

Title	Cocrystallization of organic compounds
Authors	Huang, Shan
Publication date	2023
Original Citation	Huang, S. 2023. Cocrystallization of organic compounds. PhD Thesis, University College Cork.
Type of publication	Doctoral thesis
Rights	© 2023, Shan Huang. - https://creativecommons.org/licenses/by-nc-sa/4.0/
Download date	2025-07-03 21:52:25
Item downloaded from	https://hdl.handle.net/10468/15050



UCC

University College Cork, Ireland
Coláiste na hOllscoile Corcaigh

Ollscoil na hÉireann, Corcaigh
National University of Ireland, Cork



Cocrystallization of Organic Compounds

Thesis presented by

Shan Huang, B.Sc, M.Sc

0000-0002-2521-4107

for the degree of

Doctor of Philosophy

University College Cork

School of Chemistry

Head of School/Department: Prof Anita Maguire

Supervisor: Dr Simon Lawrence

2023

Contents

DECLARATION	1
Abstract	2
Acknowledgements	4
Disseminations	7
Abbreviation List	9
Chapter 1 Introduction	11
1.1 Pharmaceutical Solids.....	12
1.2 Solid Forms of APIs	13
1.2.1 Amorphous Solids	14
1.2.2 Crystalline Solids	16
1.2.2.1 Single-component crystalline materials.....	17
1.2.2.2 Multi-component crystalline materials	18
1.2.2.2.1 Hydrates / solvates	18
1.2.2.2.2 Salts	19
1.2.2.2.3 Cocrystals.....	21
1.3 Design of Pharmaceutical Cocrystals and Salts	22
1.3.1 Etter’s Rules and Graph-set Notation	25
1.3.2 Rule of Three.....	26
1.3.3 The Selection of Cofomers	28
1.4 Cocrystal Synthesis Methodology	30

1.4.1 Solid-State Methods	30
1.4.1.1 Spontaneous formation	30
1.4.1.2 Melting crystallization	31
1.4.1.3 Mechanochemical techniques	31
1.4.1.3.1 Neat grinding	32
1.4.1.3.2 Liquid-assisted grinding	33
1.4.1.4 Extrusion crystallization	33
1.4.1.5 Hot melt extrusion	33
1.4.2 Solution-Based Methods	34
1.4.2.1 Solvent evaporation method	35
1.4.2.2 Reaction crystallization	36
1.4.2.3 Cooling crystallization	36
1.4.2.4 Antisolvent method	37
1.4.2.5 Slurry method	38
1.5 Characterization	40
1.5.1 Thermal Analysis	40
1.5.2 Spectroscopic Characterization	42
1.5.3 X-ray Diffraction Techniques	43
1.6 Application of Pharmaceutical Cocrystals and Salts	44
1.6.1 Melting Points	45
1.6.2 Solubility and Dissolution Rate	45
1.6.3 Bioavailability	46
1.6.4 Stability	46
1.6.5 Mechanical Properties	46
1.6.6 Luminescent Properties	47

1.6.7 Chiral Resolution	48
1.6.7.1 Diastereomeric salt formation	50
1.6.7.2 Cocrystal formation	50
1.7 Research Aim.....	52
1.8 Thesis Structure	53
REFERENCES	54

**Chapter 2 Exploring the Crystal Structure Landscape of Sulfasalazine
through Various Multi-component Crystals..... 76**

2.1 Abstract.....	77
2.2 Introduction	77
2.3 Experimental Section.....	83
2.3.1 Materials.....	83
2.3.2 Solid Form Screening and Crystallization Experiments	83
2.3.2.1 Liquid-assisted grinding (LAG) method	83
2.3.2.2 Slurry method	84
2.3.2.3 Solution Crystallization	84
2.3.3 Physical Measurements.....	85
2.3.4 Computational Studies	86
2.4 Results and Discussion	89
2.4.1 Physical Characterization	89
2.4.2 Crystal Structures	91
2.4.3 Conformation of SSZ.....	101
2.4.4 Array of SSZ.....	104

2.4.5 Hirshfeld Surface Analysis	106
2.4.6 HOMO-LUMO Analysis	107
2.5 Conclusions	110
REFERENCES	111
Supporting Information	118
Chapter 3 Experimental and Theoretical Investigation of Hydrogen-	
Bonding Interactions in Cocrystals of Sulfaguanidine	141
3.1 Abstract	142
3.2 Introduction	142
3.3 Experimental Section.....	148
3.3.1 Materials.....	148
3.3.2 Synthesis	148
3.3.3 Physical Measurements.....	149
3.3.4 Computational Studies	150
3.4 Results and Discussion	154
3.4.1 Physical Characterization.....	154
3.4.2 Crystal Structure Analysis.....	156
3.4.3 Computational Studies	170
3.4.3.1 Hirshfeld Surface Analysis	170
3.4.3.2 MEPS Analysis	172
3.4.3.3 QTAIM Analysis.....	174
3.5 Conclusions	180
REFERENCES	180

Supporting Information	190
Chapter 4 Pharmaceutical Salts of Piroxicam and Meloxicam with Organic Counterions.....	208
4.1 Abstract.....	209
4.2 Introduction	209
4.3 Experimental Section.....	217
4.3.1 Materials.....	217
4.3.2 Synthesis of Salts	217
4.3.3 Physical Measurements	219
4.3.4 Computational Studies	223
4.3.5 Solubility Experiments.....	223
4.3.6 Optical-Physical Measurements.....	224
4.4 Results and Discussions.....	224
4.4.1 Crystal Structure Analysis.....	224
4.4.2 Physical Characterization.....	237
4.4.3 Solubility Studies	238
4.4.4 Luminescence Studies.....	241
4.5 Conclusions	246
REFERENCES	247
Supporting Information	260
Chapter 5 Study of Enantiospecific Cocrystals and Diastereomeric Cocrystal Pairs between L-Amino Acids and Chiral Cocrystal Formers.....	279
5.1 Abstract.....	280

5.2 Introduction	280
5.3 Experimental Section.....	284
5.3.1 Materials.....	284
5.3.2 Screening Experiment	284
5.3.2.1 Liquid-assisted grinding	284
5.3.2.2 Slurry experiments.....	285
5.3.2.3 Solution cocrystallization	285
5.3.3 Physical Measurements	286
5.4 Results and Discussion	289
5.4.1 Screening Outcome	289
5.4.2 Physical Characterization.....	293
5.4.3 Crystal Structure Analysis.....	295
5.5 Conclusions	305
REFERENCES	306
Supporting Information	311
Chapter 6 Exploring the Crystal Landscape of Mandelamide	337
6.1 Abstract.....	338
6.2 Introduction	338
6.3 Experimental Section.....	343
6.3.1 Materials.....	343
6.3.2 Liquid-Assisted Grinding.....	343
6.3.3 Crystallization of (\pm)-MDM.....	343
6.3.4 Crystallization of <i>S</i> -MDM.....	344

6.3.5 Crystallization of MDM (94 <i>S</i> :6 <i>R</i>).....	344
6.3.6 Crystallization of Cocrystals	345
6.3.7 Physical Measurements.....	345
6.3.8 Computational Studies	347
6.3.9 Analysis of the Cambridge Structural Database.....	347
6.3.10 Chiral High Performance Liquid Chromatography Analysis.....	347
6.4 Results and Discussion	350
6.4.1 Structures of Racemic MDM and <i>S</i> -MDM	350
6.4.2 The Diastereomeric Cocrystal Pair of <i>S</i> -MDM and <i>S</i> / <i>R</i> -MDA.....	359
6.4.3 The Diastereomeric Cocrystal Pair of <i>S</i> -MDM and <i>L</i> / <i>D</i> -Pro	363
6.4.4 Analysis of Diastereomeric Cocrystal Pairs of <i>S</i> -MDM	367
6.5 Conclusions	370
REFERENCES	371
Supporting Information	378
Chapter 7 Conclusions and Future Work	405
REFERENCES	408

DECLARATION

This is to certify that the work I am submitting is my own and has not been submitted for another degree, either at University College Cork or elsewhere. All external references and sources are clearly acknowledged and identified within the contents. I have read and understood the regulations of University College Cork concerning plagiarism and intellectual property.

Abstract

This thesis discusses the synthesis, characterization, and properties of multi-component crystalline materials of active pharmaceutical ingredients. A special emphasis is placed on cocrystallization, which is the supramolecular phenomenon of aggregation of two or more different chemical entities in a crystalline lattice through non-covalent interactions. This research has been divided into seven chapters.

Chapter 1 gives an overview of the concept of multi-component crystalline materials and cocrystallization, where the design, methodology, characterization and application of cocrystals are also included.

Chapter 2 discusses the synthesis of multi-component crystal forms of a sulfonamide compound, sulfasalazine, through cocrystallization and explores the crystal structure landscape of sulfasalazine. Furthermore, the differences are illustrated between cocrystals and salts of sulfasalazine via structural analysis, Hirshfeld surface analysis and frontier molecular orbitals analysis.

Chapter 3 investigates the hydrogen bonding interactions in cocrystals of a frequently used sulfonamide compound, sulfaguanidine, by both experimental methods and theoretical calculations including the analysis of Hirshfeld surface, molecular electrostatic potential surfaces and quantum theory of atoms in molecules.

Chapter 4 focuses on pharmaceutical salts of piroxicam and meloxicam with three basic organic counterions, respectively. The solubility of six salts and two parent drugs in sodium phosphate solution were conducted. Furthermore, piroxicam and its salts exhibited different luminescent properties, thus, the different luminescent

mechanisms were discussed.

Chapter 5 explores cocrystallization of 19 natural L-amino acids and both enantiomers of four pharmaceutically relevant chiral compounds. The formation of diastereomeric or enantiospecific systems were explored using an examination of their hydrogen bonding motifs.

Chapter 6 investigates the formation of diastereomeric cocrystal pairs of *S*-mandelamide with both enantiomers of mandelic acid and proline, respectively. In addition, the crystal structures of (\pm)-mandelamide, *S*-mandelamide and enantio-enriched mandelamide (94 *S*:6 *R*) were determined. Detailed crystal structural analyses together with Hirshfeld surface analysis were carried out.

Chapter 7 summarizes the main findings of the entire work and examines future work, such as the use of ternary phase diagrams to assist in developing chiral separation processes.

Acknowledgements

This thesis is dedicated to my supervisor, parents, peers and friends, who tremendously supported and encouraged me throughout my PhD time.

First and foremost, I would like to sincerely express my deep gratitude to my supervisor, Dr Simon Lawrence. The memory of the first time I stepped into his office upon arriving in Ireland remains vivid in my mind. His warm smile and kind introduction immediately alleviated my anxieties about embarking on my PhD journey. Throughout my PhD, Dr Simon Lawrence has consistently provided unwavering support, promptly addressing all my inquiries and questions. Moreover, he has spent a significant amount of time reviewing my papers and offering constructive feedback to enhance the quality of my work, even working during evenings and weekends. Without his guidance and assistance, this thesis would not have been completed. Furthermore, he has provided me with excellent opportunities to participate in international conferences and engage in academic communications. He has always been my first audience whenever I prepared a presentation, offering invaluable advice and guidance. Following each presentation, he never forgets to send me a supportive "well done" message, which consistently boosts my confidence. I consider myself extremely fortunate to have him as my PhD supervisor who showed me patience, motivation and enthusiasm, as well as shared with me his immense knowledge. His mentorship has had a profound impact on my personal and academic growth.

I would like to extend my thanks to Dr Humphrey Moynihan and Dr Davide Tiana for being my assessment panel, reviewing my progress and providing constructive feedback on my projects. Special thanks go to Prof Anita Maguire and Dr Dean

Venables for their professional advice and valuable insights into my research.

I am deeply grateful to the following people for sharing their expertise: William Daly, my previous lab mate and a great friend, provided continuous help throughout my PhD journey. Vinay Cheemarla generously shared his experiences with me and provided support with theoretical calculations. Mark Lynch offered valuable advice in all the lab work when I joined the group. Dr Michael Cronin assisted me with the training of the DSC and TGA. Dr Nuala Maguire kindly provided assistance with the FT-IR and HPLC training and discussions. Dr Matteo Lusi and Dr Chiara Cappuccino collected and solved the single crystal data during the COVID-19 pandemic. Furthermore, I would like to extend my gratitude to all my colleagues and technical staff at the School of Chemistry for their help and technical support. Thank you to the members of the Manufacturing Science and Technology department at Janssen Sciences Ireland UC for their invaluable support and expertise during my three-month placement. Their guidance and knowledge have significantly contributed to my professional growth and development. Special thanks to my previous and current lab mates, John Downey, Keith Andrew O'Shaughnessy and Si Lok Ko, for their moral support from beginning to end.

I am immensely grateful to my dear friends, Dr Tianjiao Geng, Dr Jia Xu, Dr Yuan Su, Wanyun Li, Keyi Liu, Qi Tang, Dr Shengyu Wang, Dr Qingqing Xiao, and Xiaojun Zhou, for their unwavering love, support, and encouragement throughout my PhD journey. Their presence has alleviated the feeling of loneliness and enriched my life with excitement and joy.

I would like to acknowledge SSPC and Science Foundation Ireland for funding my research and providing opportunities to present my work at various

conferences, which sharpened my expertise and expanded my scholarly network. Last but not least, I want to express my deepest gratitude to my family, with special thanks to my mother, for supporting, listening, and cheering me up during times of struggle and doubt. They are my most solid support and give me reasons to work hard forever and continue moving forward with my career and life.

The past four years of pursuing my PhD at the University College Cork have been the most important period in my life. The challenges I faced and overcame, the friendships I forged, and the knowledge I gained have made this chapter of my life truly unparalleled. Cork will forever hold a special place in my heart, and the memories I created here will continue to inspire and guide me as I embark on new endeavours.

Disseminations

Publications

1. Shan Huang, Vinay K. R. Cheemarla, Davide Tiana, and Simon E. Lawrence, Experimental and Theoretical Investigation of Hydrogen-Bonding Interactions in Cocrystals of Sulfaguanidine. *Cryst. Growth Des.* **2023**, 23, 4, 2306–2320.
2. Shan Huang, Dean S. Venables, and Simon E. Lawrence, Pharmaceutical Salts of Piroxicam and Meloxicam with Organic Counterions. *Cryst. Growth Des.* **2022**, 22, 11, 6504–6520.
3. Shan Huang, Vinay K. R. Cheemarla, Davide Tiana, and Simon E. Lawrence, Exploring the Crystal Structure Landscape of Sulfasalazine through Various Multi-component Crystals. *Cryst. Growth Des.* **2023**, 23, 8, 5446–5461.
4. Shan Huang, Deirbhile Fitzgerald, Stuart G. Collins, Anita R. Maguire, and Simon E. Lawrence, Exploring the Crystal Landscape of Mandelamide. In Revision.
5. Shan Huang, and Simon E. Lawrence, Study of Enantiospecific Cocrystals and Diastereomeric Cocrystal Pairs between L-Amino Acids and Chiral Cocrystal Formers. In preparation.

Conference presentations

1. Shan Huang, Vinay K. R. Cheemarla, Davide Tiana and Simon E. Lawrence, Experimental and Theoretical Investigation of Hydrogen Bonding Interactions in Cocrystals of Sulfaguanidine. 26th Congress and General Assemble of the International Union of Crystallography (IUCr 2023), August 2023, Melbourne, Australia. [Poster]

2. Shan Huang, Dean S. Venables and Simon E. Lawrence, Pharmaceutical Salts of Piroxicam and Meloxicam with Organic Counterions. ACS Spring 2023, March 2023, Indianapolis, USA. [Oral]
3. Shan Huang, Dean S. Venables and Simon E. Lawrence, Pharmaceutical Salts of Piroxicam and Meloxicam with Organic Counterions. 25th International Conference on the Chemistry of the Organic Solid State (ICCOSS XXV), July 2022, Ohrid, Macedonia. [Poster]
4. Shan Huang, Dean S. Venables and Simon E. Lawrence, Pharmaceutical Salts of Piroxicam and Meloxicam with Organic Counterions. 73rd Irish Universities Chemistry Research Colloquium, June 2022, Dublin, Ireland. [Poster]
5. Shan Huang, Chiara Cappuccino, Matteo Lusi, Nuala M. Maguire, Anita R. Maguire and Simon E. Lawrence, Pharmaceutical Salts of Piroxicam and Meloxicam with Organic Counterions. SFI Science Summit 2021, November 2021, Ireland. [Poster]

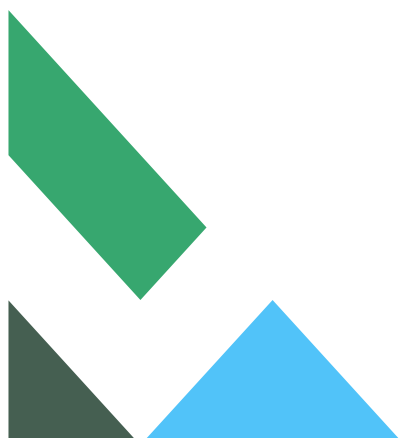
Abbreviation List

Abbreviation	Full name
ACQ	Aggregation-Caused Quenching
APIs	Active Pharmaceutical Ingredients
BCPs	Bond Critical Points
BCS	Biopharmaceutics Classification System
CAB	Conjugated Acid Base
CSD	Cambridge Structural Database
CSP	Crystal Structure Prediction
CSP	Chiral Stationary Phase
DFT	Density Functional Theory
DSC	Differential Scanning Calorimetry
EFSA	European Food Safety Authority
ESIPT	Excited-State Intramolecular Proton Transfer
FDA	Food and Drug Administration
FMO	Frontier Molecular Orbitals
FTIR	Fourier Transform Infrared Spectroscopy
GAS	Gas Antisolvent
GRAS	Generally Regarded as Safe
HOMO	Highest Occupied Molecular Orbital
HPLC	High-Performance Liquid Chromatography
ICCs	Ionic Cocrystals
LAG	Liquid-Assisted Grinding
LUMO	Lowest Unoccupied Molecular Orbital

MCCMs	Multi-Component Crystalline Materials
MEPSs	Molecular Electrostatic Potential Surfaces
NCE	New Chemical Entity
PAT	Process Analytical Technology
PXRD	Powder X-Ray Diffraction
QTAIM	Quantum Theory of Atoms in Molecules
Raman	Raman Spectroscopy
SAS	Supercritical Antisolvent
SCCs	Salt Cocrystals
SCXRD	Single Crystal X-Ray Diffraction
ssNMR	Solid State Nuclear Magnetic Resonance
TGA	Thermogravimetric Analysis
TPDs	Ternary Phase Diagrams
TSE	Twin Screw Extrusion



Chapter 1 Introduction



1.1 Pharmaceutical Solids

Solid-state drug substances or active pharmaceutical ingredients (APIs) play an ever increasing and important role in pharmaceutical development due to the ease of synthesis, low cost, patient compliance, suitability for large scale production and the physicochemical stability.¹ However, the development of solid-state drugs also has met many obstacles. Research currently estimates that about 40% of approved drugs and approximately 90% of developmental pipeline drugs may exhibit solubility problems.²⁻⁴ The Biopharmaceutics Classification System (BCS) classifies APIs into four major categories according to their solubility and permeability behaviour as shown in Figure 1.1.⁵ Solubility and permeability are relevant to the development of immediate release drugs, while poorly soluble APIs present a sizeable challenge to the pharmaceutical industry due to their low oral bioavailability, which greatly influences the therapeutic response, etc. In terms of improving the effectiveness of drug, it should be more focused on the enhancement of the solubility and bioavailability of low water-soluble BCS Class II and IV drugs.⁶ Meanwhile, solid drug forms may also affect stability, flow, compression, hygroscopicity, and a number of other properties. Therefore, optimizing the solid state form of API has become a major challenge in the early stage of drug development, i.e., preformulation study.^{7,8}

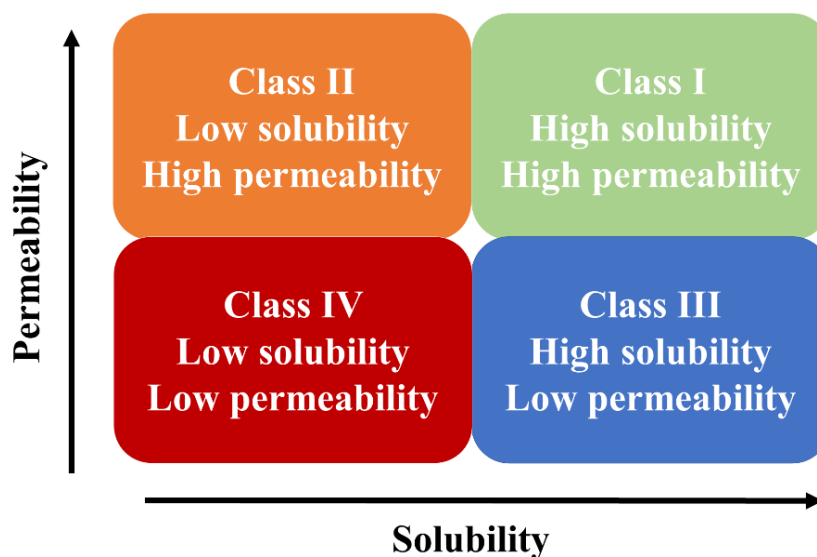


Figure 1.1. Scheme of biopharmaceutics classification system.

Preformulation study is a phase in drug development that is initiated after the discovery of a new chemical entity (NCE), focusing on characterizing and establishing the physicochemical properties of a drug substance that could affect the drug performance and the development of a dosage form.⁹ Preformulation studies include selection of the drug candidate itself, selection of formulation components, etc., while the studies on the solid forms such as potential polymorphs, hydrates and solvates of APIs are necessary and of great importance in this stage.¹⁰

1.2 Solid Forms of APIs

Solids can be categorized into two groups based on their degree of long-range order: amorphous and crystalline solids, depicted in Figure 1.2.

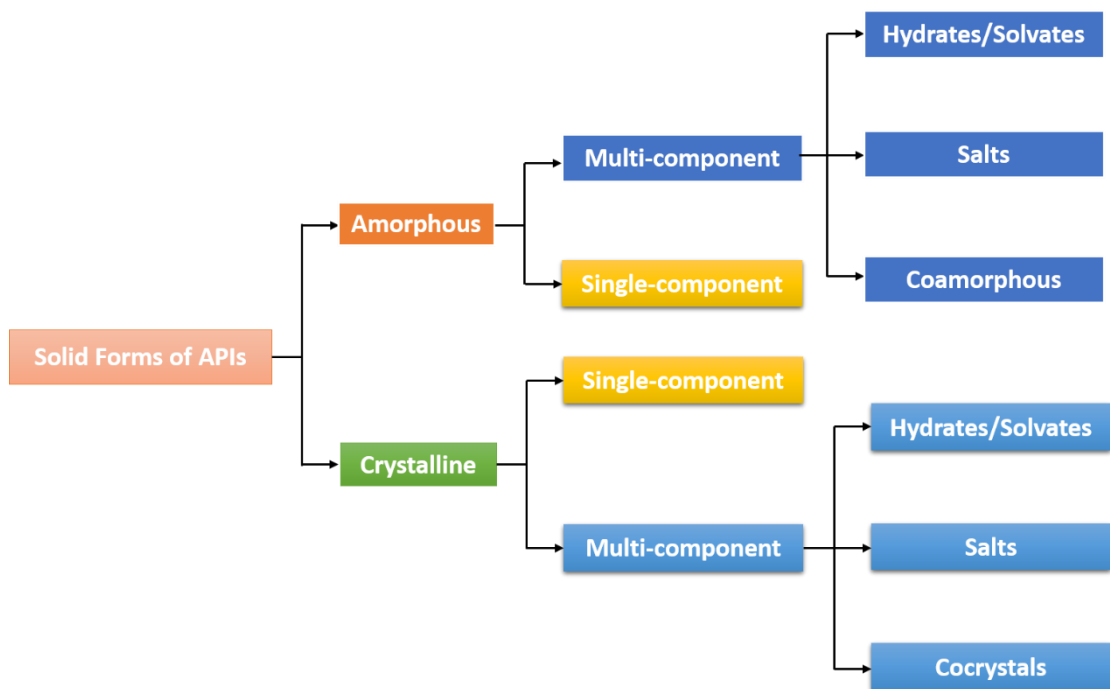


Figure 1.2. The diversity of solid forms that can exist for an API.

1.2.1 Amorphous Solids

Amorphous or non-crystalline solids may have short-range molecular order, but unlike a crystalline solid, they have no long-range order (Figure 1.3). Several drugs currently in use are amorphous¹¹ as, in general, amorphous solids have higher solubility, dissolution rate and bioavailability than crystalline solids.¹²

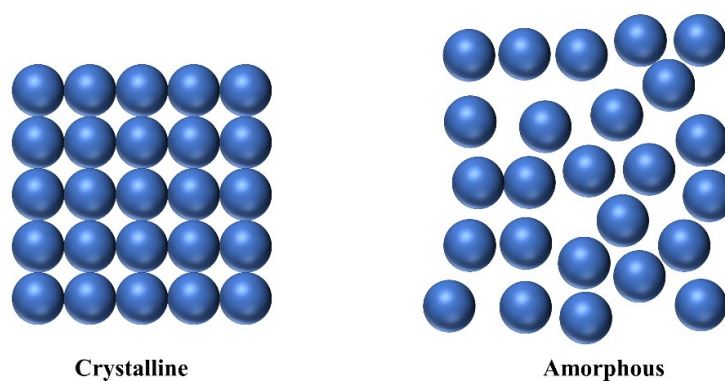


Figure 1.3. Degrees of order between the crystalline form and amorphous form.

Hussain and co-workers showed that amorphous ibuprofen made by co-milling with an excipient (such as HPMC or Soluplus[®]) has enhanced kinetic solubility and dissolution rate compared to the crystalline API.¹³ However, amorphous solids are usually less stable physically and chemically than corresponding crystalline solids.^{14, 15} Neupro[™] patch, for example, was a transdermal delivery system of rotigotine for the treatment of Parkinson's disease and restless leg syndrome. Rotigotine existed as non-crystalline form in the patch; however, unexpected crystals appeared in the form of snowflakes during storage (Figure 1.4), which caused the decrease of solubility and its efficacy. As a consequence, Neupro[™] patches were withdrawn from the US market and not available until the reformulation in 2012, which caused financial losses to the manufacturer.¹⁶

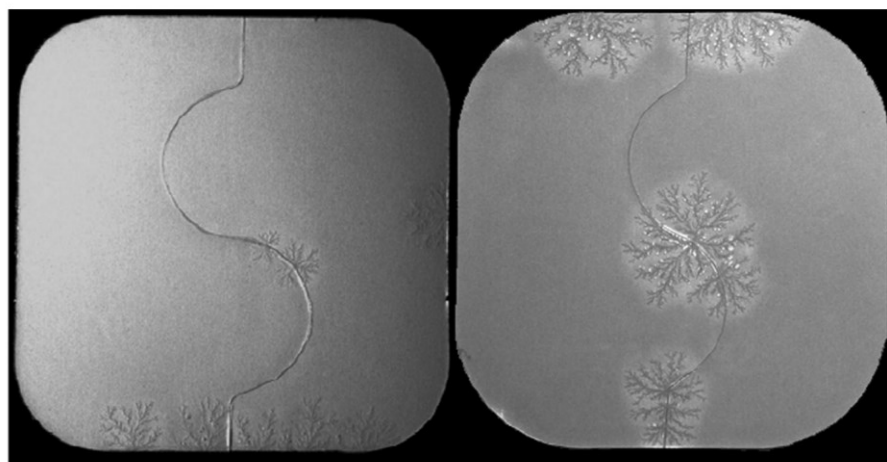


Figure 1.4. Rotigotine was crystallized during the storage of Neupro[™] patches.¹⁶

Consequently, crystalline materials have been preferred in drug development owing to their greater thermodynamic stability, reproducible nature and tendency to be isolated in a higher purity than their amorphous counterparts.

1.2.2 Crystalline Solids

A crystal or crystalline solid is a solid material whose constituents (such as atoms, molecules, or ions) are arranged in a regular repeating fashion that extends in three dimensions, called a crystal lattice.¹⁷ Different components and different crystal packing can result in different physicochemical properties of crystalline drugs, so the physicochemical properties of crystalline drugs in favourable cases can be modified by adjusting the constituents and arrangement of molecules or ions in a crystal.

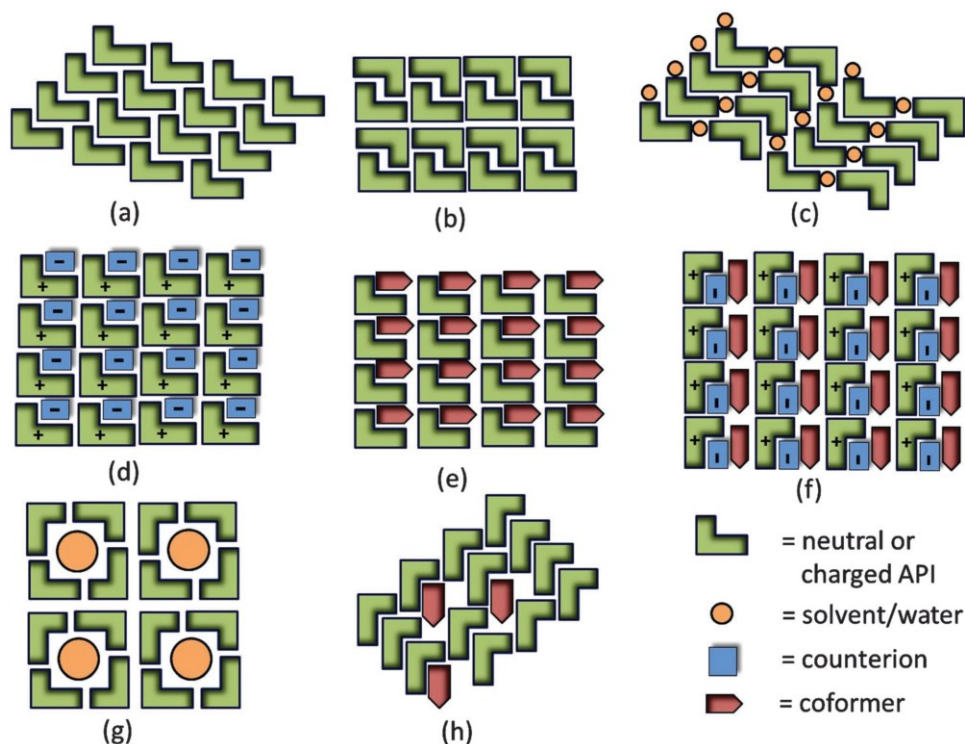


Figure 1.5. Possible crystalline forms for an API: (a) and (b) polymorphs, (c) solvate / hydrate, (d) salt, (e) molecular cocrystal, (f) ionic cocrystal, (g) non-stoichiometric inclusion compounds including channel hydrates / solvates, (h) solid solutions (mixed crystals).¹⁰

1.2.2.1 Single-component crystalline materials

It is quite common that many substances exist in more than one crystalline form; hence, different polymorphs of a compound possess different physicochemical properties due to the different arrangements of ions, atoms or molecules (Figure 1.5 a and b). One example is 5-methyl-2-[(2-nitrophenyl) amino]-3-thiophenecarbonitrile, a pharmaceutical intermediate which is known as ‘ROY’ for its red, orange and yellow crystals. Over the past twenty-five years, twelve ROY crystal structures have been discovered and definitively characterized,¹⁸⁻²⁶ while the structure for a thirteenth RPL polymorph has been proposed, but has not yet been fully characterized.^{27, 28} As these polymorphs differ in the torsional angle θ , the degree of π -conjugation existing between the thiophene and phenyl aromatic rings is different, resulting in different colours. Furthermore, polymorph Y is the most stable both thermodynamically and kinetically, and for other polymorphs, kinetic stability approximately follows thermodynamic stability: higher free-energy polymorphs tend to be shorter-lived.²⁹

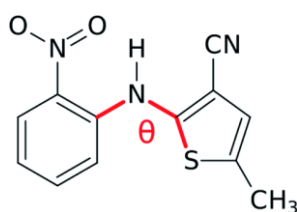


Figure 1.6. The molecular structure of ROY.²⁹

As already mentioned, the solubility and bioavailability of different polymorphs may be different. Ritonavir, marketed in 1996 and sold under the trade name Norvir[®], was an antiretroviral medication used along with other medications to treat HIV / AIDS. However, the drug was withdrawn from the market when an

undiscovered more stable and less soluble 2nd polymorph was found in Norvir[®] semi-solid capsules in 1998. After further research and development Norvir[®] was remarketed, causing at least \$ 250 M losses to Abbott Laboratories.³⁰ These examples show that investigating the solid forms of APIs is of significant importance. Chloramphenicol palmitate, which is a prodrug being readily hydrolyzed by acid and esterase in the human gut to release chloramphenicol, has three polymorphic forms: the stable form A, the metastable form B and the unstable form C.³¹ It is reported that form B has a faster dissolution rate and a much higher solubility than form A.³² Therefore, for some poor-soluble APIs, developing different polymorphs may improve the solubility because the solubility of a metastable polymorph is kinetically higher than that of a thermodynamically more stable polymorph.³³ However, generally the ratio of solubility between two different polymorphs is less than two, which sets limits on the extent to which one can alter the physicochemical properties of APIs via polymorph control.³⁴

1.2.2.2 Multi-component crystalline materials

Compared with single-component crystals, multi-component crystalline materials (MCCMs) have much more possibilities of modifying the physicochemical properties of APIs. Pharmaceutical MCCMs can be defined as multiple component crystalline materials in which at least one component is a drug substance or API, and they have the potential to profoundly impact the subsequent research of the drug.

1.2.2.2.1 Hydrates / solvates

Hydrates and solvates (Figure 1.5c) are crystalline molecular adducts containing both the host molecule (API or excipient) and guest molecule [water (hydrate) or

other solvents (solvate)] incorporated in the crystal lattice structure. Different hydrates and solvates often show differences in physicochemical properties, such as stability, hygroscopicity, solubility, colour, fluorescence, etc.^{35, 36} For example, Xiong and co-workers conducted a detailed investigation on the hydrates and solvates of rebamipide (RBM) and found that RBM hydrate presented better stability and solubility than three other solvates, i.e. dimethyl sulfoxide solvate, dichloromethane solvate and hemimethanol hemihydrate.³⁷ Rifampicin, one of the drugs for tuberculosis treatment, has a monohydrate, a dihydrate, an acetone solvate and a 2-pyrrolidone solvate. Compared with its two amorphous forms, the 2-pyrrolidone solvate was the most soluble in phosphate buffer saline at pH 7.4, while the dihydrate would have the best *in vivo* performance in 0.1 M HCl solution.³⁸ Mei *et al.* demonstrated that six emodin solvates showed different fluorescent colours, and believed that the significant differences were attributed to the different non-covalent interactions of these solvates.³⁶ To date, several solvates are on the market, for example, Mekinist[®] (Trametinib DMSO solvate), Jevtana[®] (Cabazitaxel acetone solvate) and Prezista[®] (Darunavir Ethanolate), etc.³⁹ However, hydrates or solvates, along with non-stoichiometric inclusion compounds (Figure 1.4g), are the last choice for the screening and development of crystalline drugs. This is because hydrates and solvates are often less stable over time, due to solvent loss. In addition, some solvates are not suitable for pharmaceutical applications due to safety issues of the solvent.

1.2.2.2.2 Salts

The salification of an API (Figure 1.5d) is the most common approach to modify its physicochemical properties. In general, a stable salt can be formed when the

difference of pK_a between acid and base is more than three. However, when that difference is small, a complex may be formed but it may rapidly dissociate in an aqueous environment back into its components with no desirable influence on the drug properties.⁴⁰ From the perspective of salt screening, HCl, H₂SO₄ and HBr are more frequently used to form salts with organic bases, while NaOH, Ca(OH)₂ and KOH are commonly used to form salts with organic acids.⁴¹ In recent decades, the pharmaceutical industry increasingly used this strategy to enhance the solubility and bioavailability of poorly soluble basic / acidic APIs due to the relative ease of synthesis and crystallization. Lu *et al.* synthesized three salts of phenazopyridine, a local anesthetic and analgesic drug that belongs to BCS class II, with benzoic acid, 4-hydroxyphenylacetic acid, or saccharin and found significant solubility enhancement compared to pure drug.⁴² Other desirable physicochemical properties and biopharmaceutical properties including enhanced thermal properties, photostability, organoleptic properties and mechanical properties of an API can also be obtained by salt formation. Furthermore, salt formation can achieve a controlled release of a drug through the control of the drug microenvironment's pH.⁴³ At present, more than 50% of drugs currently on the market are sold as salts,⁴⁴ for example, Zontivity[®] (Vorapaxar sulfate), Kisqali[®] (Ribociclib succinate) and Ofev[®] (Nintedanib esylate), etc. However, the weakly acidic or basic groups of some APIs are nonionizable near physiological pH; thus, they are unlikely to form salts.⁴⁵ In addition, solid solutions (Figure 1.5h) have difficulty in their design and reproducibility,⁴⁶ which might limit their further applicability. For these APIs, cocrystallization is emerging as a promising alternative in the modification of APIs during design and development of drugs.

1.2.2.2.3 Cocrystals

The first reported cocrystal is quinhydrone, a 1:1 molar ratio compound of quinone and hydroquinone, discovered by Friedrich Wöhler in 1844.³ With the rapid development of supramolecular chemistry and crystal engineering, pharmaceutical scientists applied the theory into the design and development of pharmaceutical cocrystals. Cocrystals (Figure 1.5e) are multi-component crystalline materials assembled via hydrogen bonds, halogen bonds, or π - π stacking, while pharmaceutical cocrystals are molecular adducts of definite stoichiometry where one component is a neutral API and the other is a neutral pharmaceutically acceptable coformer.⁴⁷ In addition, an interesting subset of cocrystals is ionic cocrystals (ICCs, Figure 1.5f) which features an API and inorganic salt like NaCl, or a salified API and a coformer in the same unit cell.

Cocrystals represent a promising approach for tuning properties of a given crystalline API, by selecting an appropriate coformer which can form hydrogen bonds and other non-covalent interactions to produce a specific supramolecular structure. Hence, cocrystals offer many opportunities to modify the melting point, solubility, dissolution rate, bioavailability, stability and mechanical properties, etc. of APIs.⁴⁸⁻⁵¹ These properties can directly or indirectly impact the efficacy of the API dosage form. Dai and co-workers synthesized four novel cocrystals of agomelatine (an antidepressant with low water solubility) with urea, glycolic acid, isonicotinamide and methyl 4-hydroxybenzoate. The solubility study showed that the solubility values of the four cocrystals in pH 6.8 phosphate buffer saline are approximately 2.2, 2.9, 4.7 and 3.5 times as large as that of agomelatine market form (form II). Furthermore, they demonstrated that the coformer with higher solubility may dissolve faster during dissolution and dissociate more quickly from

corresponding cocrystals.⁵² Nifedipine is one of the effective antihypertensive drugs, yet suffers from photo-induced decomposition processes both in solid state and in solution. After cocrystallization with isonicotinamide, the molecular conformation and hydrogen bonds were changed and, hence, the photo-stability properties were improved.⁵¹

Currently, there are several pharmaceutical cocrystals approved by the United State Food and Drug Administration (FDA), for example, Entresto[®] (sacubitril-valsartan), Suglat[®] (ipragliflozin-L-proline) and Steglatro[®] (ertugliflozin-L-pyrogutamic acid). Some drugs were marketed as salts at first, but then it was proved that these drugs existed as cocrystals, such as Lexapro[®] (escitalopram oxalate) and Depakote[®] (valproate sodium cocrystal with valproic acid), etc., as shown in Figure 1.6.⁵³

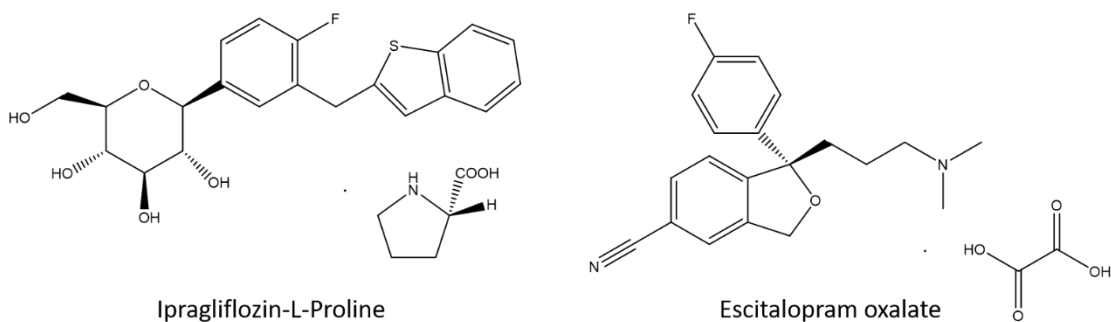


Figure 1.6. Chemical structures of Suglat[®] (ipragliflozin-L-proline) and Lexapro[®] (escitalopram oxalate).

1.3 Design of Pharmaceutical Cocrystals and Salts

The 1987 Nobel Prize in Chemistry was awarded to Charles J Pedersen, Donald J Cram and Jean-Marie Lehn, marking the emergency of a new branch of chemistry,

that is supramolecular chemistry.⁵⁴ In 1978, Lehn introduced the term “supramolecular chemistry” and defined it as “chemistry beyond the molecule”, i.e., the chemistry of molecular ensembles and intermolecular associates.⁵⁵ Traditional chemistry generally focuses on the covalent bonding to create various molecules while supramolecular chemistry relies on non-covalent interactions, such as hydrogen-bonding and electrostatic interactions, etc., between small molecules to self-assemble into molecular assemblies (Figure 1.7). Nowadays, supramolecular chemistry plays a fundamental and major role in the design and investigation of MCCMs based upon non-covalent interactions.

Crystal engineering was first introduced by Pepinsky in 1955, and then implemented by Schmidt on the investigation of photodimerizable compounds.⁵⁴

⁵⁵ In 1986, Desiraju rationalized Schmidt’s observations on the unit cell parameters of chloroaromatic compounds and subsequently came up with the definition of crystal engineering, i.e., crystal engineering is the understanding of intermolecular interactions in the context of crystal packing and the utilization of such understanding in design of new solids with desired physical and chemical properties.⁵⁶

In 1967, Corey first put forward the term “synthon” which is traditionally used to represent key structural features in a target molecule in organic synthesis. Subsequently, Desiraju proposed the definition of supramolecular synthon as “a structural unit within a supermolecule which can be formed and / or assembled by known or conceivable synthetic operations involving intermolecular interactions.”^{57, 58} Undoubtedly, the introduction of the term ‘supramolecular synthon’ is of great importance in terms of the development of the synthesis of cocrystals and molecular salts.

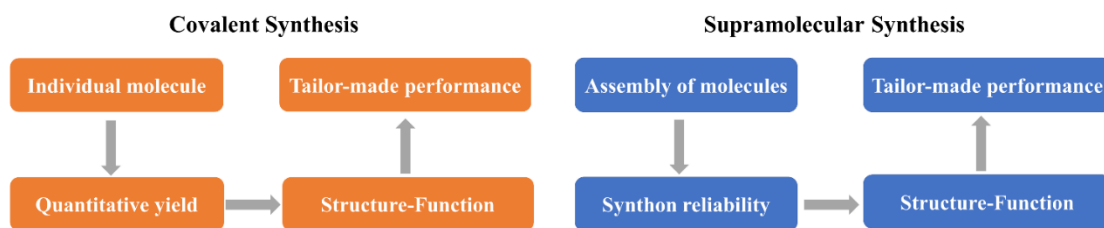


Figure 1.7. Covalent and supramolecular synthesis routes.

For crystal engineering there are two distinct categories of supramolecular synthon: supramolecular homosynths, which are composed of self-complementary functional groups, as exemplified by the acid-acid homodimer and amide-amide homodimer (Figure 1.8); and supramolecular heterosynths, which are composed of different but complementary functional groups such as the acid-amide and acid-pyridine synthons (Figure 1.8).^{59, 60} Both homo- and heterosynths have been widely exploited in cocrystallization and can be the primary driving force for cocrystallization.

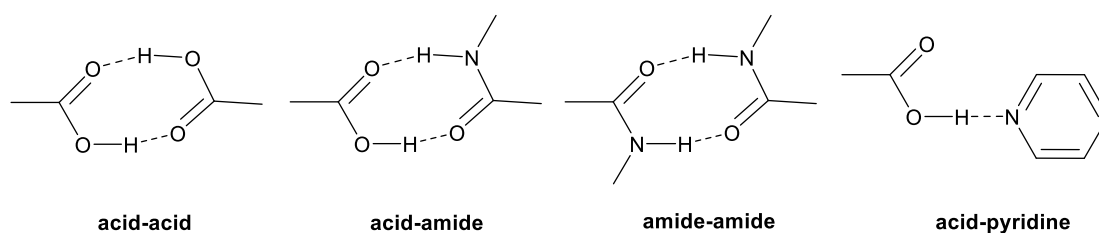


Figure 1.8. Examples of supramolecular synthons: (a) acid-acid, (b) acid-amide, (c) amide-amide, and (d) acid-pyridine.

1.3.1 Etter's Rules and Graph-set Notation

Based on the theory of supramolecular chemistry and crystal engineering, one of the most important non-covalent interactions regarding the design of pharmaceutical cocrystals and salts is hydrogen bonds. In the early 1990s, Etter *et al.* proposed three hydrogen bonding rules,⁶¹ which facilitate the design of hydrogen bonded solids.

- i. All good proton donors and acceptors are used in hydrogen bonding.
- ii. Six-membered-ring intramolecular hydrogen bonds form in preference to intermolecular hydrogen bonds.
- iii. The best proton donors and acceptors remaining after intramolecular hydrogen bond formation form intermolecular hydrogen bonds.

In addition, Etter *et al.* also introduced a graph-set notation system for describing and labelling hydrogen bond motifs / synthons.^{61, 62} In the graph-set system four principal motifs are used: (i) S (self) for intramolecular hydrogen bonds; (ii) C (chain) for infinite chains; (iii) R (ring) for intermolecular rings; and (iv) D (discrete) for finite structures. Some typical graph-set notations are given below (Figure 1.9). Based on these hydrogen-bonding rules, the formation of supramolecular synthons and hydrogen bonds between the functional groups of an API and a coformer can be designed and predicted.

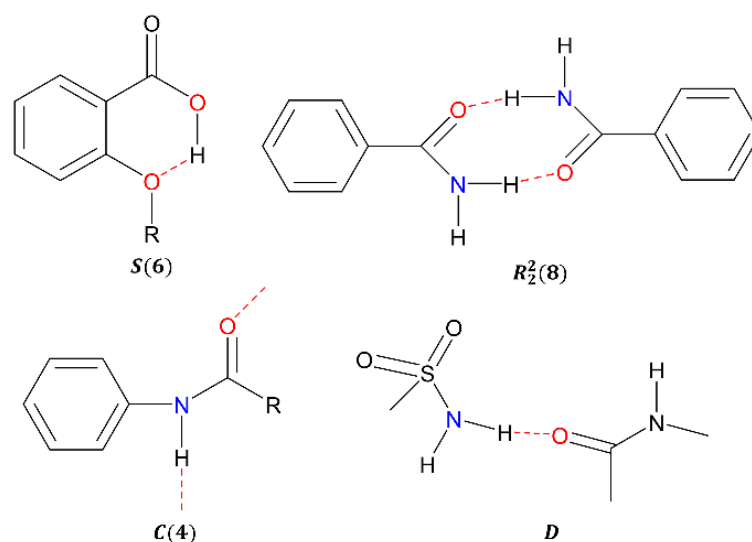


Figure 1.9. Examples of graph-set notations.

1.3.2 Rule of Three

In 1999, Wiechert *et al.* successfully synthesized both a cocrystal and a salt involving pyridine and formic acid, where the stoichiometric ratio is 1:1 for the cocrystal and 1:4 for the salt.⁶³ More recently, Losev and Boldyreva reported a system “ β -alanine-DL-tartaric acid” where a cocrystal and a salt in the same stoichiometric ratio are formed by dry co-grinding and liquid-assisted grinding, respectively.⁶⁴ If cocrystals are viewed as multi-component solids containing only neutral species, and salts contain anions and cations, then whether the as-synthesized MCCMs are cocrystals or salts remains ambiguous as both neutral and charged species may be present in the cocrystallization process.^{64, 65} This problem is not only a scientific challenge, but also of great importance in terms of the intellectual property in the pharmaceutical industry.

One strategy that can be utilized to predict whether cocrystals are formed or not is the degree of proton transfer between the components, namely the Rule of Three, which states that the systems with $\Delta pK_a < 0$ leads to cocrystals, $\Delta pK_a > 3$ results

in salts, while $0 < \Delta pK_a < 3$ can form either of them [where $\Delta pK_a = pK_a (\text{base}) - pK_a (\text{acid})$].⁶⁶

More recently, Cruz-Cabeza performed calculations to assess the differences in the predicted ΔpK_a values across 6465 crystalline complexes comprising ionized and non-ionized acid-base pairs sourced from the Cambridge Structural Database (CSD), and demonstrated that ionized acid–base systems (salts) are observed for $\Delta pK_a > 4$; $\Delta pK_a < -1$ was observed in non-ionized acid–base systems (cocrystals); while a linear relationship between the probability of salt formation and their ΔpK_a value was established for the systems with $-1 < \Delta pK_a < 4$.⁶⁷

Further to these, two interesting subsets of cocrystals are ionic cocrystals (ICCs) and salt cocrystals (SCCs), which have attracted increasing attention in recent years (Figure 1.10). ICCs consist of an API and an inorganic alkaline or alkaline earth salt in the same unit cell, such as NaCl or CaCl₂.^{68, 69} SCCs are crystalline materials wherein a salified API and a coformer (or vice versa) are in the same unit cell.^{70, 71} Notably, a conjugated acid base (CAB) cocrystal, composed of the API and its salt counterpart, has attracted major attention both within the industry and academia recently because the API is not “diluted” by any extrinsic substance.⁷²⁻⁷⁴ Perumalla *et al.* demonstrated that CAB cocrystals of benzoic acid and phenoxy acetic acid present greater physicochemical stability compared with their corresponding salts, revealing CAB cocrystals are advantageous in the manufacturing, shipping, and storage of these chemicals.⁷⁴

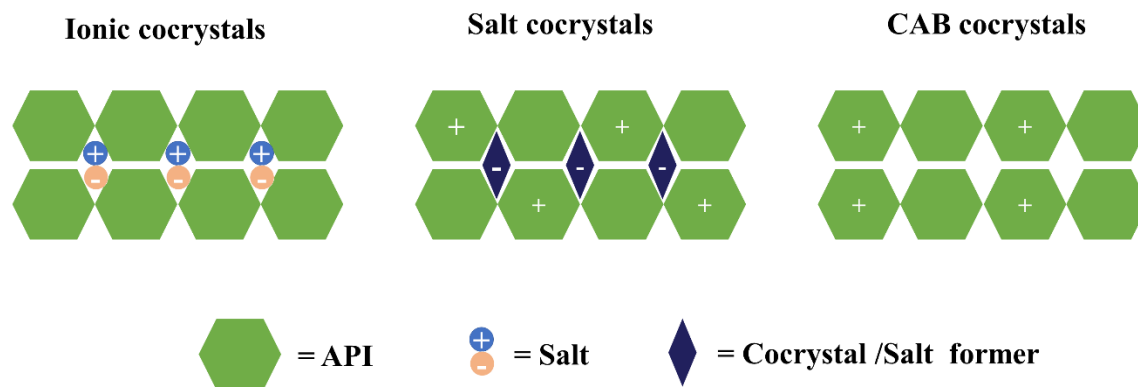


Figure 1.10. Representative molecular arrangements of ICCs (left), SCCs (middle) and CAB cococrystals (right).

1.3.3 The Selection of Cofomers

One of the main challenges in pharmaceutical cococrystal development is the selection of cofomers that can form robust supramolecular synthons with a particular API, as well as meet the as-mentioned empirical guidelines of intermolecular interaction complementarity. The traditional approach to cofomer selection is by “trial and error” cococrystal screening, which can be time-wasting and labour-consuming. Therefore, strategies to reduce the time and effort required in the new cococrystal form development are necessary. For instance, CSD can be applied to identify a common and robust supramolecular synthon for the APIs.⁷⁵ The Isostar search software enables the discovery of common arrangements of hydrogen bonding within crystals.⁷⁶ The components within *CSD-Materials* (Mercury), especially *polymorph assessment* and *co-crystal design*, provide in-depth understanding of experimentally determined crystal structures as well as insight into the likely solid-form behaviour of new compounds, based on a sophisticated assessment of preferred intra- and intermolecular interactions.^{76, 77} A

number of computational-based coformer screening methods have been presented in the literature. For instance, molecular electrostatic potential surfaces (MEPSs) can provide most promising hydrogen-bonding interaction sites and calculate the interaction site pairing energy differences for the ranking of coformer.⁷⁸ Lawrence, Cooper and co-workers established a data-driven approach of predicting cocrystal formation, which can be used to reduce the number of experiments required to obtain new cocrystals.⁷⁹ The fluid-phase thermodynamics theory conductor-like screening model for real solvents (COSMO-RS) as implemented in the COSMO*therm* software has been demonstrated to be an accurate and efficient approach to screen cofomers for cocrystallization.⁸⁰ Mswahili and co-workers developed machine learning models to select cofomers and found their Artificial Neural Network shows best accuracy, sensitivity, which can contribute to faster and more accurate cocrystal development.⁸¹ The Rasmuson group created different models to predict the melting point, lattice energy, crystal density and ideal solubility of cocrystals using a machine learning Artificial Neural Network approach. In addition, these models illustrated how the coformer structure can influence the targeted physical properties of cocrystals.⁸²⁻⁸⁴ Crystal structure prediction (CSP) approaches have been developed to find the lowest energy crystal structure of an organic molecule, and it has emerged as a complementary tool to solid form screening for identifying potential thermodynamically feasible polymorphs. This is of significant importance for the pharmaceutical industry as a change in polymorph can change the solubility and dissolution rate.^{85, 86} Recently, CSP methods have already been applied to cocrystal prediction by exploring the complete space of crystal packing possibilities of the single components and their cocrystals and an evaluation of the possible energetic gain of cocrystallization.⁸⁷⁻⁸⁹

For pharmaceutical applications, coformers are usually selected from the generally regarded as safe (GRAS) list published by the FDA and need to be commercial drug products that are pharmaceutically acceptable and non-toxic.⁹⁰

1.4 Cocrystal Synthesis Methodology

With the rapid development and an increasing demand of cocrystals, a wide range of methods for synthesis of cocrystals have been reported, which can be broadly categorized as solid-state methods and solution-based methods. Common techniques are listed below.

1.4.1 Solid-State Methods

Solid-state methods, wherein no or little solvent is required, have become a growing trend in cocrystal synthesis due to reduced cost, waste and environmental impact. However, high energy inputs are often necessary to facilitate molecule migration and product formation and crystal lattice disintegration.^{91,92}

1.4.1.1 Spontaneous formation

Although spontaneous cocrystal formation is not as common as other solid-state methods, there are quite a few examples documented in the literature. Cocrystal can be synthesized spontaneously by physically mixing or gently grinding stoichiometric ratios of the particular API and the corresponding coformer, if the reaction is thermodynamically and kinetically favoured. Rodríguez-Hornedo and co-workers investigated spontaneous formation of cocrystals of carbamazepine with form I nicotinamide or saccharin, and demonstrated that increasing temperature and relative humidity, as well as individually milling reactants can

accelerate cocrystal formation rates during storage.⁹³ MacFhionnghaile *et al.* investigated cocrystal formation of caffeine and urea via a spontaneous solid-state reaction under low energy mixing of the solids at room temperature and low relative humidity (< 30%), revealing that premilling the two components separately can accelerate the process.⁹⁴ Ervasti and colleagues found that theophylline-nicotinamide cocrystal can be formed from physical mixture of these two components without any mechanical activation during storage. Similarly, their conclusions about moisture playing a critical role in determining the spontaneous cocrystal formation, and an increasing temperature accelerating the rate of transformation, are in agreement with Rodríguez-Hornedo's conclusions.⁹⁵

1.4.1.2 Melting crystallization

Melting crystallization, a green alternative technique for identifying the formation of cocrystals, involves heating a physical mixture of an API and coformer until they melt, cooling slightly and maintaining at a temperature below the melt temperature until the crystallization process is completed.⁹⁶ Therefore, although solvents are not needed, this approach could only be applied to thermally stable compounds with appropriate melting points.⁹⁷ Yan *et al.* successfully prepared melatonin-pimelic acid cocrystal via melting crystallization by controlling the crystallization within a specific temperature range.⁹⁸

1.4.1.3 Mechanochemical techniques

The term “mechanochemistry” refers to chemical synthesis which is enabled or sustained by mechanical force and is an alternative approach to synthesize cocrystals (Figure 1.11).⁹⁹ It is the chemical transformation between two components induced by mechanical energy by grinding or milling, and therefore,

requires limited or no solvent.^{92, 100} Solid-state grinding can be split in to neat grinding and liquid-assisted grinding (LAG).

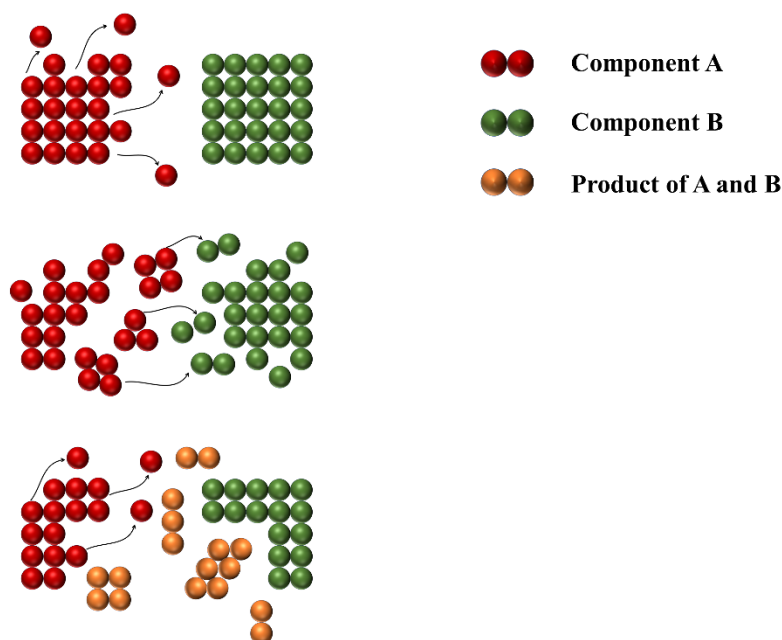


Figure 1.11. Schematic of cocrystal formation mechanism via mechanochemical reaction (adapted from ref. 7).

1.4.1.3.1 Neat grinding

Neat grinding or dry grinding, involves mixing the particular API and coformer together and grinding them through manual (mortar and pestle) or mechanical (ball mill) methods without the addition of any solvent. It differs from melt crystallization (see section 1.4.1.2) since the starting materials are not considered to be molten during grinding.⁹⁷ Numerous cocrystals obtained by neat grinding have been well documented so far, for example, Fischer *et al.* successfully synthesized several cocrystals of theophylline with benzamide, benzoic acid and isonicotinamide.¹⁰¹ Friščić and Jones indicate three possible mechanisms for

cocrystallization: molecular diffusion, mediated via liquid phase and mediated by an amorphous phase.¹⁰²

1.4.1.3.2 Liquid-assisted grinding

Liquid-assisted grinding (LAG), or wet grinding,¹⁰³ (sometimes called solvent-drop grinding) involves the addition of a solvent, typically in a very small amount, to the dry solid materials before grinding.¹⁰⁴ It is thought that the solvent plays a catalytic role in assisting cocrystal formation by accelerating the formation rate, and requires at least one of the components to be partly soluble in the solvent.^{97,}

105

1.4.1.4 Extrusion crystallization

Cocrystal formation by twin-screw extrusion is a scalable and solvent-free process, which operates at temperatures below the melting points of starting materials and takes place in a twin screw extruder (TSE). This technology was first utilized to synthesize the cocrystal of caffeine and AMG 517 by Medina *et al.*¹⁰⁶ This research group subsequently investigated the application of TSE in the manufacture of caffeine-oxalic acid, nicotinamide-trans cinnamic acid, carbamazepine-saccharin, and theophylline-citric acid cocrystals.¹⁰⁷

1.4.1.5 Hot melt extrusion

Hot melt extrusion, a recently developing branch of mechanochemistry, has been gaining increasing interest from both industry and academia as a continuous production tool for cocrystal synthesis. This approach involves simultaneous melting and mixing of the API and coformer via a heated screw extruder. Efficient mixing and close material packing lead to enhanced surface contact between the

API and coformer, resulting in the direct nucleation of the cocrystal in the melt, allowing the cocrystal to extrude from the extruder continuously.^{108, 109} A 1:1 cocrystal of ibuprofen and nicotinamide synthesized using this technology allowed the effect of process parameters such as barrel temperature and screw speed to be investigated.¹¹⁰

1.4.2 Solution-Based Methods

In solution-based methods, high solvent consumption is required for dissolving the cocrystal constituents. In addition, the choice of the solvent affects the results of cocrystallization, as it can change the intermolecular interactions between APIs and coformers. In general, there are two strategies that can be applied to synthesize cocrystals by solution-based methods:

- (i) when the starting materials have similar solubility in the solvent or solvent mixture, the cocrystal will saturate congruently.
- (ii) when the solubility of the starting materials varies significantly, the cocrystal stability region in non-congruently saturating solvents can be achieved by the utilization of non-equivalent reactant concentrations.^{7, 111}

Isothermal ternary phase diagrams (TPDs) are helpful to determine the behaviours of the solvent, starting materials and cocrystals, and provides a quick way to determine the cocrystal composition and stability.^{59, 112} Figure 1.12 presents different TPDs in the above two scenarios. Specifically, region 1 comprises undersaturated solutions; reactant A and B are the stable solid phases in regions 2 and 4, respectively; regions 3 and 5 are invariant regions, each containing mixtures of A or B and cocrystal, respectively; and the cocrystal is the stable solid phase in region 6. For two cocrystal reactants A and B which have similar solubilities in

solvent (Figure 1.12 left), solution cocrystallization with equimolar components can result in the formation of the 1:1 cocrystal by slow evaporation. When the two reactants A and B have dissimilar solubilities (Figure 1.12 right), the same method may lead to the crystallization of single component. Notably, Path R reveals the evolution of solution composition when adding reactant B to solutions at close to saturation with B.^{112, 113}

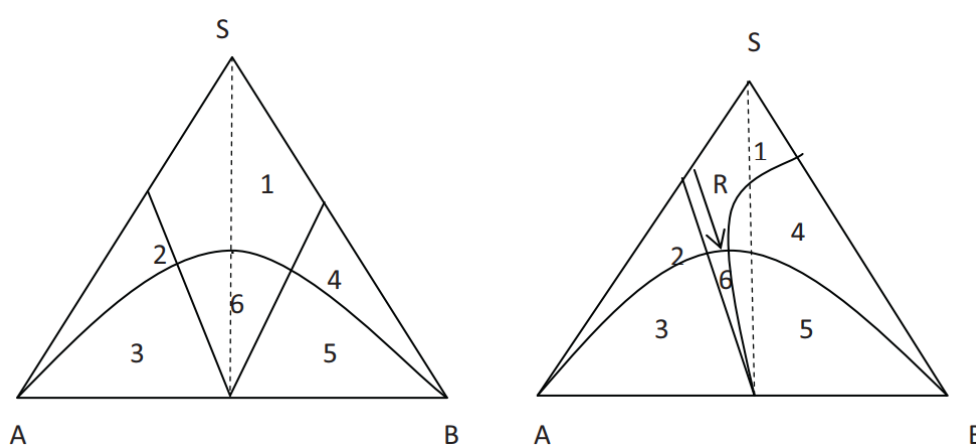


Figure 1.12. TPDs with two components having similar (left) or dissimilar solubilities (right).⁵⁹

1.4.2.1 Solvent evaporation method

This method comprises the dissolution of the API and coformer in a suitable solvent, followed by evaporation of stoichiometric solutions based on strategy (i), which has been the most frequently used solution-based method for cocrystal synthesis due to its simplicity and efficiency. The solvent evaporation experiments can be conducted by a rotary evaporator¹¹⁴ or left in a controlled environment such as an incubator or a fume hood until crystals appear.¹¹⁵ The duration of solvent removal may range from a few minutes to several weeks; as a result, the rate and

temperature of evaporation can significantly affect the formation of cocrystals. For example, Xuan *et al.* tried to synthesize cocrystals of isoniazid and curcumin by both a slow evaporation method and a rapid solvent removal. The cocrystal was only obtained using the rapid solvent removal method, indicating the rate of solvent evaporation was a critical processing parameter for controlling the phase purity of the cocrystal.¹¹⁶ In contrast, Ghosh and co-workers demonstrated that evaporation at a rate restricted to $\leq 1 \text{ mL min}^{-1}$ yielded pure cocrystals for a different system.¹¹⁷

1.4.2.2 Reaction crystallization

The solvent evaporation method may lead to the precipitation or crystallization of the single components when the cocrystallization components have different solubilities, so reaction cocrystallization can be applied for this situation. It involves adding reactant B to a saturated or approximately saturated solution of reactant A until it becomes the saturation solution of cocrystal AB, where cocrystallization proceeds along the route R as shown in Figure 1.12. This method is of increasing importance for reaction scale-up since it is based on thermodynamically stable crystal conditions.¹¹⁸ Shimpi *et al.* obtained tadalafil-malonic acid cocrystal with high purity by this method.¹¹⁹ To synthesize lamotrigine-nicotinamide·H₂O, anhydrous lamotrigine was added to the 3.5 M nicotinamide aqueous solution and stirred for 72 h at ambient temperature.¹²⁰

1.4.2.3 Cooling crystallization

Cooling crystallization involves changing the temperature of the crystallization system to achieve crystal formation, which has been extensively employed in the pharmaceutical industry. It has also been utilized for cocrystal production. The

cocrystallization components are totally dissolved in a solvent or solvent mixture at a higher temperature, and cocrystals will precipitate when the solution becomes supersaturated by reducing the temperature. TPDs have been used to depict the regions of thermodynamic stability in cooling cocrystallization. Munshi *et al.* revealed the complex crystallization behaviour of 1:1 or 2:1 cocrystals of benzoic acid and isonicotinamide by undertaking TPDs at the initial and final temperatures used in the step cooling profile.¹²¹

1.4.2.4 Antisolvent method

Antisolvent crystallization is one of the most popular techniques widely used for crystallization, where an antisolvent is added to reduce the solubility of the solute for generating supersaturation. In practice, the solvent and the antisolvent must be miscible to reach a homogeneous phase.^{122, 123} This technique has been applied as a substitute for evaporation or cooling cocrystallization techniques, in which any heating and cooling processes can be avoided.^{124, 125} Consequently, this approach can be utilized on the cocrystallization of heat sensitive materials. Water can be employed as an antisolvent due to its high miscibility with some organic solvents such as methanol, acetonitrile, etc. when the API has low aqueous solubility.¹²⁵ Wang *et al.* obtained high-purity carbamazepine-saccharin cocrystal by an antisolvent method, and demonstrated among various solvents tested, methanol was the only one that performed successfully with water as the antisolvent.¹²⁶ More recently, supercritical fluids and gas have been increasingly employed for the cocrystallization of pharmaceuticals. Supercritical antisolvent (SAS) technique involves spraying a solute-containing solution from a nozzle into a high-pressure vessel containing supercritical CO₂. The supersaturation and crystallization will

occur as the interdiffusion between organic solvent and CO₂ proceeds. For the gas antisolvent (GAS) method, compressed CO₂ is added to a solute-containing solution in a high-pressure vessel. With the dissolving of CO₂ into the liquid solvent, the solvency power of the solvent decreases, and the crystal will appear subsequently.¹²⁴ Ober and Gupta synthesized the cocrystal of itraconazole and succinic acid by GAS technique using pressurized CO₂ to improve itraconazole dissolution.¹²⁷

1.4.2.5 Slurry method

The slurry technique is a common method of screening cocrystals, typically employing a mixture of the target molecule and coformer in a fixed molar ratio suspending in a small amount of solvent, with the solids partially dissolved in the solvent. Compared with other approaches, the slurry method is not labour intensive, and it usually results in thermodynamically stable products. However, as the formation of cocrystals with high purity usually requires complete conversion of the starting materials, and the solubilities of the components can vary between systems, it is possible to isolate the stable products with prudent choice of experimental conditions.^{7, 125, 128, 129} For example, Soares and Carneiro synthesized carbamazepine-nicotinamide cocrystal by slurry method in water in four different temperatures, and found pure cocrystal bulk was only obtained at the highest temperature of 80 °C.¹³⁰

A summary of the advantages and disadvantages of these experimental methods is provided in Table 1.1.

Table 1.1 Advantages and disadvantages of different methods of cocrystal synthesis.

Technique	Categories	Advantages	Disadvantages
Solid-State	Spontaneous formation	No or less energy inputs required	The reaction needs to be thermodynamically and kinetically favoured. Selecting the correct experimental conditions can be time-consuming.
	Melting crystallization	A green alternative technique. No specific instrument required	Not appropriate for thermally labile drugs
	Grinding	Green technique due to avoidance of solvent. Avoids formation of solvates. Single-step process	Poor control on crystal properties. Difficulty in real-time monitoring. The resulting products often contain amorphous impurity
	Twin screw extrusion	An efficient, scalable, and environmentally friendly continuous process	Higher capital costs and higher operating costs
	Hot melt extrusion	Ease of scale-up. Rapid and continuous processing. Monitoring by PAT. Cost-effectiveness	Not appropriate for compounds that are subject to thermal degradation
Solution-based	Solvent evaporation	High purity cocrystals. High quality cocrystals for SCXRD	Time-consuming solvent selection. The potential for single component crystallization and solvate formation
	Reaction crystallization	Less possibility to form single component crystals	TPDs can be complicated and time-consuming to generate. Large amount of solvent required
	Cooling crystallization	Suitable for scale up	TPDs can be complicated and intensive to generate for multi-component systems.
	Antisolvent method	Adaptable for continuous operations. Size reduction by antisolvent crystallization	Tendency for organic compounds to oil out or agglomerate as fine particles into amorphous undefined structures.
	Slurry method	High efficiency. Low solvent requirement	Material loss due to residual solubility in the solvent

1.5 Characterization

Cocrystals and other crystalline materials can be characterized by a combination of analytical techniques, including (i) thermal methods, such as differential scanning calorimetry (DSC) and thermogravimetric analysis (TGA), (ii) spectroscopic methods, including vibrational spectroscopy [Fourier transform infrared spectroscopy, (FTIR) and Raman spectroscopy, (Raman)] and solid state nuclear magnetic resonance (ssNMR), and (iii) diffraction techniques, such as powder X-ray diffraction (PXRD) and single crystal X-ray diffraction (SCXRD), as shown in Figure 1.13.

1.5.1 Thermal Analysis

Thermal techniques play a vital role in providing significant information when characterizing crystalline materials including polymorphs, cocrystals, salts, etc., and when used to distinguish crystalline forms from the amorphous state. DSC and TGA are two main thermal characterization techniques.

The technique of DSC involves measuring the amount of energy absorbed or released by a sample as it is heated, cooled or held at a constant temperature. This energy correlates to the difference in heat flow between a sample and a reference standard. Integration of the area under the heat flow curve yields the enthalpy. The endothermic peak represents melting event, dehydration / desolvation, and heat-consuming thermo-degradation, etc., while exothermic peak represents a heat release event, such as crystallization or decomposition, etc.^{4, 35, 131}

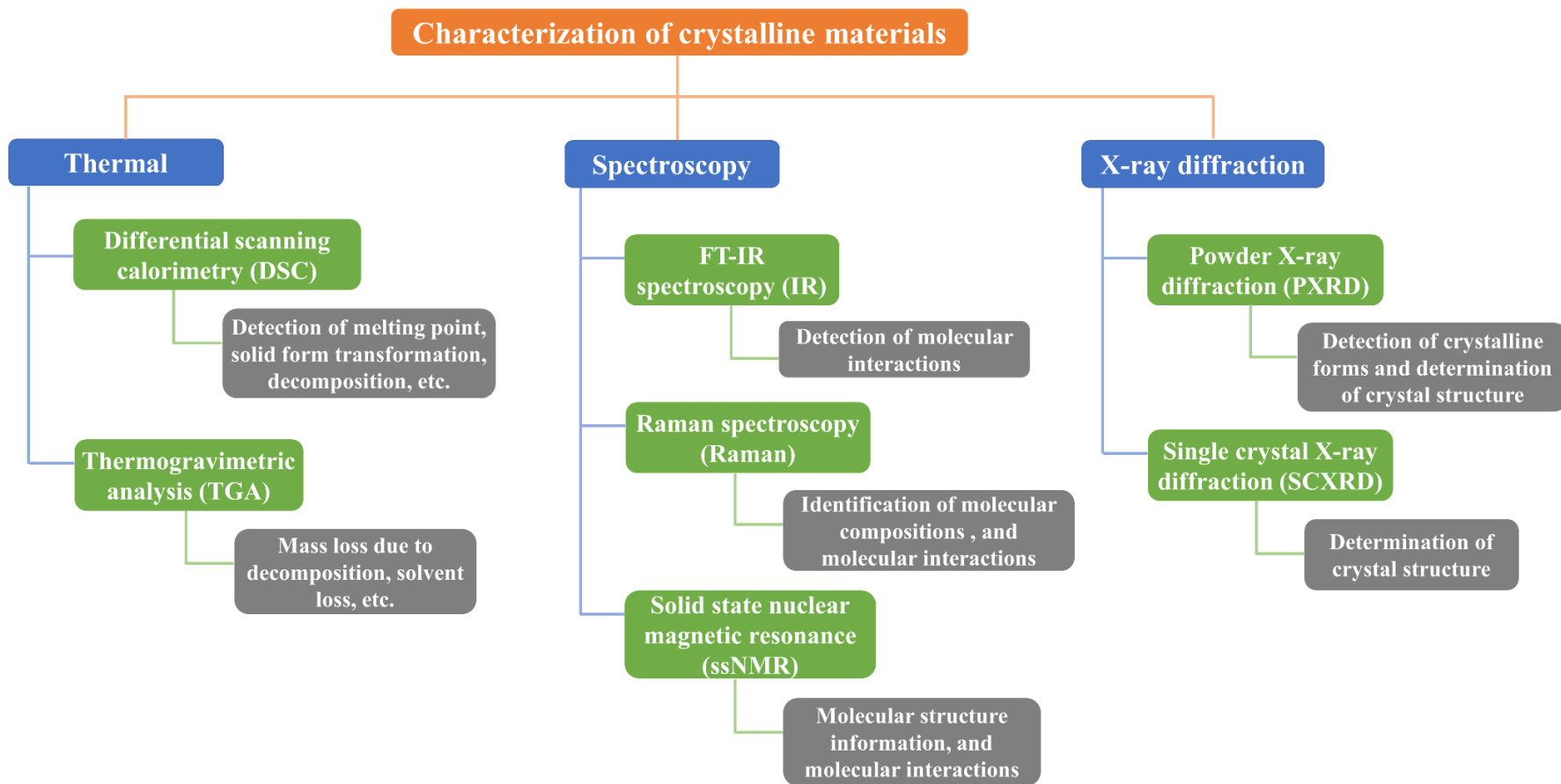


Figure 1.13. Solid state characterization techniques for crystalline materials.

No chemical information can be obtained from DSC data, and the outcome of DSC experiments can be significantly affected by the sample and experimental conditions, e.g., sample size and its distribution, purge gas type, flow rate, pan type and the heating or cooling rate.¹³² For example, fast heating and cooling rates have been used for metallic systems to increase the sensitivity, although there is a trade-off between sensitivity and sample size as the rate is increased dramatically.¹³³ Recent years have witnessed the application of DSC as a simple and rapid approach towards cocrystal screening and the exploration of the thermal behaviour of physical mixtures and the cocrystals.³⁵ Saganowska and Wesolowski conducted DSC experiments on 1:1 physical mixtures of eight benzodiazepines and nine cofomers, and demonstrated that the formation of potential cocrystals can be detected by additional endothermic or exothermic peaks.¹³⁴ Zhang *et al.* reported a method for determining the formation enthalpies of cocrystals where enthalpies of melting are measured by DSC for a cocrystal and the physical mixture.¹³⁵ TGA is another important thermal technique of measuring weight loss of the sample during heating and examining the decomposition of solid-state materials.^{4,}³⁵ Grecu and co-workers investigated weight loss from a griseofulvin-4-*tert*-butylphenol cocrystal on heating, and found the weight loss of 29.5% corresponding to the evaporation or sublimation of 4-*tert*-butylphenol (theoretically 29.8% of the overall molecular weight).¹³⁶

1.5.2 Spectroscopic Characterization

Spectroscopic techniques, providing information on molecular mobility and intermolecular interactions, have been widely used to determine the solid-state form of target compounds as they are (i) fast and non-destructive, (ii) allow for the

study of small amounts of powders and (iii) are sensitive to the hydrogen bond environment and local conformational changes.^{3, 35, 137} FTIR is a well-established technique that shows bond vibrational modes and, thus, it can reveal changes in energy for vibrational bands according to their solid-state environment.^{4, 131, 137} Similarly, Raman spectroscopy is a well-known process analytical technology (PAT) tool for identifying molecular compositions from the vibration frequencies of the molecular bonds. The improvements in optical filters make it possible to extract small Raman shifts and directly distinguish intermolecular bonds in addition to intramolecular bonds.^{35, 138} For example, Rodríguez-Hornedo and co-workers monitored the formation of carbamazepine-nicotinamide cocrystal using a Raman probe in real time.¹³⁹ However, Raman may not work sensitively if the concentration of target compound is less than 1% of the bulk material, while FTIR can accurately determine the sample of interest even if the concentration is below 1%.^{35, 131} ssNMR, an analytical technique designed specifically to probe structure and dynamics with site selectivity, provides information on several types of contacts related to a local molecular environment due to its ability to probe carbon, nitrogen and hydrogen atoms, which can be employed to analyze the different crystalline forms of solid-state materials.^{3, 4, 35, 131}

1.5.3 X-ray Diffraction Techniques

X-ray diffraction techniques include PXRD and SCXRD, and have been employed as one of the most reliable and powerful techniques for the identification and determination of crystalline forms of solid-state materials. SCXRD is the main technique for the determination of crystal structures, unit cell dimensions, related space group and three-dimensional molecular arrangement. Whether proton

transfer has occurred can also be revealed by this method. Therefore, SCXRD is regarded as the ‘gold standard’ for structural characterization of polymorphs, cocrystals, salts, hydrates and solvates, etc. However, the size and quality requirements of crystals for SCXRD is relatively high, which is a natural limitation of this technique.^{3, 4, 35} As it is easy for most solid-state crystalline materials to be prepared as microcrystalline powders, PXRD has been utilized as a predominant technique to quickly determine the crystalline forms of the samples. Each substance will produce a specific pattern depending on the structure of its unique crystal lattice, thus, PXRD can provide “fingerprint” patterns of specific crystalline forms of different solid-state materials. One of the main sources of error in PXRD technique is the preferred orientation of crystals, which can be minimized by transmission mode analysis.^{4, 35, 131} In addition, there is increasing use of structure solution using PXRD data with Rietveld analysis for the determination of crystal structures for those cases when high quality single crystals cannot be obtained.¹⁴⁰

1.6 Application of Pharmaceutical Cocrystals and Salts

Cocrystallization can modify properties of drug substances without any impact on the intrinsic pharmacological activity due to the new crystal structures imparting new physical properties, such as melting points, solubility, stability and mechanical properties, etc. Interest in pharmaceutical cocrystals and salts and their applications are continuing to grow due to these potential physical property improvements. Some key physicochemical properties of pharmaceutical cocrystals are summarized as follows:

1.6.1 Melting Points

The melting point is a fundamental property of a crystalline solid, which is the temperature at which the solid begins to change to the liquid phase. A cocrystal has a distinct melting point which usually differ from the starting materials as they have relatively different crystal packing and intermolecular interactions. In 2015 Perlovich built up a database including melting temperatures of two-component cocrystals (727 cocrystals) and individual components, and found out that the melting points of 55.3% of the cocrystals are in the range between the two components, 15.8% are higher, and 28.9% are lower.¹⁴¹ The melting points not only play an important role in characterization and purity identification, they also correlate with drug solubility and dissolution rate.¹⁴²

1.6.2 Solubility and Dissolution Rate

It is well-known that the solubility and intrinsic dissolution rate of APIs are key parameters affecting their biopharmaceutical performance; however, many drugs currently in use and NCEs belong to BCS class II and IV, which have poor solubility and / or dissolution rate. In addition to solid dispersion,¹⁴³ cyclodextrin complexation¹⁴⁴ and other methods, cocrystallization is another potential technique to conquer solubility problems. Naringenin, a natural flavanone compound, holds a poor solubility and then has difficulty being absorbed. Four cocrystals of naringenin with enhanced equilibrium solubility and intrinsic dissolution rate were prepared by Zhang *et al.*, which highlighted their potential for further pharmaceutical application.¹⁴⁵

1.6.3 Bioavailability

Bioavailability is a measure of the rate and extent at which an API reaches the systemic circulation.¹⁴⁶ Generally, improvements in solubility and dissolution rate would result in enhanced bioavailability of APIs. After demonstrating that cocrystallization can be utilized to improve the solubility of the poorly water-soluble drug quercetin, Zawarotko and colleagues investigated the pharmacokinetics of quercetin cocrystals. The bioavailability of quercetin-isonicotinamide and quercetin-caffeine cocrystals were improved by 5.46-fold and 2.57-fold respectively compared with pure quercetin.¹⁴⁷

1.6.4 Stability

The improvement of solubility, dissolution rate and bioavailability has been the subject of many researchers, but less focus has been given to investigating improvements in stability. Stability is a vital factor to evaluate the properties of an NCE and its formulation, and the consequences of drug instability can give rise to toxicity and safety concerns. Mei's group prepared two cocrystals of the physically and chemically unstable vitamin D₃ that involved a four-membered square-shaped hydrogen bonding structure, which presented superior chemical and physical stability compared with vitamin D₃ alone.¹⁴⁸

1.6.5 Mechanical Properties

The ability to modify the molecular arrangement in a crystal lattice by cocrystallization affords an opportunity to control the mechanical properties of drugs, affecting key industrial manufacturing processes, such as tableting, etc. Resveratrol, one of the most intensively studied natural polyphenolic compounds,

has poor tableability. Isoniazid and 4-aminobenzamide exhibit only slightly better tableability than resveratrol, however, the two cocrystals resveratrol-4-aminobenzamide and resveratrol-isoniazid showed significantly improved tableability.¹⁴⁹ Paracetamol has two well-known polymorphs, form 1 and 2, while form 3 has not yet been fully characterized.¹⁵⁰⁻¹⁵² Form 2 has superior compaction property compared with form 1 because of its flat hydrogen-bonded layer structure, but its lower thermodynamic stability prevents it from further use commercially. Jones *et al.* successfully produced four paracetamol cocrystals and demonstrated that these cocrystals exhibited superior tableability compared to form 1, and similar tableability but more thermodynamical stability in comparison to form 2.¹⁵³

1.6.6 Luminescent Properties

Luminescent properties of solid-state organic materials have attracted great interest owing to their wide applications in optoelectronic devices, such as organic light-emitting diodes, organic photonics and fluorescent sensors.¹⁵⁴ Cocrystallization has been established as an effective approach to modify the luminescent properties of the organic materials, where the optical properties of cocrystals are affected by different intermolecular interactions, molecular stacking modes, charge transfer and crystal packing arrangement, etc.¹⁵⁵ More recently, this technique has been applied to drug substances. Zhang *et al.* investigated the fluorescence behaviour of favipiravir-4-amino benzoic acid cocrystal and illustrated fluorescence could also be utilized as a promising tool in screening cocrystals because of the fluorescent emission nature of nitrogen heterocyclic nucleoside analog.¹⁵⁶ Two cocrystals of phloretin with nicotinamide and

isonicotinamide possessed different photoluminescence compared with the starting material, which can be attributed to the addition of coformer that created a different local molecular environment of the target API, leading to different crystal packing and intermolecular interactions.¹⁵⁷

1.6.7 Chiral Resolution

Chirality is a property possessed by a molecule with spatial arrangement of atoms which is non-superimposable with its mirror image.¹⁵⁸ For drug molecules it is necessary to investigate whether changes in chirality affect their *in vivo* activity. Based on a document entitled “Development of new stereoisomeric drugs” published by FDA in 1992,¹⁵⁹ it is a requirement to collect enough animal testing data and clinical trials of each enantiomer of a chiral drug in order to avoid unnecessary side effects. Therefore, although the investigation of chiral drugs increases the costs and time associated with pharmaceutical development, there are also opportunities for making better medicines. As a result, chiral synthesis and separation play an important role in the research and development of chiral drugs. In the pharmaceutical industry, the techniques of physical chiral resolution can be divided into two categories: classical methods and modern methods (Figure 1.14).¹⁶⁰ Diastereomeric salt formation is the most commonly used method to achieve chiral separation, which will be described in detail in the following section (1.6.7.1).¹⁶¹ Another method is called enzymatic or kinetic resolution. Some specific enantiomers of racemates can only be degraded by enzymatic assimilation, while the other enantiomer remains in solution; thus enabling separation.¹⁶²

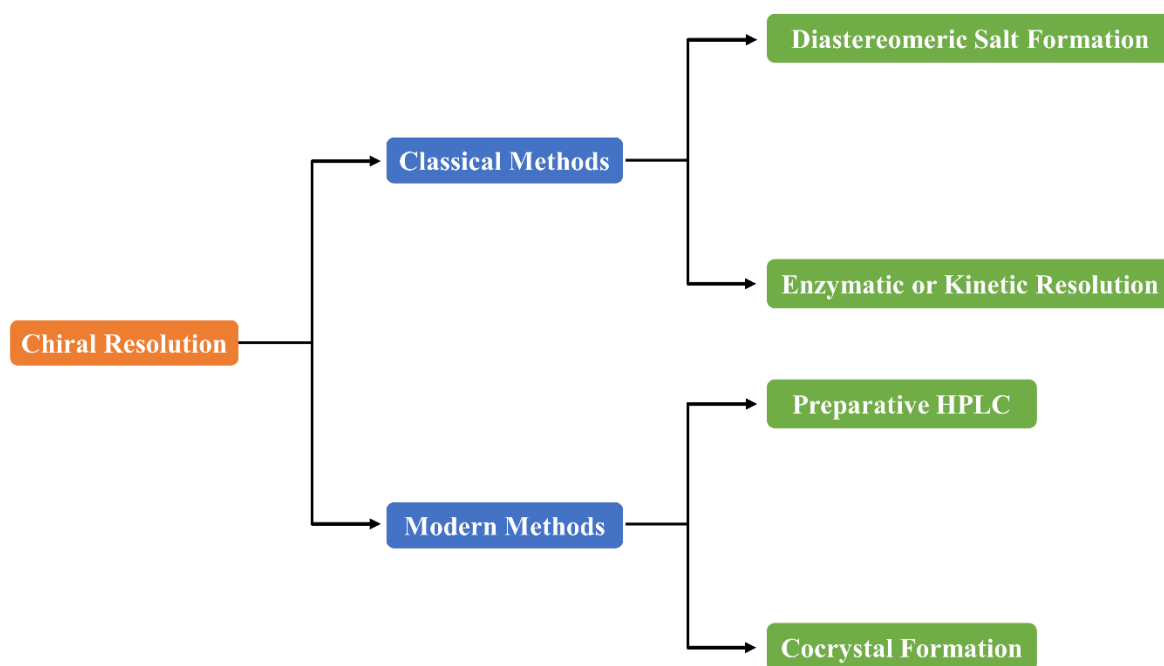


Figure 1.14. Different methods of physical chiral resolutions.

For the modern techniques, preparative HPLC is the method of choice for chiral separation. This method refers to the separation of enantiomers using a chiral HPLC column, either an HPLC column that is packed with a chiral stationary phase (CSP) or chiral mobile phase additives that are added in the mobile phase.¹⁶³ The former method is more widely used and more designable than the latter one.¹⁶⁴ However, there is no HPLC CSP that can be used for all racemic compounds, so choosing an appropriate column for different chiral compounds is of key importance, which is expensive. Another drawback is the limited throughput,¹⁶⁵ which may not be attractive for the pharmaceutical industry. The other modern technology for chiral separation is cocrystal formation, an emerging method for achieving chiral resolution with significant potential for future development in both academic research and the pharmaceutical industry.¹⁶⁶ For more details of this method, see 1.6.7.2 section.

1.6.7.1 Diastereomeric salt formation

As mentioned above, diastereomeric salt formation is the most commonly used method for chiral separation. The acid-base reaction involved is between a racemic drug and a pure single enantiomer (also called resolving agent).¹⁶⁷ Two diastereomeric salts can be obtained with different physicochemical properties so that different methods can be selected to separate the obtained diastereomeric salt pair. For example, if they have different melting points, crystallization can be utilized to achieve separation easily, while if the two salts possess different solubility or one is soluble and the other is insoluble, separation can be achieved through filtration. Subsequently, the salt is treated with either acid or base, and finally the enantiomer is released. Racemic *N*-formylphenylalanine can form a diastereomeric salt pair with (*S*)-(-)-1-phenylethylamine, and the two salts were characterized by DSC and SCXRD. When observing the growth of these two salts, a great difference in the crystal growth kinetics of the diastereomers was found, which allowed successful optical resolution.¹⁶⁸ Two of the most widely used starting materials for preparation of pharmaceuticals, namely β -aminoalcohols and 1,2-diamines, were resolved using dehydroabiatic acid. In addition, Zhang *et al.* found that dehydroabiatic acid could be easily and efficiently recovered in a reusable form.¹⁶⁹ Overall, this method is a relatively less costly process compared to chiral HPLC but can only be successfully applied when the target chiral compound can readily form salts.

1.6.7.2 Cocrystal formation

The majority of APIs lack functional groups suitable for diastereomeric salt formation,¹⁷⁰ and cocrystal formation has been proven to offer an alternative

resolution method.¹⁷¹ There are two possible outcomes for cocrystal formation: the two components can either form a diastereomeric cocrystal pair or behave enantiospecifically (Figure 1.15).¹⁷⁰ Structural modifications in the supramolecular assembly in enantiospecific cocrystals or diastereomeric cocrystal pairs result in changes in the crystal lattice energy and related physical and physicochemical properties, enabling separation. Therefore, both possible outcomes can be used to develop a chiral resolution process. In this method, the crucial step is to screen and find chiral molecules that can form cocrystals with the target chiral compounds that are stable for future development.

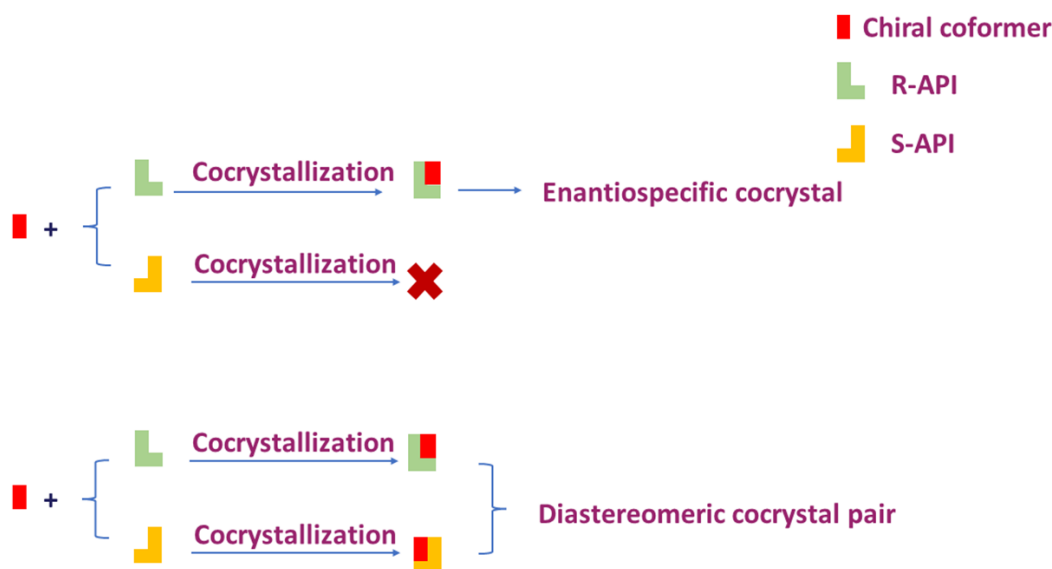


Figure 1.15. Two possible scenarios of achieving chiral resolution by cocrystal formation (adapted from ref. 171).

Leyssens's group developed a dual-drug chiral resolution process based on the ibuprofen-levetiracetam system. The resolving agent levetiracetam can form a cocrystal with *S*-ibuprofen in an enantiospecific manner. They were able to achieve enantio-enrichment by using the appropriate phase diagrams and ultimately obtain

resolution.¹⁷² Praziquantel (PZQ), an important chiral drug for the treatment of gastrointestinal parasites, is commercially available only in the form of its racemic mixture.¹⁷³ The biologically active component is *R*-PZQ while there is a bitter taste associated with *S*-PZQ. *R* / *S*-PZQ form a diastereomeric cocrystal pair with L-malic acid (L-MA). Phase-decomposition of the *R*-PZQ:L-MA cocrystal by treatment with water enabled chiral separation due to the different aqueous solubilities of the diastereomeric cocrystals.¹⁷⁰

1.7 Research Aim

The overall aim of this thesis is to investigate the modification of the physicochemical properties of drug substances by crystal engineering and examine the potential to achieve chiral separation by cocrystal formation. There are four objectives to achieve this:

- (i) to investigate the synthesis and characterization of pharmaceutical cocrystals and salts and discuss the differences between them.
- (ii) to analyse the nature of non-covalent interactions (especially hydrogen bonds) within cocrystals structurally and theoretically.
- (iii) to explore the modification of physicochemical properties of drug substances by crystal engineering.
- (iv) to screen and synthesize diastereomeric and enantiospecific cocrystals between chiral molecules and develop methods for chiral resolution.

1.8 Thesis Structure

The thesis has seven chapters. Chapter 1 is a literature review on multi-component crystalline materials, research aims and thesis structure. Chapter 2 explores the crystal structure landscape of sulfasalazine through various multi-component crystals. In this study, Shan Huang conducted all the experimental work, with assistance from Dr Matteo Lusi and Dr Chiara Cappuccino in determining the single-crystal structures of $(SSZ)_2$ -PHE, SSZ-4AP, SSZ-TMD and SSZ-IMZ-MeCN. Vinay K. R. Cheemarla and Dr Davide Tiana contributed to the HOMO-LUMO calculations. Dr Simon Lawrence provided support on determining the single-crystal structures of $(SSZ)_2$ -BPY-Tol_{0.8} and $(SSZ)_2$ -BPE-EtOH₂, and overall guidance and supervision. Chapter 3 is the experimental and theoretical investigation of non-covalent interactions in cocrystals of sulfaguanidine. Shan Huang performed all the experimental work and part of the theoretical calculations including Hirshfeld surface and MEPS, Vinay K. R. Cheemarla and Dr Davide Tiana provided helping hands in the QTAIM calculations. Dr Simon Lawrence provided overall guidance and supervision. Chapter 4 examines pharmaceutical salts of piroxicam and meloxicam with organic counterions. Shan Huang conducted all the experiments, except for the measurements of solid-state luminescence of piroxicam and its three salts, which were performed by commercial sources. Dr Matteo Lusi and Dr Chiara Cappuccino helped to determine the single-crystal structures of PRM-4AP, PRM-PPZ, MEL-4DMP and MEL-PPZ. Dr Dean Venables provided assistance in the fluorescence analysis. Dr Simon Lawrence provided overall guidance and supervision. Chapter 5 investigates the formation of enantiospecific cocrystals and

diastereomeric cocrystal pairs of amino acids and chiral cofomers. Shan Huang conducted all the experiments with the assistance of Dr Matteo Lusi and Dr Chiara Cappuccino for the crystal structure of L-Met-L-MDA. Dr Simon Lawrence provided overall guidance and supervision. Chapter 6 examines potential diastereomeric cocrystals with mandelamide. Shan Huang performed all the experiments, Deirbhile Fitzgerald contributed by synthesizing the starting materials, while Dr Stuart Collins and Prof Anita Maguire provided discussions and insights throughout the study. Dr Simon Lawrence provided support on determining the single-crystal structures and overall guidance. Chapter 7 is a summary of the previous chapters and future work.

REFERENCES

- (1) Alqahtani, M. S.; Kazi, M.; Alsenaidy, M. A.; Ahmad, M. Z., Advances in Oral Drug Delivery. *Front. Pharmacol.* **2021**, 12, 10.3389/fphar.2021.618411.
- (2) Kalepu, S.; Nekkanti, V., Insoluble drug delivery strategies: review of recent advances and business prospects. *Acta Pharm. Sin. B* **2015**, 5, (5), 442–453.
- (3) Cerreia Vioglio, P.; Chierotti, M. R.; Gobetto, R., Pharmaceutical aspects of salt and cocrystal forms of APIs and characterization challenges. *Adv. Drug Deliv. Rev.* **2017**, 117, 86–110.
- (4) Pindelska, E.; Sokal, A.; Kolodziejcki, W., Pharmaceutical cocrystals, salts and polymorphs: Advanced characterization techniques. *Adv. Drug Deliv. Rev.* **2017**, 117, 111–146.
- (5) Amidon, G. L.; Lennernäs, H.; Shah, V. P.; Crison, J. R., A theoretical basis for a biopharmaceutic drug classification: the correlation of in vitro drug

- product dissolution and in vivo bioavailability. *Pharm. Res.* **1995**, 12, (3), 413–420.
- (6) Dahan, A.; Beig, A.; Lindley, D.; Miller, J. M., The solubility–permeability interplay and oral drug formulation design: Two heads are better than one. *Adv. Drug Deliv. Rev.* **2016**, 101, (1), 99–107.
- (7) Karimi-Jafari, M.; Padrela, L.; Walker, G. M.; Croker, D. M., Creating Cocrystals: A Review of Pharmaceutical Cocrystal Preparation Routes and Applications. *Cryst. Growth Des* **2018**, 18, (10), 6370–6387.
- (8) Ngilirabanga, J. B.; Samsodien, H., Pharmaceutical co-crystal: An alternative strategy for enhanced physicochemical properties and drug synergy. *Nano Select.* **2021**, 2, (3), 512–526.
- (9) Tambe, S.; Jain, D.; Meruva, S. K.; Rongala, G.; Juluri, A.; Nihalani, G.; Mamidi, H. K.; Nukala, P. K.; Bolla, P. K., Recent Advances in Amorphous Solid Dispersions: Preformulation, Formulation Strategies, Technological Advancements and Characterization. *Pharmaceutics* **2022**, 14, (10), 2203.
- (10) Duggirala, N. K.; Perry, M. L.; Almarsson, O.; Zaworotko, M. J., Pharmaceutical cocrystals: along the path to improved medicines. *Chem. Commun.* **2016**, 52, (4), 640–655.
- (11) Patel, M. A.; Luthra, S.; Shamblin, S. L.; Arora, K.; Krzyzaniak, J. F.; Taylor, L. S., Impact of Solid-State Form on the Disproportionation of Miconazole Mesylate. *Mol. Pharm.* **2018**, 15, (1), 40–52.
- (12) Purohit, H. S.; Trasi, N. S.; Osterling, D. J.; Stolarik, D. F.; Jenkins, G. J.; Gao, W.; Zhang, G. G. Z.; Taylor, L. S., Assessing the Impact of Endogenously Derived Crystalline Drug on the in Vivo Performance of Amorphous Formulations. *Mol. Pharm.* **2019**, 16, (8), 3617–3625.

- (13) Hussain, A.; Smith, G.; Khan, K. A.; Bukhari, N. I.; Pedge, N. I.; Ermolina, I., Solubility and dissolution rate enhancement of ibuprofen by co-milling with polymeric excipients. *Eur. J. Pharm. Sci.* **2018**, 123, 395–403.
- (14) Zhu, L.; Wong, L.; Yu, L., Surface-Enhanced Crystallization of Amorphous Nifedipine. *Mol. Pharm.* **2008**, 5, (6), 921–926.
- (15) Schittny, A.; Huwyler, J.; Puchkov, M., Mechanisms of increased bioavailability through amorphous solid dispersions: a review. *Drug Deliv.* **2020**, 27, (1), 110–127.
- (16) Rietveld, I. B.; Ceolin, R., Rotigotine: Unexpected Polymorphism with Predictable Overall Monotropic Behaviour. *J. Pharm. Sci.* **2015**, 104, (12), 4117–4122.
- (17) Stahly, G. P., Diversity in Single- and Multiple-Component Crystals. The Search for and Prevalence of Polymorphs and Cocrystals. *Cryst. Growth Des.* **2007**, 7, (6), 1007–1026.
- (18) Stephenson, G. A.; Borchardt, T. B.; Byrn, S. R.; Bowyer, J. J.; Bunnell, C. A.; Snorek, S. V.; Yu, L., Conformational and Color Polymorphism of 5-Methyl-2-[(2-nitrophenyl)amino]-3-thiophenecarbonitrile. *J. Pharm. Sci.* **1995**, 84, (11), 1385–1386.
- (19) Yu, L.; Stephenson, G. A.; Mitchell, C. A.; Bunnell, C. A.; Snorek, S. V.; Bowyer, J. J.; Borchardt, T. B.; Stowell, J. G.; Byrn, S. R., Thermochemistry and Conformational Polymorphism of a Hexamorphic Crystal System. *J. Am. Chem. Soc.* **2000**, 122, (4), 585–591.
- (20) Chen, S.; Guzei, I. A.; Yu, L., New Polymorphs of ROY and New Record for Coexisting Polymorphs of Solved Structures. *J. Am. Chem. Soc.* **2005**, 127, (27), 9881–9885.

- (21) Li, X.; Ou, X.; Rong, H.; Huang, S.; Nyman, J.; Yu, L.; Lu, M., The Twelfth Solved Structure of ROY: Single Crystals of Y04 Grown from Melt Microdroplets. *Cryst. Growth Des.* **2020**, 20, (11), 7093–7097.
- (22) Chen, S.; Xi, H.; Yu, L., Cross-Nucleation between ROY Polymorphs. *J. Am. Chem. Soc.* **2005**, 127, (49), 17439–17444.
- (23) Tan, M.; Shtukenberg, A. G.; Zhu, S.; Xu, W.; Dooryhee, E.; Nichols, S. M.; Ward, M. D.; Kahr, B.; Zhu, Q., ROY revisited, again: the eighth solved structure. *Faraday Discuss.* **2018**, 211, 477–491.
- (24) Gushurst, K. S.; Nyman, J.; Boerrigter, S. X. M., The PO13 crystal structure of ROY. *CrystEngComm* **2019**, 21, 1363–1368.
- (25) Lévesque, A.; Maris, T.; Wuest, J. D., ROY Reclaims Its Crown: New Ways To Increase Polymorphic Diversity. *J. Am. Chem. Soc.* **2020**, 142, (27), 11873–11883.
- (26) Mitchell, C. A.; Yu, L.; Ward, M. D., Selective Nucleation and Discovery of Organic Polymorphs through Epitaxy with Single Crystal Substrates. *J. Am. Chem. Soc.* **2001**, 123, (44), 10830–10839.
- (27) Tyler, A. R.; Ragbirsingh, R.; McMonagle, C. J.; Waddell, P. G.; Heaps, S. E.; Steed, J. W.; Thaw, P.; Hall, M. J.; Probert, M. R., Encapsulated Nanodroplet Crystallization of Organic-Soluble Small Molecules. *Chem* **2020**, 6, (7), 1755–1765.
- (28) Nyman, J.; Yu, L.; Reutzel-Edens, S. M., Accuracy and reproducibility in crystal structure prediction: the curious case of ROY. *CrystEngComm* **2019**, 21, 2080–2088.
- (29) Beran, G. J. O.; Sugden, I. J.; Greenwell, C.; Bowskill, D. H.; Pantelides, C. C.; Adjiman, C. S., How many more polymorphs of ROY remain

- undiscovered. *Chem. Sci.* **2022**, 13, 1288–1297.
- (30) Bauer, J.; Spanton, S.; Henry, R.; Quick, J.; Dziki, W.; Porter, W.; Morris, J., Ritonavir: An Extraordinary Example of Conformational Polymorphism. *Pharm. Res.* **2001**, 18, (6), 859–866.
- (31) Gamberini, M. C.; Baraldi, C.; Tinti, A.; Rustichelli, C.; Ferioli, V.; Gamberini, G., Solid state characterization of chloramphenicol palmitate. Raman spectroscopy applied to pharmaceutical polymorphs. *J. Mol. Struct.* **2006**, 785, (1-3), 216–224.
- (32) Aguiar, A. J.; Zelmer, J. E., Dissolution Behaviour of Polymorphs of Chloramphenicol Palmitate and Mefenamic Acid. *J. Pharm. Pharm.* **1969**, 58, (8), 983–987.
- (33) Censi, R.; Di Martino, P., Polymorph Impact on the Bioavailability and Stability of Poorly Soluble Drugs. *Molecules.* **2015**, 20, (10), 18759–18776.
- (34) Pudipeddi, M.; Serajuddin, A. T., Trends in solubility of polymorphs. *J. Pharm. Sci.* **2005**, 94, (5), 929–939.
- (35) Healy, A. M.; Worku, Z. A.; Kumar D.; Madi, A. M., Pharmaceutical solvates, hydrates and amorphous forms: A special emphasis on cocrystals. *Adv. Drug Deliv. Rev.* **2017**, 117, (1), 25–46.
- (36) Li, M.; Zhang, Q.; He, H.; Wang, J.; Mei, X., Vapor triggered fluorescent color changes among solvates of Emodin. *J. Mater. Chem. C.* **2017**, 5, (24), 5970–5976.
- (37) Xiong, X.; Du, Q.; Zeng, X.; He, J.; Yang, H.; Li, H., Solvates and polymorphs of rebamipide: preparation, characterization, and physicochemical analysis. *RSC Adv.* **2017**, 7, (38), 23279–23286.
- (38) Henwood, S. Q.; Liebenberg, W.; Tiedt, L. R.; Lotter, A. P.; Villiers, M. M.

- d., Characterization of the Solubility and Dissolution Properties of Several New Rifampicin Polymorphs, Solvates, and Hydrates. *Drug Dev. Ind. Pharm.* **2001**, 27, (10), 1017–1030.
- (39) Tieger, E.; Kiss, V.; Pokol, G.; Finta, Z.; Rohlíček, J.; Skořepová, E.; Dušek, M., Rationalization of the formation and stability of bosutinib solvated forms. *CrystEngComm* **2016**, 18, (48), 9260–9274.
- (40) Serajuddin, A. T., Salt formation to improve drug solubility. *Adv. Drug Deliv. Rev.* **2007**, 59, (7), 603–616.
- (41) U.Riebesehl, B., Drug Delivery with Organic Solvents or Colloidal Dispersed Systems. In *The Practice of Medicinal Chemistry (Fourth Edition)*, Wermuth, C.; Aldous, D.; Raboisson, P.; Rognan, D., Eds. 2015; pp 699–722.
- (42) Tao, Q.; Chen, J.; Ma, L.; Lu, T., Phenazopyridine Cocrystal and Salts That Exhibit Enhanced Solubility and Stability. *Cryst. Growth Des.* **2012**, 12, (6), 3144–3152.
- (43) Badawy, S. I. F., Effect of salt form on chemical stability of an ester prodrug of a glycoprotein IIb/IIIa receptor antagonist in solid dosage forms. *Int. J. Pharm.* **2001**, 223, 81–87.
- (44) Tantardini, C.; Arkhipov, S. G.; Cherkashina, K. A.; Kil'met'ev, A. S.; Boldyreva, E. V., Crystal structure of a 2:1 co-crystal of meloxicam with acetylenedicarboxylic acid. *Acta Cryst.* **2016**, E72, 1856–1859.
- (45) Huang, S.; Xue, Q.; Xu, J.; Ruan, S.; Cai, T., Simultaneously Improving the Physicochemical Properties, Dissolution Performance, and Bioavailability of Apigenin and Daidzein by Co-Crystallization With Theophylline. *J. Pharm. Sci.* **2019**, 108, (9), 2982–2993.

- (46) Lusi, M.; Vitorica-Yrezabal, I. J.; Zaworotko, M. J., Expanding the Scope of Molecular Mixed Crystals Enabled by Three Component Solid Solutions. *Cryst. Growth Des.* **2015**, 15, (8), 4098–4103.
- (47) Sinha, A. S.; Maguire, A. R.; Lawrence, S. E., Cocrystallization of Nutraceuticals. *Cryst. Growth Des.* **2015**, 15, (2), 984–1009.
- (48) Kuminek, G.; Rodríguez-Hornedo, N.; Siedler, S.; Rocha, H. V. A.; Cuffini, S. L.; Cardoso, S. G., How cocrystals of weakly basic drugs and acidic cofomers might modulate solubility and stability. *Chem. Commun.* **2016**, 52, 5832–5835.
- (49) Suresh, K.; Mannava, M. K. C.; Nangia, A., Cocrystals and alloys of nitazoxanide: enhanced pharmacokinetics. *Chem. Commun.* **2016**, 52, 4223–4226.
- (50) Saha, S.; Desiraju, G. R., Using structural modularity in cocrystals to engineer properties: elasticity. *Chem. Commun.* **2016**, 52, 7676–7679.
- (51) Yu, Q.; Yan, Z.; Bao, J.; Wang, J.; Mei, X., Taming photo-induced oxidation degradation of dihydropyridine drugs through cocrystallization. *Chem. Commun.* **2017**, 53, 12266–12269.
- (52) Dai, X. L.; Chen, J. M.; Lu, T. B., Pharmaceutical cocrystallization: an effective approach to modulate the physicochemical properties of solid-state drugs. *CrystEngComm* **2018**, 20, 5292–5316.
- (53) Karagianni, A.; Malamataris, M.; Kachrimanis, K., Pharmaceutical Cocrystals: New Solid Phase Modification Approaches for the Formulation of APIs. *Pharmaceutics* **2018**, 10, (1), 18.
- (54) Nangia, A., Supramolecular chemistry and crystal engineering. *J. Chem. Sci.* **2010**, 122, 295–310.

- (55) Soldatov, D. V.; Terekhova, I. S., Supramolecular chemistry and crystal engineering. *J. Struct. Chem.* **2005**, 46, S1–S8.
- (56) Desiraju, G. R., Crystal Engineering: From Molecule to Crystal. *J. Am. Chem. Soc.* **2013**, 135, (27), 9952–9967.
- (57) Desiraju, G. R., Supramolecular Synthons in Crystal Engineering—A New Organic Synthesis. *Angew. Chem., Int. Ed. Engl.* **1995**, 34, (21), 2311–2327.
- (58) Thalladi, V. R.; Goud, B. S.; Hoy, V. J.; Allen, F. H.; Howard, J. A. K.; Desiraju, G. R., Supramolecular synthons in crystal engineering. Structure simplification, synthon robustness and supramolecular retrosynthesis. *Chem. Commun.* **1996**, 3, 401–402.
- (59) Qiao, N.; Li, M.; Schlindwein, W.; Malek, N.; Davies, A.; Trappitt, G., Pharmaceutical cocrystals: an overview. *Int. J. Pharm.* **2011**, 419, (1-2), 1–11.
- (60) Shattock, T. R.; Arora, K. K.; Vishweshwar, P.; Zaworotko, M. J., Hierarchy of Supramolecular Synthons: Persistent Carboxylic Acid···Pyridine Hydrogen Bonds in Cocrystals That also Contain a Hydroxyl Moiety. *Cryst. Growth Des.* **2008**, 8, (12), 4533–4545.
- (61) Etter, M. C., Encoding and decoding hydrogen-bond patterns of organic compounds. *Acc. Chem. Res.* **1990**, 23, (4), 120–126.
- (62) Etter, M. C., Hydrogen bonds as design elements in organic chemistry. *J. Phys. Chem.* **1991**, 95, (12), 4601–4610.
- (63) Wiechert, D.; Mootz, D., Molecular Beside Ionic: Crystal Structures of a 1/1 and a 1/4 Adduct of Pyridine and Formic Acid. *Angew. Chem. Int. Ed.* **1999**, 38, (13/14), 1974–1976.
- (64) Losev, E. A.; Boldyreva, E. V., A salt or a co-crystal – when crystallization

- protocol matters. *CrystEngComm* **2018**, 20, 2299–2305.
- (65) Aakeröy, C. B.; Fasulo, M. E.; Desper, J., Cocrystal or Salt: Does It Really Matter? *Mol. Pharmaceutics* **2007**, 4, (3), 317–322.
- (66) Buddhadev, S. S.; Garala, K. C., Pharmaceutical Cocrystals—A Review. *Proceedings* **2020**, 62, (1), 14.
- (67) Cruz-Cabeza, A. J., Acid–Base Crystalline Complexes and the Pka Rule. *CrystEngComm* **2012**, 14, 6362–6365.
- (68) Oertling, H.; Orcid, C. B.; Alzieu, T.; Wissenmeyer, M.; Vinay, C.; Mahieux, J.; Fumeaux, R., Ionic Cocrystals of Sodium Chloride with Carbohydrates. *Cryst. Growth Des.* **2017**, 17, (1), 262–270.
- (69) Song, L.; Robeyns, K.; Leysens, T., Crystallizing Ionic Cocrystals: Structural Characteristics, Thermal Behaviour, and Crystallization Development of a Piracetam-CaCl₂ Cocrystallization Process. *Cryst. Growth Des.* **2018**, 18, (5), 3215–3221.
- (70) Nugrahani, I.; Kumalasari, R. A.; Auli, W. N.; Horikawa, A.; Uekusa, H., Salt Cocrystal of Diclofenac Sodium-L-Proline: Structural, Pseudopolymorphism, and Pharmaceutics Performance Study. *Pharmaceutics* **2020**, 12, (7), 690.
- (71) Grifasi, F.; Chierotti, M. R.; Gaglioti, K.; Gobetto, R.; Maini, L.; Braga, D.; Dichiarante, E.; Curzi, M., Using Salt Cocrystals to Improve the Solubility of Niclosamide. *Cryst. Growth Des.* **2015**, 15, (4), 1939–1948.
- (72) Perumalla, S. R.; Sun, C. C., Design and Preparation of a 4:1 Lamivudine–Oxalic Acid CAB Cocrystal for Improving the Lamivudine Purification Process. *Cryst. Growth Des.* **2014**, 14, (8), 3990–3995.
- (73) Perumalla, S. R.; Paul, S.; Sun, C. C., Enabling the Tablet Product

- Development of 5-Fluorocytosine by Conjugate Acid Base Cocrystals. *J. Pharm. Sci.* **2016**, 105, (6), 1960–1966.
- (74) Perumalla, S. R.; Sun, C. C., Improved solid-state stability of salts by cocrystallization between conjugate acid–base pairs. *CrystEngComm* **2013**, 15, 5756–5759.
- (75) Cheney, M. L.; Weyna, D. R.; Shan, N.; Hanna, M.; Wojtas, L.; Zaworotko, M. J., Cofomer Selection in Pharmaceutical Cocrystal Development: a Case Study of a Meloxicam Aspirin Cocrystal That Exhibits Enhanced Solubility and Pharmacokinetics. *J. Pharm. Sci.* **2011**, 100, (6), 2172–2181.
- (76) Macrae, C. F.; Sovago, I.; Cottrell, S. J.; Galek, P. T. A.; McCabe, P.; Pidcock, E.; Platings, M.; Shields, G. P.; Stevens, J. S.; Towler, M.; Wood, P. A., Mercury 4.0: from visualization to analysis, design and prediction. *J. Appl. Cryst.* **2020**, 53, 226–235.
- (77) Khalaji, M.; Potrzebowski, M. J.; Dudek, M. K., Virtual Cocrystal Screening Methods as Tools to Understand the Formation of Pharmaceutical Cocrystals—A Case Study of Linezolid, a Wide-Range Antibacterial Drug. *Cryst. Growth Des.* **2021**, 21, (4), 2301–2314.
- (78) Krueger, E. L.; Sinha, A. S.; Desper, J.; Aakeröy, C. B., Exploring binding preferences in co-crystals of conformationally flexible multitopic ligands. *CrystEngComm* **2017**, 19, 4605–4614.
- (79) Wicker, J. G. P.; Crowley, L. M.; Robshaw, O.; Little, E. J.; Stokes, S. P.; Cooper, R. I.; Lawrence, S. E., Will they co-crystallize? *CrystEngComm* **2017**, 19, (36), 5336–5340.
- (80) Abramov, Y. A.; Loschen, C.; Klamt, A., Rational Cofomer or Solvent Selection for Pharmaceutical Cocrystallization or Desolvation. *J. Pharm. Sci.*

- 2012**, 101, (10), 3687–3697.
- (81) Mswahili, M. E.; Lee, M.-J.; Martin, G. L.; Kim, J.; Kim, P.; Choi, G. J.; Jeong, Y.-S., Cocrystal Prediction Using Machine Learning Models and Descriptors. *Appl. Sci.* **2021**, 11, (3), 1323.
- (82) Gamidi, R. K.; Rasmuson, Å. C., Estimation of Melting Temperature of Molecular Cocrystals Using Artificial Neural Network Model. *Cryst. Growth Des.* **2017**, 17, (1), 175–182.
- (83) Krishna, G. R.; Ukrainczyk, M.; Zeglinski, J.; Rasmuson, Å. C., Prediction of Solid State Properties of Cocrystals Using Artificial Neural Network Modeling. *Cryst. Growth Des.* **2018**, 18, (1), 133–144.
- (84) Gamidi, R. K.; Rasmuson, Å. C., Analysis and Artificial Neural Network Prediction of Melting Properties and Ideal Mole fraction Solubility of Cocrystals. *Cryst. Growth Des.* **2020**, 20, (9), 5745–5759.
- (85) Price, S. L., Predicting crystal structures of organic compounds. *Chem. Soc. Rev.* **2014**, 43, 2098–2111.
- (86) Dudek, M. K.; Druzbicki, K., Along the road to crystal structure prediction(CSP) of pharmaceutical-like molecules. *CrystEngComm* **2022**, 24, 1665–1678.
- (87) Mattei, A.; Hong, R. S.; Dietrich, H.; Firaha, D.; Helfferich, J.; Liu, Y. M.; Sasikumar, K.; Abraham, N. S.; Bhardwaj, R. M.; Neumann, M. A.; Sheikh, A. Y., Efficient Crystal Structure Prediction for Structurally Related Molecules with Accurate and Transferable Tailor-Made Force Fields. *J. Chem. Theory Comput.* **2022**, 18, (9), 5725–5738.
- (88) Sugden, I. J.; Braun, D. E.; Bowskill, D. H.; Adjiman, C. S.; Pantelides, C. C., Efficient Screening of Cofomers for Active Pharmaceutical Ingredient

- Cocrystallization. *Cryst. Growth Des.* **2022**, 22, (7), 4513–4527.
- (89) Sun, G.; Jin, Y.; Li, S.; Yang, Z.; Shi, B.; Chang, C.; Abramov, Y. A., Virtual Coformer Screening by Crystal Structure Predictions: Crucial Role of Crystallinity in Pharmaceutical Cocrystallization. *J. Phys. Chem. Lett.* **2020**, 11, (20), 8832–8838.
- (90) Bolla, G.; Nangia, A., Pharmaceutical cocrystals: walking the talk. *Chem Commun* **2016**, 52, (54), 8342–8360.
- (91) Kaupp, G., Solid-state molecular syntheses: complete reactions without auxiliaries based on the new solid-state mechanism. *CrystEngComm* **2003**, 5, (23), 117–133.
- (92) Solares-Briones, M.; Coyote-Dotor, G.; Paez-Franco, J. C.; Zermeno-Ortega, M. R.; de la, O. C. C. M.; Canseco-Gonzalez, D.; Avila-Sorrosa, A.; Morales-Morales, D.; German-Acacio, J. M., Mechanochemistry: A Green Approach in the Preparation of Pharmaceutical Cocrystals. *Pharmaceutics* **2021**, 13, (6), 790.
- (93) Maheshwari, C.; Jayasankar, A.; Khan, N. A.; Amidon, G. E.; Rodríguez-Hornedo, N., Factors that influence the spontaneous formation of pharmaceutical cocrystals by simply mixing solid reactants. *CrystEngComm* **2009**, 11, (3), 493–500.
- (94) MacFhionnghaile, P.; Crowley, C. M.; McArdle, P.; Erxleben, A., Spontaneous Solid-State Cocrystallization of Caffeine and Urea. *Cryst. Growth Des* **2020**, 20, (2), 736–745.
- (95) Ervasti, T.; Aaltonen, J.; Ketolainen, J., Theophylline-nicotinamide cocrystal formation in physical mixture during storage. *Int. J. Pharm.* **2015**, 486, (1–2), 121–130.

- (96) Ulrich, J., Is Melt Crystallization a Green Technology? *Cryst. Growth Des.* **2004**, 4, (5), 879–880.
- (97) Guo, M.; Sun, X.; Chen, J.; Cai, T., Pharmaceutical cocrystals: A review of preparations, physicochemical properties and applications. *Acta. Pharm. Sin. B.* **2021**, 11, (8), 2537–2564.
- (98) Yan, Y.; Chen, J.-M.; Lu, T.-B., Thermodynamics and preliminary pharmaceutical characterization of a melatonin–pimelic acid cocrystal prepared by a melt crystallization method. *CrystEngComm* **2015**, 17, (3), 612–620.
- (99) Do, J.-L.; Friščić, T., Mechanochemistry: A Force of Synthesis. *ACS Cent. Sci.* **2017**, 3, (1), 13–19.
- (100) Tan, D.; Loots, L.; Friscic, T., Towards medicinal mechanochemistry: evolution of milling from pharmaceutical solid form screening to the synthesis of active pharmaceutical ingredients (APIs). *Chem. Commun.* **2016**, 52, (50), 7760–7781.
- (101) Fischer, F.; Lubjuhn, D.; Greiser, S.; Rademann, K.; Emmerling, F., Supply and Demand in the Ball Mill: Competitive Cocrystal Reactions. *Cryst. Growth Des.* **2016**, 16, (10), 5843–5851.
- (102) Friščić, T.; Jones, W., Recent Advances in Understanding the Mechanism of Cocrystal Formation via Grinding. *Cryst. Growth Des.* **2009**, 9, (3), 1621–1637.
- (103) Shan, N.; Toda, F.; Jones, W., Mechanochemistry and co-crystal formation: effect of solvent on reaction kinetics. *Chem. Commun.* **2002**, 2372–2373.
- (104) Karki, S.; Friščić, T.; Jones, W.; Motherwell, W. D. S., Screening for Pharmaceutical Cocrystal Hydrates via Neat and Liquid-Assisted Grinding.

- Mol. Pharmaceutics* **2007**, 4, (3), 347–354.
- (105) Ying, P.; Yu, J.; Su, W., Liquid-Assisted Grinding Mechanochemistry in the Synthesis of Pharmaceuticals. *Adv. Synth. Catal.* **2021**, 363, (5), 1159–1462.
- (106) Medina, C.; Daurio, D.; Nagapudi, K.; Alvarez-Nunez, F., Manufacture of pharmaceutical co-crystals using twin screw extrusion: a solvent-less and scalable process. *J. Pharm. Sci.* **2010**, 99, (4), 1693–1696.
- (107) Daurio, D.; Medina, C.; Saw, R.; Nagapudi, K.; Alvarez-Núñez, F., Application of Twin Screw Extrusion in the Manufacture of Cocrystals, Part I: Four Case Studies. *Pharmaceutics* **2011**, 3, 582–600.
- (108) Panzade, P. S.; Shendarkar, G. R.; Kulkarni, D. A., Hot Melt Extrusion: an Emerging Green Technique for the Synthesis of High-Quality Pharmaceutical Cocrystals. *J. Pharm. Innov.* **2022**, 17, 283–293.
- (109) Gajda, M.; Nartowski, K. P.; Pluta, J.; Karolewicz, B., Continuous, one-step synthesis of pharmaceutical cocrystals via hot melt extrusion from neat to matrix-assisted processing - State of the art. *Int. J. Pharm.* **2019**, 558, 426–440.
- (110) Karimi-Jafari, M.; Ziaee, A.; Iqbal, J.; O'Reilly, E.; Croker, D.; Walker, G., Impact of polymeric excipient on cocrystal formation via hot-melt extrusion and subsequent downstream processing. *Int. J. Pharm.* **2019**, 566, 745–755.
- (111) Jia, Q.; Wang, J.; Zhang, S.; Zhang, J.; Liu, N.; Kou, K., Investigation of the solid–liquid ternary phase diagrams of 2HNIW·HMX cocrystal. *RSC Adv.* **2021**, 11, 9542–9549.
- (112) Holaň, J.; Stěpánek, F.; Billot, P.; Ridvan, L., The construction, prediction and measurement of co-crystal ternary phase diagrams as a tool for solvent selection. *Eur. J. Pharm. Sci.* **2014**, 63, (15), 124–131.

- (113) Chiarella, R. A.; Davey, R. J.; Peterson, M. L., Making Co-Crystals The Utility of Ternary Phase Diagrams. *Cryst. Growth Des.* **2007**, 7, (7), 1223–1226.
- (114) Bag, P. P.; Patni, M.; Reddy, C. M., A kinetically controlled crystallization process for identifying new co-crystal forms: fast evaporation of solvent from solutions to dryness. *CrystEngComm* **2011**, 13, 5650–5652.
- (115) Khandavilli, U. B. R.; Skořepová, E.; Sinha, A. S.; Bhogala, B. R.; Maguire, N. M.; Maguire, A. R.; Lawrence, S. E., Cocrystals and a Salt of the Bioactive Flavonoid: Naringenin. *Cryst. Growth Des.* **2018**, 18, (8), 4571–4577.
- (116) Xuan, B.; Wong, S. N.; Zhang, Y.; Weng, J.; Tong, H. H. Y.; Wang, C.; Sun, C. C.; Chow, S. F., Extended Release of Highly Water Soluble Isoniazid Attained through Cocrystallization with Curcumin. *Cryst. Growth Des.* **2020**, 20, (3), 1951–1960.
- (117) Ghosh, M.; Sikder, A. K.; Banerjee, S.; Gonnade, R. G., Studies on CL-20/HMX (2:1) Cocrystal: A New Preparation Method and Structural and Thermokinetic Analysis. *Cryst. Growth Des.* **2018**, 18, (7), 3781–3793.
- (118) Biscaia, I. F. B.; Gomes, S. N.; Bernardi, L. S.; Oliveira, P. R., Obtaining Cocrystals by Reaction Crystallization Method: Pharmaceutical Applications. *Pharmaceutics* **2021**, 13, (6), 898.
- (119) Shimpi, M. R.; Alhayali, A.; Cavanagh, K. L.; Rodríguez-Hornedo, N.; Velaga, S. P., Tadalafil–Malonic Acid Cocrystal: Physicochemical Characterization, pH-Solubility, and Supersaturation Studies. *Cryst. Growth Des.* **2018**, 18, (8), 4378–4387.
- (120) Cavanagh, K. L.; Maheshwari, C.; Rodríguez-Hornedo, N., Understanding the Differences Between Cocrystal and Salt Aqueous Solubilities. *J. Pharm.*

- Sci* **2018**, 107, (1), 113–120.
- (121) Munshi, T.; Redha, B.; Feeder, N.; Meenan, P.; Blagde, N., Impact of Mixed Solvent on Co-Crystal Solubility, Ternary Phase Diagram, and Crystallization Scale Up. *Cryst. Growth Des.* **2016**, 16, (4), 1817–1823.
- (122) Madane, K.; Ranade, V. V., Anti-solvent crystallization: Particle size distribution with different devices. *J. Chem. Eng.* **2022**, 446, (15), 137235.
- (123) Shahid, M.; Sanxaridou, G.; Ottoboni, S.; Lue, L.; Price, C., Exploring the Role of Anti-solvent Effects during Washing on Active Pharmaceutical Ingredient Purity. *Org. Process Res. Dev.* **2021**, 25, (4), 969–981.
- (124) Park, M.-W.; Yeo, S.-D., Antisolvent crystallization of carbamazepine from organic solutions. *Chem. Eng. Res. Des.* **2012**, 90, (12), 2202–2208.
- (125) Pawar, N.; Saha, A.; Nandan, N.; Parambil, J. V., Solution Cocrystallization: A Scalable Approach for Cocrystal Production. *Crystals* **2021**, 11, (3), 303.
- (126) Wang, I.-C.; Lee, M.-J.; Sim, S.-J.; Kim, W.-S.; Chun, N.-H.; J. Choi, G., Anti-solvent co-crystallization of carbamazepine and saccharin. *Int. J. Pharm* **2013**, 450, (1-2), 311–322.
- (127) Ober, C. A.; Gupta, R. B., Formation of Itraconazole–Succinic Acid Cocrystals by Gas Antisolvent Cocrystallization. *AAPS PharmSciTech* **2012**, 13, (4), 1396–1406.
- (128) Haskins, M. M.; Zaworotko, M. J., Screening and Preparation of Cocrystals: A Comparative Study of Mechanochemistry vs Slurry Methods. *Cryst. Growth Des.* **2021**, 21, (7), 4141–4150.
- (129) Zhang, S.-W.; Brunskill, A. P. J.; Schwartz, E.; Sun, S., Celecoxib–Nicotinamide Cocrystal Revisited: Can Entropy Control Cocrystal Formation? *Cryst. Growth Des.* **2017**, 17, (5), 2836–2843.

- (130) Soares, F. L. F.; Carneiro, R. L., In-line monitoring of cocrystallization process and quantification of carbamazepine-nicotinamide cocrystal using Raman spectroscopy and chemometric tools. *Spectrochim. Acta A Mol. Biomol. Spectrosc.* **2017**, 180, 1–8.
- (131) Rodríguez-Spong, B.; Price, C. P.; Jayasankar, A.; Matzger, A. J.; Rodríguez-Hornedo, N., General principles of pharmaceutical solid polymorphism: a supramolecular perspective. *Adv. Drug Deliv. Rev.* **2004**, 56, (3), 241–274.
- (132) Practical Purity Determination by DSC. *PerkinElmer*
https://resources.perkinelmer.com/labsolutions/resources/docs/app_011667_a_01_practical_purity_determination_by_dsc.pdf.
- (133) Cassel, R.B., High Heating Rate DSC. TA Instruments
<https://www.tainstruments.com/pdf/literature/TA297.pdf>.
- (134) Saganowska, P.; Wesolowski, M., DSC as a screening tool for rapid co-crystal detection in binary mixtures of benzodiazepines with co-formers. *J. Therm. Anal. Calorim.* **2018**, 133, 785–795.
- (135) Zhang, S.-W.; Guzei, I. A.; Villiers, M. M. d.; Yu, L.; Krzyzaniak, J. F., Formation Enthalpies and Polymorphs of Nicotinamide–R-Mandelic Acid Co-Crystals. *Cryst. Growth Des.* **2012**, 12, (8), 4090–4097.
- (136) Grecu, T.; Prohens, R.; McCabe, J. F.; Carrington, E. J.; Wright, J. S.; Brammer, L.; Hunter, C. A., Cocrystals of spironolactone and griseofulvin based on an in silico screening method. *CrystEngComm* **2017**, 19, 3592–3599.
- (137) Ali, H. R. H.; Alhalaweh, A.; Mendes, N. F. C.; Ribeiro-Claro, P.; Velaga, S. P., Solid-state vibrational spectroscopic investigation of cocrystals and salt of indomethacin. *CrystEngComm* **2012**, 14, 6665–6674.
- (138) Ohta, R.; Ueno, Y.; Ajito, K., Raman Spectroscopy of Pharmaceutical

- Cocrystals in Nanosized Pores of Mesoporous Silica. *Anal. Sci* **2017**, 33, (1), 47–52.
- (139) Rodríguez-Hornedo, N.; Nehm, S. J.; Seefeldt, K. F.; Pagán-Torres, Y.; Falkiewicz, C. J., Reaction Crystallization of Pharmaceutical Molecular Complexes. *Mol. Pharm.* **2006**, 3, (3), 362–367.
- (140) Kenneth, S., Analytical Techniques in the Pharmaceutical Sciences: An Overview of Powder X-ray Diffraction and Its Relevance to Pharmaceutical Crystal Structures. *Advances in Delivery Science and Technology*. Springer: **2016**.
- (141) Perlovich, G. L., Thermodynamic characteristics of cocrystal formation and melting points for rational design of pharmaceutical two-component systems. *CrystEngComm* **2015**, 17, 7019–7028.
- (142) Luo, Y.; Sun, B., Pharmaceutical Co-Crystals of Pyrazinecarboxamide (PZA) with Various Carboxylic Acids: Crystallography, Hirshfeld Surfaces, and Dissolution Study. *Cryst. Growth Des.* **2013**, 13, (5), 2098–2106.
- (143) Jung, J. Y.; Yoo, S. D.; Lee, S. H.; Kim, K. H.; Yoon, D. S.; Lee, K. H., Enhanced solubility and dissolution rate of itraconazole by a solid dispersion technique. *Int. J. Pharm.* **1999**, 187, 209–218.
- (144) Kang, J.; Kumar, V.; Yang, D.; Chowdhury, P. R.; Hohl, R. J., Cyclodextrin complexation: influence on the solubility, stability, and cytotoxicity of camptothecin, an antineoplastic agent. *Eur. J. Pharm. Biopharm.* **2002**, 15, 163–170.
- (145) Luo, C.; Liang, W.; Chen, X.; Wang, J.; Deng, Z.; Zhang, H., Pharmaceutical cocrystals of naringenin with improved dissolution performance. *CrystEngComm* **2018**, 20, 3025–3033.

- (146) Price, G.; Patel, D. A., ed.; Drug Bioavailability. In: StatPearls [Internet]. Treasure Island (FL): StatPearls Publishing; **2023**. Available from: <https://www.ncbi.nlm.nih.gov/books/NBK557852/>
- (147) Smith, A. J.; Kavuru, P.; Wojtas, L.; Zaworotko, M. J.; Shytle, R. D., Cocrystals of quercetin with improved solubility and oral bioavailability. *Mol. Pharm.* **2011**, 8, (5), 1867–1876.
- (148) Wang, J. R.; Zhou, C.; Yu, X.; Mei, X., Stabilizing vitamin D(3) by conformationally selective co-crystallization. *Chem. Commun.* **2014**, 50, (7), 855–858.
- (149) Zhou, Z.; Li, W.; Sun, W. J.; Lu, T.; Tong, H. H. Y.; Sun, C. C.; Zheng, Y., Resveratrol cocrystals with enhanced solubility and tabletability. *Int. J. Pharm.* **2016**, 509, (1-2), 391–399.
- (150) Drebushchak, T. N.; Boldyreva, E. V., Variable temperature (100–360 K) single-crystal X-ray diffraction study of the orthorhombic polymorph of paracetamol (p-hydroxyacetanilide). *Z. Kristallogr.* **2004**, 219, 506–512.
- (151) Burley, J. C.; Duer, M. J.; Stein, R. S.; Vrceelj, R. M., Enforcing Ostwald's rule of stages: isolation of paracetamol forms III and II. *Eur. J. Pharm. Sci.* **2007**, 31, (5), 271–276.
- (152) Wilson, C. C., Variable temperature study of the crystal structure of paracetamol (p-hydroxyacetanilide), by single crystal neutron diffraction. *Z. Kristallogr.* **2000**, 215, 693–701.
- (153) Karki, S.; Friščić, T.; Fábíán, L.; Laity, P. R.; Day, G. M.; Jones, W., Improving Mechanical Properties of Crystalline Solids by Cocrystal Formation: New Compressible Forms of Paracetamol. *Adv. Mater.* **2009**, 21, (38-39), 3905–3909.

- (154) Younis, O.; Sayed, M.; Mohammed, A. A. K.; Tolba, M. S.; Hassanien, R.; El-Dean, A. M. K.; Tsutsumi, O.; Ahmed, M., Solid-State Luminescent Materials Containing Both Indole and Pyrimidine Moieties: Design, Synthesis, and Density Functional Theory Calculations. *ACS Omega* **2022**, 7, (17), 15016–15026.
- (155) Liu, Y.; Li, A.; Xu, S.; Xu, W.; Liu, Y.; Tian, W.; Xu, B., Reversible Luminescent Switching in an Organic Cocrystal: Multi-Stimuli-Induced Crystal-to-Crystal Phase Transformation. *Angew. Chem. Int. Ed.* **2020**, 59, 15098.
- (156) Zhang, T.; Wang, X.; Zhou, H.; He, Y., Screening and fluorescence investigation on favipiravir cocrystal. *Mol. Cryst. Liq.* **2022**, 732, (1), 102–117.
- (157) Huang, S.; Xu, J.; Peng, Y.; Guo, M.; Cai, T., Facile Tuning of the Photoluminescence and Dissolution Properties of Phloretin through Cocrystallization. *Cryst. Growth Des.* **2019**, 19, (12), 6837–6844.
- (158) Mislow, K., Stereochemical Terminology and Its Discontents. *Chirality* **2002**, 14, 126–134.
- (159) Brooks, W. H.; Guida, W. C.; Daniel, K. G., The Significance of Chirality in Drug Design and Development. *Curr. Top. Med. Chem.* **2011**, 11, (7), 760–770.
- (160) Nguyen, L. A.; He, H.; Pham-Huy, C., Chiral Drugs: An Overview. *Int. J. Biomed. Sci.* **2006**, 2, (2), 85–100.
- (161) Báthori, N. B.; Jacobs, A.; Nassimbeni, L. R.; Sebogisi, B. K., Quininium Malates: Partial Chiral Discrimination via Diastereomeric Salt Formation. *S. Afr. J. Chem.* **2014**, 67, 160–166.

- (162) Pàmies, O.; Bäckvall, J.-E., Enzymatic Kinetic Resolution and Chemoenzymatic Dynamic Kinetic Resolution of δ -Hydroxy Esters. An Efficient Route to Chiral δ -Lactones. *J. Org. Chem.* **2002**, *67*, (4), 1261–1265.
- (163) Leonard, W. R., Jr.; Henderson, D. W.; Miller, R. A.; Spencer, G. A.; Sudah, O. S.; Biba, M.; Welch, C. J., Strategic use of preparative chiral chromatography for the synthesis of a preclinical pharmaceutical candidate. *Chirality* **2007**, *19*, (9), 693–700.
- (164) Mudi, S. Y.; Muhammad, A., Chiral chromatography and its application to the pharmaceutical industry: A review. *Chemsearch Journal* **2011**, *2*, (1), 8–11.
- (165) Harmsen, B.; Leyssens, T., Enabling Enantiopurity: Combining Racemization and Dual-Drug Co-crystal Resolution. *Cryst. Growth Des.* **2018**, *18*, (6), 3654–3660.
- (166) Putman, J. I.; Armstrong, D. W., Recent advances in the field of chiral crystallization. *Chirality* **2022**, *34*, (10), 1338–1354.
- (167) Córdova-Villanueva, E. N.; Rodríguez-Ruiz, C.; Sánchez-Guadarrama, O.; Rivera-Islas, J.; Herrera-Ruiz, D.; Morales-Rojas, H.; Höpfl, H., Diastereomeric Salt Formation by the γ -Amino Acid *RS*-Baclofen and *L*-Malic Acid: Stabilization by Strong Heterosynthons Based on Hydrogen Bonds between RNH^{3+} and COOH/COO^- Groups. *Cryst. Growth Des.* **2018**, *18*, (12), 7356–7367.
- (168) Bereczki, L.; Pálovics, E.; Bombicz, P.; Pokol, G.; Fogassy, E.; Marthi, K., Optical resolution of *N*-formylphenylalanine succeeds by crystal growth rate differences of diastereomeric salts. *Tetrahedron: Asymmetry* **2007**, *18*, (2), 260–264.

- (169) Guangyou, Z.; Yuqing, L.; Zhaohui, W.; Nohira, H.; Hirose, T., Resolution of β -aminoalcohols and 1,2-diamines using fractional crystallization of diastereomeric salts of dehydroabiatic acid. *Tetrahedron: Asymmetry* **2003**, 14, (21), 3297–3300.
- (170) Sánchez-Guadarrama, O.; Mendoza-Navarro, F.; Cedillo-Cruz, A.; Jung-Cook, H.; Arenas-García, J. I.; Delgado-Díaz, A.; Herrera-Ruiz, D.; Morales-Rojas, H.; Höpfl, H., Chiral Resolution of *RS*-Praziquantel via Diastereomeric Co-Crystal Pair Formation with L-Malic Acid. *Cryst. Growth Des.* **2015**, 16, (1), 307–314.
- (171) Springuel, G.; Robeyns, K.; Norberg, B.; Wouters, J.; Leyssens, T., Cocrystal Formation between Chiral Compounds: How Cocrystals Differ from Salts. *Cryst. Growth Des.* **2014**, 14, (8), 3996–4004.
- (172) Harmsen, B.; Leyssens, T., Dual-Drug Chiral Resolution: Enantiospecific Cocrystallization of (*S*)-Ibuprofen Using Levetiracetam. *Cryst. Growth Des.* **2017**, 18, (1), 441–448.
- (173) Cugovčan, M.; Jablan, J.; Lovrić, J.; Cinčić, D.; Galić, N.; Jug, M., Biopharmaceutical characterization of praziquantel cocrystals and cyclodextrin complexes prepared by grinding. *J. Pharm. Biomed. Anal.* **2017**, 137, 42–53.



Chapter 2 Exploring the Crystal Structure Landscape of Sulfasalazine through Various Multi-component Crystals

(Cryst. Growth Des. **2023**, 23, 8, 5446–5461)



2.1 Abstract

Sulfasalazine is used as an anti-inflammatory drug to treat large intestine diseases and atrophic arthritis. In the solid state two tautomers are known: an amide tautomer (triclinic polymorph) and an imide tautomer (monoclinic polymorph). Crystallization of six new multi-component solids of sulfasalazine with three cocrystal formers and three salt formers has been achieved by slurry, liquid-assisted grinding and slow evaporation methods. All the solid forms were characterized by X-ray diffraction techniques, thermal analysis, and Fourier transform infrared spectroscopy. The crystal structural analysis reveals that two sulfasalazine molecules or anions arrange in a head-to-head fashion involving their pyridyl, amide and sulfonyl groups in an $R_2^2(7):R_2^2(8):R_2^2(7)$ motif. This is the key structural unit appearing in both the sulfasalazine imide polymorph and all six multi-component crystals. In addition, sulfasalazine exists in the amide form in all unsolvated multi-component crystals obtained in this work, and adopts the imide tautomer in the solvated cocrystals and salt. Hirshfeld surface analysis and the associated 2D fingerprint plots demonstrate that sulfasalazine has significant hydrogen bond donor capability when cocrystallized and is a significant hydrogen bond acceptor in the salts. The frontier molecular orbitals analysis indicates sulfasalazine cocrystals are chemically more stable than the salts.

2.2 Introduction

Sulfasalazine (SSZ, Figure 2.1), a conjugate of an anti-inflammatory drug, 5-aminosalicylic acid, and an anti-bacterial drug, sulfapyridine, is successfully used as a disease-modifying anti-rheumatic drug to treat large intestine diseases

and atrophic arthritis.¹ As one of the sulfonamide compounds containing a pyridine or pyrimidine moiety, SSZ can adopt two different tautomeric conformations in its crystal forms. The first reported tautomer of SSZ was the triclinic amide form, which was obtained from ethanol by recrystallization;² while the monoclinic imide tautomer was obtained by cooling after heating an ethanolic solution of SSZ in a Teflon-lined stainless-steel autoclave.³ The migration of a hydrogen atom, accompanied by the switch of a single bond and adjacent double bond significantly alters the crystal packing and intermolecular interactions of these two tautomers.

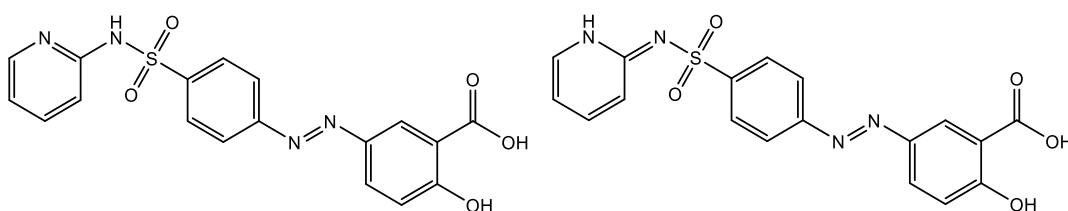


Figure 2.1. The amide form of sulfasalazine observed in the triclinic polymorph, left, and the imide form seen in the monoclinic polymorph, right.

To further investigate the molecular arrangements and hydrogen bonding motifs in different SSZ crystal forms a detailed analysis of the crystal structures of the known SSZ amide and imide forms was conducted. The hydrogen-bonded network and π - π interactions of the amide polymorph are presented in Figures 2.2 and S2.7(a), respectively, and the corresponding hydrogen bond and π - π interaction data are displayed in Table S2.2. Two SSZ molecules are assembled in a head-to-tail fashion through discrete N-H \cdots O and O-H \cdots N hydrogen bonds (taking the pyridyl group as the head and the carboxyl acid group as the tail), generating binary

level $R_2^2(8)$ and $R_2^2(28)$ motifs (Figure 2.2a). The structure is extended through C–H \cdots O discrete hydrogen bonds, forming an $R_2^2(14)$ motif (Figure 2.2b).

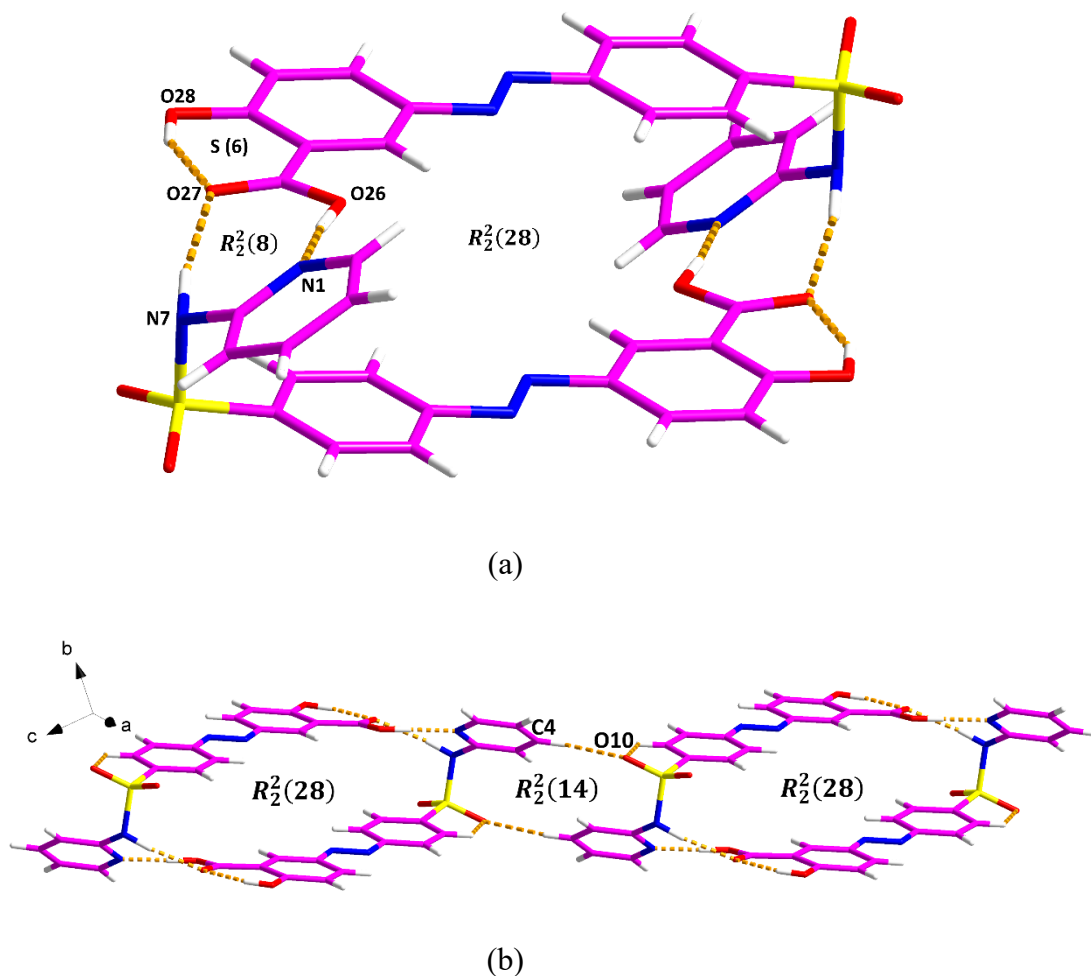


Figure 2.2. Crystal packing and intermolecular interactions in the SSZ amide form: (a) the $R_2^2(8)$ and $R_2^2(28)$ motifs and (b) the $R_2^2(14)$ motif.

In contrast, in the structure of the imide form pairs of SSZ molecules are arranged in a head-to-head manner (Figure 2.3 and Table S2.3). The two SSZ molecules are linked via a N–H \cdots N discrete hydrogen bond and a C–H \cdots O discrete hydrogen bond, generating an $R_2^2(7):R_2^2(8):R_2^2(7)$ motif (Figure 2.3a). Additional C–H \cdots O discrete hydrogen bond form an $R_2^2(14)$ motif (Figure 2.3b). Furthermore, the π –

π interactions between two pyridyl rings from SSZ also contribute to the extended crystal packing (Figure S2.7b).

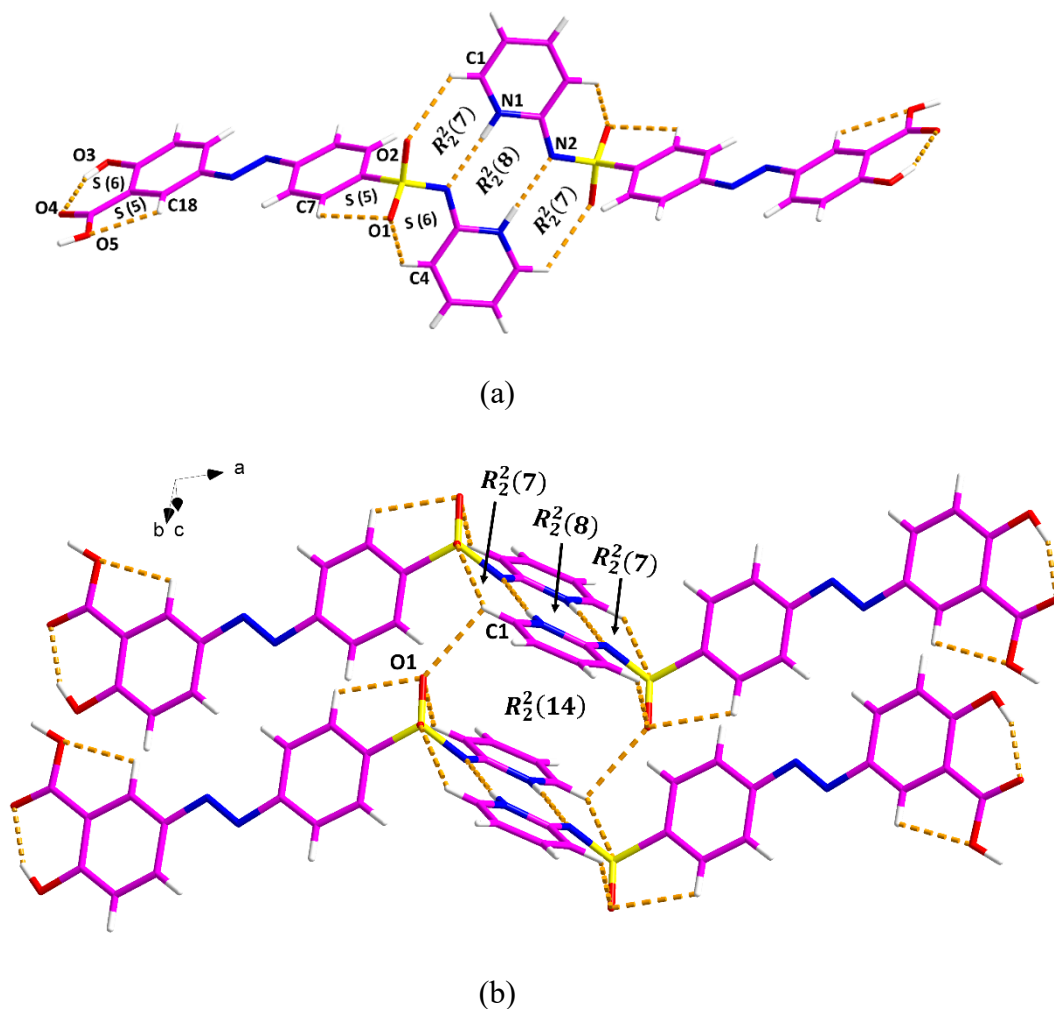


Figure 2.3. Crystal packing and intermolecular interactions in the SSZ monoclinic imide form: (a) the $R_2^2(7):R_2^2(8):R_2^2(7)$ motif and (b) the $R_2^2(14)$ motif.

Sulfasalazine has low solubility and permeability and is a class IV drug⁴ using the Biopharmaceutics Classification System.⁵ Different approaches have been investigated to improve its bioavailability. For example, Shadid *et al.* successfully improved the solubility and bioavailability of SSZ by ionic liquid formation.⁶ Priyam and co-workers synthesized an amphiphilic derivative of SSZ to modify

the solubility by conjugating it with polyethylene glycol.⁷ In addition, nanocrystallization,⁸ solid dispersion⁹ and noisome techniques¹⁰ have been explored to improve the solubility and / or dissolution performance of SSZ.

During the past decades, crystal engineering has developed for predicting and designing the crystals that contain more than one molecule, for example cocrystals and salts.¹¹⁻¹⁴ A significant driver has been the design of improved drugs with optimal physicochemical properties. Cocrystals are multi-component crystalline materials of two or more different molecular and / or ionic compounds in a stoichiometric ratio that are neither solvates nor simple salts.¹⁵ They are generally assembled via hydrogen bonds,¹⁶ halogen bonds,¹⁷ or π - π stacking.¹⁸ The term pharmaceutical cocrystal has been used when at least one component is an active pharmaceutical ingredient and the others are pharmaceutically acceptable.¹⁹ Similarly, the term pharmaceutical salt has been used for related systems where intermolecular proton transfer has occurred between complementary acid and basic functional groups.²⁰ Empirically, when the ΔpK_a [$\Delta pK_a = pK_a$ (base) - pK_a (acid)] is greater than 4, the two components form a salt, when the ΔpK_a is less than -1, the system results in a cocrystal. When it comes to systems with ΔpK_a between -1 and 4, a linear relationship between ΔpK_a and the probability of proton transfer between two components were derived.^{21, 22} Other techniques are required for distinguishing crystal forms, for instance, by using solid-state nuclear magnetic resonance,²³ vibrational spectroscopy,²⁴ and single crystal X-ray diffraction (SCXRD).²⁵

From the crystal engineering perspective, SSZ would be expected to readily form cocrystals or salts because it has multiple functional groups, with multiple hydrogen bond donor and acceptor sites. Four multi-component crystalline

materials of SSZ have been reported: SSZ-trimethoprim (one cocrystal and one salt), SSZ-nicotinamide cocrystal and SSZ-theobromine cocrystal. They all have enhanced dissolution performance compared with pure SSZ,^{26,27} however, none of their crystal structures are available in version 2022.2.0 of the Cambridge Structural Database (CSD).²⁸

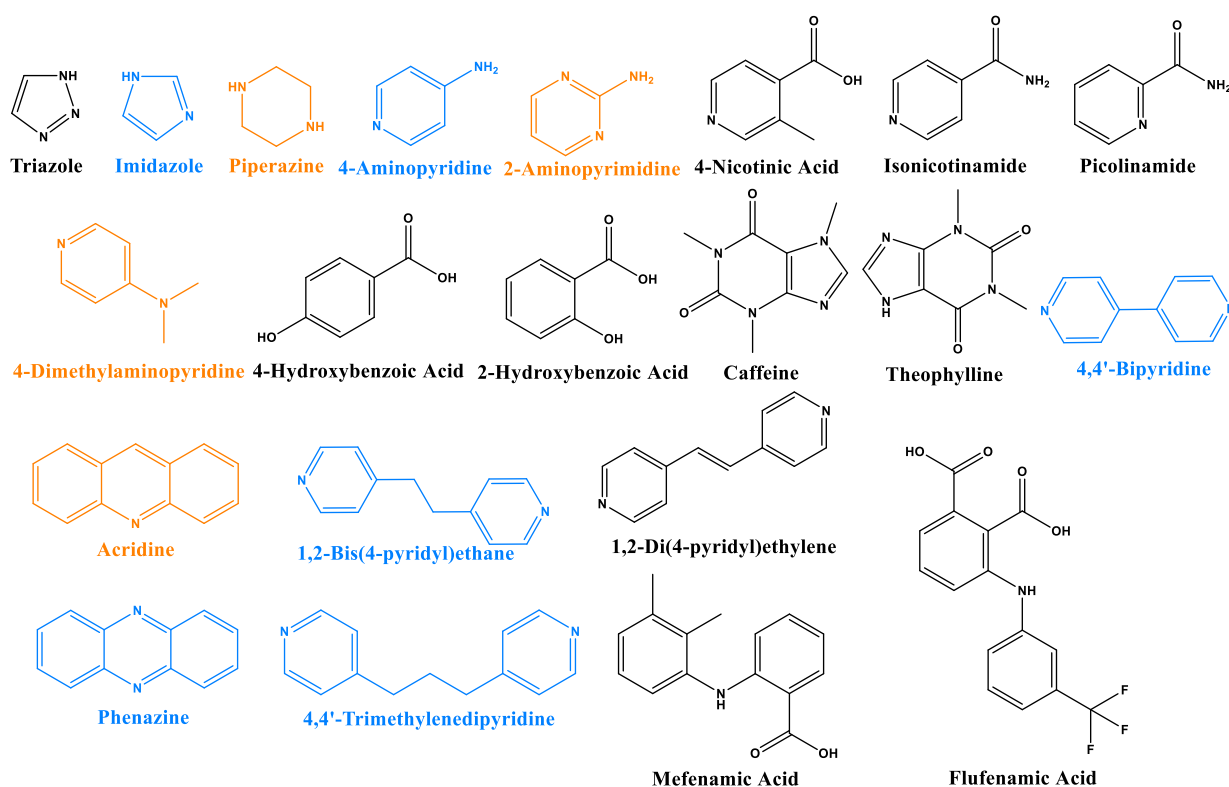


Figure 2.4. Cocrystal formers and salt formers investigated in this study (successful cocrystal / salt formers analysed by SCXRD in blue, successful cocrystal/salt formers based on PXRD in orange, unsuccessful cocrystal / salt formers in black).

Herein, the crystalline form diversity of SSZ with a series of pharmaceutically relevant cocrystal / salt formers (Figure 2.4) was explored. Three cocrystals of SSZ with 4,4'-bipyridine (BPY), 1,2-bis(4-pyridyl) ethane (BPE) and phenazine (PHE),

and three salts of SSZ with 4-aminopyridine (4AP), 4,4'-trimethylenedipyridine (TMD) and imidazole (IMZ) were successfully prepared, fully characterized, and their crystal structures obtained. Four more products of SSZ with piperazine (PPZ), 2-aminopyrimidine (2-APM), 4-dimethylaminopyridine (4-DMP) and acridine (ACRI) were determined as new multi-component crystalline solids by powder X-ray diffraction (PXRD) (Figure S2.5). However, multiple attempts to grow suitable crystals for SCXRD analysis were unsuccessful.

2.3 Experimental Section

2.3.1 Materials

Sulfasalazine (monoclinic imide form) was purchased from Fluorochem and used as received without further purification. Isonicotinamide, mefenamic acid and picolinamide were purchased from TCI chemicals; other cocrystal / salt formers were obtained from Sigma-Aldrich and used as received. Solvents were purchased from Honeywell International, Inc. and used as received.

2.3.2 Solid Form Screening and Crystallization Experiments

2.3.2.1 Liquid-assisted grinding (LAG) method

Mechanical grinding experiments were conducted in a Retsch MM400 Mixer mill, equipped with stainless steel 5 mL grinding jars and one 2.5 mm stainless steel grinding ball per jar. The mill was operated at a rate of 30 Hz for 30 min and the molar ratio of 1:1 / 1:2 / 2:1 of SSZ with cocrystal / salt formers was used. The powdered products were isolated and analyzed by PXRD.¹² Experimental details are displayed in Table S2.1.

2.3.2.2 Slurry method

SSZ and cocrystal / salt formers in a 1:1 / 1:2 / 2:1 molar ratio were slurried in methanol or ethanol for 2-3 days. The resulting suspension was filtered and allowed to dry in the fume hood for up to 24 h. The powdered products were isolated and analyzed by PXRD. Experimental details are displayed in Table S2.1.

2.3.2.3 Solution Crystallization

(SSZ)₂·BPY·(Tol)_{0.8} cocrystal solvate. The powdered product from the 2:1 SSZ:BPY slurry experiment (48.6 mg) was dissolved in 20 mL of toluene-ethanol (1:1, v/v) in a sample vial, covered with perforated parafilm, and left at room temperature until the solvent had almost completely evaporated (~ one week). Red plate-like single crystals were obtained.

(SSZ)₂·BPE·(EtOH)₂ cocrystal solvate. The powdered (SSZ)₂·BPE·(EtOH)₂ (51.1 mg) obtained from slurry experiments was dissolved in 10 mL of ethanol in a sample vial, covered with perforated parafilm, and left at room temperature until the solvent had almost completely evaporated (1-2 weeks). Orange plate-like single crystals were obtained.

(SSZ)₂·PHE cocrystal. The powdered (SSZ)₂·PHE (50.8 mg) obtained from slurry experiments was dissolved in 10 mL of ethanol in a sample vial, covered with perforated parafilm, and left at room temperature until the solvent had almost completely evaporated (1-2 weeks). Orange needle-like single crystals were obtained.

SSZ·4AP salt. The powdered SSZ·4AP (49.6 mg) obtained from slurry experiments was dissolved in 5 mL of methanol in a sample vial, covered with perforated parafilm, and left at room temperature until the solvent had almost

completely evaporated (~ one week). Red plate-like single crystals were obtained. **SSZ·TMD salt.** SSZ (19.9 mg, 0.05 mmol) and TMD (9.9 mg, 0.05 mmol) in a 1:1 molar ratio were dissolved in 10 mL of deionized water in a sample vial and left at room temperature until the solvent had almost completely evaporated (3-4 months). The orange plate-like single crystals of SSZ·TMD salt were obtained on one occasion. Attempts to obtain other crystals or bulk material were unsuccessful. **SSZ·IMZ·MeCN salt solvate.** The powdered product from the 1:1 SSZ: IMZ LAG experiment (49.2 mg) was dissolved in 15 mL of acetonitrile in a sample vial, covered with perforated parafilm, and left at room temperature until the solvent had almost completely evaporated (1-2 weeks). Orange needle-like single crystals were obtained.

2.3.3 Physical Measurements

Differential scanning calorimetry (DSC) data were collected using a TA Instruments Q1000. Samples (2-6 mg) were crimped in nonhermetic aluminum pans and scanned from 25 to 300 °C at a heating rate of 10 °C min⁻¹ under a continuously purged dry nitrogen atmosphere. Thermogravimetric analysis (TGA) data were collected using a TA Instruments Q500 thermogravimetric analyzer. The sample was placed in an aluminum sample pan and heated under nitrogen at a rate of 20 °C min⁻¹ from 25 to 500 °C. IR spectra were recorded on a PerkinElmer UATR Two spectrophotometer using a diamond attenuated total reflectance accessory over a range of 400-4000 cm⁻¹. An average of four scans was taken for each spectrum obtained with a resolution of 4 cm⁻¹. PXRD data were collected using a STOE STADI MP diffractometer with Cu K α radiation using a linear position-sensitive detector over the 2θ range of 3.5-45.5° with an increment of 0.05°

at a rate of 2° min^{-1} . The samples were prepared as transmission foils and the data were viewed via STOE WinXPOW POWDAT software.²⁹ SCXRD data of $(\text{SSZ})_2 \cdot \text{BPY} \cdot (\text{Tol})_{0.8}$ and $(\text{SSZ})_2 \cdot \text{BPE} \cdot (\text{EtOH})_2$ were collected using a Bruker APEX II DUO with monochromated Cu K α radiation ($\lambda = 1.54178 \text{ \AA}$). SCXRD data of the other SSZ cocrystals and salts were collected on a Bruker Quest D8 diffractometer with monochromated Cu K α radiation ($\lambda = 1.54184 \text{ \AA}$). All calculations and refinements were made using Bruker APEX software with the SHELX suite of programs.^{30, 31} Nonhydrogen atoms were refined anisotropically. For $(\text{SSZ})_2 \cdot \text{BPY} \cdot (\text{Tol})_{0.8}$ and $(\text{SSZ})_2 \cdot \text{BPE} \cdot (\text{EtOH})_2$ the N–H hydrogen atoms were located and refined. All other hydrogen atoms were placed in geometrically calculated positions using the riding model, with C–H = 0.93–0.97 \AA and N–H = 0.86–0.89 \AA , and Uiso (H) (in the range 1.2–1.5 times Ueq of the parent atom). DIAMOND was used for creating figures,³² and PLATON was used for the analysis of potential hydrogen bonds and short ring interactions.^{33, 34} Crystallographic parameters are listed in Table 2.1.

2.3.4 Computational Studies

Density functional theory (DFT) calculations using the Gaussian 09 program package employing the M06-2X functional with 6-31+G (d, p) basis set were performed on the six obtained crystals without conducting structural optimization.^{13, 35} The molecular orbitals were viewed using Multiwfn 3.8 program and plotted by VMD.^{36, 37} Hirshfeld surface analyses and 2D fingerprint plots were carried out using the CrystalExplorer 21.5 program.³⁸

Table 2.1. Crystallographic data for SSZ cocrystals and salts.

Crystallographic data	(SSZ) ₂ ·BPY·(Tol) _{0.8}	(SSZ) ₂ ·BPE·(EtOH) ₂	(SSZ) ₂ ·PHE	SSZ·4AP	SSZ·TMD	SSZ·IMZ·MeCN
Chemical formula	C _{51.6} H _{42.4} N ₁₀ O ₁₀ S ₂	C ₂₆ H ₂₆ N ₅ O ₆ S	C ₂₄ H ₁₈ N ₅ O ₅ S	C ₂₃ H ₂₀ N ₆ O ₅ S	C ₃₁ H ₂₈ N ₆ O ₅ S	C ₂₃ H ₂₁ N ₇ O ₅ S
Formula weight	1026.67	536.58	488.49	492.51	596.65	507.53
Crystal system	monoclinic	triclinic	monoclinic	triclinic	triclinic	monoclinic
Space group, <i>Z</i>	<i>P</i> 2/ <i>n</i> , 2	<i>P</i> $\bar{1}$, 2	<i>C</i> 2/ <i>c</i> , 8	<i>P</i> $\bar{1}$, 4	<i>P</i> $\bar{1}$, 2	<i>P</i> 2 ₁ / <i>c</i> , 4
Temperature (K)	296(2)	296(2)	293(2)	293(2)	298(2)	302(2)
<i>a</i> (Å)	14.2397(5)	8.7750(7)	7.683(5)	10.7519(17)	7.826(13)	25.134(3)
<i>b</i> (Å)	6.4706(2)	12.8102(10)	33.62(3)	15.5563(18)	13.715(17)	10.0917(14)
<i>c</i> (Å)	26.7698(9)	12.9300(10)	22.610(9)	15.7326(17)	15.243(18)	9.409(2)
<i>α</i> (°)	90	68.159(3)	90	64.838(7)	64.54(10)	90
<i>β</i> (°)	90.5000(10)	77.234(4)	98.78(2)	74.725(10)	81.12(7)	91.511(12)
<i>γ</i> (°)	90	82.571(4)	90	87.389(10)	75.13(12)	90
Volume (Å ³)	2466.46(14)	1313.99(18)	5771(6)	2290.9(5)	1426(4)	2385.8(7)
<i>ρ</i> calc (g cm ⁻³)	1.382	1.356	1.124	1.428	1.390	1.413
<i>μ</i> (mm ⁻¹)	1.571	1.524	1.320	1.678	1.449	1.640
Reflns measured	30288	16382	20087	73865	11530	54017
Reflns independent	4321	4409	2835	8952	6638	4714
<i>R</i> _{int}	0.0220	0.0201	0.0491	0.0887	0.0738	0.0629

Significant [$I > 2\sigma(I)$]	4140	3996	2277	5947	1163	4055
Parameters refined	338	366	319	628	390	328
$\Delta\rho_{\max}, \Delta\rho_{\min}$ ($e \text{ \AA}^{-3}$)	0.484, -0.355	0.508, -0.422	0.198, -0.300	1.050, -0.526	0.137, -0.204	0.508, -0.287
$F(000)$	1068	562	2024	1024	624	1056
R_I [$I > 2\sigma(I)$]	0.0473	0.0673	0.0512	0.0872	0.0593	0.0573
wR_2 (all data)	0.1492	0.1988	0.2007	0.2842	0.1647	0.1829
CCDC	2109809	2109810	2109811	2064484	2109807	2109808

2.4 Results and Discussion

2.4.1 Physical Characterization

The thermal behaviour of the SSZ cocrystals / salts was assessed using DSC and TGA techniques. The melting points of $(SSZ)_2 \cdot BPY \cdot (Tol)_{0.8}$, $(SSZ)_2 \cdot BPE \cdot (EtOH)_2$, $SSZ \cdot 4AP$, $SSZ \cdot TMD$ and $SSZ \cdot IMZ \cdot MeCN$ are in between those of the individual components, while $(SSZ)_2 \cdot PHE$ cocrystal melts at a lower temperature than the starting materials (Figure S2.1). Additionally, small endothermic peaks before the melting peaks were observed in the DSC traces for $(SSZ)_2 \cdot BPY \cdot (Tol)_{0.8}$, $(SSZ)_2 \cdot BPE \cdot (EtOH)_2$ and $SSZ \cdot IMZ \cdot MeCN$, indicating the presence of solvent within the crystal lattice, which is consistent with the SCXRD data. This is also supported by the TGA results (Figure S2.2). A weight loss of 6.8% is observed for $(SSZ)_2 \cdot BPY \cdot (Tol)_{0.8}$, which corresponds to 0.8 equivalents of toluene (calculated as 6.7%). For $(SSZ)_2 \cdot BPE \cdot (EtOH)_2$, a weight loss of 8.7%, corresponding to 1 equivalent of EtOH (calculated 8.6%) is observed. Similarly, $SSZ \cdot IMZ \cdot MeCN$ exhibits a significant weight loss of 7.8%, which corresponds to 1 equivalent of MeCN (calculated value is 8.1%). No significant weight loss before the decomposition temperature is observed for the other SSZ solids, suggesting that they are not solvated or hydrated. After cocrystallization of SSZ, the FTIR spectrum (Figure S2.3) of cocrystals and salts showed the shifts in the hydroxyl peak of SSZ from 3027 cm^{-1} to 2974 [$(SSZ)_2 \cdot BPY \cdot (Tol)_{0.8}$], 2978 [$(SSZ)_2 \cdot BPE \cdot (EtOH)_2$], 3059 [$(SSZ)_2 \cdot PHE$], 2980 ($SSZ \cdot 4AP$), 3058 ($SSZ \cdot IMZ \cdot MeCN$), 3052 ($SSZ \cdot TMD$) cm^{-1} , suggesting the formation of new crystalline forms of SSZ, respectively. The PXRD patterns of the $(SSZ)_2 \cdot BPY \cdot (Tol)_{0.8}$, $(SSZ)_2 \cdot BPE \cdot (EtOH)_2$, $(SSZ)_2 \cdot PHE$, $SSZ \cdot 4AP$, and

SSZ·IMZ·MeCN (Figure S2.4) matched with the theoretical patterns obtained from the SCXRD analysis, demonstrating these cocrystals can be reproduced in bulk quantities by the slurry or LAG method. The PXRD pattern of SSZ·TMD cannot be obtained since attempts to synthesize crystals or bulk material of SSZ·TMD were unsuccessful.

Table 2.2. p*K*_a values of SSZ, cocrystal / salt formers and Δp*K*_a values of the new solid forms.

	p <i>K</i> _a	Δp <i>K</i> _a	Solid state
SSZ	2.70 ^a	-	
BPY	3.27 ^a	0.57	2:1 cocrystal solvate
BPE	6.13 ^a	3.43	2:1 cocrystal solvate
PHE	1.60 ^a	-1.10	2:1 cocrystal
4AP	9.17 ³⁹	6.47	1:1 salt
TMD	6.30 ^a	3.60	1:1 salt
IMZ	6.97 ⁴⁰	4.27	1:1:1 salt solvate

^a p*K*_a values were obtained from CAS SciFinderⁿ

As for the solid states of these obtained new crystals, according to the Δp*K*_a rule, (SSZ)₂·PHE is expected to be a cocrystal (Δp*K*_a < -1), while SSZ·4AP and SSZ·IMZ·MeCN are expected to be salts (Δp*K*_a > 4), which are confirmed by the SCXRD results. The solid state of (SSZ)₂·BPY·(Tol)_{0.8}, (SSZ)₂·BPE·(EtOH)₂, and SSZ·TMD could be either salt or cocrystal (-1 < Δp*K*_a < 4), and SCXRD data confirms (SSZ)₂·BPY·(Tol)_{0.8}, (SSZ)₂·BPE·(EtOH)₂ are cocrystals and SSZ·TMD is a salt, which follows the linear relationship proposed by Cruz-Cabeza.²²

2.4.2 Crystal Structures

The structure analyses of the six multi-component systems are presented below. Hydrogen bond and π - π interaction data are displayed in Tables S2.4-S2.9.

(SSZ)₂·BPY·(Tol)_{0.8} Cocrystal Solvate

The (SSZ)₂·BPY·(Tol)_{0.8} crystal has one SSZ molecule and half of the BPY molecule in the asymmetric unit. Disordered toluene is present in voids in the structure. An $R_2^2(7)$ motif is formed by SSZ and BPY molecules through O1–H1···N5 and C23–H23···O2 discrete hydrogen bonds, and the BPY molecule links another SSZ molecule via discrete C20–H20···O4 hydrogen bond. The latter SSZ molecule is involved in two hydrogen bonds (N4–H4N···N3 and C18–H18···O5) with the adjacent SSZ molecule, forming an $R_2^2(7):R_2^2(8):R_2^2(7)$ motif, which leads to the formation of three-dimensional (3D) hydrogen bonded layers (Figure 2.5). The structure is further stabilized by the π - π interactions between the SSZ and SSZ, SSZ and BPY, and SSZ and toluene molecules, Figure S2.8 and Table S2.4.

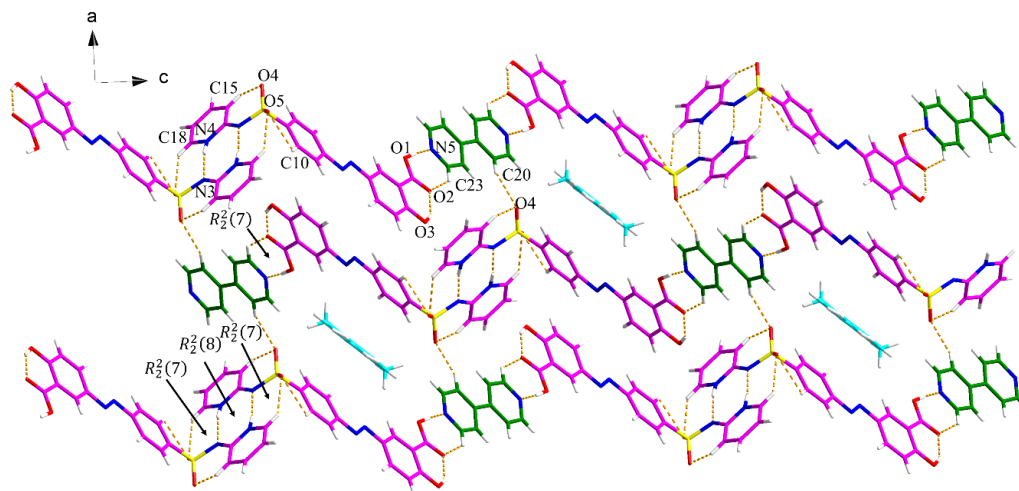
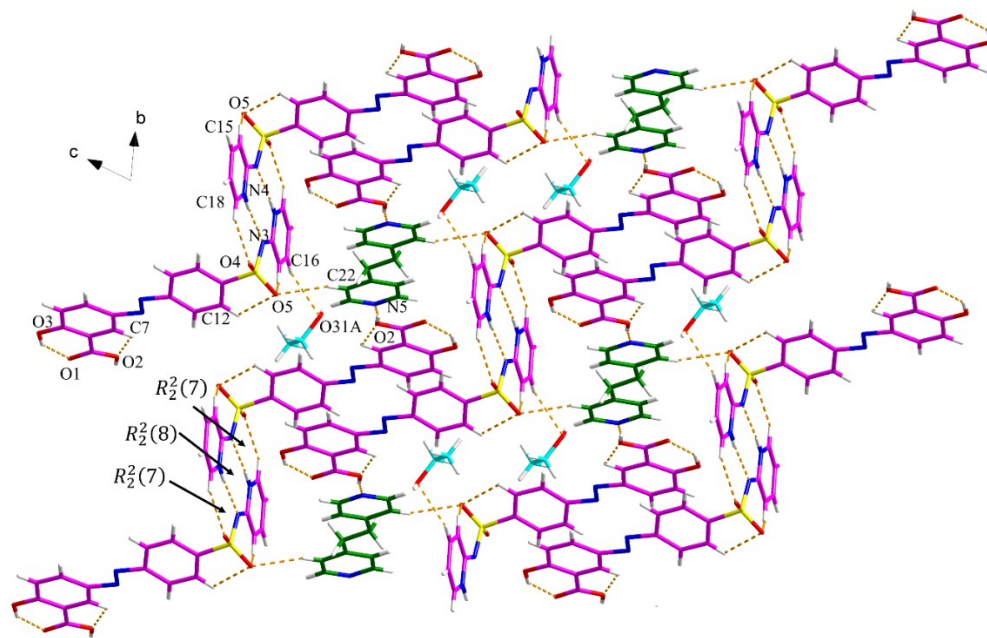


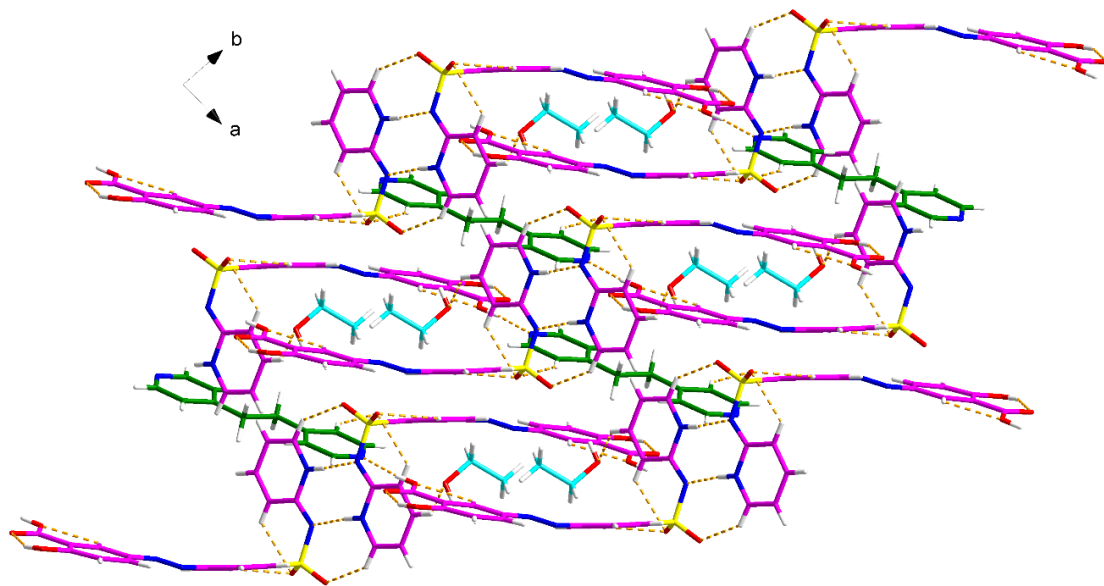
Figure 2.5. Crystal packing and intermolecular interactions in the $(\text{SSZ})_2 \cdot \text{BPY} \cdot (\text{Tol})_{0.8}$ cocrystal solvate (pink is SSZ, green is BPY, and blue is toluene).

$(\text{SSZ})_2 \cdot \text{BPE} \cdot (\text{EtOH})_2$ Cocrystal Solvate

The $(\text{SSZ})_2 \cdot \text{BPE} \cdot (\text{EtOH})_2$ cocrystal solvate crystallizes in the triclinic $P\bar{1}$ space group with one SSZ molecule, half of the BPE molecule, and one EtOH molecule in the asymmetric unit. The SSZ molecule is disordered over the N=N group (75:25), and the EtOH molecule is disordered (75:25). As shown in Figure 2.6a, the BPE molecule links two SSZ molecules through discrete O2–H2···N5 and C22–H22···O5 hydrogen bonds, and the EtOH molecule links one SSZ molecule via C16–H16···O31A hydrogen bonds. Along the *a* axis, the 3D hydrogen bonding network is further stabilized by the $R_2^2(7):R_2^2(8):R_2^2(7)$ motif between two adjacent SSZ molecules. Along the *c* axis, the voids containing EtOH molecules can be observed (Figure 2.6b). Additional π – π interactions between the phenyl rings from SSZ and the pyridyl rings from BPE (Cg2–Cg3, Cg2–Cg4 and Cg4–Cg4) contribute to the extended 3D structure (Figure S2.9, Table S2.5).



(a)

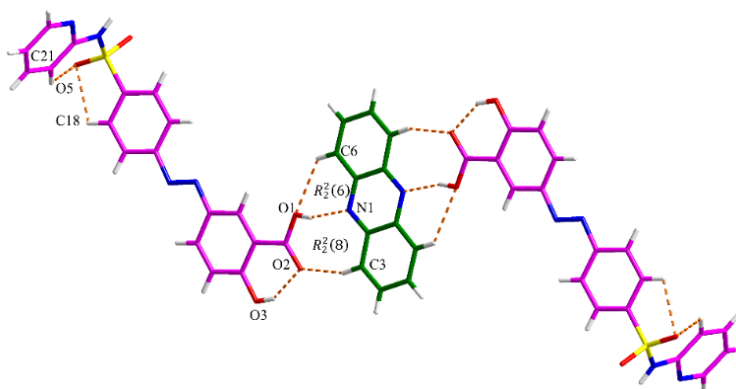


(b)

Figure 2.6. Crystal packing and intermolecular interactions in the $(\text{SSZ})_2 \cdot \text{BPE} \cdot (\text{EtOH})_2$: (a) along the a axis (pink is SSZ, green is BPE, and blue is EtOH), and (b) along the c axis. The minor component of the disordered structure has been omitted for clarity.

(SSZ)₂·PHE Cocrystal

The asymmetric unit of (SSZ)₂·PHE has one SSZ molecule and half of the PHE molecule. PHE and two SSZ molecules form an $R_2^2(6)R_2^2(8)$ motif through C6–H6···O1, O1–H1···N1 and C3–H3···O2 discrete hydrogen bonds (Figure 2.7a). The hydrogen-bonding network is extended through N4–H40···N5 and C24–H24···O4 hydrogen bonds, resulting in the same $R_2^2(7):R_2^2(8):R_2^2(7)$ motif between adjacent SSZ molecules as mentioned previously (Figure 2.7b). In addition, an $R_6^4(32)$ ring is formed via C22–H22···O3 interaction between two SSZ molecules, and an $R_8^8(54)$ ring is formed between six SSZ molecules and two PHE molecules. The π – π interactions between two phenyl rings from SSZ and PHE (Cg2–Cg2, Cg3–Cg5) also contribute to the extended crystal packing (Figure S2.10, Table S2.6).



(a)

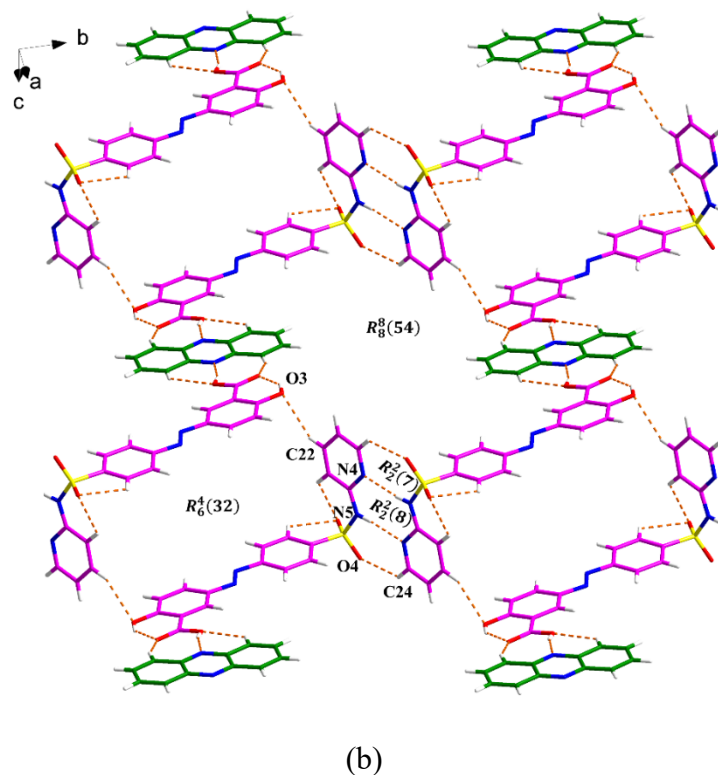
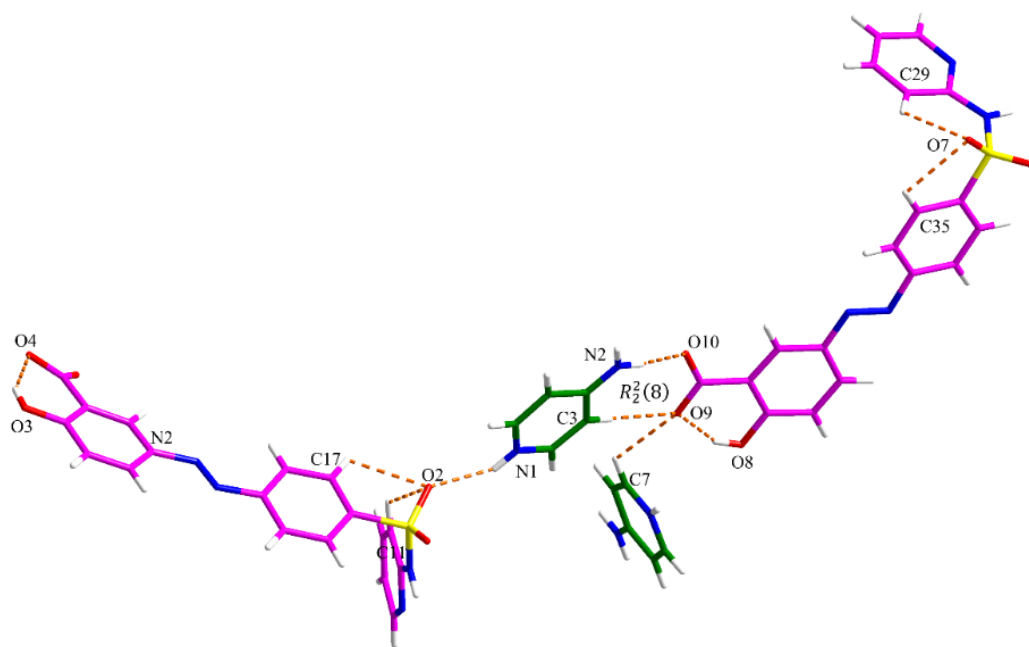


Figure 2.7. Crystal packing and intermolecular interactions in the $(\text{SSZ})_2 \cdot \text{PHE}$: (a) asymmetric unit (pink is SSZ and green is PHE) and (b) hydrogen-bonded network.

SSZ·4AP Salt

The SSZ·4AP salt crystallizes with two SSZ^- anions and two 4AP^+ cations in the asymmetric unit. The proton is transferred from the carboxylic acid group of SSZ to the pyridyl ring of 4AP. SSZ^- and 4AP^+ are linked through $\text{N1-H1N} \cdots \text{O2}$, $\text{C7-H7} \cdots \text{O9}$, $\text{N2-H2A} \cdots \text{O10}$ and $\text{C3-H3} \cdots \text{O9}$ discrete hydrogen bonds, the latter two forming an $R_2^2(8)$ motif (Figure 2.8a). The assembly is further sustained by intermolecular interactions ($\text{C9-H9} \cdots \text{O5}$, $\text{N4-H4B} \cdots \text{O4}$, $\text{N2-H2B} \cdots \text{O5}$, $\text{N3-H3N} \cdots \text{O6}$, $\text{N4-H4A} \cdots \text{O10}$, and $\text{N3-H3N} \cdots \text{O7}$) between two SSZ^- anions and two 4AP^+ cations in the same manner. The two adjacent SSZ^- interact via $\text{N-H} \cdots \text{N}$ and $\text{C-H} \cdots \text{O}$ hydrogen bonds, which constitute

an $R_2^2(7):R_2^2(8):R_2^2(7)$ motif (Figure 2.8b). Additional π - π stacking interactions between adjacent phenyl rings from SSZ^- also contribute to the extended structure (Figure S2.11, Table S2.7).



(a)

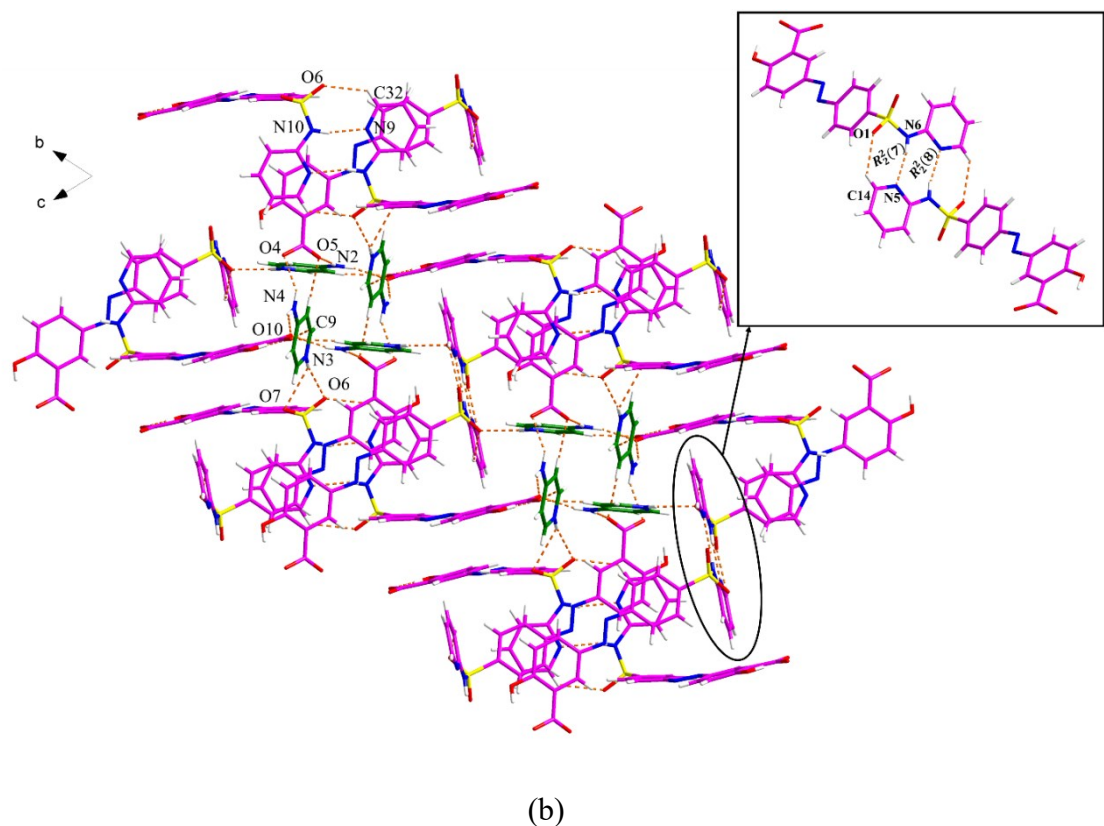


Figure 2.8. Crystal packing and intermolecular interactions in the SSZ·4AP: (a) asymmetric unit (pink is SSZ and green is 4AP) and (b) three-dimensional hydrogen-bonded network.

SSZ·TMD Salt

SSZ and TMD form a salt that crystallizes with one TMD⁺ cation and one SSZ⁻ anion in the asymmetric unit. The two components interact with each other through N5–H5···O5 discrete hydrogen bond (Figure 2.9a). What is interesting is that only in this crystal is the N atom of azo group from SSZ⁻ anion involved in the formation of intermolecular hydrogen bonds, producing an $R_2^2(26)$ motif between two asymmetric units via C24–H24B···N4 hydrogen bond. Two adjacent SSZ⁻ anions connect through N2–H2···N1 and

C1-H1 \cdots O2 hydrogen bonds, forming the same $R_2^2(7):R_2^2(8):R_2^2(7)$ motif as the previous described crystals (Figure 2.9b). As shown in Figure S2.12 and Table S2.8, the packing is further stabilized by the π - π interactions between the phenyl rings from SSZ^- and the pyridyl rings from TMD^+ (Cg2-Cg3, Cg4-Cg4 and Cg5-Cg5).

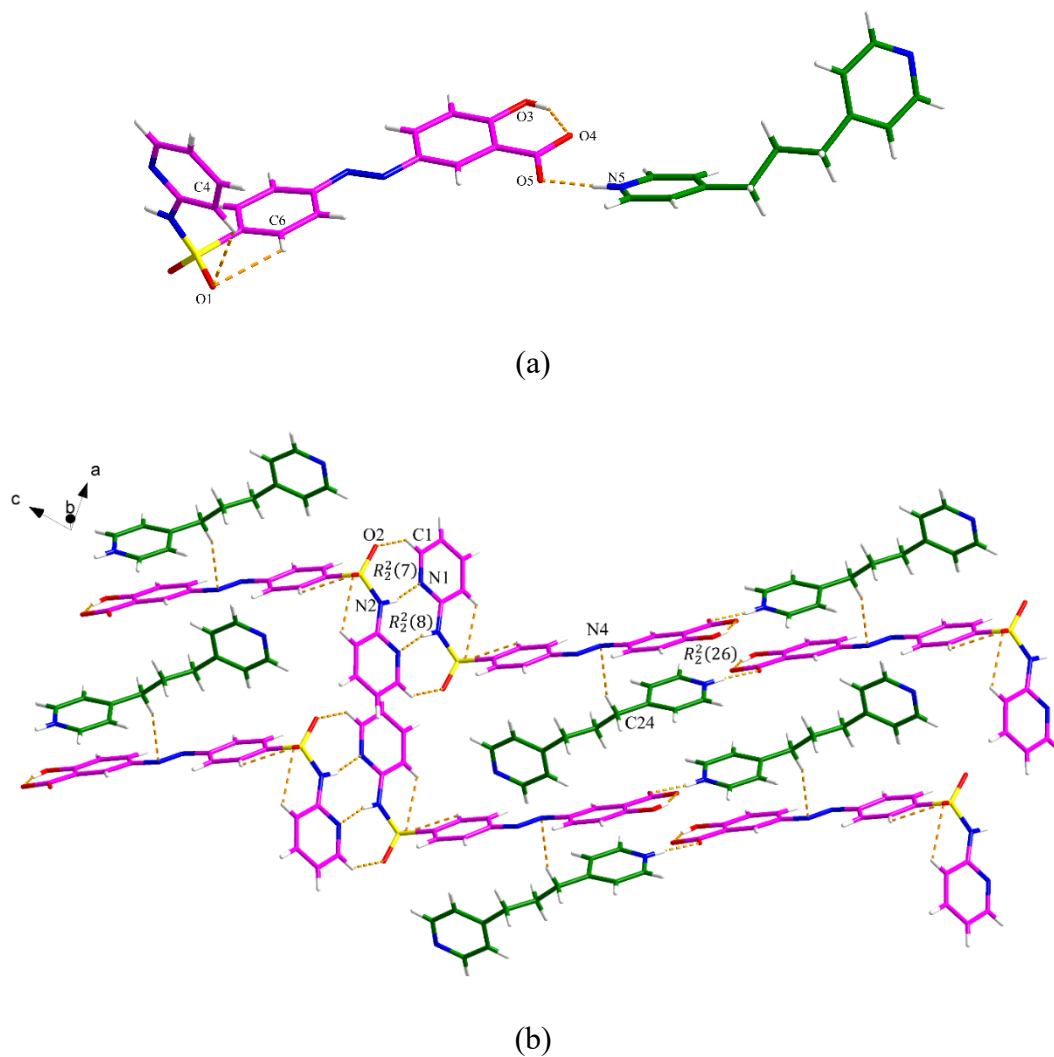
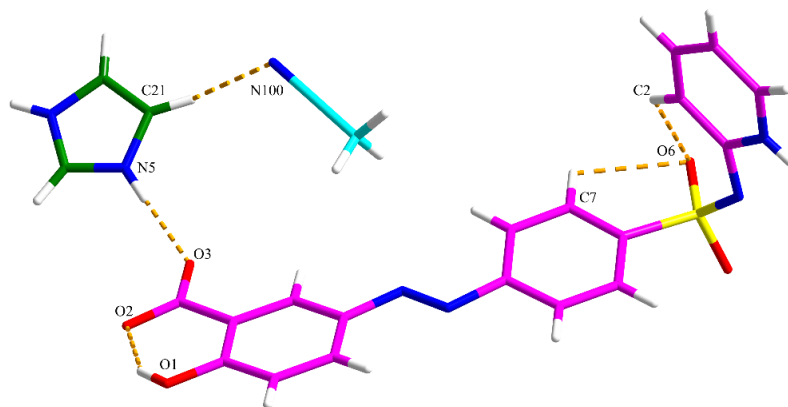


Figure 2.9. Crystal packing and intermolecular interactions in the $\text{SSZ}\cdot\text{TMD}$: (a) asymmetric unit (pink is SSZ^- and green is TMD^+) and (b) hydrogen-bonded network.

SSZ·IMZ·MeCN Salt Solvate

SSZ·IMZ·MeCN salt solvate crystallizes with one SSZ^- anion, one IMZ^+ cation, and one acetonitrile molecule in the asymmetric unit. The proton is transferred from the carboxylic acid of SSZ to the basic nitrogen of the imidazole ring (Figure 2.10a). Along the b axis, the IMZ^+ cation acts as hydrogen bond donors and interacts with SSZ^- and MeCN through $\text{N5-H5A}\cdots\text{O3}$, $\text{N6-H6}\cdots\text{O2}$ and $\text{C21-H21}\cdots\text{N100}$ discrete hydrogen bonds, respectively (Figure 2.10b). In addition, $R_3^3(14)$ and $R_4^4(25)$ motifs are formed via the above interactions and $\text{C100-H10B}\cdots\text{N100}$, $\text{C100-H10C}\cdots\text{O5}$, $\text{C22-H22}\cdots\text{O3}$ hydrogen bonds. The two adjacent SSZ^- anions interact with each other through $\text{C5-H5}\cdots\text{O5}$ and $\text{N1-H1A}\cdots\text{N2}$ hydrogen bonds, forming a related $R_2^2(7):R_2^2(8):R_2^2(7)$ motif. As shown in Figure S2.13 and Table S2.9, the 3D structure is further stabilized by the π - π interactions between the phenyl rings and pyridyl rings from SSZ (Cg1-Cg1 and Cg2-Cg3).



(a)

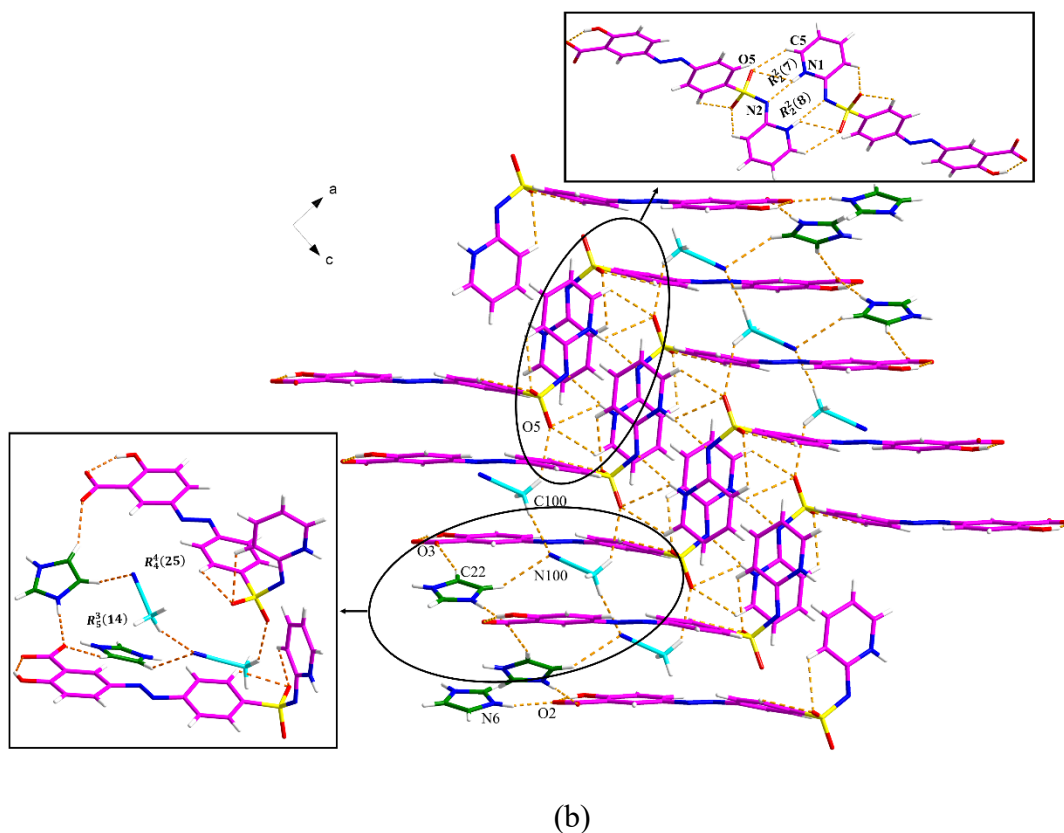


Figure 2.10. Crystal packing and intermolecular interactions in the SSZ·IMZ·MeCN: (a) asymmetric unit (pink is SSZ, green is IMZ, and blue is MeCN) and (b) hydrogen-bonded network.

Overall, the introduction of cocrystal / salt formers have disrupted the hydrogen bonds involving the pairs of SSZ molecules in the imide SSZ, forming six multi-component systems with different molecular arrangements and crystal packings with the $R_2^2(7):R_2^2(8):R_2^2(7)$ motif of pairs of SSZ molecules maintained (Figure 2.11).

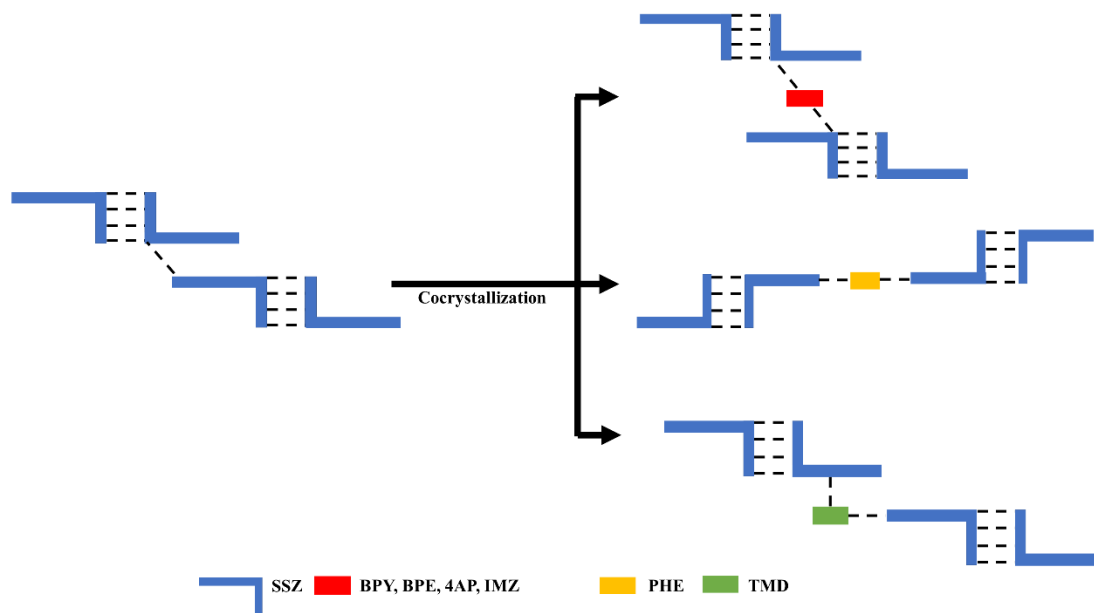


Figure 2.11. Hydrogen bonds in pure SSZ (starting material), left, and the different arrangements with the head-to-head SSZ pairs of molecules, right.

2.4.3 Conformation of SSZ

The starting material SSZ used in this work is in conformation A, where the two intramolecular hydrogen bonds ($C-H \cdots O$ and $O-H \cdots O$) form an $S_2^1(9)$ motif and direct the orientation of the carboxylic acid group (Figure 2.12). The oxygen atom of the sulfonyl group in the amide tautomer of SSZ (conformation B) is involved in one intramolecular hydrogen bonding, forming a four-membered $N-S=O \cdots H$ intramolecular hydrogen bond. SSZ exists in different conformations when cocrystallized with the different cocrystal / salt formers, with the amide tautomer seen in three unsolvated crystals and the imide tautomer seen in the solvated cocrystals and salt. For the $(SSZ)_2 \cdot BPY \cdot (Tol)_{0.8}$ cocrystal solvate, the intramolecular hydrogen bonds $C-H \cdots O=S=O \cdots H-C$ involving both oxygen

atoms of the sulfonyl group lock the conformation of the SSZ molecules (conformation C), while in $(SSZ)_2 \cdot BPE \cdot (EtOH)_2$ the conformation of the SSZ is the same as the pure starting material (imide form, conformation A). In the solvated salt $SSZ \cdot IMZ \cdot MeCN$, the SSZ exists in conformation F which only differs by the absence of the $S(5)$ motif due to proton transfer. For $(SSZ)_2 \cdot PHE$ cocrystal (conformation D), $SSZ \cdot 4AP$ salt and $SSZ \cdot TMD$ salt (conformation E), only one oxygen atom of the sulfonyl group is utilized, leading to an $S_2^1(9)$ motif, and the carbonyl oxygen atom has an intramolecular interaction with the hydroxyl group, creating an $S(6)$ motif. The only difference between conformation D and E is whether the hydroxyl group from the carboxyl group is involved in the formation of an $S(5)$ motif.

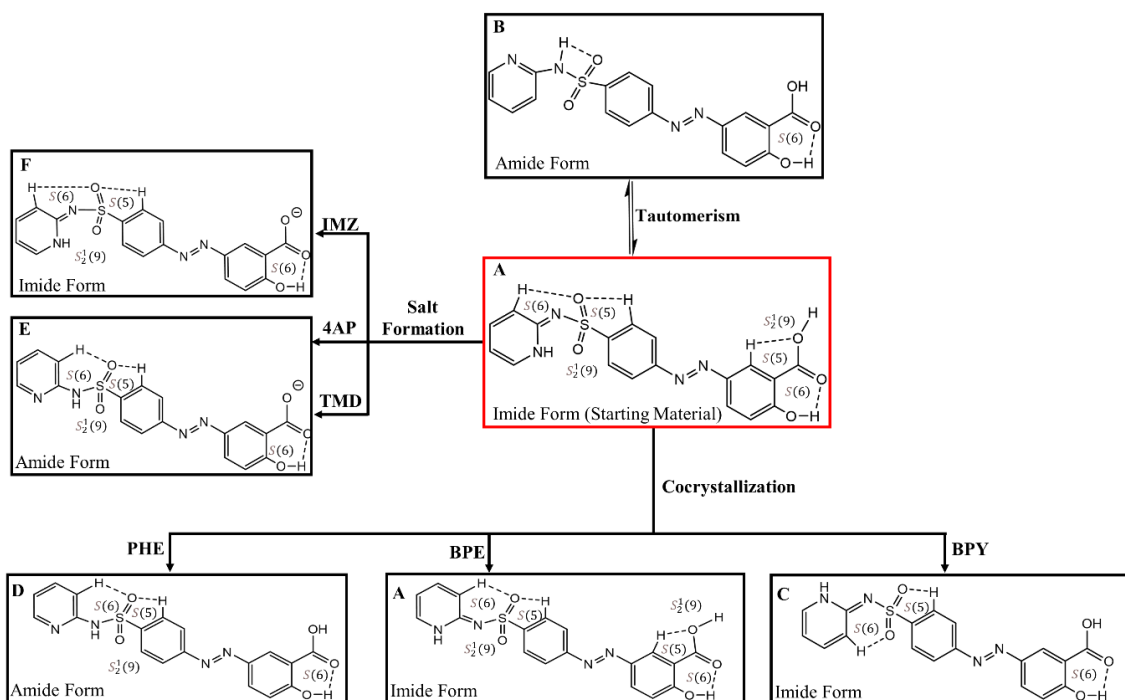


Figure 2.12. Molecular conformations of SSZ / SSZ^- in solid forms.

Molecular overlay (Figure 2.13a) indicates the bulk of the molecule (including the sulfur atom, the phenyl ring, the azo bridge and the hydroxybenzoic acid segment) is almost planar, while the orientation of the (2-pyridylamino) sulfonyl group vary significantly. In the imide form, both C1–N2 and N2–S1 bond lengths [1.35 (4) and 1.59 (3) Å] are much shorter than those in the amide form [1.43 (2) and 1.65 (16) Å], revealing conjugation between the pyridine ring and the side chain. Moreover, the N1–C1–N2–S1 and N2–S1–C2–C3 torsion angles of the two tautomers differ.^{2, 3} Regardless of the conformation of SSZ, the C1–N2 and N2–S1 bond lengths of SSZ in the six systems are closer to those of the pure imide SSZ, and no general rule in the N1–C1–N2–S1 and N2–S1–C2–C3 torsion angles can be found (Table S2.10).

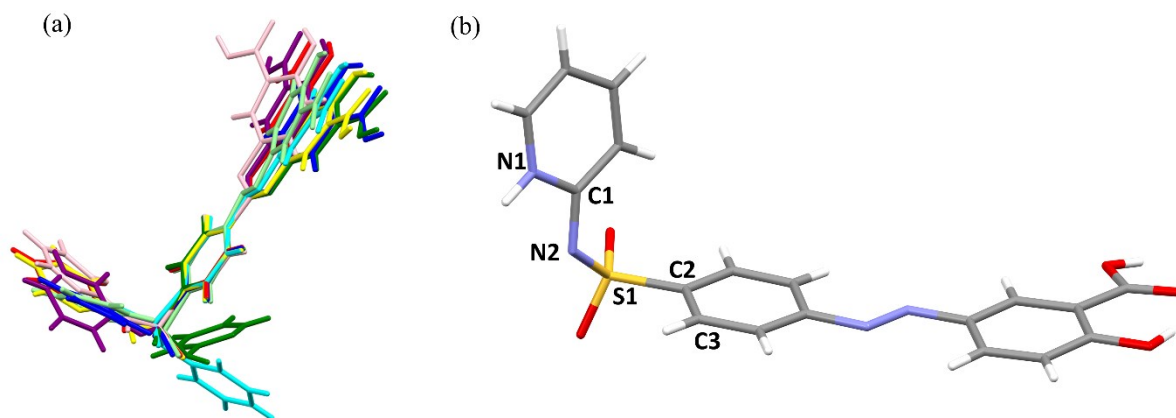


Figure 2.13. (a) Molecular overlay of SSZ: SSZ (starting material, imide form) purple, SSZ (amide form) green, (SSZ)₂·BPY·(Tol)_{0.8} blue, (SSZ)₂·BPE·(EtOH)₂ pink, (SSZ)₂·PHE yellow, SSZ·4AP light green, SSZ·TMD red, SSZ·IMZ·MeCN cyan, and (b) the selected bonds and torsions in the SSZ molecule.

2.4.4 Array of SSZ

There are two scenarios of the $R_2^2(7):R_2^2(8):R_2^2(7)$ motif involving two adjacent SSZ molecules observed in the six multi-component crystals. These arise due to the different positions of the hydrogen atom: the imide tautomer leads to the AADD array (Figure 2.14, left) while the amide tautomer leads to the ADAD array (D: hydrogen bond donor, A: hydrogen bond acceptor) (Figure 2.14, right). The three unsolvated SSZ multi-component materials in this work have the ADAD array in their crystal structures. In contrast, the AADD array is observed in the solvated SSZ multi-component materials, and this array is also present in the pure imide form of SSZ.³

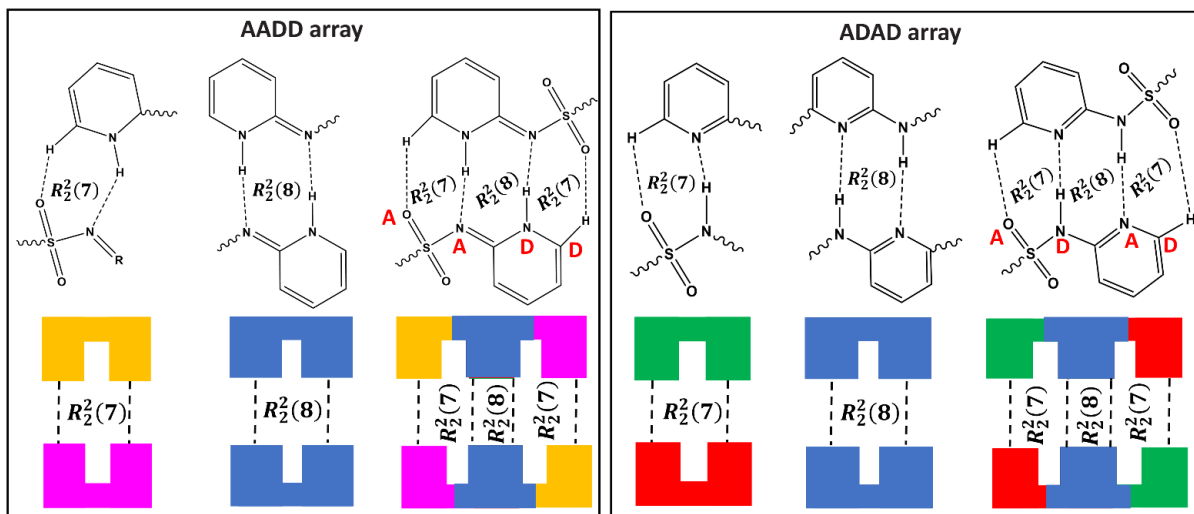


Figure 2.14. AADD / ADAD array (from sulfonyl group to pyridyl group) observed between two SSZ molecules / SSZ^- anions in SSZ solids.

To further investigate the occurrence of these two kinds of array in other multi-component crystalline materials of sulfonamide compounds, a CSD search was conducted using

ConQuest (version 2022.2.0) and the results were filtered by “3D coordinates determined”, “only single crystal structures” and “only organics”. Both of the two arrays can be found in multi-component crystalline materials of sulfapyridine (Figure 2.15, left), which is not surprising since the molecular structure of sulfapyridine is a sub-structure of SSZ. The AADD array is found in sulfapyridine 1,3-dioxane and sulfapyridine tetrahydrofuran solvate,⁴¹ while the ADAD array is observed in sulfapyridine oxalic acid dibutyl ester cocrystal.⁴² In addition to this, the ADAD array also exists in three complexes of SSZ with calcium, magnesium and strontium, and a methanol solvate of a sulfonamide compound (Figure 2.15, right). Therefore, it appears that the pyridine-2-amine moiety in sulfonamide compounds plays an important role in the formation of AADD or ADAD array in the crystal structures.

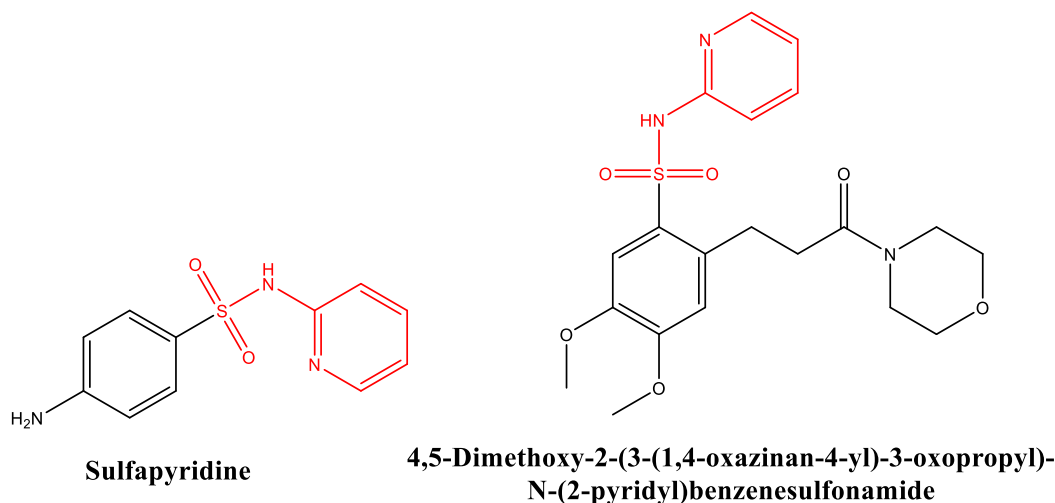


Figure 2.15. Chemical structure of sulfapyridine and 4,5-Dimethoxy-2-(3-(1,4-oxazinan-4-yl)-3-oxopropyl)-N-(2-pyridyl)benzenesulfonamide.

2.4.5 Hirshfeld Surface Analysis

Hirshfeld surfaces have proven to be a unique tool to investigate and visualize different types of intermolecular interactions in the crystal, and the 2D fingerprint plots provide quantitative information on these interactions.^{43,44} To investigate the influence of different cocrystal / salt formers on the intermolecular interactions of SSZ in different cocrystals / salts, the Hirshfeld surface analysis was performed using CrystalExplorer 21.5 program. Figures S2.14 and 2.16 illustrate the Hirshfeld surfaces of SSZ that have been mapped over d_{norm} , and the corresponding 2D fingerprint plots, respectively. Table S2.11 summarizes the main close contact contributions to the SSZ Hirshfeld surface area in different SSZ solids.

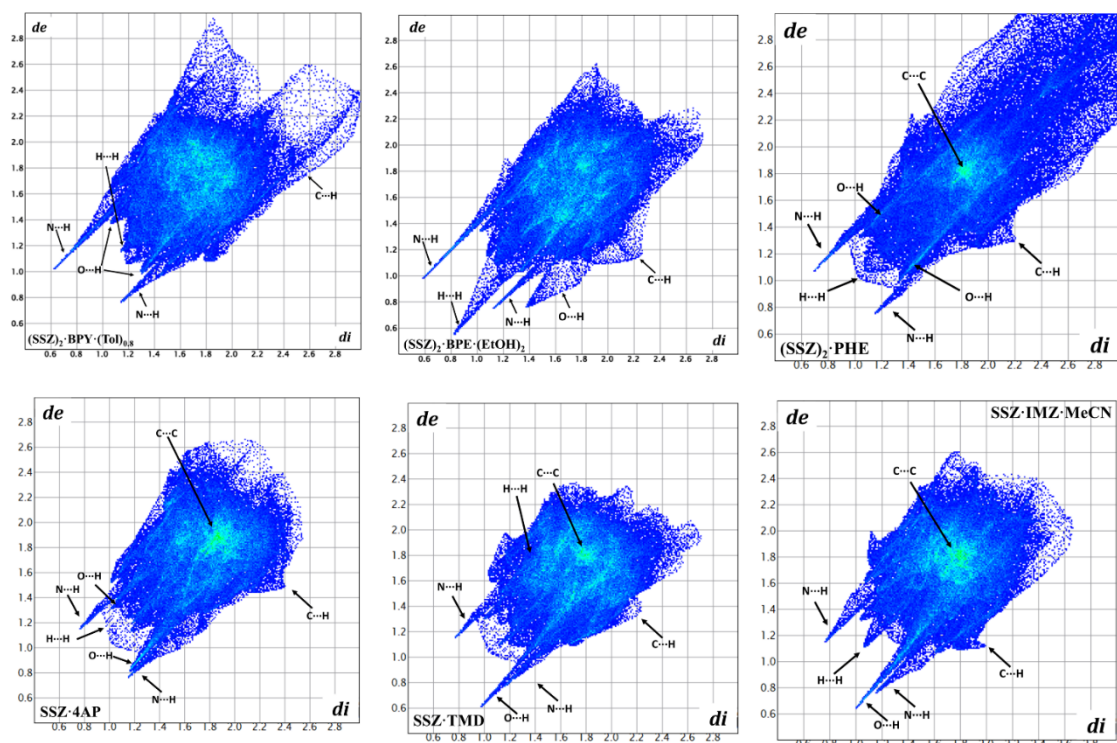


Figure 2.16. 2D fingerprint plots of SSZ in six crystalline solids.

The large circular depressions (deep red) stand for the hydrogen bonding contacts (i.e. $\text{H}\cdots\text{O}$ and $\text{H}\cdots\text{N}$) whereas other visible spots represent the $\text{H}\cdots\text{H}$ contacts (Figure S14).⁴⁵ The $\text{H}\cdots\text{H}$ interactions have the most significant contribution to the total Hirshfeld surfaces (37.8% and 40.6%) in $(\text{SSZ})_2\cdot\text{BPE}\cdot(\text{EtOH})_2$ and $(\text{SSZ})_2\cdot\text{PHE}$, while make up the second-largest proportion (32.8%, 27.5%, 32.2% and 27.1%) of the total Hirshfeld surfaces in $(\text{SSZ})_2\cdot\text{BPY}\cdot(\text{Tol})_{0.8}$, $\text{SSZ}\cdot 4\text{AP}$, $\text{SSZ}\cdot\text{TMD}$ and $\text{SSZ}\cdot\text{IMZ}\cdot\text{MeCN}$. This could be because the ratios between SSZ and cocrystal / salt formers are 2:1 and 1:1, respectively, therefore, the more hydrophobic moiety (in the SSZ structure) in SSZ cocrystals leads to a higher proportion of $\text{H}\cdots\text{H}$ contacts compared with SSZ salts. In the 2D fingerprint plots, the longest upper spike ($d_e > d_i$) stands for the hydrogen bond donor, whereas the lower longest spike ($d_e < d_i$) represents the hydrogen bond acceptor.³⁵ Therefore, when cocrystallized with BPY, BPE and PHE, respectively, SSZ acted more as hydrogen bond donor; when involved in salt formation, especially with TMD and IMZ, SSZ acted more as hydrogen bond acceptor due to the proton transfer, which is in line with the crystal structure analysis.

2.4.6 HOMO-LUMO Analysis

The frontier molecular orbitals play an important role in the reactivity of chemical systems and they can also be used to predict the most reactive position in the conjugated systems.⁴⁶⁻⁴⁸ In particular, the energy gap between highest occupied molecular orbital (HOMO) and lowest unoccupied molecular orbital (LUMO) can determine the kinetic stability and chemical reactivity of the system.^{48, 49} The distribution of the HOMO and the

LUMO of the imide and amide tautomers of SSZ are similar (Figure 2.17). For $(\text{SSZ})_2 \cdot \text{BPY} \cdot (\text{Tol})_{0.8}$, $(\text{SSZ})_2 \cdot \text{BPE} \cdot (\text{EtOH})_2$ and $\text{SSZ} \cdot 4\text{AP}$, the HOMOs and the LUMOs are located on the SSZ molecule / anion (Figure 2.18). The HOMOs are mainly localized on the azo group and hydroxybenzoic acid moiety, whereas the LUMOs mainly spreads around the benzene ring and the azo group. On the contrary, for $(\text{SSZ})_2 \cdot \text{PHE}$, both HOMO and LUMO are distributed on the PHE skeleton. For $\text{SSZ} \cdot \text{TMD}$, the HOMO is mainly localized on the azo group and hydroxybenzoate moiety of SSZ^- , and the LUMO is distributed on the protonated pyridyl ring of TMD^+ . For $\text{SSZ} \cdot \text{IMZ} \cdot \text{MeCN}$, the HOMO mainly spreads around the carboxylate group of the SSZ^- anion and the LUMO is located on the imidazolium moiety.

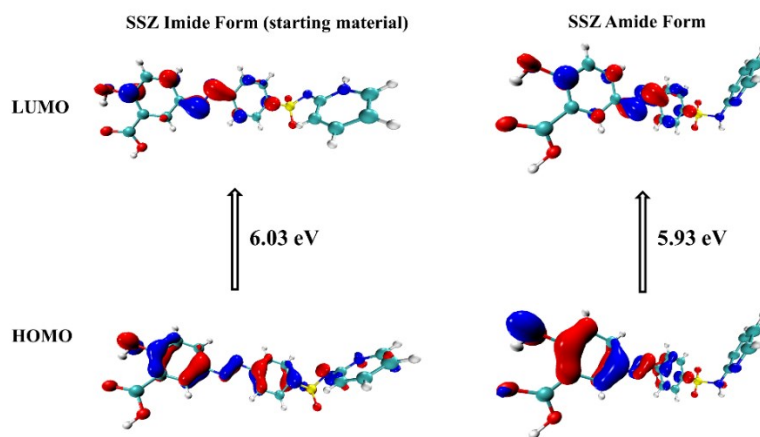


Figure 2.17. The HOMOs and LUMOs of the imide (left) and amide (right) tautomers of SSZ.

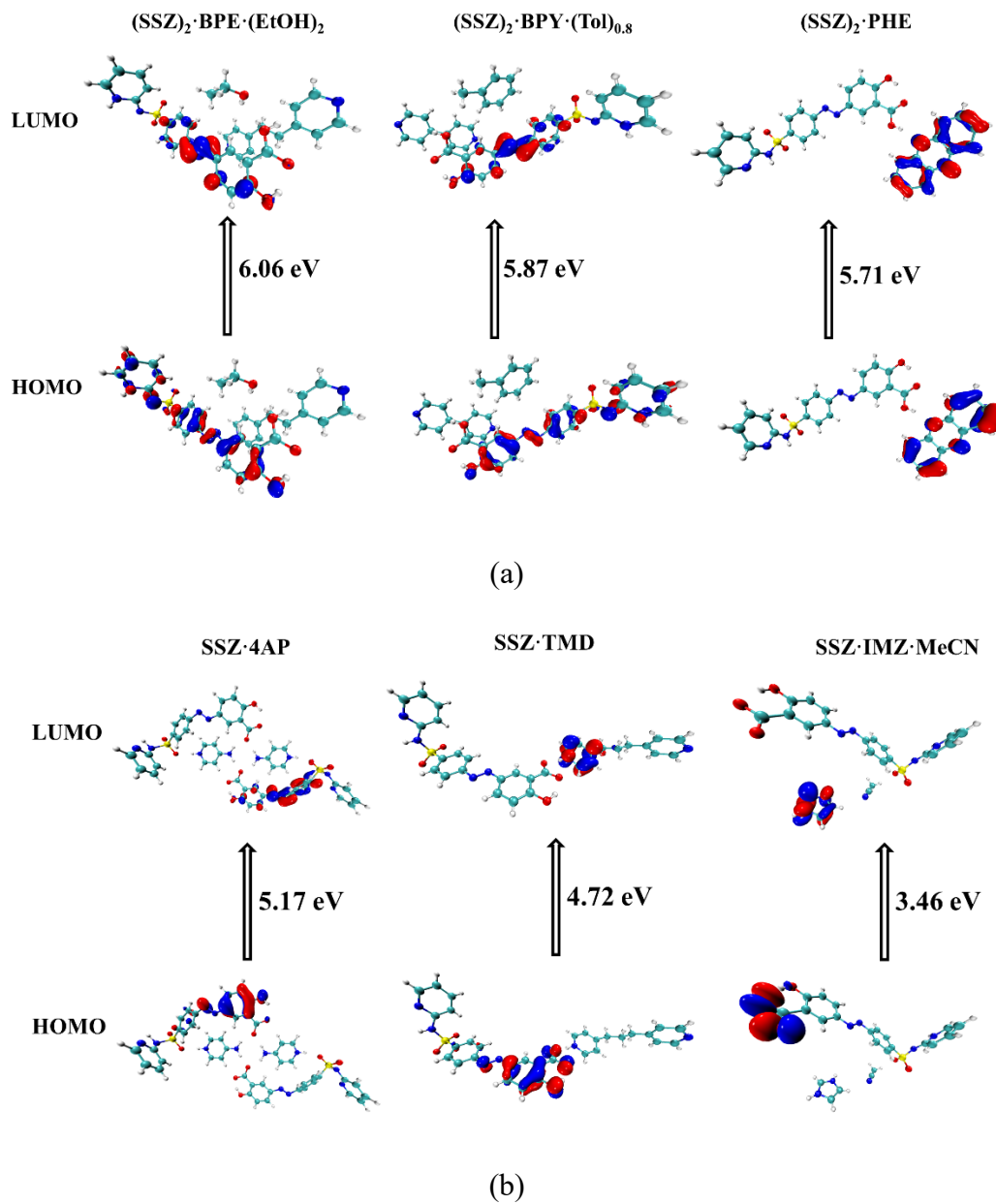


Figure 2.18. The HOMOs and LUMOs of (a) the SSZ cocrystals, and (b) the SSZ salts.

It has been reported that larger HOMO and LUMO energy gaps lead to higher chemical stability and lower chemical reactivity, and vice versa.⁴⁸ As illustrated in Figure 2.17, the energy gap in the imide is greater than the amide for pure SSZ, suggesting the imide form

is more stable than amide form. This may be supported by the fact that the amide form was the first synthesized polymorph at ambient environment, while the imide form was obtained under high temperature and high pressure. The order of energy gaps in the SSZ cocrystals and salts is $(SSZ)_2 \cdot BPE \cdot (EtOH)_2 > (SSZ)_2 \cdot BPY \cdot (Tol)_{0.8} > (SSZ)_2 \cdot PHE > SSZ \cdot 4AP > SSZ \cdot TMD > SSZ \cdot IMZ \cdot MeCN$. Notably, the cocrystals are more stable than the salts and there is a significant difference for the solvated salt $SSZ \cdot IMZ \cdot MeCN$.

2.5 Conclusions

Sulfasalazine has a strong tendency to form multi-component crystalline materials with a variety of cocrystal / salt formers because it has multiple hydrogen bond acceptor and donor sites in the structure and exhibits tautomerism. In these multi-component forms SSZ exists in different conformations. The $R_2^2(7) : R_2^2(8) : R_2^2(7)$ motif between two adjacent SSZ occurs in all the multi-component forms, presenting an ADAD array in three unsolvated SSZ solids while the AADD array is observed in solvated cocrystals and salt $(SSZ)_2 \cdot BPY \cdot (Tol)_{0.8}$, $(SSZ)_2 \cdot BPE \cdot (EtOH)_2$ and $SSZ \cdot IMZ \cdot MeCN$, which is also present in the imide form of SSZ. In addition, the azo group from SSZ participates in hydrogen bonding only in SSZ-TMD salt. Hirshfeld surface analysis indicates that SSZ acts as a hydrogen bond donor when forming cocrystals and as a hydrogen bond acceptor when it forms salts, which is consistent with proton transfer occurring determined by SCXRD results. HOMO-LUMO results suggested the cocrystals are chemically more stable than the salts.

REFERENCES

- (1) Gardner, G.; Furst, D. E., Disease-Modifying Antirheumatic Drugs. *Drugs Aging*. **1995**, *7*, 420–437.
- (2) Filip, L. A.; Caira, M. R.; Farcas, S. I.; Bojit, M. T., Triclinic polymorph of sulfasalazine. *Acta Cryst.* **2001**, *C57*, 435–436.
- (3) Blake, A. J.; Lin, X.; Schroder, M.; Wilson, C.; Yuan, R. X., The imide tautomer of sulfasalazine. *Acta Cryst.* **2004**, *C60*, o226–228.
- (4) Ol'khovich, M. V.; Sharapova, A. V.; Blokhina, S. V.; Perlovich, G. L., Sulfasalazine: Dissolution and Distribution in Pharmaceutically Relevant Mediums. *J. Chem. Eng. Data*. **2016**, *62*, (1), 123–128.
- (5) Amidon, G. L.; Lennernäs, H.; Shah, V. P.; Crison, J. R., A theoretical basis for a biopharmaceutic drug classification: the correlation of in vitro drug product dissolution and in vivo bioavailability. *Pharm. Res.* **1995**, *12*, (3), 413–420.
- (6) Shadid, M.; Gurau, G.; Shamshina, J. L.; Chuang, B. C.; Hailu, S.; Guan, E.; Chowdhury, S. K.; Wu, J. T.; Rizvi, S. A. A.; Griffin, R. J.; Rogers, R. D., Sulfasalazine in ionic liquid form with improved solubility and exposure. *MedChemComm.* **2015**, *6*, (10), 1837–1841.
- (7) Priyam, A.; Shivhare, K.; Yadav, S.; Sharma, A. K.; Kumar, P., Enhanced solubility and self-assembly of amphiphilic sulfasalazine-PEG-OMe (S-PEG) conjugate into core-shell nanostructures useful for colonic drug delivery. *Colloids Surf. A: Physicochem. Eng. Asp.* **2018**, *547*, 157–167.
- (8) Rao, M. R.; Pawar, V. M., Evaporative nanocrystallization for enhanced

- solubility and bioavailability of sulfasalazine. *World J. Pharm. Res.* **2016**, *5*, (9), 814–832.
- (9) D. M. Shinkar, A. N. Patil, R. B. Saudagar, Solubility and Dissolution Enhancement of Sulfasalazine by Solid Dispersion Technique. *Res. J. Pharm. Technol.* **2018**, *11*, (4), 1277–1282.
- (10) rad, S. m.; Abdolahi, N.; Soltani, A., Improving Drug Solubility For Inflammatory Arthritis Treatment: Sulfasalazine Niosome. *Ann. Rheum. Dis.* **2019**, *78*, 1657.
- (11) Desiraju, G. R., Crystal engineering: from molecule to crystal. *J. Am. Chem. Soc.* **2013**, *135*, (27), 9952–9967.
- (12) Khandavilli, U. B. R.; Skořepová, E.; Sinha, A. S.; Bhogala, B. R.; Maguire, N. M.; Maguire, A. R.; Lawrence, S. E., Cocrystals and a Salt of the Bioactive Flavonoid: Naringenin. *Cryst. Growth Des.* **2018**, *18*, (8), 4571–4577.
- (13) Huang, S.; Xu, J.; Peng, Y.; Guo, M.; Cai, T., Facile Tuning of the Photoluminescence and Dissolution Properties of Phloretin through Cocrystallization. *Cryst. Growth Des.* **2019**, *19*, (12), 6837–6844.
- (14) Huang, S.; Xue, Q.; Xu, J.; Ruan, S.; Cai, T., Simultaneously Improving the Physicochemical Properties, Dissolution Performance, and Bioavailability of Apigenin and Daidzein by Co-Crystallization With Theophylline. *J. Pharm. Sci.* **2019**, *108*, (9), 2982–2993.
- (15) Sinha, A. S.; Maguire, A. R.; Lawrence, S. E., Cocrystallization of Nutraceuticals. *Cryst. Growth Des.* **2015**, *15*, (2), 984–1009.
- (16) Bolla, G.; Sarma, B.; Nangia, A. K., Crystal Engineering of Pharmaceutical

- Cocrystals in the Discovery and Development of Improved Drugs. *Chem. Rev.* **2022**, 122, (13), 11514–11603.
- (17) Choquesillo-Lazarte, D.; Nemečb, V.; Cinčić, D., Halogen bonded cocrystals of active pharmaceutical ingredients: pyrazinamide, lidocaine and pentoxifylline in combination with haloperfluorinated compounds. *CrystEngComm* **2017**, 19, 5293–5299.
- (18) Zhang, Y.; Wang, J.-G.; Wang, W., Unexpected Sandwiched-Layer Structure of the Cocrystal Formed by Hexamethylbenzene with 1,3-Diiodotetrafluorobenzene: A Combined Theoretical and Crystallographic Study. *Crystals* **2020**, 10, (5), 379.
- (19) Karimi-Jafari, M.; Padrela, L.; Walker, G. M.; Croker, D. M., Creating Cocrystals: A Review of Pharmaceutical Cocrystal Preparation Routes and Applications. *Cryst. Growth Des.* **2018**, 18, 6370–6387.
- (20) Lemmerer, A.; Govindraj, S.; Johnston, M.; Motloug, X.; Savig, K. L., Cocrystals and molecular salts of carboxylic acid/pyridine complexes: can calculated pKa's predict proton transfer? A case study of nine complexes. *CrystEngComm* **2015**, 17, 3591–3595.
- (21) Childs, S. L.; Stahly, G. P.; Park, A., The Salt–Cocrystal Continuum: The Influence of Crystal Structure on Ionization State. *Mol. Pharmaceutics* **2007**, 4, (3), 323–338.
- (22) Cruz-Cabeza, A. J., Acid–base crystalline complexes and the pKa rule. *CrystEngComm* **2012**, 14, 6362–6365.
- (23) Zhao, L.; Hanrahan, M. P.; Chakravarty, P.; DiPasquale, A. G.; Sirois, L. E.;

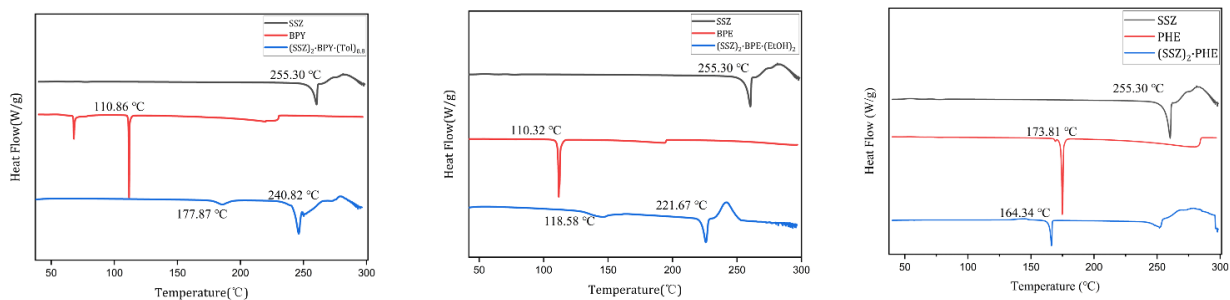
- Nagapudi, K.; Lubach, J. W.; Rossini, A. J., Characterization of Pharmaceutical Cocrystals and Salts by Dynamic Nuclear Polarization-Enhanced Solid-State NMR Spectroscopy. *Cryst. Growth Des.* **2018**, 18, (4), 2588–2601.
- (24) Ali, H. R. H.; Alhalaweh, A.; Mendes, N. F. C.; Ribeiro-Claro, P.; Velaga, S. P., Solid-state vibrational spectroscopic investigation of cocrystals and salt of indomethacin. *CrystEngComm* **2012**, 14, 6665–6674.
- (25) Mohamed, S.; Tocher, D. A.; Vickers, M.; Karamertzanis, P. G.; Price, S. L., Salt or Cocrystal? A New Series of Crystal Structures Formed from Simple Pyridines and Carboxylic Acids. *Cryst. Growth Des.* **2009**, 9, (6), 2881–2889.
- (26) Elbakush, R. E. A Crystal Engineering Study of Selected Sulfa Drugs and Trimethoprim. University of the Western Cape, South Africa, **2014**.
- (27) Bala, M.; Gautam, M. K.; Chadha, R., Development of non-covalent derivative of sulfasalazine with theobromine for its properties optimization. *Innov. Pharm. Pharmacother.* **2017**, 5, (3), 154–158.
- (28) Groom, C. R.; Bruno, I. J.; Lightfoot, M. P.; Ward, S. C., The Cambridge Structural Database. *Acta Cryst.* **2016**, B72, 171–179.
- (29) Sinha, A. S.; Rao Khandavilli, U. B.; O'Connor, E. L.; Deadman, B. J.; Maguire, A. R.; Lawrence, S. E., Novel co-crystals of the nutraceutical sinapic acid. *CrystEngComm* **2015**, 17, (26), 4832–4841.
- (30) Sheldrick, G. M., Crystal structure refinement with SHELXL. *Acta Cryst.* **2015**, C71, 3–8.
- (31) APEX2 v2009.3-0. Bruker AXS. **2009**.
- (32) Huang, S.; Venables, D. S.; Lawrence, S. E., Pharmaceutical Salts of Piroxicam

- and Meloxicam with Organic Counterions. *Cryst. Growth Des.* **2022**, 22, (11), 6504–6520.
- (33) Xu, J.; Huang, Y.; Ruan, S.; Chi, Z.; Qin, K.; Cai, B.; Cai, T., Cocrystals of isoliquiritigenin with enhanced pharmacokinetic performance. *CrystEngComm* **2016**, 18, (45), 8776–8786.
- (34) Spek, A. L., Structure validation in chemical crystallography. *Acta Cryst.* **2009**, D65, 148–155.
- (35) Yang, D.; Wang, R.; Jin, G.; Zhang, B.; Zhang, L.; Lu, Y.; Du, G., Structural and Computational Insights into Cocrystal Interactions: A Case on Cocrystals of Antipyrine and Aminophenazone. *Cryst. Growth Des.* **2019**, 19, (11), 6175–6183.
- (36) Lu, T.; Chen, F., Quantitative analysis of molecular surface based on improved Marching Tetrahedra algorithm. *J. Mol. Graph. Model.* **2012**, 38, 314–323.
- (37) Lu, T.; Chen, F., Multiwfn: a multifunctional wavefunction analyzer. *J. Comput. Chem.* **2012**, 33, (5), 580–592.
- (38) Spackman, P. R.; Turner, M. J.; McKinnon, J. J.; Wolff, S. K.; Grimwood, D. J.; Jayatilaka, D.; Spackman, M. A., CrystalExplorer: a program for Hirshfeld surface analysis, visualization and quantitative analysis of molecular crystals. *J. Appl. Cryst.* **2021**, 54, 1006–1011.
- (39) Kostadinova, I.; Danchev, N., 4-aminopyridine- the new old drug for the treatment of neurodegenerative diseases. *Pharmacia* **2019**, 66, (2), 67–74.
- (40) Liang, M.-K.; Patwardhan, S. V.; Danilovtseva, E. N.; Annenkov, V. V.; Perry, C. C., Imidazole catalyzed silica synthesis: Progress toward understanding the

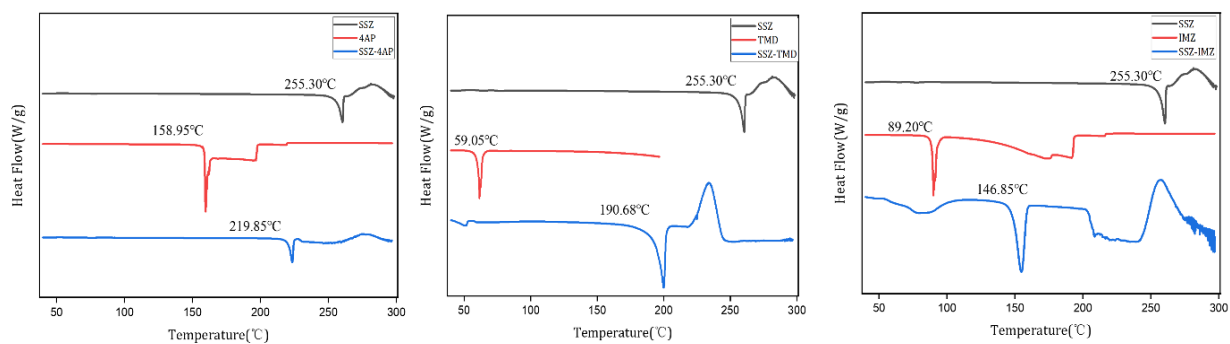
- role of histidine in (bio)silicification. *J. Mater. Res.* **2011**, 24, (5), 1700–1708.
- (41) Pratt, J.; Hutchinson, J.; Stevens, C. L. K., Sulfapyridine (polymorph III), sulfapyridine dioxane solvate, sulfapyridine tetrahydrofuran solvate and sulfapyridine piperidine solvate, all at 173 K. *Acta Cryst.* **2011**, C67, o487–o491.
- (42) Coles, S. J.; Hursthouse, M. B.; Mayer, T. A.; Threlfall, T. L., University of Southampton. *Crystal Structure Report Archive* **2000**, 196.
- (43) Yang, J.; Yin, L.; Gong, X.-D.; Sinditskii, V. P.; Zhang, J.-G., Origins of Salt Formation and Cocrystallization: A Combined Experimental and Theoretical Study. *Cryst. Growth Des.* **2020**, 20, (9), 5834–5842.
- (44) Luo, Y. H.; Sun, B. W., Pharmaceutical Co-Crystals of Pyrazinecarboxamide (PZA) with Various Carboxylic Acids: Crystallography, Hirshfeld Surfaces, and Dissolution Study. *Cryst. Growth Des.* **2013**, 13, (5), 2098–2106.
- (45) Seth, S. K.; Das, N. K.; Aich, K.; Sen, D.; Fun, H.-K.; Goswami, S., Exploring contribution of intermolecular interactions in supramolecular layered assembly of naphthyridine co-crystals: Insights from Hirshfeld surface analysis of their crystalline states. *J. Mol. Struct.* **2013**, 1048, 157–165.
- (46) Li, K.; Ren, X.; Fu, S.; Zhu, J., Cocrystal structure, thermal behaviour, and DFT calculations between FOX-7 and 1,10-Phenanthroline. *J. Mol. Struct.* **2018**, 1173, (5), 26–32.
- (47) Kumar, G. S. S.; Prabhu, A. A. M.; N.Bhuvanesh; X.A.V.Ronica; Kumaresan, S., Molecular structure investigation of organic cocrystals of 1,10-phenanthroline-5,6-dione with aryloxyacetic acid: A combined experimental

- and theoretical study. *Spectrochimica. Acta Part A.* **2014**, 132, (11), 465–476.
- (48) Velmurugan, V.; Nandini Asha, R.; Ravindran Durai Nayagam, B.; Kumaresan, S.; Bhuvanesh, N., Synthesis, Characterization and Biological Activity of (Phenylthio)Acetic Acid:Theophylline Cocrystal. *J. Chem. Crystallogr.* **2020**, 51, (2), 225–234.
- (49) Hao, L.; Wang, J.; Zhai, D.; Ma, P.; Ma, C.; Pan, Y.; Jiang, J., Theoretical Study on CL-20-Based Cocrystal Energetic Compounds in an External Electric Field. *ACS Omega* **2020**, 5, (24), 14767–14775.

Supporting Information

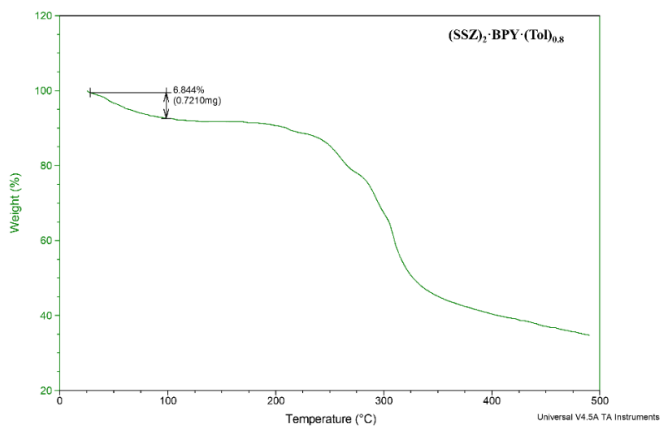


(a)

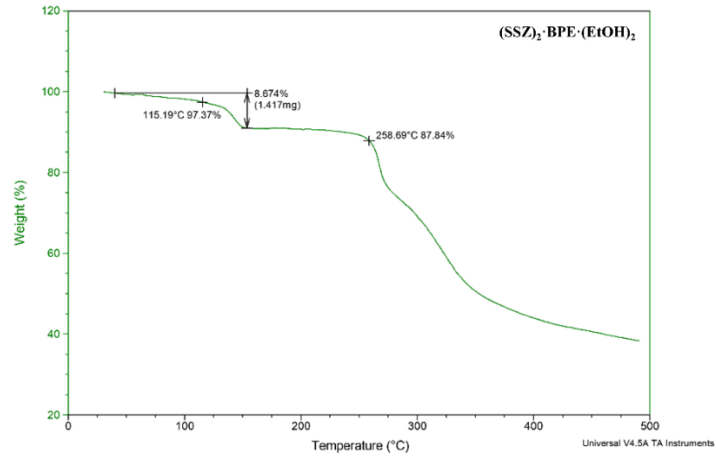


(b)

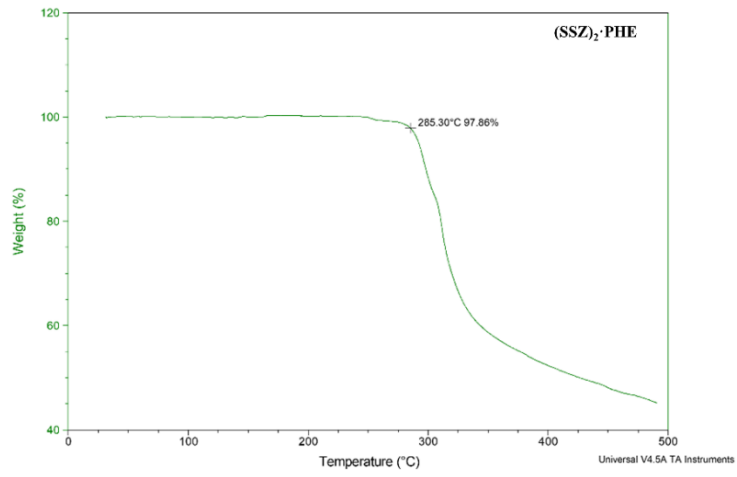
Figure S2.1. DSC traces of (a) SSZ, BPY, BPE, PHE and (SSZ)₂·BPY·(Tol)_{0.8}, (SSZ)₂·BPE·(EtOH)₂ and (SSZ)₂·PHE, and (b) SSZ, 4AP, TMD, IMZ and SSZ·4AP, SSZ·TMD and SSZ·IMZ·MeCN.



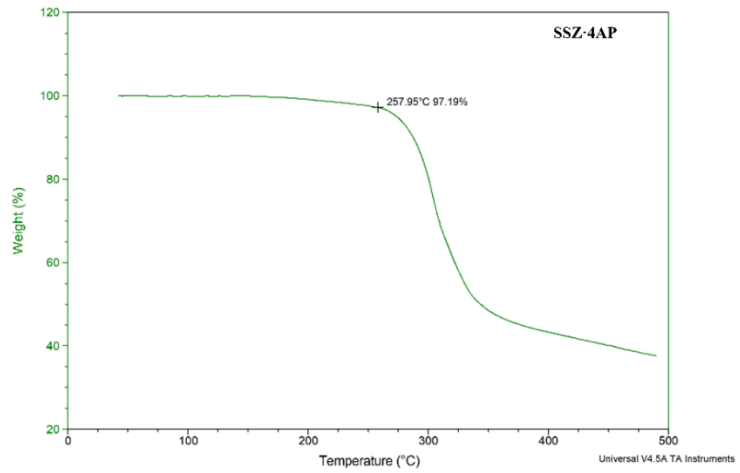
(a)



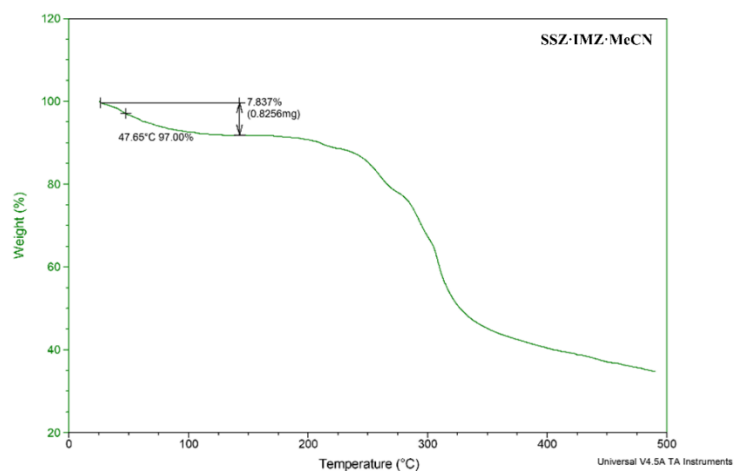
(b)



(c)

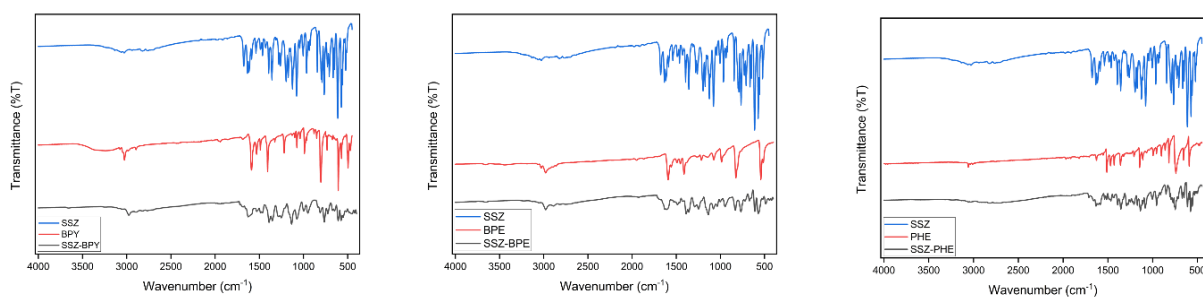


(d)

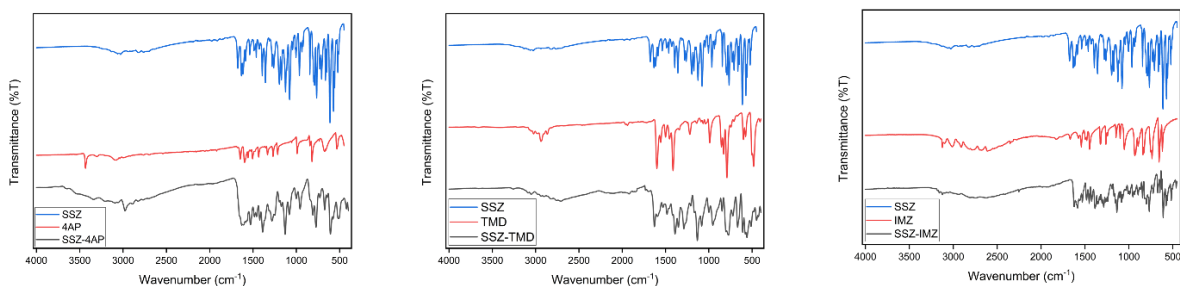


(e)

Figure S2.2. TGA plots of (a) $(\text{SSZ})_2 \cdot \text{BPY} \cdot (\text{Tol})_{0.8}$, (b) $(\text{SSZ})_2 \cdot \text{BPE} \cdot (\text{EtOH})_2$, (c) $(\text{SSZ})_2 \cdot \text{PHE}$, (d) $\text{SSZ} \cdot 4\text{AP}$, and (e) $\text{SSZ} \cdot \text{IMZ} \cdot \text{MeCN}$.

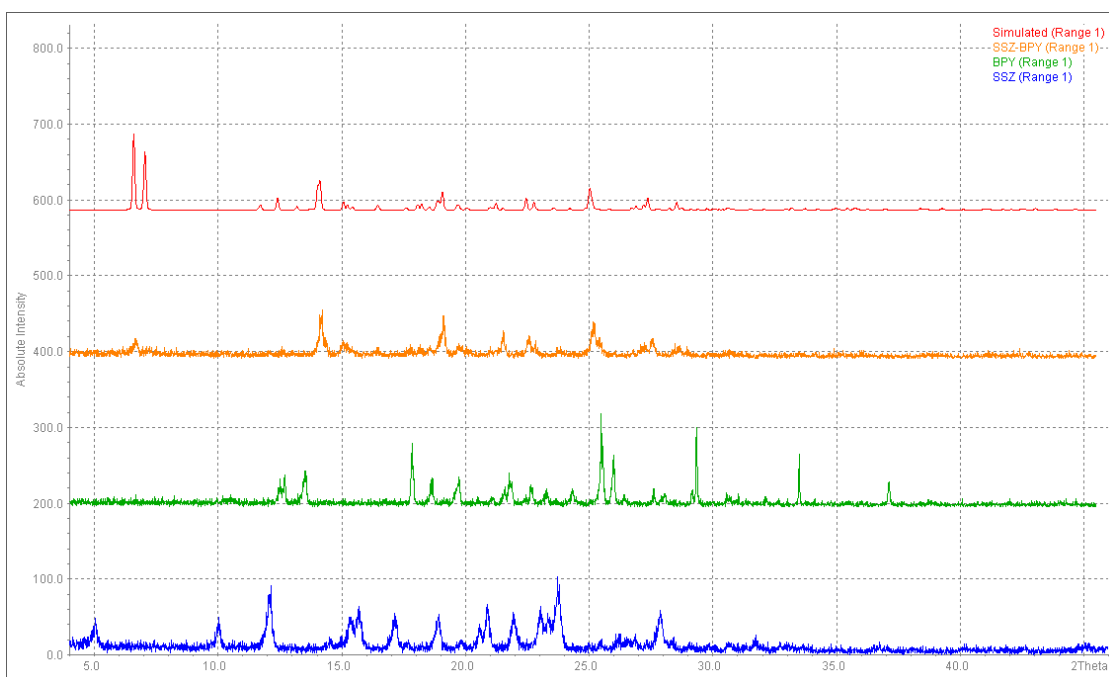


(a)

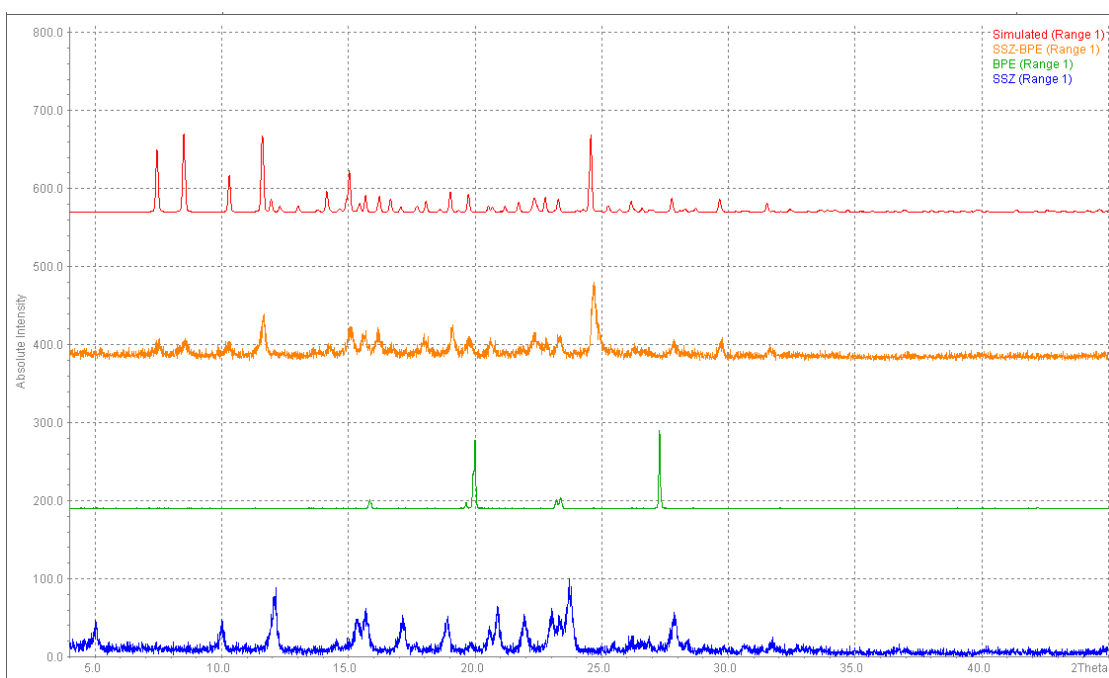


(b)

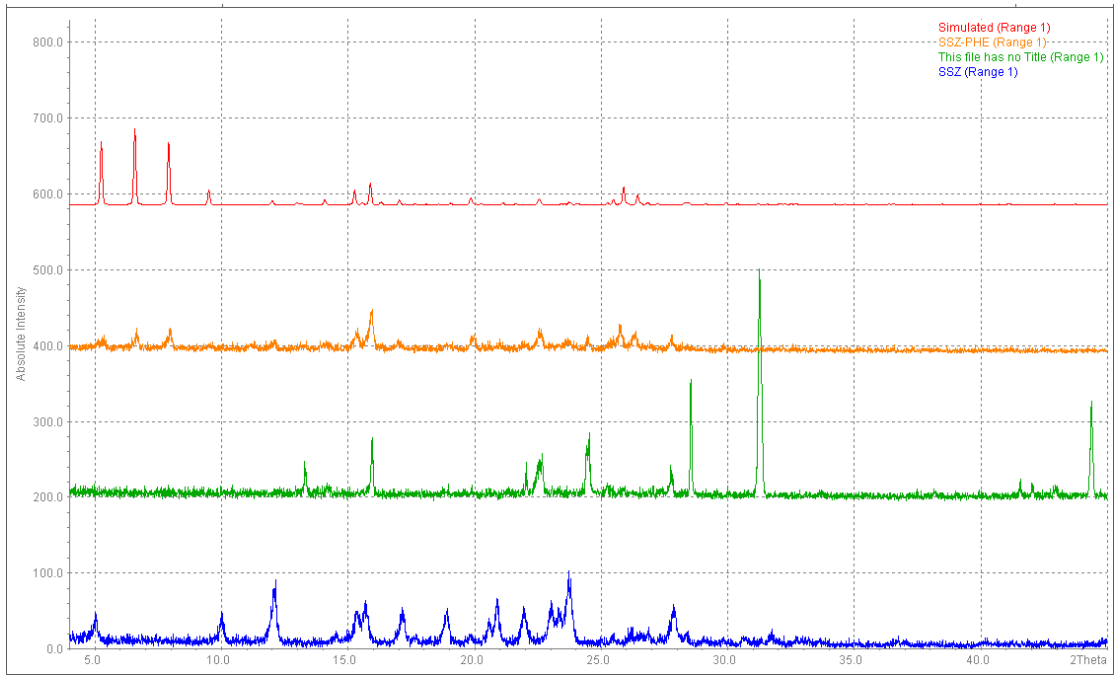
Figure S2.3. IR spectra of (a) SSZ, BPY, BPE, PHE and $(\text{SSZ})_2 \cdot \text{BPY} \cdot (\text{Tol})_{0.8}$, $(\text{SSZ})_2 \cdot \text{BPE} \cdot (\text{EtOH})_2$ and $(\text{SSZ})_2 \cdot \text{PHE}$, and (b) SSZ, 4AP, TMD, IMZ and $\text{SSZ} \cdot 4\text{AP}$, $\text{SSZ} \cdot \text{TMD}$ and $\text{SSZ} \cdot \text{IMZ} \cdot \text{MeCN}$.



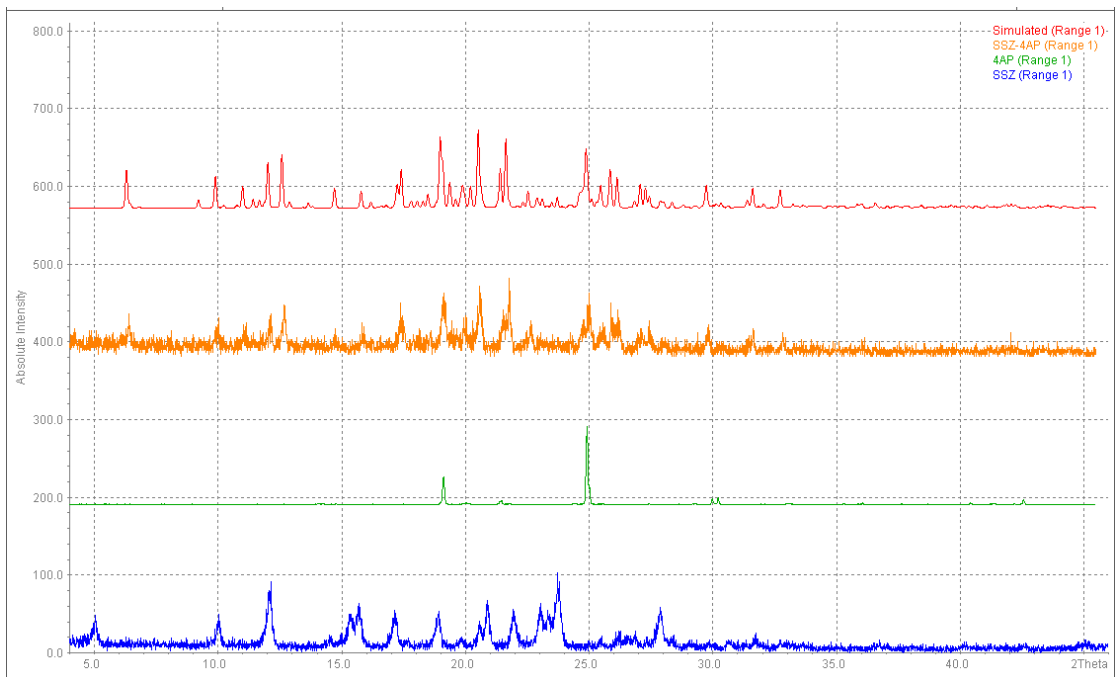
(a)



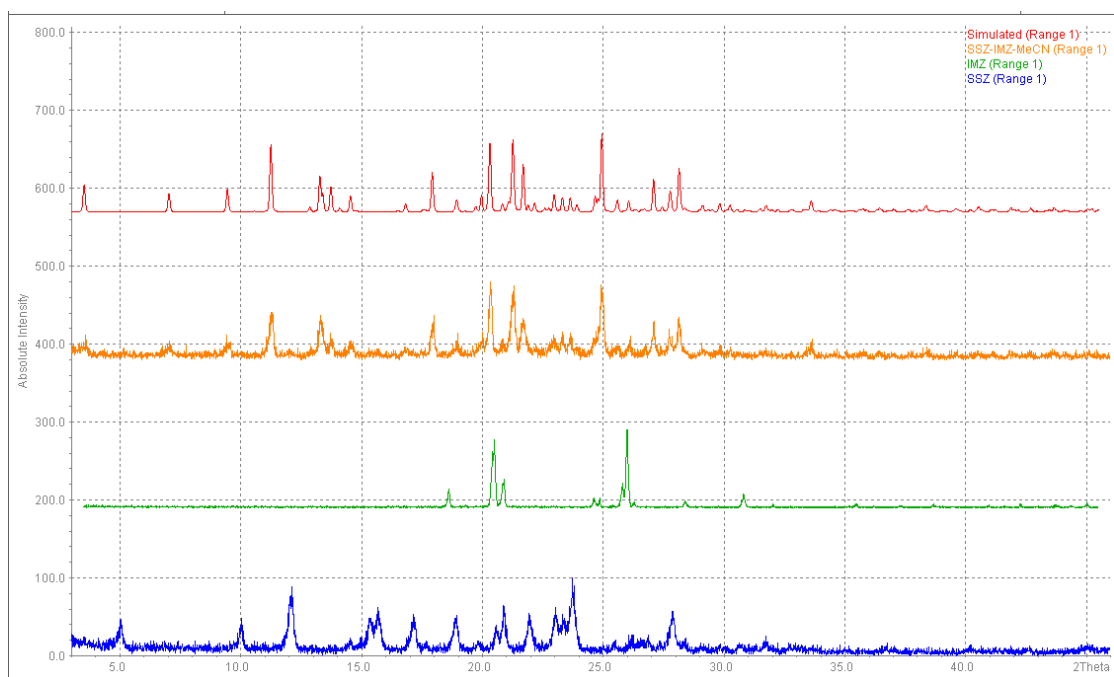
(b)



(c)

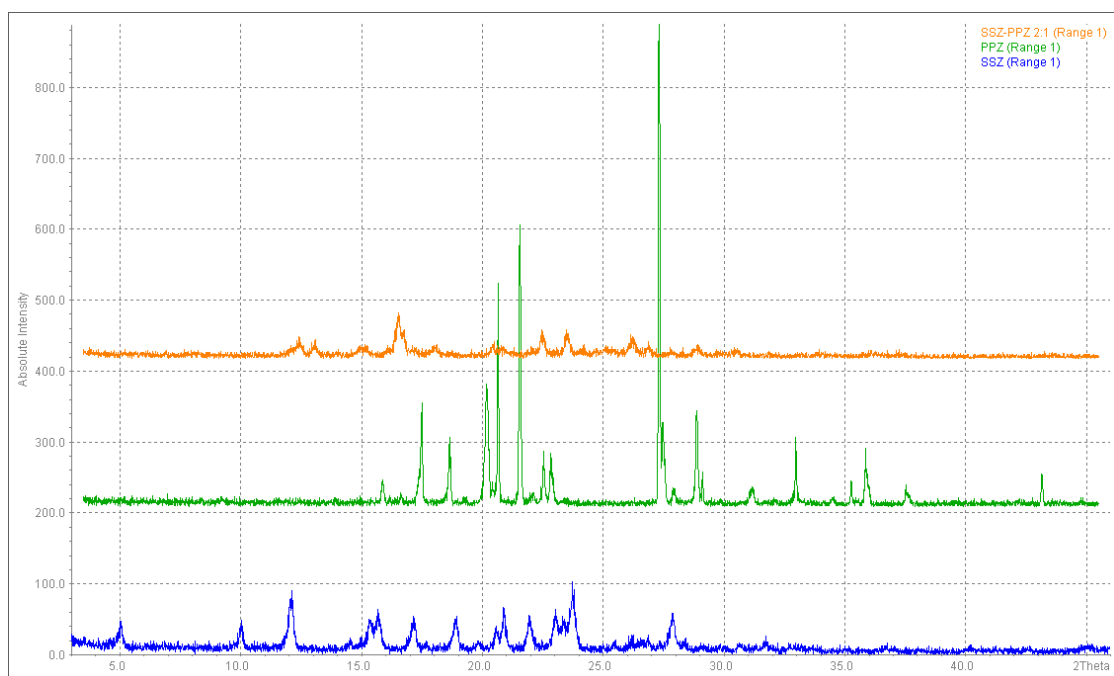


(d)

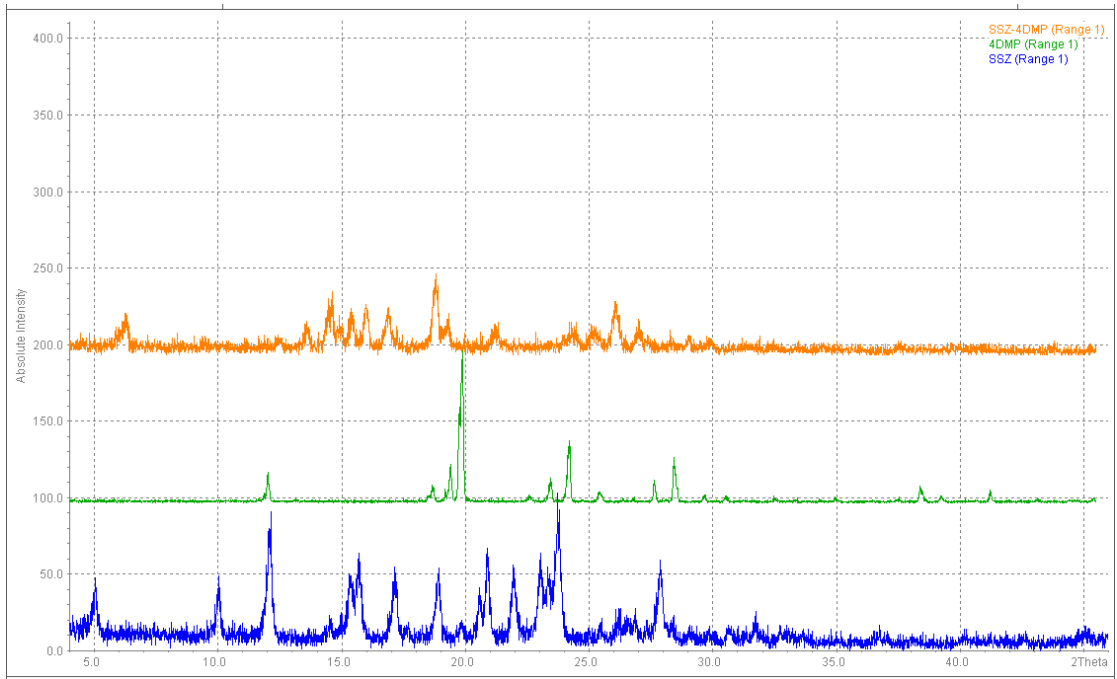


(e)

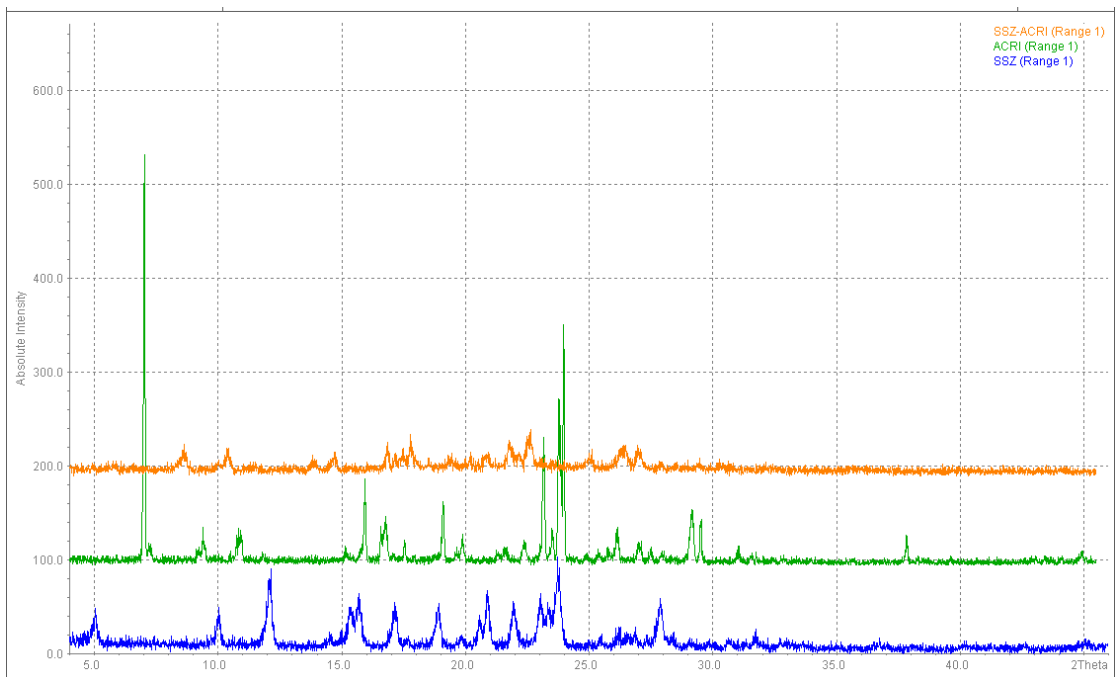
Figure S2.4. PXRD patterns of (a) $(SSZ)_2 \cdot BPY \cdot (Tol)_{0.8}$, (b) $(SSZ)_2 \cdot BPE \cdot (EtOH)_2$, (c) $(SSZ)_2 \cdot PHE$, (d) $SSZ \cdot 4AP$, and (e) $SSZ \cdot IMZ \cdot MeCN$.



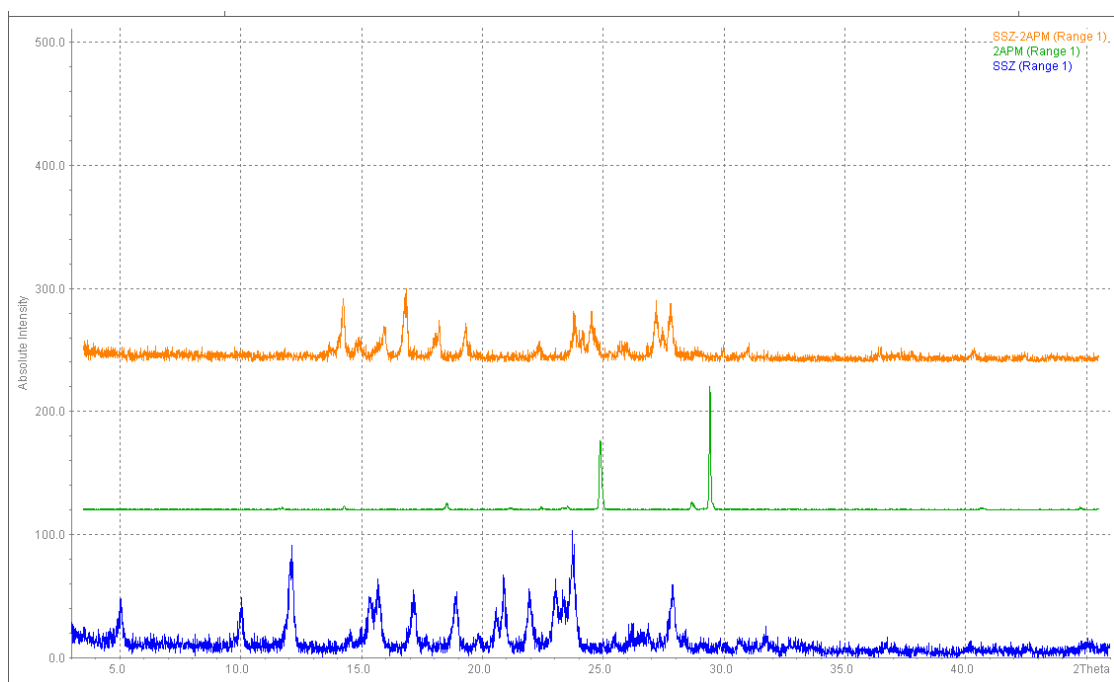
(a)



(b)

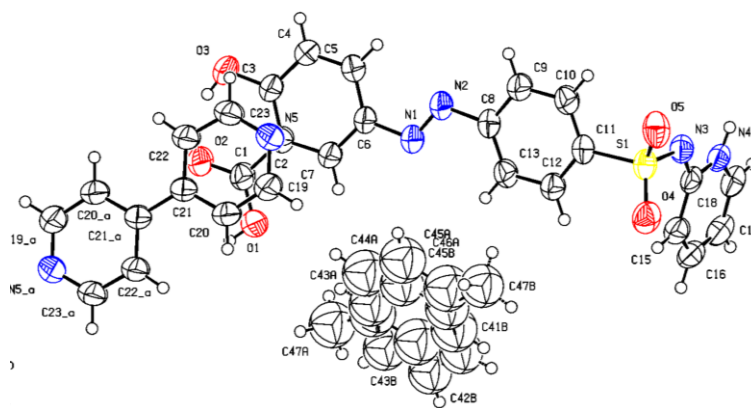


(c)

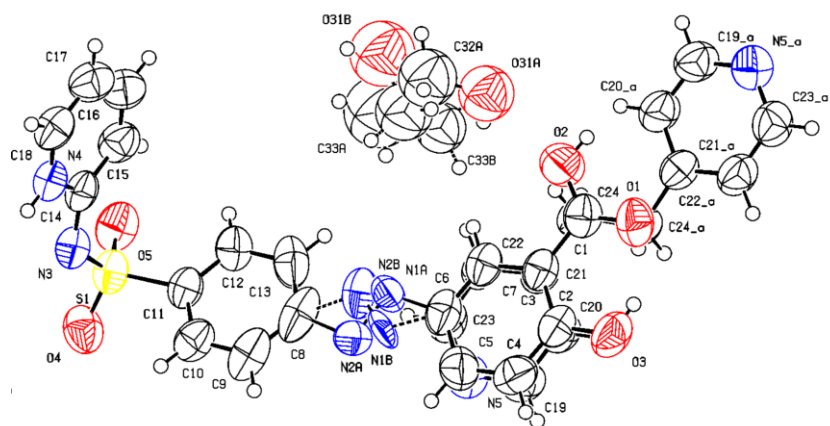


(d)

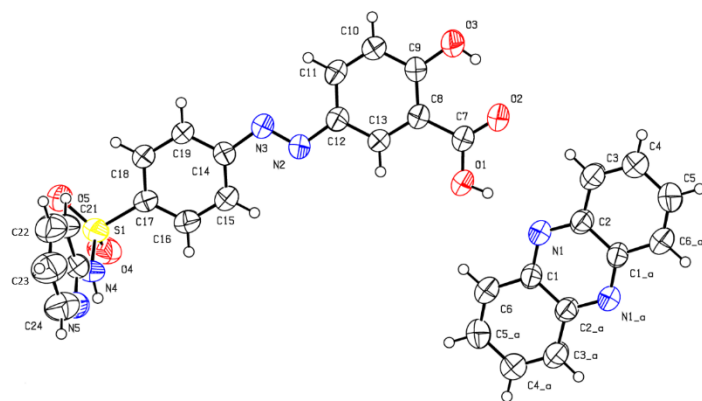
Figure S2.5. PXRD patterns of (a) SSZ-PPZ, (b) SSZ-4DMP, (c) SSZ-ACRI and (d) SSZ-2AMP.



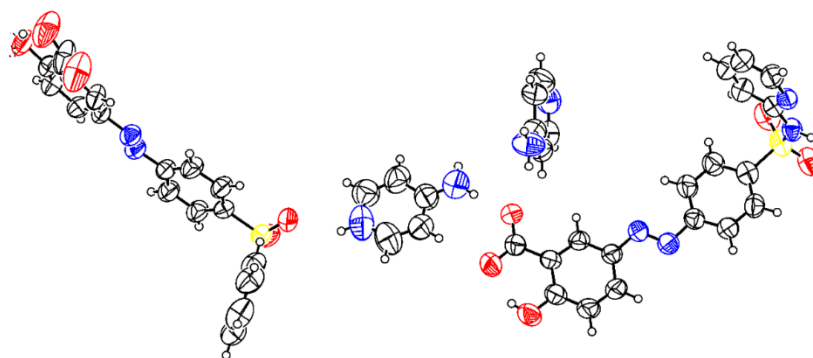
(a)



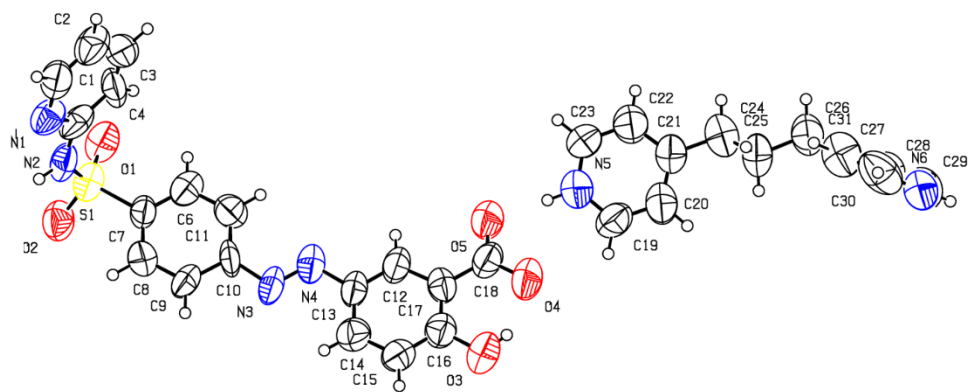
(b)



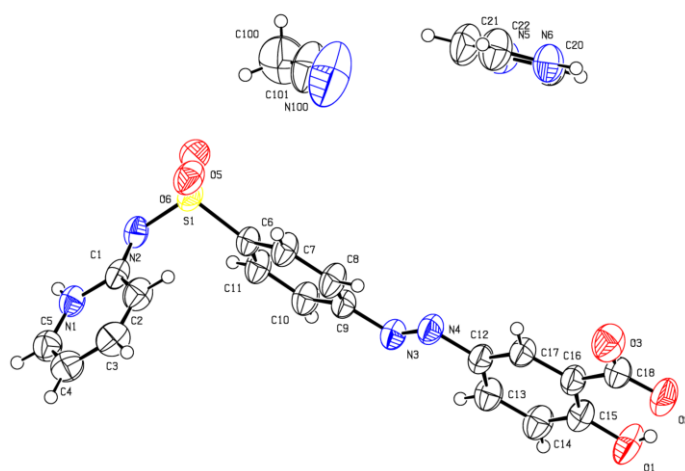
(c)



(d)

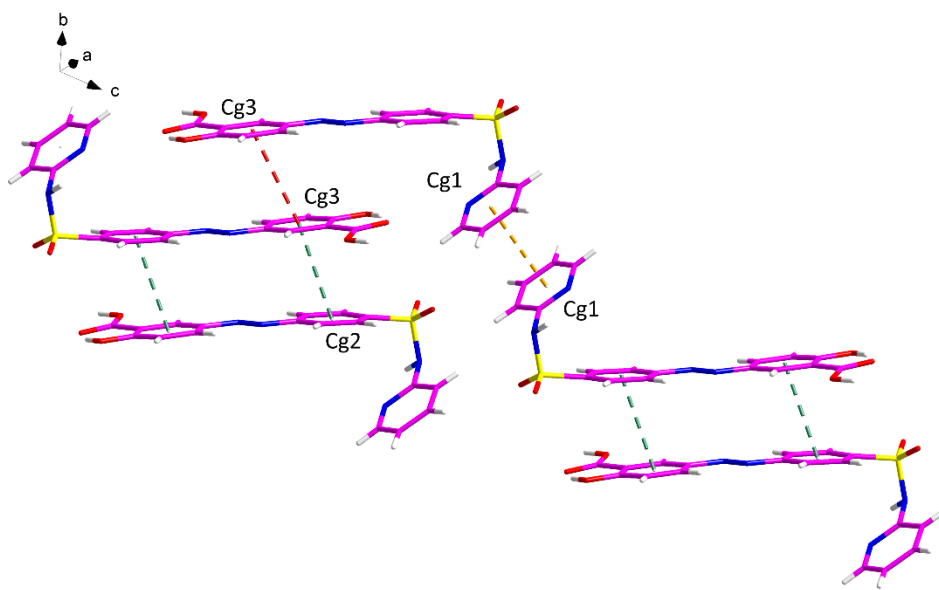


(e)

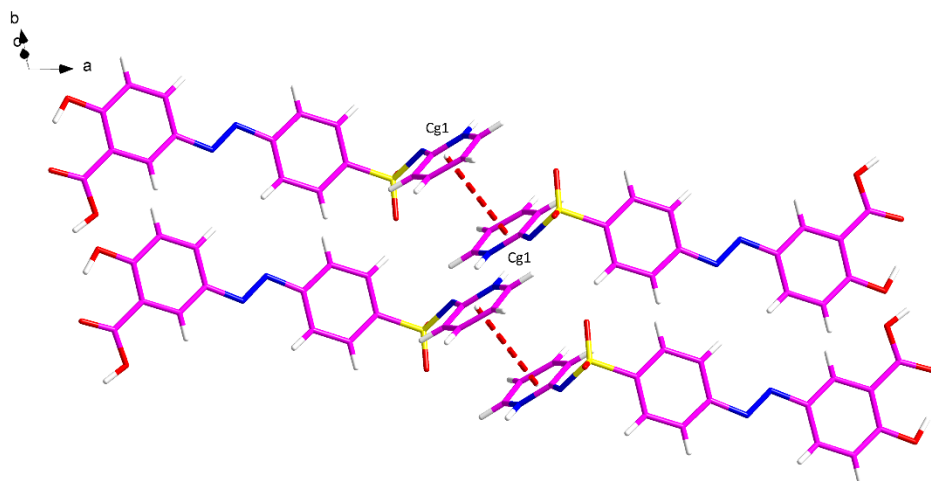


(f)

Figure S2.6. Ellipsoid plots of (a) $(SSZ)_2 \cdot BPY \cdot (Tol)_{0.8}$, (b) $(SSZ)_2 \cdot BPE \cdot (EtOH)_2$, (c) $(SSZ)_2 \cdot PHE$, (d) $SSZ \cdot 4AP$, (e) $SSZ \cdot TMD$ and (f) $SSZ \cdot IMZ \cdot MeCN$.



(a)



(b)

Figure S2.7. π - π interactions of (a) in the SSZ triclinic amide form, and (b) in the SSZ monoclinic imide form as indicated by dashed lines (hydrogen bonding is not displayed for clarity).

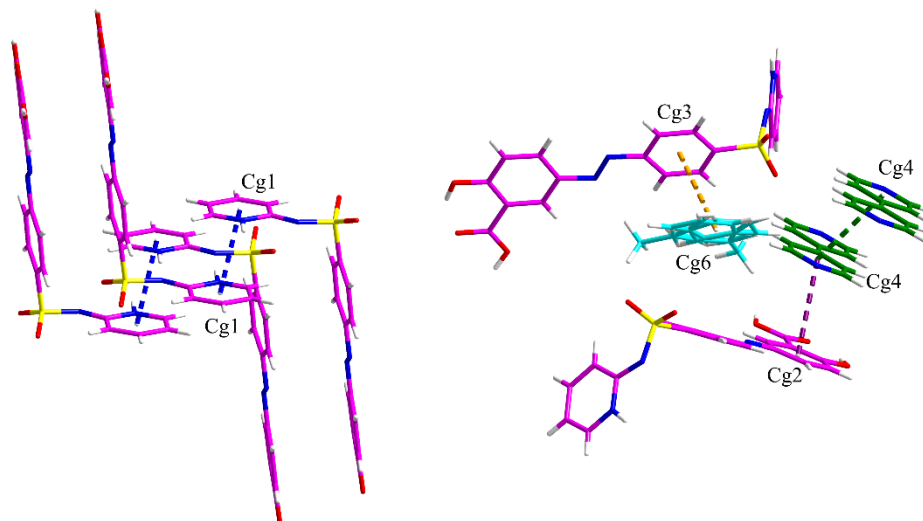


Figure S2.8. π - π interactions of $(\text{SSZ})_2 \cdot \text{BPY} \cdot (\text{Tol})_{0.8}$ cocrystal solvate.

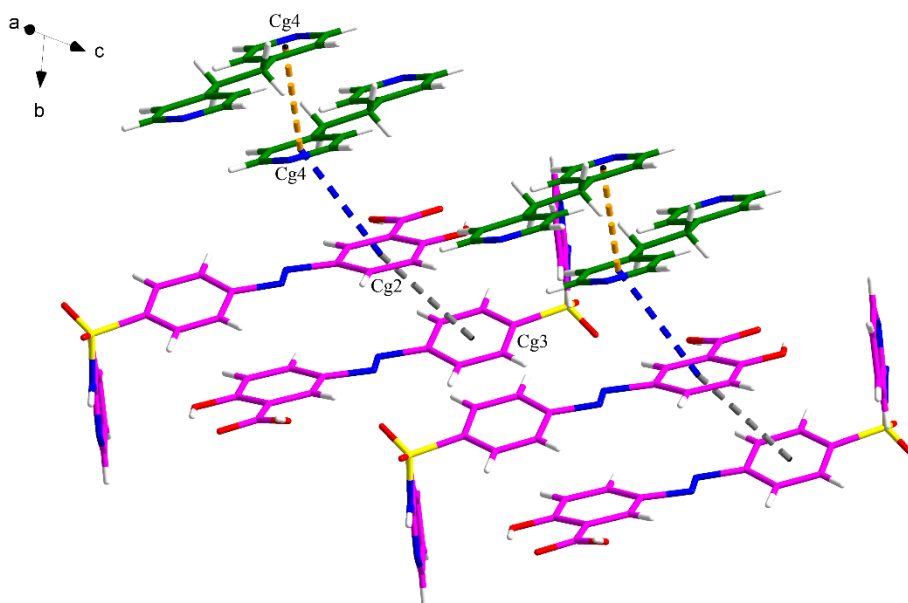


Figure S2.9. π - π interactions of $(\text{SSZ})_2 \cdot \text{BPE} \cdot (\text{EtOH})_2$ cocrystal solvate.

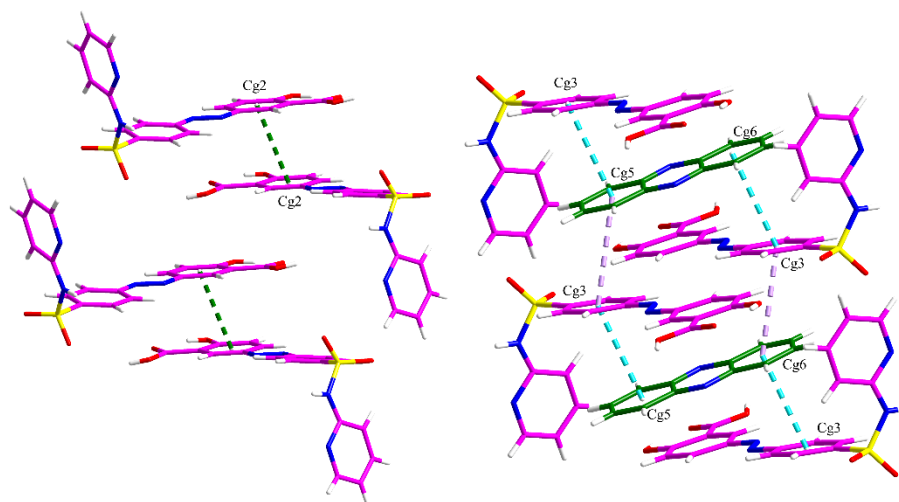


Figure S2.10. π - π interactions of $(SSZ)_2 \cdot PHE$ cocrystal.

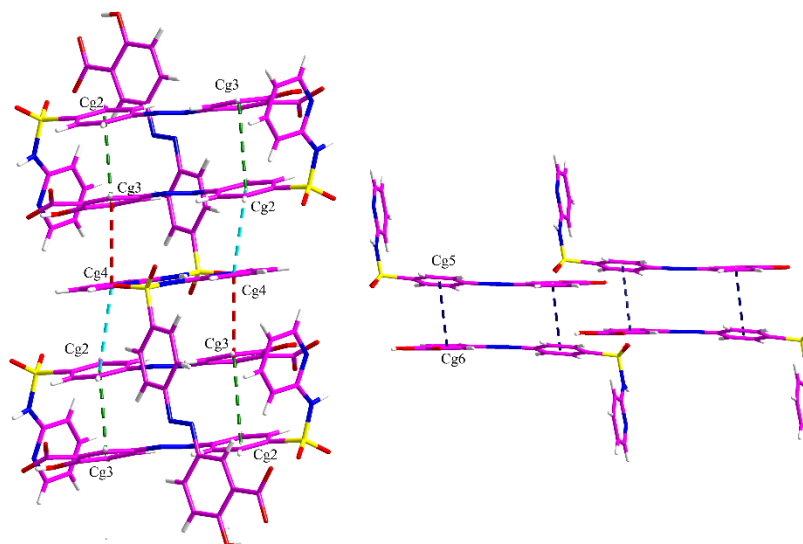


Figure S2.11. π - π interactions of $SSZ \cdot 4AP$ salt.

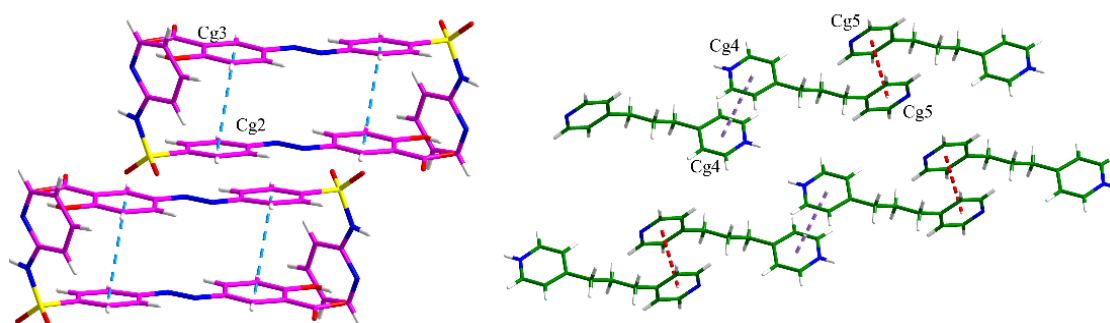


Figure S2.12. π - π interactions of $SSZ \cdot TMD$ salt.

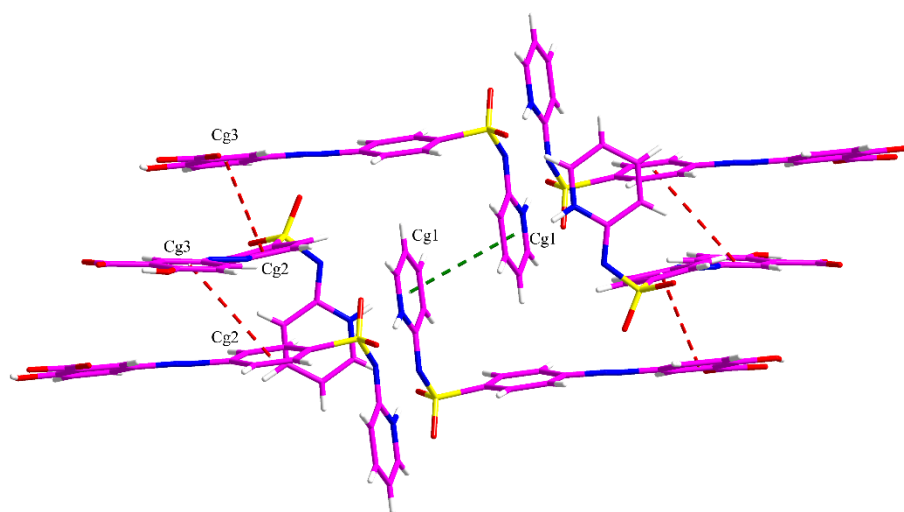


Figure S2.13. π - π interactions of SSZ·IMZ·MeCN salt solvate.

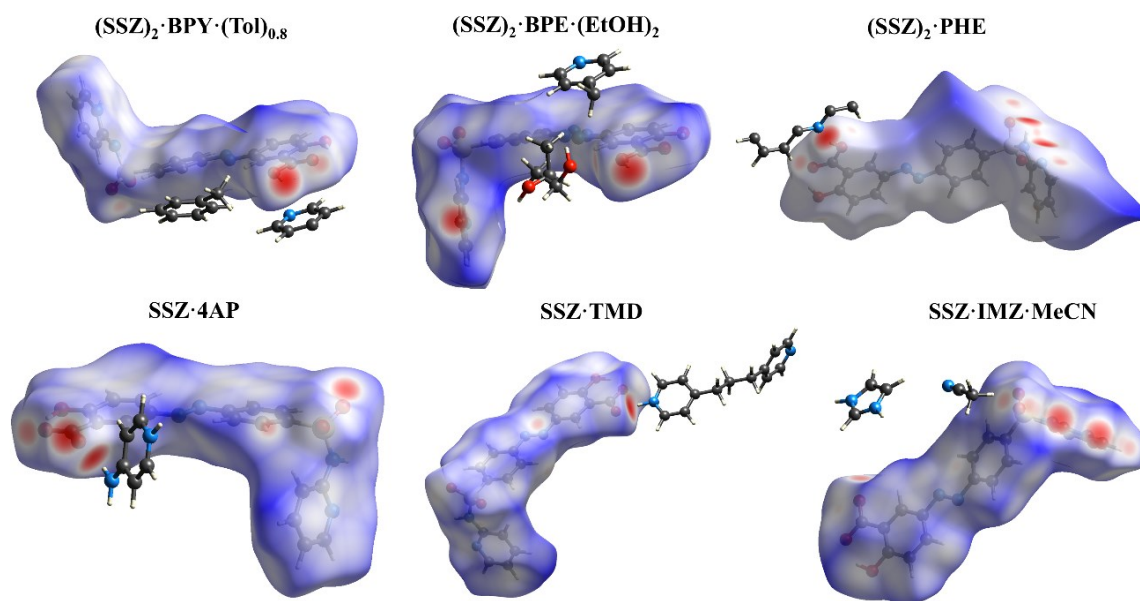


Figure S2.14. 3D d_{norm} surfaces of SSZ in six crystalline solids.

Table S2.1. Summary of experiments for SSZ cocrystals and salts.

Crystal forms	SSZ	CCF / Salt former	Method	Solvent
(SSZ) ₂ ·BPY	398.4 mg, 1 mmol	78.1 mg, 0.5 mmol	Slurry	MeOH 3 mL
(SSZ) ₂ ·BPE·(EtOH) ₂	398.4 mg, 1 mmol	92.1 mg, 0.5 mmol	Slurry	EtOH 3 mL
(SSZ) ₂ ·PHE	398.4 mg, 1 mmol	90.1 mg, 0.5 mmol	Slurry	EtOH 3 mL
SSZ·4AP	398.4 mg, 1 mmol	94.1 mg, 1 mmol	Slurry	MeOH 3 mL
SSZ·IMZ	398.4 mg, 1 mmol	68.1 mg, 1 mmol	LAG	MeCN 30 μ L
SSZ·PPZ	398.4 mg, 1 mmol	43.1 mg, 0.5 mmol	Slurry	MeOH 3 mL
SSZ-2APM	398.4 mg, 1 mmol	95.1 mg, 1 mmol	Slurry	MeOH 3 mL
SSZ-ACRI	398.4 mg, 1 mmol	179.1 mg, 1 mmol	Slurry	MeOH 3 mL
SSZ-4DMP	398.4 mg, 1 mmol	94.1 mg, 1 mmol	Slurry	MeOH 3 mL

Table S2.2. Hydrogen bond and π - π interaction geometries (\AA , $^\circ$) in the SSZ triclinic amide form.^{1,a}

Type	D-H \cdots A	D-H	H \cdots A	D \cdots A	D-H \cdots A	ARU (J)
1	N7-H7 \cdots O27	0.993(17)	1.966(16)	2.948(2)	169.3(17)	[2655.01]
2	O26-H26 \cdots N1	1.01(2)	1.62(2)	2.623(2)	173(2)	[2655.01]
3	Intra O28-H28 \cdots O27	0.91(3)	1.76(3)	2.604(2)	154(3)	
4	C4-H4 \cdots O10	0.93	2.6	3.416(3)	147	[2666.01]
5	C6-H6 \cdots O9	0.93	2.58	3.403(3)	147	[1445.01]
6	Intra C12-H12 \cdots O10	0.93	2.6	2.950(2)	103	
7	C13-H13 \cdots O9	0.93	2.47	3.190(3)	135	[1455.01]
Cg(I)	Cg(J)	Cg-Cg	Interplanar distance	Dihedral Angle	Beta	ARU (J)
1	1	3.6802(13)	3.4095(8)	0.03(10)	22.1	[2656.01]
2	3	3.8848(12)	3.4943(8)	3.87(9)	27.1	[2665.01]

3 3 4.0449(12) 3.5925(7) 0.00(9) 27.4 [2555.01]

^a Symmetry codes: [2666.] = 1-x, 1-y, 1-z; [2655.] = 1-x, -y, -z; [1455.] = -1+x, y, z; [1445.] = -1+x, -1+y, z; [2656] = 1-x, -y, 1-z; [2665] = 1-x, 1-y, -z; [2555] = -x, -y, -z. Cg1, Cg2 and Cg3 are centroids of N1, C2–C6, C11–C16 and C19–C24, respectively. Cg(I) = plane number I; Cg–Cg = distance between ring centroids (Ang.). Beta is the displacement angle between the ring normal of plane I and the centroid vector.

Table S2.3. Hydrogen bond and π – π interaction geometries (Å, °) in the SSZ monoclinic imide form^{2,a}

	Type	D-H...A	D-H	H...A	D...A	D-H...A	ARU (J)
1		N1-H1N...N2	0.90(3)	1.98(3)	2.878(4)	173(3)	[3766.01]
2	Intra	O3-H3O...O4	0.91(4)	1.75(3)	2.612(4)	157(4)	
3		O5-H5O...O2	0.91(4)	1.77(4)	2.635(4)	158(4)	[2645.01]
4		C1-H1...O1	0.93	2.56	2.945(5)	105	[3756.01]
5		C1-H1...O2	0.93	2.54	3.161(4)	124	[3766.01]
6		C3-H3...O4	0.93	2.48	3.404(5)	171	[3656.01]
7	Intra	C4-H4...O1	0.93	2.55	2.982(5)	109	
8	Intra	C7-H7...O1	0.93	2.49	2.869(5)	105	
9	Intra	C18-H18...O5	0.93	2.38	2.695(5)	100	
Cg(I)	Cg(J)	Cg-Cg	Interplanar distance	Dihedral Angle	Beta	ARU (J)	
1	1	4.267(2)	3.9237(15)	0.00(18)	23.1	[3756.01]	

^a Symmetry codes: [3766.] = 2-x, 1-y, 1-z; [2645.] = 1-x, -1/2+y, 1/2-z; [3756.] = 2-x, -y, 1-z; [3656.] = 1-x, -y, 1-z; [3756] = 2-x, -y, 1-z. Cg1 is centroid of N1, C1–C5. Cg(I) = plane number I; Cg–Cg = distance between ring centroids (Ang.). Beta is the displacement angle between the ring normal of plane I and the centroid vector.

Table S2.4. Hydrogen bond and π – π interaction geometries (Å, °) in the (SSZ)₂·BPY·(Tol)_{0.8} cocrystal solvate ^a

	Type	D-H...A	D-H	H...A	D...A	D-H...A	ARU (J)
1		O1-H1...N5	0.82	1.79	2.613(2)	176	[1545.02]

2	Intra	O3-H3A...O2	0.82	1.79	2.514(2)	147	
3		N4-H4N...N3	0.862(14)	2.074(14)	2.927(2)	169.9(19)	[3686.01]
4	Intra	C10-H10...O5	0.93	2.59	2.933(3)	102	
5	Intra	C15-H15...O4	0.93	2.32	2.928(3)	122	
6		C18-H18...O5	0.93	2.55	3.224(3)	130	[3686.01]
7		C20-H20...O4	0.93	2.45	3.338(3)	160	[2545.01]
8		C23-H23...O2	0.93	2.4	3.082(3)	130	[1565.01]

Cg(I)	Cg(J)	Cg-Cg	Interplanar distance	Dihedral Angle	Beta	ARU (J)
1	1	3.4630(11)	3.2495 (8)	0.02(9)	20.2	[3676.01]
2	4	4.0140(12)	3.4478(8)	4.43(10)	27.6	[1555.02]
3	6	4.019(7)	3.6470(8)	23.6(6)	15.2	[1565.04]
4	4	3.8910(13)	3.5740(10)	0.00(11)	23.3	[3675.02]

^a Symmetry codes: [3686.] = [3_686] = 1-x, 3-y, 1-z; [1545.] = [1_545] = x, -1+y, z; [1565.] = [1_565] = x, 1+y, z; [2545.] = [2_545] = 1/2-x, -1+y, 1/2-z; [3676] = 1-x, 2-y, 1-z; [1555.] = x, y, z; [1565] = x, 1+y, z; [3675] = 1-x, 2-y, -z. Cg1, Cg2, C3, C4 and Cg6 are centroids of N4/C14-C18, C2-C7, C8-C13, N5/C19-C23 and C41B-C46B, respectively. Cg(I) = plane number I; Cg-Cg = distance between ring centroids (Ang.). Beta is the displacement angle between the ring normal of plane I and the centroid vector.

Table S2.5. Hydrogen bond and π - π interaction geometries (\AA , $^\circ$) in the (SSZ)₂·BPE·(EtOH)₂ cocrystal solvate ^a

Type	D-H...A	D-H	H...A	D...A	D-H...A	ARU (J)
1	O2-H2...N5	0.82	1.74	2.556(4)	171	[1655.02]
2	Intra O3-H3...O1	0.82	1.83	2.551(4)	146	
3	N4-H4N...N3	0.86(3)	2.04(3)	2.891(4)	172(3)	[2557.01]
4	Intra C7-H7...O2	0.93	2.44	2.762(4)	100	

5	Intra	C12-H12···O5	0.93	2.59	2.935(4)	103	
6	Intra	C15-H15···O5	0.93	2.42	3.009(5)	121	
7		C16-H16···O31A	0.93	2.44	3.194(7)	138	[2667.03]
8		C18-H18···O4	0.93	2.47	3.174(5)	132	[2557.01]
9		C22-H22···O5	0.93	2.51	3.310(4)	144	[2567.01]

Cg(I)	Cg(J)	Cg-Cg	Interplanar distance	Dihedral Angle	Beta	ARU (J)
2	3	4.290(2)	3.6647(14)	15.42(17)	36.1	[2666.01]
2	4	4.140(2)	3.8293(14)	12.32(17)	28.9	[1555.02]
4	4	3.943(2)	3.5232(15)	0.00(18)	26.7	[2576.02]

^a Symmetry codes: [1555] = x, y, z; [1655.] = [1_655] = 1+x, y, z; [2557.] = [2_557] = -x, -y, 2-z; [2667.] = [2_667] = 1-x, 1-y, 2-z; [2567.] = [2_567] = -x, 1-y, 2-z; [2666] = 1-x, 1-y, 1-z; [2576] = -x, 2-y, 1-z. Cg2, Cg3 and Cg4 are centroids of C2–C7, C8–C13 and N5/C19–C23, respectively. Cg(I) = plane number I; Cg–Cg = distance between ring centroids (Ang.). Beta is the displacement angle between the ring normal of plane I and the centroid vector.

Table S2.6. Hydrogen bond and π – π interaction geometries (\AA , $^\circ$) in the (SSZ)₂·PHE cocrystal ^a

Type	D-H···A	D-H	H···A	D···A	D-H···A	ARU (J)	
1	O1-H1···N1	0.82	1.94	2.733(4)	163	[1555.02]	
2	Intra	O3-H30···O2	0.82	1.85	2.575(4)	146	
3		N4-H40···N5	0.86	2.06	2.899(5)	164	[7656.01]
4		C3-H3···O2	0.93	2.48	3.354(5)	158	[1555.01]
5		C6-H6···O1	0.93	2.59	3.281(5)	132	[1555.01]
6	Intra	C18-H18···O5	0.93	2.48	2.872(5)	105	
7	Intra	C21-H21···O5	0.93	2.43	2.982(7)	118	
8		C22-H22···O3	0.93	2.59	3.379(6)	143	[3766.01]
9		C24-H24···O4	0.93	2.46	3.129(6)	129	[7656.01]

Cg(I)	Cg(J)	Cg-Cg	Interplanar distance	Dihedral Angle	Beta	ARU (J)
Cg2	Cg2	3.607(4)	3.4329(14)	0.72(16)	17.9	[2655.01]
Cg3	Cg5	4.168(4)	3.2938(16)	13.64(18)	25.1	[2655.02]
Cg3	Cg5	3.841(4)	3.5585(16)	13.64(18)	23.6	[2755.02]
Cg3	Cg6	4.168(4)	3.2938(16)	13.64(18)	25.1	[4465.02]
Cg3	Cg6	3.841(4)	3.5585(16)	13.64(18)	23.6	[4565.02]

^a Symmetry codes: [3766.] = 2-x, 1-y, 1-z; [7656.] = 3/2-x, 1/2-y, 1-z; [2655.] = 1-x, y, 1/2-z; [2755.] = 2-x, y, 1/2-z; [2755.] = 2-x, y, 1/2-z; [4565] = x, 1-y, 1/2+z. Cg2, Cg3, Cg5 and Cg6 are centroids of C8–C13, C14–C19 and C1–C6, respectively. Cg(I) = plane number I; Cg–Cg = distance between ring centroids (Ang.). Beta is the displacement angle between the ring normal of plane I and the centroid vector.

Table S2.7. Hydrogen bond and π – π interaction geometries (\AA , $^\circ$) in the SSZ·4AP salt ^a

	Type	D-H...A	D-H	H...A	D...A	D-H...A	ARU (J)
1		N1-H1N...O2	0.86	2.15	2.878	142	[1555.01]
2		N2-H2A...O10	0.86	2.03	2.880	168	[1555.02]
3		N2-H2B...O5	0.86	2.17	3.031	178	[1654.01]
4		N3-H3N...O6	0.86	2.31	3.137	162	[2865.02]
5		N3-H3N...O7	0.86	2.59	3.155	124	[2865.02]
6	Intra	O3-H3O...O4	0.82	1.84	2.564	146	
7		N4-H4A...O10	0.86	2.02	2.812	153	[1555.02]
8		N4-H4B...O4	0.86	2.12	2.900	150	[2667.01]
9		N6-H6N...N5	0.86	2.08	2.926	167	[2576.01]
10	Intra	O8-H8O...O9	0.82	1.76	2.492	148	
11		N10-H10N...N9	0.86	2.05	2.894	166	[2855.02]
12		C3-H3...O9	0.93	2.39	3.314	170	[1555.02]
13		C7-H7...O9	0.93	2.59	3.105	116	[1655.02]

14		C9-H9...O5	0.93	2.27	3.137	155	[2667.01]
15	Intra	C11-H11...O2	0.93	2.47	3.029	119	
16		C14-H14...O1	0.93	2.44	3.110	129	[2576.01]
17	Intra	C17-H17...O2	0.93	2.58	2.923	103	
18	Intra	C29-H29...O7	0.93	2.44	3.004	119	
19		C32-H32...O6	0.93	2.47	3.141	129	[2855.02]
20	Intra	C35-H35...O7	0.93	2.54	2.916	104	

Cg(I)	Cg(J)	Cg-Cg	Interplanar distance	Dihedral Angle	Beta	ARU (J)
Cg2	Cg3	3.908(3)	3.731(2)	16.4(2)	33.7	[2577.01]
Cg2	Cg4	3.733(3)	3.512(2)	8.9(2)	17.9	[2766.02]
Cg3	Cg4	3.955(3)	3.549(2)	7.7(2)	33.8	[1466.02]
Cg5	Cg6	4.085(3)	3.655(2)	13.4(2)	39.8	[2765.02]

^a Symmetry codes: [2576.] = -x, 2-y, 1-z; [2855.] = 3-x, -y, -z; [1655.] = 1+x, y, z; [1654.] = 1+x, y, -1+z; [2865.] = 3-x, 1-y, -z; [2667.] = 1-x, 1-y, 2-z; [2577.] = -x, 2-y, 2-z; [2766.] = 2-x, 1-y, 1-z; [1466.] = -1+x, 1+y, 1+z; [1644.] = 1+x, -1+y, -1+z; [2765.] = 2-x, 1-y, -z. Cg2, Cg3, Cg4, Cg5 and Cg6 are centroids of C16–C21, C22–C27, N9/C29–C33, C34–C39 and C40–C45, respectively. Cg(I) = plane number I; Cg–Cg = distance between ring centroids (Ang.). Beta is the displacement angle between the ring normal of plane I and the centroid vector.

Table S2.8. Hydrogen bond and π – π interaction geometries (Å, °) in the SSZ·TMD salt ^a

	Type	D-H...A	D-H	H...A	D...A	D-H...A	ARU (J)
1	Intra	O3-H03...O4	0.82	1.78	2.513(11)	147	
2		N2-H2...N1	0.86	2.09	2.920(13)	162	[2558.01]
3		N5-H5...O5	0.86	1.75	2.610(13)	175	[1555.01]
4		C1-H1...O2	0.93	2.42	3.124(14)	133	[2558.01]
5	Intra	C4-H4...O1	0.93	2.49	3.046(17)	119	
6	Intra	C6-H6...O1	0.93	2.51	2.900(16)	106	

7		C24-H24B...N4	0.97	2.54	3.458(17)	159	[2666.01]
Cg(I)	Cg(J)	Cg-Cg	Interplanar distance	Dihedral Angle	Beta	ARU (J)	
2	3	3.964(11)	3.407(5)	5.2(6)	26.5	[2657.01]	
4	4	4.104(11)	3.326(6)	0.0(7)	35.9	[2766.02]	
5	5	3.647(13)	3.610(8)	0	8.1	[2865.02]	

^a Symmetry codes: [2558.] = -x, -y, 3-z; [2666.] = 1-x, 1-y, 1-z; [2657.] = 1-x, -y, 2-z; [2766.] = 2-x, 1-y, 1-z. Cg2, Cg3, Cg4 and Cg5 are centroids of C6-C11, C12-C17, N5/C19-C23 and N6/C27-C31, respectively. Cg(I) = plane number I; Cg-Cg = distance between ring centroids (Ang.). Beta is the displacement angle between the ring normal of plane I and the centroid vector.

Table S2.9. Hydrogen bond and π - π interaction geometries (\AA , $^\circ$) in the SSZ·IMZ·MeCN salt solvate^a

	Type	D-H...A	D-H	H...A	D...A	D-H...A	ARU (J)
1	Intra	O1-H1...O2	0.82	1.8	2.530(4)	147	
2		N1-H1A...O5	0.86	2.56	3.129(3)	125	[3667.01]
3		N1-H1A...N2	0.86	2.09	2.944(3)	170	[3667.01]
4		N5-H5A...O3	0.86	1.82	2.673(4)	174	[1556.01]
5		N6-H6...O2	0.86	1.86	2.672(3)	156	[2555.01]
6	Intra	C2-H2...O6	0.93	2.51	3.057(3)	118	
7		C5-H5...O5	0.93	2.46	3.085(3)	124	[3667.01]
8	Intra	C7-H7...O6	0.93	2.53	2.911(3)	105	
9		C100-H10B...N100	0.96	2.57	3.487(8)	160	[4565.03]
10		C100-H10C...O5	0.96	2.41	3.212(5)	141	[1555.01]
11		C21-H21...N100	0.93	2.57	3.365(6)	144	[1555.03]
12		C22-H22...O3	0.93	2.35	3.220(4)	155	[4565.01]
Cg(I)	Cg(J)	Cg-Cg	Interplanar distance	Dihedral Angle	Beta	ARU (J)	
1	1	4.1552(17)	3.3891(11)	0.00(13)	35.3	[3666.01]	

2 3 4.2756(17) 3.0805(10) 11.01(12) 33.8 [4555.01]

^a Symmetry codes: [3667.] = 1-x, 1-y, 2-z; [4565.] = x, 3/2-y, 1/2+z; [1556.] = x, y, 1+z; [2555.] = -x, 1/2+y, 1/2-z; [3666.] = 1-x, 1-y, 1-z; [4555.] = x, 1/2-y, 1/2+z; [4554] = x, 1/2-y, -1/2+z. Cg1, Cg2 and Cg3 are centroids of N1/C1-C5, C6-C11 and C12-C17, respectively. Cg(I) = plane number I; Cg-Cg = distance between ring centroids (Ang.). Beta is the displacement angle between the ring normal of plane I and the centroid vector.

Table S2.10. Selected geometric parameters (Å, °)

Solid State	C1-N2	N2-S1	N1-C1-N2-S1	N2-S1-C2-C3
SSZ (imide form)	1.348 (4)	1.586 (3)	164.70	43.90
SSZ (amide form)	1.425 (2)	1.6539 (16)	107.13	86.38
(SSZ) ₂ ·BPY·(Tol) _{0.8}	1.350 (6)	1.604 (4)	173.40	94.94
(SSZ) ₂ ·BPE·(EtOH) ₂	1.351 (2)	1.597 (8)	-173.62	74.53
(SSZ) ₂ ·PHE	1.331 (5)	1.594 (3)	179.70	-117.89
SSZ·4AP	1.339 (5)	1.582 (4)	178.95	-74.11
SSZ·TMD	1.350 (2)	1.597 (8)	-178.26	78.38
SSZ·IMZ·MeCN	1.343 (3)	1.603 (2)	-178.45	56.11

Table S2.11. Summary of the various contact contributions to the SSZ Hirshfeld surface area in different cocrystals and salts.

	O-H	H-H	C-H	C-O	C-C	N-H	O-N	N-C	N-N	H-S	O-O
(SSZ)₂·BPY·(Tol)_{0.8}	21.5	32.8	21.6	3.8	4.5	12.4	1.5	1.9	0	0	0
(SSZ)₂·BPE·(EtOH)₂	23	37.8	15.6	3.9	3.8	9.3	1.3	4.3	0.5	0	0.5
(SSZ)₂·PHE	24.3	40.6	13.1	2.7	6.0	10.0	1.2	1.2	0.3	0	0.6
SSZ·4AP	21.7	27.5	23.4	3.6	6.5	9.7	2.9	2.2	1.7	0	0.8
SSZ·TMD	23.3	32.2	22.5	4.0	3.8	9.7	3.1	1.0	0.3	0	0
SSZ·IMZ·MeCN	25.0	27.1	22.2	3.2	4.9	12.1	1.0	4.4	0	0.1	0.1

REFERENCES

- (1) Filip, L. A.; Caira, M. R.; Farcas, S. I.; Bojit, M. T., Triclinic polymorph of sulfasalazine. *Acta Cryst.* **2001**, C57, 435–436.
- (2) Blake, A. J.; Lin, X.; Schroder, M.; Wilson, C.; Yuan, R. X., The imide tautomer of sulfasalazine. *Acta Cryst.* **2004**, C60, o226-228.



**Chapter 3 Experimental and Theoretical
Investigation of Hydrogen-Bonding
Interactions in Cocrystals of Sulfaguanidine**

(Cryst. Growth Des. **2023**, 23, 4, 2306–2320)



3.1 Abstract

Pharmaceutical cocrystals, a type of multi-component crystalline materials incorporating two or more molecular and / or ionic compounds connected by non-covalent interactions (such as hydrogen bonds, π - π interactions, and halogen bonds), are attracting increasing attention in crystal engineering. Sulfaguanidine (SGD), one of the most frequently used sulfonamide compounds, was chosen as a model compound in this work to further investigate the hydrogen bond interactions in cocrystals, since it possesses various hydrogen bond donor and acceptor sites. Five cocrystals of SGD, synthesized successfully by slurry and slow evaporation methods, were fully characterized by thermal analysis, X-ray techniques and Fourier transform infrared spectroscopy. To gain an insight into the nature of hydrogen-bonding interactions, theoretical calculations including the analysis of Hirshfeld surface, MEPS (molecular electrostatic potential surface) and QTAIM (quantum theory of atoms in molecules) were conducted. The results are a part of a systematic study of cocrystals of sulfonamides that aims to establish synthon hierarchies in cocrystals containing molecules with multiple hydrogen-bonding functional groups.

3.2 Introduction

Crystal engineering, as an important part of supramolecular chemistry, deals with the understanding of intermolecular interactions in the context of crystal packing and the utilization of such understanding in the design of new solids with expected physiochemical properties,¹ which has been widely used in academia and industry

including pharmaceutical,² chemical,³ photographic processing,⁴ textile⁵ and electronics,⁶ etc. With the exploitation of the crystal engineering strategies, recent decades have witnessed an enormous interest in the design of multi-component crystalline materials (e.g., cocrystals, salts, hydrates / solvates).^{7, 8} In particular, cocrystals offer many possibilities when it comes to crystal engineering since there are various coformers which can be assembled with target compounds by non-covalent interactions, such as hydrogen bonding interactions, π - π interactions, halogen bonds, etc.⁹ These interactions can manipulate the molecular arrangement in crystal structures, resulting in the modification of the physicochemical properties, such as solubility, luminescence and stability, etc.¹⁰⁻¹³

Among different non-covalent intermolecular contacts, hydrogen bonds are of particular interest. Conventional hydrogen bonds ($A-H\cdots B$, where A and B can be elements such as N, O, or F) represent the strongest interactions,¹⁴ while $C-H\cdots O$ / N belong to non-conventional hydrogen bonds, which are much weaker than conventional hydrogen bonds.¹⁵ Furthermore, the contribution of hydrogen bonds to the crystal stability is not an additive one, hence, one strong hydrogen bond interaction is not equivalent to the sum of several weak ones.¹⁶ In the late 1980s, Etter provided three general rules for hydrogen bond patterns in molecular solids,¹⁷ which are nowadays widely applied and have proven to be of great use in the design and development of cocrystals. From the perspective of supramolecular chemistry, cocrystals can be considered as a structure composed of subunits (i.e., supramolecular synthons), the majority of which are joined by hydrogen bond interactions. Therefore, an in-depth understanding of hydrogen bond interactions will aid in the design of the cocrystals with desired physicochemical properties.

More recently, several computational techniques have been developed to explain

the intermolecular interactions in crystalline solids. The Hirshfeld surface is a unique tool to investigate and visualize different types of intermolecular interactions in crystals. The corresponding two-dimensional fingerprint plots can provide quantitative information on these interactions, for example demonstrating common features and trends in specific compounds present in cocrystals.¹⁸⁻²⁰ Luo *et al.* performed the Hirshfeld surface analysis of pyrazinecarboxamide in twelve cocrystals and compared the quantitative information of intermolecular interactions with their crystal structures, revealing the influence in different contacts by different coformers.¹⁹ In addition, DFT calculations are also widely applied to elucidate whether cocrystal formation is possible in terms of the structure and interaction of molecules, gaining additional insight into the complex information on intermolecular interactions in different cocrystals. As the formation of hydrogen bonds is primarily driven by electrostatic interactions, molecular electrostatic potential surfaces (MEPSs) can illustrate electrostatic interactions by visualizing the potential hydrogen donor and acceptor sites.^{21, 22} Sarkar *et al.* synthesized eight cocrystals of thiophene-based compounds and conducted MEPS calculations, indicating the prediction of the homomeric and heteromeric synthon matched the experimental cocrystallization studies in seven out of eight cases.²³ In addition, QTAIM (quantum theory of atoms in molecules) analysis has been applied in the decoding of weak interactions of cocrystals, providing a pathway for comparing the experimental with the theoretically derived electron density based on the topological properties of the electron density (ρ).²⁴ Bankiewicz and Wojtulewski investigated the molecular arrangement of dipicolinic acid with two coformers in their crystal structures by DFT and subsequent QTAIM analysis, and obtained more detailed information about the topology and energy of interaction

in the two cocrystals.²⁵ Prediction of the stability based on the strongest intermolecular hydrogen bonds was performed on ten polymeric drug systems using this methodology. It was found that predictions made with QTAIM analysis are more reliable than the ones made using the COMPASS force-field, DFT and DFT-D calculations.¹⁶

Sulfonamides are an important class of antibiotics used in veterinary and human medicine (Figure 3.1),²⁶ and the crystal structure landscape of many sulfonamide drugs has been explored to date.²⁷ For instance, Nangia *et al.* synthesized a series of cocrystals of celecoxib with carboxamide and investigated the synthons in different crystals and their physicochemical properties.²⁸ Elacqua and co-workers explored the cocrystals and salts of sulfadiazine and pyridines, demonstrating the “chameleon-like” behaviour of tautomers at the cocrystal–salt boundary.²⁹

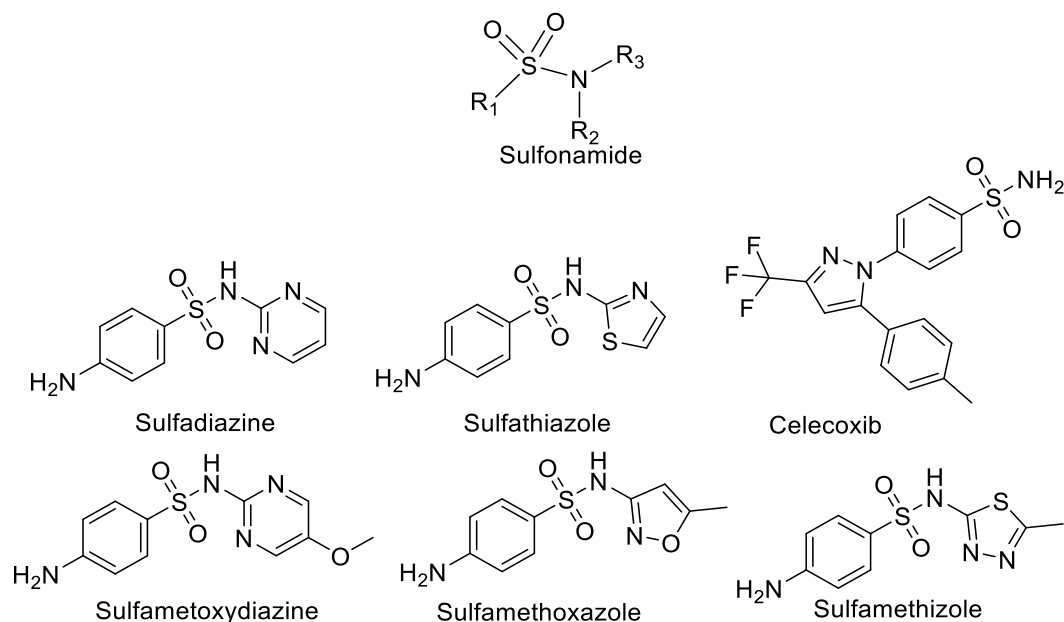


Figure 3.1. Chemical structures of some common sulfonamide drugs.

Sulfaguanidine (SGD, Figure 3.2), one of the most frequently used sulfonamide compounds in medicated feeds, is used to treat enteric infections such as bacillary dysentery.³⁰⁻³² The amino group, sulfonyl group and guanidyl group of SGD molecule can participate in hydrogen bond interactions as donor and/or acceptor sites and form a variety of supramolecular synthons, which creates challenges in predicting supramolecular synthon behaviour in different SGD crystal forms. To best of our knowledge, the crystal form landscape of SGD has not been well explored yet. According to the Cambridge Structural Database (CSD) search,³³ the first SGD-related structure SGD·H₂O (CCDC refcode: 1261309) was published by Alléaume *et al.* in 1976, and demonstrated that the amino form of SGD is present in SGD·H₂O while the imino form of SGD appears in some metal complexes of SGD (Figure 3.2).³⁴ In 1977, three polymorphs of SGD (CCDC refcodes: 1317914-1317916) and SGD acetone solvate (CCDC refcode: 1317913) were published by Alberola *et al.*,³⁵ however, their 3D structures and the original literature are not available in the CSD. The crystal structure of SGD (CCDC refcode: 1317917) was reported by Kálmán and co-workers in 1981.³⁶ In 1986, the first SGD cocrystal SGD-ATP (antipyrine) (CCDC refcode: 1317714) was reported.³⁷ Other two SGD cocrystals SGD-PT (1,10-phenanthroline) and SGD-TBA (thiobarbituric acid)·2H₂O were analyzed structurally by Abidi and colleagues.³⁰ These possess higher antibacterial activity and lower hemolytic toxicity compared with the starting materials.

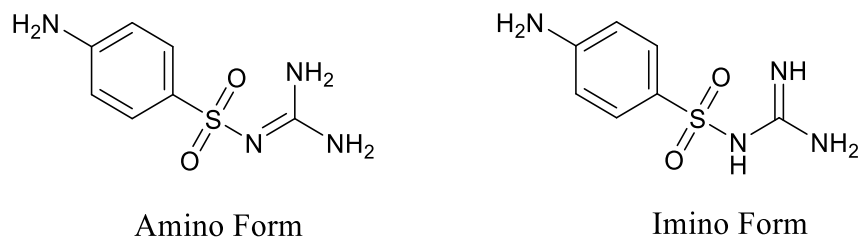


Figure 3.2. Molecular structures of sulfaguanidine (amino form on the left and imino form on the right).

In this study, five novel cocrystals of SGD with 1,2-di(4-pyridyl)ethylene (DPEL), 4-nitrobenzoic acid (4NBA), 3-nitrobenzoic acid (3NBA) and phenazine (PHE) (Figure 3.3) are reported. All these cocrystals were fully characterized by thermal analysis, X-ray techniques and FT-IR spectroscopy. To establish hierarchies of supramolecular synthons and gain an insight into the intermolecular interactions of SGD cocrystals, Hirshfeld surfaces, MEPS and QTAIM analysis were conducted on the five new SGD cocrystals, as well as the three previously reported SGD cocrystals.

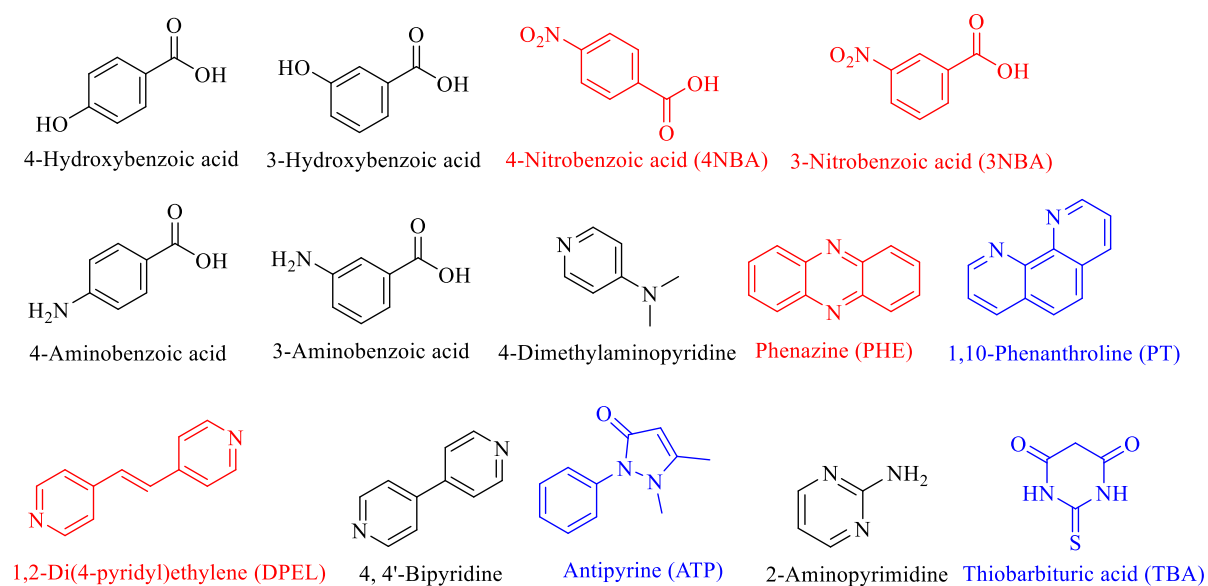


Figure 3.3. Molecular structures of coformers present in this work (successful are red, unsuccessful are black) and reported in the literature (blue).

3.3 Experimental Section

3.3.1 Materials

Sulfaguanidine monohydrate was purchased from Fluorochem and used as received without further purification. All the coformers were purchased from Sigma-Aldrich and used as received. Solvents were obtained from Honeywell International, Inc. and used as received without further purification.

3.3.2 Synthesis

The cocrystals were produced by dissolving the components in solvents and allowing the solutions to evaporate before harvesting the crystals for single crystal analysis. Bulk products were made by slurring a mixture of components in solvent at room temperature for 2-3 days. The resulting suspension was allowed to dry in the fume hood overnight. The powdered product was collected and analyzed by powder X-ray diffraction (PXRD).

SGD-DPEL: For the crystallization experiment a 1:1 molar ratio of SGD·H₂O (34.8 mg, 0.15 mmol) and DPEL (27.3 mg, 0.15 mmol) were placed in a mixture of acetonitrile and methanol (1:1, v/v). Colourless plate-like crystals were harvested after 3-5 days. A 1:1 mixture of SGD·H₂O (232.3 mg, 1 mmol) and DPEL (182.2 mg, 1 mmol) in methanol were used for the slurry experiments.

SGD-4NBA: Crystals were produced by dissolving a 1:1 molar ratio of SGD·H₂O (34.8 mg, 0.15 mmol) and 4NBA (25.1 mg, 0.15 mmol) in methanol to yield yellow plate-like crystals after 3-5 days. A 1:1 mixture of SGD·H₂O (232.3 mg, 1 mmol) and 4NBA (167.1 mg, 1 mmol) in methanol were used for the slurry experiments.

SGD-3NBA: Crystals were produced by dissolving a 1:1 molar ratio of SGD·H₂O (34.8 mg, 0.15 mmol) and 3NBA (25.1 mg, 0.15 mmol) in methanol to afford yellow plate-like crystals after 3-5 days. For the slurry experiments a 1:1 mixture of SGD·H₂O (232.3 mg, 1 mmol) and 3NBA (167.1 mg, 1 mmol) in methanol was used.

SGD-3NBA·MeCN: The cocrystal solvate was produced by dissolving a 1:2 molar ratio of SGD·H₂O (34.8 mg, 0.15 mmol) and 3NBA (50.2 mg, 0.3 mmol) in a mixture of acetonitrile and deionized water (1:1, v/v). Yellow plate-like crystals were harvested after 3-5 days in the fume hood. Bulk amounts of the solvated cocrystal were made by slurring a 1:2 mixture of SGD·H₂O (232.3 mg, 1 mmol) and 3NBA (334.2 mg, 2 mmol) in acetonitrile for 3 days.

SGD-PHE: Yellow plate-like crystals were produced by dissolving a 1:1 molar ratio of SGD·H₂O (34.8 mg, 0.15 mmol) and PHE (27.0 mg, 0.15 mmol) in ethanol and harvesting after 1-2 days. A 1:1 mixture of SGD·H₂O (232.3 mg, 1 mmol) and PHE (180.2 mg, 1 mmol) in ethanol was used for the slurring experiments.

3.3.3 Physical Measurements

Differential scanning calorimetry (DSC) experiments were conducted on a TA Instruments Q1000 under a continuously purged dry nitrogen atmosphere. Powdered samples (2-6 mg) were crimped in nonhermetic aluminum pans and analyzed from 25 to 300 °C at a heating rate of 10 °C min⁻¹. IR spectra were performed on a PerkinElmer UATR Two spectrophotometer using a diamond attenuated total reflectance accessory. Powdered samples were scanned over a range of 400-4000 cm⁻¹ and an average of four scans was taken for each spectrum obtained with a resolution of 4 cm⁻¹. PXRD data were recorded using a STOE

STADI MP diffractometer with Cu K α radiation using a linear position-sensitive detector over the 2θ range of 3.5–45.5° with an increment of 0.05° at a rate of 2° min⁻¹. The powdered samples were made between transmission foils and the data were analyzed via STOE WinXPOW POWDAT software.³⁸ Single crystal X-ray diffraction (SCXRD) data were collected on a Bruker APEX II DUO with monochromated Mo K α radiation ($\lambda = 0.7107 \text{ \AA}$). All calculations and refinements were made using Bruker APEX software with the SHELX suite of programs.^{39,40} Nonhydrogen atoms were refined anisotropically. All hydrogen atoms were placed in geometrically calculated positions using the riding model, with C–H = 0.93–0.97 Å and N–H = 0.86–0.89 Å, and Uiso (H) (in the range 1.2–1.5 times Ueq of the parent atom). Crystal structures were viewed and analyzed using the DIAMOND 4.6 software package,⁴¹ and the data of potential hydrogen bonds and π – π interactions were obtained using the PLATON program.^{42,43} Crystallographic parameters are listed in Table 3.1.

3.3.4 Computational Studies

Hirshfeld surface analysis and two-dimensional fingerprint plots were analyzed using the CrystalExplorer 21.5 program.²⁰ The optimized geometries and energies of the SGD cocrystals in the ground state were obtained by the density functional theory (DFT) methods using the Gaussian 09 program package employing the B3LYP functional with 6-311G (d,p) basis set.²¹ MEPSs were computed at the same level of theory using Multiwfn 3.8 program and plotted using VMD.^{24, 44, 45} QTAIM analysis was carried on geometry optimized cocrystal structures using a periodic plane wave DFT using the QE package.⁴⁶ Ultrasoft pseudo potential with kinetic energy cutoff 45 Ry and 425 Ry charge density cutoff was employed for

the calculations. Critic2 was used for topology analysis to locate the bond critical points.⁴⁷ Estimated hydrogen bonding energy was calculated from the theoretical equation fitted with experimental data.⁴⁸

Table 3.1. Crystallographic data for SGD-DPEL, SGD-4NBA, SGD-3NBA and SGD-3NBA·MeCN cocrystals.

	SGD-DPEL 1:1	SGD-4NBA 1:1	SGD-3NBA 1:1	SGD-3NBA·MeCN 1:2:1	SGD-PHE 1:1
chemical formula	C ₁₉ H ₂₀ N ₆ O ₂ S	C ₁₄ H ₁₅ N ₅ O ₆ S	C ₁₄ H ₁₅ N ₅ O ₆ S	C ₂₃ H ₂₃ N ₇ O ₁₀ S	C ₁₉ H ₁₈ N ₆ O ₂ S
formula weight	396.47	381.37	381.37	589.54	394.45
crystal system	triclinic	monoclinic	monoclinic	triclinic	monoclinic
space group, <i>Z</i>	<i>P</i> $\bar{1}$, 2	<i>C</i> 2/ <i>c</i> , 8	<i>C</i> 2/ <i>c</i> , 8	<i>P</i> $\bar{1}$, 2	<i>P</i> 2 ₁ / <i>c</i> , 4
temperature (K)	296(2)	296	296	296(2)	296(2)
<i>a</i> (Å)	9.2182(6)	29.597(7)	23.0253(18)	8.3188(10)	8.7472(5)
<i>b</i> (Å)	10.1853(7)	7.0348(17)	12.2300(9)	10.4106(14)	13.0128(9)
<i>c</i> (Å)	11.3564(8)	16.074(4)	14.775(2)	16.261(2)	16.8853(9)
α (°)	84.599(2)	90	90	105.555(3)	90
β (°)	79.857(2)	96.582(5)	124.408(1)	90.390(4)	102.097(2)
γ (°)	66.6940(10)	90	90	102.618(2)	90
volume (Å ³)	963.60(11)	3324.7(14)	3432.7(6)	1320.7(3)	1879.3(2)
ρ_{calc} (g cm ⁻³)	1.366	1.524	1.476	1.483	1.394
radiation type	Mo K α	Mo K α	Mo K α	Mo K α	Mo K α
μ (mm ⁻¹)	0.196	0.240	0.232	0.193	0.201
reflns measured	18145	14795	16726	25438	18949
reflns independent	4808	4171	4294	6638	4685
significant [<i>I</i> >2 σ (<i>I</i>)]	4150	3378	3647	4922	3651
parameters refined	277	256	256	373	253
restraints	18	13	13	24	0

$\Delta\rho_{max}, \Delta\rho_{min}$ (e Å ⁻³)	0.25, -0.47	0.39, -0.64	0.26, -0.63	0.389, -0.393	0.357, -0.327
$F(000)$	416	1584	1584	612	824
$R_I [I > 2\sigma(I)]$	0.0379	0.0501	0.0364	0.0547	0.0424
w R_2 (all data)	0.1076	0.1719	0.1070	0.1647	0.1063
CCDC number	2190690	2190688	2190691	2190689	2190692

3.4 Results and Discussion

3.4.1 Physical Characterization

The thermal behaviour of the SGD cocrystals was assessed using DSC. The DSC traces of five cocrystals that were obtained and the corresponding single components are shown in Figure S3.1. Table 3.2 displays the melting points of five cocrystals and their starting materials. SGD-DPEL and SGD-PHE cocrystals melt at a higher temperature than the starting materials, respectively, while the melting points of SGD-4NBA, SGD-3NBA and SGD-3NBA·MeCN are in between those of the individual components. IR spectra of the cocrystals and the starting materials are shown in Figures S3.2-S3.5. As shown in Table 3.3, the -NH₂, C=N and sulfonyl group bands of SGD·H₂O exhibit a blue shift in all five cocrystals. Meanwhile, all the observed differences indicated that the sulfonyl group, amino group and / or guanidyl group are involved in the formation of hydrogen bonds in different cocrystals, confirming the formation of the new crystalline forms of SGD.

Table 3.2. Melting points of cocrystals and starting materials.

solids	T _m (°C)	solids	T _m (°C)
SGD·H ₂ O	189–190 ⁴⁹	SGD-DPEL	193–196
DPEL	150–153 ⁵⁰	SGD-4NBA	218–220
4NBA	240–241 ⁵¹	SGD-3NBA	178–181
3NBA	142–143 ⁵²	SGD-3NBA·MeCN	175–178
PHE	175–176 ⁵³	SGD-PHE	209–211

Table 3.3. Distinctive bands (cm^{-1}) in the FTIR spectra of $\text{SGD}\cdot\text{H}_2\text{O}$ and the cocrystals.

solid form	ν_{NH_2}	ν_{SO_2}	$\nu_{\text{C}=\text{N}}$
$\text{SGD}\cdot\text{H}_2\text{O}$	3394, 3337	1123, 1082	1612
SGD-DPEL	3398, 3339	1132, 1082	1634
SGD-4NBA	3407, 3368	1130, 1090	1627
SGD-3NBA	3438, 3367	1136, 1094	1629
$\text{SGD-3NBA}\cdot\text{MeCN}$	3454, 3374	1133, 1092	1625
SGD-PHE	3401, 3358	1122, 1088	1634

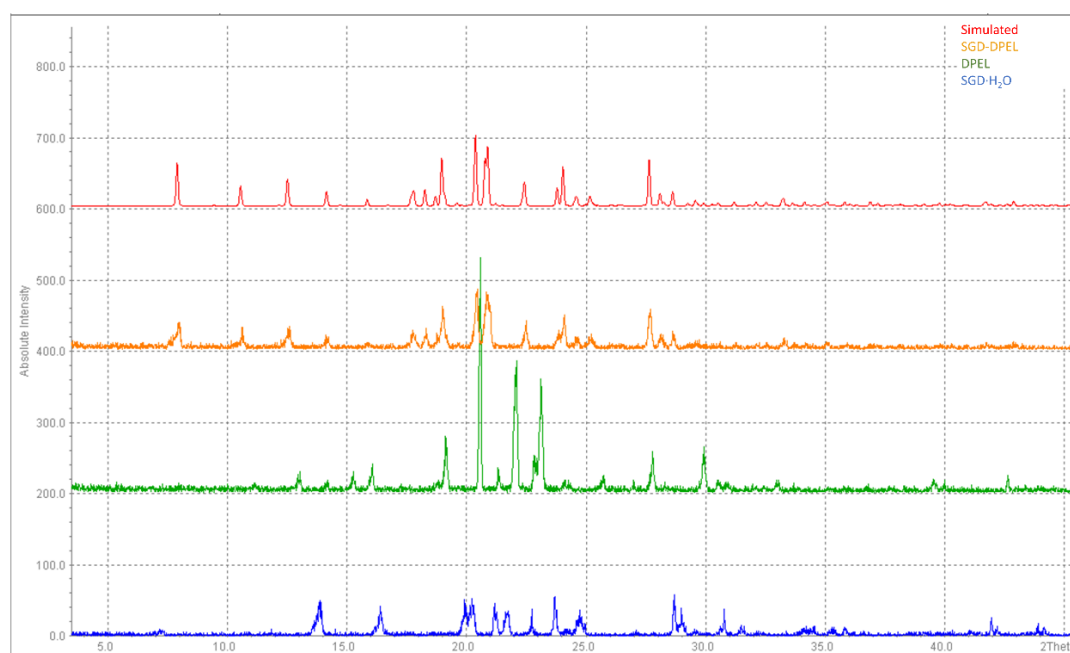


Figure 3.4. PXRD patterns of (a) $\text{SGD}\cdot\text{H}_2\text{O}$ (blue), DPEL (green), SGD-DPEL (orange) and simulated pattern of SGD-DPEL from the crystal structure analysis (red).

PXRD patterns of SGD-DPEL, the two starting materials and simulated patterns of SGD-DPEL from SCXRD analysis are shown in Figure 3.4. SGD-DPEL

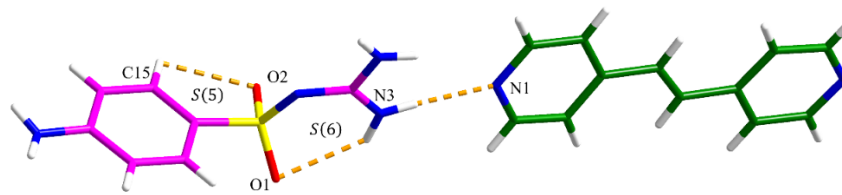
cocrystal exhibits several new diffraction peaks at 2θ values of 7.9° , 10.5° and 12.7° , etc, which are not present in the patterns of the two starting materials, suggesting the formation of new crystalline forms. The PXRD patterns of the other four cocrystals are displayed in Figure S3.6. All the PXRD patterns of the five cocrystals match with the simulated patterns extracted from the SCXRD analysis, indicating these cocrystals can be reproduced in bulk quantities by the slurry method.

3.4.2 Crystal Structure Analysis

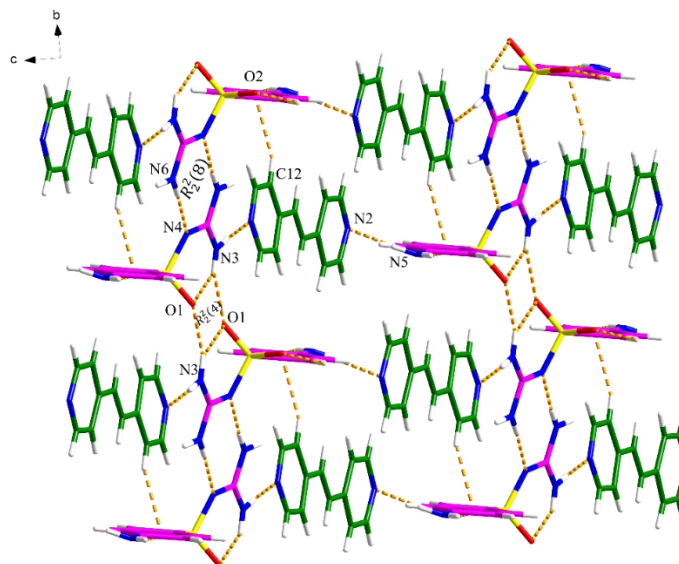
Single crystals of the five cocrystals were obtained and their structures were determined by SCXRD. Ellipsoid plots are shown in Figure S3.7. Hydrogen bonds and π - π interaction geometries are displayed in Tables S3.1-S3.5, respectively.

SGD-DPEL Cocrystal

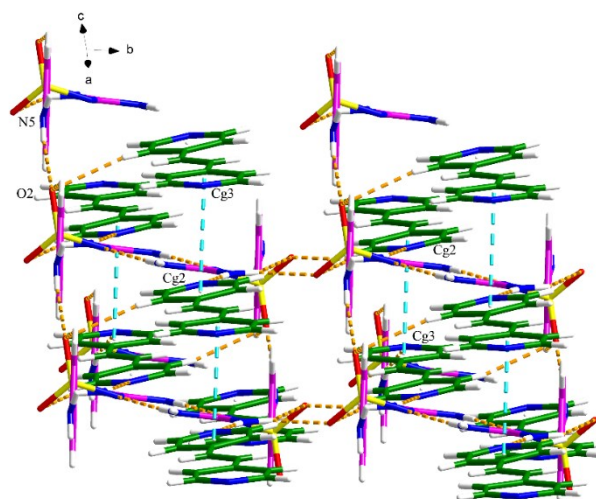
The SGD-DPEL cocrystal crystallizes in the triclinic space group $P\bar{1}$. The asymmetric unit consists of one SGD molecule and one DPEL molecule. As shown in Figure 3.5a, the two components interact with each other via a discrete N3-H11 \cdots N1 hydrogen bond. Along the a axis, an $R_2^2(8)$ motif and an $R_2^2(4)$ ring are generated by two SGD molecules through N6-H14 \cdots N4 and N3-H20 \cdots O1 hydrogen bond interactions. The 2D hydrogen-bonding network is extended via C-H \cdots O and N-H \cdots N discrete hydrogen bonds (Figure 3.5b). The three-dimensional crystal lattice is stabilized by the N5-H15 \cdots O2 hydrogen bond interaction and the π - π interactions through the pyridyl rings of DPEL molecules between the layers (Figure 3.5c).



(a)



(b)

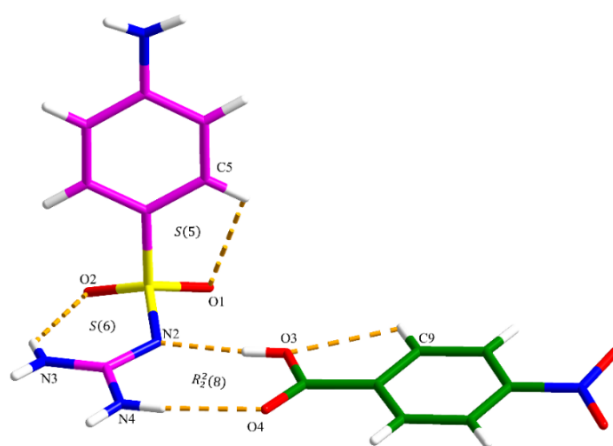


(c)

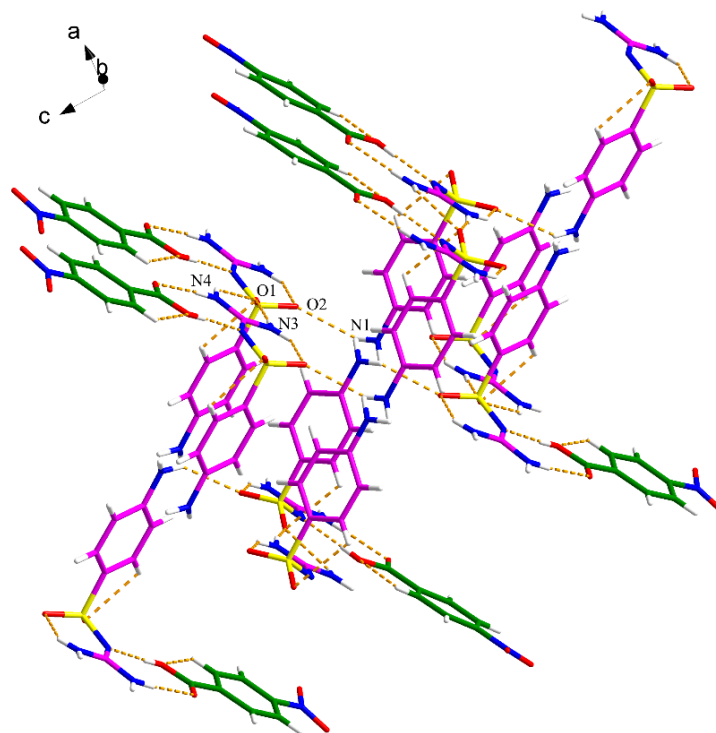
Figure 3.5. Crystal packing diagrams of the SGD-DPEL cocrystal: (a) asymmetric unit (pink is SGD and green is DPEL), (b) two-dimensional hydrogen bonding network, and (c) three-dimensional network (hydrogen bonding is displayed by orange dashed lines and π - π interaction is displayed by blue dashed lines).

SGD-4NBA Cocrystal

SGD and 4NBA form a cocrystal that crystallizes with one SGD molecule and one 4NBA molecule in the asymmetric unit. As shown in Figure 3.6a, the two components interact with each other through $N4-H17\cdots O4$ and $O3-H15\cdots N2$ discrete hydrogen bonds, resulting in an $R_2^2(8)$ motif. The basic unit is extended via three discrete $N-H\cdots O$ hydrogen-bonding interactions, i.e., $N3-H13\cdots O1$, $N4-H16\cdots O1$ and $N1-H18\cdots O2$, resulting in the 3D hydrogen bonding network (Figure 3.6b). No $\pi-\pi$ interactions participate in stabilizing the three-dimensional structure of the SGD-4NBA cocrystal.



(a)



(b)

Figure 3.6. Crystal packing diagrams of the SGD-4NBA cocrystal: (a) asymmetric unit (pink is SGD and green is 4NBA), (b) three-dimensional hydrogen bonding network (hydrogen bonding is displayed by orange dashed lines).

SGD-3NBA Cocrystal

The SGD-3NBA cocrystal crystallizes in the monoclinic system with the $C2/c$ space group. The asymmetric unit contains one SGD molecule and one 3NBA molecule (Figure 3.7a). As shown in Figure 3.7b, four continuous motifs are produced between two SGD molecules and two 3NBA molecules. Specifically, the amino group of SGD 1, the sulfonyl guanidyl group of SGD 2, the carboxyl group from 3NBA 1 and the nitro group from 3NBA 2 are involved in the formation of (from left to right) an $R_2^2(7)$ motif, an $R_2^3(6)$ motif and two $R_2^2(8)$ motifs via $N-H\cdots O$, $O-H\cdots N$ and $C-H\cdots N$ discrete hydrogen bond interactions. The 3D structure is further assembled by the $N-H\cdots O$ and $C-H\cdots O$ discrete

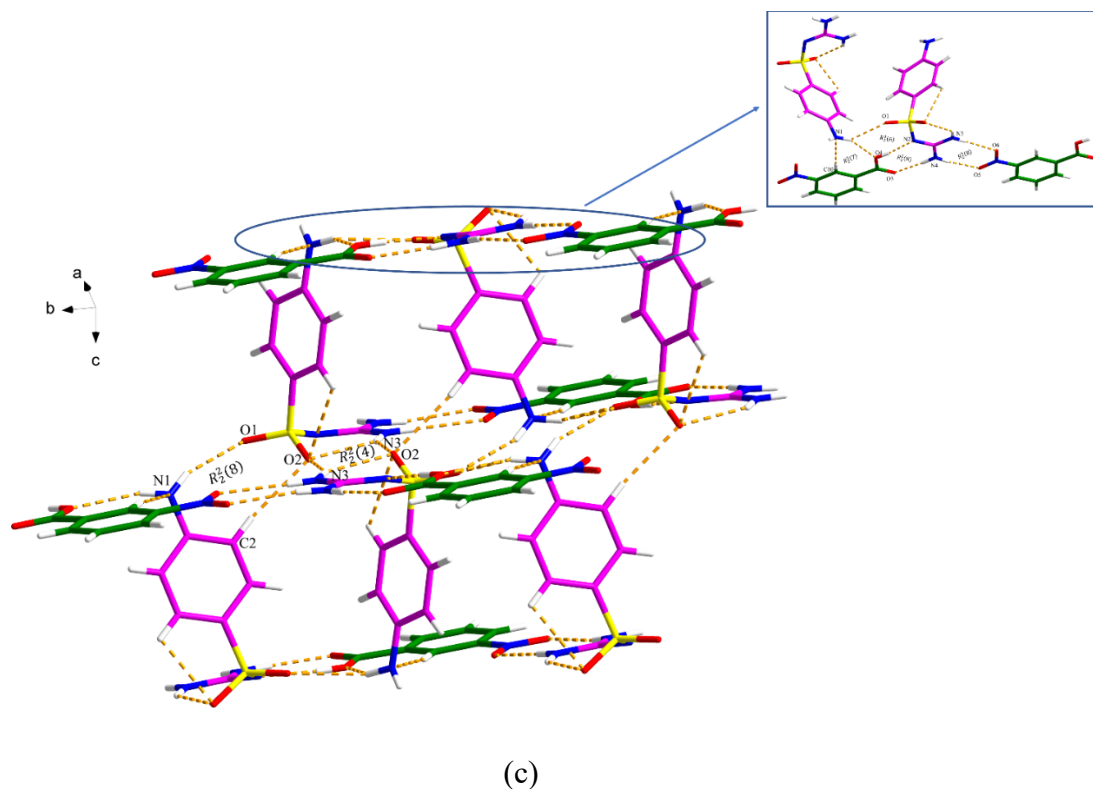


Figure 3.7. Crystal packing diagrams of the SGD-3NBA cocrystal: (a) asymmetric unit (pink is SGD and green is 3NBA), (b) four motifs between two SGD molecules and 3NBA molecules, and (c) three-dimensional hydrogen bonding network (hydrogen bonding is displayed by orange dashed lines).

SGD-3NBA·MeCN Cocrystal Solvate

SGD-3NBA·MeCN crystallizes in the triclinic space group $P\bar{1}$ with one molecule of SGD, two molecules of 3NBA and one molecule of MeCN in the asymmetric unit. As shown in Figure 3.8a, $R_2^2(8)$, $R_2^1(6)$ and $R_4^3(12)$ motifs are generated among these four components via N–H···O, C–H···O and O–H···N discrete hydrogen bond interactions. The hydrogen bonding network is extended via the C–H···O and N–H···O hydrogen bond interactions, the latter hydrogen bond interactions forming an $R_2^2(4)$ ring. Furthermore, two 3NBA are linked by two C11–H11···O5 discrete hydrogen bond interactions, resulting in an $R_2^2(10)$ motif

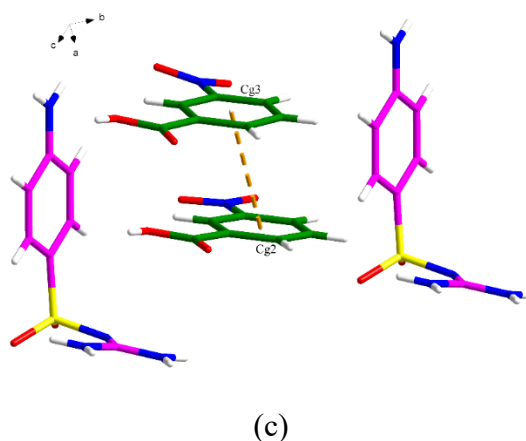


Figure 3.8. Crystal packing diagrams of the SGD-3NBA·MeCN cocrystal: (a) asymmetric unit (pink is SGD, green is 3NBA and blue is MeCN), (b) hydrogen bonding network (hydrogen bonding is displayed by orange dashed lines) and (c) the three-dimensional network resulting from interstack π - π interactions as shown by orange dashed lines (hydrogen bonding is not displayed for clarity).

SGD-PHE Cocrystal

SGD-PHE cocrystallizes in the $P2_1/c$ space group with $Z = 4$, the asymmetric unit consisting of one SGD molecule and one PHE molecule (Figure 3.9a). Notably, the guanidyl group of SGD molecule is only involved as a hydrogen donor in this cocrystal. Along the a axis, the guanidyl group of SGD links PHE molecule via two $N-H\cdots N$ discrete hydrogen bond interactions. The 3D structure is extended through $N3-H3A\cdots O2$ and $N4-H4A\cdots O1$ hydrogen-bonding interactions, forming an $R_2^2(8)$ motif (Figure 3.9b). The $N1-H1A\cdots O2$ hydrogen-bonding interactions between the amino group and sulfonyl group of SGD molecule and the additional π - π interactions between the phenyl rings and pyrazine rings from PHE also contribute to the extended 3D structure of SGD-PHE cocrystal (Figure 3.9c).

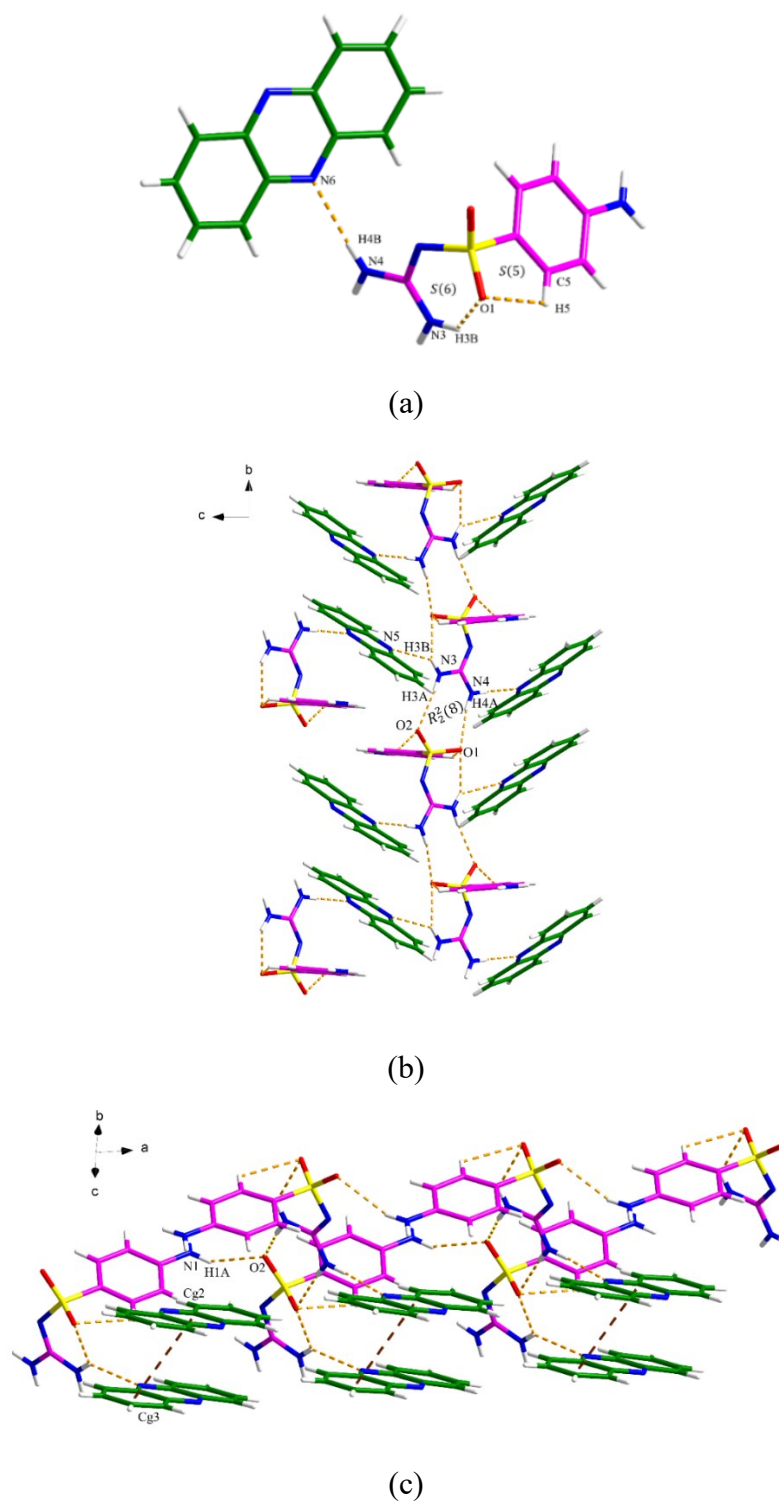
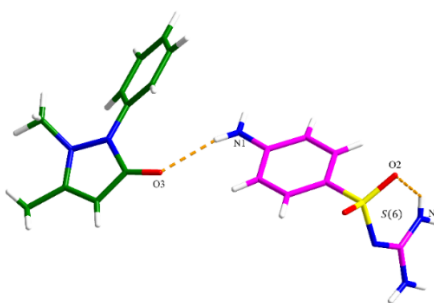


Figure 3.9. Crystal packing diagrams of the SGD-PHE cocrystal: (a) asymmetric unit (pink is SGD and green is PHE), (b) hydrogen bonding network (hydrogen bonding is displayed by orange dashed lines), and (c) the three-dimensional network resulting from interstack π - π interactions as shown by red-brown dashed lines.

The structural analysis of SGD-ATP³⁷ was also conducted prior to the investigation of hydrogen-bonding interactions of SGD cocrystals. Hydrogen bond and π - π interaction geometries are displayed in Tables S3.6.

SGD-ATP Cocrystal

SGD-ATP cocrystallizes in the monoclinic crystal system, $P2_1/c$ space group, with one SGD molecule and ATP molecule in the asymmetric unit, which interact via the N1-H3 \cdots O3 hydrogen bond interaction (Figure 3.10a). As shown in Figure 3.10b, the same ATP molecule connects with another adjacent SGD molecule through N1-H3 \cdots O3 hydrogen bond interaction. The crystal structure is further extended by the hydrogen bond interactions between SGD molecules, generating three different motifs. Specifically, an $R_2^1(6)$ motif is formed via N3-H7 \cdots O1 and N4-H8 \cdots O1, and an $R_2^2(4)$ motif is formed via N4-H9 \cdots O2 inter- and intra-hydrogen bond interactions between the guanidyl and sulfonyl groups in SGD. In addition, an $R_2^2(8)$ homosynthon is generated through N3-H6 \cdots N2 from the two guanidyl groups. The 3D structure is also stabilized by π - π interactions through the pyrazole and phenyl rings of ATP molecules between the layers (Figure 3.10c).



(a)

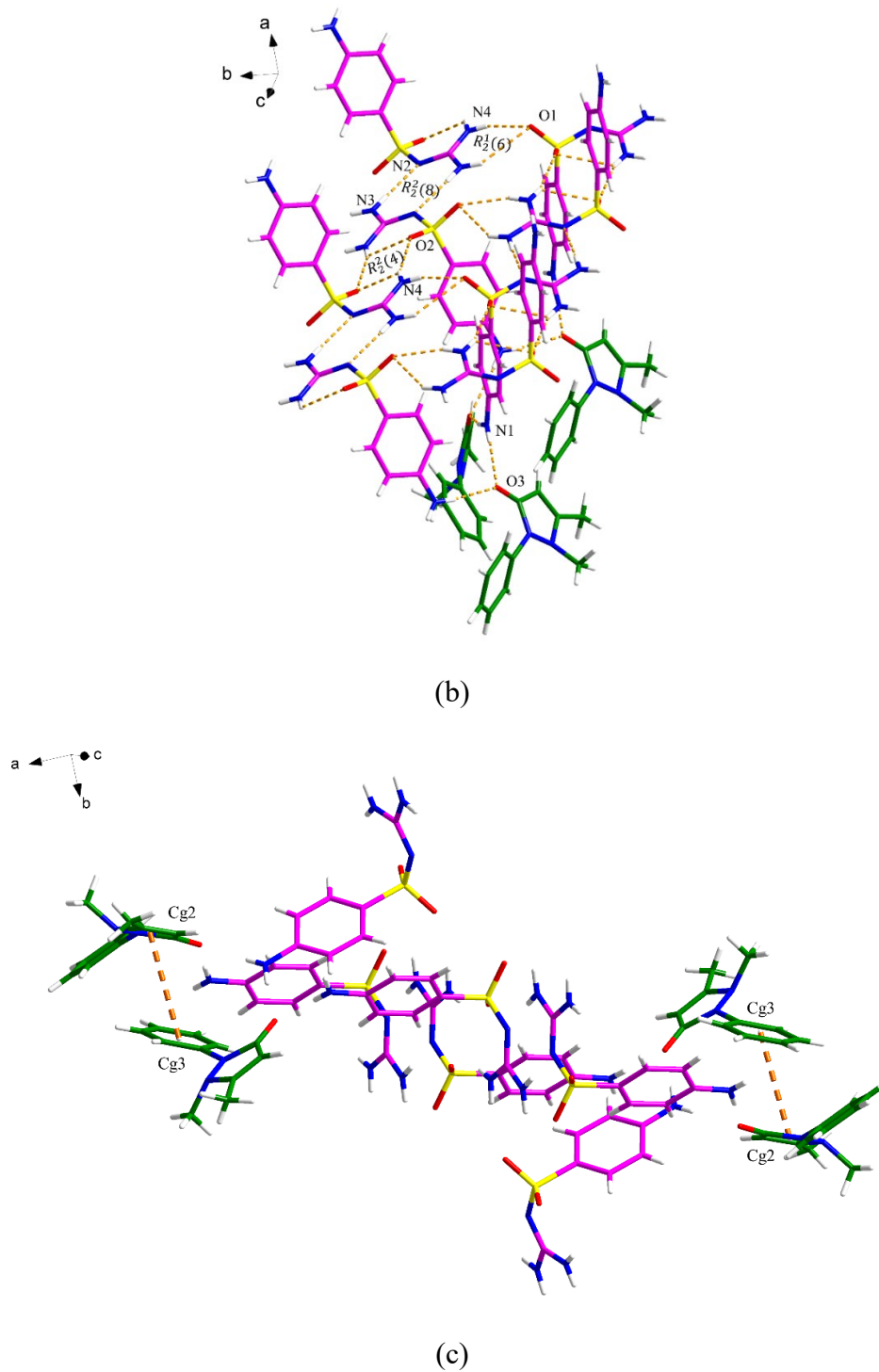
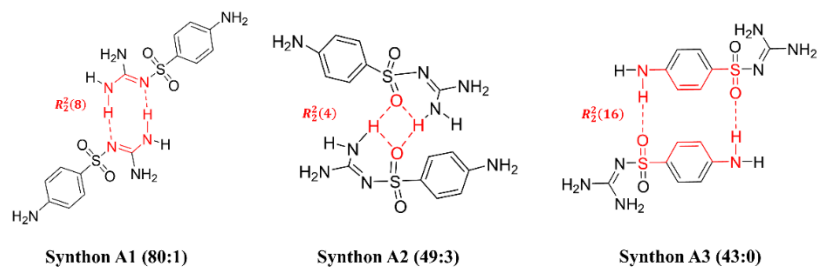


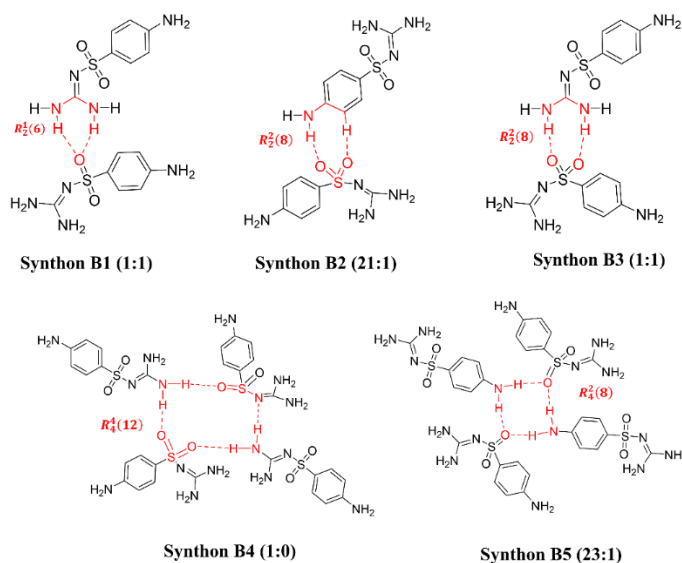
Figure 3.10. Crystal packing diagrams of the SGD-ATP cocrystal: (a) asymmetric unit (pink is SGD and green is ATP), (b) hydrogen bonding network (hydrogen bonding is displayed by orange dashed lines), and (c) three-dimensional network resulting from interstack π - π interactions as shown by orange dashed lines (hydrogen bonding is not displayed for clarity).

Based on the structural analysis above, SGD molecule can form different types of synthons with either SGD molecules or coformer molecules due to the various kinds of hydrogen bond donor and acceptor sites in the molecules. Figure 3.11 illustrates the different types of supramolecular synthons⁵⁴ in the SGD cocrystals, their graph set notation,^{55, 56} and the frequency of occurrence of each synthon in multi-component solids of sulfonamides deposited in CSD. The results of CSD search were obtained and filtered by: 3D coordinates determined, only single crystal structures and only organics, using ConQuest (version 2022.2.0). Table 3.4 displays the frequency of occurrence of each synthon in the different SGD cocrystals. Among all SGD-SGD synthons, synthon A1 has been widely reported in the multi-component solids of sulfonamides in the CSD. However, this robust synthon is less likely to occur when forming cocrystals with acids since in these cases the SGD-coformer interactions might be relatively weaker resulting in the failure of cocrystal formation.⁵⁷ In this work, synthon A1 was observed in SGD-DPEL and SGD-PT cocrystals, which is reasonable as these cofomers can form strong interactions with SGD through the extra hydrogen atoms from the guanidyl group, resulting in the formation of the robust synthon C3. When cocrystallizing with benzoic acid or its derivatives, the guanidyl group from SGD is more likely to form a heterosynthon (C4) with the carboxylic group from the acid instead of forming a homosynthon (A1) with the guanidyl group from another SGD, which is usually energetically more favored.^{58, 59} Synthons C5-C9 are specific to the structures of the cofomers used in this work.

A. SGD-SGD Homosynthons



B. SGD-SGD Heterosynthons



C. SGD-Coformer Heterosynthons

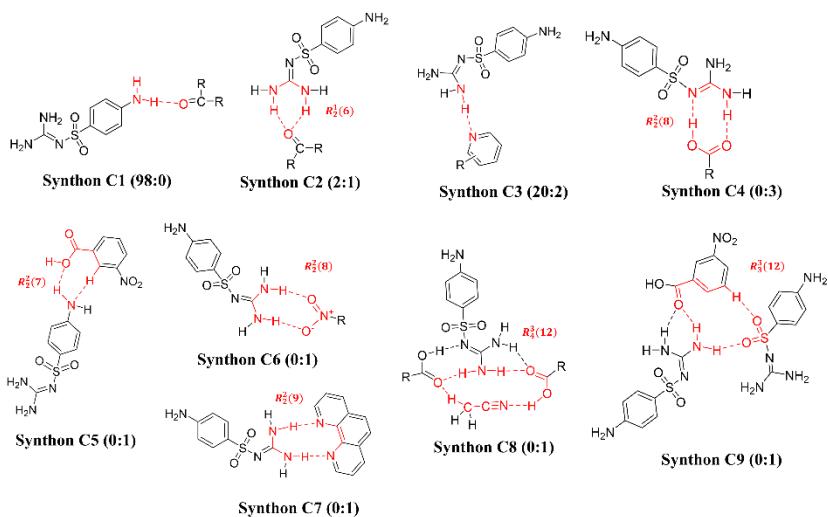


Figure 3.11. The types of synthons identified in the eight SGD cocrystals. Numbers indicate # occurrences in the CSD (left) and in this work (right).

Table 3.4. List of the occurrence of synthons in SGD cocrystals.

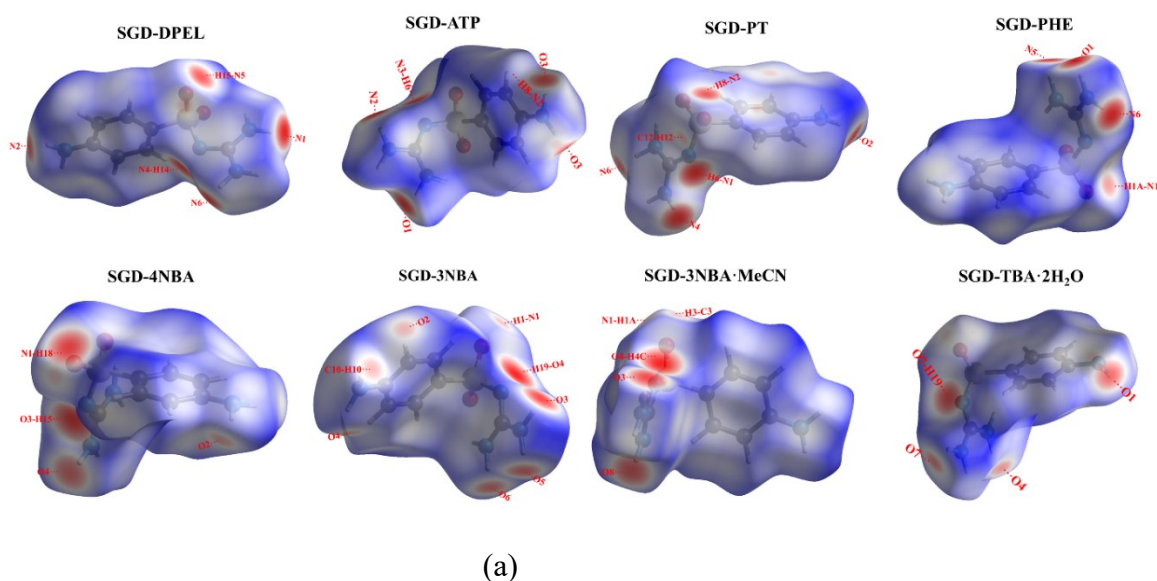
	Synthon	SGD-DPEL ^a	SGD-4NBA ^a	SGD-3NBA ^a	SGD-3NBA·MeCN ^a	SGD-PHE ^a	SGD-PT ³⁰	SGD-TBA·2H ₂ O ³⁰	SGD-ATP ³⁷
SGD- SGD	A1	✓					✓		✓
	A2	✓		✓	✓				✓
	A3							✓	
	B1		✓						✓
	B2			✓					
	B3					✓			
	B4								✓
	B5			✓					
SGD- Coformer	C1								✓
	C2				✓			✓	
	C3	✓				✓	✓		
	C4		✓	✓	✓				
	C5			✓					
	C6			✓					
	C7						✓		
	C8				✓				
	C9				✓				

^a Crystal structure obtained in this work

3.4.3 Computational Studies

3.4.3.1 Hirshfeld Surface Analysis

The Hirshfeld surface analysis has been utilized to investigate and visualize different types of intermolecular interactions in the crystal, and the 2D fingerprint plots provide quantitative information on these interactions.^{18, 19} Figure 3.12a illustrates the Hirshfeld surfaces of SGD that have been mapped over d_{norm} , where the large circular depressions (deep red) stand for the hydrogen bonding contacts (i.e. $\text{H}\cdots\text{O}$ and $\text{H}\cdots\text{N}$) whereas other visible spots represent the $\text{H}\cdots\text{H}$ contacts.⁶⁰ Figure 3.12b demonstrates the corresponding 2D fingerprint plots. In particular, the hydrogen bonding contacts, (appeared as spike-like tips), $\text{H}\cdots\text{H}$ contacts (appeared as asymmetric points spread over a large area) and the $\text{C}\cdots\text{H}$ contacts (presented as symmetric pair of wings) are three most significant contacts in the eight cocrystals.¹⁹



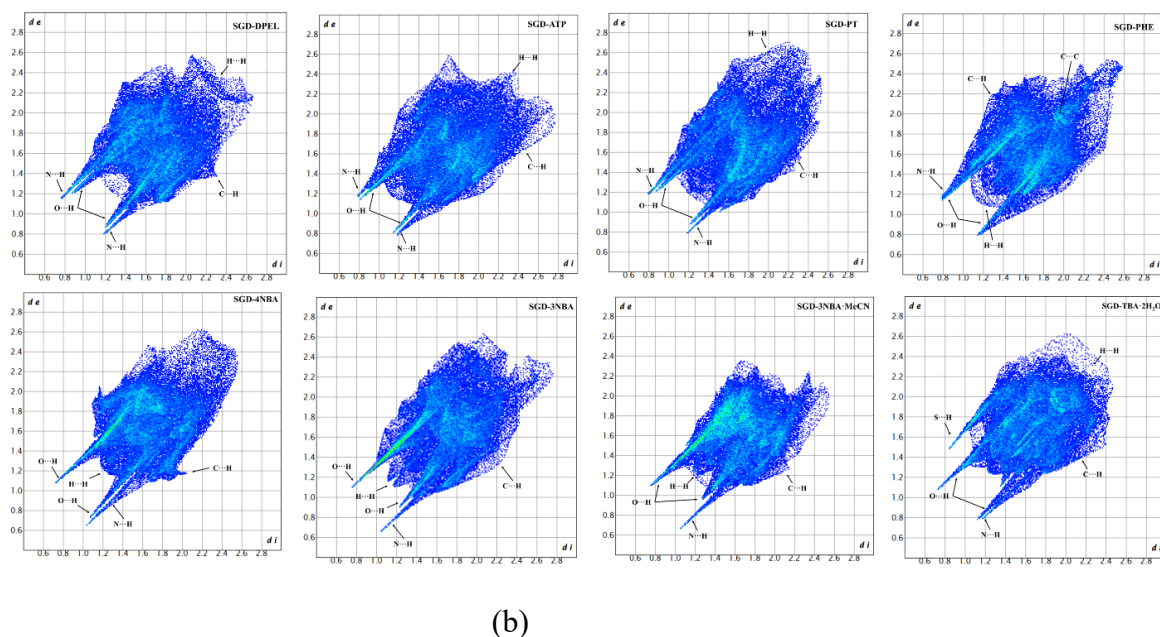


Figure 3.12. (a) Hirshfeld surfaces, and (b) 2D fingerprint plots of SGD in SGD cocrystals.

Table 3.5. Summary of the various contact contributions in SGD cocrystals (%)

	H···H	Hydrogen bond		C···H	C···C	N···C	O···C	others
		H···N	H···O					
SGD-ATP	50.6	7.5	15.4	22.1	3.9	0.1	0.2	0.2
SGD-PHE	46.9	12.7	4.8	22.4	8.3	4.3	0.2	0.4
SGD-DPEL	44.5	13.1	5.4	27.1	2.5	6.4	0.1	0.9
SGD-PT	39.9	16	4.9	24.9	9.1	4.5	0.6	0.1
SGD-4NBA	19.2	7.5	41	12.6	4.2	0.4	12.1	3
SGD-3NBA	15.3	6.6	33.2	25.4	0.1	2	10.2	7.2

According to the structural analysis and Table 3.4, the SGD molecule in any SGD cocrystals can not only interact with coformer molecules but also other SGD

molecules. However, the majority of coformer molecules only interact with SGD molecules in the SGD cocrystals. The exceptions involve three component systems, namely SGD-3NBA·MeCN, this work, and SGD-TBA·2H₂O.³⁰ Therefore, the various contact contributions of coformers were obtained to investigate the influence of different coformers on the intermolecular interactions of the SGD molecule in different SGD cocrystals (Table 3.5).

As shown in Table 3.5, H···H, hydrogen bonding interactions (N···H and O···H) and C···H are the three significant contacts. For SGD-ATP, SGD-PHE, SGD-DPEL and SGD-PT cocrystals, H···H contacts make the largest contribution, which is to be expected since the limited hydrogen bonding sites result in the increase of the contribution of van der Waals force to form cocrystals.⁶¹ The hydrogen bonding interactions (mainly O···H–N for SGD-ATP and N···H–N for these other three cocrystals) make the second or third largest contribution. For SGD-4NBA and SGD-3NBA cocrystals, the increasing hydrogen bonding sites in the coformers lead to the increase of hydrogen bonding interactions (mainly by providing hydrogen bond acceptors and forming O···H–N hydrogen bonds) and the decrease of H···H contacts.

3.4.3.2 MEPS Analysis

MEPS is critical for identifying and ranking sites for hydrogen bonding,²² which has been utilized as an important tool to understand and predict intermolecular interaction in the formation of cocrystals.^{21, 62} The MEPS of SGD cocrystals are shown in Figure 3.13, where the red region represents positive potential and blue shows negative potential.

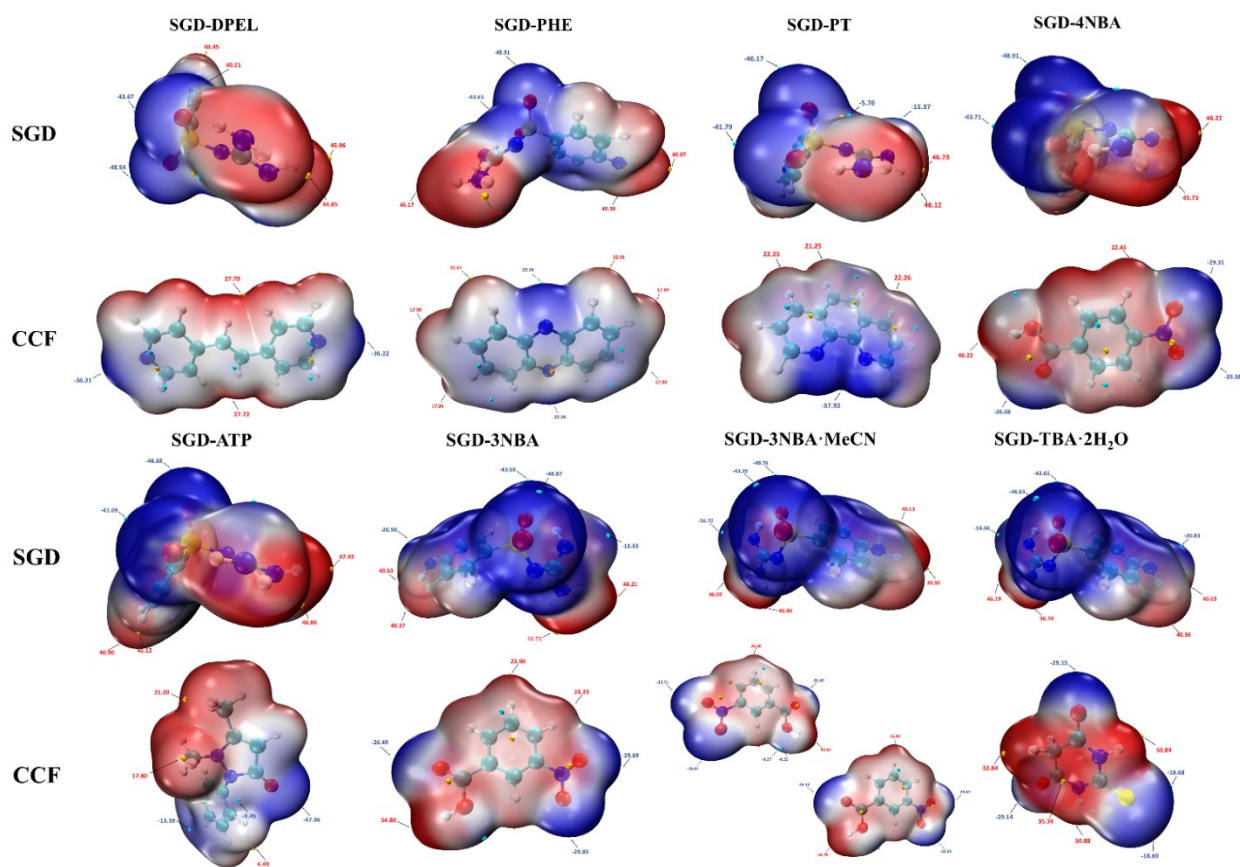


Figure 3.13. The MEPS for SGD cococrystals (significant local minima and maxima of MEPS are labelled by blue and red text, respectively, and the units are kJ mol^{-1}).

After computation, the maxima site of the MEPS for the SGD molecule in all cococrystals is the amino groups of the guanidyl group, the second maxima site is the amino group on the phenyl ring, while the minima values of the MEPS correspond to the two oxygen atoms from the sulfonyl group. These functional groups possess the highest hydrogen bond propensity compared to other groups and sites in the SGD molecule, while the global maxima and minima values of the MEPS for the conformers in the different cococrystals vary significantly.

According to the hierarchical organization of functional group interactions theory, the main site of interaction in cococrystal formation should first occur pairwise in the

minima and maxima of the MEPS.^{63, 64} The formation of four SGD cocrystals (C3 in SGD-DPEL and SGD-PHE, C7 in SGD-PT, and C4 in SGD-4NBA) follow this rule, where a discrete hydrogen bond or a heterodimer occurs between the amino group from guanidyl group in SGD and the global minima site in cofomers, respectively. For SGD-ATP cocrystal, the hydrogen bond (C1) is formed between the oxygen atom (global minima site) from ATP molecules and the amino group on the phenyl ring (second global maxima site) from SGD molecules. For SGD-3NBA, SGD-3NBA·MeCN and SGD-TBA·H₂O, the global maxima sites as hydrogen bond donors in cofomers are engaged in the formation of hydrogen bonds with the SGD molecules where the hydrogen bond acceptors are neither the minima nor the second minima sites. Due to the complexity of multiple hydrogen bond donor and acceptor sites in both SGD molecule and the cofomer molecules, the information of hydrogen bonding ranking sites and the prediction of the most robust synthons cannot be obtained only by MEPS. To further rank the hydrogen bonding sites and quantify the strength of hydrogen bond interactions in SGD cocrystals, QTAIM analysis was conducted.

3.4.3.3 QTAIM Analysis

The basic motive of QTAIM is to investigate the nature of bonding in molecular systems by exploring the charge density or electron density (ρ) of molecules and the Laplacian ($\nabla^2\rho$) of electron density at bond critical points (BCPs), which can be utilized to distinguish between non-covalent and covalent interactions.^{16, 24, 65} Moreover, hydrogen bonding interactions can also be characterized by binding energy, $E_{\text{HBbinding}}$, which can be calculated using equation 1.⁴⁸

$$E_{\text{HBbinding}} = -223.08 * \rho_{\text{bcp}} + 0.7423 \quad (1)$$

In the current work, QTAIM analysis was conducted to gain insight into the nature and quantify the characteristics of non-covalent interactions stabilizing the structures of the SGD cocrystals. Figure 3.14 and Table S3.7 demonstrate the relationship between basic QTAIM parameters (ρ_{bcp} , $E_{\text{HBbinding}}$ and $\nabla^2\rho$) and H...A (acceptor) distances.

As shown in Figure 3.14a, the $\nabla^2\rho$ values of 83 out of 88 contacts fall into the 0-0.2 a.u. range, suggesting the electron density is depleted and representing non-covalent interactions, such as ionic, van der Waals or hydrogen bonds. The $\nabla^2\rho$ values of 5 out of 88 contacts are less than zero, which demonstrates the density is locally concentrated, resulting in covalent bond or covalent character of interaction.²⁴ Based on $\nabla^2\rho$ and H_{BCP} (total electron energy density at bond critical point), Rozas and co-workers classified hydrogen bonds as follows: (i) $\nabla^2\rho > 0$ and $H_{\text{BCP}} > 0$ for weak hydrogen bonds, (ii) $\nabla^2\rho > 0$ and $H_{\text{BCP}} < 0$ for medium and strong hydrogen bonds and (iii) $\nabla^2\rho < 0$ and $H_{\text{BCP}} < 0$ for very strong hydrogen bonds.⁶⁶ Therefore, the 5 contacts are very strong hydrogen bonds.

The value of ρ_{bcp} reflects the strength of hydrogen bonds, with low values corresponding to weak interactions, and the ρ_{bcp} value increases as the strength of the interaction increases. As shown in Table S3.7, the ρ_{bcp} values are in the ranges 0.007–0.262 a.u., and most hydrogen bonds are in line with the criteria proposed by Koch and Popelier,⁶⁷ while 8 out of 88 hydrogen bonds do not correlate well with ρ_{bcp} value (Figure 3.14b). The upper five data points with negative values of both $\nabla^2\rho$ and H_{BCP} are very strong hydrogen bonds, and three data with relatively higher ρ_{bcp} values lie in the middle region, representing the medium-strong hydrogen bonds, which are also supported by the positive $\nabla^2\rho$ values and negative

H_{BCP} values of these interactions. The value of $E_{HBbinding}$ is another approach to quantify the strength of hydrogen bonds, the lower $E_{HBbinding}$ value corresponding to stronger interactions, and vice versa (Figure 3.14c).

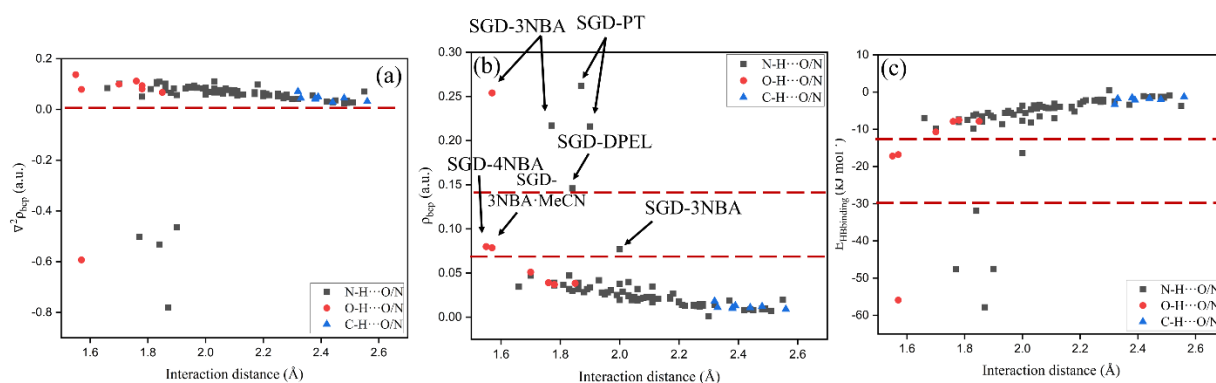


Figure 3.14. Relationship between basic QTAIM parameters (a) $\nabla^2\rho$, (b) ρ_{bcp} , and (c) $E_{HBbinding}$ and $H\cdots A$ (acceptor) distances.

All the medium-strong and very strong hydrogen bonds are involved in the formation of heterosynthons between the guanidyl group of SGD and the cofomers, except one interaction in SGD-PT which forms the homosynthon between two SGD molecules. More specifically, for SGD-3NBA, the very strong and medium-strong hydrogen bonds are involved in the formation of two $R_2^2(8)$ motifs (C4 and C6) between SGD and two 3NBA molecules. The two very strong hydrogen bonds in SGD-PT cocrystal are engaged in the formation of an $R_2^2(8)$ homosynthon (A1) between two SGD molecules and an $R_2^2(9)$ heterosynthon (C7) between SGD and PT molecules; respectively. The very strong hydrogen bond in SGD-DPEL and medium strong hydrogen bond in SGD-PHE form a discrete synthon (C3) between SGD and cofomers, respectively. Both of the medium-strong hydrogen bonds in SGD-4NBA and SGD-3NBA·MeCN are found in the

structures of the $R_2^2(8)$ heterosynthons (C4). This reveals that it is both experimentally and computationally favorable for those cocrystals to form.

According to Table S3.7, no strong hydrogen bonds can be found in the SGD-ATP cocrystal, and the first three relatively stronger hydrogen bond interactions occur between SGD molecules instead of SGD and ATP molecules with the strength of hydrogen bonds in the order: C1 < A2 < B1 < A1. For SGD-TBA·2H₂O, the first six relatively stronger hydrogen bonds are between two TBA molecules or SGD and H₂O molecules, indicating the propensity of forming hydrogen bonds between SGD and TBA is weaker. From the crystal packing (Figure 3.15) there are more hydrogen bond interactions between two SGD molecules, or between two coformer molecules, than there are between SGD and coformer molecules.

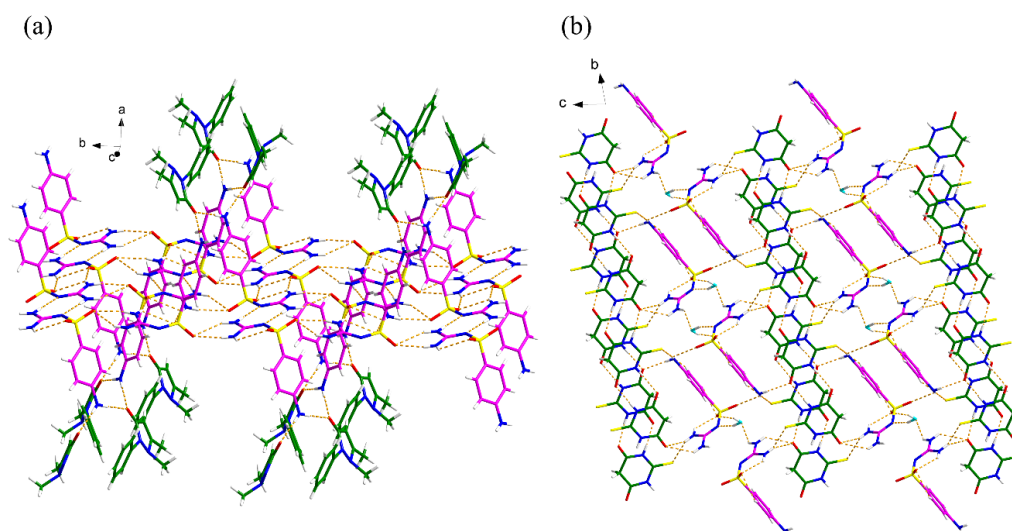


Figure 3.15. Crystal packing of (a) SGD-ATP and (b) SGD-TBA·2H₂O (pink is SGD, green is coformer, blue is H₂O).

Current study on hydrogen bonds within cocrystals has focused most attention upon the ability of functional groups to form conventional hydrogen bonds of the

O–H···O or N–H···O type because these traditional hydrogen bonds can be expected to represent the strongest sort of interaction, which are considered the main driving forces for the cocrystal formation. As mentioned above, for the studied cocrystals, all the robust hydrogen bonds are conventional hydrogen bonds. For N–H···O / N hydrogen bonds, an exponential dependence between the distance and ρ_{bcP} can be found, with R^2 factors of 0.7210 (Figure 3.16a). The exponential correlation ($R^2 = 0.9669$) is also found between the ρ_{bcP} and H···A distances for O–H···O / N contacts (Figure 3.16b), revealing that ρ_{bcP} is a good descriptor of the strength of weak conventional hydrogen bonds. Non-conventional hydrogen bonds such as C–H···O / N hydrogen bonds also play non-negligible role in the stabilization of 3D structure of the SGD cocrystals. However, no significant correlation between the ρ_{bcP} and H···A distances for C–H···O / N contacts can be found ($R^2 = 0.3210$), which may be due to the relatively low strength of this type of hydrogen bond (Figure 3.16c).

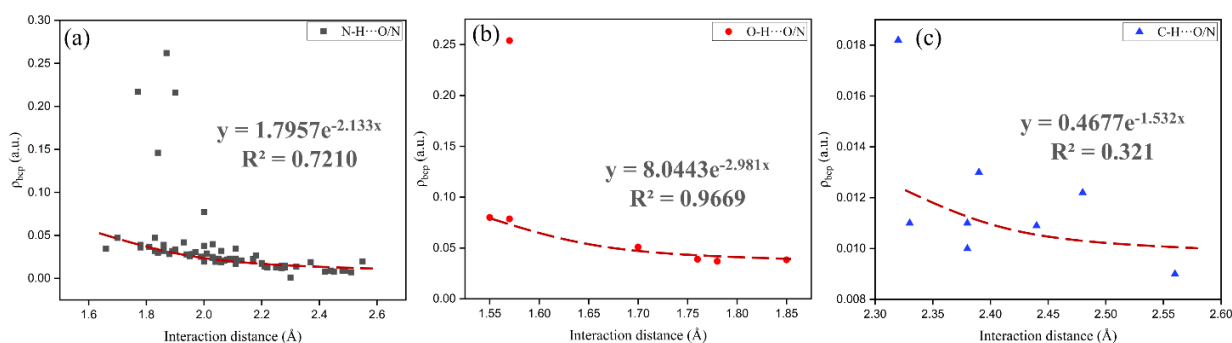


Figure 3.16. Relationship between the interaction distance and the electron density (ρ_{bcP}) of (a) N–H···O / N, (b) O–H···O / N, and (c) non-conventional hydrogen bond interactions (C–H···O / N) (Strong and medium strong hydrogen bonds ignored for the regression).

Some work reported that the QTAIM analysis is not able to detect all expected weak non-covalent interactions,^{68, 69} which is also found in this work. As shown in Figure 3.17, SGD adopts conformation 1 in SGD·H₂O, SGD-3NBA, SGD-PHE, SGD-PT and SGD-TBA·2H₂O, generating S(6) and S(5) rings.

In SGD-3NBA·MeCN and SGD-ATP, only one N–H···O intramolecular hydrogen bond interaction forming an S(6) ring can be found in SGD conformation 2. For conformation 3 in SGD, SGD-4NBA and SGD-DPEL, two oxygen atoms from sulfonyl group are involved in the construction of S(6) and S(5) rings. Notably, the bond angles of all hydrogen bonds forming S(5) rings in SGD molecules are less than 110°, which are not in the common range 120–180°. ⁷⁰ However, these angles fall inside the range of geometric limits provided by the IUPAC definition of the hydrogen bond. ⁷¹ The bond critical points of the C–H···O intramolecular hydrogen bonds involving the formation of an S(5) ring in the crystal structures were not found after optimization. This suggests that conformations 1 and 3 may be not the preferable molecular geometry of SGD, and the conformation of SGD moiety in those cocrystals are changed with the breakage of the C–H···O intramolecular hydrogen bonds after optimization, resulting in no critical points for those intramolecular hydrogen bonds.

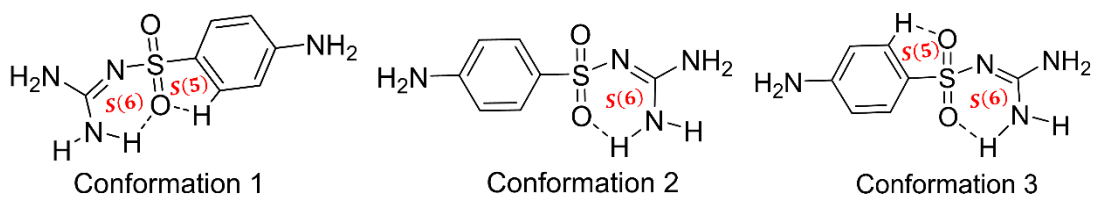


Figure 3.17. Conformations of SGD molecule existing in different crystalline forms.

3.5 Conclusions

This study reports the synthesis and characterization of five novel cocrystals of SGD with four cofomers (DPEL, PHE, 4NBA and 3NBA). A detailed crystal structural analysis was performed and computational calculations including Hirshfeld Surface, MEPS and QTAIM analysis have been applied to investigate the different hydrogen bonding interactions within all SGD cocrystals. Hirshfeld surface analysis revealed that the increasing hydrogen donor / acceptor sites in the cofomers lead to the increase of hydrogen bonding interactions and decrease of H...H contacts in SGD cocrystals and vice versa. The main site of interaction in the formation of four out of eight cocrystals first occurred pairwise in the minima and maxima of the MEPS, however, the prediction of the most robust synthons cannot be obtained correctly by MEPS due to the complexity of the various hydrogen bond donor and acceptor sites in both SGD and the cofomer molecules. QTAIM analysis was conducted as a complementary tool to quantify the strength of hydrogen bond interactions, illustrating that all the medium-strong and very strong hydrogen bonds are involved in the formation of heterosynthons between SGD and cofomers. This indicates that the formation of those SGD cocrystals is both experimentally and computationally favourable. In this study QTAIM analysis showed superiority over MEPS analysis to obtain comprehensive understanding of hydrogen bond interactions when there are multiple hydrogen bond donor and acceptor sites in cocrystallizing components.

REFERENCES

- (1) Desiraju, G. R., Crystal engineering: from molecule to crystal. *J. Am. Chem. Soc.* **2013**, 135, (27), 9952–9967.

- (2) Blagden, N.; de Matas, M.; Gavan, P. T.; York, P., Crystal engineering of active pharmaceutical ingredients to improve solubility and dissolution rates. *Adv. Drug. Deliv. Rev.* **2007**, *59*, (7), 617–630.
- (3) Brammer, L., Developments in inorganic crystal engineering. *Chem. Soc. Rev.* **2004**, *33*, (8), 476–489.
- (4) Nwambaekwe, K. C.; John-Denk, V. S.; Douman, S. F.; Mathumba, P.; Yussuf, S. T.; Uhuo, O. V.; Ekwere, P. I.; Iwuoha, E. I., Crystal engineering and thin-film deposition strategies towards improving the performance of kesterite photovoltaic cell. *J. Mater. Res. Technol.* **2021**, *12*, 1252–1287.
- (5) Du, H.; Wang, Q.; Tian, M.; Yang, X., Simple crystallization approach for enhancing function of plant-based madder dye and performance of dyed fabric. *Heliyon.* **2019**, *5*, (8), e02232.
- (6) Yu, P.; Zhen, Y.; Dong, H.; Hu, W., Crystal Engineering of Organic Optoelectronic Materials. *Chem.* **2019**, *5*, (11), 2814–2853.
- (7) Duggirala, N. K.; Perry, M. L.; Almarsson, Ö.; Zaworotko, M. J., Pharmaceutical cocrystals: along the path to improved medicines. *Chem. Commun.* **2016**, *52*, 640–655.
- (8) Bolla, G.; Sarma, B.; Nangia, A. K., Crystal Engineering of Pharmaceutical Cocrystals in the Discovery and Development of Improved Drugs. *Chem. Rev.* **2022**, *122*, (13), 11514–11603.
- (9) Sinha, A. S.; Maguire, A. R.; Lawrence, S. E., Cocrystallization of Nutraceuticals. *Cryst. Growth Des.* **2015**, *15*, (2), 984–1009.
- (10) Ren, B.Y.; Dai, X.L.; Zhang, F.; Long, X.; Huang, Y.-L.; Chen, J.-M.; Lu, T.-B., “Drug-Cofomer-Drug” Multi-component Crystals to Simultaneously Improve the Solubility of Two Insoluble Combined Drugs by Introduction of

- a Soluble Coformer. *Cryst. Growth Des.* **2022**, 22, (10), 5785–5790.
- (11) Bommaka, M. K.; Mannava, M. K. C.; Suresh, K.; Gunnam, A.; Nangia, A., Entacapone: Improving Aqueous Solubility, Diffusion Permeability, and Cocrystal Stability with Theophylline. *Cryst. Growth Des.* **2018**, 18, (10), 6061–6069.
- (12) Ding, Z.; Shang, H.; Zhang, S.; Han, W.; Li, B.; Jiang, S., Insight from Molecular Packing: Charge Transfer and Emission Modulation through Cocrystal Strategies. *Cryst. Growth Des.* **2020**, 20, (8), 5203–5210.
- (13) Huang, S.; Venables, D. S.; Lawrence, S. E., Pharmaceutical Salts of Piroxicam and Meloxicam with Organic Counterions. *Cryst. Growth Des.* **2022**, 22, (11), 6504–6520.
- (14) Scheiner, S.; Kar, T.; Pattanayak, J., Comparison of Various Types of Hydrogen Bonds Involving Aromatic Amino Acids. *J. Am. Chem. Soc.* **2002**, 124, (44), 13257–13264.
- (15) Alkorta, I.; Rozas, I.; Elguero, J., Non-conventional hydrogen bonds. *Chem. Soc. Rev.* **1998**, 27, 163–170.
- (16) Abramov, Y. A., QTAIM application in drug development: prediction of relative stability of drug polymorphs from experimental crystal structures. *J. Phys. Chem. A.* **2011**, 115, (45), 12809–12817.
- (17) Etter, M. C., Encoding and decoding hydrogen-bond patterns of organic compounds. *Acc. Chem. Res.* **1990**, 23, (4), 120–126.
- (18) Yang, J.; Yin, L.; Gong, X.D.; Sinditskii, V. P.; Zhang, J.-G., Origins of Salt Formation and Cocrystallization: A Combined Experimental and Theoretical Study. *Cryst. Growth Des.* **2020**, 20, (9), 5834–5842.
- (19) Luo, Y.H.; Sun, B.W., Pharmaceutical Co-Crystals of Pyrazinecarboxamide

- (PZA) with Various Carboxylic Acids: Crystallography, Hirshfeld Surfaces, and Dissolution Study. *Cryst. Growth Des.* **2013**, 13, (5), 2098–2106.
- (20) Spackman, P. R.; Turner, M. J.; McKinnon, J. J.; Wolff, S. K.; Grimwood, D. J.; Jayatilaka, D.; Spackman, M. A., CrystalExplorer: a program for Hirshfeld surface analysis, visualization and quantitative analysis of molecular crystals. *J. Appl. Cryst.* **2021**, 54, 1006–1011.
- (21) Yang, D.; Wang, R.; Jin, G.; Zhang, B.; Zhang, L.; Lu, Y.; Du, G., Structural and Computational Insights into Cocrystal Interactions: A Case on Cocrystals of Antipyrine and Aminophenazone. *Cryst. Growth Des.* **2019**, 19, (11), 6175–6183.
- (22) Politzer, P.; Murray, J. S., Quantitative Analyses of Molecular Surface Electrostatic Potentials in Relation to Hydrogen Bonding and Cocrystallization. *Cryst. Growth Des.* **2015**, 15, (8), 3767–3774.
- (23) Sarkar, N.; Parkin, S.; Huckaba, A. J., Structural Study of Hydrogen-Bond Driven Cocrystallization of Pyridyl-Bithiophene Based Compounds. *Cryst. Growth Des.* **2021**, 21, (8), 4337–4345.
- (24) Kowalik, M.; Brzeski, J.; Gawrońska, M.; Kazimierczuk, K.; Makowski, M., Experimental and theoretical investigation of conformational states and non-covalent interactions in crystalline sulfonamides with a methoxyphenyl moiety. *CrystEngComm.* **2021**, 23, (35), 6137–6162.
- (25) Bankiewicz, B.; Wojtulewski, S., Two New Cocrystals of the Dipicolinic Acid. Hirshfeld Atom Refinement of Crystal Structures and Quantum Theory of Atoms in Molecules Analysis of Molecular Complexes. *Cryst. Growth Des.* **2019**, 19, (12), 6860–6872.
- (26) Perlovich, G. L.; Ryzhakov, A. M.; Tkachev, V. V.; Hansen, L. K.; Raevsky, O.

- A., Sulfonamide Molecular Crystals: Structure, Sublimation Thermodynamic Characteristics, Molecular Packing, Hydrogen Bonds Networks. *Cryst. Growth Des.* **2013**, 13, (9), 4002–4016.
- (27) Cairra, M. R., Sulfa Drugs as Model Cocrystal Formers. *Mol. Pharmaceutics.* **2007**, 4, (3), 310–316.
- (28) Bolla, G.; Mittapalli, S.; Nangia, A., Celecoxib cocrystal polymorphs with cyclic amides: synthons of a sulfonamide drug with carboxamide cofomers. *CrystEngComm.* **2014**, 16, 24–27.
- (29) Elacqua, E.; Bučar, D.-K.; Henry, R. F.; Zhang, G. G. Z.; MacGillivray, L. R., Supramolecular Complexes of Sulfadiazine and Pyridines: Reconfigurable Exteriors and Chameleon-like Behaviour of Tautomers at the Co-Crystal-Salt Boundary. *Cryst. Growth Des.* **2012**, 13, (1), 393–403.
- (30) Abidi, S. S. A.; Azim, Y.; Khan, S. N.; Khan, A. U., Sulfaguanidine cocrystals: Synthesis, structural characterization and their antibacterial and hemolytic analysis. *J. Pharm. Biomed. Anal.* **2018**, 149, 351–357.
- (31) Bialk-Bielinska, A.; Maszkowska, J.; Mroziak, W.; Bielawska, A.; Kolodziejka, M.; Palavinskas, R.; Stepnowski, P.; Kumirska, J., Sulfadimethoxine and sulfaguanidine: their sorption potential on natural soils. *Chemosphere.* **2012**, 86, (10), 1059–1065.
- (32) Najlaoui, D.; Echabaane, M.; Khélifa, A. B.; Rouis, A., Development of a selective and highly sensitive optical chemical sensor for determination of sulfaguanidine based on a novel mixed isopolymolybdates. *Optik.* **2021**, 231.
- (33) Groom, C. R.; Bruno, I. J.; Lightfoot, M. P.; Ward, S. C., The Cambridge Structural Database. *Acta Cryst.* **2016**, B72, 171–179.
- (34) Alléaume, M.; Gulko, A.; Herbstein, F. H.; Kapon, M.; Marsh, R. E.,

- Comparison of the dimensions and conformation of the sulfaguanidine moiety in sulfaguanidine monohydrate and trans-dichlorobis (sulfaguanidine) palladium(II). *Acta. Cryst.* **1976**, B32, 669–682.
- (35) Serge, A.; Joelle, R.; Fernand, S., Study of the polymorphism of sulfaguanidine. *Bull. Soc. Chim. Fr.* **1977**, 3-4, 181–184.
- (36) Kálmán, A.; Czugler, M.; Argay, G., Conformational characteristics of anhydrous sulfaguanidine: computer retrieval and analysis of N-substituted arylsulfonamides. *Acta. Cryst.* **1981**, B37, 868–877.
- (37) Serge, A.; Joelle, R.; Fernand, S., Study of the antipyrine-sulfaguanidine system by x-ray diffraction and differential enthalpic analysis. *Ann. Pharm. Fr.* **1976**, 34, (3-4), 95–99.
- (38) Sinha, A. S.; Rao Khandavilli, U. B.; O'Connor, E. L.; Deadman, B. J.; Maguire, A. R.; Lawrence, S. E., Novel co-crystals of the nutraceutical sinapic acid. *CrystEngComm.* **2015**, 17, (26), 4832–4841.
- (39) Sheldrick, G. M., Crystal structure refinement with SHELXL. *Acta. Cryst.* **2015**, C71, 3–8.
- (40) APEX2 v2009.3-0. Bruker AXS. **2009**.
- (41) Huang, S.; Xu, J.; Peng, Y.; Guo, M.; Cai, T., Facile Tuning of the Photoluminescence and Dissolution Properties of Phloretin through Cocrystallization. *Cryst. Growth Des.* **2019**, 19, (12), 6837–6844.
- (42) Xu, J.; Huang, Y.; Ruan, S.; Chi, Z.; Qin, K.; Cai, B.; Cai, T., Cocrystals of isoliquiritigenin with enhanced pharmacokinetic performance. *CrystEngComm.* **2016**, 18, (45), 8776–8786.
- (43) Spek, A. L., Structure validation in chemical crystallography. *Acta Cryst.* **2009**, D65, 148–155.

- (44) Lu, T.; Chen, F., Quantitative analysis of molecular surface based on improved Marching Tetrahedra algorithm. *J. Mol. Graph. Model.* **2012**, *38*, 314–323.
- (45) Lu, T.; Chen, F., Multiwfn: a multifunctional wavefunction analyzer. *J. Comput. Chem.* **2012**, *33*, (5), 580–592.
- (46) Giannozzi, P.; Baroni, S.; Bonini, N.; Calandra, M.; Car, R.; Cavazzoni, C.; Ceresoli, D.; Chiarotti, G. L.; Cococcioni, M.; Dabo, I., QUANTUM ESPRESSO: a modular and open-source software project for quantum simulations of materials. *J. Phys.: Condens. Matter.* **2009**, *21*, 395502.
- (47) Otero-de-la-Roza, A.; Johnson, E. R.; Luaña, V., Critic2: A program for real-space analysis of quantum chemical interactions in solids. *Comput. Phys. Commun.* **2014**, *185*, (3), 1007–1018.
- (48) Emamian, S.; Lu, T.; Kruse, H.; Emamian, H., Exploring Nature and Predicting Strength of Hydrogen Bonds: A Correlation Analysis Between Atoms-in-Molecules Descriptors, Binding Energies, and Energy Components of Symmetry-Adapted Perturbation Theory. *J. Comput. Chem.* **2019**, *40*, (32), 2868–2881.
- (49) Jr, R. O. R.; Williams, J. H.; Winnek, P. S.; English, J. P., Chemotherapy. II. Some sulfanilamido heterocycles. *J. Am. Chem. Soc.* **1940**, *62*, (8), 2002–2005.
- (50) Bis, J. A.; Vishweshwar, P.; Weyna, D.; Zaworotko, M. J., Hierarchy of Supramolecular Synthons: Persistent Hydroxyl···Pyridine Hydrogen Bonds in Cocrystals That Contain a Cyano Acceptor. *Mol. Pharmaceutics.* **2007**, *4*, (3), 401–416.
- (51) Heravi, M. M.; Farhangi, N.; Bakhtiari, K.; Ghassemzadeh, M., Oxidation of Primary Alcohols to Carboxylic Acids Using Silica Supported CrO₃/H₅IO₆ Under Microwave Irradiation in a Solvent-Free System. *J. Chin. Chem. Soc.*

- 2006**, 53, (3), 643–645.
- (52) Yang, H.; Li, Y.; Jiang, M.; Wang, J.; Fu, H., General Copper-Catalyzed Transformations of Functional Groups from Arylboronic Acids in Water. *Eur. J. Chem.* **2011**, 17, (20), 5652–5660.
- (53) Urleb, U.; Gobec, S., Product Class 16: Phenazines. *Sci. Synth.* **2004**, 16, 913–943.
- (54) Desiraju, G. R., Supramolecular Synthons in Crystal Engineering—A New Organic Synthesis. *Angew. Chem., Int. Ed. Engl.* **1995**, 34, (21), 2311–2327.
- (55) Bernstein, J.; Davis, R. E.; Shimoni, L.; Chang, N.-L., Patterns in Hydrogen Bonding: Functionality and Graph Set Analysis in Crystals. *Angew. Chem., Int. Ed. Engl.* **1995**, 34, 1555–1573.
- (56) Etter, M. C.; Macdonald, J. C.; Bernstein, J., Graph-set analysis of hydrogen-bond patterns in organic crystals. *Acta Cryst.* **1990**, B46, 256–262.
- (57) Kumar, V.; Thaimattam, R.; Dutta, S.; Munshi, P.; Ramanan, A., Structural landscape of multi-component solids based on sulfa drugs. *CrystEngComm* **2017**, 19, (21), 2914–2924.
- (58) Scheepers, M. C.; Lemmerer, A., In Pursuit of Multi-component Crystals of the Sulfa Drugs Sulfapyridine, Sulfathiazole, and Sulfamethoxazole. *Cryst. Growth Des.* **2022**, 22, (1), 98–122.
- (59) Adalder, T. K.; Sankolli, R.; Dastidar, P., Homo- or Heterosynthon? A Crystallographic Study on a Series of New Cocrystals Derived from Pyrazinecarboxamide and Various Carboxylic Acids Equipped with Additional Hydrogen Bonding Sites. *Cryst. Growth Des.* **2012**, 12, (5), 2533–2542.
- (60) Seth, S. K.; Das, N. K.; Aich, K.; Sen, D.; Fun, H.-K.; Goswami, S., Exploring contribution of intermolecular interactions in supramolecular layered assembly

- of naphthyridine co-crystals: Insights from Hirshfeld surface analysis of their crystalline states. *J. Mol. Struct.* **2013**, 1048, 157–165.
- (61) Wang, Y.; Wang, L.; Zhang, F.; Wang, N.; Gao, Y.; Xiao, Y.; Wang, Z.; Bao, Y., Structure analysis and insight into hydrogen bond and van der waals interactions of etoricoxib cocrystals and cocrystal solvate. *J. Mol. Struct.* **2022**, 1258, (15), 132665.
- (62) Admond, D. A.; Sinha, A. S.; Khandavilli, U. B. R.; Maguire, A. R.; Lawrence, S. E., Design and Synthesis of Ternary Cocrystals Using Carboxyphenols and Two Complementary Acceptor Compounds. *Cryst. Growth Des.* **2016**, 16, (1), 59–69.
- (63) Fu, Q.; Lu, H. D.; Xie, Y. F.; Liu, J. Y.; Han, Y.; Gong, N. B.; Guo, F., Salt formation of two BCS II drugs (indomethacin and naproxen) with (1*R*, 2*R*)-1,2-diphenylethylenediamine: Crystal structures, solubility and thermodynamics analysis. *J. Mol. Struct.* **2019**, 1185, 281–289.
- (64) Etter, M. C.; Admond, D. A., The use of cocrystallization as a method of studying hydrogen bond preferences of 2-aminopyrimidine. *J. Chem. Soc., Chem. Commun.* **1990**, 589–591.
- (65) Kumar, P. S. V.; Raghavendra, V.; Subramanian, V., Bader's Theory of Atoms in Molecules (AIM) and its Applications to Chemical Bonding. *J. Chem. Sci.* **2016**, 128, 1527–1536.
- (66) Rozas, I.; Alkorta, I.; Elguero, J., Behaviour of Ylides Containing N, O, and C Atoms as Hydrogen Bond Acceptors. *J. Am. Chem. Soc.* **2000**, 122, 11154–11161.
- (67) Koch, U.; Popelier, P. L. A., Characterization of C \cdots H-O hydrogen bonds on the basis of the charge density. *J. Phys. Chem.* **1995**, 99, 9747–9754.

- (68) Kalinowska-Tluscik, J.; Staron, J.; Krawczuk, A.; Mordalski, S.; Warszycki, D.; Satala, G.; Hogendorf, A. S.; Bojarski, A. J., The effect of the intramolecular C-Hcdots, three dots, centeredO interactions on the conformational preferences of bis-arylsulfones-5-HT6 receptor antagonists and beyond. *RSC Adv.* **2018**, 8, (33), 18672–18681.
- (69) Lane, J. R.; Contreras-Garcia, J.; Piquemal, J. P.; Miller, B. J.; Kjaergaard, H. G., Are Bond Critical Points Really Critical for Hydrogen Bonding? *J. Chem. Theory. Comput.* **2013**, 9, (8), 3263–3266.
- (70) Steiner, T.; Desiraju, G. R., Distinction between the weak hydrogen bond and the van der Waals interaction. *Chem. Commun.* **1998**, 891–892.
- (71) Steiner, T., The Hydrogen Bond in the Solid State. *Angew. Chem. Int. Ed.* **2002**, 41, 48–76.

Supporting Information

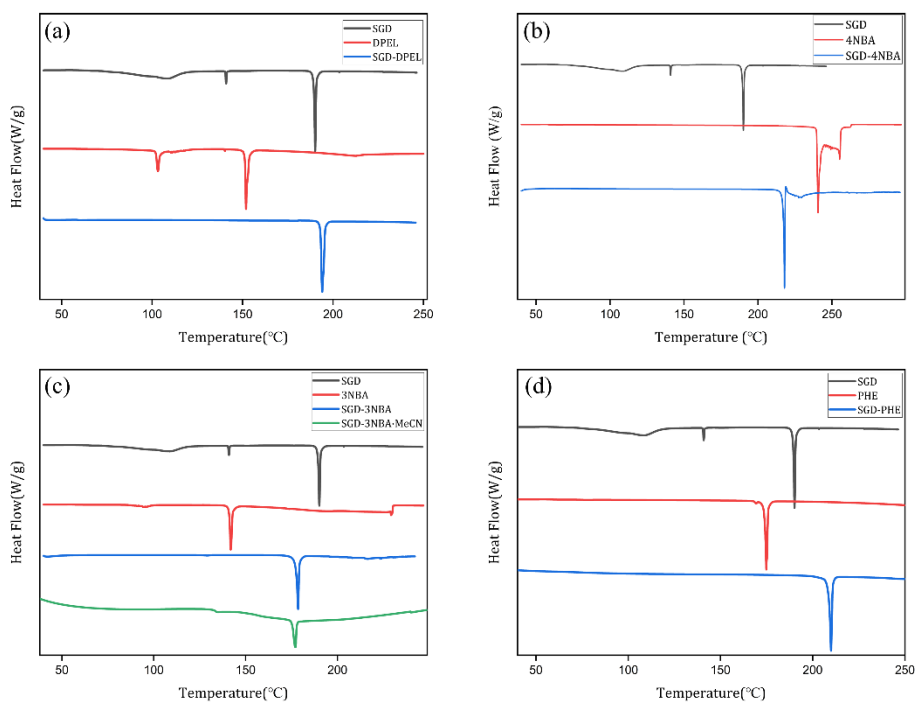


Figure S3.1. DSC traces of (a) SGD·H₂O (black), DPEL (red) and SGD-DPEL cocrystal (blue); (b) SGD·H₂O (black), 4NBA (red) and SGD-4NBA cocrystal (blue); (c) SGD·H₂O (black), 3NBA (red), SGD-3NBA cocrystal (blue) and SGD-3NBA·MeCN cocrystal (green); and (d) SGD·H₂O (black), PHE (red) and SGD-PHE cocrystal (blue).

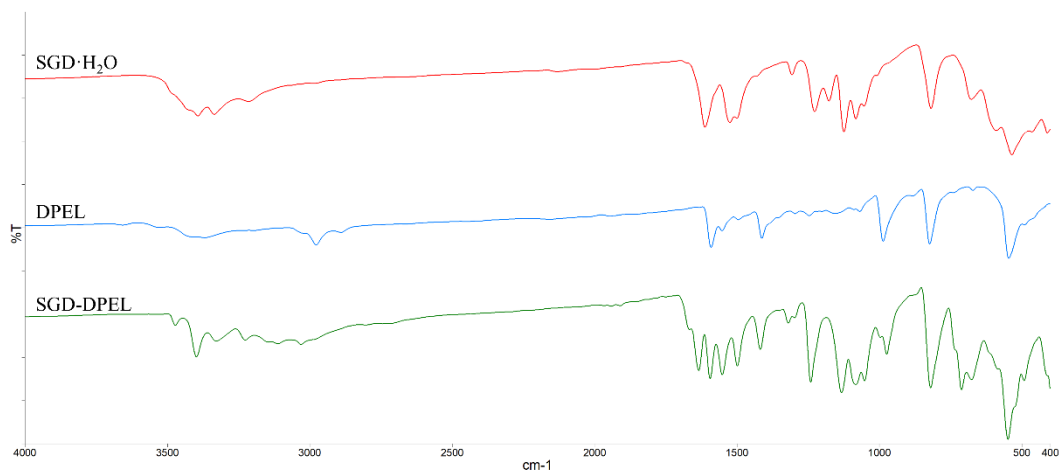


Figure S3.2. IR spectra of (a) SGD·H₂O, DPEL and SGD-DPEL cocrystal.

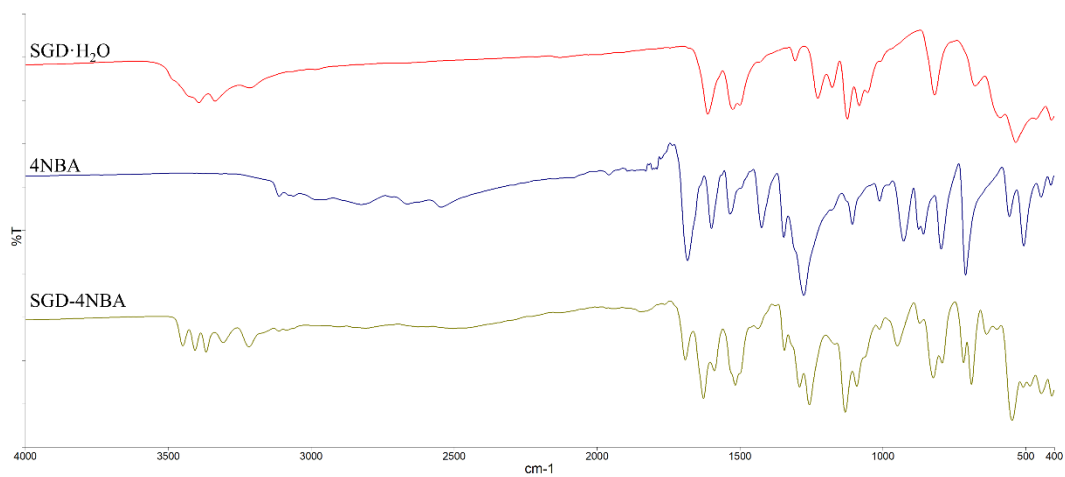


Figure S3.3. IR spectra of SGD·H₂O, 4NBA and SGD-4NBA cocrystal.

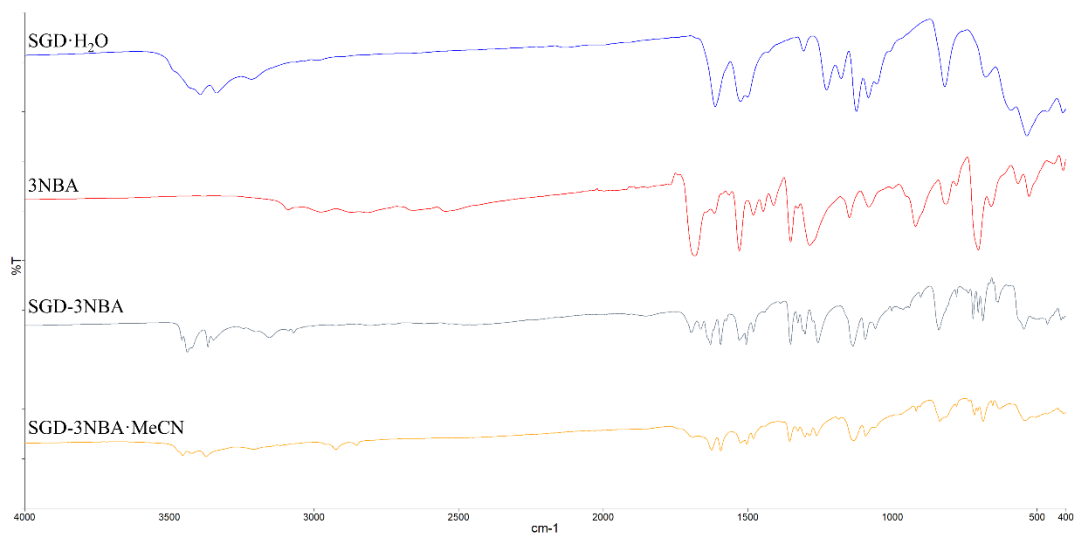


Figure S3.4. IR spectra of SGD-H₂O, 3NBA, SGD-3NBA cocrystal.

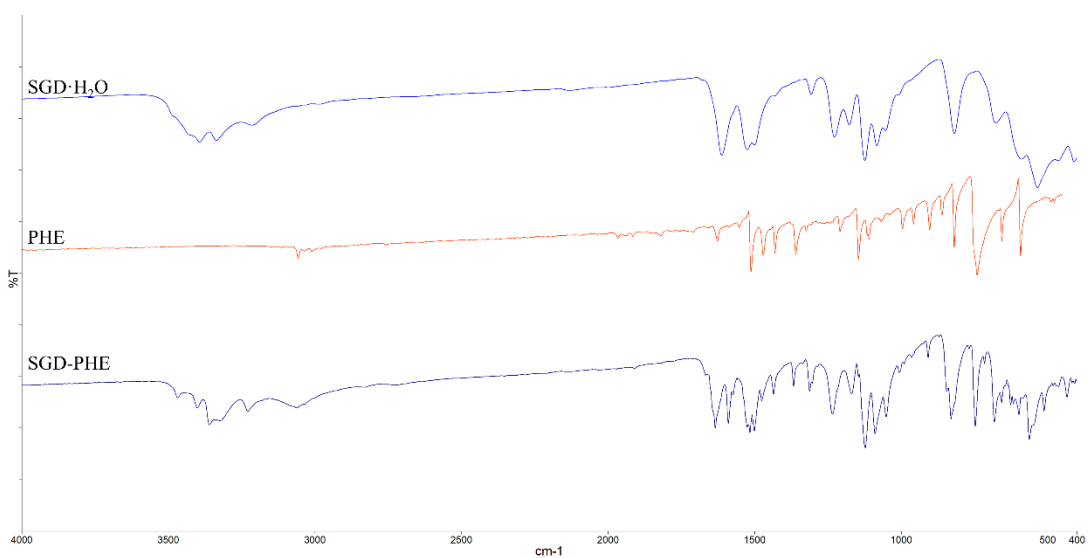


Figure S3.5. IR spectra of SGD-H₂O, PHE and SGD-PHE cocrystal.

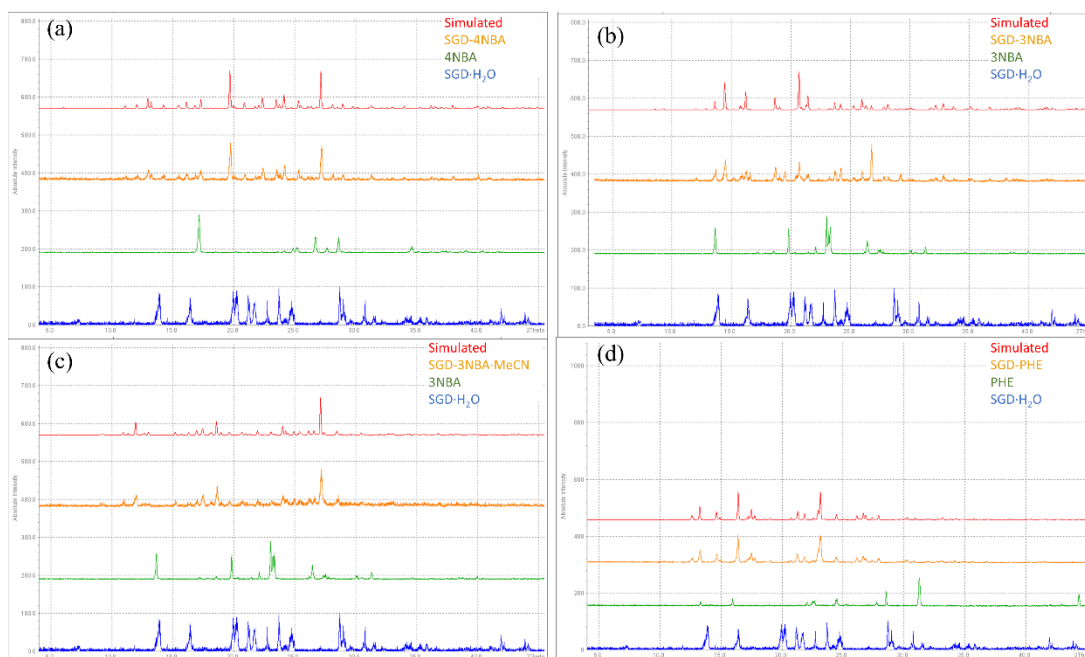
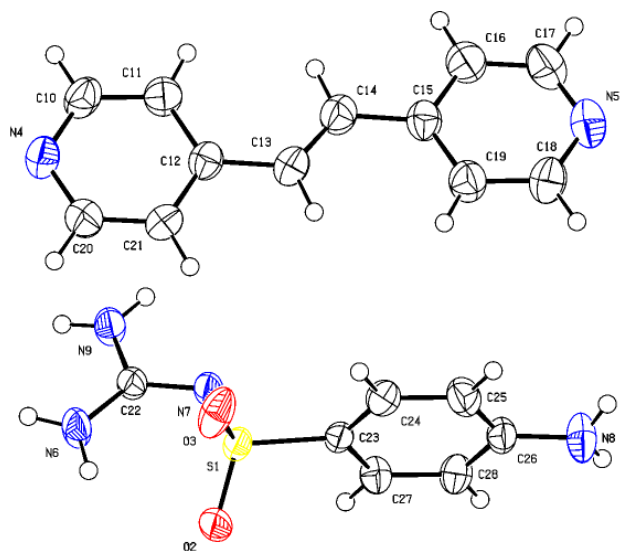
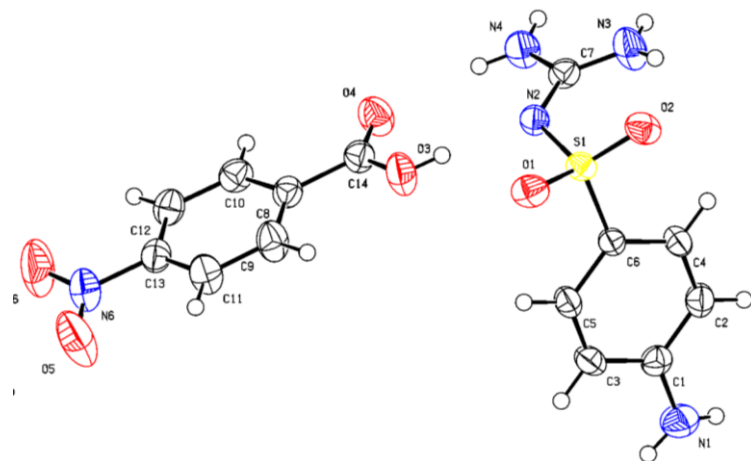


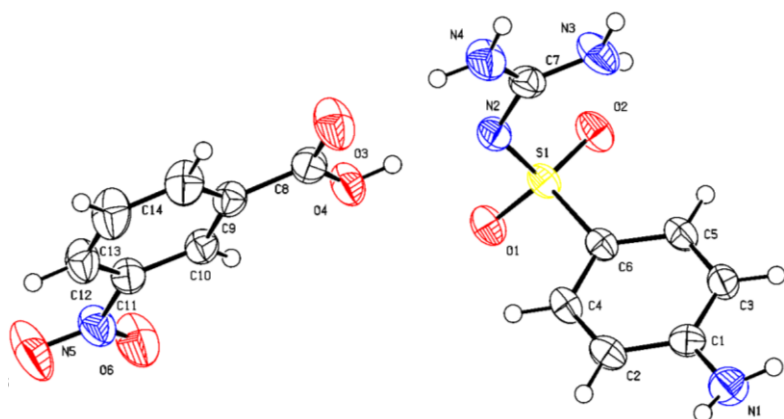
Figure S3.6. PXRD patterns of (a) SGD-H₂O (blue), 4NBA (green), SGD-4NBA (orange) and simulated pattern from the crystal structure (red); (b) PXRD patterns of SGD-H₂O (blue), 3NBA (green), SGD-3NBA (orange) and simulated pattern from the crystal structure (red); (c) PXRD patterns of SGD-H₂O (blue), 3NBA (green), SGD-3NBA·MeCN (orange) and simulated pattern from the crystal structure (red); (d) PXRD patterns of SGD-H₂O (blue), PHE (green), SGD-PHE (orange) and simulated pattern from the crystal structure (red).



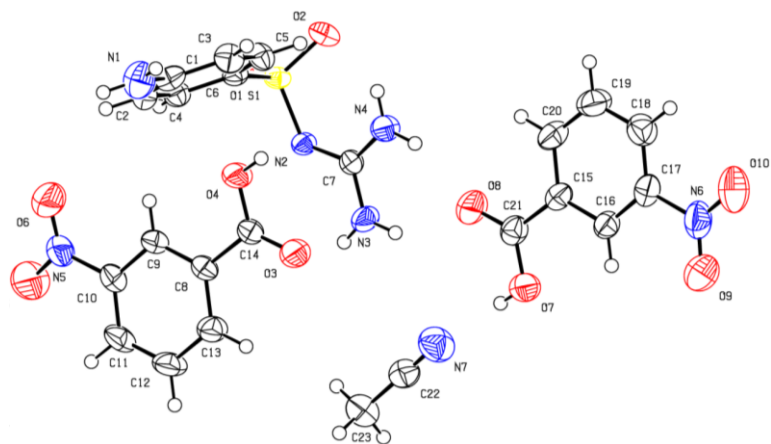
(a)



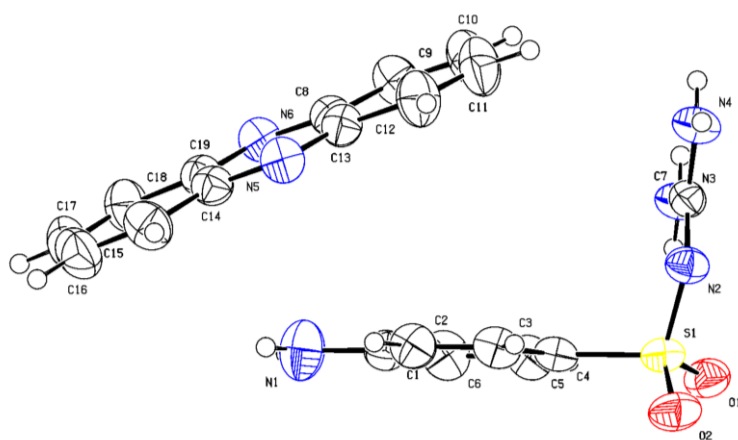
(b)



(c)



(d)



(e)

Figure S3.7. Ellipsoid plot of (a) SGD-DPEL, (b) SGD-4NBA, (c) SGD-3NBA, (d) SGGD-3NBA·MeCN and (e) SGD-PHE.

Table S3.1. Hydrogen bond and π - π interaction geometries (\AA , $^\circ$) in the SGD-DPEL cocrystal. ^a

	Type	D-H...A	D-H	H...A	D...A	D-H...A	ARU (J)
1		N3-H11...N1	0.852(19)	2.065(19)	2.914(2)	175.4(18)	[1455.02]
2		N5-H12...N2	0.856(15)	2.28(2)	3.049(2)	150(2)	[1656.02]
3		N6-H14...N4	0.858(18)	2.134(18)	2.9912(18)	176.6(18)	[2666.01]
4		N5-H15...O2	0.842(19)	2.22(2)	3.016(2)	157.8(17)	[1655.01]
5	Intra	N3-H20...O1	0.851(11)	2.419(18)	2.9941(19)	125.5(15)	
6		N3-H20...O1	0.851(11)	2.201(13)	2.9151(16)	141.4(18)	[2656.01]
7		C12-H5...O2	0.93	2.58	3.4553(19)	157	[2666.01]
8	Intra	C15-H17...O2	0.93	2.55	2.917(2)	104	
Cg(I)	Cg(J)	Cg-Cg	Interplanar distance	Dihedral Angle	Beta	ARU (J)	
2	3	3.8818(11)	3.3836(7)	6.22(8)	31.2	[1655.02]	

^a Symmetry codes: [2656.] = [2_656] = 1-x, -y, 1-z; [1455.] = [1_455] = -1+x, y, z; [2666.] = [2_666] = 1-x, 1-y, 1-z; [1655.] = [1_655] = 1+x, y, z; [1656.] = [1_656] = 1+x, y, 1+z. Cg2 represents the centroid of N1-C1-C2-C3-C12-C11 and Cg3 represents the centroid of N2-C8-C7-C6-C10-C9. Cg(I) = plane number I; Cg-Cg = distance between ring centroids (Ang.). Beta is the displacement angle between the ring normal of plane I and the centroid vector.

Table S3.2. Hydrogen bond and π - π interaction geometries (\AA , $^\circ$) in the SGD-4NBA cocrystal.^a

	Type	D-H \cdots A	D-H	H \cdots A	D \cdots A	D-H \cdots A	ARU (J)
1		N3-H13 \cdots O1	0.865(13)	1.962(13)	2.8155(16)	168.8(14)	[1565.01]
2	Intra	N3-H14 \cdots O2	0.800(15)	2.151(14)	2.7601(17)	133.2(13)	
3		O3-H15 \cdots N2	0.836(15)	1.854(15)	2.6859(15)	173.2(14)	[1555.01]
4		N4-H16 \cdots O1	0.842(13)	2.571(13)	3.2482(17)	138.4(11)	[1565.01]
5		N4-H17 \cdots O4	0.872(13)	2.145(13)	3.0093(17)	171.2(12)	[1555.02]
6		N1-H18 \cdots O2	0.871(13)	2.411(12)	3.1442(16)	142.1(11)	[4564.01]
7	Intra	C5-H5 \cdots O1	0.93	2.57	2.9272(15)	103	
8	Intra	C9-H9 \cdots O3	0.93	2.4	2.7166(18)	100	

^aSymmetry codes: [4564.] = [6_564] = x, 1-y, -1/2+z; [1565.] = [1_565] = x, 1+y, z.

Table S3.3. Hydrogen bond and π - π interaction geometries (\AA , $^\circ$) in the SGD-3NBA cocrystal. ^a

	Type	D-H...A	D-H	H...A	D...A	D-H...A	ARU (J)
1		N1-H1...O1	0.894(10)	2.465(10)	3.2091(11)	141.0(11)	[6545.01]
2		N1-H1...O4	0.894(10)	2.585(11)	3.2905(12)	136.4(8)'	[6545.02]
3		N3-H15...O6	0.851(10)	2.249(10)	3.0998(11)	177.7(8)	[1545.02]
4	Intra	N3-H16...O2	0.855(11)	2.227(10)	2.8558(11)	130.3(8)	
5		N3-H16...O2	0.855(11)	2.270(10)	3.0144(12)	145.5(9)'	[7555.01]
6		N4-H17...O5	0.838(10)	2.196(10)	3.0285(12)	173.0(12)	[1545.02]
7		N4-H18...O3	0.905(10)	1.959(10)	2.8588(11)	173.0(10)	[1555.02]
8		O4-H19...N2	0.847(11)	1.842(12)	2.6835(10)	172.2(15)	[1555.01]
9		N1-H20...O1	0.849(10)	2.475(10)	3.2707(11)	156.6(12)	[4565.01]
10		C2-H2...O2	0.93	2.51	3.4397(10)	173	[4565.01]
11	Intra	C5-H2...O2	0.93	2.58	2.9415(12)	103	
12		C10-H10...N1	0.93	2.62	3.5427(14)	172	[6555.01]

^a Symmetry codes: [6555.] = [7_555] = 1/2-x, 1/2+y, 1/2-z; [7555.] = [4_555] = 1/2-x, 1/2-y, -z; [6545.] = [7_545] = 1/2-x, -1/2+y, 1/2-z; [1545.] = [1_545] = x, -1+y, z; [4565.] = [6_565] = x, 1-y, 1/2+z.

Table S3.4. Hydrogen bond and π - π interaction geometries (\AA , $^\circ$) in the SGD-3NBA·MeCN.^a

	Type	D-H...A	D-H	H...A	D...A	D-H...A	ARU (J)
1		N1-H1A...O1	0.86	2.57	3.354(3)	153	[1655.01]
2		N3-H3A...O8	0.86	2.35	3.086(3)	144	[1555.03]
3		N3-H3B...O3	0.86	2.01	2.870(3)	174	[1455.02]
4		N4-H4A...O8	0.86	2.03	2.848(3)	158	[1555.03]
5	Intra	N4-H4B...O2	0.86	2.19	2.812(3)	129	
6		N4-H4B...O2	0.86	2.33	2.939(3)	129	[2676.01]
7		O4-H4C...N2	0.82	1.87	2.681(3)	170	[1655.01]
8		O7-H7...N7	0.82	2.01	2.829(4)	174	[1555.04]
9		C3-H3...O1	0.93	2.54	3.385(3)	151	[1655.01]
10		C11-H11...O5	0.93	2.53	3.259(4)	136	[2667.02]
11		C19-H19...O1	0.93	2.56	3.313(4)	138	[2676.01]
12		C23-H23C...O3	0.96	2.53	3.425(4)	155	[1455.02]
Cg(I)	Cg(J)	Cg-Cg	Interplanar distance	Dihedral Angle	Beta	ARU (J)	
2	3	3.8615(17)	3.4490(11)	3.98(14)	23	[2666.03]	

^a Symmetry codes: [1455.] = [1_455] = -1+x, y, z; [2676.] = [2_676] = 1-x, 2-y, 1-z; [1655.] = [1_655] = 1+x, y, z; [2667.] = [2_667] = 1-x, 1-y, 2-z; [2666] = 1-x, 1-y, 1-z. Cg2 represents the centroid of C8-C13 and Cg2 represents the centroid of C15-C20. Cg(I) = plane number I; Cg-Cg = distance between ring centroids (Ang.). Beta is the displacement angle between the ring normal of plane I and the centroid vector.

Table S3.5. Hydrogen bond and π - π interaction geometries (\AA , $^\circ$) in the SGD-PHE cocrystal.^a

	Type	D-H...A	D-H	H...A	D...A	D-H...A	ARU (J)
1		N1-H1A...O2	0.86	2.46	3.220(2)	148	[1455.01]
2		N3-H3A...O2	0.86	2.14	2.985(2)	169	[2655.01]
3	Intra	N3-H3B...O1	0.86	2.29	2.8953(19)	128	
4		N3-H3B...N5	0.86	2.62	3.313(2)	139	[4564.02]
5		N4-H4A...O1	0.86	2.08	2.930(2)	169	[2655.01]
6		N4-H4B...N6	0.86	2.08	2.936(2)	175	[1655.02]
7	Intra	C5-H5...O1	0.93	2.53	2.903(2)	105	
Cg(I)	Cg(J)	Cg-Cg	Interplanar distance	Dihedral Angle	Beta	ARU (J)	
2	3	4.0823(12)	3.6008(7)	1.96(9)	28.6	[3576.02]	

^a Symmetry codes: [4564.] = [4_575] = x, 3/2-y, -1/2+z; [1455.] = [1_455] = -1+x, y, z; [2655.] = [2_655] = 1-x, 1/2+y, 1/2-z; [1655.] = [1_655] = 1+x, y, z; [3576] = -x, 2-y, 1-z. Cg2 represents the centroid of N5-C13-C8-N6-C19-C14 and Cg3 represents the centroid of C8-C9-C10-C12-C12-C13. Cg(I) = plane number I; Cg-Cg = distance between ring centroids (Ang.). Beta is the displacement angle between the ring normal of plane I and the centroid vector.

Table S3.6. Hydrogen bond and π – π interaction geometries (Å, °) in the SGD-ATP cocrystal.^{1 a}

	Type	D-H...A	D-H	H...A	D...A	D-H...A	ARU (J)
1		N1-H3...O3	0.83(7)	2.24(7)	3.056(9)	167(7)	[2756.02]
2		N1-H5...O3	0.77(7)	2.38(7)	3.145(9)	175(8)	[3756.02]
3		N3-H6...N2	0.86(7)	2.11(7)	2.974(7)	176(9)	[3656.01]
4		N3-H7...O1	0.85(7)	2.57(7)	3.279(7)	142(6)	[2645.01]
5		N4-H8...O1	0.82(7)	2.15(7)	2.937(7)	161(7)	[2645.01]
6	Intra	N4-H9...O2	0.75(8)	2.43(7)	2.832(7)	116(7)	
7		N4-H9...O2	0.75(8)	2.20(8)	2.912(7)	160(7)	[3655.01]
Cg(I)	Cg(J)	Cg-Cg	Interplanar distance	Dihedral Angle	Beta	ARU (J)	
2	3	4.025(5)	3.341(3)	16.4(4)	22.1	[4544.02]	
3	2	4.026(5)	3.731(4)	16.4(4)	33.9	[4545.02]	

^a Symmetry codes: [3656.] = [3_656] = 1-x, -y, 1-z; [3655.] = [3_655] = 1-x, -y, -z; [2756.] = [2_756] = 2-x, 1/2+y, 3/2-z; [3756.] = [3_756] = 2-x, -y, 1-z; [2645.] = [2_645] = 1-x, -1/2+y, 1/2-z; [4544] = x, -1/2-y, -1/2+z; [4545] = x, -1/2-y, 1/2+z. Cg2 represents the centroid of N5-N6-C10-C9-C8 and Cg3 represents the centroid of C13-C14-C15-C16-C17-C18. Cg(I) = plane number I; Cg-Cg = distance between ring centroids (Ang.). Beta is the displacement angle between the ring normal of plane I and the centroid vector.

Table S3.7. Selected topological parameters of electron density distribution [a.u.] for SGD crystals.

	Type	D-H...A	H...A ^a	ρ_{bcp} (a.u.)	$\nabla^2 \rho_{\text{bcp}}$ (a.u.)	G_{bcp} kJ mol ⁻¹	V_{bcp} kJ mol ⁻¹	H_{bcp} kJ mol ⁻¹	E_{binding} kJ mol ⁻¹
SGD·H ₂ O ²		O3-H4...O2	1.78	0.037	0.0939	30.975	-0.462	30.513	-7.530
		O3-H3...O1	1.76	0.039	0.112	33.338	6.851	40.189	-7.870
		N3-H11...O3	1.94	0.028	0.0902	19.924	19.346	39.270	-5.590
		N3-H10...O3	2.04	0.022	0.0769	13.414	23.599	37.013	-4.260
		N4-H2...O2	2.11	0.017	0.0617	8.636	23.179	31.815	-3.100
		N4-H12...O3	2.21	0.014	0.0611	6.458	27.300	33.758	-2.480
	Intra	N4-H2...O1	2.28	0.0149	0.0584	6.799	24.728	31.526	-2.580
SGD-DPEL		N3-H11...N1	1.84	0.146	-0.532	304.500	-960.750	-656.250	-480.375
		N6-H14...N4	1.93	0.042	0.083	38.063	-21.236	16.826	-10.618
		N5-H12...N2	2.06	0.032	0.063	24.728	-8.111	16.616	-4.056
		N5-H15...O2	2.03	0.025	0.067	15.619	12.784	28.403	6.392
		N3-H20...O1	2.06	0.020	0.077	11.183	27.825	39.008	13.913
	Intra	N3-H20...O1	2.37	0.019	0.056	9.739	17.430	27.169	8.715
		C12-H5...O2	2.39	0.013	0.050	5.381	22.050	27.431	11.025
SGD-4NBA		O3-H15...N2	1.57	0.0786	0.0793	108.675	-165.375	-56.700	-16.800
		N3-H13...O1	1.78	0.0361	0.0504	29.663	-26.513	3.150	-7.320
		N4-H17...O4	1.89	0.0319	0.0823	24.150	5.670	29.820	-6.370
	Intra	N3-H14...O2	1.97	0.0306	0.0852	22.628	10.658	33.285	-6.090
		N1-H18...O2	2.18	0.0268	0.0986	18.086	28.613	46.699	-5.230

		N4-H16...O1	2.51	0.00718	0.0268	2.013	13.545	15.558	-0.859
SGD-3NBA		O4-H19...N2	1.57	0.254	-0.593	769.125	-1924.125	-1155.000	-55.900
		N4-H18...O3	1.77	0.217	-0.502	590.625	-1509.375	-918.750	-47.600
		N4-H17...O5	2.00	0.077	0.0858	105.000	-153.825	-48.825	-16.400
	Intra	N3-H16...O2	2.17	0.0226	0.0607	13.624	12.548	26.171	-4.300
		N3-H15...O6	2.03	0.0399	0.111	35.175	2.544	37.719	-8.150
		N3-H16...O2	2.17	0.0213	0.0677	12.285	19.845	32.130	-4.000
		N1-H1...O1	2.27	0.0122	0.0441	4.909	4.909	9.818	-1.990
		N1-H20...O1	2.25	0.0139	0.0625	6.038	28.875	34.913	-2.360
		C2-H2...O2	2.32	0.0182	0.071	9.476	27.563	37.039	-3.320
		N1-H1...O4	2.49	0.01	0.0263	3.491	10.264	13.755	-1.490
	C10-H10...N1	2.48	0.0122	0.0449	4.856	19.766	24.623	-1.980	
SGD-3NBA·MeCN		O4-H4C...N2	1.55	0.08	0.137	112.613	-135.188	-22.575	-17.200
		O7-H7...N7	1.70	0.051	0.0996	53.288	-41.213	12.075	-10.700
		N3-H3B...O3	1.78	0.039	0.0842	34.388	-13.571	20.816	-8.050
		N4-H4A...O8	1.83	0.032	0.108	23.861	23.048	46.909	-6.320
	Intra	N4-H4B...O2	2.08	0.022	0.0769	13.046	24.386	37.433	-4.170
		N4-H4B...O2	2.22	0.013	0.0566	5.513	26.093	31.605	-2.190
		N3-H3A...O8	2.25	0.013	0.051	5.618	22.208	27.825	-2.220
		C23-H23C...O3	2.33	0.011	0.0446	4.174	20.921	25.095	-1.740
		C11-H11...O5	3.00	0.002	0.0085	0.243	5.119	5.361	0.293

		C3-H3...O1	2.38	0.01	0.041	3.465	19.950	23.415	-1.480
		C19-H19...O1	2.38	0.011	0.0447	3.780	21.788	25.568	-1.590
		N1-H1A...O1	2.42	0.008	0.0309	2.449	15.356	17.805	-1.060
SGD ³		N3-H8...O4	1.84	0.030	0.109	21.788	28.147	49.935	-5.942
		N3-H7...N8	2.01	0.029	0.070	20.181	5.759	25.940	-5.642
	Intra	N6-H15...O3	2.03	0.024	0.082	15.041	23.625	38.666	-4.612
		N4-H10...O3	2.06	0.019	0.069	9.765	25.751	35.516	-3.391
	Intra	N2-H5...O1	2.07	0.021	0.083	13.140	28.481	41.621	-3.994
		N7-H18...N1	2.09	0.023	0.064	13.650	14.385	28.035	-4.299
		N6-H16...N4	2.11	0.023	0.055	13.571	9.004	22.575	-4.277
		N8-H19...N5	2.13	0.021	0.059	12.180	14.464	26.644	-3.965
		N7-H17...N5	2.20	0.018	0.053	9.240	15.960	25.200	-3.251
		N2-H6...O2	2.30	0.001	0.041	3.431	20.213	23.643	0.522
		N4-H9...O2	2.32	0.014	0.042	4.383	18.579	22.961	-2.489
		N8-H20...O2	2.44	0.009	0.028	3.045	12.338	15.383	-1.306
		N6-H15...O1	2.45	0.008	0.036	2.651	18.113	20.764	-1.149
		C5-H3...O3	2.56	0.009	0.032	2.861	15.041	17.903	-1.239
	SGD-PHE		N4-H4A...O1	1.86	0.032	0.102	24.649	17.955	42.604
		N4-H4B...N6	1.86	0.039	0.075	33.600	-18.139	15.461	-7.930
		N3-H3A...O2	1.95	0.026	0.086	17.010	22.076	39.086	-5.020
Intra		N3-H3B...O1	2.27	0.015	0.054	6.983	21.105	28.088	-2.640

		N1-H1A···O2	2.28	0.013	0.048	5.119	20.974	26.093	-2.050
		N3-H3B···N5	2.48	0.010	0.031	3.754	12.653	16.406	-1.590
SGD-PT		N1-H6···N4	1.90	0.216	-0.464	588.000	-1480.500	-892.500	-47.500
	Intra	N3-H7···O2	2.00	0.0379	0.059	32.288	-25.778	6.510	-7.710
		N1-H5···N5	1.87	0.262	-0.781	811.125	-2131.500	-1320.375	-57.800
		N2-H9···O2	1.99	0.0252	0.0827	16.380	21.499	37.879	-4.890
		N2-H8···O1	2.05	0.023	0.067	13.965	16.013	29.978	-4.380
		N3-H10···N6	2.11	0.0348	0.073	28.088	-8.111	19.976	-7.030
		N1-H5···N6	2.55	0.0198	0.0707	10.920	24.544	35.464	-3.680
		C12-H12···O1	2.44	0.0109	0.0288	4.043	10.841	14.884	-1.690
	SGD-ATP ¹		N3-H6···N2	1.90	0.0339	0.0569	26.775	-16.170	10.605
		N4-H8···O1	1.88	0.0284	0.0654	19.898	3.124	23.021	-5.590
		N4-H9···O2	2.04	0.0193	0.0767	10.500	29.400	39.900	-3.570
		N1-H4···O3	2.00	0.0195	0.0711	10.684	25.331	36.015	-3.620
		N1-H5···O3	2.10	0.0225	0.0759	13.519	22.759	36.278	-4.280
Intra		N4-H9···O2	2.20	0.0171	0.0641	8.531	25.016	33.548	-3.060
		N3-H7···O1	2.48	0.00896	0.0244	2.914	10.185	13.099	-1.260
SGD-TBA·2H ₂ O		N5-H11···O5	1.83	0.0472	0.102	46.463	25.804	72.266	-9.790
		O7-H19···N1	1.85	0.0384	0.067	33.075	-21.998	11.078	-7.830
		N6-H12···O6	1.81	0.0368	0.0806	30.713	-8.505	22.208	-7.470
		N8-H16···O4	1.70	0.0472	0.102	46.463	-25.804	20.659	-9.790

		O7-H20...O2	1.78	0.0369	0.0808	30.975	-8.689	22.286	-7.500
		N7-H15...O3	1.66	0.0346	0.0845	27.563	0.185	27.748	-6.970
		N4-H9...O5	3.65	0.00898	0.0351	2.914	17.168	20.081	-1.260
	Intra	N3-H4...O2	1.96	0.0283	0.0945	19.793	22.418	42.210	-5.570
		N2-H2...O7	1.86	0.0335	0.0967	26.250	10.894	37.144	-6.740
		N3-H3...O4	2.26	0.0126	0.0512	5.145	23.310	28.455	-2.070
		N2-H1...O4	2.49	0.00898	0.0351	2.914	17.168	20.081	-1.260
		C14-H17...O3	2.39	0.0106	0.0419	3.833	19.819	23.651	-1.620
		N4-H10...S3	2.74	0.00875	0.0274	2.809	12.416	15.225	-1.210
		N4-H10...O1	2.06	0.0197	0.0703	10.815	24.518	35.333	-3.650
		N3-H3...S2	2.59	0.0133	0.0361	5.618	12.495	18.113	-2.220
		C3-H6...S3	3.88	0.00673	0.0223	1.809	11.025	12.834	-0.759

^a H...A represented the DFT calculated H...A distances.

REFERENCES

- (1) Serge, A.; Joelle, R.; Fernand, S., Study of the antipyrine-sulfaguanidine system by x-ray diffraction and differential enthalpic analysis. *Ann. Pharm. Fr.* **1976**, 34, (3-4), 95–99.
- (2) Alléaume, M.; Gulko, A.; Herbstein, F. H.; Kapon, M.; Marsh, R. E., Comparison of the dimensions and conformation of the sulfaguanidine moiety in sulfaguanidine monohydrate and trans-dichlorobis (sulfaguanidine) palladium(II). *Acta Cryst.* **1976**, B32, 669–682.
- (3) Kálmán, A.; Czugler, M.; Argay, G., Conformational characteristics of anhydrous sulfaguanidine: computer retrieval and analysis of N-substituted arylsulfonamides. *Acta Cryst.* **1981**, B37, 868–877.



Chapter 4 Pharmaceutical Salts of Piroxicam and Meloxicam with Organic Counterions

(Cryst. Growth Des. **2022**, *22*, 11, 6504–6520)



4.1 Abstract

Piroxicam (PRM) and meloxicam (MEL) are two nonsteroidal anti-inflammatory drugs, belonging to the Biopharmaceutics Classification System (BCS) Class II drugs. In this study, six novel pharmaceutical salts of PRM and MEL with three basic organic counterions, i.e., 4-aminopyridine (4AP), 4-dimethylaminopyridine (4DMP) and piperazine (PPZ) were prepared by both slurring and slow evaporation. These salts were characterized by single-crystal and powder X-ray diffraction, thermal analysis, and Fourier transform infrared spectroscopy. All six salts, especially MEL-4DMP and MEL-4AP, showed a significantly improved apparent solubility and dissolution rate in sodium phosphate solution compared with the pure APIs. Notably, PRM-4AP and PRM-4DMP salts exhibited enhanced fluorescence, and the PRM-PPZ salt showed weaker fluorescence compared with that of pure PRM due to different luminescent mechanisms.

4.2 Introduction

Over the past few decades, the wide application of high-throughput screening in drug design and discovery has resulted in more drug candidates exhibiting low aqueous solubility. Many approaches, including the use of nanoparticles,¹ lipid-based drug delivery systems² and cyclodextrin inclusion techniques,³ have been successfully developed to enhance the solubility of active pharmaceutical ingredients (APIs). For ionizable (acidic, basic and zwitterionic) APIs, salt formation is the most commonly used method for enhancing aqueous solubility.⁴⁻⁶ To some extent, this approach can produce predictable and designable physicochemical properties and performance of drug substances.⁷⁻¹¹

Approximately 50% of all drug molecules present in marketed products are administered as salts,^{12, 13} for example, Zontivity[®] (Vorapaxar sulfate), Kisqali[®] (Ribociclib succinate) and Ofev[®] (Nintedanib esylate). For the preparation of pharmaceutical salts, ΔpK_a is one of the most important factors, and salts can be distinguished from cocrystals by the degree of proton transfer between the components. Generally, systems with $\Delta pK_a < -1$ leads to cocrystals, $\Delta pK_a > 4$ results in salts, while $-1 < \Delta pK_a < 4$ can form either of them [where $\Delta pK_a = pK_a$ (base) – pK_a (acid)].¹⁴ In addition, complementary hydrogen bond acceptors /donors should exist in the structures of the drug molecule and salt formers.¹⁵ It is also important that the salt formers should be pharmaceutically acceptable or on the generally recognized as safe (GRAS) and the European Food Safety Authority (EFSA) lists to ensure that the resulting pharmaceutical salts are safe. Based on the presence of acidic or basic functional groups in ionizable APIs, potential counterions can be selected. For basic drugs, chloride and sulfate are typically the most popular inorganic counterions, while acidic drugs usually form salts with simple inorganic cations such as sodium, magnesium and potassium.¹⁶ Recently, pharmaceutically acceptable organic counterions have received increasing attention because they tend to have preferable dissolution behaviours. There is no common ion effect in gastric media for the systems compared to the hydrochloride salts, and salt disproportionation may be reduced owing to the regulation of the microenvironmental pH by the organic counterions.^{17, 18}

Piroxicam (PRM, brand name Feldene[®], Figure 4.1) and meloxicam (MEL, brand name Mobic[®], Figure 4.2) are nonsteroidal anti-inflammatory drugs, prescribed for the symptomatic relief of rheumatoid arthritis and osteoarthritis, which belong to the Biopharmaceutics Classification System Class II drugs and, thus, the

bioavailability is considered to be dissolution rate limited.^{19, 20} Moreover, PRM and MEL are zwitterionic compounds with $pK_{a1} = 1.86$ (hydroxyl group) and $pK_{a2} = 5.46$ (pyridyl group),²¹ and $pK_{a1} = 1.09$ (hydroxyl group) and $pK_{a2} = 4.18$ (nitrogen of the 5-methyl-1,3-thiazolyl group),²² respectively. When forming salts with acid counterions, the nitrogen atom of the pyridine ring or the thiazole ring from PRM or MEL is deprotonated, whereas when basic counterions are involved in the salt formation, the phenolic hydroxyl group is deprotonated (Figures 4.1 and 4.2).

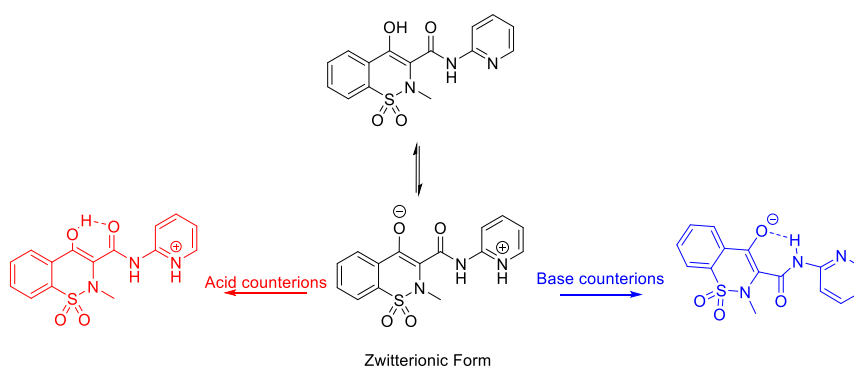


Figure 4.1. Neutral, zwitterionic (middle), acid (left) and base (right) salt forms of PRM.

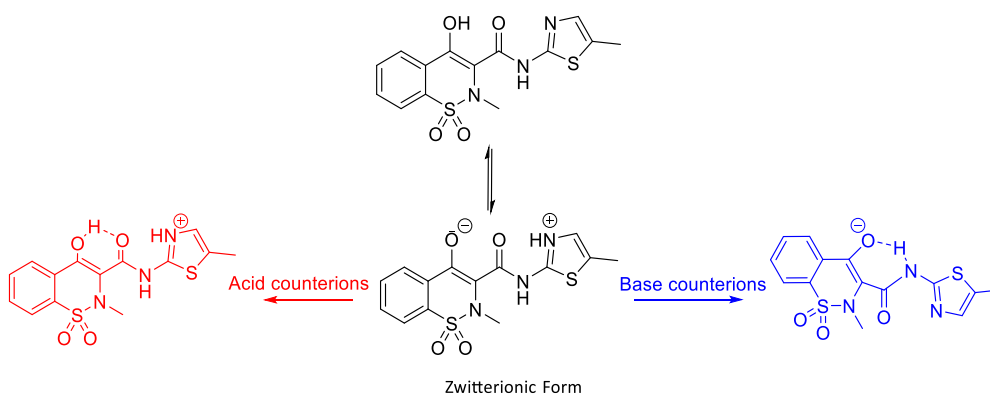


Figure 4.2. Neutral, zwitterionic form (middle), acid (left) and base (right) salt forms of MEL.

Both PRM and MEL are polymorphic. PRM has six polymorphs (forms I, α 1, II, III, VI and VII),²³ and it exists as zwitterionic form in its monohydrate,²⁴ while five polymorphs (forms I, II, III, IV and V) of MEL have been reported,²⁵ and the zwitterionic form of MEL in the solid form can be found in form IV²⁶ and its monohydrate.²⁷

Childs and Hardcastle investigated the cocrystal formation of PRM with pharmaceutically acceptable carboxylic acids using a crystal engineering approach.²⁰ Wilson *et al.* demonstrated the PRM molecule can exist in two possible tautomers when cocrystallizing with mono-substituted benzoic acids.²⁸ Subsequently, they synthesized different multi-component molecular crystals (including cocrystals and salts) of PRM with *N*-heterocycles and haloanilic acids, and significantly enhanced solubility can be found in some crystals.²⁹ Zaworotko and co-workers synthesized 12 cocrystal forms of MEL with carboxylic acids via crystal engineering and the supramolecular synthon approach. Solubility tests and pharmacokinetics studies on these MEL cocrystals revealed 9 out of 12 cocrystals exhibited a greater apparent solubility and higher oral bioavailability compared to pure MEL.^{19,30} In addition to PRM and MEL, two more oxycam drugs (lornoxicam, LRM, and tenoxicam, TNM) have had multi-component forms synthesized and their physicochemical properties investigated. Nangia *et al.* synthesized a series of cocrystals and salts of LRM and TNM, indicating the solubility advantages of those new multi-component crystalline forms.^{31, 32} The known multi-component forms of these four oxycam drugs are displayed in Table 4.1.

Table 4.1. Summary of salts and cocrystals and their physicochemical properties of piroxicam, meloxicam, lornoxicam and tenoxicam.

Name	System	Multi-component formers	Physicochemical properties ^a
Piroxicam	Salt / Salt solvate	4-Aminopyridine, 4-dimethylaminopyridine, piperazine (this work)	Higher solubility at pH 6.5, modified luminescence
		L-arginine ^{b 33}	Higher solubility in H ₂ O, greater bioavailability (x 1.38)
		Ethanolamine, ^b diethanolamine, ^b triethanolamine ^{b 21}	No improvement in solubility at pH 1.2, higher bioavailability & solubility at pH 6.8
		Norfloxacin MeOH ³⁴	Higher solubility at pH 6.8 (x 1.4)
	Cocrystal / Cocrystal solvate	Benzoic acid ³⁵	Increased solubility (x 3), increased dissolution rate in H ₂ O (x 2) improved oral bioavailability in rats (x 15)
		Clonixin ethyl acetate ³⁶	Improved moisture stability
		Febuxostat ³⁷	Improved dissolution at pH 6.8 (x 2.8), improved flow & compressibility
		Ferulic acid ³⁸	Improved IDR at pH 2 (x 1.7), improved powder flowability
		Furosemide ³⁹	Good thermal stability, good stability under accelerated ageing
		Nicotinamide, ^b resorcinol, ^b saccharin sodium, ^b urea ^{b 40}	No solubility advantage
		Methylparaben, ^b vanillin ^{b 41}	No solubility & IDR advantages at pH 1.2 superior dissolution rates in the sink condition at pH 1.2
		Saccharin ⁴²	Reduced plasticity & significantly deteriorated tableting behaviour
	Sodium acetate ^{b 40}	Improved solubility (x 5), improved flow & compressibility	
Meloxicam	Salt / Salt solvate	4-Aminopyridine, 4-dimethylaminopyridine, piperazine (this work)	Higher solubility at pH 6.5
		Arginine ^{b 43, 44}	Improved dissolution behaviour at pH 1.2 (x 9.4) & 7.5
		Ciprofloxacin MeCN ³⁴	Higher solubility at pH 6.8 (x 3)
		Cysteine, ^b glycine ^{b 43}	Improved dissolution behaviour at pH 7.5
		Meglumine ^{b 45}	Improved solubility at pH 6
		KOH H ₂ O ^{b 46}	Improved dissolution behaviour at pH 5.6, no bioavailability advantage <i>in vivo</i>
	Di/tri-ethanolamine, ^b tris(hydroxymethyl)aminomethane, ^b KOH ^{b 44}	Improved dissolution behaviours at pH 1.2 (x 3.7– 7.2)	
	Salt cocrystal	L-Malic acid ^{19, 30}	No solubility advantage at pH 6.5, improved bioavailability (x 1.2)
	Cocrystal / Cocrystal	Adipic acid ^{30, 47}	No solubility advantage at pH 6.8
		Aspirin ⁴⁸	Improved solubility at pH 7.4 (x 44), improved bioavailability (x 4.4)
		Benzoic acid, ^{19, 49} 4- hydroxybenzoic acid, ^{b 19, 30} 1-hydroxy-2-	Higher solubility at pH 6.5, improved bioavailability (x 1.1– 1.6)

	solvate	naphthoic acid, ^{19, 30} DL-malic acid, ^{b 19, 30, 50} salicylic acid, ¹⁹ succinic acid ^{19, 30, 47}	
		(+)-Camphoric acid ^{b 30}	No solubility advantage at pH 6.5
		Fumaric acid ^{19, 30, 50}	Higher solubility at pH 6.5 & 6.7, no bioavailability advantage
		Glutaric acid ^{19, 30}	No solubility advantage at pH 6.5, improved bioavailability (x 1.2)
		Glycolic acid ^{b 19, 30}	No solubility advantage at pH 6.5, no bioavailability advantage
		Hydrocinnamic acid ^{b 19, 30}	Higher solubility at pH 6.5, no bioavailability advantage
		Maleic acid ^{b 19, 30, 51}	Higher solubility at pH 1.6, 5.0 & 6.5, improved bioavailability (x 1.2)
		Salicylic acid ^{30, 50-52}	Higher solubility at pH 1.6, 5.0 & 6.5, enhanced drug permeation coefficient
		Terephthalic acid ⁴⁷	Higher solubility at pH 6.8
Lornoxicam	Salt / Salt solvate	HCl, methanesulfonic acid, NH ₃ , piperazine, ³¹	Improved dissolution at pH 7 (x 1.3 – 1.6)
		Norfloxacin H ₂ O MeOH ³⁴	Improved dissolution at pH 6.8 (x 1.6)
	Cocrystal / Cocrystal solvate	Ascorbic acid, ^b benzoic acid, ^b cinnamic acid, ^b citric acid, ^b fumaric acid, ^b glutaric acid, ^b hippuric acid, ^b malonic acid, ^b salicylic acid, ^b succinic acid, ^b tartaric acid ^{b 53}	No solubility advantage in H ₂ O
		4-Aminobenzoic acid, ^b anthranilic acid, ^b ferulic acid, ^b 4-hydroxy benzoic acid, ^b oxalic acid, ^b resorcinol, ^b saccharin sodium, ^b urea ^{b 53}	Improved solubility in H ₂ O (x 1.6 – 6.9)
		1,3-Dimethyl urea ^{b 54}	Increased IDR at pH 1.2 (x 28) & 7.4 (x 19), improved tabletability (x 2.5) & bioavailability (x 2.5)
Tenoxicam	Salt / Salt solvate	Ciprofloxacin MeOH ³⁴	Improved dissolution at pH 6.8 (x 1.1)
		HCl, methanesulfonic acid ³²	No solubility & IDR advantages at pH 7
		Piperazine ³²	Improved solubility (x 5.5) & IDR (x 2.5) at pH 7
	Cocrystal / Cocrystal solvate	Benzoic acid ³²	No solubility advantage, improved IDR (x 2) at pH 7
		Catechol, pyrogallol, resorcinol ³²	Improved solubility (x 5.8 – 10.1) & IDR (x 2.4 – 4.2) at pH 7
		Glycolic acid, ^b saccharin, ^b salicylic acid, ^b succinic acid, ^{b 55}	No IDR advantage at pH 4.5 & 6.8
		Salicylic acid ³²	No solubility & IDR advantages at pH 7

^a no reported physicochemical properties of multi-component forms for PRM^{20, 28, 36, 56, 57}, MEL^{27, 30, 58} and TNM⁵⁵; ^b no crystal structure reported

It is known that PRM exhibits luminescence in solution,⁵⁹ and there has been recent interest in the solid-state luminescent properties of organic multi-component crystalline materials, with applications including organic light-emitting diodes, semiconductor lasers, and fluorescent sensors.⁶⁰⁻⁶³

In many conventional systems, fluorophores that exhibit intensive fluorescence in the solution state can experience partial or complete emission quenching in the aggregate state. This is due to the effects of excited state energy transfer in the solid state and is known as aggregation-caused quenching (ACQ).⁶⁴⁻⁶⁶ In 2001, Tang's group reported that silole derivatives exhibited significantly enhanced fluorescence in the aggregated state and proposed the concept of aggregation-induced emission to explain this phenomenon.⁶⁷ Recent years have witnessed the wide application of solid-state fluorescence in the pharmaceutical, food, chemical, and optoelectronic industries. For example, Tang's group developed a real-time, on-site and non-destructive fluorescence imaging technique to monitor the crystal formation and transformation based on the crystallization-induced emission properties of (Z)-1-phenyl-2-(3-phenylquinoxalin-2(1H)-ylidene) ethenone. Based on in-depth analysis of the crystal structures of two crystalline polymorphs, Li *et al.* demonstrated that the mechanoluminescence performance is related to the molecular packing rather than the chemical structure.⁶⁸

To date, the reports of cocrystals / salts of PRM or MEL with organic basic cocrystal / salt formers are rare, and the solid-state luminescent properties of PRM have not been reported. Therefore, one motivation for this study is to explore whether the crystal landscape of PRM and MEL can be expanded with more bases and, if so, is there any improvement in solubility. Another motivation is to investigate the solid-state luminescent behaviour of PRM and its salts and expand

the understanding of crystal engineering in modifying the luminescent properties of organic materials.

In this work, six novel pharmaceutical salts of PRM or MEL with 4-aminopyridine (4AP), 4-dimethylaminopyridine (4DMP) or piperazine (PPZ) (Figure 4.3), were prepared and characterized by various solid-state analytical techniques, including thermal analysis, X-ray techniques and Fourier transform infrared (FT-IR) spectroscopy. The solubility behaviour of the six salts was measured and compared with those of parent materials. The distinct luminescent properties of PRM and its salts were investigated by optical-physical techniques together with the Hirshfeld surface analysis and the frontier molecular orbitals (FMOs) analysis.

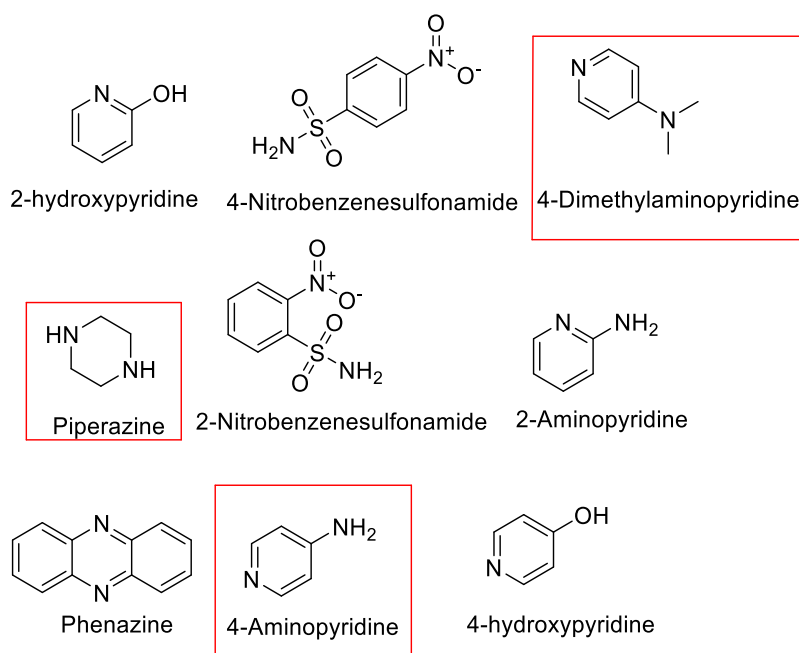


Figure 4.3. Molecular structures of the salt formers used in this study (the red boxes indicate those compounds that successfully formed salts with PRM and MEL).

4.3 Experimental Section

4.3.1 Materials

Piroxicam (form I) and meloxicam (form I) were purchased from Fluorochem and used as received without further purification. All salt formers were obtained from Sigma-Aldrich and used as received. Solvents were purchased from Honeywell International, Inc. and used as received.

4.3.2 Synthesis of Salts

PRM-4AP salt: PRM (49.7 mg, 0.15 mmol) and 4AP (14.1 mg, 0.15 mmol) in a 1:1 molar ratio were dissolved in 5 mL of methanol by heating. Red plate-like crystals were obtained by slowly evaporating the filtered solution for 3 days. Bulk materials were made by slurring a stoichiometric amount (1:1) of PRM (331.5 mg, 1 mmol) and 4AP (94.1 mg, 1 mmol) in 3 mL of methanol at room temperature for 3 days. The resulting suspension was allowed to dry in the fume hood. The powdered product was isolated and analyzed by powder X-ray diffraction (PXRD).

PRM-4DMP salt: PRM (49.7 mg, 0.15 mmol) and 4DMP (18.3 mg, 0.15 mmol) in a 1:1 molar ratio were dissolved in 10 mL of acetone by heating. Yellow plate-like crystals were obtained by slowly evaporating the filtered solution for 3 days. Bulk materials were made by slurring a stoichiometric amount (1:1) of PRM (331.5 mg, 1 mmol) and 4DMP (122.2 mg, 1 mmol) in 3 mL of methanol at room temperature for 3 days. The resulting suspension was allowed to dry in the fume hood. The powdered product was isolated and analyzed by PXRD.

PRM-PPZ salt: PRM (49.7 mg, 0.15 mmol) and PPZ (6.5 mg, 0.075 mmol) in a 2:1 molar ratio were dissolved in 5 mL of nitromethane by heating. Yellow needle-like crystals were obtained by slowly evaporating the filtered solution for 5-8 days.

Bulk materials were made by slurring a stoichiometric amount (2:1) of PRM (331.5 mg, 1 mmol) and PPZ (43.1 mg, 0.5 mmol) in 3 mL of methanol at room temperature for 3 days. The resulting suspension was allowed to dry in the fume hood. The powdered product was isolated and analyzed by PXRD.

MEL-4AP salt: MEL (52.7 mg, 0.15 mmol) and 4AP (14.1 mg, 0.15 mmol) in a 1:1 molar ratio were dissolved in 10 mL of acetone by heating. Yellow needle-like crystals were obtained by slowly evaporating the filtered solution for 5-8 days. Bulk materials were made by slurring a stoichiometric amount (1:1) of MEL (351.4 mg, 1 mmol) and 4AP (94.1 mg, 1 mmol) in 3 mL of acetone at room temperature for 3 days. The resulting suspension was allowed to dry in the fume hood. The powdered product was isolated and analyzed by PXRD.

MEL-4DMP salt: MEL (52.7 mg, 0.15 mmol) and 4DMP (18.3 mg, 0.15 mmol) in a 1:1 molar ratio were dissolved in 5 mL of methanol by heating. Yellow plate-like crystals were obtained by slowly evaporating the filtered solution for 8-10 days. Bulk materials were made by slurring a stoichiometric amount (1:1) of MEL (351.4 mg, 1 mmol) and 4DMP (122.2 mg, 1 mmol) in 3 mL of methanol at room temperature for 3 days. The resulting suspension was allowed to dry in the fume hood. The powdered product was isolated and analyzed by PXRD.

MEL-PPZ salt: MEL (52.7 mg, 0.15 mmol) and PPZ (6.5 mg, 0.075 mmol) in a 2:1 molar ratio were dissolved in 10 mL of DMF-EtOAc (1:1, v/v) by heating. Yellow needle-like crystals were obtained by slowly evaporating the filtered solution for 5-8 days. Bulk materials were made by slurring a stoichiometric amount (2:1) of MEL (351.4 mg, 1 mmol) and PPZ (43.1 mg, 0.5 mmol) in 3 mL of methanol at room temperature for 3 days. The resulting suspension was allowed

to dry in the fume hood. The powdered product was isolated and analyzed by PXRD.

4.3.3 Physical Measurements

Differential scanning calorimetry (DSC) data were collected using a TA Instruments Q1000. Samples (2-6 mg) were crimped in nonhermetic aluminum pans and scanned from 25 to 300 °C at a heating rate of 10 °C min⁻¹ under a continuously purged dry nitrogen atmosphere. Thermogravimetric analysis (TGA) data were collected using a TA Instruments Q500 thermogravimetric analyzer. The sample was placed in an aluminum sample pan and heated under nitrogen at a rate of 20 °C min⁻¹ from 25 to 500 °C. IR spectra were recorded on a PerkinElmer UATR Two spectrophotometer using a diamond ATR accessory over a range of 400–4000 cm⁻¹. An average of four scans was taken for each spectrum obtained with a resolution of 4 cm⁻¹. PXRD data were collected using a STOE STADI MP diffractometer with Cu K α radiation using a linear PSD over the 2 θ range of 3.5–45.5° with increments of 0.05° at a rate of 2° min⁻¹. The samples were prepared using transmission foils and the data were viewed via STOE WinXPOW POWDAT software.⁶⁹ Single-crystal X-ray diffraction (SCXRD) data were collected on a Bruker APEX II DUO with monochromated Cu K α radiation for PRM-4AP and MEL-4DMP ($\lambda = 1.54184 \text{ \AA}$) and Mo K α radiation for PRM-4DMP, PRM-PPZ, MEL-4AP and MEL-PPZ ($\lambda = 0.7107 \text{ \AA}$), respectively. All calculations and refinements were made using the Bruker APEX software with the SHELXL program.^{70, 71} Nonhydrogen atoms were refined anisotropically. All hydrogen atoms were placed in geometrically calculated positions using the riding model, with C–H = 0.93–0.97 Å and N–H = 0.86–0.89 Å, and $U_{iso}(\text{H})$ (in the range

1.2–1.5 times U_{eq} of the parent atom). For PRM-PPZ and MEL-PPZ, there was disorder in the methyl group, which was modeled in two conformations in a 50:50 ratio. DIAMOND was used for creating figures,⁶² and PLATON was used for analysis of potential hydrogen bonds and short ring interactions.⁷² Crystallographic parameters are listed in Table 4.2.

Table 4.2. Crystallographic data for PRM-4AP, PRM-4DMP, PRM-PPZ, MEL-4AP, MEL-4DMP and MEL-PPZ salts.

	PRM-4AP 1:1	PRM-4DMP 1:1	PRM-PPZ 1:0.5	MEL-4AP 1:1	MEL-4DMP 1:1	MEL-PPZ 1:0.5
Chemical formula	C ₂₀ H ₁₉ N ₅ O ₄ S	C ₂₂ H ₂₃ N ₅ O ₄ S	C ₁₇ H ₁₈ N ₄ O ₄ S	C ₁₉ H ₁₉ N ₅ O ₄ S ₂	C ₂₁ H ₂₃ N ₅ O ₄ S ₂	C ₁₆ H ₁₈ N ₄ O ₄ S ₂
Formula weight	425.46	453.52	374.41	445.51	473.56	394.46
Crystal system	triclinic	monoclinic	monoclinic	monoclinic	triclinic	monoclinic
Space group	<i>P</i> $\bar{1}$	<i>C</i> 2/ <i>c</i>	<i>P</i> 2 ₁ / <i>c</i>	<i>C</i> <i>c</i>	<i>P</i> $\bar{1}$	<i>P</i> 2 ₁ / <i>c</i>
Temperature (K)	293(2)	296	299(2)	296	298(2)	298(2)
<i>a</i> (Å)	8.2328(12)	22.431(3)	9.944(4)	11.813(2)	8.3482(7)	8.002(4)
<i>b</i> (Å)	10.6200(16)	16.048(3)	7.906(3)	20.427(4)	10.4251(15)	29.90(2)
<i>c</i> (Å)	12.361(4)	12.900(2)	22.650(12)	10.2167(17)	12.6635(7)	7.512(4)
<i>α</i> (°)	75.393(16)	90	90	90	90.789(7)	90
<i>β</i> (°)	71.368(12)	109.888(6)	96.56(2)	123.016(3)	95.355(5)	106.380(18)
<i>γ</i> (°)	89.872(10)	90	90	90	95.567(7)	90
Volume (Å ³)	987.4(4)	4366.7(13)	1769.1(13)	2067.1(6)	1091.84(19)	1724.6(18)
<i>Z</i>	2	8	4	4	2	4
ρ_{calc} (g cm ⁻³)	1.431	1.380	1.406	1.432	1.444	1.519

Radiation type	Cu K α	Mo K α	Mo K α	Mo K α	Cu K α	Mo K α
μ (mm ⁻¹)	1.795	0.188	0.214	0.295	2.551	0.340
Reflns measured	40074	27903	57483	7186	57119	76271
Reflns independent	3809	5504	9923	3309	4267	6931
Significant [$I > 2\sigma(I)$]	3670	4248	7423	3236	4010	3067
Parameters refined	272	292	235	273	290	235
Restraints	0	6	0	26	0	0
$\Delta\rho_{max}, \Delta\rho_{min}$ (e Å ⁻³)	0.367, -0.465	0.381, -0.451	0.404, -0.417	0.140, -0.232	0.331, -0.559	0.385, -0.445
$F(000)$	444	1904	784	928	498	824
R_I [$I > 2\sigma(I)$]	0.0435	0.0561	0.0425	0.0260	0.0344	0.0609
wR_2 (all data)	0.1193	0.1200	0.1338	0.0654	0.1017	0.1916
CCDC Number	2064483	2109805	2064485	2109802	2109803	2109804

4.3.4 Computational Studies

Hirshfeld surface analyses and two-dimensional (2D) fingerprint plots were carried out using the CrystalExplorer 21.5 program.⁷³ Density functional theory (DFT) calculations using the Gaussian 09 program package employing the RB3LYP functional with 6-31G (d, p) basis set were performed on PRM, MEL and the six obtained crystals without conducting structural optimization.^{62, 74} The molecular orbitals were viewing using Multiwfn 3.8 program and plotted by VMD.^{75, 76}

4.3.5 Solubility Experiments

Solubility experiments were conducted in sodium phosphate buffer solutions at pH 6.5 and 37 °C to simulate intestinal physiological conditions. For each experiment, an excess crystalline solid was sieved through a 300 µm sieve and introduced into a flask with a screw top containing 100 mL of the medium. The solution was stirred at 200 rpm by a magnetic stir bar for 48 h to reach the equilibrium state. Sampling was performed at 5, 10, 15, 20, 30, 45, 60, 90, 120, 180, 240, 300, 360, 540, 720, 1440, 2160 and 2880 min. After each sampling, the volume of the liquid removed from the suspension was not compensated. The withdrawn suspension was filtered through 0.2 µm nylon filters and diluted prior to high-performance liquid chromatography (HPLC) analysis. The solubility experiment for each crystal form was repeated in triplicate. After the last sample collection, the remaining solid material in the suspension was filtered, dried and characterized by IR and PXRD. The HPLC method was developed to determine the concentration of PRM and MEL using an Agilent 1260 series Infinite HPLC system (Agilent Technologies, Waldbronn, Germany). A C18 HPLC column (YMC-Pack ODS-A column, 4.6 mm

× 250 mm, 5 μm) with a flow rate of 1 mL min⁻¹ was employed, and the column temperature was set at 25 °C. The binary mobile phase consisted of acetonitrile and sodium phosphate buffer (pH 6.5) in a volume ratio of 25:75. The samples were diluted appropriately with the mobile phase, and the absorbance was measured at 347 nm. The retention times of PRM and MEL were 7.1 min and 10.9 min, respectively.

4.3.6 Optical-Physical Measurements

Solid-state UV-vis spectra were recorded on a Shimadzu 3200 UV spectrometer. Solid-state fluorescent spectra were collected by a Cary Eclipse Fluorescence Spectrometer (Agilent, United States) with 365 nm excitation light. The fluorescence quantum yield values were performed on a Hamamatsu Photonics C9920-02G Instrument (Hamamatsu Photonics Co., Ltd).

4.4 Results and Discussions

4.4.1 Crystal Structure Analysis

The salt formation of PRM or MEL can be rationalized by ΔpK_a values. The ΔpK_a values are greater than 4 in all cases since 4AP, 4DMP and PPZ are strong organic bases (Table 4.3). Therefore, it is expected that the hydroxyl group of PRM or MEL will be deprotonated and form charge-assisted hydrogen-bonded salts with these organic counterions. Single crystals of the six salts suitable for SCXRD were obtained and their structures determined. Ellipsoid plots of PRM-4AP, PRM-4DMP and PRM-PPZ are shown in Figure S4.5 and those of MEL-4AP, MEL-4DMP and MEL-PPZ are shown in Figure S4.13. Hydrogen bonds and π - π interaction geometries are shown in Tables S4.1-S4.3 for PRM-4AP, PRM-4DMP

and PRM-PPZ salts, and in Tables S4.5-S4.7 for MEL-4AP, MEL-4DMP and MEL-PPZ salts.

Table 4.3. p*K*_a Values of PRM, MEL, salt formers and their Δ*pK*_a values.

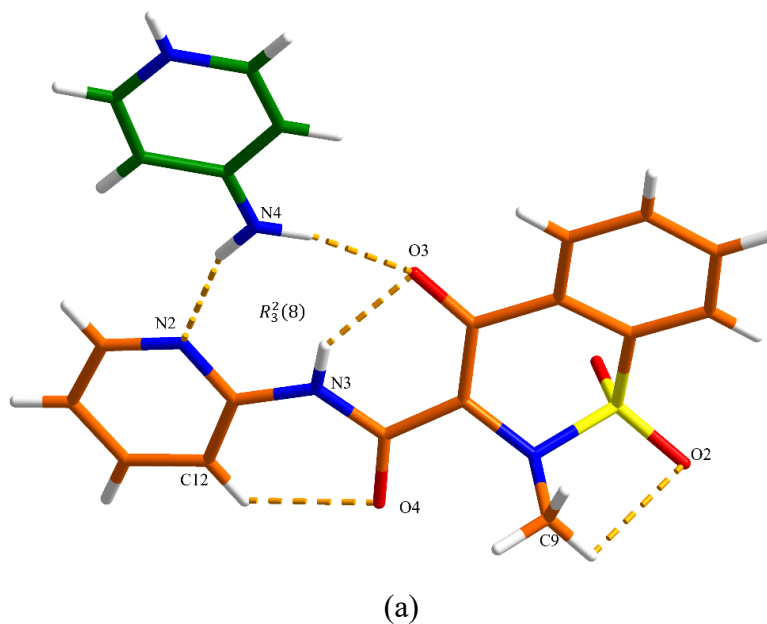
	p <i>K</i> _a in water	Δ <i>pK</i> _a for PRM	Δ <i>pK</i> _a for MEL	structure
PRM	1.86, ^a 5.46 ²¹			
MEL	1.09, ^a 4.18 ²²			
4AP	9.17 ⁷⁷	7.31	8.08	1:1 salt
4DMP	9.70 ⁷⁸	7.84	8.61	1:1 salt
PPZ	9.72 ⁷⁹	7.86	8.63	2:1 salt

^a it is the hydroxyl group that is deprotonated in this work.

PRM-4AP Salt

PRM-4AP crystallizes in $P\bar{1}$ space group with $Z = 2$, the asymmetric unit consisting of one PRM⁻ anion and one 4-aminopyridinium (4APH⁺) cation. As shown in Figure 4.4a, an $R_3^2(8)$ motif is formed between PRM⁻ and 4APH⁺ through two discrete hydrogen bonds (N4–H4A···N2, 2.99 Å; and N4–H4B···O3, 2.89 Å) and intramolecular hydrogen-bonding interactions [S(6), N3–H3N···O3, 2.65 Å]. There are two more intramolecular interactions within the PRM⁻ anion (C12–H12···O4, 2.87 Å and C9–H9B···O2, 2.85 Å), forming an S(6) motif and an S(5) motif, respectively. Notice the bond angle of the methyl C–H···O intramolecular interaction is smaller than that of other interactions, which is reasonable since five-membered ring intramolecular hydrogen bonds usually have the smallest angles and the longest distances compared to the six-eight-membered intramolecular hydrogen bonds and are within the geometric limits of a hydrogen bond as defined.⁸⁰ Moreover, the angle (τ) formed between the methyl hydrogen

and the plane of a sp^2 oxygen in PRM^- anion is 45.4° , which falls within the required range ($< 50^\circ$)⁸¹. This methyl $C-H\cdots O$ intramolecular interaction in PRM^- anion can also be found in $PRM-4DMP$ and $PRM-PPZ$ salts, and their dihedral angles (τ) are listed in Figure S4.6. The basic unit is extended via two discrete hydrogen bonding interactions, i.e., $N5-H5N\cdots O4$ (2.65 Å) and $C19-H19\cdots O1$ (3.28 Å), resulting in a double-layer 2D network (Figure 4.4b). As shown in Figure 4.4c, the $\pi-\pi$ interactions between layers participate in the construction of the three-dimensional (3D) structure. The centroid-centroid distances of $\pi-\pi$ interactions from Cg2 to Cg5 (orange), Cg5 to Cg2 (blue), and Cg3 to Cg3 (purple) are 4.18, 4.17, and 3.64 Å, respectively (Table S4.1).



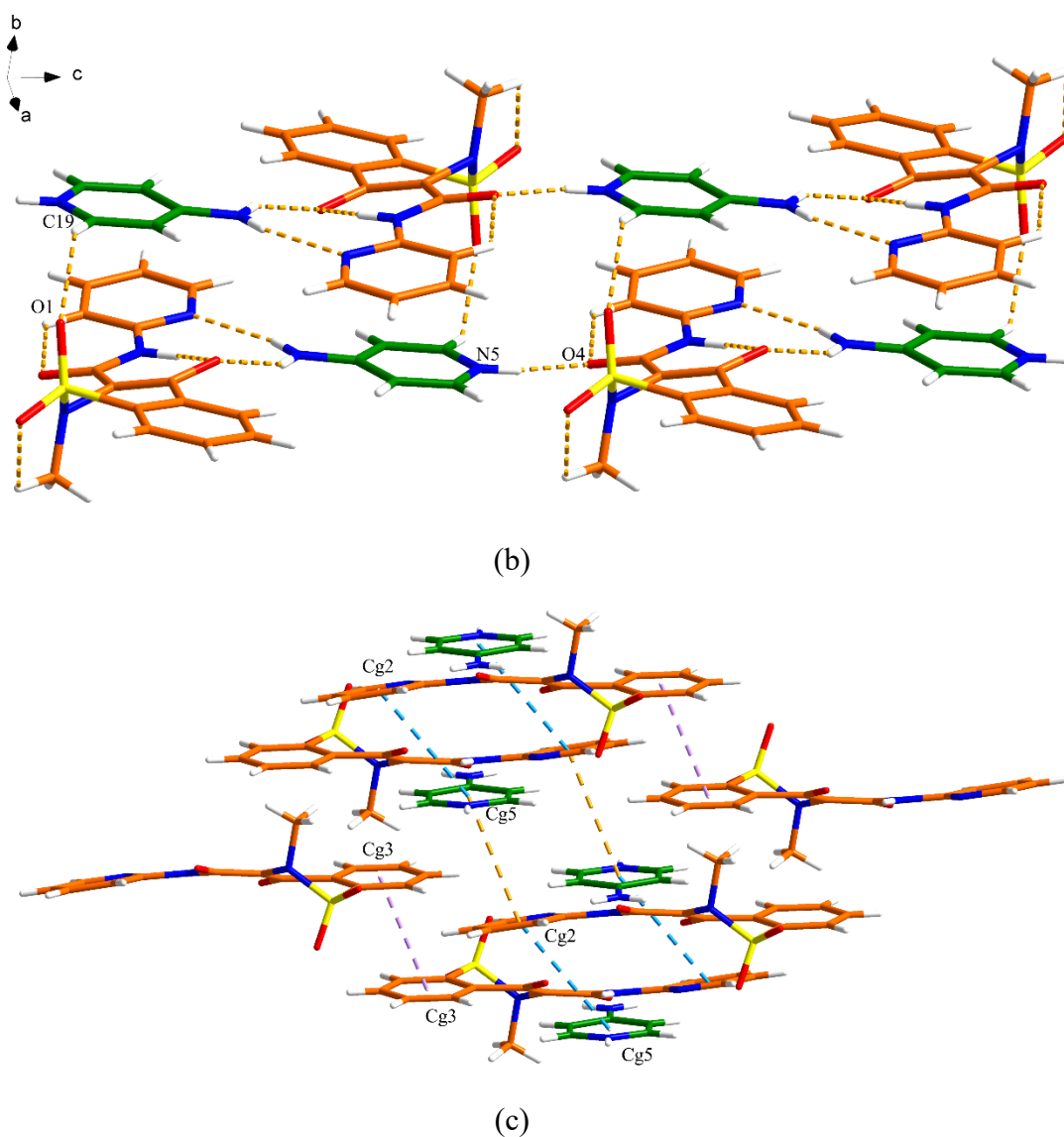
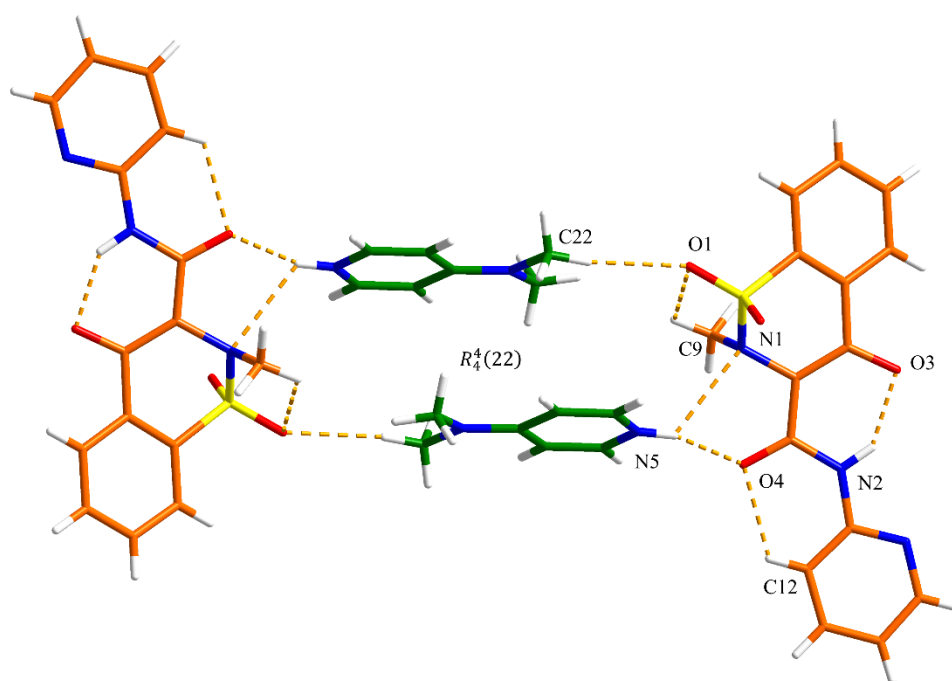


Figure 4.4. Crystal packing and intermolecular interactions in the PRM-4AP salt: (a) asymmetric unit (orange is PRM and green is 4AP), (b) 2D hydrogen-bonded network (hydrogen bonding is displayed by dashed lines), and (c) 3D network resulting from π - π interactions as indicated by dashed lines (hydrogen bonding is not displayed for clarity).

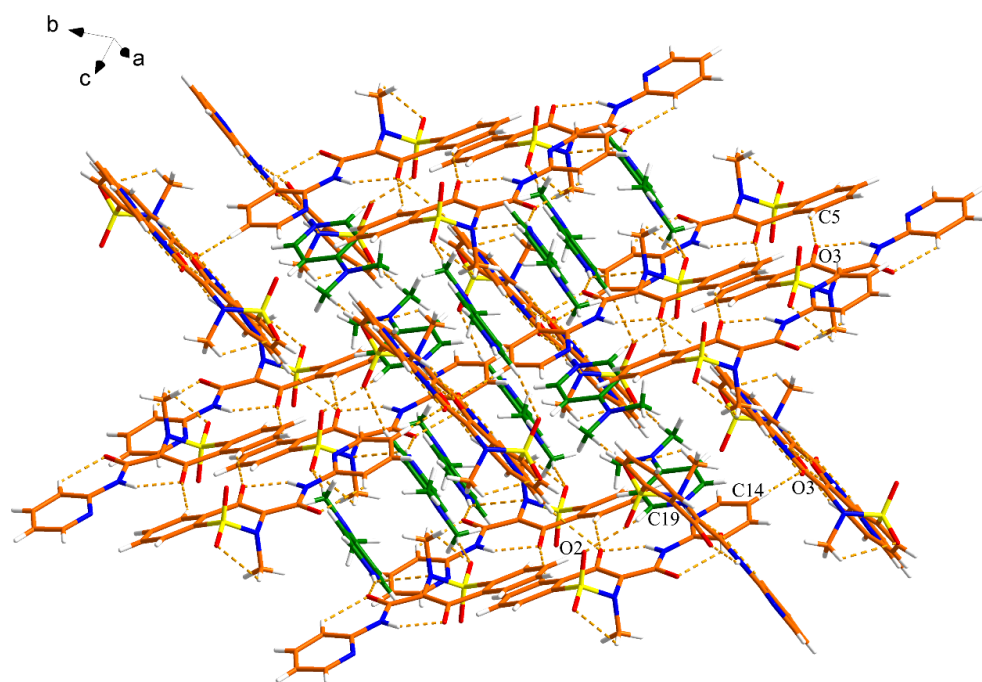
PRM-4DMP Salt

PRM-4DMP crystallizes in the monoclinic $C2/c$ space group and contains, in the asymmetric unit, one PRM^- anion and one 4DMPH^+ cation. As shown in Figure 4.5a, one S(5) and two S(6) can be found in the structure of the PRM^- anion. The

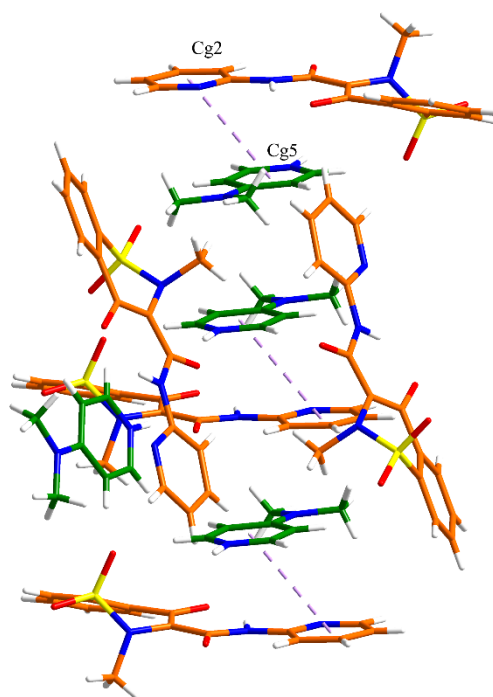
two PRM^- anions and two 4DMPH^+ cations form an $R_4^4(22)$ motif around an inversion center via two discrete $\text{N5-H24}\cdots\text{N1}$ (3.15 Å) and $\text{C22-H29}\cdots\text{O1}$ (3.40 Å) hydrogen-bonding interactions. The discrete $\text{N5-H24}\cdots\text{O4}$ (2.69 Å) hydrogen bond is also responsible for the construction of the tetramer. This tetramer is then extended by four $\text{C-H}\cdots\text{O}$ hydrogen bond interactions, displaying the 3D hydrogen bonding network (Figure 4.5b and Table S4.2). As shown in Figure 4.5c and Table S4.2, the 3D structure is further stabilized by π - π interactions between the two pyridyl rings of PRM and 4DMP (Cg2-Cg5 , 4.07 Å).



(a)



(b)



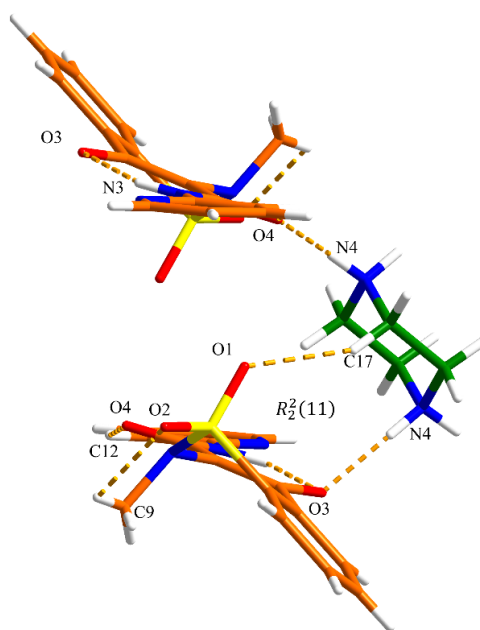
(c)

Figure 4.5. Crystal packing and intermolecular interactions in the PRM-4DMP salt: (a) tetramer (orange is PRM and green is 4DMP), (b) 3D hydrogen-bonded network (hydrogen bonding is displayed by dashed lines), and (c) 3D network

resulting from π - π interactions as indicated by dashed lines (hydrogen bonding is not displayed for clarity).

PRM-PPZ Salt

The PRM-PPZ salt crystallizes in the monoclinic system, space group $P2_1/c$ with one PRM^- anion and half of the PPZH_2^{2+} dication in the asymmetric unit. As shown in Figure 4.6a, the PPZH_2^{2+} dication is located on an inversion center (protons abstracted each from two PRM molecules) and the two PRM^- anions are at the general position in the unit cell. An $R_2^2(11)$ motif is formed between PPZH_2^{2+} and PRM^- through discrete $\text{N-H}\cdots\text{O}$ hydrogen bond interaction ($\text{N4-H4B}\cdots\text{O3}$, 2.70 Å) and $\text{C-H}\cdots\text{O}$ hydrogen bond interaction ($\text{C17-H17A}\cdots\text{O1}$, 3.48 Å). Along the c axis, there are discrete $\text{N-H}\cdots\text{O}$ hydrogen bonds ($\text{N4-H4A}\cdots\text{O4}$, 2.65 Å) between PPZH_2^{2+} and another PRM^- anion. No significant π - π interactions participate in stabilizing the 3D structure of PRM-PPZ salts (Figure 4.6b and Table S4.3).



(a)

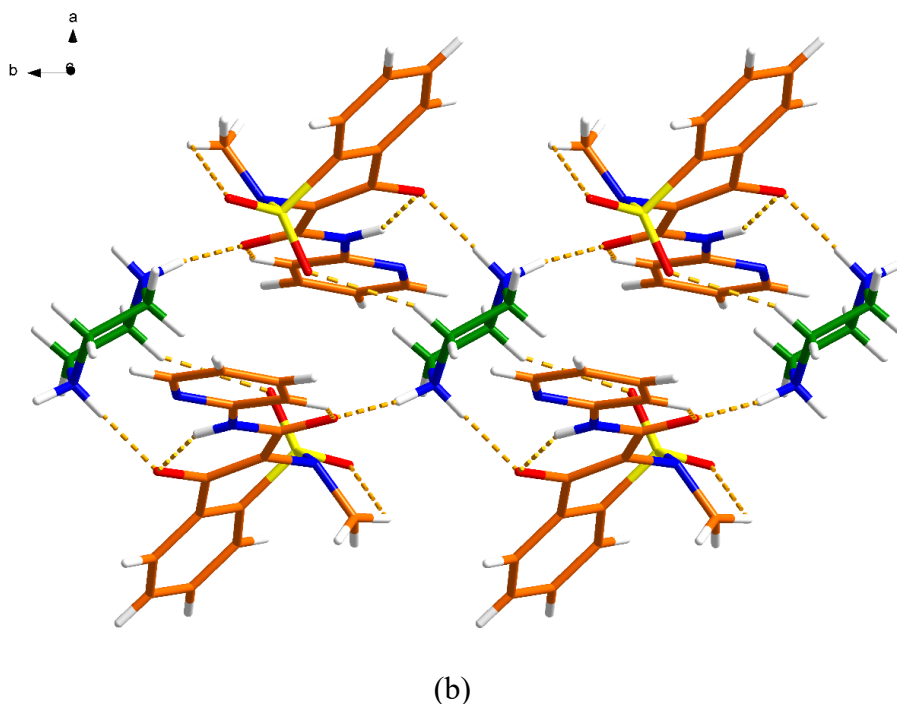
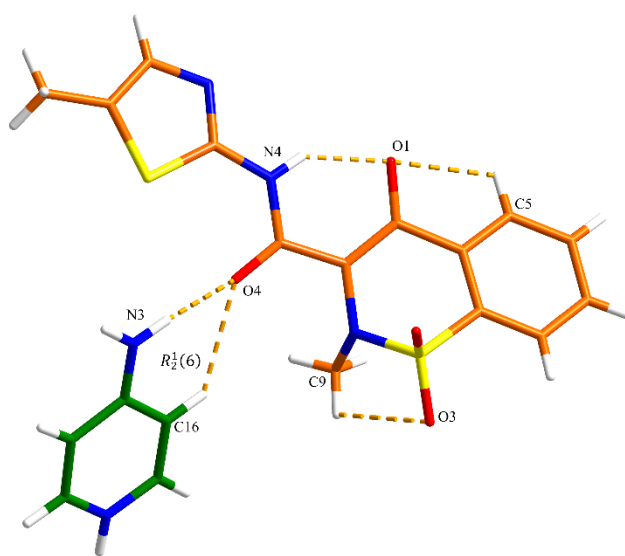


Figure 4.6. Crystal packing and intermolecular interactions in the PRM-PPZ salt: (a) basic unit (orange is PRM and green is PPZ) and (b) 3D hydrogen-bonded network (hydrogen bonding is displayed by dashed lines). One of the disordered methyl hydrogen atom conformations has been omitted for clarity.

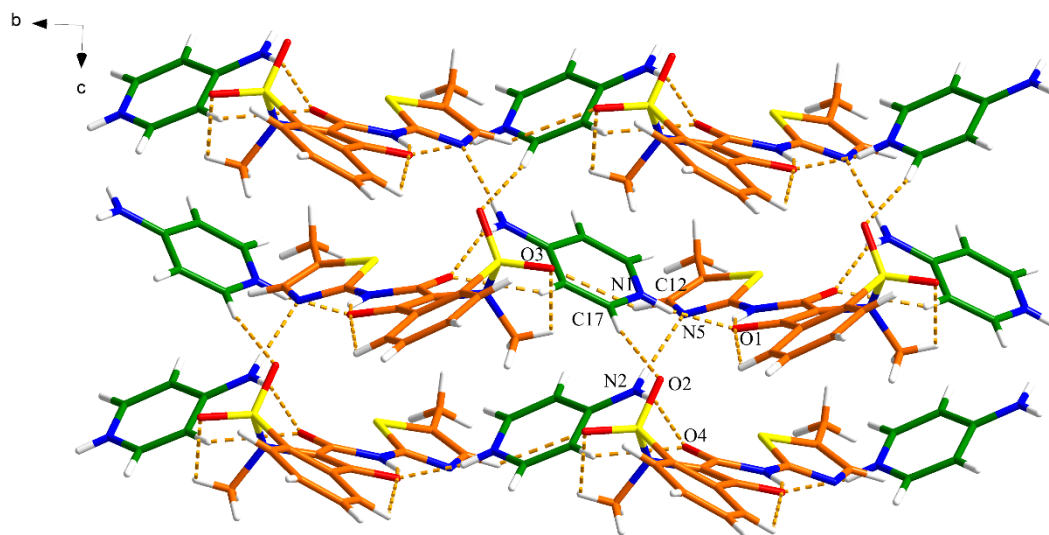
MEL-4AP Salt

MEL-4AP salt crystallizes as a 1:1 salt consistent with the acid – base donor–acceptor ratio. One MEL[−] anion and one 4APH⁺ cation are present in the asymmetric unit of a monoclinic *Cc* crystal structure. As shown in Figure 4.7a, an $R_2^1(6)$ supramolecular heterosynthon is formed between one 4APH⁺ and one MEL[−] via N–H \cdots O and C–H \cdots O discrete hydrogen bond interactions (N2–H20 \cdots O4, 2.89 Å; C16–H16 \cdots O, 3.27 Å). The methyl C–H \cdots O intramolecular interaction can be observed in three MEL salts and their dihedral angles (τ) are listed in Figure S4.14. Along the *a* axis, the MEL[−] anion in this unit is further connected with other MEL[−] and 4APH⁺ through C12–H12 \cdots O3 (3.26 Å) and N1–H1 \cdots O1 (2.69 Å) hydrogen bonds, respectively, extending into a 2D sheet.

These 2D sheets are further linked through N2–H21⋯N5 (3.02 Å) and C17–H17⋯O2 (3.29 Å) hydrogen bonds to construct a 3D network, as shown in Figure 4.7b. The structure is also stabilized by intermolecular π – π stacking interactions between the phenyl ring of MEL and the pyridyl ring of 4AP with a centroid–centroid distance (Cg–Cg) of around 4.22 Å (Figure 4.7c and Table S4.5).



(a)



(b)

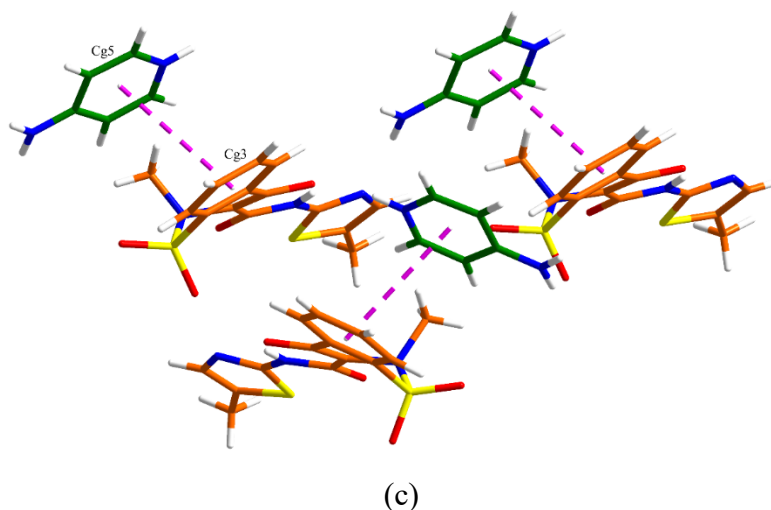


Figure 4.7. Crystal packing and intermolecular interactions in the MEL-4AP salt: (a) asymmetric unit (orange is MEL and green is 4AP), (b) 3D hydrogen-bonded network (hydrogen bonding is displayed by dashed lines), and (c) 3D network resulting from π - π interactions as indicated by dashed lines (hydrogen bonding is not displayed for clarity).

MEL-4DMP Salt

The MEL-4DMP salt crystallizes in the $P\bar{1}$ space group. The asymmetric unit contains one MEL^- anion and 4DMPH^+ cation (Figure 4.8a). The two components interact via $\text{N}-\text{H}\cdots\text{N}$ ($\text{N5}-\text{H05}\cdots\text{N3}$, 2.79 Å) discrete hydrogen bond interactions. The 3D structure is further assembled by the $\text{C}-\text{H}\cdots\text{O}$ ($\text{C15}-\text{H15A}\cdots\text{O3}$, 3.35 Å; $\text{C16}-\text{H16A}\cdots\text{O3}$, 3.45 Å; $\text{C16}-\text{H16C}\cdots\text{O2}$, 3.24 Å and $\text{C20}-\text{H20}\cdots\text{O4}$, 3.16 Å) hydrogen bond interactions between the 4DMPH^+ cation and adjacent MEL^- anions. Additional π - π interactions between the phenyl rings from MEL^- ($\text{Cg3}-\text{Cg3}$, 3.80 Å) contribute to the extended 3D structure (Figures 4.8b, c and Table S4.6).

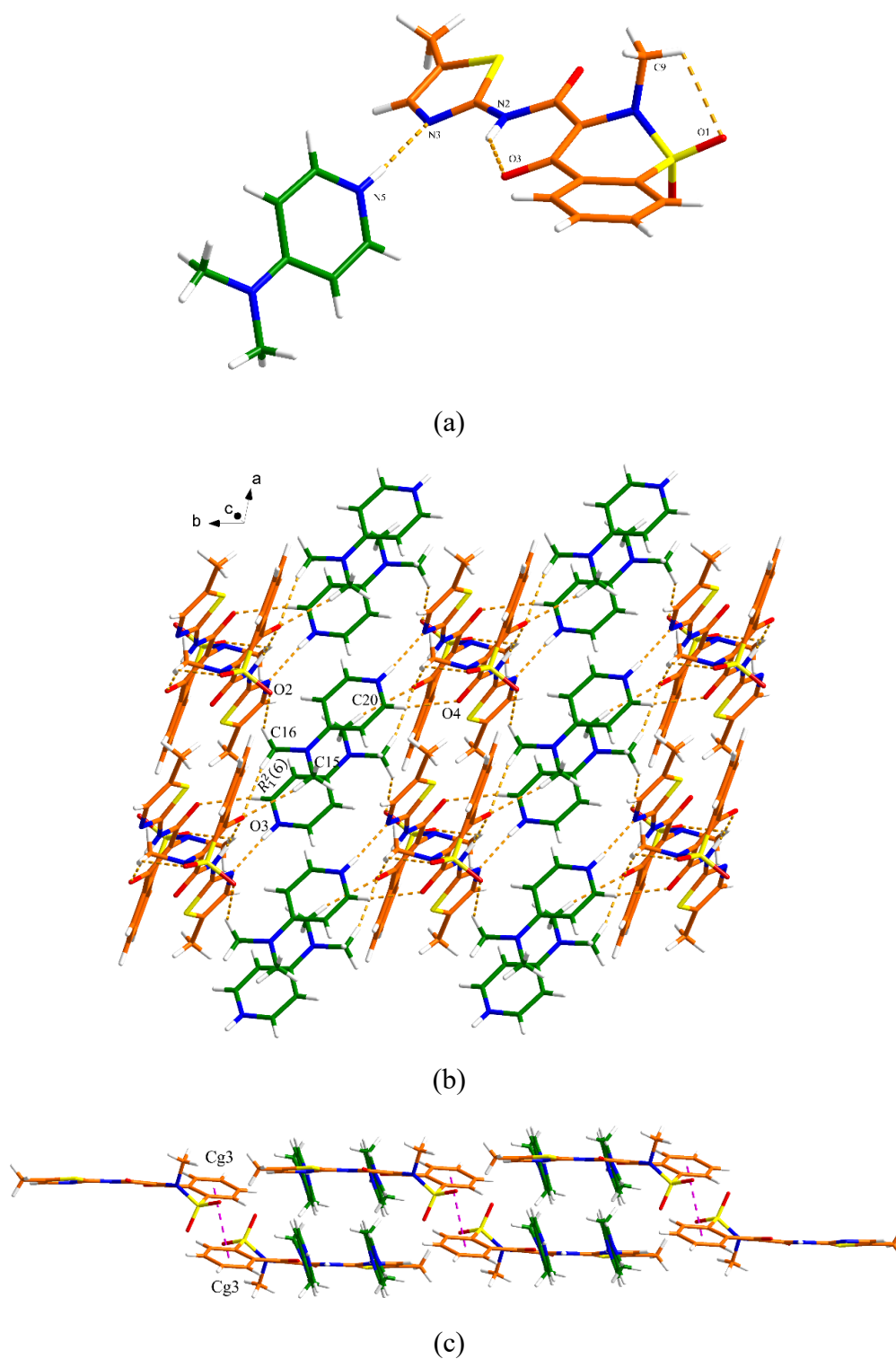
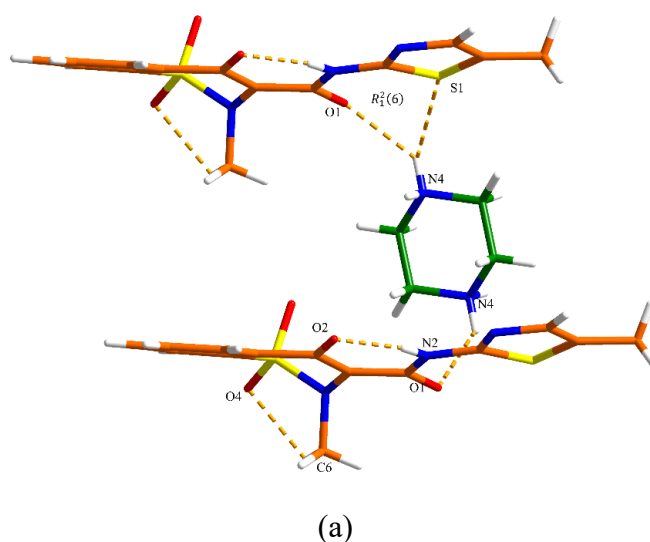


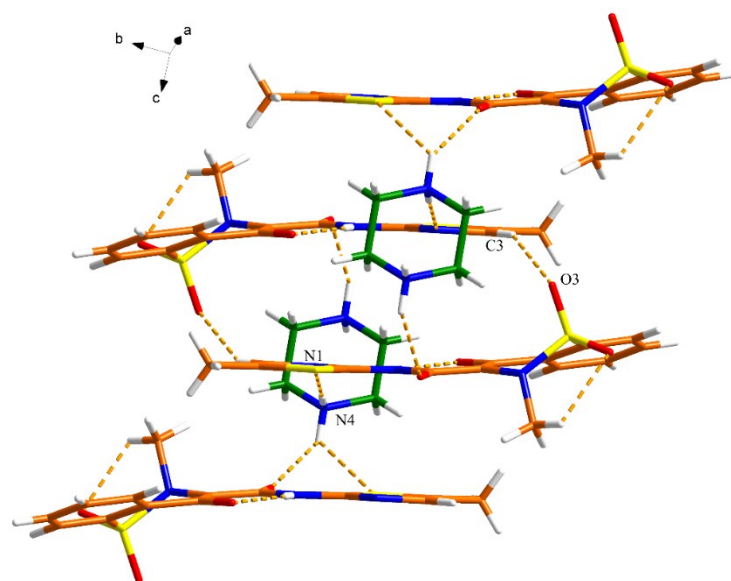
Figure 4.8. Crystal packing and intermolecular interactions in the MEL-4DMP salt: (a) asymmetric unit (orange is MEL and green is 4DMP), (b) 3D hydrogen-bonded network (hydrogen bonding is displayed by dashed lines), and (c) 3D

network resulting from π - π interactions as indicated by dashed lines (hydrogen bonding is not displayed for clarity).

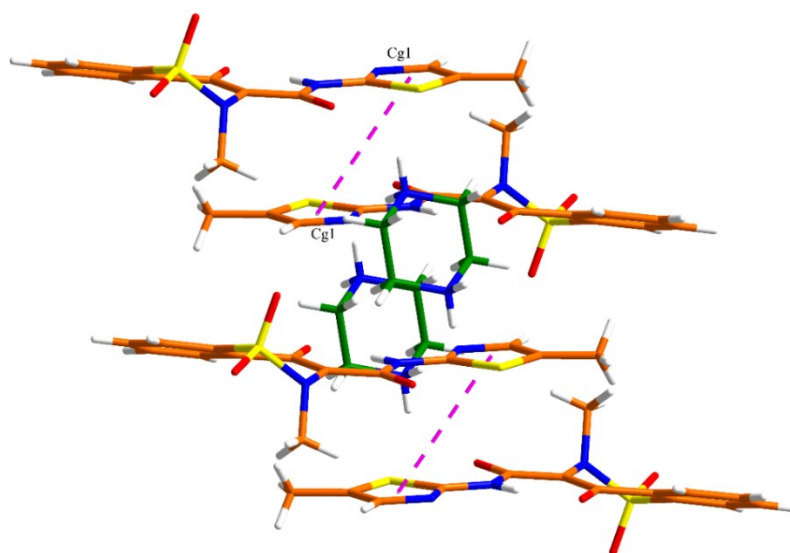
MEL-PPZ Salt

MEL-PPZ salt crystallizes in the monoclinic $P2_1/c$ space group. The asymmetric unit contains one MEL⁻ anion and half of the PPZH₂²⁺ dication. As shown in the top of Figure 4.9a, the PPZH₂²⁺ dication connects to two MEL⁻ anions via N-H \cdots O and N-H \cdots S (N4-H4B \cdots O1, 2.93 Å; N4-H4B \cdots S1, 3.31 Å) discrete hydrogen bond interactions, generating an $R_1^2(6)$ motif (as shown in the top of Figure 4.9a), and N4-H4B \cdots O1 (2.93 Å) discrete hydrogen bonding interactions (in the bottom of Figure 4.9a). This trimer is connected with adjacent MEL⁻ and PPZH₂²⁺ via N-H \cdots N and C-H \cdots O (N4-H4A \cdots N1, 2.85 Å and C3-H3 \cdots O3, 3.28 Å) discrete hydrogen bond interactions, stabilizing the 3D hydrogen bonding network. The neighboring layers are further held together via π - π interactions (\sim 4.2 Å) to generate a 3D structure (Figures 4.9b, c and Table S4.7).





(b)



(c)

Figure 4.9. Crystal packing and intermolecular interactions in the MEL-PPZ salt: (a) basic unit (orange is MEL and green is PPZ), (b) 3D hydrogen-bonded network (hydrogen bonding is displayed by dashed lines), and (c) 3D network resulting from π - π interactions as indicated by dashed lines (hydrogen bonding is not displayed for clarity). One of the disordered methyl hydrogen atom conformations has been omitted for clarity.

These are the first examples of the oxicam salts with 4AP and 4DMP; the salts of LRM and TNM with PPZ are known.^{31,32} Comparing the crystal structures of the four oxicam-PPZ salts reveals that they all have a 2:1 stoichiometry. The PPZH₂²⁺ dication lies over an inversion center, with a proton abstracted from each of the oxicam molecules, and it bridges the two oxicam anions through N⁺-H···O⁻ hydrogen bonds. Notably, for MEL-PPZ salt, the PPZH₂²⁺ dication is involved in more hydrogen bonding interactions than the other three oxicams.

4.4.2 Physical Characterization

The PXRD patterns of the PRM system and the MEL system are shown in Figures S4.4 and S4.12, respectively. For all six salts, the experimental PXRD patterns match the theoretical patterns obtained from the SCXRD analysis, revealing these salts were reproduced in bulk quantities by the slurry method.

FT-IR spectra of PRM and MEL systems are shown in Figures S4.3 and S4.11, respectively. The new crystalline solids exhibit different vibrational frequencies compared with those of the pure API and the salt formers, for example, for PRM, the characteristic absorption peak at 1628 cm⁻¹ assigned to the C=O stretching vibration is red-shifted to 1626 cm⁻¹, 1618 cm⁻¹ and 1615 cm⁻¹ in PRM-4AP, PRM-4DMP and PRM-PPZ salts, respectively. For MEL the C=O stretching vibration is red-shifted from 1617 cm⁻¹ to 1614 cm⁻¹ (MEL-4AP), 1611 cm⁻¹ (MEL-4DMP) and 1616 cm⁻¹ (MEL-PPZ). Furthermore, the unencumbered -NH stretch in PRM (3337 cm⁻¹) and MEL (3287 cm⁻¹) is lost in the PRM or MEL salts, revealing the -NH group is engaged in the formation of hydrogen bonds. These changes suggest the re-construction of hydrogen bond networks in those solids and indicate the formation of new crystalline solids.

DSC and TGA studies were conducted on the six salts and their individual components to obtain the melting points and decomposition temperatures. The melting trace and decomposition behaviour of each salt and the starting materials are given in the Supporting Information (Figures S4.1 and S4.2 for the PRM system, and Figures S4.9 and S4.10 for the MEL system). Each salt shows a single sharp endothermic peak, suggesting that each product is in a homogeneous phase. Moreover, the TGA traces indicate that no solvent or water molecule are involved in the crystal lattice of these salts.

4.4.3 Solubility Studies

PRM is dissolved and absorbed mainly in the intestine (in pH 6–8), and MEL undergoes significant degradation at lower pH (< 3).^{21, 82} Therefore, solubility tests of PRM, MEL, and their salts were performed in sodium phosphate buffer solutions (pH = 6.5) to investigate the ability of salt formation to improve the solubility of the poorly water-soluble APIs. As shown in Figure 4.10a, pure PRM reaches its highest solubility (0.39 mg mL⁻¹) at 60 min. Subsequently, the concentration of pure PRM decreases slowly over time due to the crystal transformation from PRM anhydrate to PRM monohydrate and forms a plateau (0.14 mg mL⁻¹). Similar behaviour is observed for theophylline and caffeine.⁸³ All the PRM salts exhibit the “spring and parachute” phenomenon,⁸⁴ in that they dissolve faster than pure PRM and reach their maximum solubility within 5 min, and then the solubility decreases slowly over time owing to the transformation of the salts into the less soluble PRM monohydrate in solution (see Figure S4.7 for PXRD analysis confirming formation of the monohydrate). The dissolved PRM of PRM-4AP, PRM-4DMP, and PRM-PPZ salts are 1.08, 1.07 and 0.43 mg mL⁻¹,

which are 2.8, 2.8 and 1.1 times higher than that of the anhydrous PRM, respectively (Table 4.4). Looking at Table 4.1, while some reported cocrystals and salts do not show any solubility advantage, these results are similar to the majority of the PRM salts and cocrystals in the literature, demonstrating enhanced solubility performance.

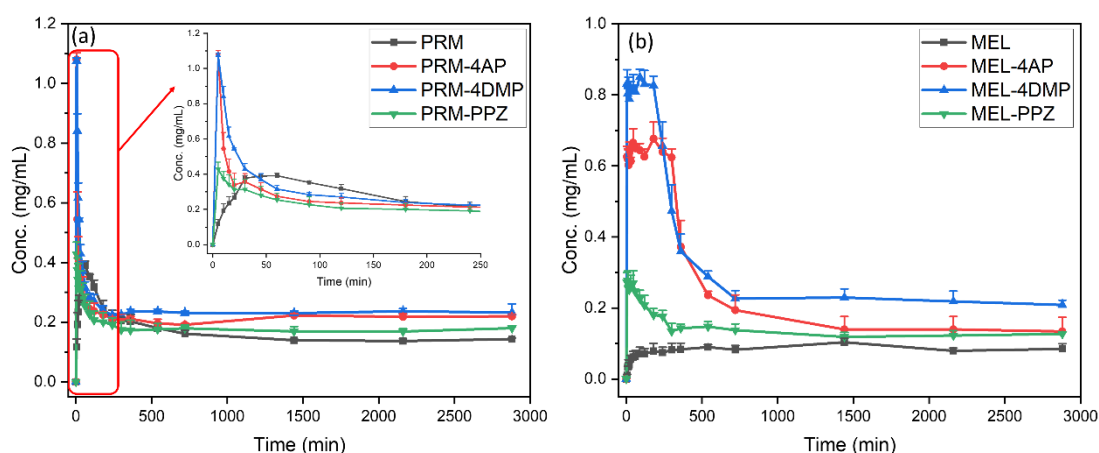


Figure 4.10. Solubility profiles of (a) PRM, PRM-4AP, PRM-4DMP, and PRM-PPZ and (b) MEL, MEL-4AP, MEL-4DMP, and MEL-PPZ.

Table 4.4. Melting point (T_m) and dissolved API of PRM, MEL and the six salts.

Solids	T_m ($^{\circ}\text{C}$)	Dissolved PRM (mg mL^{-1})	Solids	T_m ($^{\circ}\text{C}$)	Dissolved MEL (mg mL^{-1})
PRM	198–200	0.39 ± 0.01	MEL	259 (dec)	0.08 ± 0.02
PRM-4AP	213–216	1.08 ± 0.02	MEL-4AP	227–232	0.68 ± 0.05
PRM-4DMP	207–209	1.07 ± 0.01	MEL-4DMP	212–216	0.85 ± 0.02
PRM-PPZ	208–213	0.43 ± 0.04	MEL-PPZ	246–251	0.28 ± 0.03

Similarly, the solubility and dissolution rate of MEL are significantly enhanced by salt formation. As shown in Figure 4.10b, pure MEL dissolves slowly and reaches

equilibrium (0.08 mg mL^{-1}) at 90 min. The “spring and parachute” phenomenon is also observed for all the MEL salts, with PXRD analysis of the solid residues collected after the solubility experiments indicating these undissolved solids had transformed to MEL (Figure S4.15). The time to maximum dissolved concentration of the salts is extended to 5 min, demonstrating the remarkably improved dissolution rate in comparison with that of pure MEL. The dissolved MEL of MEL-4AP, MEL-4DMP, and MEL-PPZ salts is 8.1, 10.2 and 3.3 times higher than that of the pure MEL, respectively. Furthermore, MEL-4DMP and MEL-4AP can maintain the supersaturation state for more than 200 and 300 min, respectively, indicating the two salts of MEL could be promising formulations for achieving extended release without using polymers.^{85, 86} These two salts have better solubility behaviour when compared to most reported MEL cocrystals and salts, although the MEL aspirin cocrystal has significantly improved solubility compared to all other systems (Table 4.1).⁴⁸

More recently, there have been reports of a correlation between the melting point and the solubility of cocrystals.^{87,88} In this study, no correlation was identified when examining the melting point and solubility of PRM salts; however, a semiempirical negative correlation between the drug melting point and drug solubility was found in the MEL system (Table 4.4).^{62, 88} The melting point of the MEL salts increase in the following order: MEL-4DMP < MEL-4AP < MEL-PPZ, while the apparent solubility increases in the opposite order: MEL-PPZ < MEL-4AP < MEL-4DMP.

4.4.4 Luminescence Studies

It is known that PRM is fluorescent in dilute solution,⁵⁹ and we observed that PRM and the three salts exhibit relatively strong solid-state luminescence. As shown in Figure 4.11, PRM, PRM-4AP, and PRM-4DMP are yellow and PRM-PPZ is pale pink in color under white light illumination. However, upon irradiating with UV light, the PRM-4AP and PRM-4DMP salts exhibit strong cyan fluorescence, while PRM and PRM-PPZ show blue fluorescence. Solid-state UV–vis absorption spectra for PRM and its three salts were measured to further investigate the luminescent properties (Figure 4.12a). The wavelength of maximum absorption for all four solids is ca. 405 nm, and there is a weaker absorption which peaks around 560 nm in all three salts. In addition, the absorption bands for PRM-4AP and PRM-4DMP demonstrate a broad trend with a slight redshift in the higher energy absorption band. Based on analysis by Lu *et al.* on a different luminescent system,⁶³ this suggests that the charge transfer interaction in these two salts is stronger than that in PRM-PPZ salt. Solid-state fluorescence spectra and quantum yields of the four PRM solids are shown in Table 4.5 and Figure 4.12b. Both PRM-4AP and PRM-4DMP salts display significantly red-shifted spectra and higher quantum yields compared to those of PRM, while a slight red shift and lower quantum yield are observed for PRM-PPZ. The difference of the luminescent properties among the three salts could be attributed to different fluorescence mechanisms, such as aggregate quenching,⁸⁹ or greater competition from non-radiative relaxation processes in the case of PRM-PPZ.

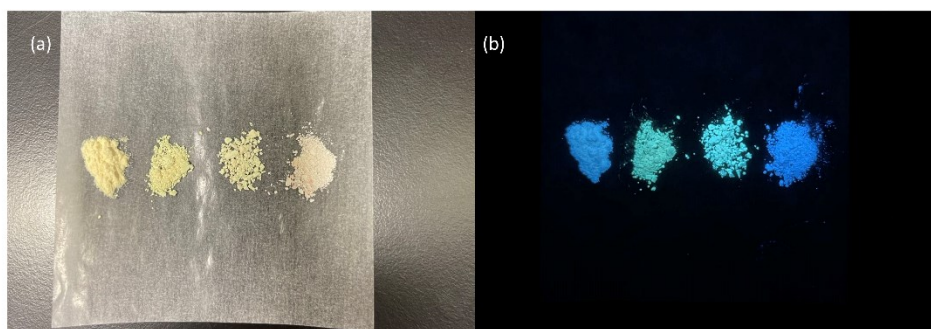


Figure 4.11. Photographs of PRM solids (from left to right: PRM, PRM-4AP, PRM-4DMP, and PRM-PPZ): (a) under white light illumination and (b) under a UV (365 nm) lamp.

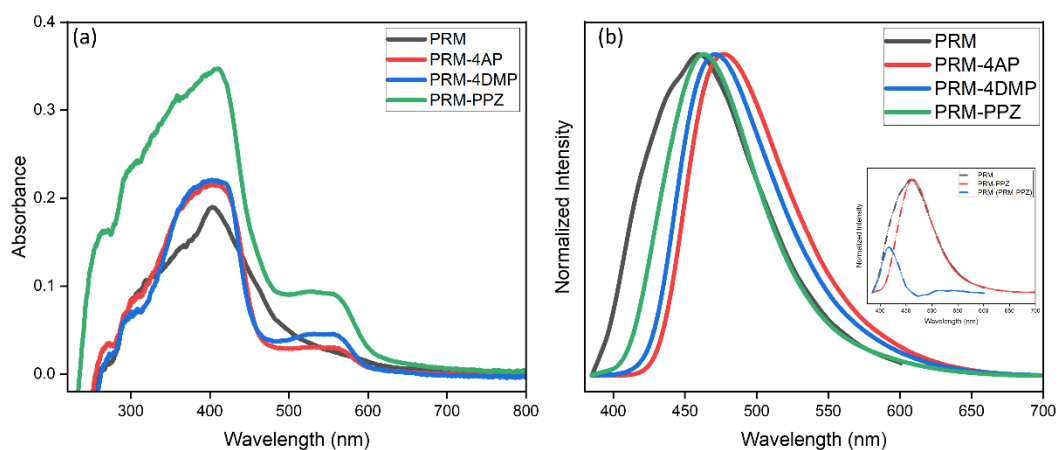


Figure 4.12. (a) Solid-state UV-vis absorption spectra and (b) normalized fluorescence spectra (excited at 365 nm) of PRM, PRM-4AP, PRM-4DMP, and PRM-PPZ. The blue line in the insert is the difference between the normalized fluorescence spectrum of PRM and that of PRM-PPZ, showing an apparent emission peak at about 417 nm in the PRM fluorescence.

Table 4.5. Comparison of maximum fluorescence emission wavelengths, fluorescence quantum yields, and contributions of π - π and hydrogen bonding of PRM, PRM-4AP, PRM-4DMP, and PRM-PPZ.

	λ_{em}^{max} (nm)	ΦF^a	π - π^b	hydrogen bonding ^b
PRM	460	0.614	6.2%	33.8%
PRM-4AP	477	0.685	5.1%	33.9%
PRM-4DMP	471	0.660	2.2%	33.7%
PRM-PPZ	463	0.408	2.3%	32.7%

^a Fluorescence quantum yields excited at 365 nm. ^b Refers to the contribution of π - π interactions and hydrogen bonding in the crystal structures. Values are obtained from Hirshfeld surfaces calculations (Table S4.4).

From the structural perspective, PRM demonstrates different conformations and intramolecular interactions before and after forming salts (Figure 4.1). In pure PRM, the hydrogen atom from the hydroxyl group forms an intramolecular hydrogen bond with the oxygen atom from the carbonyl group. In the deprotonated PRM, there is an intramolecular hydrogen bond between the hydrogen atom from secondary amine and the oxygen ion. Based on the excited-state intramolecular proton transfer (ESIPT) theory and internal charge transfer theory,^{64, 90, 91} we suggest that the fluorescence mechanism for PRM salts could be proton-transfer-induced enhanced luminescence with a moderate Stokes shift. Support for an ESIPT mechanism is seen in the apparent short wavelength emission peak in PRM that occurs on top of the longer wavelength emission, seen in PRM and its salts (Figure 4.12). Here the short wavelength peak in PRM would match an enol tautomer, while the longer wavelength emission in PRM and its salts would correspond to the lower-energy keto state. After proton transfer, the new

conformation and new intramolecular interactions lead to the red-shifted spectra of PRM-4AP and PRM-4DMP, as well as the higher quantum yields compared with pure PRM. In addition, the maximum emission wavelength of PRM-4DMP is slightly blue-shifted in comparison with that of PRM-4AP, which could be attributed to the relatively weaker π - π interactions.^{62, 92} The stronger intermolecular interactions suppress vibrational relaxation to enhance the quantum yields;⁹³ consequently, PRM-4AP presents a higher quantum yield compared with that of PRM-4DMP. However, the difference in the emission wavelength maxima between PRM and PRM-PPZ is not as significant as the difference between PRM and PRM-4AP or PRM-4DMP, which suggests the fluorescence performance of PRM-PPZ could also be affected by other factors, such as the electron distribution in the ground and excited states.

FMOs have been used to explain the reactivity in chemical systems and to predict the most reactive position in conjugated systems.⁹⁴⁻⁹⁶ A comparison of the FMOs has been undertaken to see if it provides an explanation for the luminescent properties of PRM and these three salts. As shown in Figure 13, the highest occupied molecular orbital (HOMO) of PRM is located over the skeleton of the PRM molecule, except for the phenyl ring. In contrast, it is the pyridyl ring that is not involved in the lowest unoccupied molecular orbital (LUMO). For PRM-4AP and PRM-4DMP, the HOMOs are mainly restricted in the middle of PRM, especially around two oxygen atoms and the chemical bonds in between, suggesting that these are the most reactive positions. The LUMOs are associated with the cations 4APH⁺ and 4DMPH⁺, respectively. Therefore, the deprotonation of PRM plays an important role in the structural, electronic and luminescent changes of the PRM-4AP and PRM-4DMP systems, which also supports our

proposal that the mechanism for the luminescent performance of PRM-4AP and PRM-4DMP is credited to the proton transfer of PRM. In addition, the larger energy gap of PRM-4DMP also contributes to the blue-shifted spectrum in comparison to PRM-4AP.⁹⁷

However, in the PRM-PPZ salt, although PRM is deprotonated and presents similar conformation compared to the previous two salts, the distribution of the HOMO and LUMO varies significantly. Both are mainly located around the methyl group, the benzothiazine moiety of PRM and the PPZH₂²⁺ dication, suggesting that the proton transfer sites are not the most reactive positions in this conjugated system. Therefore, the observed luminescence is likely reduced by some factors, such as crystal packing and molecular arrangement, that are known to quench fluorescence in the solid state.

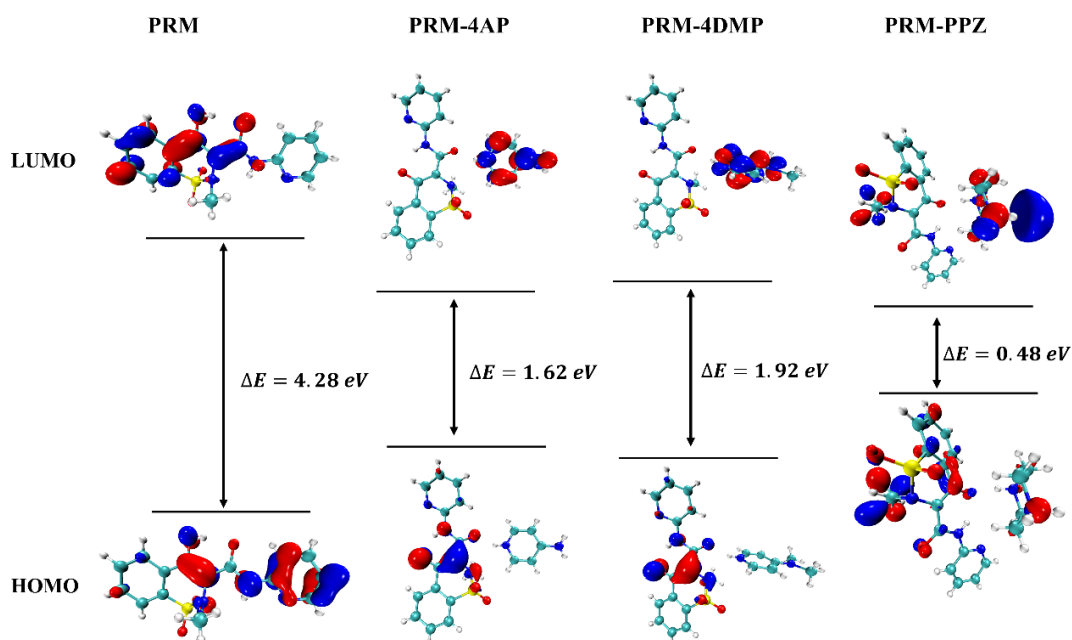


Figure 4.13. Molecular orbital plots of the HOMOs and LUMOs of PRM, PRM-4AP, PRM-4DMP, and PRM-PPZ.

MEL can exhibit fluorescence in the solution state;⁹⁸ however, it is weakly fluorescent ($\Phi_F = 0.14$, Figure S4.16) in the crystal state, possibly indicative of fluorescence quenching caused by aggregation (ACQ).⁶⁴ The MEL-4AP, MEL-4DMP, and MEL-PPZ salts present almost no fluorescence ($\Phi_F = 0.008$, 0.044 and 0.016, respectively), again indicating quenching due to aggregation.

4.5 Conclusions

In summary, six new pharmaceutical salts of PRM and MEL with three organic counterions (4AP, 4DMP, and PPZ) were successfully synthesized and characterized by various solid-state analytical techniques, including SCXRD, PXRD, DSC, TGA, and IR. In the solubility tests, the apparent solubility of all six salts was enhanced relative to that of the parent molecule (PRM / MEL) and the dissolution rate of all of six salts was also improved significantly. The salts exhibit similar solid-state luminescent properties to PRM and MEL. The proton-transfer-induced enhanced luminescence with a large red shift could be used to explain the luminescence mechanism of PRM-4AP and PRM-4DMP. For PRM-PPZ, the mechanism could be the combination of the proton transfer process together with some quenching process. Hirshfeld surface analysis and HOMO–LUMO analysis were also employed to further investigate the different luminescent behaviours of PRM solids. Overall, this study revealed that salt formation by using organic counterions is an effective approach to improve the solubility behaviour of poorly water-soluble APIs. Furthermore, the luminescent properties of organic fluorophores can be altered and modified by forming salts involved proton transfer. In this example, exposure of samples under UV illumination provides a convenient and useful tool to examine the synthesis of new crystalline materials.

REFERENCES

- (1) Kwok, P. C. L.; Chan, H. K., Nanotechnology Versus other Techniques in Improving Drug Dissolution. *Curr. Pharm. Des.* **2014**, 20, (3), 474–482.
- (2) Kalepu, S.; Manthina, M.; Padavala, V., Oral lipid-based drug delivery systems – an overview. *Acta Pharmaceutica Sinica B.* **2013**, 3, (6), 361–372.
- (3) Loh, G. O. K.; Tan, Y. T. F.; Peh, K. K., Enhancement of norfloxacin solubility via inclusion complexation with β -cyclodextrin and its derivative hydroxypropyl- β -cyclodextrin. *Asian J. Pharm. Sci.* **2016**, 11, (4), 536–546.
- (4) Oliveira, C. H. d. M.; Melo, C. C. d.; Doriguetto, A. C., Sulfamethoxazole salts: crystal structures, conformations and solubility. *New J. Chem.* **2019**, 43, (26), 10250–10258.
- (5) Fu, Q.; Lu, H. D.; Xie, Y. F.; Liu, J. Y.; Han, Y.; Gong, N. B.; Guo, F., Salt formation of two BCS II drugs (indomethacin and naproxen) with (1*R*, 2*R*)-1,2-diphenylethylenediamine: Crystal structures, solubility and thermodynamics analysis. *J. Mol. Struct.* **2019**, 1185, 281–289.
- (6) Bolla, G.; Sarma, B.; Nangia, A. K., Crystal Engineering of Pharmaceutical Cocrystals in the Discovery and Development of Improved Drugs. *Chem. Rev.* **2022**, 122, (13), 11514–11603.
- (7) Rajput, L., Stable Crystalline Salts of Haloperidol: A Highly Water-Soluble Mesylate Salt. *Cryst. Growth Des.* **2014**, 14, (10), 5196–5205.
- (8) Goud, N. R.; Suresh, K.; Nangia, A., Solubility and Stability Advantage of Aceclofenac Salts. *Cryst. Growth Des.* **2013**, 13, (4), 1590–1601.
- (9) Mannava, M. K. C.; Dandela, R.; Tothadi, S.; Solomon, K. A.; Nangia, A. K., Naftopidil Molecular Salts with Improved Dissolution and Permeation.

- Cryst. Growth Des.* **2020**, 20, (5), 3064–3076.
- (10) Domingos, S.; André, V.; Quaresma, S.; Martins, I. C. B.; Piedade, M. F. M. d.; Duarte, M. T., New forms of old drugs: improving without changing. *J. Pharm. Pharmacol.* **2015**, 67, (6), 830–846.
- (11) Duggirala, N. K.; Perry, M. L.; Almarsson, Ö.; Zaworotko, M. J., Pharmaceutical cocrystals: along the path to improved medicines. *Chem. Commun.* **2016**, 52, 640–655.
- (12) Gupta, D.; Bhatia, D.; Dave, V.; Sutariya, V.; Varghese Gupta, S., Salts of Therapeutic Agents: Chemical, Physicochemical, and Biological Considerations. *Molecules.* **2018**, 23, (7), 1719.
- (13) Tantardini, C.; Arkhipov, S. G.; Cherkashina, K. A.; Kil'met'ev, A. S.; Boldyreva, E. V., Crystal structure of a 2:1 co-crystal of meloxicam with acetylendicarboxylic acid. *Acta Cryst.* **2016**, E72, 1856–1859.
- (14) Cruz-Cabeza, A. J., Acid–base crystalline complexes and the pKa rule. *CrystEngComm.* **2012**, 14, (20), 6362–6365.
- (15) Almarsson, O.; Zaworotko, M. J., Crystal engineering of the composition of pharmaceutical phases. Do pharmaceutical co-crystals represent a new path to improved medicines? *Chem Commun.* **2004**, 7, (17), 1889–1896.
- (16) Byrn, S. R.; Zograf, G.; Chen, X. S., Solid-State Properties of Pharmaceutical Materials, **2017**; pp 48–59.
- (17) Surov, A. O.; Vasilev, N. A.; Vener, M. V.; Parashchuk, O. D.; Churakov, A. V.; Magdysyuk, O. V.; Perlovich, G. L., Pharmaceutical Salts of Fenbendazole with Organic Counterions: Structural Analysis and Solubility Performance. *Cryst. Growth Des.* **2021**. 21, (8), 4516–4530.

- (18) Thakral, N. K.; Kelly, R. C., Salt disproportionation: A material science perspective. *Int. J. Pharm.* **2017**, 520, (1-2), 228–240.
- (19) Weyna, D. R.; Cheney, M. L.; Shan, N.; Hanna, M.; Zaworotko, M. J.; Sava, V.; Song, S.; Sanchez-Ramos, J. R., Improving solubility and pharmacokinetics of meloxicam via multiple-component crystal formation. *Mol. Pharm.* **2012**, 9, (7), 2094–2102.
- (20) Childs, S. L.; Hardcastle, K. I., Cocrystals of Piroxicam with Carboxylic Acids. *Cryst. Growth Des.* **2007**, 7, (7), 1291–1304.
- (21) Gwak, H. S.; Choi, J. S.; Choi, H. K., Enhanced bioavailability of piroxicam via salt formation with ethanolamines. *Int. J. Pharm.* **2005**, 297, (1-2), 156–161.
- (22) Suzuki, H.; Yakushiji, K.; Matsunaga, S.; Yamauchi, Y.; Seto, Y.; Sato, H.; Onoue, S., Amorphous Solid Dispersion of Meloxicam Enhanced Oral Absorption in Rats With Impaired Gastric Motility. *J. Pharm. Sci.* **2018**, 107, (1), 446–452.
- (23) Yao, C.; Guzei, I. A.; Jin, Y.; Ruan, S.; Sun, G.; Gui, Y.; Wang, L.; Yu, L., Polymorphism of Piroxicam: New Polymorphs by Melt Crystallization and Crystal Structure Prediction. *Cryst. Growth Des.* **2020**, 20, (12), 7874–7881.
- (24) Thomas, L. H.; Wales, C.; Wilson, C. C., Selective preparation of elusive and alternative single component polymorphic solid forms through multi-component crystallisation routes. *Chem. Commun.* **2016**, 52, (46), 7372–7375.
- (25) Jacón Freitas, J. T.; Santos Viana, O. M. M.; Bonfilio, R.; Doriguetto, A. C.; de Araujo, M. B., Analysis of polymorphic contamination in meloxicam raw

- materials and its effects on the physicochemical quality of drug product. *Eur. J. Pharm. Sci.* **2017**, 109, 347–358.
- (26) Coppi, L.; Sanmarti, M. B.; Clavo, M. C. Crystalline forms of meloxicam and processes for their preparation and interconversion. U.S. Patent 6,967,248 B2,2005, Nov 22.
- (27) Luger, P.; Daneck, K.; Engel, W.; Trummelitz, G.; Wagner, K., Structure and physicochemical properties of meloxicam, a new NSAID. *Eur. J. Pharm. Sci.* **1996**, 4, (3), 175–187.
- (28) Wales, C.; Thomas, L. H.; Wilson, C. C., Tautomerisation and polymorphism in molecular complexes of piroxicam with mono-substituted benzoic acids. *CrystEngComm.* **2012**, 14, (21), 7264–7274.
- (29) Thomas, L. H.; Klapwijk, A. R.; Wales, C.; Wilson, C. C., Intermolecular hydrogen transfer and solubility tuning in multi-component molecular crystals of the API piroxicam. *CrystEngComm.* **2014**, 16, (26), 5924–5932.
- (30) Cheney, M. L.; Weyna, D. R.; Shan, N.; Hanna, M.; Wojtas, L.; Zaworotko, M. J., Supramolecular Architectures of Meloxicam Carboxylic Acid Cocrystals, a Crystal Engineering Case Study. *Cryst. Growth Des.* **2010**, 10, (10), 4401–4413.
- (31) Suresh, K.; Nangia, A., Lornoxicam Salts: Crystal Structures, Conformations, and Solubility. *Cryst. Growth Des.* **2014**, 14, 2945–2953.
- (32) Bolla, G.; Sanphui, P.; Nangia, A., Solubility Advantage of Tenoxicam Phenolic Cocrystals Compared to Salts. *Cryst. Growth Des.* **2013**, 13, (5), 1988–2003.
- (33) Hong, S.-C.; Yu, C.-H.; Cho, D.-H.; Shin, H.-J.; Gil, Y.-S., Improvement of Solubility and Bioavailability of Poorly Water Soluble Piroxicam with L-

Arginine Complex. *J. Kor. Pharm. Sci.* **2003**, 33, (2), 85–89.

- (34) Jiao, L.-t.; Yang, D.-z.; Zhang, L.; Yang, S.-y.; Du, G.-h.; Lu, Y., Salt solvates of quinolones and oxicams: Theoretical computation, structural characterization and dissolution studies. *J. Mol. Struct.* **2021**, 1223, 128865.
- (35) Solaimalai, R.; Shinde, G.; Dharamsi, A.; Kokare, C., Exploring the novel green eutectic solvent for the synthesis of 4-hydroxy-2-methyl-N-2-pyridinyl-2H-1,2,-benzothiazine-3-carboxamide 1,1-dioxide with benzoic acid cocrystal using a co-grinding technique. *New J. Chem.* **2020**, 44, 17088–17098.
- (36) Li, D.; Li, J.; Deng, Z.; Zhang, H., Piroxicam–clonixin drug–drug cocrystal solvates with enhanced hydration stability. *CrystEngComm.* **2019**, 21, (28), 4145–4149.
- (37) Modani, S.; Gunnam, A.; Yadav, B.; Nangia, A. K.; Shastri, N. R., Generation and Evaluation of Pharmacologically Relevant Drug–Drug Cocrystal for Gout Therapy. *Cryst. Growth Des.* **2020**, 20, 3577–3583.
- (38) Chen, H.; Wang, C.; Liu, S.; Sun, C. C., Development of piroxicam mini-tablets enabled by spherical cocrystallization. *Int. J. Pharm.* **2020**, 590, (30), 119953.
- (39) Acebedo-Martínez, F. J.; Alarcón-Payer, C.; Rodríguez-Domingo, L.; Domínguez-Martín, A.; Gómez-Morales, J.; Choquesillo-Lazarte, D., Furosemide/Non-Steroidal Anti-Inflammatory Drug–Drug Pharmaceutical Solids: Novel Opportunities in Drug Formulation. *Crystals.* **2021**, 11, (11), 1339.
- (40) Panzade, P.; Shendarkar, G.; Shaikh, S.; Balmukund Rathi, P., Pharmaceutical Cocrystal of Piroxicam: Design, Formulation and

Evaluation. *Adv. Pharm. Bull.* **2017**, 7, (3), 399–408.

- (41) Emami, S.; Adibkia, K.; Barzegar-Jalali, M.; Siahi-Shadbad, M., Piroxicam cocrystals with phenolic cofomers: preparation, characterization, and dissolution properties. *Pharm. Dev. Technol.* **2019**, 24, (2), 199–210.
- (42) Chatteraj, S.; Shi, L.; Chen, M.; Alhalaweh, A.; Velaga, S.; Sun, C. C., Origin of Deteriorated Crystal Plasticity and Compaction Properties of a 1:1 Cocrystal between Piroxicam and Saccharin. *Cryst. Growth Des.* **2014**, 14, (8), 3864–3874.
- (43) Elkholy, N. E.; Sultan, A. A.; Elosaily, G. H.; Maghraby, G. M. E., Acetone-assisted co-processing of meloxicam with amino acids for enhanced dissolution rate. *Pharm. Dev. Technol.* **2020**, 25, (7), 882–891.
- (44) Ochi, M.; Inoue, R.; Yamauchi, Y.; Yamada, S.; Onoue, S., Development of Meloxicam Salts with Improved Dissolution and Pharmacokinetic Behaviours in Rats with Impaired Gastric Motility. *Pharm. Res.* **2013**, 30, 377–386.
- (45) Haser, A.; Cao, T.; Lubach, J. W.; Zhang, F., In Situ Salt Formation during Melt Extrusion for Improved Chemical Stability and Dissolution Performance of a Meloxicam-Copovidone Amorphous Solid Dispersion. *Mol. Pharmaceutics.* **2018**, 15, 1226–1237.
- (46) Bartos, C.; Ambrus, R.; Kovács, A.; Gáspár, R.; Sztojkov-Ivanov, A.; Márki, Á.; Janáky, T.; Tömösi, F.; Kecskeméti, G.; Szabó-Révész, P., Investigation of Absorption Routes of Meloxicam and Its Salt Form from Intranasal Delivery Systems. *Molecules.* **2018**, 23, (4), 784.
- (47) Tumanov, N. A.; Myz, S. A.; Shakhtshneider, T. P.; Boldyreva, E. V., Are meloxicam dimers really the structure-forming units in the ‘meloxicam–

- carboxylic acid' co-crystals family? Relation between crystal structures and dissolution behaviour. *CrystEngComm*. **2012**, 14, 305–313.
- (48) Cheney, M. L.; Weyna, D. R.; Shan, N.; Hanna, M.; Wojtas, L.; Zaworotko, M. J., Coformer selection in pharmaceutical cocrystal development: a case study of a meloxicam aspirin cocrystal that exhibits enhanced solubility and pharmacokinetics. *J. Pharm. Sci.* **2011**, 100, (6), 2172–2181.
- (49) Tantardini, C.; Arkipov, S. G.; Cherkashina, K. A.; Kil'met'ev, A. S.; Boldyreva, E. V., Synthesis and crystal structure of a meloxicam co-crystal with benzoic acid. *Struct. Chem.* **2018**, 29, (6), 1867–1874.
- (50) Fernandes, R. P.; Nascimento, A. L. C. S. d.; Carvalho, A. C. S.; Teixeira, J. A.; Ionashiro, M.; Caires, F. J., Mechanochemical synthesis, characterization, and thermal behaviour of meloxicam cocrystals with salicylic acid, fumaric acid, and malic acid. *J. Therm. Anal. Calorim.* **2019**, 138, 765–777.
- (51) Machado, T. C.; Kuminek, G.; Cardoso, S. G.; Rodríguez-Hornedo, N., The role of pH and dose/solubility ratio on cocrystal dissolution, drug supersaturation and precipitation. *Eur. J. Pharm. Sci.* **2020**, 152, 105422.
- (52) Machado, T. C.; Gelain, A. B.; Rosa, J.; Cardoso, S. G.; Caon, T., Cocrystallization as a novel approach to enhance the transdermal administration of meloxicam. *Eur. J. Pharm. Sci.* **2018**, 123, 184–190.
- (53) Gadade, D. D.; Kulkarni, D. A.; Rathi, P. B.; Pekamwar, S. S.; Joshi, S. S., Solubility Enhancement of Lornoxicam by Crystal Engineering. *Indian J. Pharm. Sci.* **2017**, 79, (2), 277–286.
- (54) Fatima, K.; Bukhari, N. I.; Latif, S.; Afzal, H.; Hussain, A.; Shamim, R.; Abbas, N., Amelioration of physicochemical, pharmaceutical, and

- pharmacokinetic properties of lornoxicam by cocrystallization with a novel coformer. *Drug Dev. Ind. Pharm.* **2021**, 47, (3), 498–508.
- (55) Patel, J. R.; Carlton, R. A.; Needham, T. E.; Chichester, C. O.; Vogt, F. G., Preparation, structural analysis, and properties of tenoxicam cocrystals. *Int. J. Pharm.* **2012**, 436, (1-2), 685–706.
- (56) Liu, X.; Michalchuk, A. A. L.; Pulham, C. R.; Boldyreva, E. V., An acetonitrile-solvated cocrystal of piroxicam and succinic acid with co-existing zwitterionic and non-ionized piroxicam molecules. *Acta. Cryst.* **2019**, C75, 29–37.
- (57) Horstman, E. M.; Bertke, J. A.; Kim, E. H.; Gonzalez, L. C.; Zhang, G. G. Z.; Gong, Y.; Kenis, P. J. A., Crystallization and characterization of cocrystals of piroxicam and 2,5-dihydroxybenzoic acid. *CrystEngComm.* **2015**, 17, (28), 5299–5306.
- (58) D.R.Weyna; M.L.Cheney; N.Shan; M.Hanna, CCDC 927795. *Experimental Crystal Structure Determination.* **2013**.
- (59) Damiani, P. C.; Bearzotti, M.; Cabezo'n, M.; Olivieri, A. C., Spectrofluorometric determination of piroxicam. *J. Pharm. Biomed. Anal.* **1998**, 17, 233–236.
- (60) Yan, D.; Delori, A.; Lloyd, G. O.; Friscic, T.; Day, G. M.; Jones, W.; Lu, J.; Wei, M.; Evans, D. G.; Duan, X., A cocrystal strategy to tune the luminescent properties of stilbene-type organic solid-state materials. *Angew. Chem. Int. Ed.* **2011**, 50, (52), 12483–12486.
- (61) Anthony, S. P.; Varughese, S.; Draper, S. M., Switching and tuning organic solid-state luminescence via a supramolecular approach. *Chem. Commun.* **2009**, (48), 7500–7502.

- (62) Huang, S.; Xu, J.; Peng, Y. Y.; Guo, M. S.; Cai, T., Facile Tuning of the Photoluminescence and Dissolution Properties of Phloretin through Cocrystallization. *Cryst. Growth Des.* **2019**, *19*, (12), 6837–6844.
- (63) Lu, B.; Fang, X.; Yan, D., Luminescent Polymorphic Co-crystals: A Promising Way to the Diversity of Molecular Assembly, Fluorescence Polarization, and Optical Waveguide. *ACS Appl. Mater. Interfaces.* **2020**, *12*, (28), 31940–31951.
- (64) Gayathri, P.; Pannipara, M.; Al-Sehemi, A. G.; Anthony, S. P., Recent advances in excited state intramolecular proton transfer mechanism-based solid state fluorescent materials and stimuli-responsive fluorescence switching. *CrystEngComm.* **2021**, *23*, (21), 3771–3789.
- (65) Mei, J.; Leung, N. L.; Kwok, R. T.; Lam, J. W.; Tang, B. Z., Aggregation-Induced Emission: Together We Shine, United We Soar! *Chem. Rev.* **2015**, *115*, (21), 11718–11940.
- (66) Brittain, H. G.; Elder, B. J.; Isbester, P. K.; Salerno, A. H., Solid-State Fluorescence Studies of Some Polymorphs of Diflunisal. *Pharm. Res.* **2005**, *22*, 999–1006.
- (67) Luo, J.; Xie, Z.; Lam, J. W. Y.; Cheng, L.; Chen, H.; Qiu, C.; Kwok, H. S.; Zhan, X.; Liu, Y.; Zhuc, D.; Tang, B. Z., Aggregation-induced emission of 1-methyl-1,2,3,4,5-pentaphenylsilole. *Chem. Commun.* **2001**, 1740–1741.
- (68) Yu, Y.; Fan, Y.; Wang, C.; Wei, Y.; Liao, Q.; Li, Q.; Li, Z., Phenanthroimidazole derivatives with minor structural differences: crystalline polymorphisms, different molecular packing, and totally different mechanoluminescence. *J. Mater. Chem. C.* **2019**, *7*, 13759–13763.
- (69) Sinha, A. S.; Rao Khandavilli, U. B.; O'Connor, E. L.; Deadman, B. J.;

- Maguire, A. R.; Lawrence, S. E., Novel co-crystals of the nutraceutical sinapic acid. *CrystEngComm*. **2015**, 17, (26), 4832–4841.
- (70) Eccles, K. S.; Deasy, R. E.; Fábíán, L.; Braun, D. E.; Maguire, A. R.; Lawrence, S. E., Expanding the crystal landscape of isonicotinamide: concomitant polymorphism and co-crystallisation. *CrystEngComm*. **2011**, 13, (23), 6923–6925.
- (71) Sheldrick, G. M., Crystal structure refinement with SHELXL. *Acta Cryst.* **2015**, C71, 3–8.
- (72) Xu, J.; Huang, Y.; Ruan, S.; Chi, Z.; Qin, K.; Cai, B.; Cai, T., Cocrystals of isoliquiritigenin with enhanced pharmacokinetic performance. *CrystEngComm*. **2016**, 18, (45), 8776–8786.
- (73) Spackman, P. R.; Turner, M. J.; McKinnon, J. J.; Wolff, S. K.; Grimwood, D. J.; Jayatilaka, D.; Spackman, M. A., CrystalExplorer: a program for Hirshfeld surface analysis, visualization and quantitative analysis of molecular crystals. *J. Appl. Cryst.* **2021**, 54, 1006–1011.
- (74) Yang, D.; Wang, R.; Jin, G.; Zhang, B.; Zhang, L.; Lu, Y.; Du, G., Structural and Computational Insights into Cocrystal Interactions: A Case on Cocrystals of Antipyrine and Aminophenazone. *Cryst. Growth Des.* **2019**, 19, (11), 6175–6183.
- (75) Lu, T.; Chen, F., Quantitative analysis of molecular surface based on improved Marching Tetrahedra algorithm. *J. Mol. Graph. Model.* **2012**, 38, 314–323.
- (76) Lu, T.; Chen, F., Multiwfn: a multifunctional wavefunction analyzer. *J. Comput. Chem.* **2012**, 33, (5), 580–592.
- (77) Kostadinova, I.; Danchev, N., 4-aminopyridine – the new old drug for the

- treatment of neurodegenerative diseases. *Pharmacia*. **2019**, 66, (2), 67–74.
- (78) Chiriac, C. I.; Onciu, M.; Tanasa, F., Synthesis of aromatic amides at room temperature using triphenyl phosphite-4-dimethylaminopyridine as reagent. *Des. Monomers Polym.* **2012**, 7, (4), 331–335.
- (79) Suresh, K.; Nangia, A., Lornoxicam Salts: Crystal Structures, Conformations, and Solubility. *Cryst. Growth Des.* **2014**, 14, (6), 2945–2953.
- (80) Steiner, T., The Hydrogen Bond in the Solid State. *Angew. Chem. Int. Ed.* **2002**, 41, 48–76.
- (81) Yesselman, J. D.; Horowitz, S.; Brooks, C. L.; Trievel, R. C., Frequent Side Chain Methyl Carbon-Oxygen Hydrogen Bonding in Proteins Revealed by Computational and Stereochemical Analysis of Neutron Structures. *Proteins*. **2015**, 83, (3), 403–410.
- (82) Haser, A.; Huang, S.; Listro, T.; White, D.; Zhang, F., An approach for chemical stability during melt extrusion of a drug substance with a high melting point. *Int. J. Pharm.* **2017**, 524, (1-2), 55–64.
- (83) Jinno, J.; OH, D.-M.; Crison, J. R.; Amidon, G. L., Dissolution of Ionizable Water-Insoluble Drugs: The Combined Effect of pH and Surfactant. *J. Pharm. Sci.* **2000**, 89, (2), 268–274.
- (84) Bavishi, D. D.; Borkhataria, C. H., Spring and parachute: How cocrystals enhance solubility. *Prog. Cryst. Growth Charact. Mater.* **2016**, 62, (3), 1–8.
- (85) Xuan, B.; Wong, S. N.; Zhang, Y.; Weng, J.; Tong, H. H. Y.; Wang, C.; Sun, C. C.; Chow, S. F., Extended Release of Highly Water Soluble Isoniazid Attained through Cocrystallization with Curcumin. *Cryst. Growth Des.* **2020**, 20, (3), 1951–1960.
- (86) Guo, C.; Zhang, Q.; Zhu, B.; Zhang, Z.; Bao, J.; Ding, Q.; Ren, G.; Mei, X.,

Pharmaceutical Cocrystals of Nicorandil with Enhanced Chemical Stability and Sustained Release. *Cryst. Growth Des.* **2020**, 20, (10), 6995–7005.

- (87) Kilinkissa, O. E. Y.; Govender, K. K.; Báthori, N. B., Melting point–solubility–structure correlations in chiral and racemic model cocrystals. *CrystEngComm* **2020**, 22, (16), 2766–2771.
- (88) Luo, Y.-H.; Sun, B.-W., Pharmaceutical Co-Crystals of Pyrazinecarboxamide (PZA) with Various Carboxylic Acids: Crystallography, Hirshfeld Surfaces, and Dissolution Study. *Cryst. Growth Des.* **2013**, 13, (5), 2098–2106.
- (89) Huang, Y.; Xing, J.; Gong, Q.; Chen, L. C.; Liu, G.; Yao, C.; Wang, Z.; Zhang, H. L.; Chen, Z.; Zhang, Q., Reducing aggregation caused quenching effect through co-assembly of PAH chromophores and molecular barriers. *Nat. Commun.* **2019**, 10, (1), 169.
- (90) Sakai, K.-i.; Tsuchiya, S.; Kikuchi, T.; Akutagawa, T., An ESIPT fluorophore with a switchable intramolecular hydrogen bond for applications in solid-state fluorochromism and white light generation. *J. Mater. Chem. C.* **2016**, 4, (10), 2011–2016.
- (91) Sedgwick, A. C.; Wu, L.; Han, H. H.; Bull, S. D.; He, X. P.; James, T. D.; Sessler, J. L.; Tang, B. Z.; Tian, H.; Yoon, J., Excited-state intramolecular proton-transfer (ESIPT) based fluorescence sensors and imaging agents. *Chem. Soc. Rev.* **2018**, 47, (23), 8842–8880.
- (92) Mizobe, Y.; Ito, H.; Hisaki, I.; Miyata, M.; Hasegawa, Y.; Tohnai, N., A novel strategy for fluorescence enhancement in the solid-state: affording rigidity to fluorophores packing. *Chem. Commun.* **2006**, (20), 2126–2128.
- (93) Xue, P.; Wang, P.; Chen, P.; Yao, B.; Gong, P.; Sun, J.; Zhang, Z.; Lu, R.,

- Bright persistent luminescence from pure organic molecules through a moderate intermolecular heavy atom effect. *Chem. Sci.* **2017**, 8, (9), 6060–6065.
- (94) Li, K.; Ren, X.; Fu, S.; Zhu, J., Cocrystal structure, thermal behaviour, and DFT calculations between FOX-7 and 1,10-Phenanthroline. *J. Mol. Struct.* **2018**, 1173, (5), 26–32.
- (95) Kumar, G. S. S.; Prabhu, A. A. M.; N.Bhuvanesh; X.A.V.Ronica; Kumaresan, S., Molecular structure investigation of organic cocrystals of 1,10-phenanthroline-5,6-dione with aryloxyacetic acid: A combined experimental and theoretical study. *Spectrochimica. Acta. Part A.* **2014**, 132, (11), 465–476.
- (96) Velmurugan, V.; Nandini Asha, R.; Ravindran Durai Nayagam, B.; Kumaresan, S.; Bhuvanesh, N., Synthesis, Characterization and Biological Activity of (Phenylthio)Acetic Acid:Theophylline Cocrystal. *J. Chem. Crystallogr.* **2020**, 51, (2), 225–234.
- (97) Silva, G. L.; Ediz, V.; Yaron, D.; Armitage, B. A., Experimental and computational investigation of unsymmetrical cyanine dyes: understanding torsionally responsive fluorogenic dyes. *J. Am. Chem. Soc.* **2007**, 129, (17), 5710–5718.
- (98) Hassan, E. M., Spectrophotometric and fluorimetric methods for the determination of meloxicam in dosage forms. *J. Pharm. Biomed.* **2002**, 27, 771–777.

Supporting Information

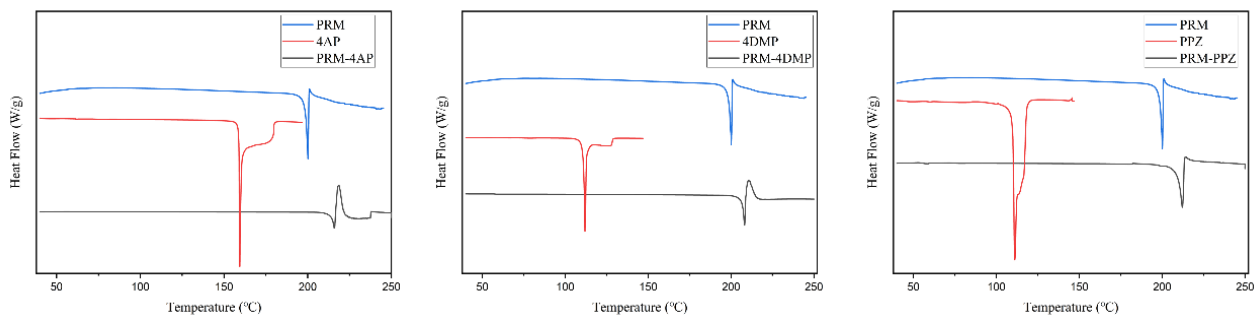


Figure S4.1. DSC traces of PRM (blue), salt formers (4AP, 4DMP and PPZ; red) and salts (PRM-4AP, PRM-4DMP and PRM-PPZ; black).

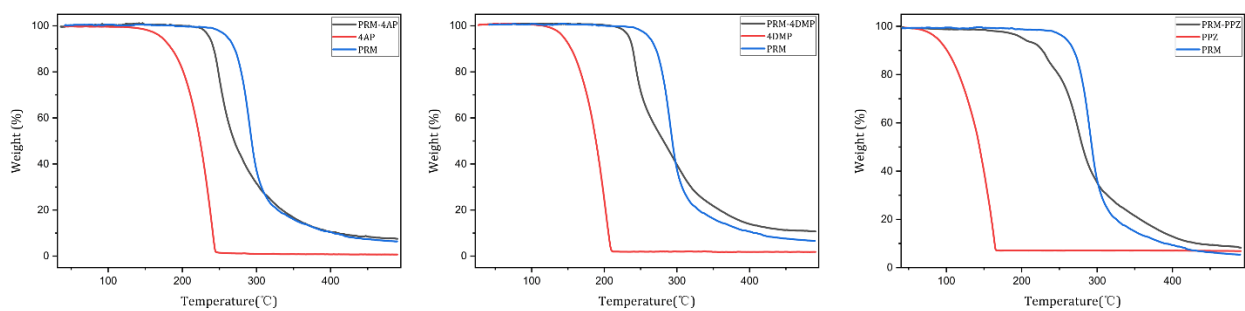
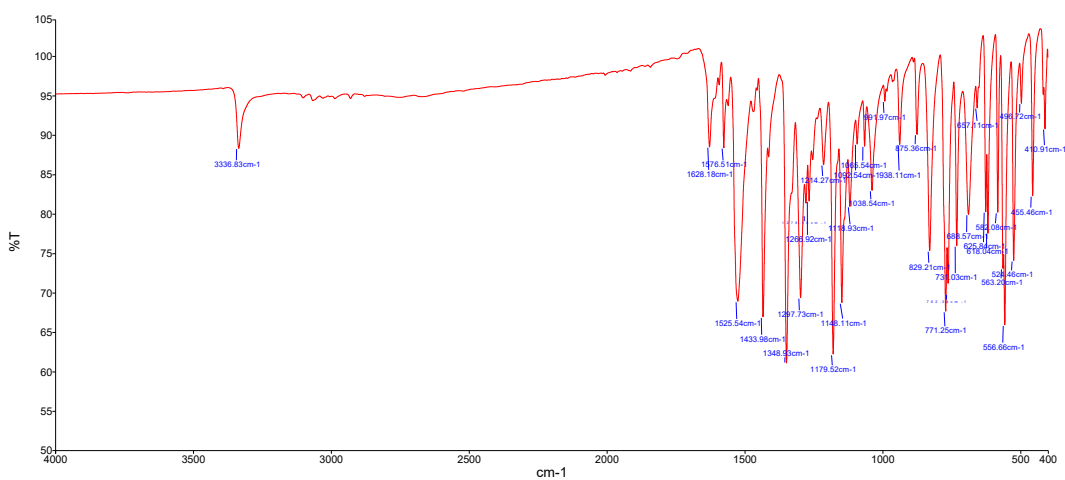
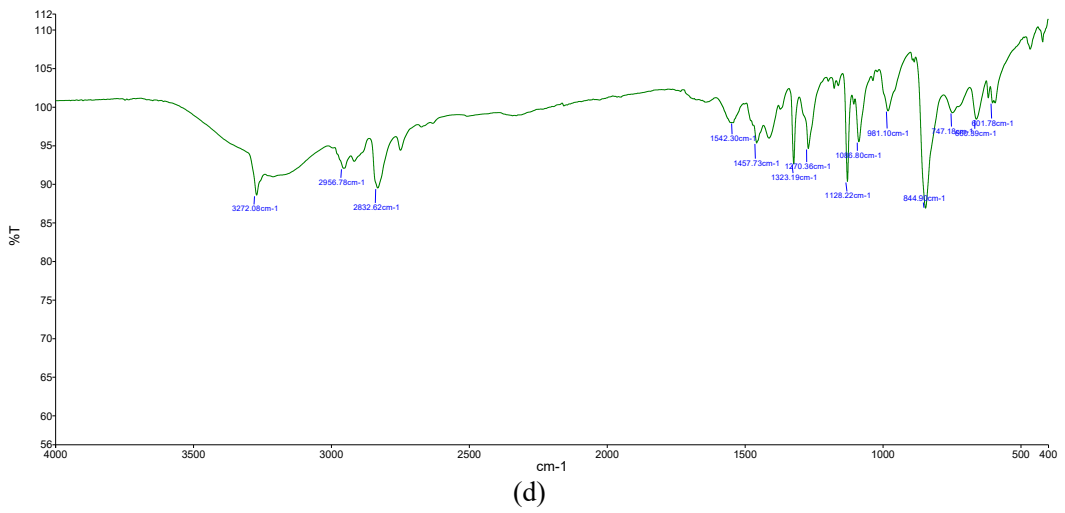
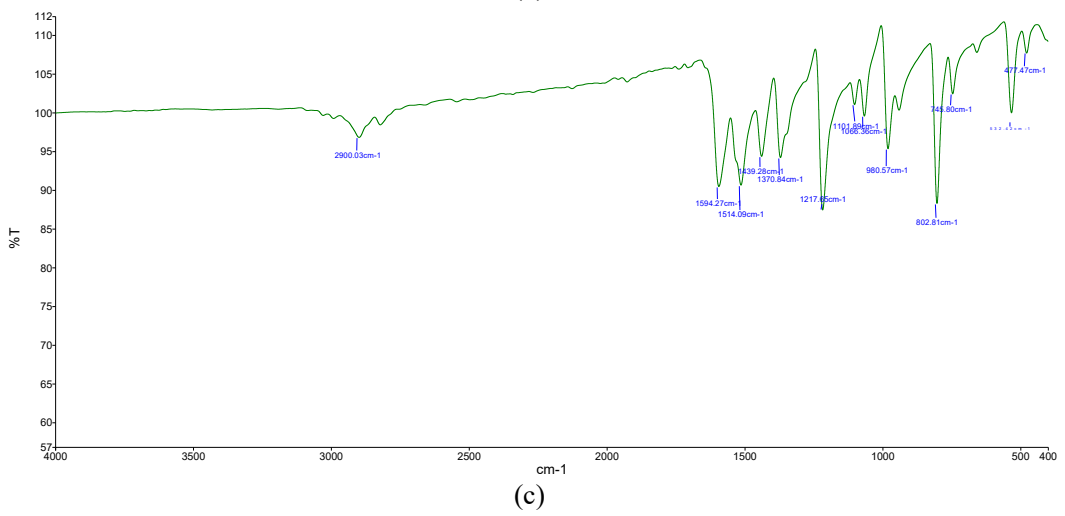
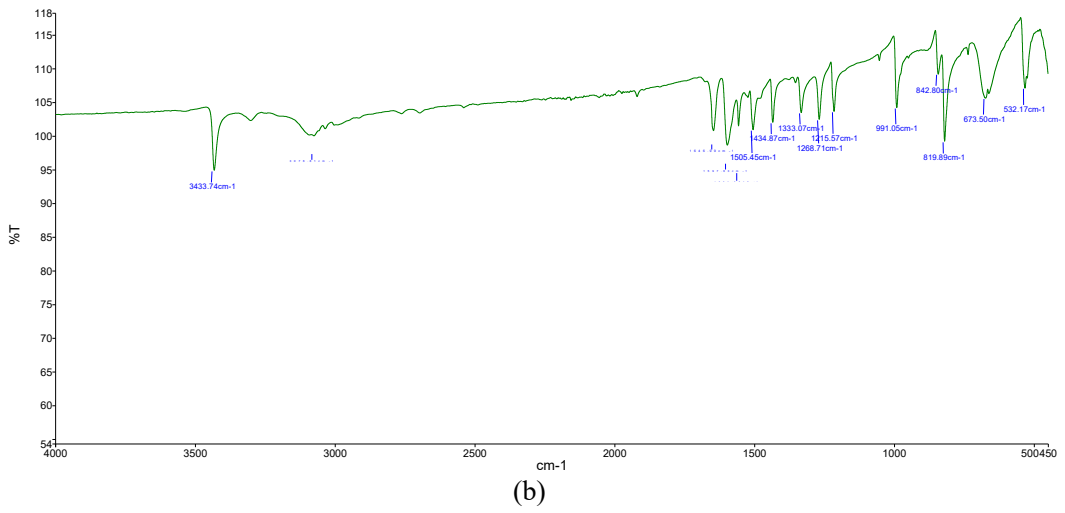


Figure S4.2. TGA traces of PRM (blue), salt formers (4AP, 4DMP and PPZ; red) and salts (PRM-4AP, PRM-4DMP and PRM-PPZ; black).



(a)



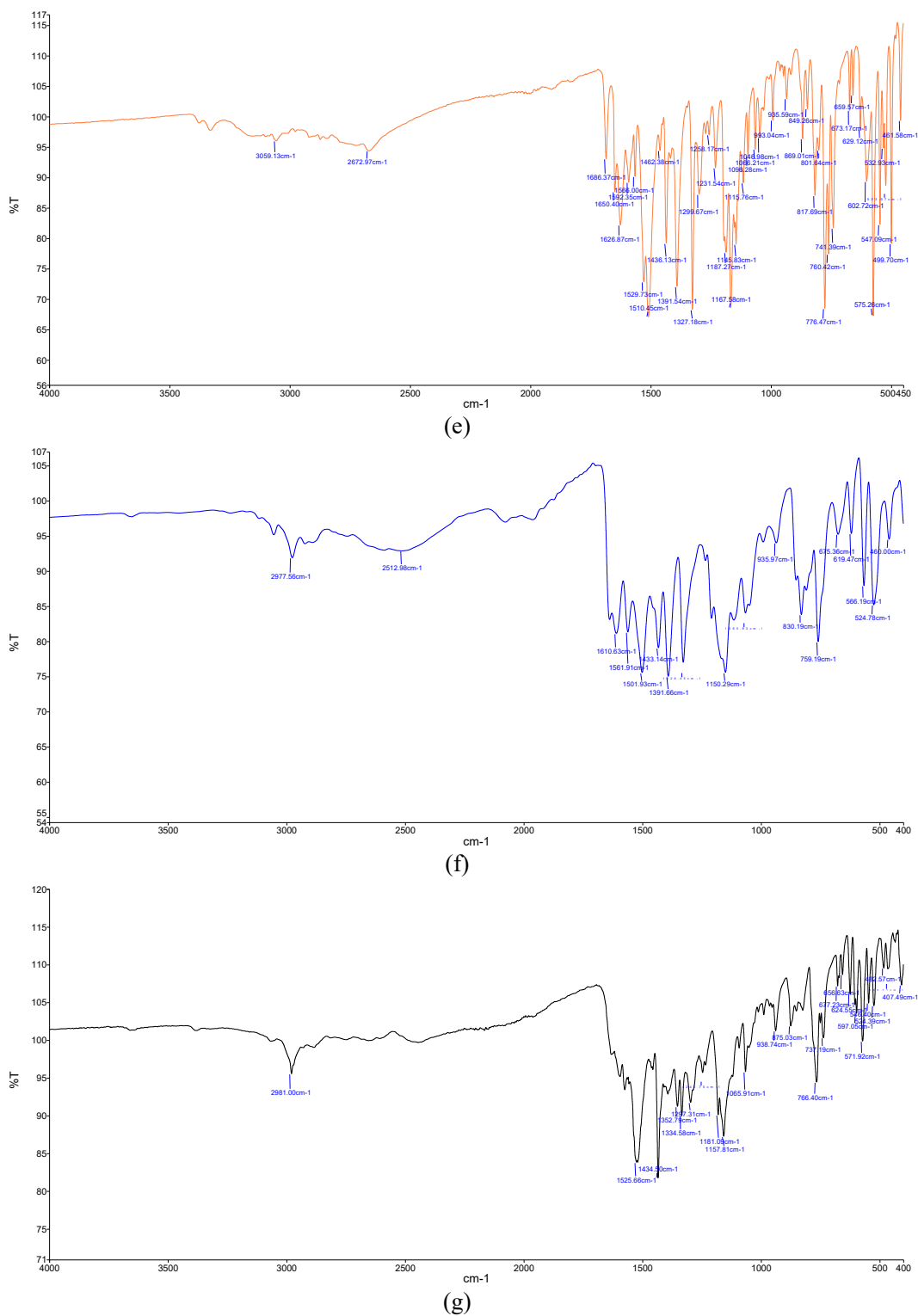
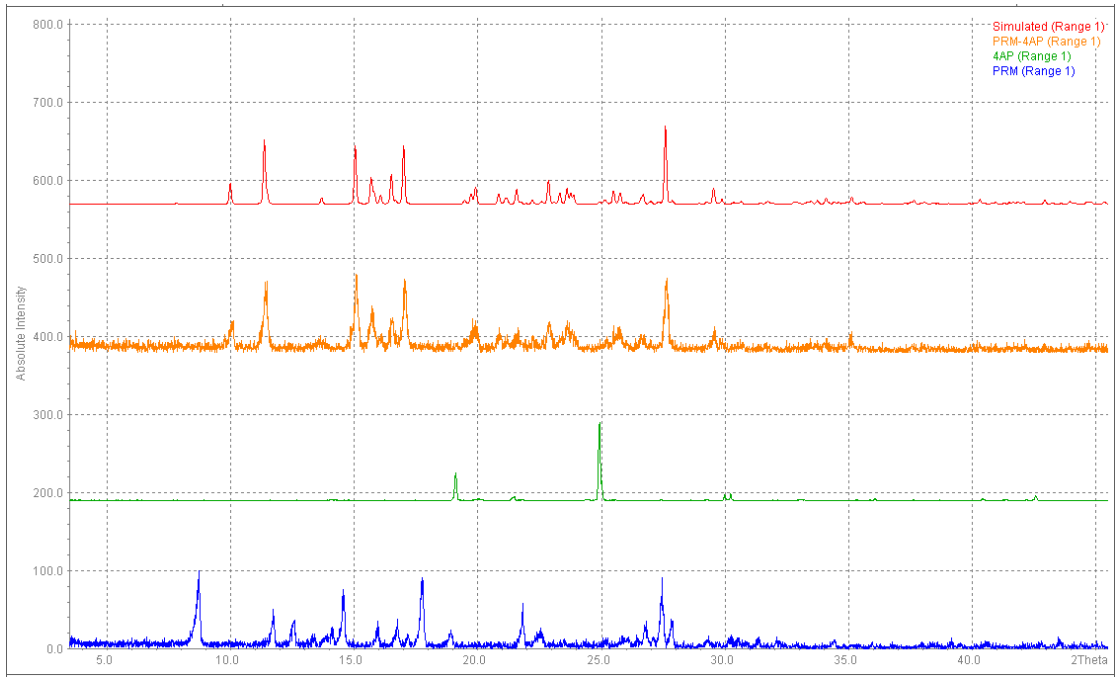
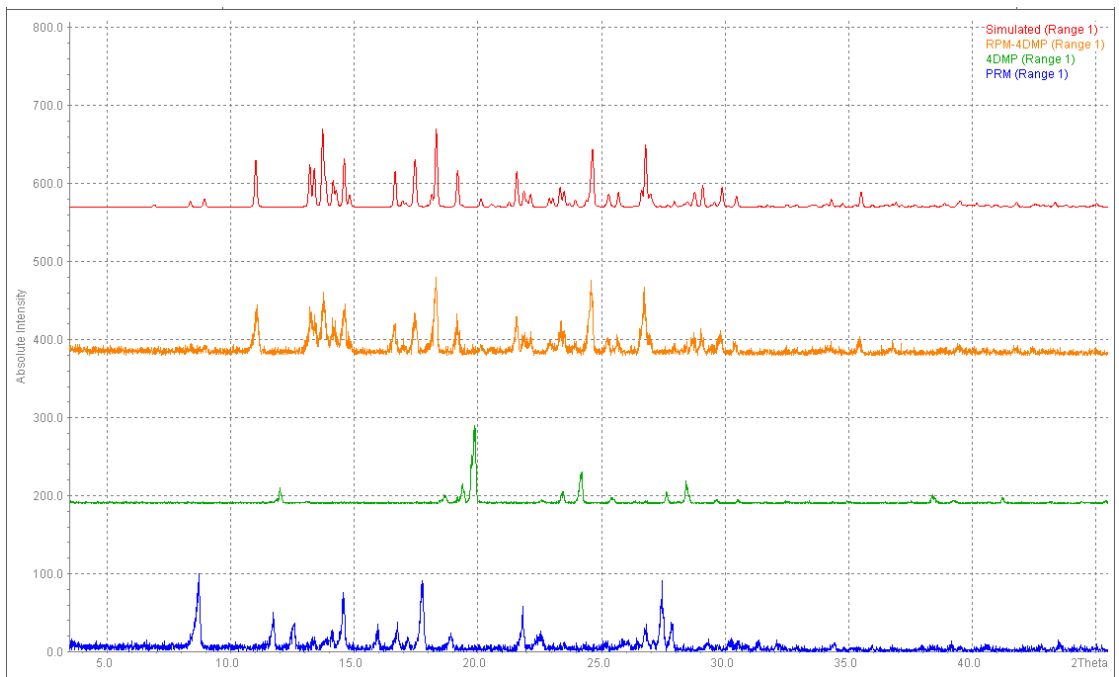


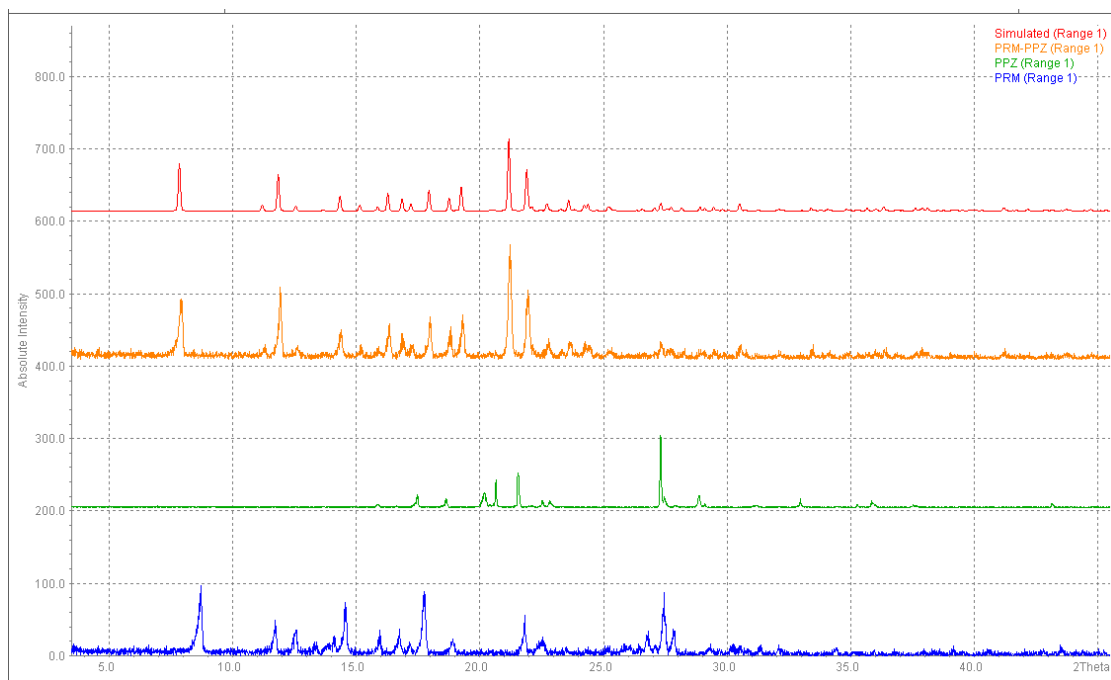
Figure S4.3. IR spectra of (a) PRM, (b) 4AP, (c) 4DMP, (d) PPZ, (e) PRM-4AP, (f) PRM-4DMP and (g) PRM-PPZ.



(a)

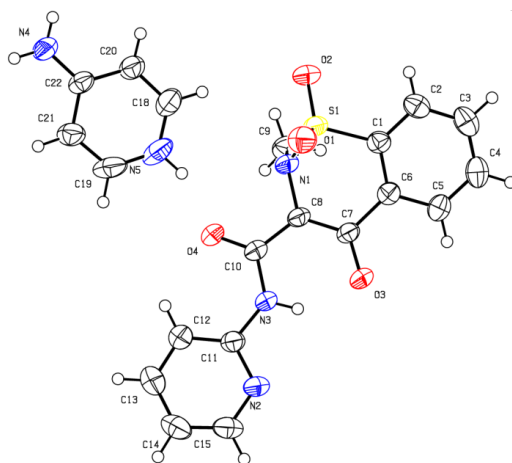


(b)



(c)

Figure S4.4. (a) PXR D patterns of PRM (blue), 4AP (green), PRM-4AP salt (orange) and simulated pattern from the crystal structure (red), (b) PXR D patterns of PRM (blue), 4DMP (green), PRM-4DMP salt (orange) and simulated pattern from the crystal structure (red) and (c) PXR D patterns of PRM (blue), PPZ (green), PRM-PPZ salt (orange) and simulated pattern from the crystal structure (red).



(a)

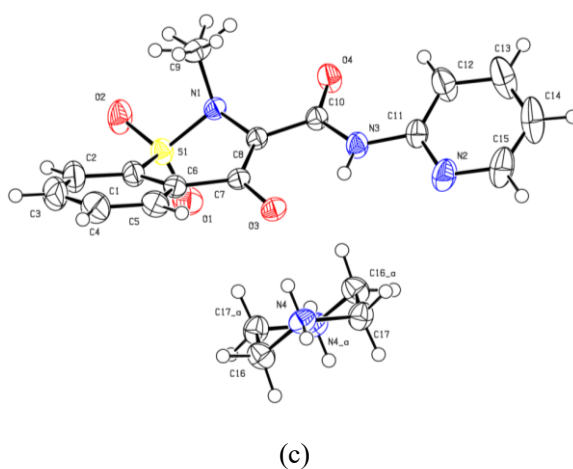
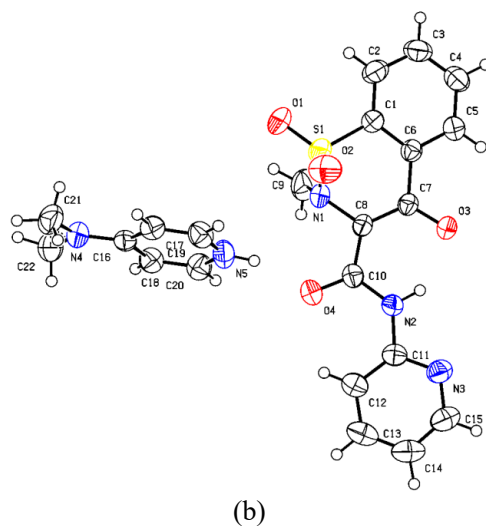


Figure S4.5. Ellipsoid plot of (a) PRM-4AP, (b) PRM-4DMP and (c) PRM-PPZ.

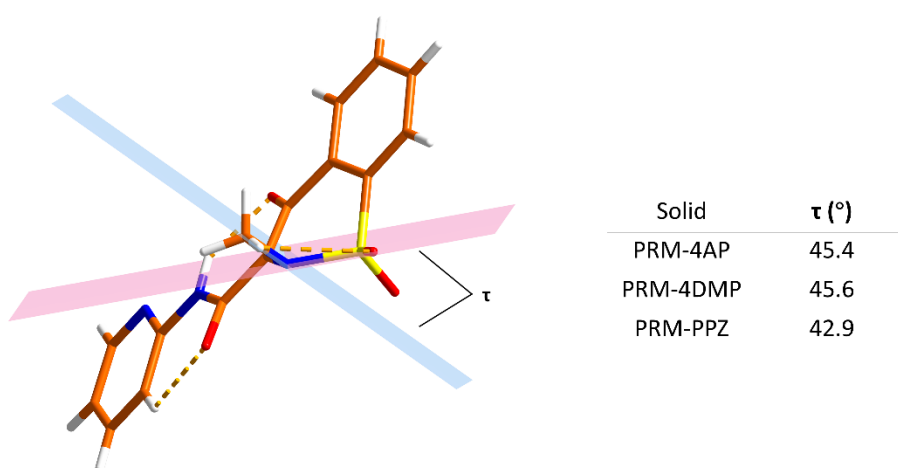


Figure S4.6. The angle (τ) formed between the methyl hydrogen and the plane of a sp^2 oxygen in PRM^- anion in PRM-4AP, PRM-4DMP and PRM-PPZ.

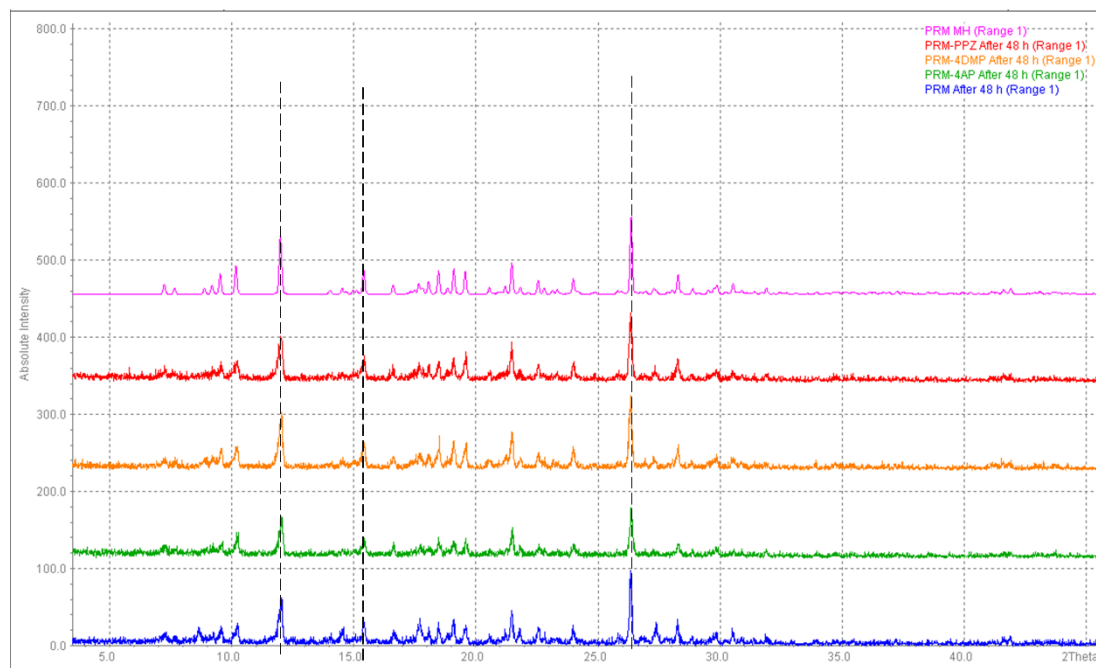


Figure S4.7. PXRD patterns of residual solids of PRM (blue), PRM-4AP (green), PRM-4DMP (orange), PRM-PPZ (red) after solubility experiments, and the simulated pattern from the crystal structure of PRM monohydrate (pink).

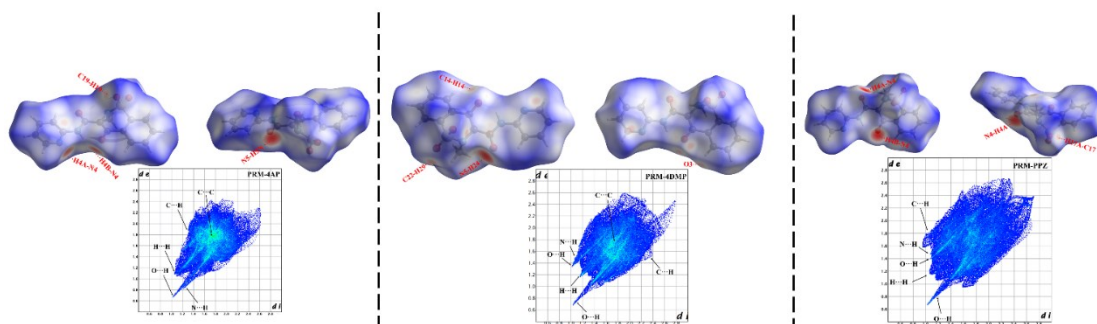


Figure S4.8. 3D d_{norm} surfaces and 2D fingerprint plots of PRM in PRM-4AP (left), PRM-4DMP (middle) and PRM-PPZ (right).

Table S4.1 Hydrogen bond and π - π interaction geometries (\AA , $^\circ$) in the PRM-4AP salt.

	Type	D-H \cdots A	D-H	H \cdots A	D \cdots A	D-H \cdots A	ARU (J)
1	Intra	N3-H3N \cdots O3	0.86	1.93	2.647	139	

2		N4-H4A...N2	0.86	2.18	2.991	157	1556.01
3		N4-H4B...O3	0.86	2.09	2.889	153	1556.01
4		N5-H5N...O4	0.86	1.83	2.653	159	1555.01
5	Intra	C9-H9B...O2	0.96	2.47	2.847	103	
6	Intra	C12-H12...O4	0.93	2.29	2.867	120	
7		C19-H19...O1	0.93	2.52	3.277	139	2666.01
Cg(I)	Cg(J)	Cg-Cg	Interplanar distance	Dihedral Angle	Beta	ARU (J)	
2	5	4.1818(19)	3.5149(9)	10.50(11)	22.3	2566.02	
5	2	4.1727(19)	3.0843(9)	10.50(11)	33	2666.02	
3	3	3.6422(16)	3.3605(7)	0.02(8)	22.7	2775.01	

^a Symmetry codes: [1556] = x, y, 1+z; [2566] = -x, 1-y, 1-z; [2666] = 1-x, 1-y, 1-z; [2775] = 2-x, 2-y, -z. Cg2 represents the centroid of N2, C11-C15; Cg3 represents the centroid of C1-C6; Cg5 represents the centroid of N5, C18-C22. Cg(I) = plane number I; Cg-Cg = distance between ring centroids (Ang.). Beta is the displacement angle between the ring normal of plane I and the centroid vector.

Table S4.2 Hydrogen bond and π - π interaction geometries (\AA , $^\circ$) in the PRM-4DMP salt.

	Type	D-H...A	D-H	H...A	D...A	D-H...A	ARU (J)
1	Intra	N2-H23...O3	0.875(9)	1.907(8)	2.6504(10)	141.8(8)	
2		N5-H24...O4	0.872(9)	1.853(9)	2.6881(11)	159.8(8)	[1555.01]
3		N5-H24...N1	0.872(9)	2.599(9)	3.1549(12)	122.6(7)	[1555.01]
4		C5-H5...O3	0.93	2.51	3.3852(12)	157	[7666.01]
5	Intra	C12-H12...O4	0.93	2.27	2.8577(12)	121	
6		C14-H14...O3	0.93	2.56	3.4297(13)	156	[6646.01]
7		C19-H19...O2	0.93	2.55	3.3241(12)	141	[2656.01]
8	Intra	C9-H25...O1	0.96	2.49	2.8560(14)	102	
9		C22-H29...O1	0.96	2.44	3.3961(14)	172	[7566.01]
Cg(I)	Cg(J)	Cg-Cg	Interplanar distance	Dihedral Angle	Beta	ARU (J)	

2	5	4.0738(9)	3.4027(4)	1.82(4)	34.9	[2656.02]
---	---	-----------	-----------	---------	------	-----------

^a Symmetry codes [7666.] = 3/2-x, 3/2-y, 1-z; [6646.] = 3/2-x, -1/2+y, 3/2-z; [2656.] = 1-x, y, 3/2-z; [7566.] = 1/2-x, 3/2-y, 1-z. Cg2 represents the centroid of N3, C11-C15 and Cg5 represents the centroid of N5, C16-C20. Cg(I) = plane number I; Cg-Cg = distance between ring centroids (Ang.). Beta is the displacement angle between the ring normal of plane I and the centroid vector.

Table S4.3 Hydrogen bond and π - π interaction geometries (\AA , $^\circ$) in the PRM-PPZ salt.

	Type	D-H...A	D-H	H...A	D...A	D-H...A	ARU (J)
1	Intra	N3-H3N...O3	0.86	1.91	2.6447	143	
2		N4-H4A...O4	0.89	1.81	2.6451	156	1545.01
3		N4-H4B...O3	0.89	1.82	2.6959	168	1555.01
4	Intra	C9-H9A...O2	0.96	2.45	2.871	106	
6	Intra	C12-H12...O4	0.93	2.32	2.892	119	
7		C17-H17A...O1	0.97	2.59	3.481	153	3556.01

^a Symmetry codes: [1545.] = x, -1+y, z; [3556.] = -x, -y, 1-z.

Table S4.4 Summary of the various contact contributions to the PRM Hirshfeld surface area in pure PRM and its salts.

	O-H	H-H	C-H	C-O	C-C	N-H	O-N	N-C	N-N	H-S	O-O
PRM	27.4	37.3	14.9	4.4	6.2	6.4	0.8	0.1	1.1	0	1.4
PRM-4AP	28.1	42.2	15.5	1.2	5.1	5.8	0.2	1.7	0.1	0	0
PRM-4DMP	26.7	43.9	18	1.1	2.2	7	0.2	0.5	0.2	0	0.2
PRM-PPZ	24.3	39.2	21.1	2.8	2.3	8.4	0.2	0	0	0.1	1.5

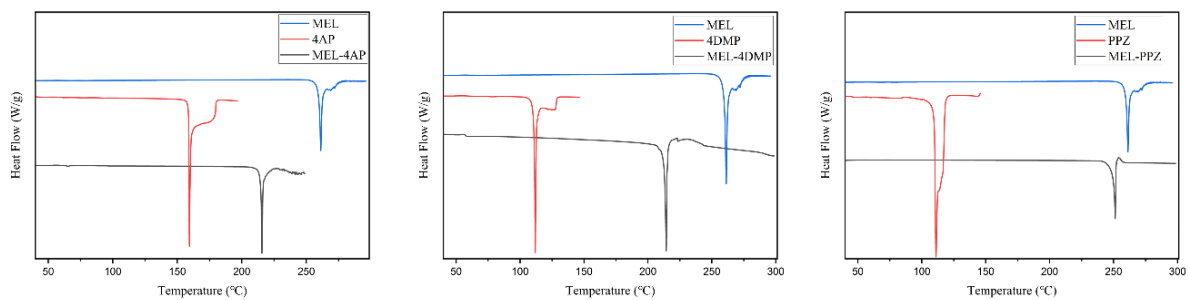


Figure S4.9. DSC traces of MEL (blue), salt formers (4AP, 4DMP and PPZ; red) and salts (MEL-4AP, MEL-4DMP and MEL-PPZ; black).

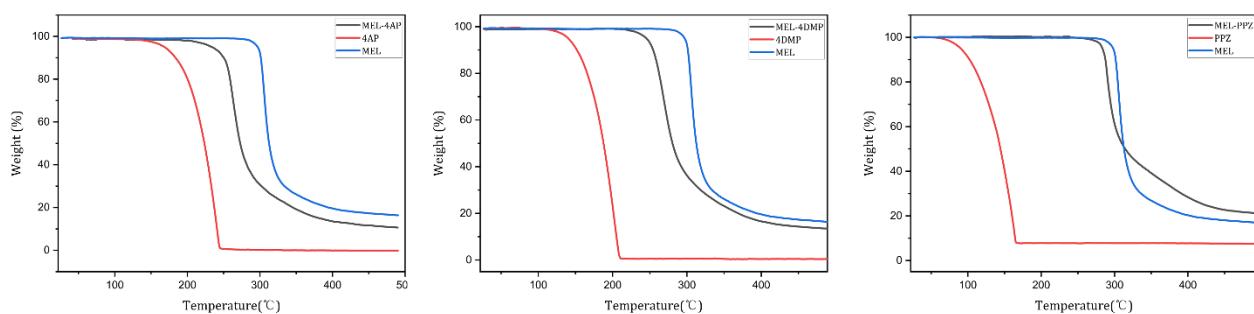
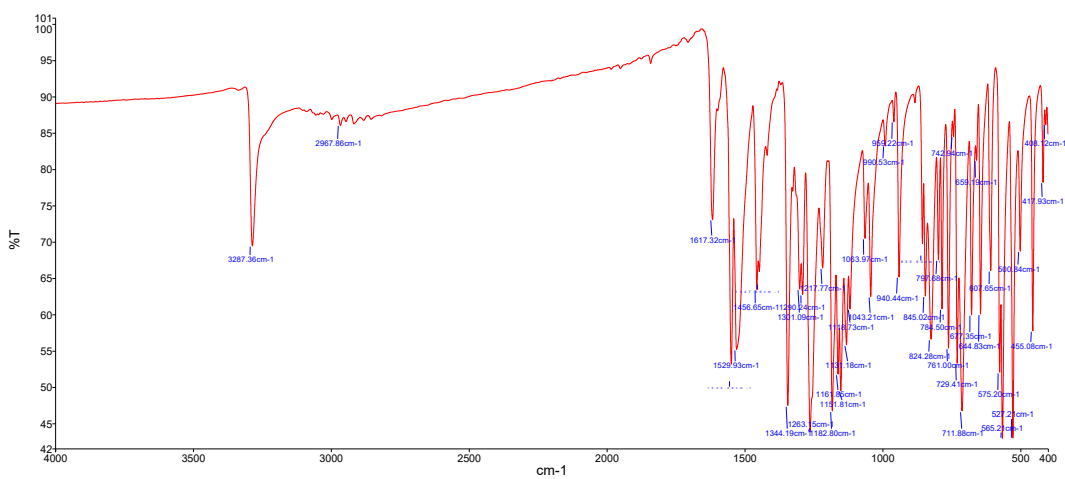


Figure S4.10. TGA traces of MEL (blue), salt formers (4AP, 4DMP and PPZ; red) and salts (MEL-4AP, MEL-4DMP and MEL-PPZ; black).



(a)

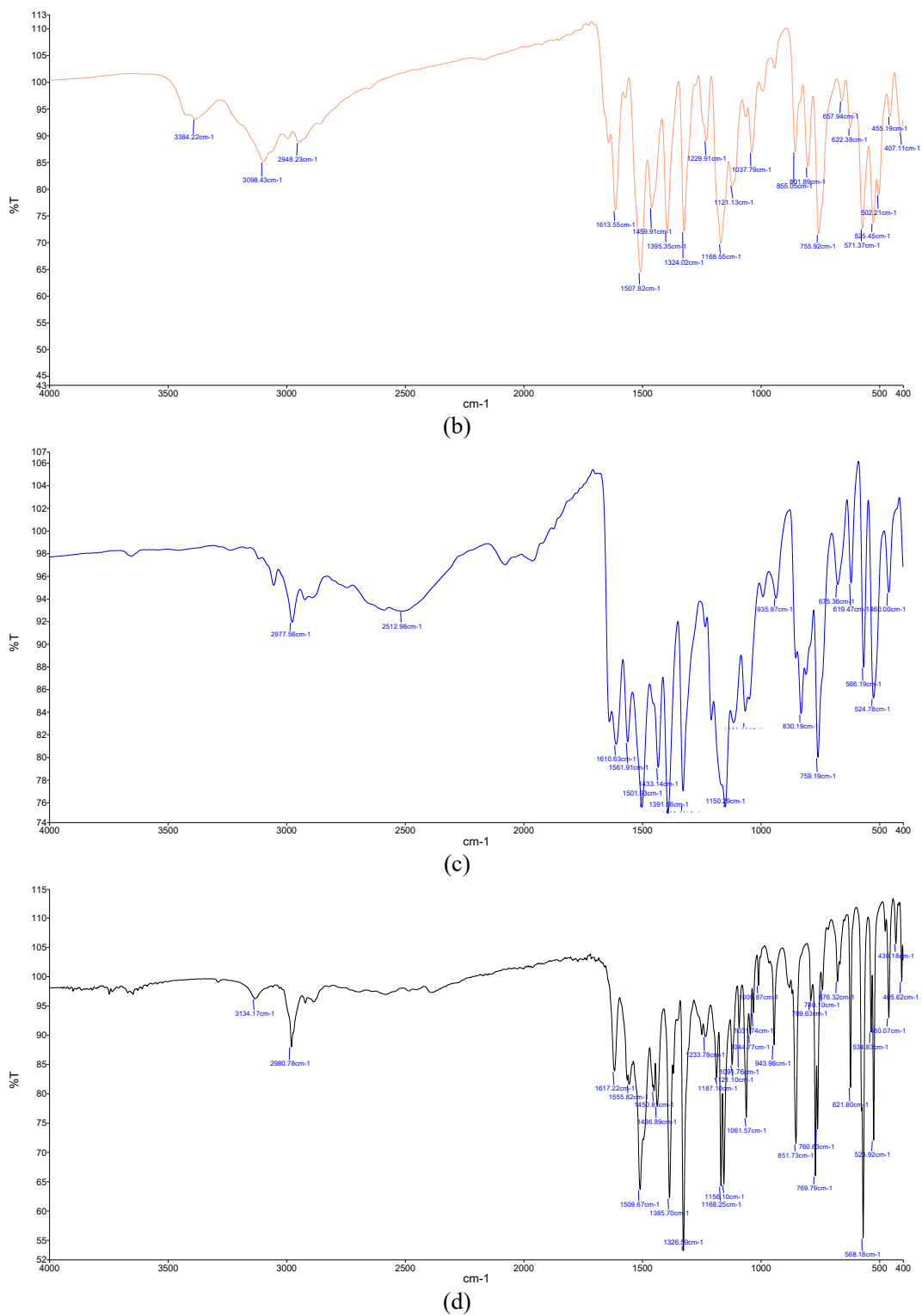
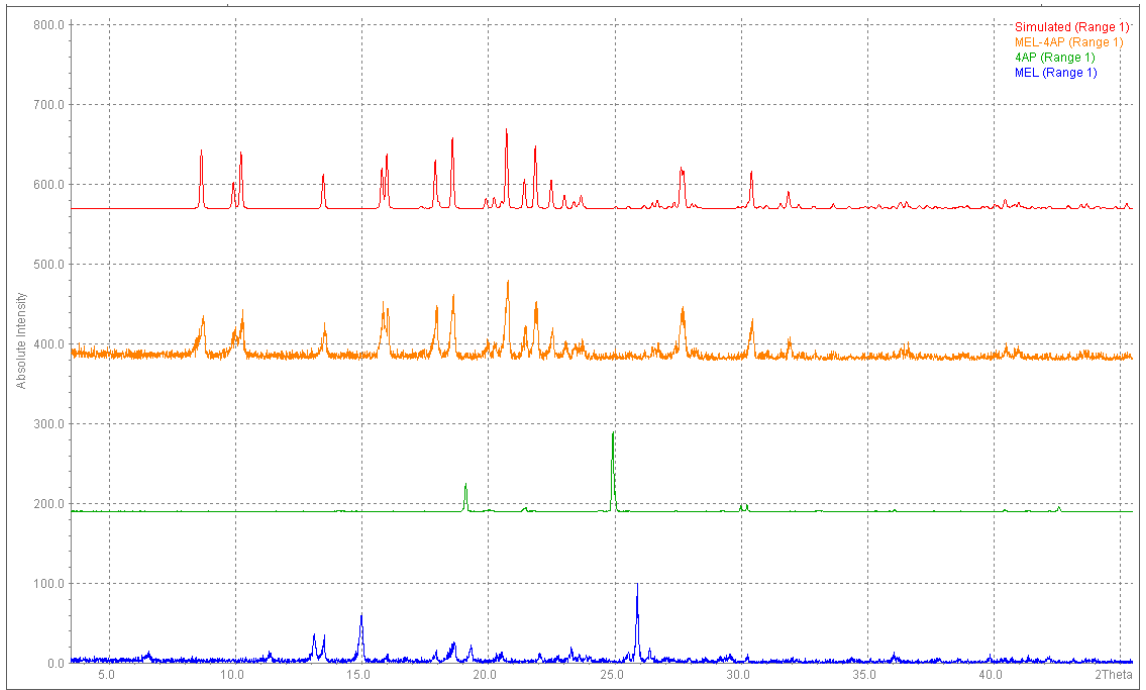
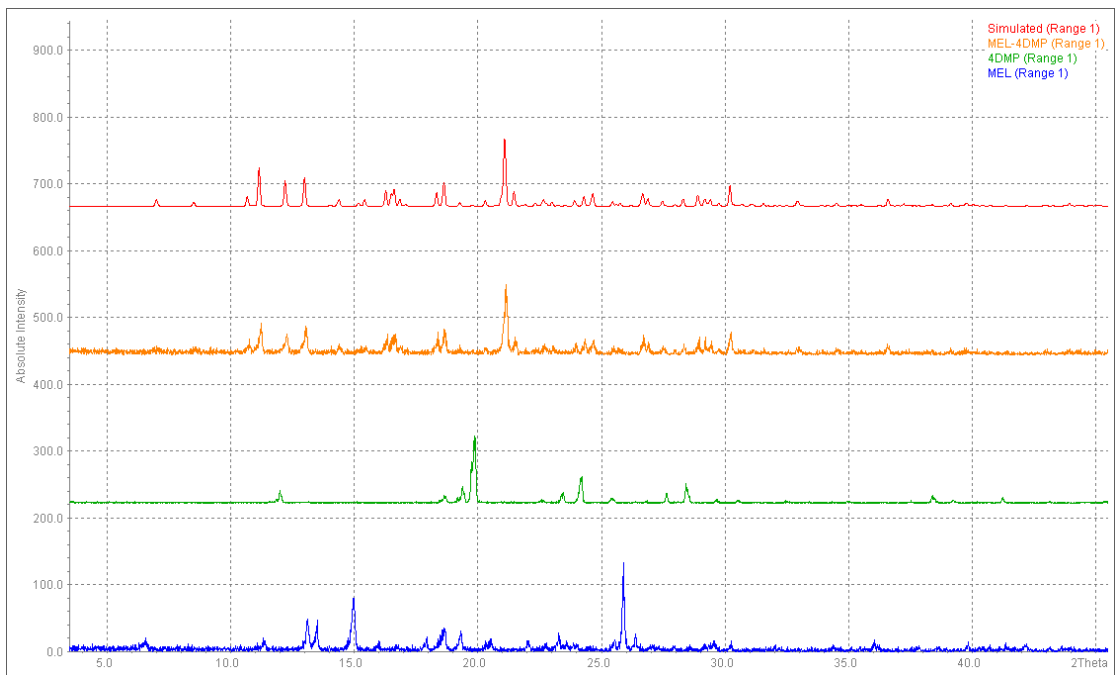


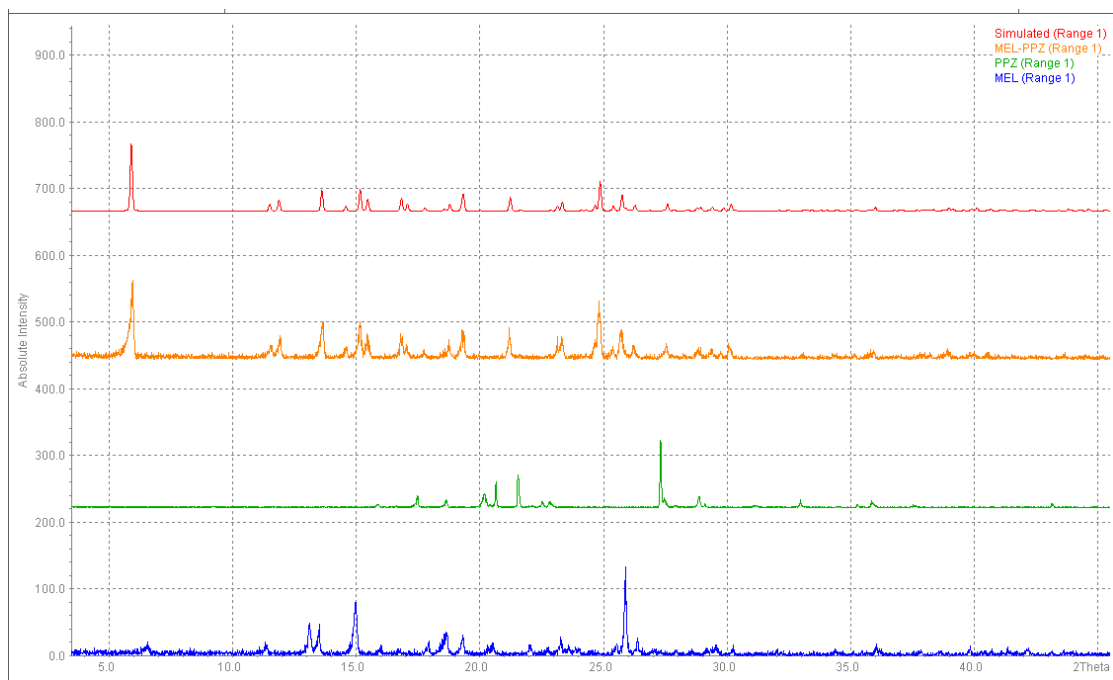
Figure S4.11. IR spectra of (a) MEL, (b) MEL-4AP, (c) MEL-4DMP and (d) MEL-PPZ.



(a)

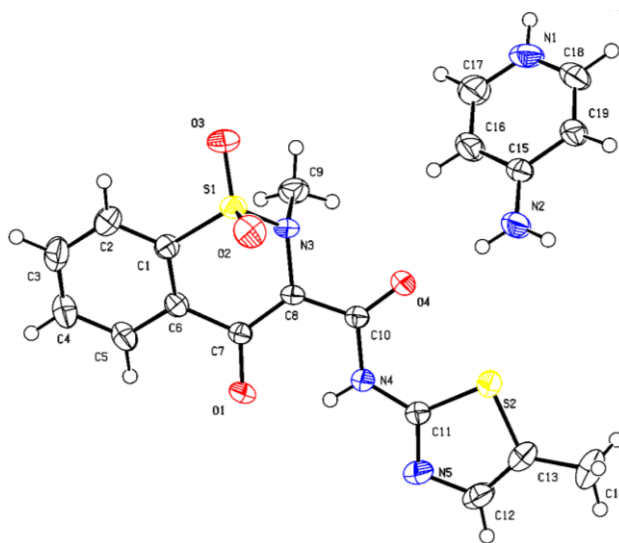


(b)

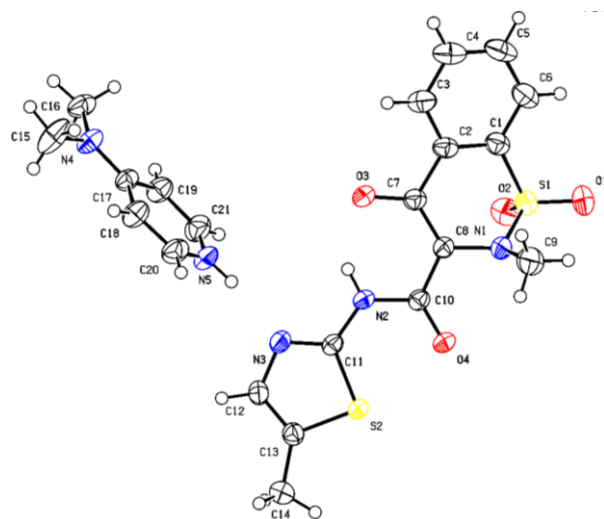


(c)

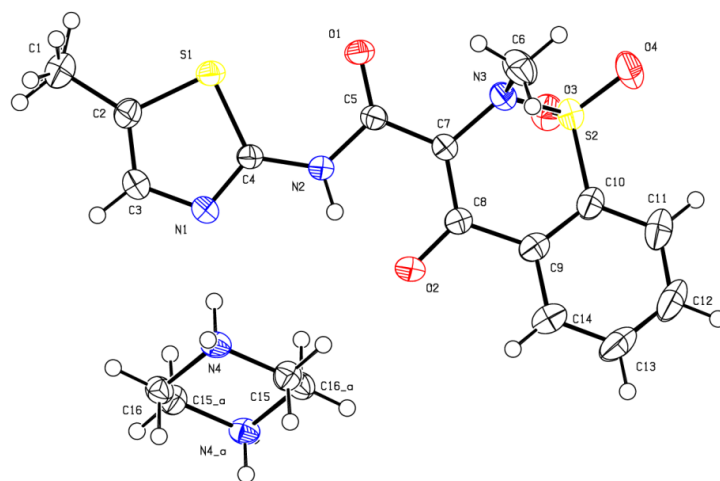
Figure S4.12. (a) PXR D patterns of MEL (blue), 4AP (green), MEL-4AP salt (orange) and simulated pattern from the crystal structure (red), (b) PXR D patterns of MEL (blue), 4DMP (green), MEL-4DMP salt (orange) and simulated pattern from the crystal structure (red) and (c) PXR D patterns of MEL (blue), PPZ (green), MEL -PPZ salt (orange) and simulated pattern from the crystal structure (red).



(a)

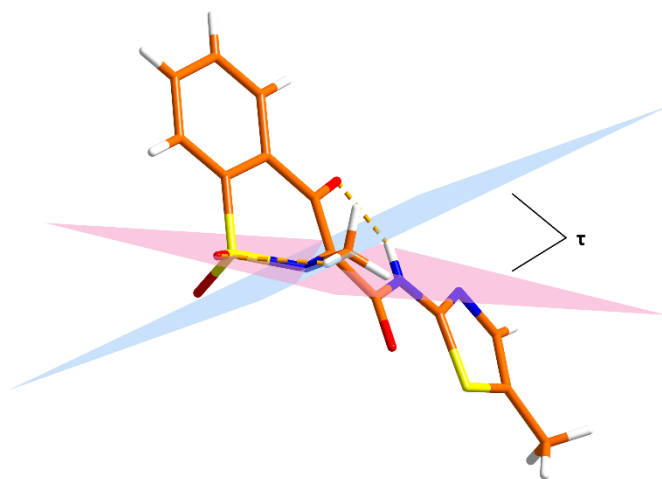


(b)



(c)

Figure S4.13. Ellipsoid plot of (a) MEL-4AP, (b) MEL-4DMP and (c) MEL-PPZ.



Solid	τ (°)
MEL-4AP	45.4
MEL-4DMP	45.6
MEL-PPZ	42.9

Figure S4.14. The angle (τ) formed between the methyl hydrogen and the plane of a sp^2 oxygen in MEL^- anion in MEL-4AP, MEL-4DMP and MEL-PPZ.

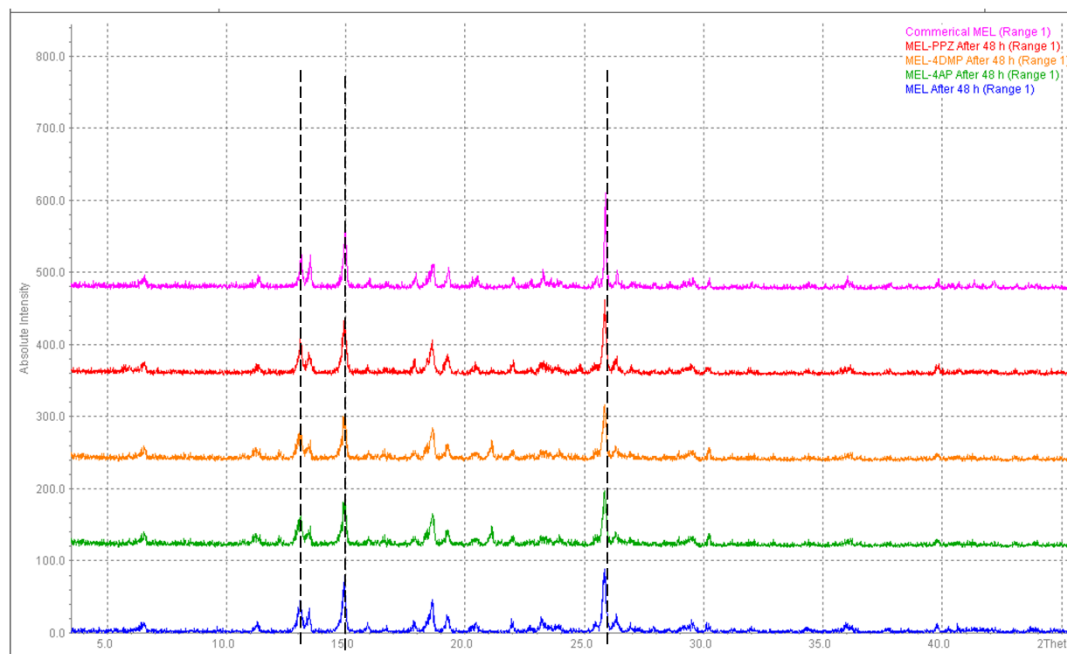


Figure S4.15. PXR D patterns of residual solids of MEL (blue), MEL-4AP (green), MEL-4DMP (orange), MEL-PPZ (red) after solubility experiments and the experimental PXR D patterns with commercial MEL (pink).

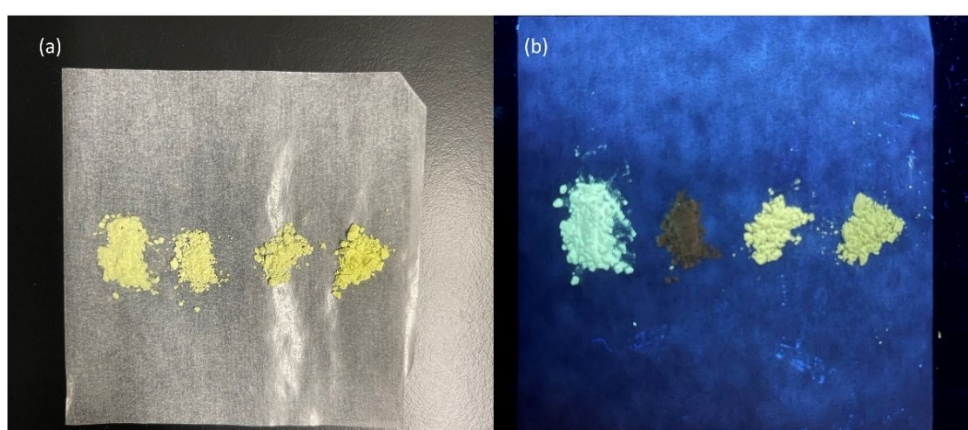


Figure S4.16. Photographs of MEL solids (from left to right: MEL, MEL-4AP, MEL-4DMP and MEL-PPZ): (a) powder samples under daylight; (b) powder samples under UV (365 nm) lamp.

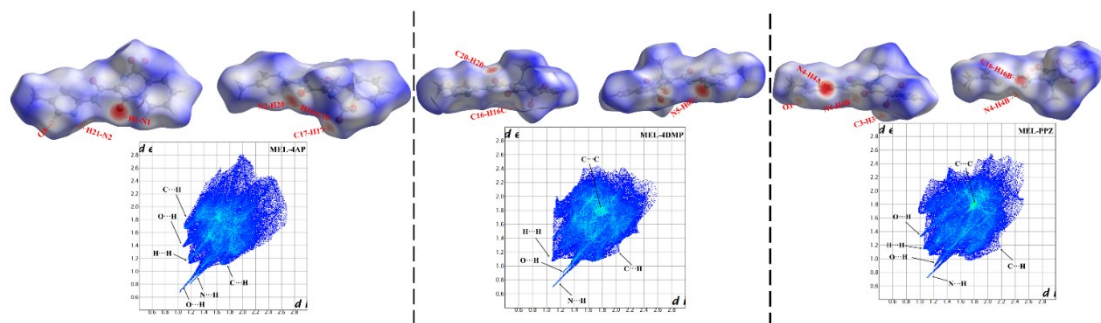


Figure S4.17. 3D d_{norm} surfaces and 2D fingerprint plots of MEL in MEL-4AP (left), MEL-4DMP (middle) and MEL-PPZ (right).

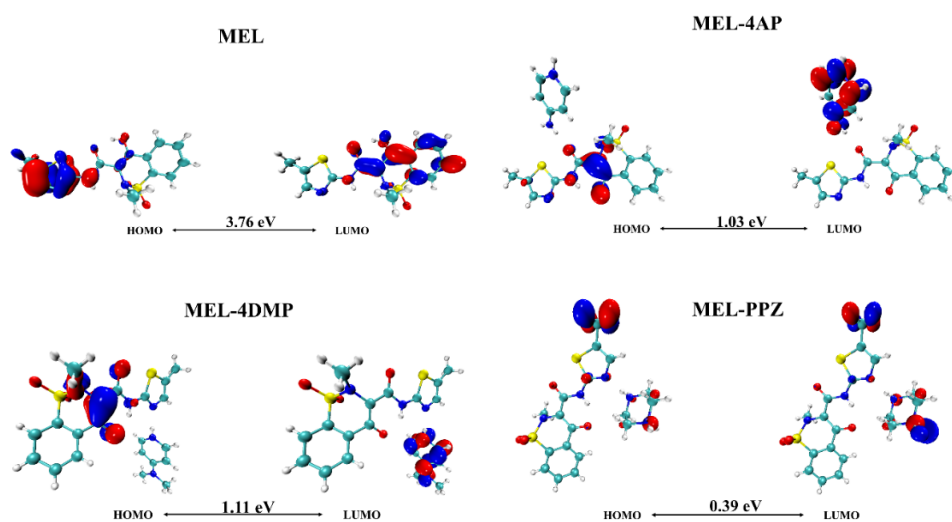


Figure S4.18. Molecular orbital plots of the HOMOs and LUMOs of MEL, MEL-4AP, MEL-4DMP and MEL-PPZ.

Table S4.5. Hydrogen bond and π - π interaction geometries (\AA , $^\circ$) in the MEL-4AP salt.

Type	D-H \cdots A	D-H	H \cdots A	D \cdots A	D-H \cdots A	ARU (J)
1	N1-H1 \cdots O1	0.87(2)	1.835(19)	2.690(2)	166(3)	3445.01
2	N2-H20 \cdots O4	0.87(3)	2.07(3)	2.892(3)	157(2)	1555.01
3	N2-H21 \cdots N5	0.86(3)	2.17(3)	3.019(4)	168(2)	4464.01
4	Intra N4-H22 \cdots O1	0.83(2)	1.88(3)	2.591(3)	142.7(19)	

5	Intra	C5-H5...O1	0.94	2.49	2.804(3)	100	
6		C12-H12...O3	0.93	2.57	3.259(3)	131	3455.01
7		C16-H16...O4	0.96	2.52	3.274(3)	135	1555.01
8		C17-H17...O2	0.94	2.37	3.290(4)	168	2565.01
9	Intra	C9-H24...O3	0.95	2.5	2.852(3)	102	
Cg(I)	Cg(J)	Cg-Cg	Interplanar distance	Dihedral Angle	Beta	ARU (J)	
3	5	4.2197(16)	2.8815(10)	20.89(13)	27.2	2665.02	

^a Symmetry codes: [3445.] = -1/2+x, -1/2+y, z; [4464.] = -1/2+x, 3/2-y, -1/2+z; [3455.] = -1/2+x, 1/2+y, z; [2565.] = x, 1-y, 1/2+z; [2665.] = 1+x, 1-y, 1/2+z; [2464.] = -1+x, 1-y, -1/2+z. Cg3 represents the centroid of C1-C6 and Cg5 represents the centroid of N1, C15-C19. Cg(I) = plane number I; Cg-Cg = distance between ring centroids (Ang.). Beta is the displacement angle between the ring normal of plane I and the centroid vector.

Table S4.6. Hydrogen bond and π - π interaction geometries (\AA , $^\circ$) in the MEL-4DMP salt.

Type	D-H...A	D-H	H...A	D...A	D-H...A	ARU (J)
1	N5-H05...N3	0.86	1.94	2.794(2)	172	[1555.01]
2	Intra N2-H2...O3	0.86	1.86	2.5810(18)	140	
3	Intra C9-H9A...O1	0.96	2.43	2.865(3)	107	
4	C15-H15A...O3	0.96	2.41	3.352(2)	169	[2766.01]
5	C16-H16A...O3	0.96	2.52	3.454(2)	163	[2766.01]
6	C16-H16C...O2	0.96	2.53	3.241(2)	131	[2666.01]
7	C20-H20...O4	0.93	2.26	3.162(2)	165	[2676.01]
Cg(I)	Cg(J)	Cg-Cg	Interplanar distance	Dihedral Angle	Beta	ARU (J)
3	3	3.7999(12)	3.4665(7)	0.00(9)	24.2	[2667.01]

^a Symmetry codes: [2676.] = 1-x, 2-y, 1-z; [2666.] = 1-x, 1-y, 1-z; [2766.] = 2-x, 1-y, 1-z; [2667.] = 1-x, 1-y, 2-z. Cg3 is the centroid of C1-C6. Cg(I) = plane number I; Cg-Cg = distance between ring centroids (Ang.). Beta is the displacement angle between the ring normal of plane I and the centroid vector.

Table S4.7 Hydrogen bond and π - π interaction geometries (\AA , $^\circ$) in the MEL-PPZ salt.

	Type	D-H \cdots A	D-H	H \cdots A	D \cdots A	D-H \cdots A	ARU (J)
1	Intra	N2-H2 \cdots O2	0.86	1.77	2.520(4)	144	
2		N4-H4A \cdots N1	0.89	1.96	2.847(4)	175	[1555.01]
3		N4-H4B \cdots O1	0.89	2.22	2.928(4)	136	[1455.01]
4		N4-H4B \cdots S1	0.89	2.83	3.314(3)	116	[3667.01]
5		N4-H4B \cdots O1	0.89	2.32	2.969(4)	129	[3667.01]
6		C3-H3 \cdots O3	0.93	2.46	3.276(4)	146	[3666.01]
7	Intra	C6-H6A \cdots O4	0.96	2.38	2.817(5)	107	

Cg(I)	Cg(J)	Cg-Cg	Interplanar distance	Dihedral Angle	Beta	ARU (J)
1	1	4.276(3)	3.3710(11)	0.00(13)	38	[3667.01]

^aSymmetry codes: [3666.] = 1-x, 1-y, 1-z; [3667.] = 1-x, 1-y, 2-z; [1455.] = -1+x, y, z. Cg1 is the centroid of S1, C2-C4, N1. Cg(I) = plane number I; Cg-Cg = distance between ring centroids (Ang.). Beta is the displacement angle between the ring normal of plane I and the centroid vector.

Table S4.8. Summary of the various contact contributions to the MEL Hirshfeld surface area in pure MEL and its salts.

	O-H	H-H	C-H	C-O	C-C	N-H	O-N	N-C	N-N	H-S	O-O	S-C	S-N	S-O	S-S
MEL	28.9	35.1	9.9	2.2	4.6	5.1	0.9	4.6	0	7.2	0	0	0	1.3	0.2
MEL-4AP	26.5	32	20.8	1.1	1.9	7.5	0.1	0.8	0	5.7	0.7	1.6	0.7	0.6	0
MEL-4DMP	27.8	36.6	17.6	0.7	3.3	5.8	0.3	1.2	0.6	4.8	0	0	0.1	0.7	0.5
MEL-PPZ	27.3	38.9	16.6	1.4	3.0	5.2	0.3	1.2	0.6	4.4	0	0	0.1	0.9	0



**Chapter 5 Study of Enantiospecific Cocrystals
and Diastereomeric Cocrystal Pairs between
L-Amino Acids and Chiral Cocrystal Formers**



5.1 Abstract

A comprehensive cocrystal screen of 19 L-amino acids with both enantiomers of four chiral cofomers (tartaric acid, mandelic acid, malic acid, and 3-phenyllactic acid) was conducted to investigate the cocrystallizing behaviour between two chiral components. In addition to the four previously reported diastereomeric systems and five enantiospecific systems found in the literature, seven new diastereomeric systems and eight distinct enantiospecific systems were discovered in this study. Thus, a total of eleven diastereomeric systems and thirteen enantiospecific systems were identified. Among them, three enantiospecific systems and one diastereomeric cocrystal pair that form in different stoichiometric ratios were structurally characterized. The formation of diastereomeric or enantiospecific systems was explored using an examination of their hydrogen bonding motifs.

5.2 Introduction

Chiral chemistry was discovered by Louis Pasteur when investigating the crystallization of racemic sodium ammonium tartrate tetrahydrate from aqueous solution in 1848.¹ However, it took about 100 years to recognize the importance of chirality in the pharmaceutical industry.² The vast majority of proteins, amino acids, enzymes, carbohydrates are chiral compounds. Furthermore, more than 50% of drugs currently in use are chiral,³ and there are many more drugs which are sold

as racemates, meaning they consist of an equimolar mixture of two enantiomers.⁴ From a regulatory viewpoint,⁵ it is necessary to figure out what role(s) each enantiomer play(s) *in vivo* in order to avoid, or at least reduce, unwanted side effects. The investigation of chiral drugs increases the costs and time associated with pharmaceutical development yet provides opportunities for making better medicines. Therefore, chiral resolution plays an important role in the research and development of chiral drugs.

Despite the fact that asymmetric synthesis has made significant advancements,⁶ there are still chiral compounds that are synthesized as racemates and then separated through appropriate physical separation methods, such as preparative HPLC. This method involves separating enantiomers using a chiral HPLC column, which can be either an HPLC column packed with a chiral stationary phase or chiral mobile phase additives added to the mobile phase.⁷ In recent years, cocrystal formation has emerged as an alternative approach for achieving chiral resolution. According to The European Medicines Agency, cocrystals are defined as homogeneous (single-phase) crystalline structures composed of two or more components in a specific stoichiometric ratio. Unlike salts, the arrangement of components in the crystal lattice of cocrystals is not governed by ionic bonds. Instead, cocrystals are formed through weaker interactions, such as hydrogen bonding, π - π stacking, or van der Waals interactions.⁸

Cocrystallization presents two new variations for chiral resolution (Figure 5.1). Enantiospecific cocrystallization requires the target chiral API to cocrystallize

with only one enantiomer but not the other.⁹ The first enantiospecific cocrystal system of levetiracetam and *S*-mandelic acid was introduced by Leyssens *et al.* in 2012, along with a separation method that could separate 70% of the *S*-mandelic acid from the racemic mixture in a single cocrystallization step.¹⁰ In contrast, the target chiral API can form a cocrystal with each enantiomer of a chiral cofomer, giving rise to a diastereomeric cocrystal pair, which is similar to diastereomeric salts yet without proton transfer occurring between the two components. A two-step protocol for the chiral resolution of *RS*-praziquantel was developed on the basis of the formation of a diastereomeric cocrystal pair of *RS*-praziquantel with L-malic acid.⁹

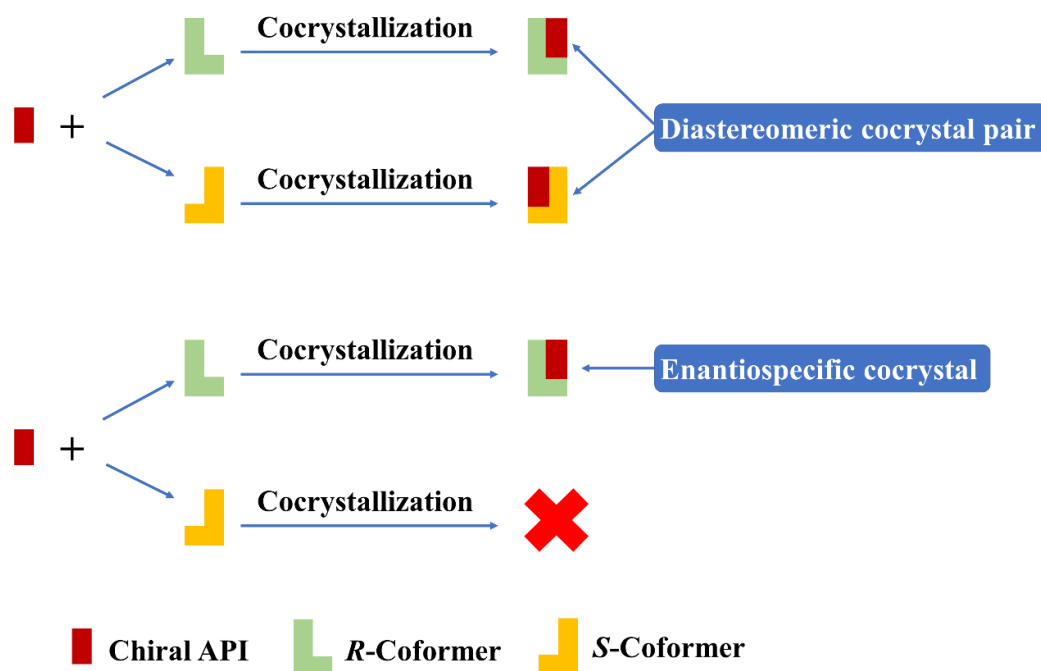


Figure 5.1. Two possible scenarios of achieving chiral resolution by cocrystallization (adapted from ref. 31).

Amino acids are important bioactive substances, which are widely used in the food, chemical and pharmaceutical industries. In addition, all naturally occurring proteins from all living organisms consist of L-amino acids (with the exception of glycine, whose side chain is H atom).^{11, 12} In this work, to explore the formation of enantiospecific cocrystals and diastereomeric cocrystal pairs of amino acids, 19 essential L-amino acids (Figure 5.2) were chosen as target compounds. Four readily available and pharmaceutically relevant chiral compounds α -hydroxy acids were selected as cofomers,^{13, 14} namely tartaric acid (D/L-TA), mandelic acid (D/L-MDA), malic acid (D/L-MA) and 3-phenyllactic acid (D/L-PLA) (Figure 5.3). A comprehensive cocrystal screening of 19 L-amino acids with both enantiomers of the four cofomers was undertaken and four crystal structures were reliably determined.

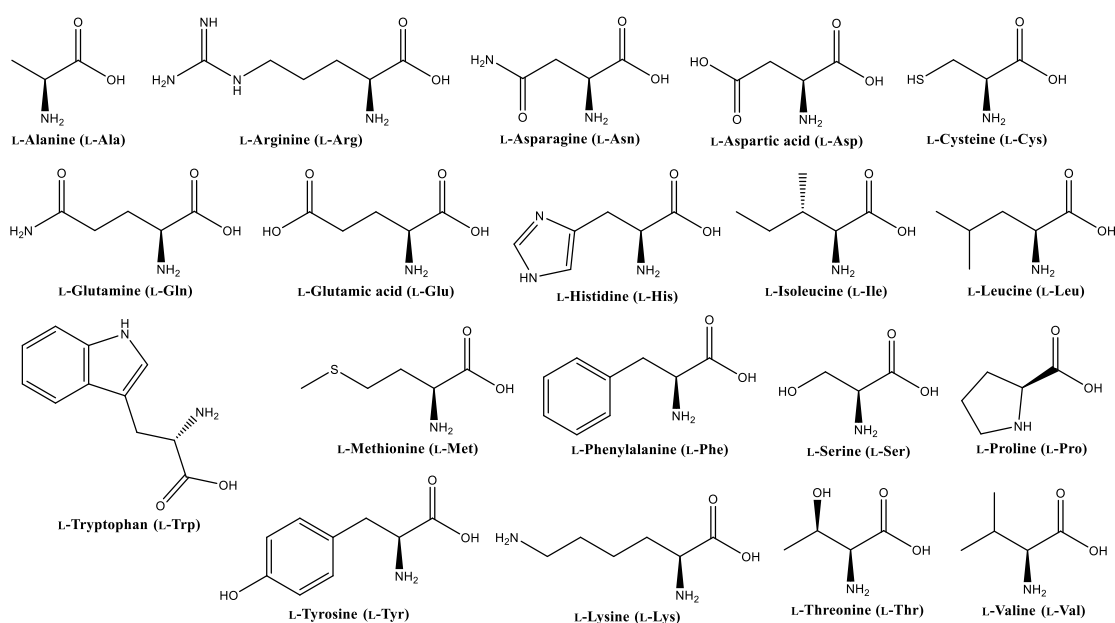


Figure 5.2. Chemical structures of 19 common L-amino acids.

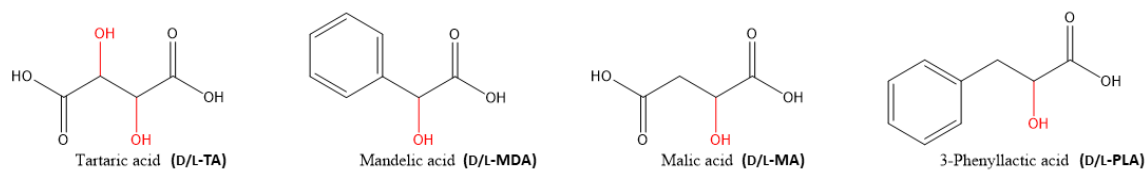


Figure 5.3. Chemical structures of chiral cofomers used in this work.

5.3 Experimental Section

5.3.1 Materials

All materials were obtained from commercial suppliers and used without further purification. L-Lysine, L-histidine, L-serine, L-tryptophan, L-threonine, L-mandelic acid, D-mandelic acid, D/L-mandelic acid, L-malic acid, D-malic acid, D/L-malic acid, L-3-phenyllactic acid, D-3-phenyllactic acid and D/L-3-phenyllactic acid were purchased from Fluorochem. L-Glutamic acid, L-leucine, L-alanine, L-cysteine, L-aspartic acid, L-methionine, L-glutamine, L-valine, L-tartaric acid and D/L-tartaric acid were purchased from TCI chemicals. L-Asparagine, L-phenylalanine, L-arginine, L-proline, L-tyrosine, L-isoleucine and D-tartaric acid were purchased from Sigma-Aldrich. Methanol, ethanol, acetone, isopropanol and ethyl acetate were obtained from Honeywell International Inc.

5.3.2 Screening Experiment

5.3.2.1 Liquid-assisted grinding

Mechanical grinding experiments were performed in a Retsch MM400 Mixer mill (30 min at 30 Hz), equipped with stainless steel 5 mL grinding jars and one 2.5

mm stainless steel grinding ball per jar. Before starting, 10 μL of ethyl acetate was added to the mixture of the amino acid and the coformer in the correct stoichiometric ratio. Initial experiments examined the 1:1 stoichiometry and subsequently 1:2 and / or 2:1 ratio were examined, where appropriate. The resulting powder was obtained and analyzed by powder X-ray diffraction (PXRD).

5.3.2.2 Slurry experiments

Amino acids and coformers in 1:1, 1:2 and 2:1 were stirred at 400 rpm in methanol-deionized water (4:1, v/v) at room temperature for 72 h, respectively. The resulting suspensions were left in the fume hood and allowed to dry. The obtained powdered samples were isolated and analyzed by PXRD.

5.3.2.3 Solution cocrystallization

In all cases, the starting material was dissolved by heating in solvent in a laboratory vial, which was covered with parafilm and a pinhole made in the parafilm. The vial was left over a period of time until only a small amount of solvent remained. The resulting solid / crystal was isolated for further single crystal X-ray diffraction (SCXRD) analysis.

L-Met-L-MDA: L-Met (50.5 mg, 0.34 mmol) and L-MDA (152.9 mg, 1 mmol) were dissolved in 20 mL of a mixture of acetone and deionized water (1:1, v/v) and white plate-like crystals were obtained after 1-2 weeks.

L-Met-D-MDA: L-Met (50.8 mg, 0.34 mmol) and D-MDA (51.7 mg, 0.34 mmol) were dissolved in 5 mL of a mixture of MeOH and deionized water (1:1, v/v) and colourless plate-like crystals were obtained after 1-2 weeks.

L-His-L-MA: L-His (77.6 mg, 0.5 mmol) and L-MA (67.1 mg, 0.5 mmol) were dissolved in 10 mL of a mixture of THF and deionized water (1:1, v/v) and colourless needle-like crystals were obtained after 1-2 weeks.

L-Leu-D-MDA: L-Leu (65.6 mg, 0.5 mmol) and D-MDA (51.7 mg, 0.34 mmol) were dissolved in 10 mL of a mixture of MeOH and deionized water (1:1, v/v) and white needle-like crystals were obtained after 1-2 weeks.

L-Ile-L-PLA: L-Ile (65.6 mg, 0.5 mmol) and L-PLA (83.1 mg, 0.5 mmol) were dissolved in 10 mL of deionized water and white needle-like crystals were obtained after 4-5 weeks.

5.3.3 Physical Measurements

Differential scanning calorimetry (DSC) data were collected using a TA Instruments Q1000. Samples (2-6 mg) were crimped in nonhermetic aluminum pans and scanned from 40 to 350 °C at a heating rate of 10 °C min⁻¹ under a continuously purged dry nitrogen atmosphere. Fourier transform infrared spectroscopy were recorded on a PerkinElmer UATR Two spectrophotometer using a diamond attenuated total reflectance accessory over a range of 400-4000 cm⁻¹. An average of four scans was taken for each spectrum obtained with a

resolution of 4 cm^{-1} . PXRD data were collected using a STOE STADI MP diffractometer with Cu K α radiation using a linear position-sensitive detector over the 2θ range of $3.5\text{-}45.5^\circ$ with an increment of 0.05° at a rate of 2° min^{-1} . The samples were prepared as transmission foils and the data were viewed via STOE Powder Diffraction Software Package WinX^{POW}.¹⁵ SCXRD data were collected on a Bruker APEX II DUO with monochromated Cu K α radiation ($\lambda = 1.54178 \text{ \AA}$). All calculations and refinements were made using Bruker APEX software with the SHELX suite of programs.^{16, 17} Nonhydrogen atoms were refined anisotropically. All hydrogen atoms were placed in geometrically calculated positions using the riding model, with C-H = $0.93\text{-}0.97 \text{ \AA}$ and N-H = $0.86\text{-}0.89 \text{ \AA}$, and Uiso (H) (in the range 1.2-1.5 times Ueq of the parent atom). DIAMOND was used for creating figures,¹⁸ and PLATON was used for the analysis of potential hydrogen bonds and short ring interactions.^{19, 20} Crystallographic parameters of L-Met-L-MDA, L-Leu-D-MDA, L-Ile-L-PLA and L-His-L-MA are listed in Table 5.1, and crystallographic parameters of L-Met-D-MDA are listed in Table S5.1 due to the low quality of the single crystal that was analyzed and its high disordered crystal structure.

Table 5.1. Crystallographic data for L-Met-L-MDA, L-Leu-D-MDA, L-Ile-L-PLA and L-His-L-MA.

Crystallographic data	L-Met-L-MDA 1:3	L-Leu-D-MDA 1:1	L-His-L-MA 1:1	L-Ile-L-PLA 1:1
Chemical formula	C ₂₉ H ₃₅ NO ₁₁ S	C ₁₄ H ₂₁ NO ₅	C ₁₀ H ₁₅ N ₃ O ₇	C ₁₅ H ₂₃ NO ₅
Formula weight	605.64	283.32	289.25	297.34
Crystal system	orthorhombic	monoclinic	orthorhombic	orthorhombic
Space group, <i>Z</i>	<i>P2₁2₁2₁</i> , 4	<i>P2₁</i> , 2	<i>P2₁2₁2₁</i> , 4	<i>P2₁2₁2₁</i> , 4
Temperature (K)	297(2)	296(2)	296(2)	296(2)
<i>a</i> (Å)	9.554(10)	9.1735(19)	5.2310(7)	5.4029(2)
<i>b</i> (Å)	9.896(16)	5.7105(12)	13.7394(19)	10.9506(4)
<i>c</i> (Å)	31.40(3)	14.506(4)	17.546(2)	27.5295(11)
α (°)	90	90	90	90
β (°)	90	92.051(17)	90	90
γ (°)	90	90	90	90
Volume (Å ³)	2969(6)	759.4(3)	1261.0(3)	1628.78(11)
ρ_{calc} (g cm ⁻³)	1.355	1.239	1.524	1.213
Radiation type	Mo K α	Cu K α	Cu K α	Cu K α
μ (mm ⁻¹)	0.170	0.781	1.128	0.751
Reflns measured	70101	3762	8197	10677
Reflns independent	5710	2125	2176	2845
Significant [<i>I</i> >2 σ (<i>I</i>)]	3292	1879	2164	2702
Parameters refined	386	186	184	195
Restraints	0	43	6	24
$\Delta\rho_{max}$, $\Delta\rho_{min}$ (e Å ⁻³)	0.324, -0.288	0.274, -0.235	1.047, -0.478	0.447, -0.221
<i>F</i> (000)	1280	304	608	640
<i>R</i> ₁ [<i>I</i> >2 σ (<i>I</i>)]	0.0557	0.0509	0.0550	0.0387
w <i>R</i> ₂ (all data)	0.1707	0.1393	0.1598	0.1134
<i>Flack</i>	-0.08(8)	0.2(2)	0.17(4)	0.08(6)

5.4 Results and Discussion

5.4.1 Screening Outcome

The outcome of the screening experiments is summarized in Table S5.7. Based on the Cambridge Structural Database (CSD) search, thirteen cocrystals of L-amino acids with chiral cofomers used in this work have been reported and their structures have been determined.²¹⁻²⁹ To complete the cocrystal screening between the 19 L-amino acids and both enantiomers of four chiral cofomers, initial experiments examined the 1:1 stoichiometry and subsequently 1:2 and / or 2:1 ratios were examined. Therefore, more than 400 screening experiments were conducted by LAG method and / or slurry experiments in different ratios. Since no significant differences were found between the results obtained from the LAG method and the slurry experiments, the LAG experiments were discontinued for the screening of D-MA and D/L-PLA with the 19 L-amino acids. Among all the screening products, only 22 (5%) are promising new phases, based on PXRD analysis, while no new phase or no powder samples can be obtained for L-Asp, L-Gln, L-Glu, L-Ser, L-Thr and L-Tyr with any enantiomer of chiral cofomers under the experimental conditions carried out in this study. For example, as shown in Figure S5.7, no new diffraction peak can be found in the PXRD patterns of the products of L-Asp and L-TA, for all stoichiometries investigated. In other words, the PXRD patterns obtained are the simple overlay of PXRD patterns of L-Asp and L-TA.

Previous literature has reported 4 diastereomeric cocrystal pairs.^{21, 24-26, 28} In this study, we identified 5 additional diastereomeric systems, which were analyzed using PXRD (Figures S5.4 and S5.8-S5.11) and only one diastereomeric cocrystal pair was analyzed by SCXRD.

For instance, new diffraction peaks of the product of L-Phe with L-MA can be found, demonstrating the generation of a new phase of L-Phe with L-MA. However, the appropriate ratio between L-Phe and L-MA cannot be confirmed only by PXRD. For L-Phe-D-MA system, some distinct diffraction peaks at 8.1° and 16.2° are only present in the 1:1 product of L-Phe and D-MA while the 1:2 and 2:1 products exhibit characteristic diffraction peaks at 14.8° and 19.8°, suggesting there could be more than one stoichiometric ratio between L-Phe and D-MA (Figure S5.9). While suitable single crystals for SCXRD analysis were not obtained, it is evident from the PXRD patterns that L-Phe can form a diastereomeric system with both enantiomers of MA.

Out of the 76 combinations analyzed, 13 systems were found to exhibit enantiospecific behaviour. This includes 5 systems previously reported in the literature,^{21-23, 27, 29} and 8 systems discovered in this study (Figures S5.2 and S5.12-S5.16). As shown in Figure S5.16, a new phase could be produced between L-Val and D-MA as the PXRD patterns of the product of L-Val and D-MA are significantly different from the PXRD patterns of the starting materials. Some distinct peaks of the products can be found at around 12.3° and 29.8°, etc., which are not present in the PXRD patterns of L-Val and D-MA. In contrast, no distinct

PXRD diffraction peak is observed in the product of L-Val and L-MA, indicating that L-Val can form an enantiospecific system with D-MA.

Two special cases have been observed in this study. L-Ala can form new phases with both enantiomers of TA. However, the PXRD patterns of L-Ala-L-TA and L-Ala-D-TA exhibit remarkable similarity, suggesting that these two systems may have related solid forms (see Figure S5.17). One possible explanation could be that the hydrogen-bonded interactions between L-Ala and D/L-TA are identical. However, a similar phenomenon has been observed in our unpublished research,³⁰ where the PXRD patterns of a diastereomeric cocrystal pair exhibit similarity. This can be attributed to the extremely similar hydrogen bonding and crystal packing arrangements between these two cocrystallizing components. A similar trend is also observed in the L-Trp-D / L-TA system, where comparable PXRD patterns were observed for L-Trp-L-TA and L-Trp-D-TA (Figure S5.18). Therefore, it is likely that L-Ala or L-Trp with D/L-TA are forming a diastereomeric cocrystal pair with similar hydrogen bonds.

Overall, there are 11 diastereomeric systems (14%) and 13 enantiospecific systems (17%) among the 76 possible combinations, which appears that there is similar likelihood for two chiral components to form an enantiospecific system rather than a diastereomeric pair for the amino acids and the four cofomers in this study. A 2014 search in the CSD for existing enantiospecific and diastereomeric cocrystals among 44 multicomponent structures containing two optically active compounds indicated that 86% of these systems exhibit enantiospecific behaviour.³¹ However,

as indicated in Table S5.7, the formation of enantiospecific or diastereomeric cocrystals by two chiral compounds cannot be only attributed to the nature of the compounds, as certain chiral amino acids are involved in the formation of both enantiospecific and diastereomeric cocrystals (e.g., L-Cys-L-TA enantiospecific cocrystal and L-Cys-D/L-MDA diastereomeric cocrystal pair).^{27,28} The interactions between two chiral components may decide whether they can form an enantiospecific cocrystal or a diastereomeric pair. Based on computational crystal structure prediction of enantiospecific and diastereomeric cocrystal systems, Habgood suggested that the formation of a diastereomeric cocrystal pair is facilitated by a strong, orientationally restrictive interaction motif, such as double hydrogen bonding, between the two cocrystallizing components. Furthermore, it is advantageous to avoid competing motifs and to have multiple weaker secondary motifs, as the exchange of one enantiomer for the other within the "primary" motif may disrupt the weaker secondary motifs.³²

Therefore, to further explore the propensity of two chiral compounds to cocrystallize in a diastereomeric manner or behave enantiospecifically in this work, a detailed structural analysis is required. However, after numerous attempts, only a small percentage (1%) of the new phases yielded single crystals suitable for SCXRD. Among these, three systems show enantiospecific cocrystal / salt formation (L-Leu-D-MDA, L-Ile-L-PLA and L-His-L-MA) based on the experimental conditions employed in this study, while one system behaves

diastereomerically (L-Met with D/L-MDA). Hydrogen bonds geometries are displayed in Tables S5.2-S5.6, and ellipsoid plots are shown in Figure S5.5.

5.4.2 Physical Characterization

The enantiospecific cocrystals and salt, i.e., L-Leu-D-MDA, L-Ile-L-PLA and L-His-L-MA and their corresponding starting materials were characterized by DSC, IR and PXRD. The melting trace of each new product and the starting materials are displayed in Figure 5.4. Each of the three enantiospecific cocrystals show a single sharp endothermic peak, and their melting points are in between those of the starting materials. The new crystalline solids exhibit different vibrational frequencies compared with those of the starting materials (Figure S5.1). The PXRD patterns of these three systems are shown in Figure S5.2. The experimental PXRD patterns match well with the theoretical patterns obtained from the SCXRD analysis, indicating these cocrystals can be reproduced in bulk quantities.

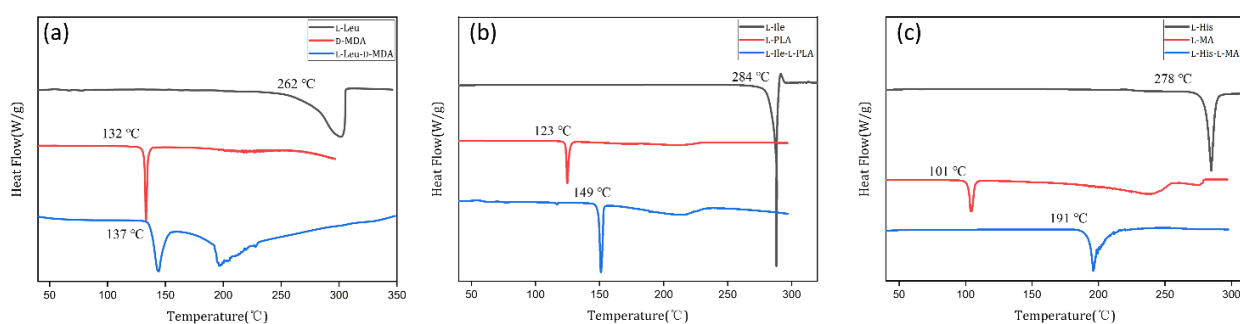


Figure 5.4. DSC traces of (a) L-Leu (black), D-MDA (red) and L-Leu-D-MDA (blue), (b) L-Ile (black), L-PLA (red) and L-Ile-L-PLA (blue), and (c) L-His (black), L-MA (red) and L-His-L-MA (blue).

The diastereomeric cocrystal pair L-Met-L-MDA and L-Met-D-MDA differ significantly in their melting points, Figure 5.5. The melting point of L-Met-D-MDA (145 °C) is between that of the two starting materials, while L-Met-L-MDA melts at 97 °C, lower than the melting point of each starting material. The ca. 50 °C difference of melting point may provide a new approach to achieve chiral separation by melting and recrystallizing at different temperatures. IR spectra of L-Met-L-MDA and L-Met-D-MDA are displayed in Figure S5.3. The differences in vibrational frequencies indicate the formation of new crystalline solids. As shown in Figure S5.4, the L-Met-L / D-MDA cocrystal pair exhibits several new diffraction peaks that are not present in the patterns of L-Met or L / D-MDA. Both simulated PXRD patterns derived from the single crystal structure match the experimental PXRD pattern, revealing the new crystalline forms with high purity can be obtained in quantities.

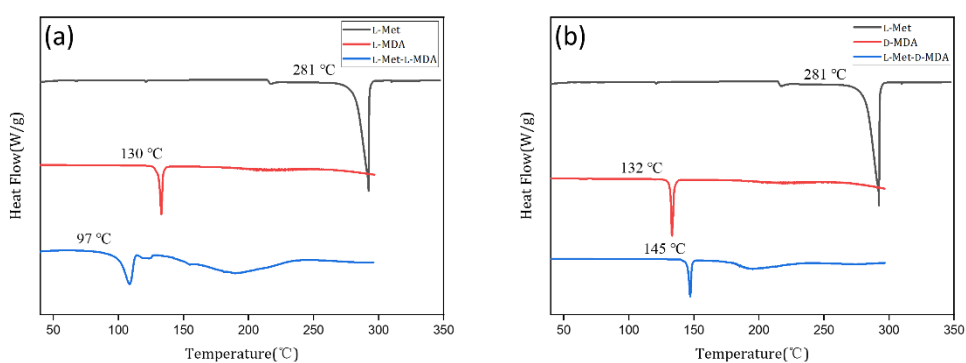
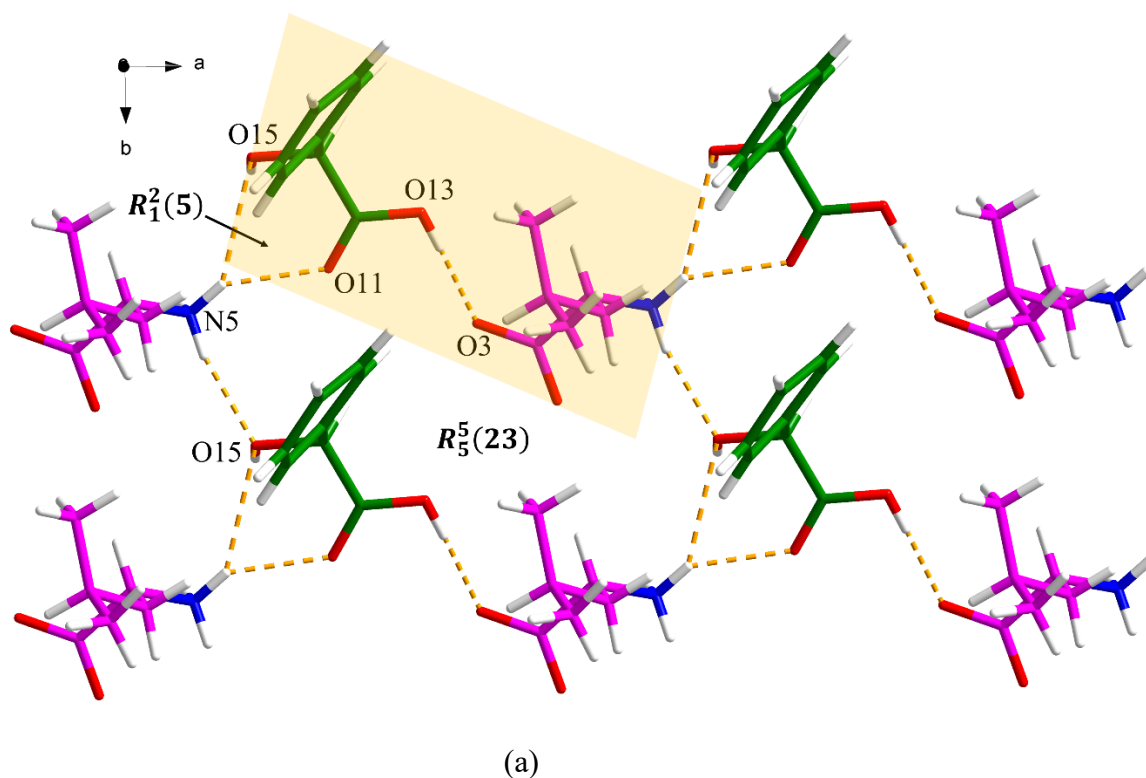


Figure 5.5. DSC traces of (a) L-Met (black), L-MDA (red) and L-Met-L-MDA (blue), and (b) L-Met (black), D-MDA (red) and L-Met-L-MDA (blue).

5.4.3 Crystal Structure Analysis

L-Leu-D-MDA crystallizes with the asymmetric unit consisting of one L-Leu zwitterion and one D-MDA molecule. As shown in Figure 5.6a, L-Leu and D-MDA connect through $N9-H9A \cdots O19$ discrete hydrogen bonding interactions. The basic unit is extended via three $N-H \cdots O$ hydrogen-bonding, i.e., $N9-H9B \cdots O8$, $N9-H9C \cdots O19$, $N9-H9C \cdots O21$, and a discrete $O19-H19 \cdots O7$ hydrogen bonding interactions, forming $R_1^2(5)$ and $R_3^3(8)$ motifs and resulting in a three-dimensional (3D) hydrogen bonding network (Figure 5.6b).



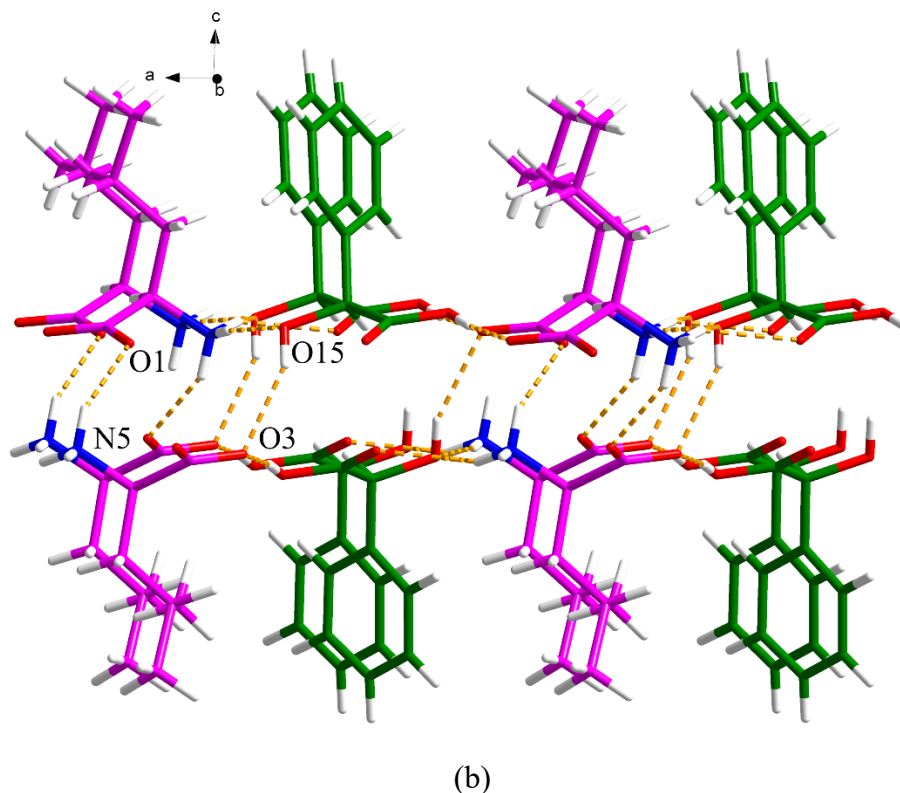
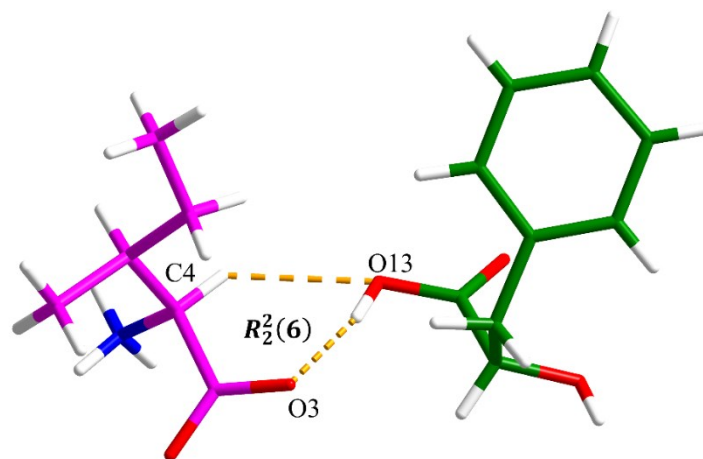
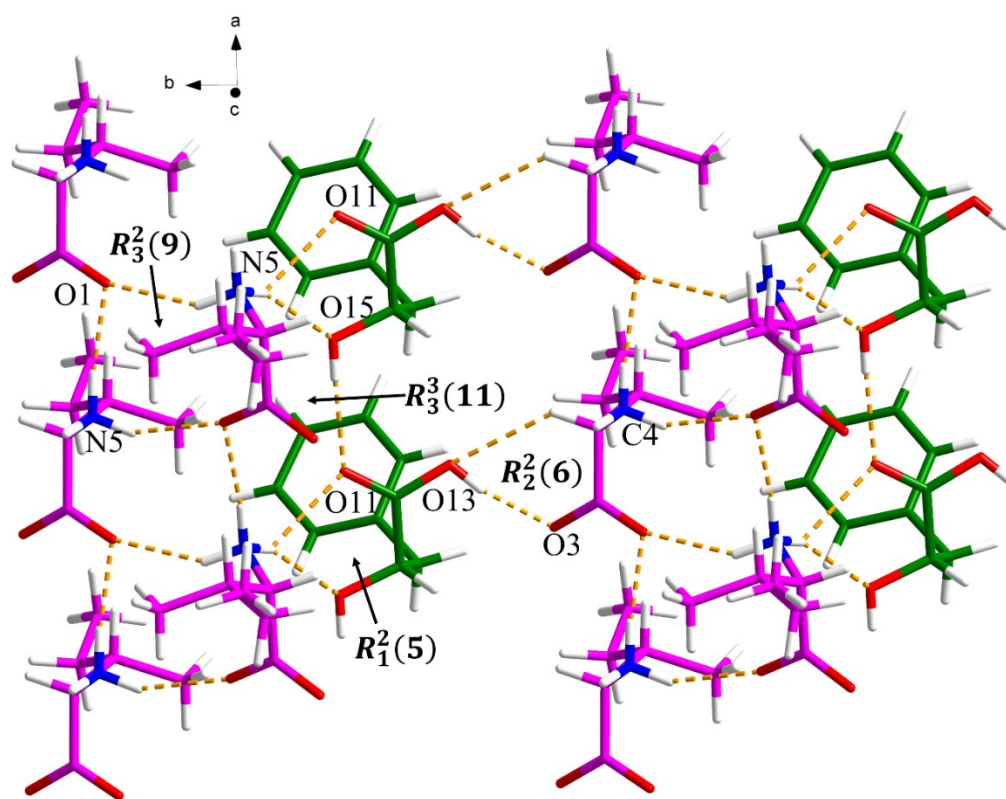


Figure 5.6. Hydrogen-bonded network in the L-Leu-D-MDA cocrystal: (a) along the *c* axis, and (b) along the *b* axis (hydrogen bonding is displayed by dashed lines).

L-Ile and L-PLA form a cocrystal that crystallizes with one L-Ile zwitterion and one L-PLA molecule in the asymmetric unit. The two components interact with each other through O13–H13···O3 and C4–H4···O13 discrete hydrogen bonds, resulting in an $R_2^2(6)$ motif (Figure 5.7a). An $R_1^2(5)$ motif connects L-Ile molecule and L-PLA molecule via N5–H5B···O11 and N5–H5B···O15. Additionally, discrete N5–H5A···O1 and N5–H5C···O1 hydrogen-bonding between L-Ile zwitterions form an $R_3^2(9)$ motif (Figure 5.7b).



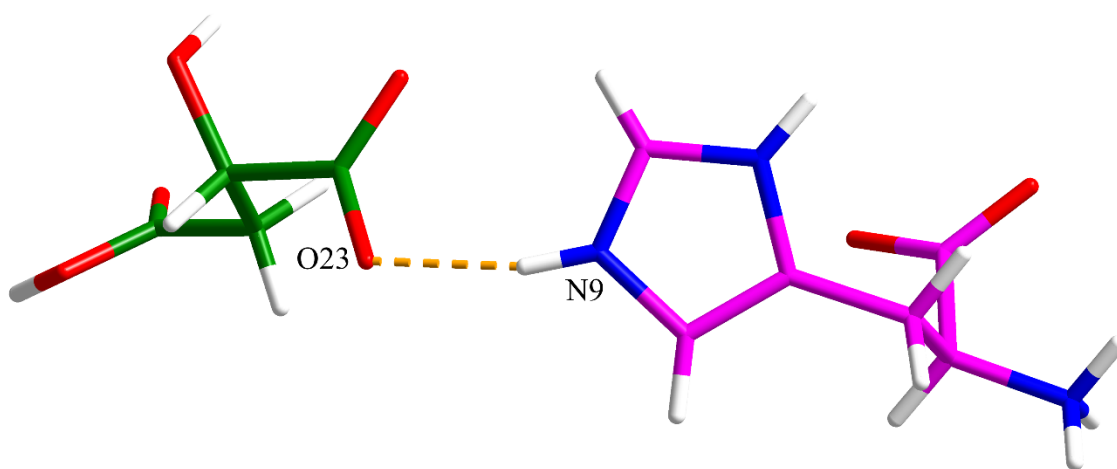
(a)



(b)

Figure 5.7. Crystal packing and intermolecular interactions in the L-Ile-L-PLA cocrystal: (a) asymmetric unit and (b) hydrogen-bonded network (hydrogen bonding is displayed by dashed lines).

L-His-L-MA is a molecular salt with the proton transfer from the carboxylate group of L-MA to the nitrogen atom of the imidazole group on L-His. L-His-L-MA crystallizes in the orthorhombic system in the $P2_12_12_1$ space group. The asymmetric unit contains one L-His⁺ and one L-MA⁻, and these two components are linked through N9–H9···O23 charge-assisted hydrogen bond (Figure 5.8a). As shown in Figure 5.8b, along the *a* axis, four L-His⁺ and four L-MA⁻ form a building block which is mainly assembled by N–H···O hydrogen bonds between NH₃⁺ of L-His⁺ and the other L-His⁺ or L-MA⁻, forming an $R_1^2(4)$ and an $R_1^2(5)$ motif. The 3D hydrogen bonded network is further extended via N–H···O, and O–H···O, and C–H···O interactions.



(a)

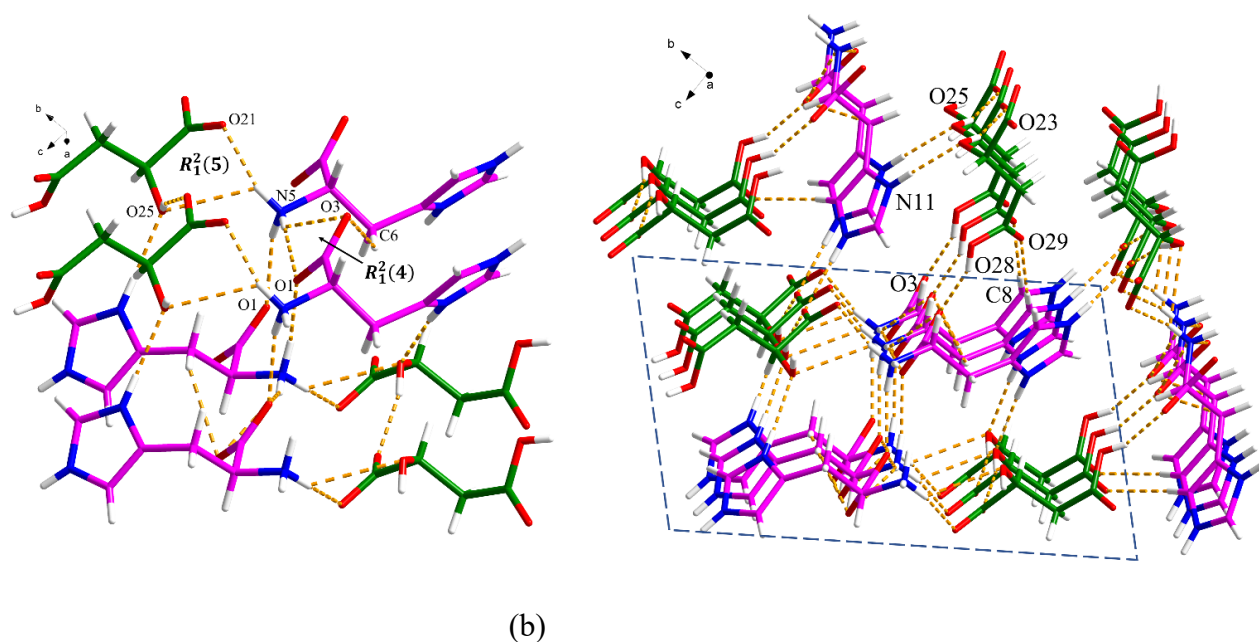
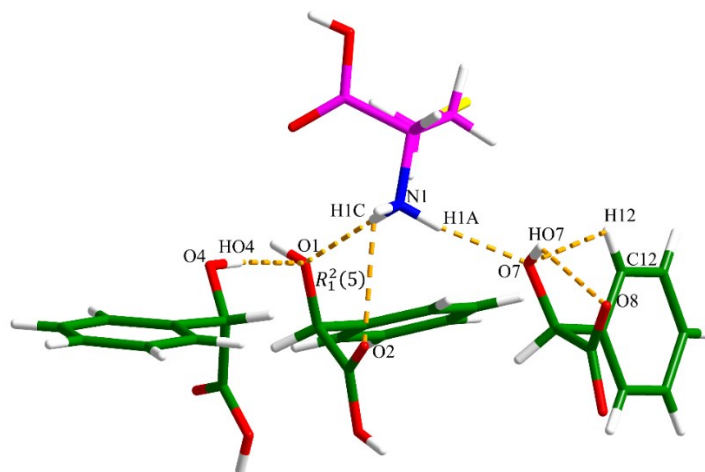


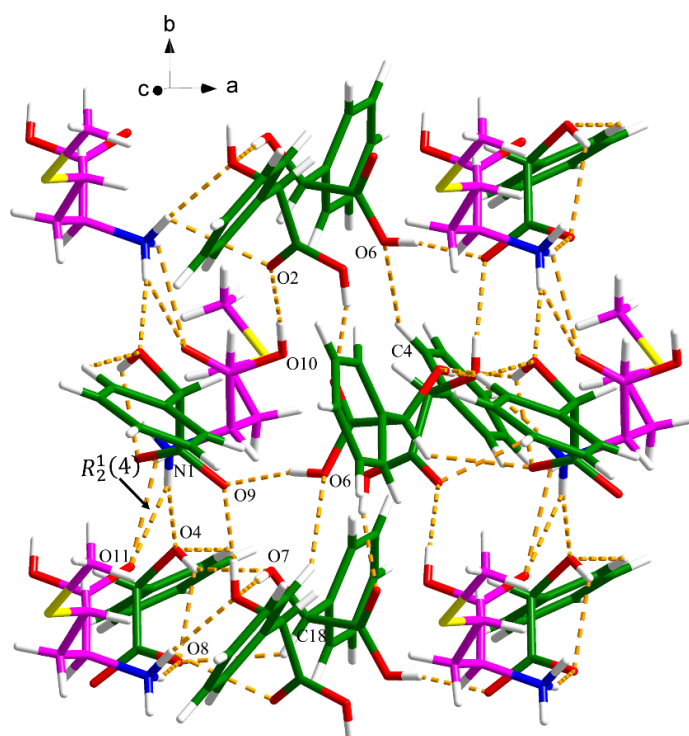
Figure 5.8. Crystal packing and intermolecular interactions in the L-His-L-MA: (a) asymmetric unit and (b) hydrogen-bonded network (hydrogen bonding is displayed by dashed lines).

L-Met-L-MDA crystallizes in the orthorhombic $P2_12_12_1$ space group in the asymmetric unit with one L-Met⁺, one L-MDA⁻ and two neutral L-MDA molecules ($Z=4$). The hydrogen atom of the carboxylate group in L-MDA is transferred to the amino group of L-Met, which are linked via discrete N1–H1A···O7 hydrogen bonding. This results in two new intramolecular interactions involving the L-MDA⁻ anion, forming two S(5) rings by O7–HO7···O8 and C12–H12···O7 hydrogen bonds. One L-MDA molecule connects with the L-Met⁺ through N1–H1C···O1 and N1–H1C···O2 hydrogen bonding interactions, generating an $R_1^2(5)$ motif, and connects with another L-MDA molecule via O4–HO4···O1 hydrogen bonding interaction (Figure 5.9a). As shown in Figure 5.9b, this unit is extended

via the N1–H1A···O11 and N1–H1B···O11 hydrogen bonding interactions between two L-Met⁺, forming an $R_2^1(4)$ motif. Other N–H···O, O–H···O and C–H···O hydrogen bonding interactions are also present.



(a)



(b)

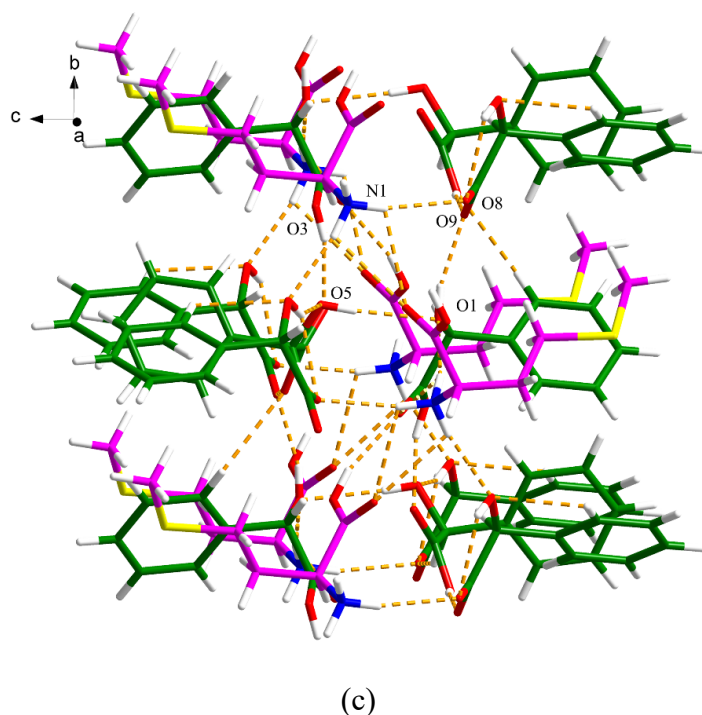


Figure 5.9. Crystal packing and intermolecular interactions in the L-Met-L-MDA: (a) asymmetric unit, (b) and (c) hydrogen-bonded network (hydrogen bonding is displayed by dashed lines).

Obtaining single crystals of L-Met-D-MDA suitable for SCXRD was extremely difficult, due to disorder in the structure, especially over the L-Met component and the phenyl ring of the D-MDA molecule. The SCXRD result from the best attempt shows that L-Met-D-MDA crystallizes with one L-Met molecule and one D-MDA molecule in the asymmetric unit. It appears L-Met-D-MDA is a cocrystal and L-Met is present as a zwitterion, although the poor quality data due to the disorder means this is not completely certain. Therefore, the following description of the crystal structure is based on this model. The two components interact with each other via a discrete $N5-H5C \cdots O15$ hydrogen bond, Figure S5.6a. As shown in

Figure S5.6b, along the c axis, an $R_3^3(9)$ motif and an $R_5^5(21)$ motif are generated among L-Met and D-MDA molecules through O11–H11···O3, N5–H5C···O15, N5–H5B···O3 and C14–H14···O1 hydrogen bond interactions. The 3D crystal lattice is further stabilized by the N5–H5A···O1 hydrogen bond interaction along the b axis.

Hydrogen bonding interactions are generally considered as the most important interactions to govern structure of cocrystals, which show directional preferences (the donor points at the acceptor and the X–H···Y angle is usually linear) and influence packing modes in crystal structures, while secondary interactions such as π – π stacking interactions, electrostatic potential of molecules, etc., may drive the hydrogen bond away from linearity.^{31, 33, 34} However, in addition to the strong hydrogen bonds, the formation of cocrystals can also be affected by van der Waals interactions and steric hindrance, etc., which is not negligible due to the low stabilization free enthalpy of cocrystal formation (on the order of kJ mol^{-1}).³⁵ Crystal lattice energy can be utilized as a quantitative indicator of the stability of cocrystals, which consists of intermolecular electrostatic energy (E_{elec}), intermolecular repulsion-dispersion potential ($E_{\text{r-d}}$), and intramolecular energies (ΔE_{intra}).³⁶ If the lattice energy of the target cocrystal is lower than the sum of each components' lattice energies, the cocrystal is expected to be thermodynamically stable and, likely, can be formed, and vice versa. Springuel *et al.* illustrated the comparison of crystal lattice energies of cocrystal and its components, and demonstrated that the stabilization free energy of cocrystal formation is usually

small ($\leq 10 \text{ kJ mol}^{-1}$) since the lattice energy of a cocrystal is generally similar to that of the sum of each component.³¹ This can explain the low successful rate when conducting cocrystal screening, and even a small change (such as the change in chirality) in the structure of the cocrystallizing component can change the outcome of cocrystal screening. The changes of these interactions may make the cocrystal lattice energy larger than that of the sum of each component, as a result, in some cases a chiral compound can only form an enantiospecific cocrystal with only one enantiomer. In this study, distinctive graph-set motifs were observed in two enantiospecific cocrystals L-Leu-D-MDA [C(5) & $R_1^2(5)$], L-Ile-L-PLA [$R_1^2(5)$ & $R_2^2(6)$], and one enantiospecific molecular salt, L-His-L-MA [$R_1^2(5)$]. Since no diastereomeric cocrystal pairs were found for these systems in the conducted experiments, a reasonable hypothesis is that these hydrogen-bonding interactions may contribute to their energetically favourable formation compared to diastereomeric systems.³⁷

For the formation of a diastereomeric cocrystal pair, more changes in the hydrogen bonding network and molecular arrangement are required in order to reduce the influence of the secondary interactions and steric effects to the total cocrystal stabilization energy.³¹ A summary of the graph-set motif of L-amino acids with enantiomers of the four chiral cofomers in both this work and the literature is displayed in Table S5.8. L-Lys can form a diastereomeric cocrystal pair with both enantiomer of TA in a 1:1 ratio.²¹ Both amino group and carboxylic group of L-Lys are involved in the formation of an $R_2^2(10)$ motif with L-TA in L-Lys-L-TA,

while a significant difference in hydrogen-bonding interactions can be observed in L-Lys-D-TA, i.e., two L-Lys and one D-TA form an $R_3^3(19)$ motif, leading to the remarkable changes in the crystal packing. Leysens and co-workers demonstrated that both *R*- and *S*-enantiomers of mandelic acid can be resolved using L-proline as a resolving agent from a racemic mixture by varying the stoichiometry (1:1 for L-proline-*R*-mandelic acid, and 2:1 for L-proline-*S*-mandelic acid),²⁸ where the hydrogen bonding of the two cocrystals vary significantly. In this example, L-Met can form a stoichiometrically diverse diastereomeric cocrystal pair with L- and D-MDA. Although the crystal structural analysis of L-Met-D-MDA was based on the disordered model, some significant differences in hydrogen bonding and crystal packing between the two cocrystals can be observed. For instance, the ratio of L-Met-L-MDA is 1:3 and the proton transfer occur between the L-Met⁺ and the L-MDA⁻. In contrast, the ratio of L-Met and D-MDA in L-Met-D-MDA cocrystal is 1:1, and L-Met exists as a zwitterion, which is similar to the form of L-amino acids in the majority cocrystals. Furthermore, an $R_1^2(5)$ motif is observed in the L-Met-L-MDA cocrystal while an $R_3^3(9)$ motif and an $R_5^5(21)$ motif can be found in the crystal structure of the L-Met-D-MDA cocrystal, which can further rationalize the formation of the diastereomeric cocrystal pair of L-Met with both enantiomers of MDA.

5.5 Conclusions

In this work, cocrystal screening of 19 L-amino acids with both enantiomers of TA, MDA, MA and 3-PLA was carried out. 22 new phases were obtained, consisting of seven diastereomeric cocrystal pairs and eight enantiospecific cocrystals. This indicates that diastereomeric cocrystals account for 14% while enantiospecific cocrystals make up 17% out of the 76 cocrystallizing systems examined. After multiple attempts, two enantiospecific cocrystals, L-Leu-D-MDA and L-Ile-L-PLA, along with one enantiospecific salt, L-His-L-MA, were successfully obtained, and their crystal structures were determined. Additionally, a diastereomeric cocrystal pair involving L-Met and D / L-MDA in stoichiometric ratios of 1:1 and 1:3, respectively, was synthesized. Although the reliable crystal structure of L-Met-D-MDA could not be determined due to significant structural disorder, the hydrogen-bonding patterns and crystal packings of these two cocrystals showed notable differences. Based on the analysis of graph-set motifs in the five crystal structures examined in this study and the previously reported enantiospecific / diastereomeric systems involving 19 L-amino acids with both enantiomers of four cofomers, the presence of hydrogen bonding in enantiospecific cocrystals may contribute to the formation of energetically favourable systems, while more changes in hydrogen bonding network and / or stoichiometric ratio of diastereomeric cocrystal pairs are observed. Overall, this investigation yielded valuable insights into the formation of diastereomeric and enantiospecific cocrystals between L-amino acids and chiral cofomers. Subsequent research will continue to focus on investigating the

cocrystallization behaviour of chiral APIs and chiral coformers, as well as the development of corresponding separation methods.

REFERENCES

- (1) Flack, H. D., Louis Pasteur's discovery of molecular chirality and spontaneous resolution in 1848, together with a complete review of his crystallographic and chemical work. *Acta Cryst.* **2009**, A65, 371–389.
- (2) Jayakumar, R.; Vadivel, R.; Ananthi, N., Role of Chirality in Drugs. *Organic & Medicinal Chem. IJ* **2018**, 5, 555661.
- (3) McConathy, J.; Owens, M. J., Stereochemistry in Drug Action. *Prim. Care Companion J. Clin. Psychiatry.* **2003**, 5, 70–73.
- (4) Ananthi, N., Role of Chirality in Drugs. *OMCIJ.* **2018**, 5, 555661.
- (5) Brooks, W. H.; Guida, W. C.; Daniel, K. G., The Significance of Chirality in Drug Design and Development. *Curr. Top. Med. Chem.* **2011**, 11, 760–770.
- (6) Cedillo-Cruz, A.; Aguilar, M. I.; Flores-Alamo, M.; Palomares-Alonso, F.; Jung-Cook, H., A straightforward and efficient synthesis of praziquantel enantiomers and their 4'-hydroxy derivatives. *Tetrahedron: Asymmetry* **2014**, 25, 133–140.
- (7) Leonard, W. R., Jr.; Henderson, D. W.; Miller, R. A.; Spencer, G. A.; Sudah, O. S.; Biba, M.; Welch, C. J., Strategic use of preparative chiral chromatography for the synthesis of a preclinical pharmaceutical candidate.

Chirality **2007**, 19, 693–700.

- (8) Reflection paper on the use of cocrystals of active substances in medicinal products. https://www.ema.europa.eu/en/documents/scientific-guideline/reflection-paper-use-cocrystals-active-substances-medicinal-products_en.pdf **2015**.
- (9) Sánchez-Guadarrama, O.; Mendoza-Navarro, F.; Cedillo-Cruz, A.; Jung-Cook, H.; Arenas-García, J. I.; Delgado-Díaz, A.; Herrera-Ruiz, D.; Morales-Rojas, H.; Höpfl, H., Chiral Resolution of *RS*-Praziquantel via Diastereomeric Co-Crystal Pair Formation with L-Malic Acid. *Cryst. Growth Des.* **2015**, 16, 307–314.
- (10) Springuel, G.; Leyssens, T., Innovative Chiral Resolution Using Enantiospecific Co-Crystallization in Solution. *Cryst. Growth Des.* **2012**, 12, 3374–3378.
- (11) Moura, A.; Savageau, M. A.; Alves, R., Relative Amino Acid Composition Signatures of Organisms and Environments. *PLoS One* **2013**, 8, e77319.
- (12) Fu, Y.; Han, Q.; Chen, Q.; Wang, Y.; Zhou, J.; Zhang, Q., A new strategy for chiral recognition of amino acids. *Chem. Commun.* **2012**, 48, 2322–2324.
- (13) Tumanova, N.; Payen, R.; Springuel, G.; Norberg, B.; Robeyns, K.; Le Duff, C.; Wouters, J.; Leyssens, T., Cocrystallization out of the blue: DL-mandelic acid/ethyl-DL-mandelate cocrystal. *J. Mol. Struct.* **2017**, 1127, 397–402.

- (14) Eddleston, M. D.; Arhangelkis, M.; Frišćić, T.; Jones, W., Solid state grinding as a tool to aid enantiomeric resolution by cocrystallisation. *Chem. Commun.* **2012**, 48, 11340–11342.
- (15) STOE Powder Diffraction Software Package WinX^{POW}, *STOE*.
<https://www.stoe.com/product/software-powder-xrd/>
- (16) Sheldrick, G. M., Crystal structure refinement with SHELXL. *Acta Cryst.* **2015**, C71, 3–8.
- (17) APEX2 v2009.3-0. *Bruker AXS* **2009**.
- (18) Huang, S.; Xu, J.; Peng, Y.; Guo, M.; Cai, T., Facile Tuning of the Photoluminescence and Dissolution Properties of Phloretin through Cocrystallization. *Cryst. Growth Des.* **2019**, 19, 6837–6844.
- (19) Xu, J.; Huang, Y.; Ruan, S.; Chi, Z.; Qin, K.; Cai, B.; Cai, T., Cocrystals of isoliquiritigenin with enhanced pharmacokinetic performance. *CrystEngComm* **2016**, 18, 8776–8786.
- (20) Spek, A. L., Structure validation in chemical crystallography. *Acta Cryst.* **2009**, D65, 148–155.
- (21) Selvaraj, M.; Thamocharan, S.; Roy, S.; Vijayan, M., X-ray studies of crystalline complexes involving amino acids and peptides. XLIV. Invariant features of supramolecular association and chiral effects in the complexes of arginine and lysine with tartaric acid. *Acta Cryst.* **2007**, B63, 459–468.
- (22) Natarajan, S.; Hema, V.; Sundar, J. K.; Suresh, J.; Lakshman, P. L., L-Asparagine-L-tartaric acid (1/1). *Acta Cryst.* **2010**, C66, o2239.

- (23) Shan, Y.; Huang, S. D., Crystal structure of L-cysteine L-tartarate monohydrate, $C_7H_{15}NO_9S$. *Z. Kristallogr. NCS.* **1999**, 214, 41–42.
- (24) Hu, Z. Q.; Xu, D. J.; Xu, Y. Z., (*S*)-Alanine–(*S*)-mandelic acid (1/1). *Acta Cryst.* **2004**, E60, o269–o271.
- (25) Hu, Z. Q.; Xu, D. J.; Xu, Y. Z.; Wu, J. Y.; Chiang, M. Y., (*R*)-Mandelic acid (*S*)-alanine hemihydrate. *Acta Cryst.* 2002, **C58**, o612–o614.
- (26) Fujii, I.; Baba, H.; Takahashi, Y., Crystal Structures of L-(*R*)-Cysteine-Mandelic Acid Diastereomers. *Anal. Sci.* **2005**, 21, x175–x176.
- (27) Okamura, K.; Aoe, K. i.; Hiramatsu, H.; Nishimura, N.; Sato, T.; Hashimoto, K., Crystal Structures of Diastereomeric 1:1 Complexes of (*R*)- and (*S*)-Phenylalanine (*S*)-Mandelic Acid. *Anal. Sci.* **1997**, 13, 315–317.
- (28) Zhou, F.; Collard, L.; Robeyns, K.; Leyssens, T.; Shemchuk, O., L-Proline, a resolution agent able to target both enantiomers of mandelic acid: an exciting case of stoichiometry controlled chiral resolution. *Chem. Commun.* **2022**, 58, 8560–8563.
- (29) Fujii, I., Crystal Structure of L-(*S*)-Tryptophane D-(*R*)-mandelate $1.5H_2O$. *X-ray Struct.* **2009**, 25, 35–36.
- (30) Huang, S.; Fitzgerald, D.; Collins, S. G.; Maguire, A. R.; Lawrence, S. E., Exploring the Crystal Landscape of Mandelamide. *Cryst. Growth Des.* **2023**, Submitted.
- (31) Springuel, G.; Robeyns, K.; Norberg, B.; Wouters, J.; Leyssens, T., Cocrystal Formation between Chiral Compounds: How Cocrystals Differ

- from Salts. *Cryst. Growth Des.* **2014**, 14, 3996–4004.
- (32) Habgood, M., Analysis of Enantiospecific and Diastereomeric Cocrystal Systems by Crystal Structure Prediction. *Cryst. Growth Des.* **2013**, 13, 4549–4558.
- (33) Arunan, E.; Desiraju, G. R.; Klein, R. A.; Sadlej, J.; Scheiner, S.; Alkorta, I.; Clary, D. C.; Crabtree, R. H.; Dannenberg, J. J.; Hobza, P.; Kjaergaard, H. G.; Legon, A. C.; Mennucci, B.; Nesbitt, a. D. J., Definition of the hydrogen bond (IUPAC Recommendations 2011). *Pure Appl. Chem.* **2011**, 83, 1637–1641.
- (34) Shahi, A.; Arunan, E., Why are Hydrogen Bonds Directional? *Chem. Sci. J.* **2016**, 128, 1571–1577.
- (35) Taylor, C. R.; Day, G. M., Evaluating the Energetic Driving Force for Cocrystal Formation. *Cryst. Growth Des.* **2018**, 18, 892–904.
- (36) Issa, N.; Karamertzanis, P. G.; Welch, G. W. A.; Price, S. L., Can the Formation of Pharmaceutical Cocrystals Be Computationally Predicted? I. Comparison of Lattice Energies. *Cryst. Growth Des.* **2009**, 9, 442–453.
- (37) Nulek, T.; Klaysri, R.; Cedeno, R.; Nalaoh, P.; Bureekaew, S.; Promarak, V.; Flood, A. E., Separation of Etiracetam Enantiomers Using Enantiospecific Cocrystallization with 2-Chloromandelic Acid. *ACS Omega* **2022**, 7, 19465–19473.

Supporting Information

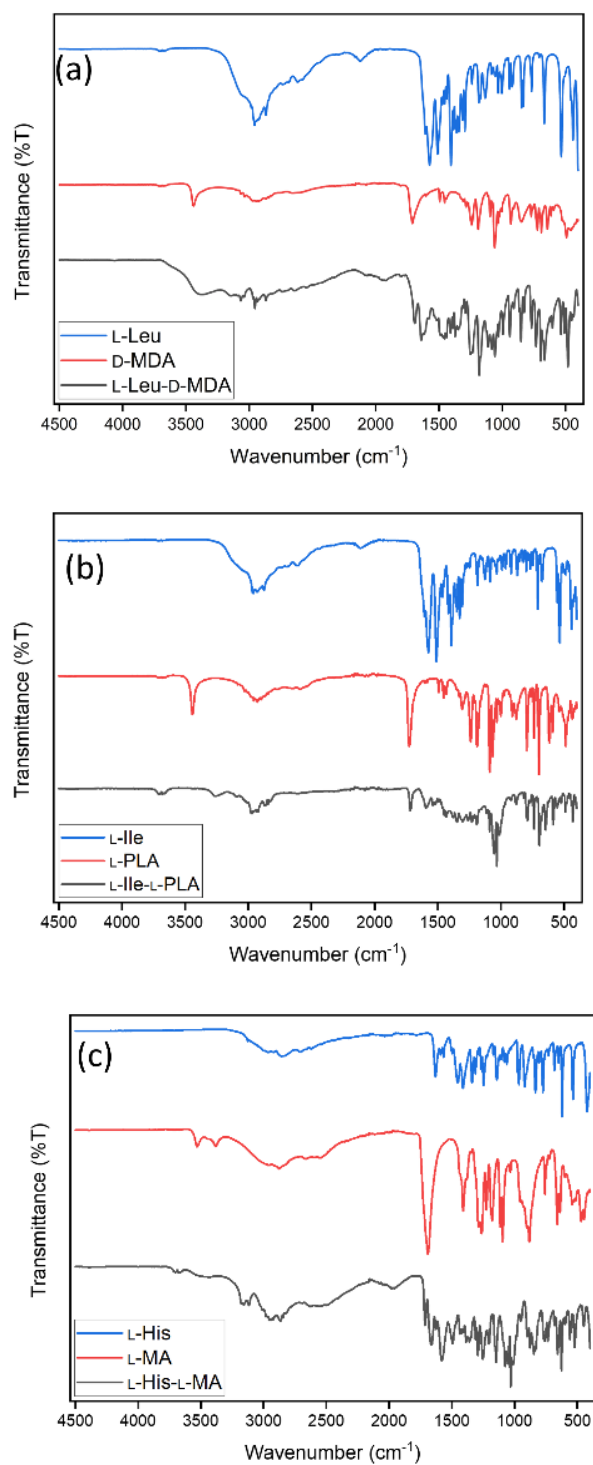
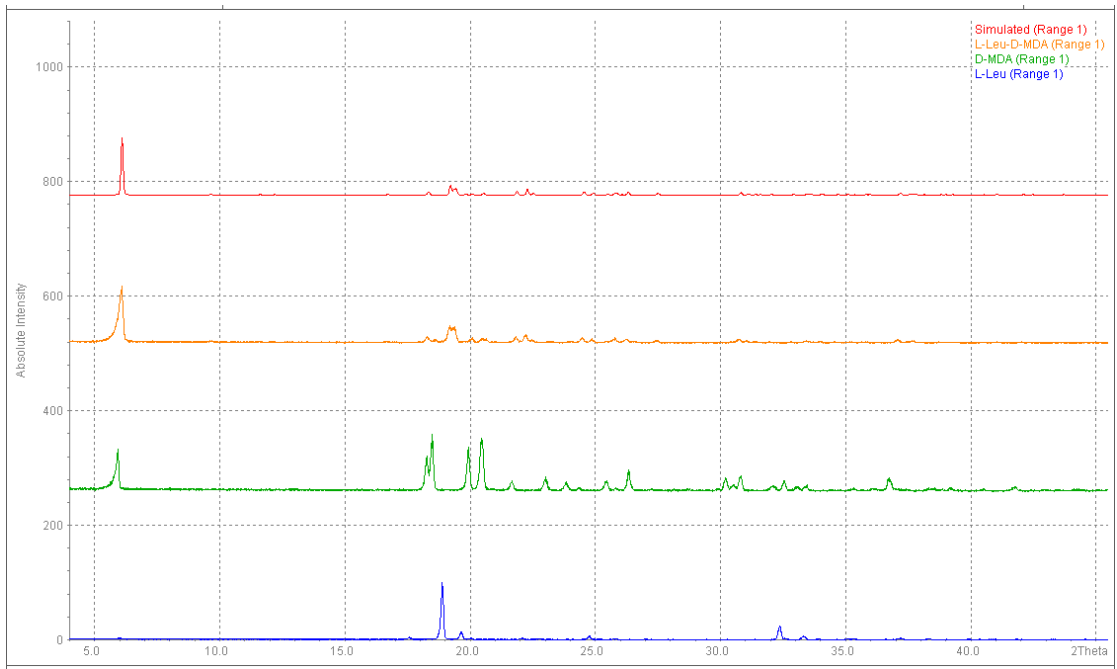
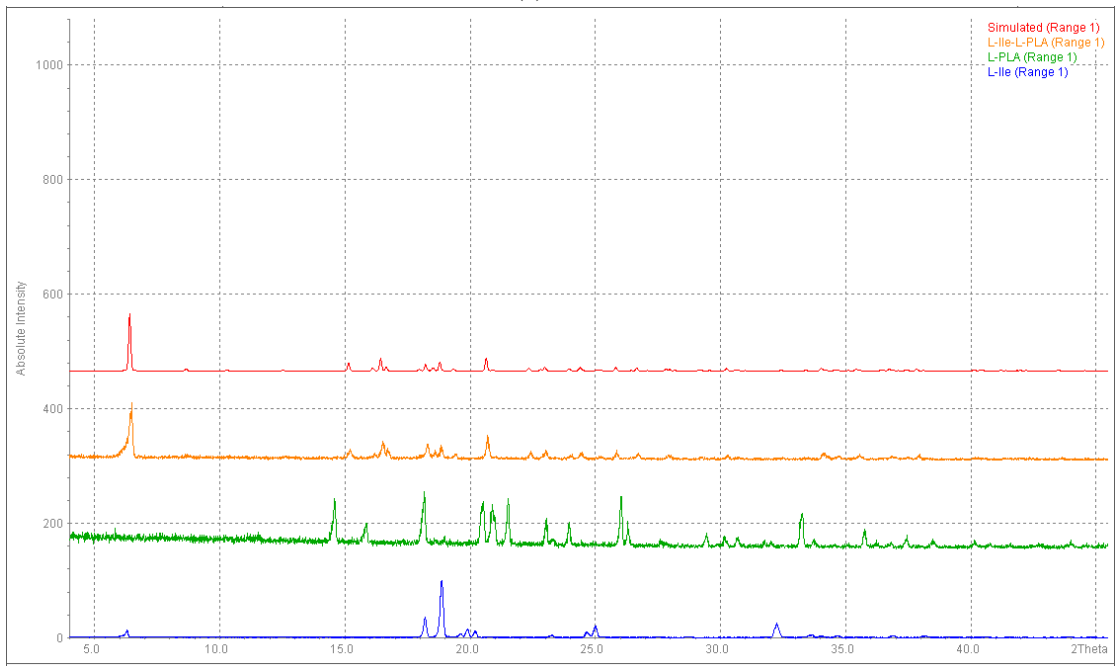


Figure S5.1. IR spectra of (a) L-Leu (blue), D-MDA (red) and L-Leu-D-MDA (black), (b) L-Ile (blue), L-PLA (red) and L-Ile-L-PLA (black), and (c) L-His (blue), L-MA (red) and L-His-L-MA (black).



(a)

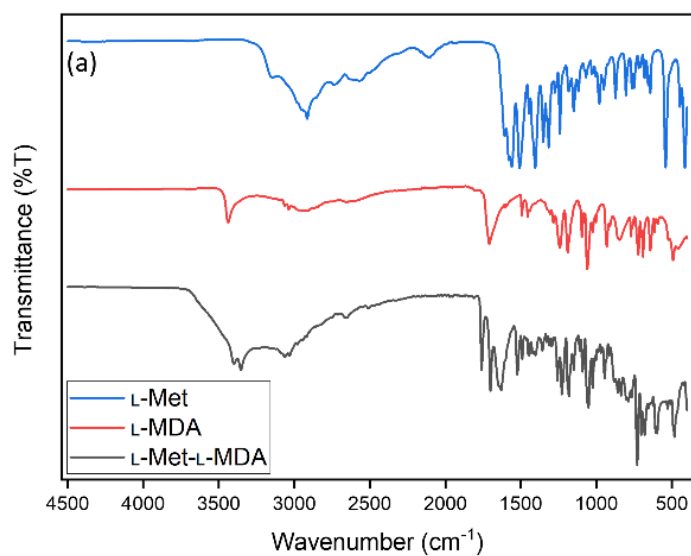


(b)



(c)

Figure S5.2. PXR D patterns of (a) L-Leu (blue), D-MDA (green) and L-Leu-D-MDA cocrystal (orange) and simulated pattern from the crystal structure (red); (b) L-Ile (orange), L-PLA (green) and L-Ile-L-PLA cocrystal (black) and simulated pattern from the crystal structure (red); and (c) L-His (blue), L-MA (green) and L-His-L-MA salt (orange) and simulated pattern from the crystal structure (red).



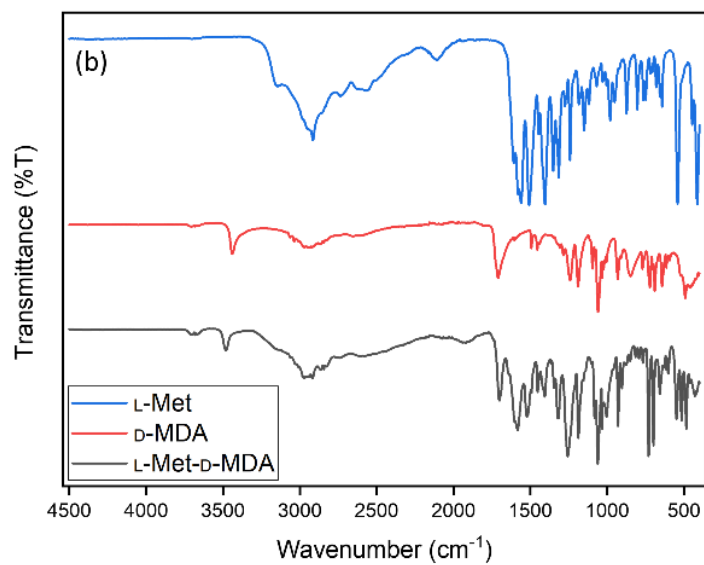
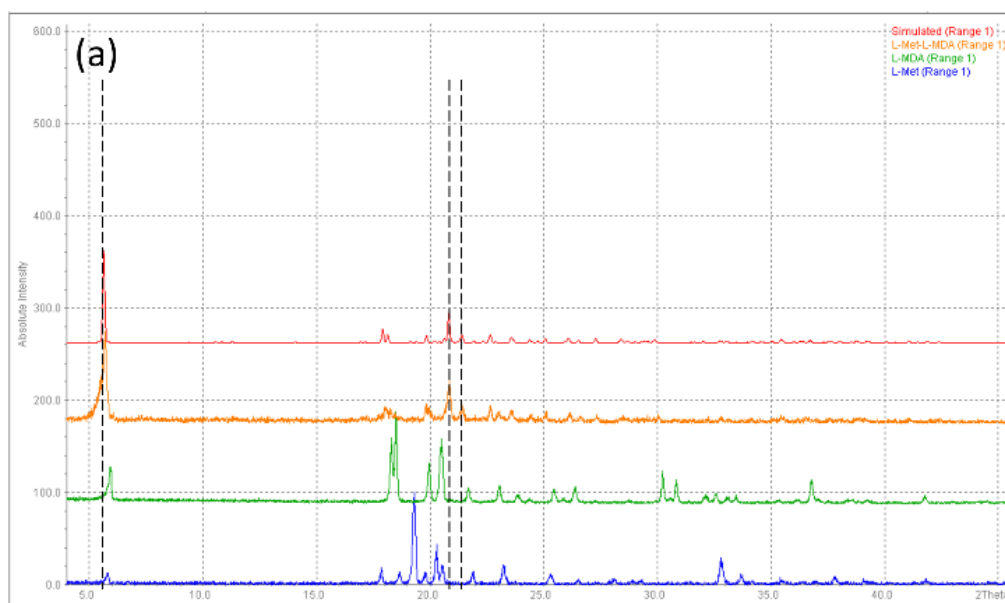


Figure S5.3. IR spectra of (a) L-Met (blue), L-MDA (red) and L-Met-L-MDA (black), and (b) L-Met (blue), D-MDA (red) and L-Met-L-MDA (black).



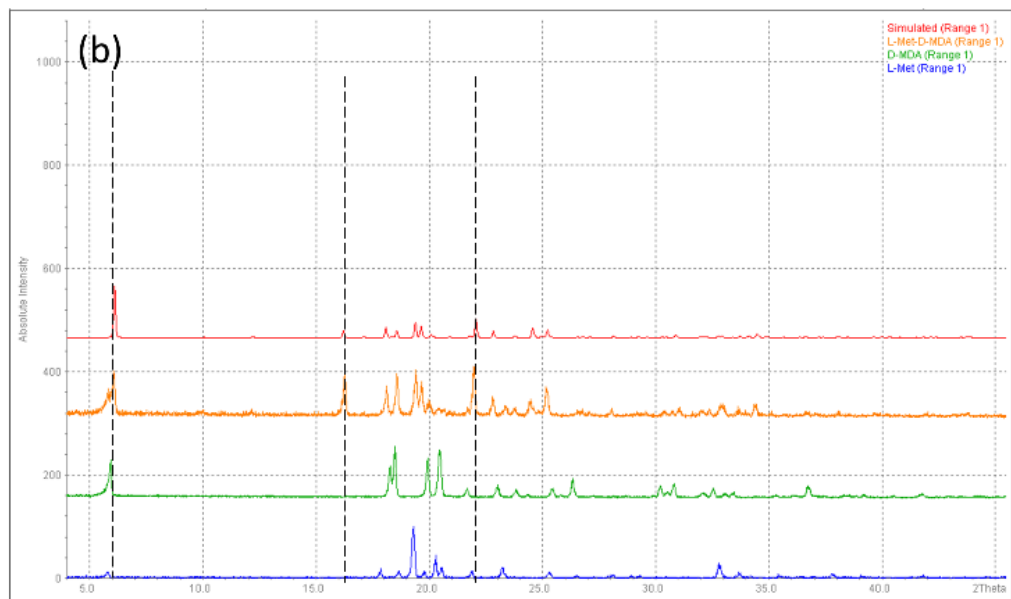
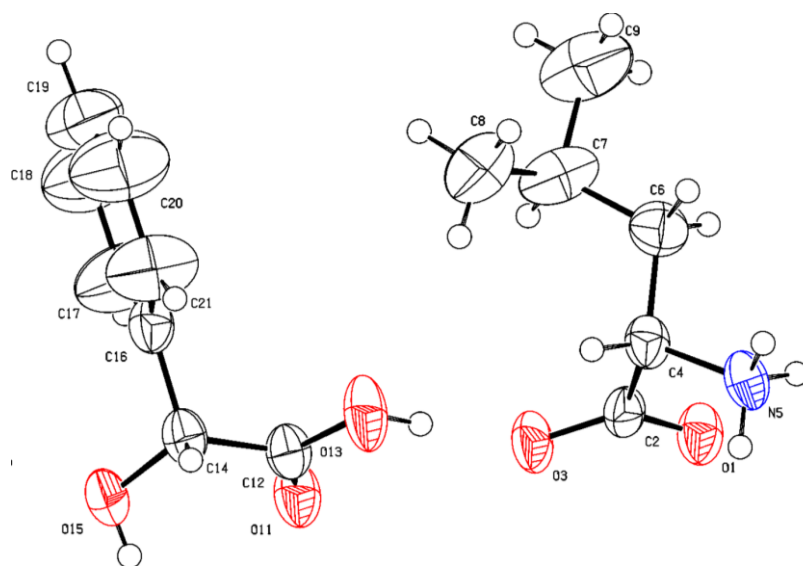
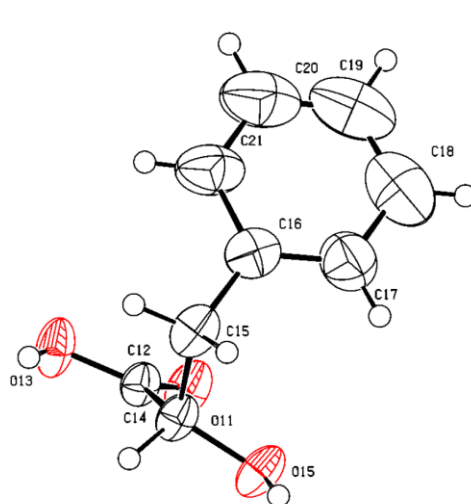
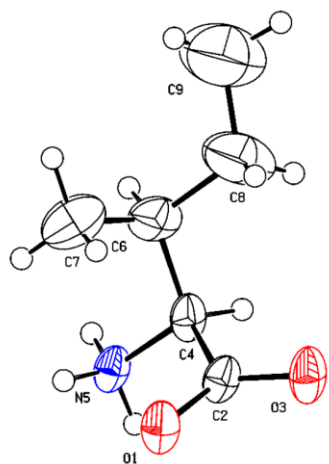


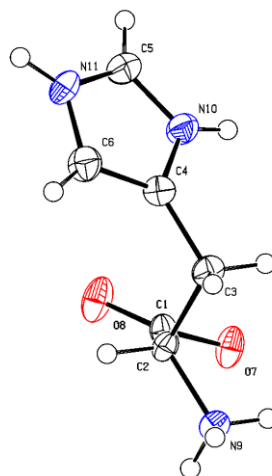
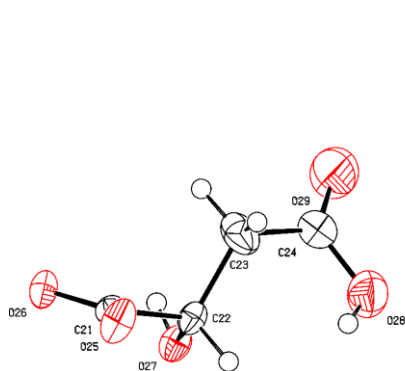
Figure S5.4. PXRD patterns of (a) L-Met (blue), L-MDA (green), L-Met-L-MDA cocystal (orange) and simulated pattern from the crystal structure (red), and (b) L-Met (blue), D-MDA (green), L-Met-D-MDA cocystal (orange) and simulated pattern from the crystal structure (red).



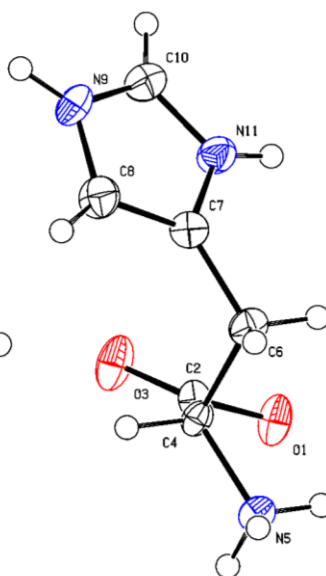
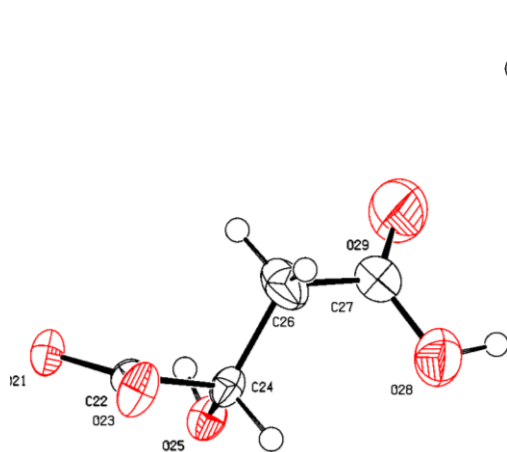
(a)



(b)



(c)



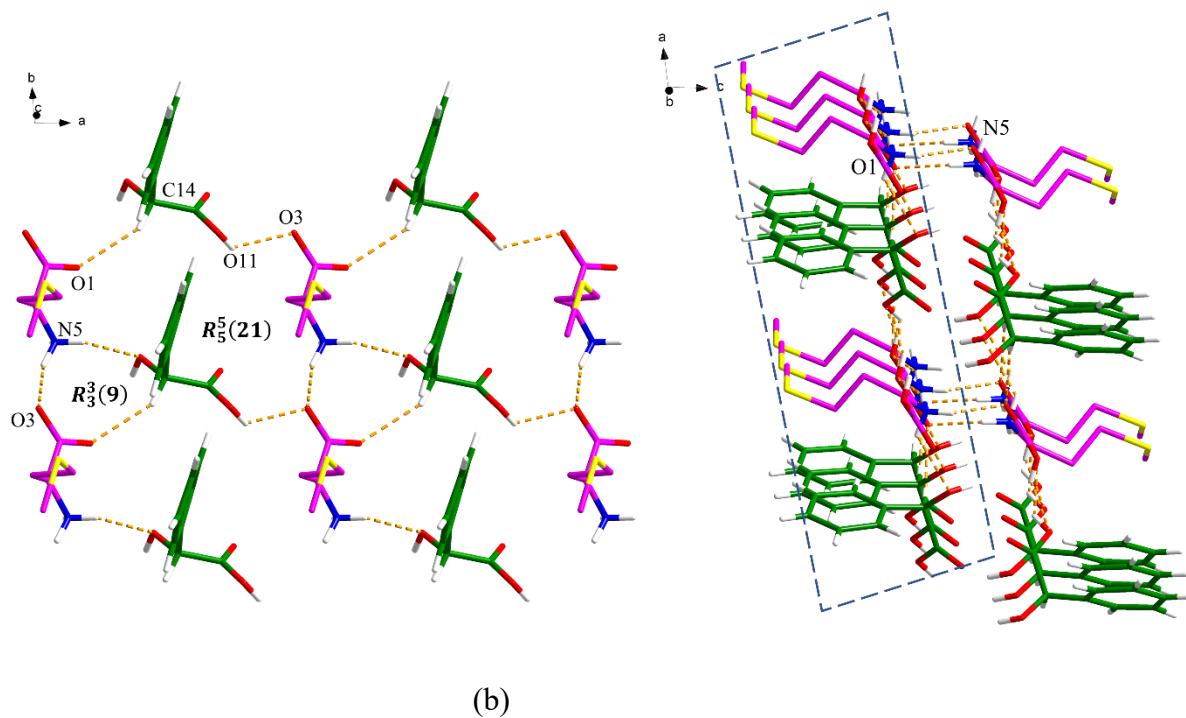


Figure S5.6. Crystal packing and intermolecular interactions in the L-Met-D-MDA: (a) asymmetric unit and (b) hydrogen-bonded network (hydrogen bonding is displayed by dashed lines).

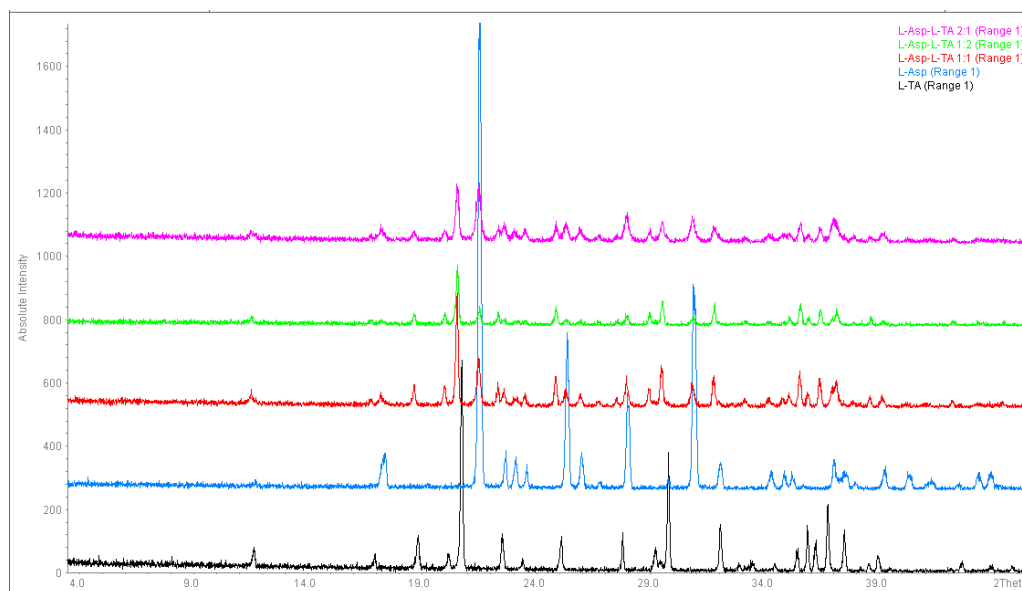


Figure S5.7. PXRD patterns of L-TA (black), L-Asp (blue) and the products obtained from the experiments of L-Asp with L-TA in 1:1 (red), 1:2 (green) and 2:1 (pink) ratio.

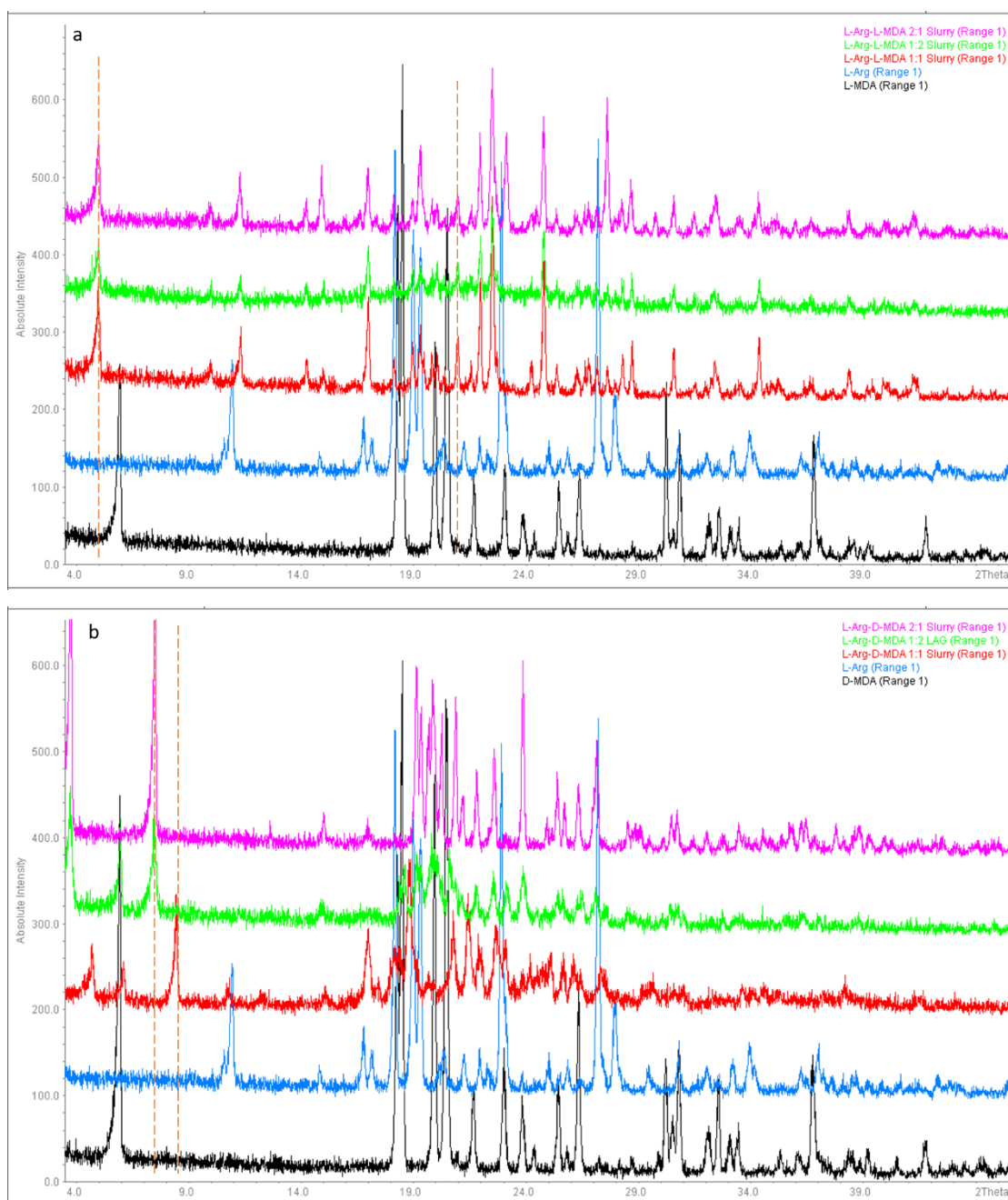


Figure S5.8. PXRD patterns of (a) L-MDA (black), L-Arg (blue) and the products obtained from the experiments of L-Arg with L-MDA in 1:1 (red), 1:2 (green) and 2:1 (pink) ratio; (b) D-MDA (black), L-Arg (blue) and the products obtained from the experiments of L-Arg with D-MDA in 1:1 (red), 1:2 (green) and 2:1 (pink) ratio.

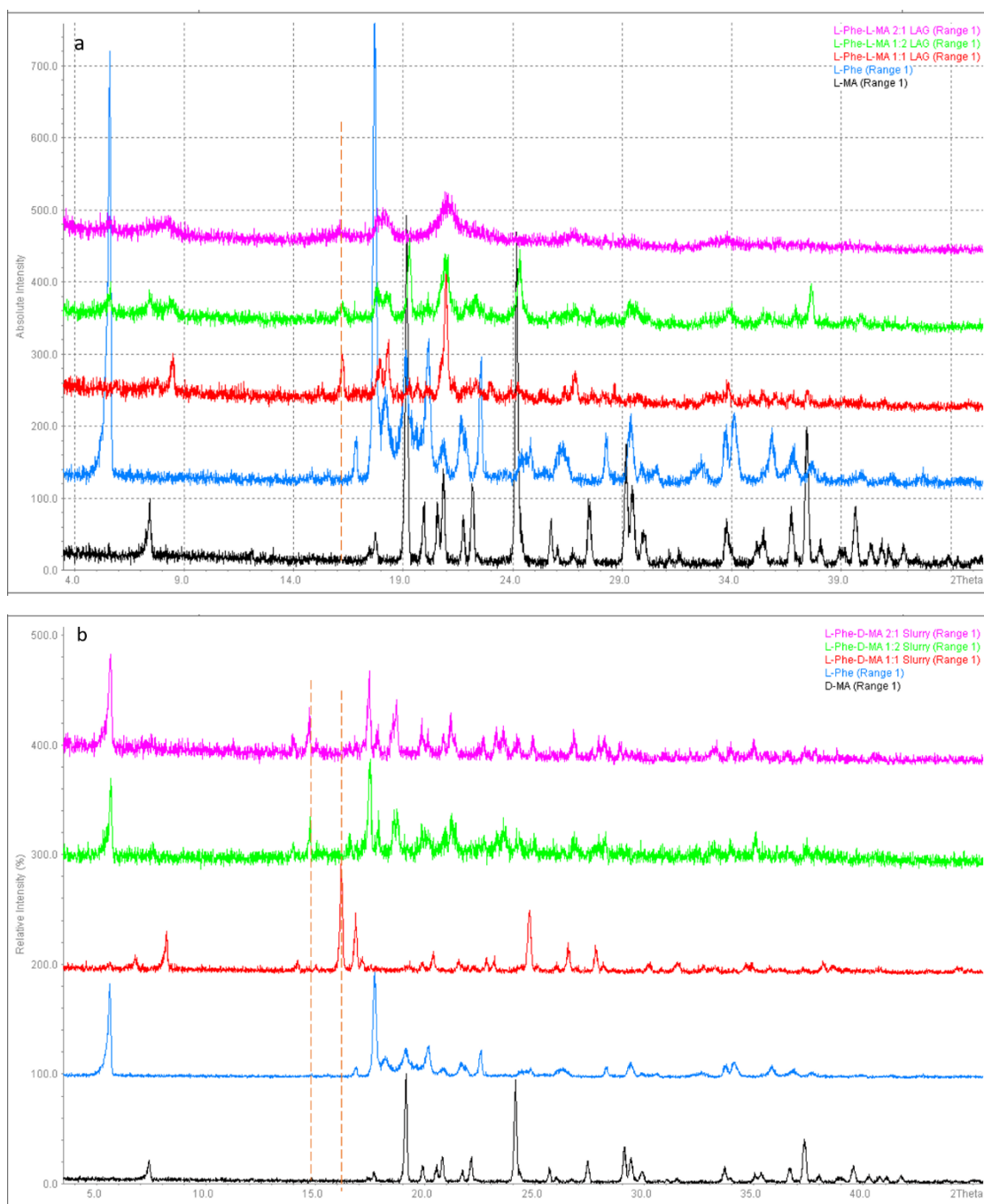


Figure S5.9. PXRD patterns of (a) L-MA (black), L-Phe (blue) and the products obtained from the experiments of L-Phe with L-MA in 1:1 (red), 1:2 (green) and 2:1 (pink) ratio; (b) D-MA (black), L-Phe (blue) and the products obtained from the experiments of L-Phe with D-MA in 1:1 (red), 1:2 (green) and 2:1 (pink) ratio.

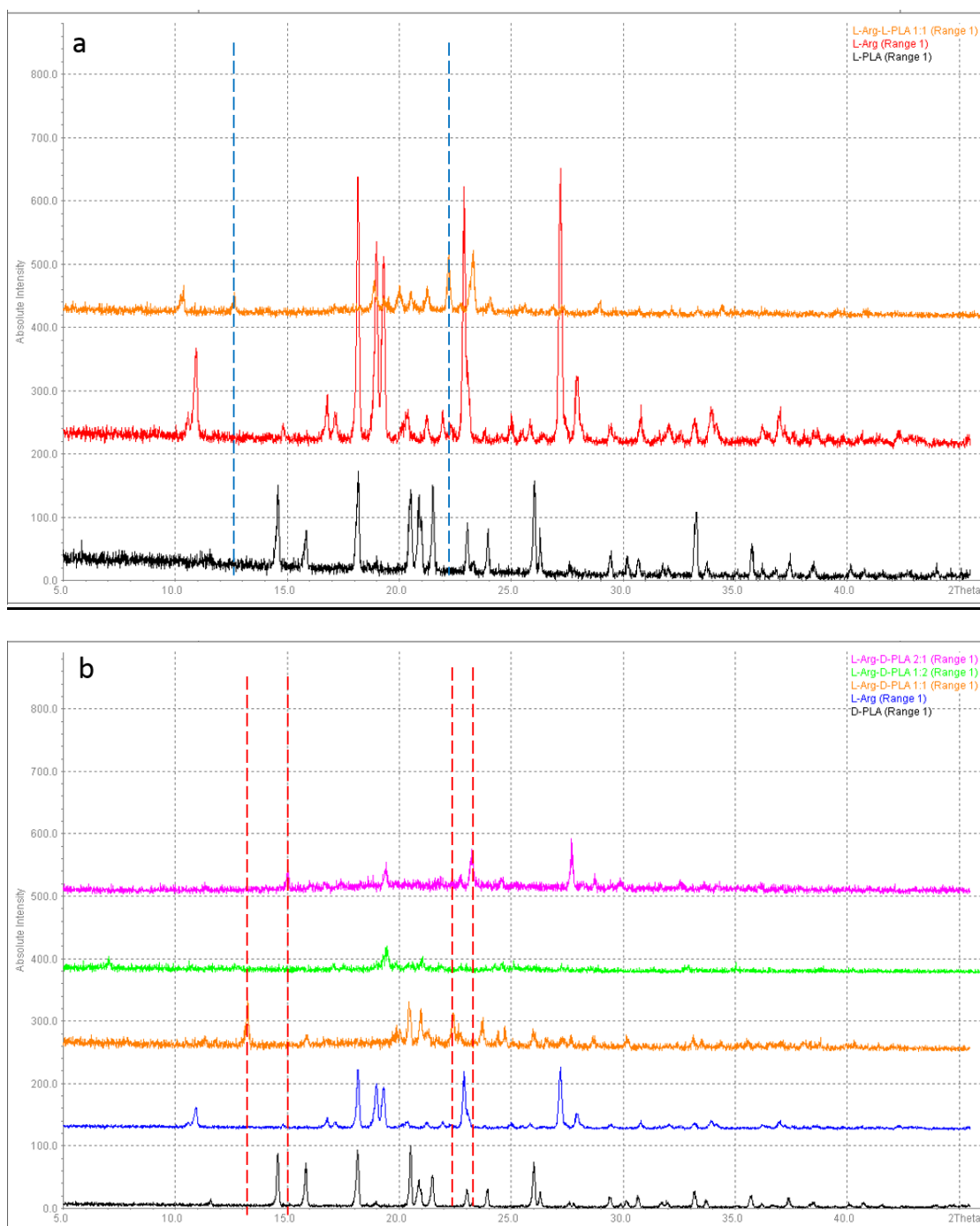


Figure S5.10. PXRD patterns of (a) L-PLA (black), L-Arg (red) and the products obtained from the experiments of L-Arg with L-PLA in 1:1 ratio (orange); (b) D-PLA (black), L-Arg (blue) and the products obtained from the experiments of L-Arg with D-PLA in 1:1 (orange), 1:2 (green) and 2:1 (pink) ratio.

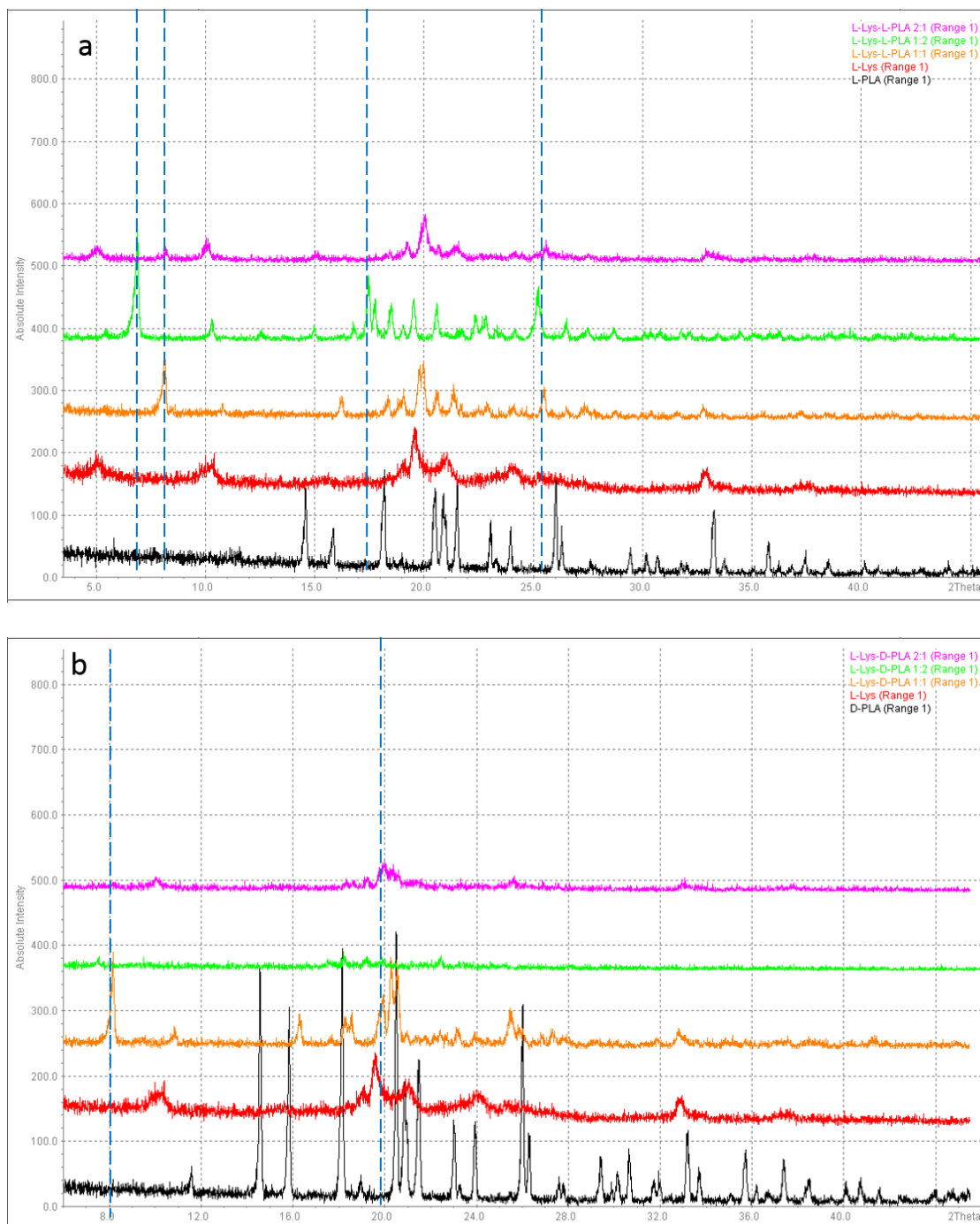


Figure S5.11. PXRD patterns of (a) L-PLA (black), L-Lys (red) and the products obtained from the experiments of L-Lys with L-PLA in 1:1 (orange), 1:2 (green) and 2:1 (pink) ratio; (b) D-PLA (black), L-Lys (red) and the products obtained from the experiments of L-Lys with D-PLA in 1:1 (orange), 1:2 (green) and 2:1 (pink) ratio.

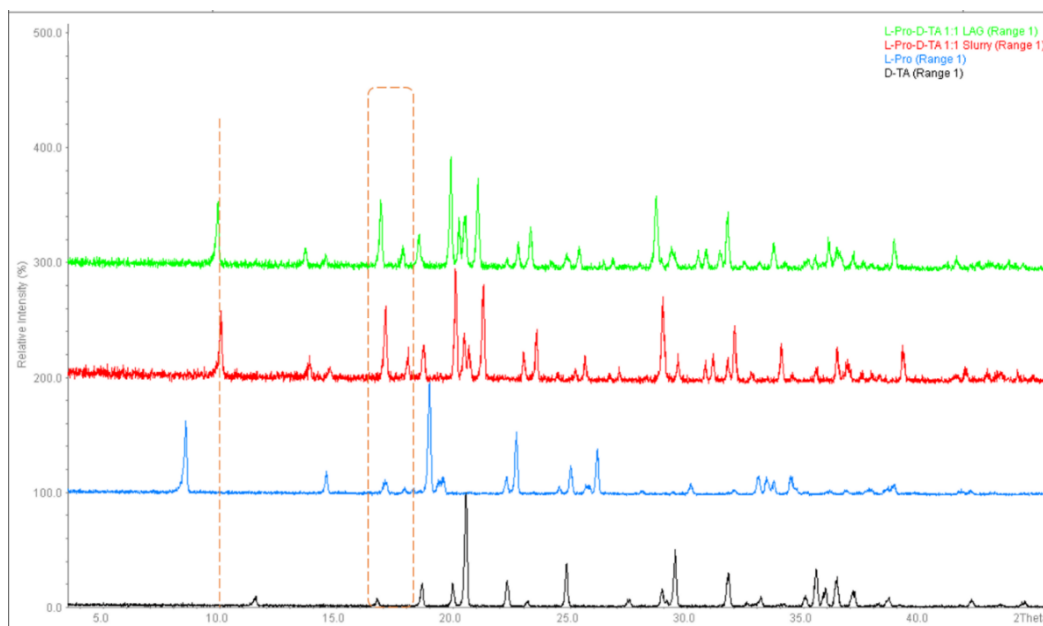


Figure S5.12. PXRD patterns of (a) D-TA (black), L-Pro (blue) and the products of L-Pro with D-TA in 1:1 obtained from the LAG experiments (red) and the slurry experiment (green).

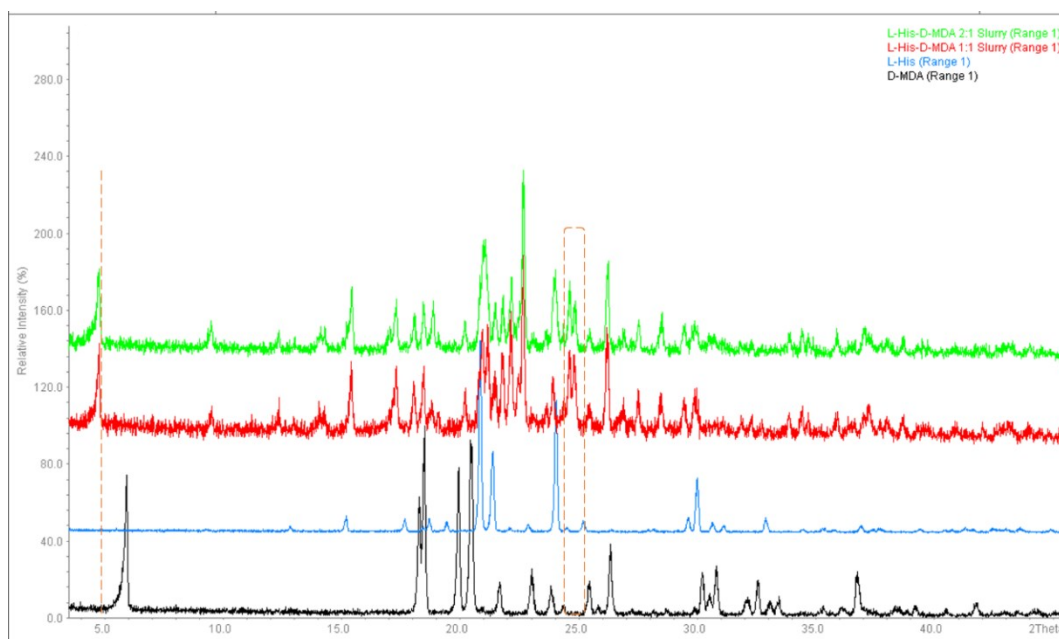


Figure S5.13. PXRD patterns of D-MDA (black), L-His (blue) and the products of L-His with D-MDA in 1:1 (red) and 2:1 (green) ratio.

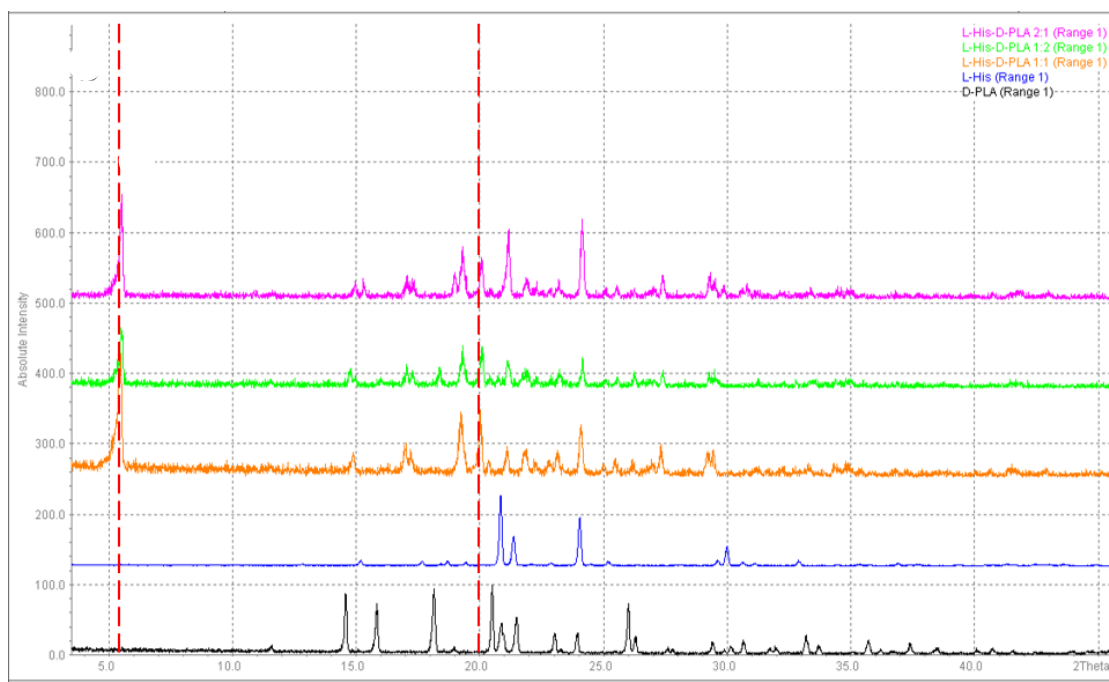


Figure S5.14. PXR D patterns of D-PLA (black), L-His (blue) and the product of L-His with D-PLA in 1:1 (orange), 1:2 (green) and 2:1 (pink) ratio.

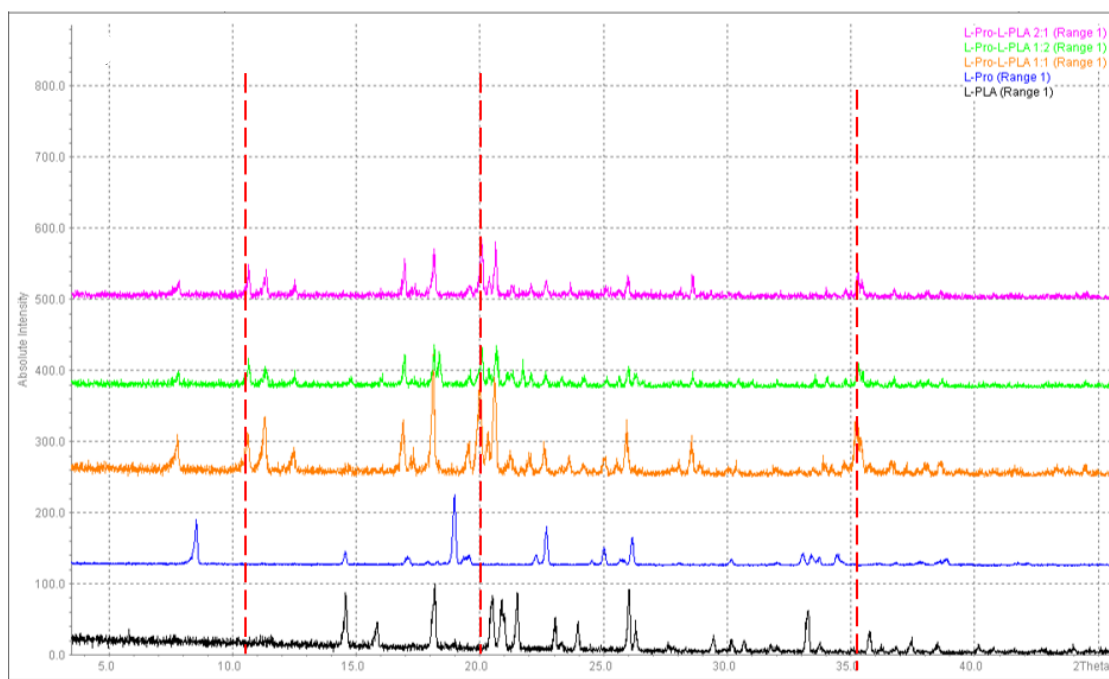


Figure S5.15. PXR D patterns of (a) L-PLA (black), L-Pro (blue) and the of L-Pro with L-PLA in 1:1 (orange), 1:2 (green) and 2:1 (pink) ratio.

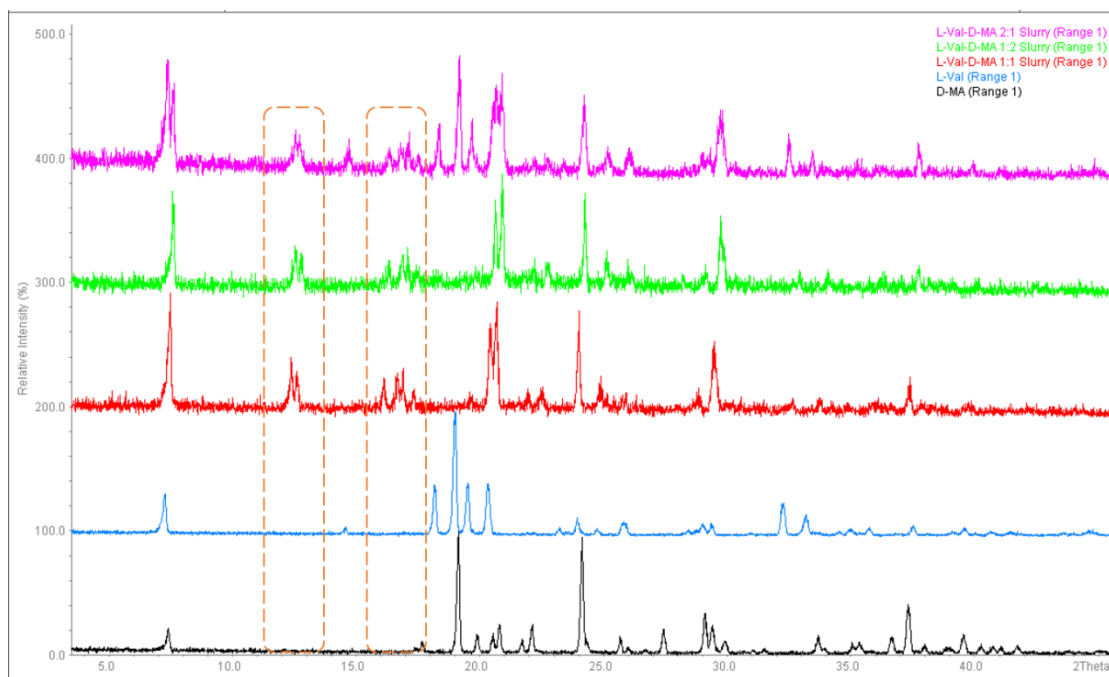
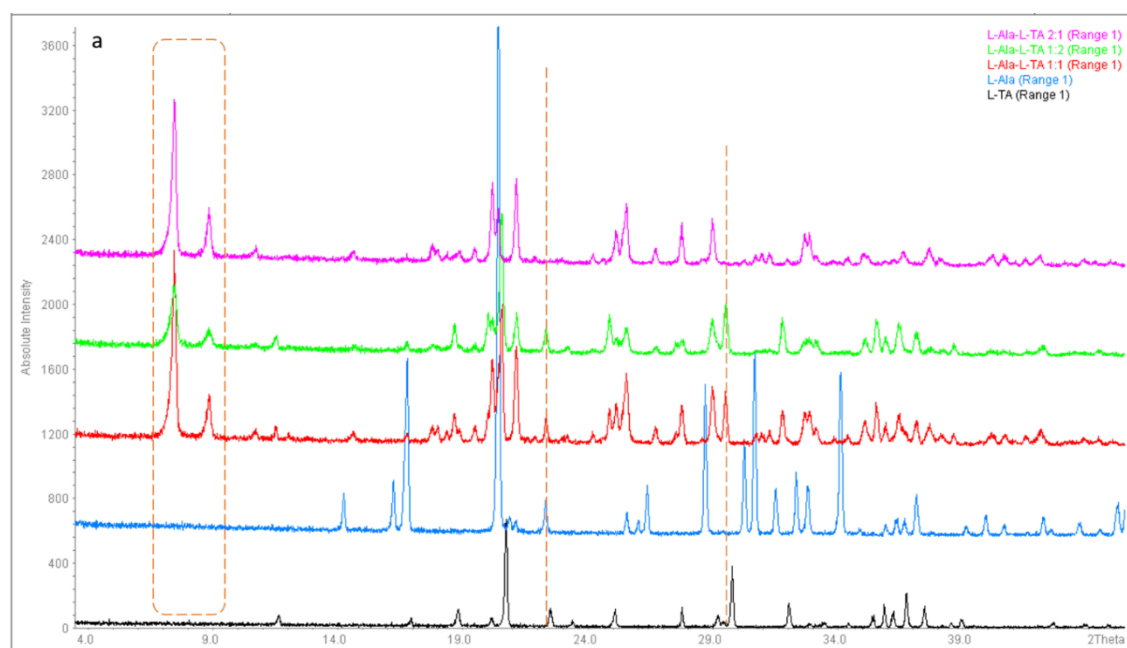


Figure S5.16. PXRD patterns of D-MA (black), L-Val (blue) and the products of L-Val with D-MA in 1:1 (red), 1:2 (green) and 2:1 (pink) ratio.



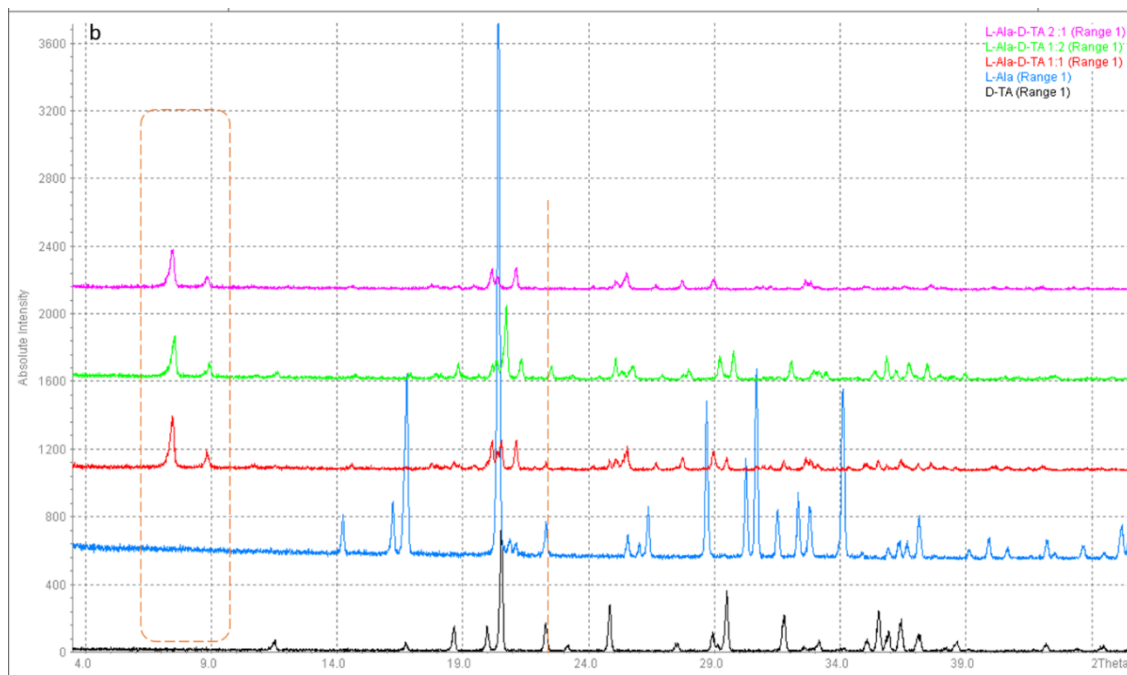
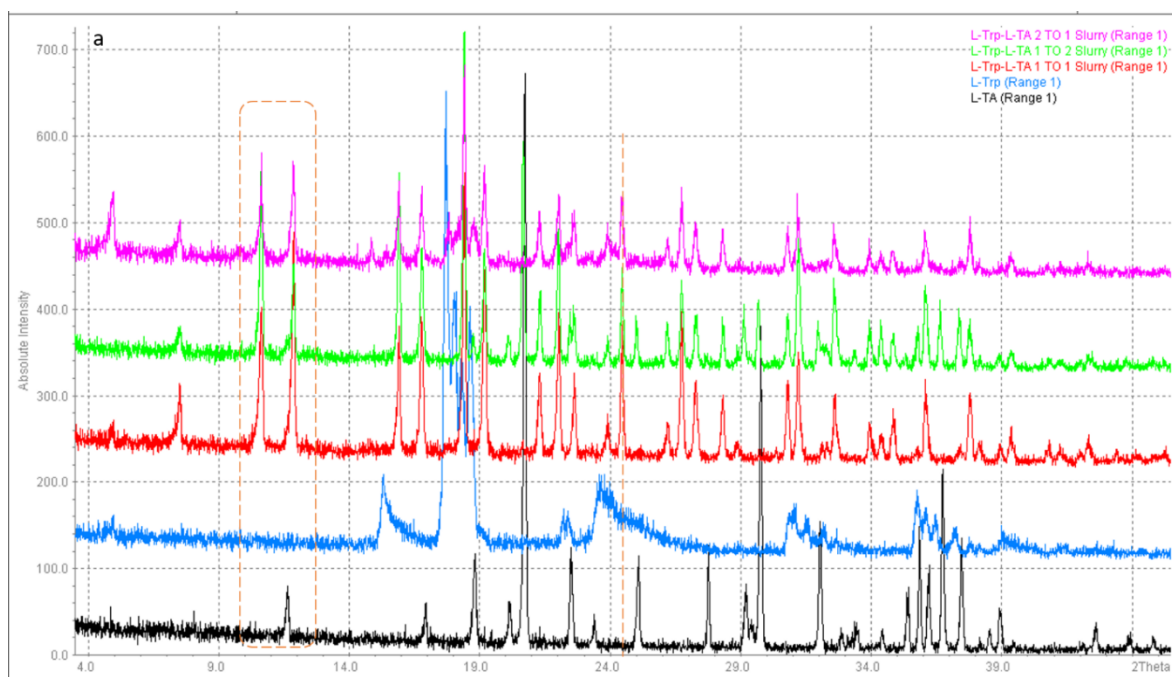


Figure S5.17. PXR D patterns of (a) L-TA (black), L-Ala (blue) and the of L-Ala with L-TA in 1:1 (red), 1:2 (green) and 2:1 (pink) ratio and (b) D-TA (black), L-Ala (blue) and the product of L-Ala with D-TA in 1:1 (red), 1:2 (green) and 2:1 (pink) ratio



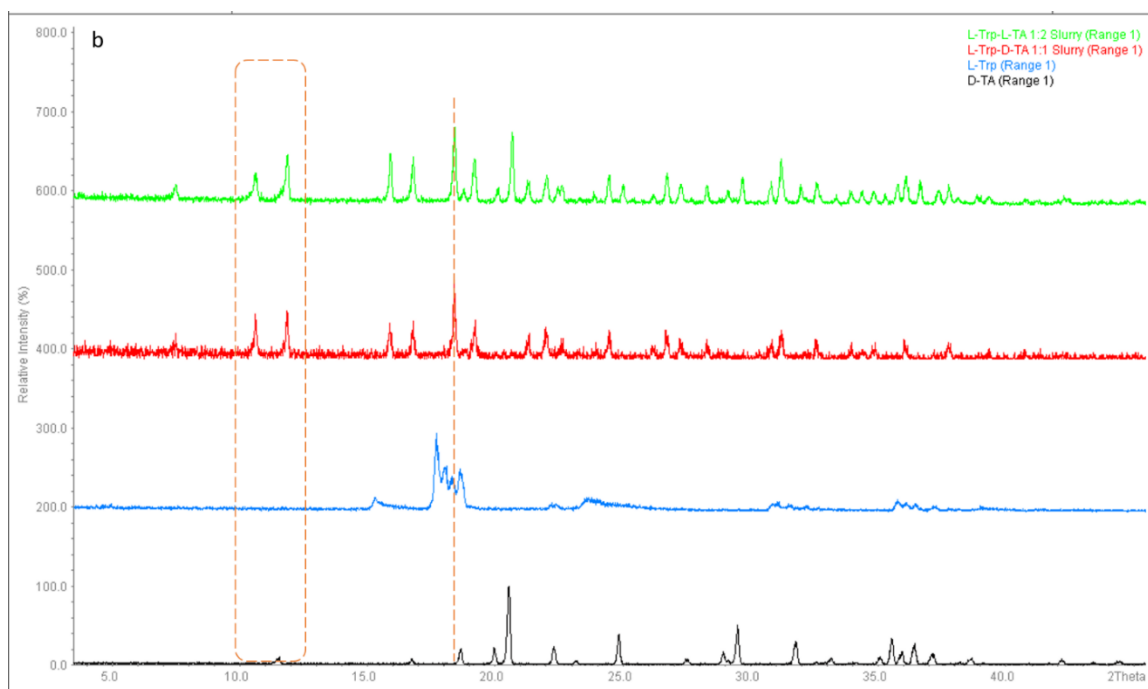


Figure S5.18. PXR D patterns of (a) L-TA (black), L-Trp (blue) and the products obtained from the experiments of L-Trp with L-TA in 1:1 (red), 1:2 (green) and 2:1 (pink) ratio; (b) D-TA (black), L-Trp (blue) and the products obtained from the experiments of L-Trp with D-TA in 1:1 (red) and 1:2 (green) ratio.

Table S5.1. Crystallographic data for L-Met-D-MDA cocrystal.

Crystallographic data	L-Met-D-MDA
Chemical formula	C ₁₃ H ₁₉ NO ₅ S
Formula weight	301.36
Crystal system	monoclinic
Space group, <i>Z</i>	<i>P</i> 2 ₁ , 2
Temperature (K)	293(2)
<i>a</i> (Å)	8.9248(17)
<i>b</i> (Å)	5.8980(10)
<i>c</i> (Å)	14.699(3)
α (°)	90
β (°)	99.671(8)
γ (°)	90
Volume (Å ³)	762.7(2)
ρ_{calc} (g cm ⁻³)	1.434
Radiation type	Cu K α
μ (mm ⁻¹)	2.105
Reflns measured	5686
Reflns independent	2310
Significant [<i>I</i> >2 σ (<i>I</i>)]	2130
Parameters refined	164
Restraints	22
$\Delta\rho_{max}, \Delta\rho_{min}$ (e Å ⁻³)	1.193, -0.928
<i>F</i> (000)	352
<i>R</i> ₁ [<i>I</i> >2 σ (<i>I</i>)]	0.1607
wR ₂ (all data)	0.5043
<i>Flack</i>	0.1(2)

Table S5.2. Hydrogen bond (Å, °) in the L-Leu-D-MDA cocrystal ^a

	D-H...A	D-H	H...A	D...A	D-H...A	ARU (J)
1	N5-H5A...O15	0.89	2.07	2.949(5)	167	[1445.01]
2	N5-H5B...O1	0.89	1.9	2.711(4)	151	[2556.02]
3	N5-H5C...O11	0.89	2.15	2.893(4)	140	[1455.01]
4	O13-H13...O3	0.82	1.7	2.520(4)	178	[1555.02]
5	O15-H15...O3	0.82	2.11	2.848(4)	151	[2656.02]

^a Symmetry codes: [2556.] = [2_556] = -x, 1/2+y, 1-z; [1455.] = [1_455] = -1+x, y, z; [1445.] = [1_445] = -1+x, -1+y, z; [2656.] = [2_656] = 1-x, 1/2+y, 1-z.

Table S5.3. Hydrogen bond (Å, °) in the L-Ile-L-PLA cocrystal ^a

	D-H...A	D-H	H...A	D...A	D-H...A	ARU (J)
1	N5-H5A...O1	0.89	2.08	2.878(2)	148	[3456.02]
2	N5-H5B...O11	0.89	2.27	2.880(3)	126	[3466.01]
3	N5-H5B...O15	0.89	2.06	2.872(3)	151	[3466.01]
4	N5-H5C...O1	0.89	1.89	2.779(2)	173	[1455.02]
5	O13-H13...O3	0.82	1.71	2.511(2)	166	[1555.02]
6	O15-H15...O11	0.82	1.98	2.795(2)	176	[1655.01]
7	C4-H4...O13	0.98	2.46	3.227(3)	134	[1555.01]

^a Symmetry codes: [1455.] = [1_455] = -1+x, y, z; [1655.] = [1_655] = 1+x, y, z; [3466.] = [4_466] = -1/2+x, 3/2-y, 1-z; [3456.] = [4_456] = -1/2+x, 1/2-y, 1-z.

Table S5.4. Hydrogen bond (Å, °) in the L-His-L-MA salt ^a

	D-H...A	D-H	H...A	D...A	D-H...A	ARU (J)
1	N5-H5A...O21	0.89	1.93	2.769(4)	157	[2564.02]
2	N5-H5A...O25	0.89	2.58	3.130(4)	121	[2564.02]
3	N5-H5B...O1	0.89	1.89	2.738(4)	158	[1655.01]
4	N5-H5B...O3	0.89	2.48	3.153(4)	133	[1655.01]
5	N5-H5C...O1	0.89	2.03	2.855(4)	154	[3565.01]
6	N9-H9...O23	0.86	1.87	2.701(5)	163	[3466.02]
7	N11-H11...O25	0.86	1.97	2.820(4)	170	[4555.02]
8	O25-H25...O23	0.82	1.93	2.730(4)	164	[1455.02]
9	O28-H28...O3	0.82	1.85	2.616(5)	155	[1555.01]
10	C6-H6A...O3	0.97	2.55	3.228(5)	127	[1655.01]
11	C8-H8...O29	0.93	2.54	3.464(7)	171	[1655.02]

^a Symmetry codes: [2564.] = [2_564] = 1/2-x, 1-y, -1/2+z; [1655.] = [1_655] = 1+x, y, z; [3565.] = [4_565] = 1/2+x, 3/2-y, -z; [3466.] = [4_466] = -1/2+x, 3/2-y, 1-z; [4555.] = [3_555] = -x, 1/2+y, 1/2-z; [1455.] = [1_455] = -1+x, y, z.

Table S5.5. Hydrogen bond (Å, °) in the L-Met-L-MDA salt cocrystal ^a

	D-H...A	D-H	H...A	D...A	D-H...A	ARU (J)
1	O1-H1...O9	0.82	1.89	2.687(7)	165	[1565.03]
2	O4-HO4...O1	0.82	2.16	2.978(8)	172	[4646.01]
3	N1-H1A...O7	0.89	1.98	2.856(8)	170	[4746.03]
4	N1-H1A...O11	0.89	2.51	2.929(8)	109	[4746.04]
5	N1-H1B...O8	0.89	2.09	2.964(8)	167	[1555.03]
6	N1-H1B...O11	0.89	2.53	2.929(8)	108	[4746.04]
7	N1-H1C...O1	0.89	2.06	2.932(8)	168	[4746.01]
8	N1-H1C...O2	0.89	2.58	2.941(8)	105	[4746.01]
9	O6-HO6...O9	0.82	1.69	2.491(7)	164	[1555.03]
10	O3-H3...O5	0.82	1.84	2.632(7)	162	[1555.02]
11	O7-HO7...O4	0.82	2.24	2.957(7)	146	[1655.02]
12	O7-HO7...O8	0.82	2.15	2.641(8)	119	Intra
13	O10-HO10...O2	0.82	1.93	2.727(8)	165	[1555.01]
14	C4-H4...O6	0.93	2.56	3.355(10)	144	[1565.02]
15	C12-H12...O7	0.93	2.38	2.745(9)	103	Intra
16	C18-H18...O8	0.98	2.5	3.177(9)	126	[1455.03]

^a Symmetry codes: [1565.] = [1_565] = x, 1+y, z; [1455.] = [1_455] = -1+x, y, z; [4646.] = [3_646] = 1-x, -1/2+y, 3/2-z; [1655.] = [1_655] = 1+x, y, z; [4746.] = [3_746] = 2-x, -1/2+y, 3/2-z.

Table S5.6. Hydrogen bond (Å, °) in the L-Met-D-MDA cocrystal ^a

	D-H...A	D-H	H...A	D...A	D-H...A	ARU (J)
1	O11-H11...O3	0.82	2.07	2.574(9)	119	[1545.02]
2	N5-H5A...O1	0.89	2.01	2.780(11)	144	[2745.02]
3	N5-H5B...O3	0.89	1.92	2.745(14)	154	[1545.02]
4	N5-H5C...O15	0.89	2.3	2.960(11)	131	[1655.01]
5	C14-H14...O1	0.98	2.42	3.296(15)	149	[1445.02]

^a Symmetry codes: [1545.] = [1_545] = x, -1+y, z; [1445.] = [1_445] = -1+x, -1+y, z; [1655.] = [1_655] = 1+x, y, z; [2745.] = [2_745] = 2-x, -1/2+y, -z.

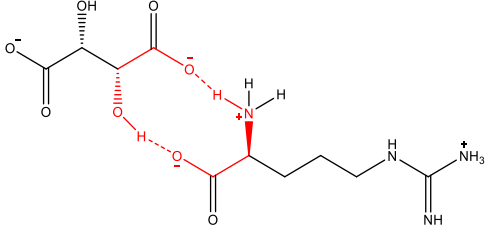
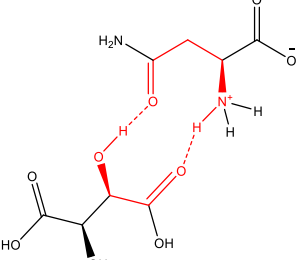
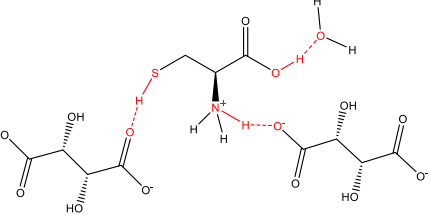
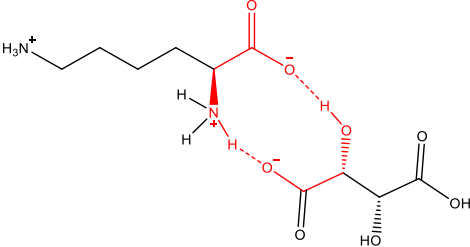
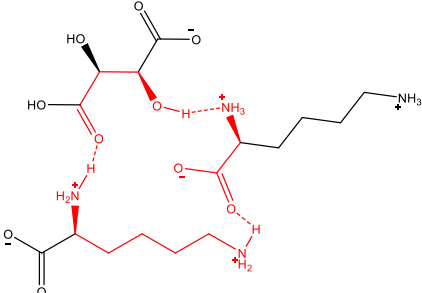
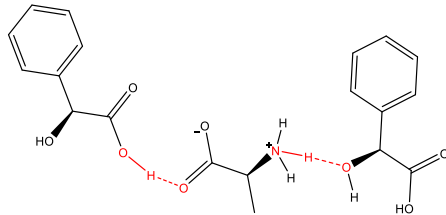
Table S5.7. Overview of screening experiments ^a

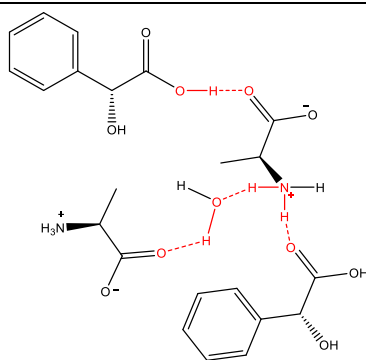
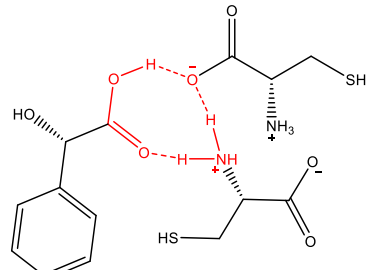
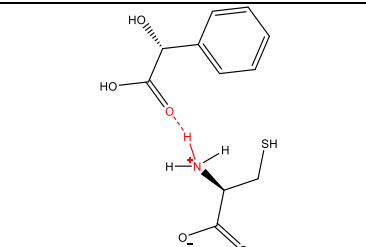
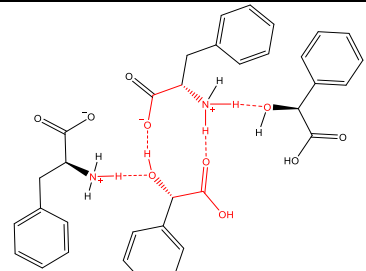
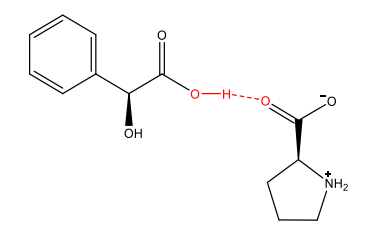
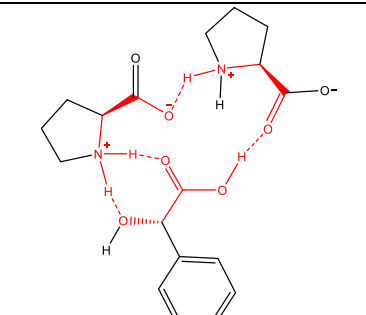
Amino acids	L-TA			D-TA			L-MDA			D-MDA			L-MA			D-MA			L-PLA			D-PLA		
	1:1	1:2	2:1	1:1	1:2	2:1	1:1	1:2	2:1	1:1	1:2	2:1	1:1	1:2	2:1	1:1	1:2	2:1	1:1	1:2	2:1	1:1	1:2	2:1
L-Ala							4			5														
L-Arg	1																							
L-Asn	2																							
L-Asp																								
L-Cys	3						6			6														
L-Gln																								
L-Glu																								
L-His													(1:1)											
L-Ile																(1:1)								
L-Leu										(1:1)														
L-Lys	1			1																				
L-Met							(1:3) ^b			(1:1)														
L-Phe							7																	
L-Pro							8			8														
L-Ser																								
L-Thr																								
L-Trp										9														
L-Tyr																								
L-Val																								

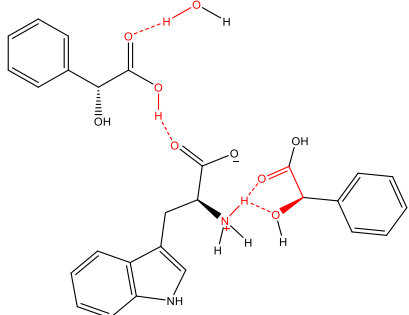
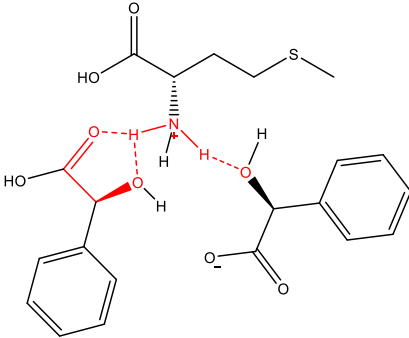
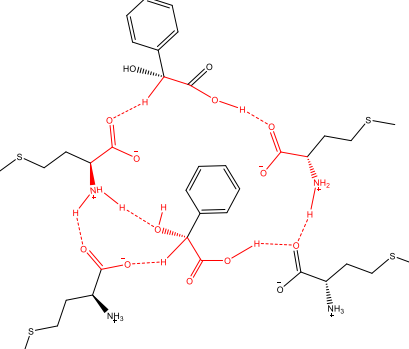
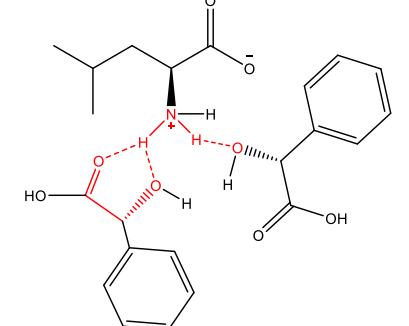
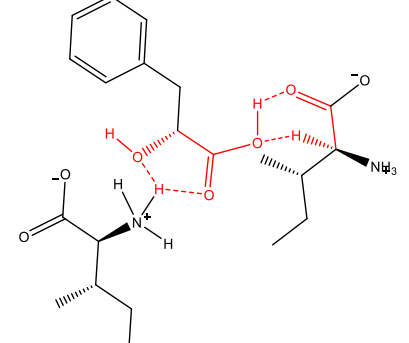
^a Gray = no new phase or powdered product obtained, blue = enantiospecific system, yellow = diastereomeric system, green = crystal structure determined in this work (ratio is marked), and numbers in boxes are references

^b L-Met and L-MDA in a 1:3 molar ratio was used in the formation of L-Met-L-MDA.

Table S5.8. Summary of graph-set motif of L-amino acids with enantiomers of TA, MDA, MA and PLA.

crystal	graph-set motif	
L-Arg-L-TA 2:1 ¹	$R_2^2(10)$	
L-Asn-L-TA 1:1 ²	$R_2^2(11)$	
L-Cys-L-TA monohydrate 1:1:1 ³	D & C(9)	
L-Lys-L-TA 1:1 ¹	$R_2^2(10)$	
L-Lys-D-TA 1:1 ¹	$R_3^3(19)$	
L-Ala-L-MDA 1:1 ⁴	C(8)	

<p>L-Ala-D-MDA hemihydrate 1:1: 0.5⁵</p>	<p>D & C(7)</p>	
<p>L-Cys-L-MDA 1:1⁶</p>	<p>R₃²(8)</p>	
<p>L-Cys-D-MDA 1:1⁶</p>	<p>D</p>	
<p>L-Phe-L-MDA 1:1⁷</p>	<p>R₂²(10)</p>	
<p>L-Pro-L-MDA 1:2⁸</p>	<p>D</p>	
<p>L-Pro-D-MDA 2:1⁸</p>	<p>R₂²(7) & R₃³(14)</p>	

L-Trp-D-MDA 1:1 ⁹	C(7) & R ₁ ² (5)	
L-Met-L-MDA 1:3	C(5) & R ₁ ² (5)	
L-Met-D-MDA 1:1	R ₃ ³ (9) & R ₅ ⁵ (21)	
L-Leu-D-MDA 1:1	C(5) & R ₁ ² (5)	
L-Ile-L-PLA 1:1	R ₁ ² (5) & R ₂ ² (6)	

L-His-L-MA 1:1	$R_1^2(5)$	
----------------	------------	--

REFERENCES

- (1) Selvaraj, M.; Thamocharan, S.; Roy, S.; Vijayan, M., X-ray studies of crystalline complexes involving amino acids and peptides. XLIV. Invariant features of supramolecular association and chiral effects in the complexes of arginine and lysine with tartaric acid. *Acta Cryst.* **2007**, B63, 459–468.
- (2) Natarajan, S.; Hema, V.; Sundar, J. K.; Suresh, J.; Lakshman, P. L., L-Asparagine-L-tartaric acid (1/1). *Acta Cryst.* **2010**, C66, o2239.
- (3) Shan, Y.; Huang, S. D., Crystal structure of L-cysteine L-tartaric acid monohydrate, $C_7H_{15}NO_9S$. *Z. Kristallogr. NCS.* **1999**, 214, 41–42.
- (4) Hu, Z. Q.; Xu, D. J.; Xu, Y. Z., (*S*)-Alanine–(*S*)-mandelic acid (1/1). *Acta Cryst.* **2004**, E60, o269–o271.
- (5) Hu, Z. Q.; Xu, D. J.; Xu, Y. Z.; Wu, J. Y.; Chiang, M. Y., (*R*)-Mandelic acid (*S*)-alanine hemihydrate. *Acta Cryst.* **2002**, C58, o612–o614.
- (6) Fujii, I.; Baba, H.; Takahashi, Y., Crystal Structures of L-(*R*)-Cysteine-Mandelic Acid Diastereomers. *Anal. Sci.* **2005**, 21, x175–x176.
- (7) Okamura, K.; Aoe, K. i.; Hiramatsu, H.; Nishimura, N.; Sato, T.; Hashimoto, K., Crystal Structures of Diastereomeric 1:1 Complexes of (*R*)- and (*S*)-Phenylalanine (*S*)-Mandelic Acid. *Anal. Sci.* **1997**, 13, 315–317.
- (8) Zhou, F.; Collard, L.; Robeyns, K.; Leyssens, T.; Shemchuk, O., L-Proline, a resolution agent able to target both enantiomers of mandelic acid: an

exciting case of stoichiometry controlled chiral resolution. *Chem. Commun.* **2022**, 58, 8560–8563.

- (9) Fujii, I., Crystal Structure of L-(*S*)-Tryptophane D-(*R*)-mandelate 1.5H₂O. *X-ray Struct.* **2009**, 25, 35-36.



Chapter 6 Exploring the Crystal Landscape of Mandelamide

(Revision)



6.1 Abstract

The crystal structures of (\pm)-mandelamide, *S*-mandelamide and enantio-enriched mandelamide (94 *S*:6 *R*) were determined. Diastereomeric cocrystal pairs of *S*-mandelamide with both enantiomers of mandelic acid and proline were synthesized as part of an investigation into the potential of *S*-mandelamide as a resolution agent for chiral resolution.

6.2 Introduction

Chirality, a distinct characteristic of objects that cannot be perfectly aligned with their mirror image, is present in various aspects of nature. For example, the standard form of the DNA double helix always twists in a right-handed manner, while snails exhibit left-right asymmetry both internally and externally.^{1,2} A large number of naturally occurring molecules, such as proteins, enzymes, amino acids, carbohydrates, etc., are chiral and contain at least one stereogenic center in the structure, typically tetrahedral (sp^3 -hybridized) carbons with four different substituents,³ and the two non-superimposable mirror-image forms of chiral molecules are called enantiomers.⁴ A review from 2003 states that approximately 50% of the pharmaceuticals marketed and used in medical treatment are chiral compounds, and 88% among them are administered as racemates.⁵ Different enantiomers of a chiral compound generally possess identical physical and chemical properties in an achiral environment, but they may exhibit significant

variations in biological activities. For example, the (*S,S*)-(+)-enantiomer of ethambutol is utilized for treating tuberculosis, while the (*R,R*)-(-)-ethambutol may lead to blindness.⁶ Nowadays, regulatory authorities require independent pharmacological tests for each enantiomer as well as their combined effects, and only the therapeutically active isomer can be used in a marketed drug product,⁷ consequently, stereochemistry and chiral resolution are of paramount importance in the pharmaceutical industry. The 2001 Nobel Prize in Chemistry was awarded to three scientists for their work in the development of asymmetric synthesis using chiral catalysts in the production of single enantiomer drugs or chemicals.⁸ In spite of the rapid development of asymmetric synthesis in recent years, there are still numerous chiral compounds synthesized as racemates, and then separated by a suitable physical separation approach.⁹ In industry, two main categories of techniques are often applied for chiral resolution. Diastereomeric salt formation and enzymatic or kinetic resolution are two classical technologies, and the modern approach is the use of preparative high-performance liquid chromatography.¹⁰⁻¹² The main restrictions of the above methods is that sometimes they are impractical and uneconomical.

Cocrystallization, the process of producing cocrystals, i.e., crystals with two or more molecular species in a specific stoichiometric ratio within a crystal lattice, has gained increasing attention recently as a feasible strategy to achieve chiral separation.¹³⁻¹⁵ This process enables the formation of new crystalline materials involving two chiral molecules, leading to changes in its physical and

physicochemical properties.¹⁶ This approach involves two possible scenarios when both cocrystallizing components are chiral: (i) the chiral coformer only forms an enantiospecific cocrystal with one enantiomer of the target compound or (ii) the chiral coformer can form a diastereomeric cocrystal pair with each enantiomer of the target compound. Structural modifications in the supramolecular assembly in enantiospecific cocrystals or diastereomeric cocrystal pairs lead to changes in the crystal lattice energy and related physical and physicochemical properties, enabling separation (Figure 6.1). Therefore, both possible outcomes can be used to develop a chiral resolution process.

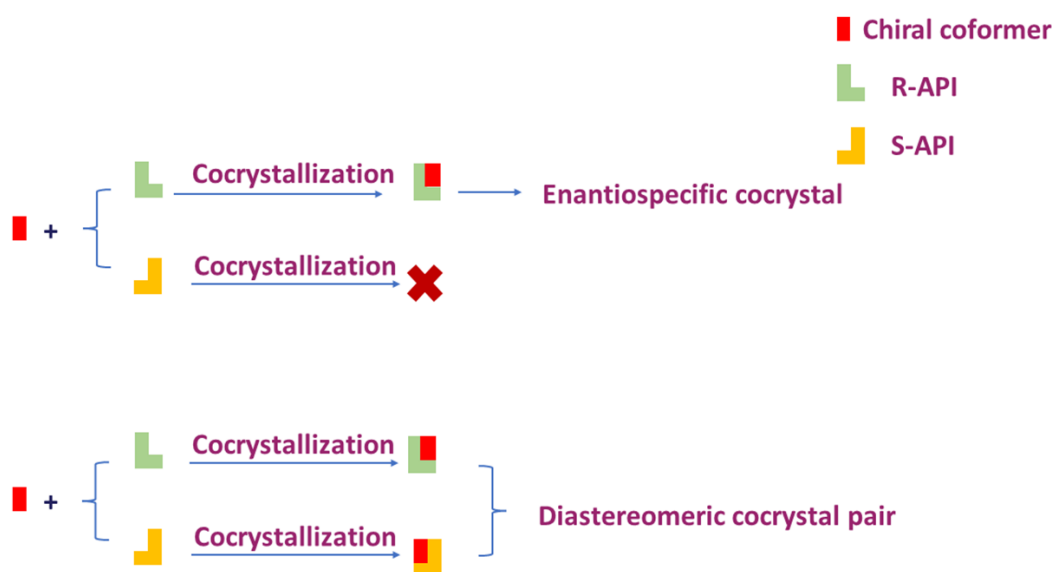


Figure 6.1. Two possible scenarios of achieving chiral resolution by cocrystal formation (adapted from ref. 14).

The application of achieving chiral resolution through enantiospecific cocrystal formation in solution was first introduced by Leyssens's group in 2012.¹⁴ They

demonstrated that only the *S*-enantiomer of 2-(2-oxopyrrolidin-1-yl) butanamide, which exhibits nootropic activity and is marketed under the name levetiracetam, can cocrystallize with *S*-mandelic acid, while the *R*-enantiomer cannot form a cocrystal with *S*-mandelic acid, leading to 70% of the *S*-enantiomer separated from the racemic mixture in a single cocrystallization step. This group further developed a dual-drug chiral resolution process based on the ibuprofen-levetiracetam system, where levetiracetam can form a cocrystal with *S*-ibuprofen in an enantiospecific manner, and the enantio-enrichment can be achieved and resolution can be ultimately obtained through constructing the appropriate phase diagrams.¹⁷ More recently, chiral resolution by formation of ionic cocrystals were explored by Leysens and co-workers.^{16, 18}

Diastereomeric cocrystal systems have been less extensively studied in comparison to enantiospecific systems. Höpfl and colleagues reported a diastereomeric cocrystal pair of *R* / *S*-praziquantel with L-malic acid, and the chiral separation was enabled by phase-decomposition of the *R*-praziquantel-L-malic acid cocrystal due to the different aqueous solubilities of the diastereomeric cocrystals.¹⁹ L-Proline was proven to form diastereomeric cocrystals with both *R*- and *S*-enantiomers of mandelic acid in different stoichiometric ratios, hence, the chiral separation can be attained by simply altering the stoichiometry of the two constituents.²⁰

Mandelic acid is a widely used compound for forming enantiospecific or diastereomeric cocrystals. The literature and Cambridge Structural Database (CSD)

search indicate that approximately 40 cocrystals / salts incorporating mandelic acid with another chiral compound have been documented (Table S6.9). Somewhat surprisingly, no cocrystals involving mandelamide, the amide derivative of mandelic acid, have been reported or deposited in the CSD,²¹ even though it is an important drug precursor.²² In this work, the crystal structure of racemic mandelamide [(±)-MDM], enantiopure mandelamide (*S*-MDM) and enantio-enriched MDM (94 *S*:6 *R*) were identified, and the potential of *S*-MDM as a chiral resolution agent via cocrystallization was considered. Two diastereomeric cocrystal pairs of *S*-MDM with both *R*- and *S*-enantiomers of mandelic acid (MDA) and proline (Pro) (Figure 6.2) were obtained by both liquid-assisted grinding and slow evaporation, and fully characterized by thermal analysis, X-ray techniques, and FT-IR spectroscopy. To further investigate the diastereomeric behaviour of *S*-MDM with the chiral cofomers, detailed analyses of crystal structures, motifs and Hirshfeld surfaces were performed.

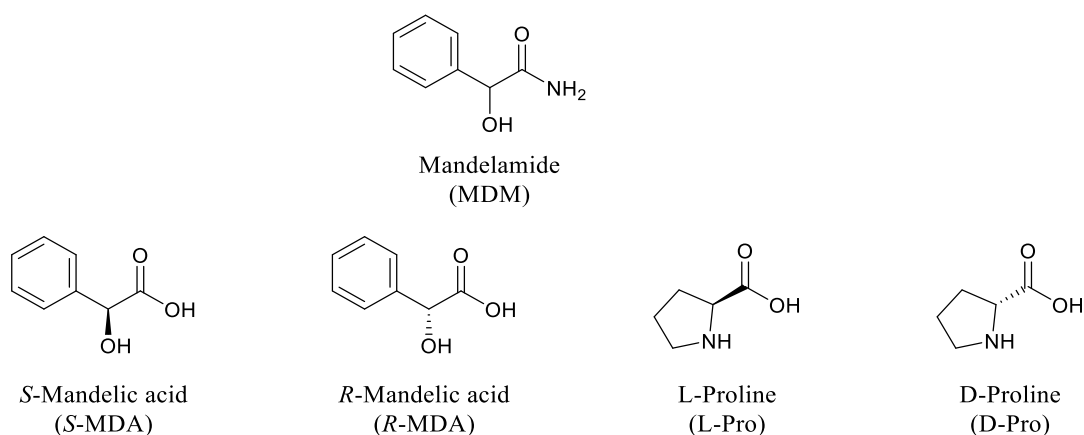


Figure 6.2. Molecular structures of *S*-MDM and cofomers present in this work.

6.3 Experimental Section

6.3.1 Materials

S-MDA, *R*-MDA and L-Pro were obtained from Fluorochem, and D-Pro from TCI chemicals. (±)-MDM was synthesized from (±)-MDA using a literature procedure,²³ and was recrystallized from hot ethanol to yield white plates. *S*-MDM was synthesized from *S*-MDA using a similar procedure to that used for (±)-MDM, see Supporting Information. Both (±)-MDA, *S*-MDA and commercial *S*-MDM were obtained from Sigma Aldrich. Solvents were purchased from Honeywell International; Inc. and all materials were used as received.

6.3.2 Liquid-Assisted Grinding

LAG experiments were performed by placing a physical mixture of *S*-MDM with each coformer in a 5 mL stainless steel grinding jar along with a 2.5 mm stainless steel grinding ball. After the addition of 30 μ L of ethyl acetate the mixture was ground using a Retsch MM400 Mixer mill at a rate of 30 Hz for 30 min. The products obtained were analyzed by powder X-ray diffraction (PXRD). A 1:1 molar ratio of *S*-MDM: coformer was used in all cases. After single crystal analysis, a 1:2 molar ratio of *S*-MDM with L-Pro was used.

6.3.3 Crystallization of (±)-MDM

20.5 mg of synthesized (±)-MDM was dissolved in 10 mL of THF by heating. Colourless plate-like crystals were obtained by slowly evaporating the filtered

solution at room temperature for 3-5 days.

6.3.4 Crystallization of *S*-MDM

20.2 mg of synthesized *S*-MDM was dissolved in 5 mL of MeOH by heating. Colourless plate-like crystals were obtained by slowly evaporating the filtered solution at room temperature for 3-5 days. The bulk commercial sample is identical by PXRD.

6.3.5 Crystallization of MDM (94 *S*:6 *R*)

20.4 mg of the commercial *S*-MDM was dissolved in 10 mL of the solvent mixture THF and toluene (1:1, v/v) by heating. Colourless plate-like crystals of MDM were obtained by slowly evaporating the filtered solution at room temperature for 3-5 days and one crystal was identified by single crystal X-ray diffraction as containing 94% *S*-MDM and 6% *R*-MDM. Bulk quantities of MDM (94 *S*:6 *R*) were obtained by dissolving 100 mg of the commercial *S*-MDM in EtOH at room temperature, and removing the solvent quickly using a rotary evaporator (Büchi, Germany) under a vacuum achieved by a diaphragm pump (Vacuubrand, Germany), with the rotary flask rotating at a speed of 40 rpm while being immersed in a water bath at 50 °C.²⁴ The resulting white powdered product was isolated and allowed to dry in the fume hood overnight.

6.3.6 Crystallization of Cocrystals

The products from the LAG experiments were dissolved in 10 mL of solvent and the filtrate allowed to crystallize by slow evaporation.

S-MDM-S-MDA: 22.7 mg of powdered *S*-MDM-*S*-MDA was used in MeOH.

Colourless plate-like crystals were harvested after 3-5 days.

S-MDM-R-MDA: 20.8 mg of powdered *S*-MDM-*R*-MDA was used in a solvent mixture of MeOH and Et₂O (1:1, v/v). Colourless needle-like crystals were after 5-7 days.

S-MDM-L-Pro: 31.4 mg of *S*-MDM-*L*-Pro was used with the solvent mixture of EtOH and CH₂Cl₂ (1:1, v/v). Colourless needle-like crystals were obtained after 3-5 days.

S-MDM-D-Pro: 19.8 mg of *S*-MDM-*D*-Pro in the mixed solvent MeOH and THF (1:1, v/v). Colourless needle-like crystals were obtained after 3-5 days.

6.3.7 Physical Measurements

Powder X-ray Diffraction (PXRD): The PXRD patterns were collected on a STOE STADI MP diffractometer with a Cu K α radiation (1.540 Å) using a linear position-sensitive detector. The tube voltage and amperage were set at 40 kV and 40 mA respectively. Each sample was scanned between 3.5 and 45.5° 2 θ with a with an increment of 0.05° at a rate of 2° min⁻¹. The samples were prepared as transmission foils and the data were viewed via STOE WinXPOW POWDAT software.²³

Differential Scanning Calorimetry (DSC): DSC was conducted on a TA Instruments Q1000. Samples (1-5 mg) were placed in nonhermetic aluminium pans and scanned in the range of 25 °C to 200 °C at a heating rate of 10 °C min⁻¹ under a continuously purged dry nitrogen atmosphere (flow rate 80 mL min⁻¹). The data were viewed and analyzed by TA Universal Analysis software.

FT-IR Spectroscopy (IR): FT-IR spectra were recorded on a PerkinElmer UATR Two spectrophotometer using a diamond attenuated total reflectance accessory over a range of 400-4000 cm⁻¹. Four scans were taken at 4 cm⁻¹ resolution for each sample, and the spectra were measured over the range of 400-4000 cm⁻¹.

Single-crystal X-ray Diffraction (SCXRD): An optical microscope (Zeiss Stemi 2000) was used to choose a suitable crystal for diffraction. SCXRD data was performed using a Bruker APEX II DUO with monochromated Cu K α radiation ($\lambda = 1.54178 \text{ \AA}$). The structure was solved and refined by the SHELX suite of programs from Bruker APEX software.^{26, 27} All non-hydrogen atoms were refined by using anisotropic displacement parameters while hydrogen atoms were fixed in geometrically calculated positions using the riding model, with C-H = 0.93-0.98 Å, O-H = 0.82 Å and N-H = 0.86-0.89 Å, and Uiso (H) (in the range 1.2-1.5 times Ueq of the parent atom). For MDM (94 *S*:6 *R*), there is disorder in two of the four crystallographically independent MDM molecules due to *R*-MDM impurity, which was modeled in two conformations in 88:12 ratio. For *S*-MDM-L-Pro and *S*-MDM-D-Pro cocrystals, there is disorder in the proline carbon that is beta to both the nitrogen and the carbon bonded to the carboxylic acid, which was

modeled in two conformations in 50:50 and 85:15 ratios, respectively. PLATON was used for the analysis of potential hydrogen bonds and short ring interactions.²⁸
²⁹ Mercury 2022.2.0 and DIAMOND 4.6 were used for viewing structures and creating diagrams.³⁰ Crystallographic parameters are listed in Table 6.1.

6.3.8 Computational Studies

Hirshfeld surface analyses and two-dimensional (2D) fingerprint plots were carried out using the CrystalExplorer 21.5 program.³¹

6.3.9 Analysis of the Cambridge Structural Database

Searches of the CSD were conducted using ConQuest version 2022.2.0.³² The following restrictions were applied: 3D coordinates; single crystal structures only; and organics only.

6.3.10 Chiral High Performance Liquid Chromatography Analysis

The enantiopurity of the commercial *S*-MDM from Sigma Aldrich, synthesized *S*-MDM and the single crystal of MDM (94 *S*:6 *R*) were determined by chiral High Performance Liquid Chromatography (HPLC) analysis on a Lux® Amylose-1 column, purchased from Daicel Chemical Industries, Japan. The HPLC parameters employed included a mobile phase of hexane / isopropanol = 90:10, a flow rate of 1 $\mu\text{L min}^{-1}$, a temperature of 25 °C and a detection wavelength of 210 nm. HPLC analysis was performed on a Waters Alliance 2695 with a Waters 2487 Dual Wavelength UV Detector. All solvents employed were of HPLC grade.

Table 6.1. Crystallographic data for (±)-MDM, S-MDM, MDM (94 S:6 R), S-MDM-S-MDA, S-MDM-R-MDA, S-MDM-L-Pro and S-MDM-D-Pro.

	(±)-MDM	S-MDM	MDM (94 S:6 R)	S-MDM-S-MDA	S-MDM-R-MDA	S-MDM-L-Pro	S-MDM-D-Pro
Chemical formula	C ₈ H ₉ NO ₂	C ₈ H ₉ NO ₂	C ₈ H ₉ NO ₂	C ₁₆ H ₁₇ NO ₅	C ₁₆ H ₁₇ NO ₅	C ₁₈ H ₂₇ N ₃ O ₆	C ₁₃ H ₁₈ N ₂ O ₄
Formula weight	151.16	151.16	151.16	303.30	303.30	381.43	266.29
Crystal system	monoclinic	orthorhombic	monoclinic	orthorhombic	orthorhombic	orthorhombic	monoclinic
Space group	P2 ₁ /c	P2 ₁ 2 ₁ 2 ₁	P2 ₁	P2 ₁ 2 ₁ 2 ₁	P2 ₁ 2 ₁ 2 ₁	P2 ₁ 2 ₁ 2 ₁	P2 ₁
Z, Z'	4, 1	4, 1	8, 4	4, 1	4, 1	4, 1	4, 2
Temperature (K)	296(2)	296(2)	296(2)	296(2)	296(2)	296(2)	296(2)
<i>a</i> (Å)	15.906(3)	5.5857(5)	8.2111(5)	6.4068(6)	6.9120(11)	5.6311(4)	5.19880(10)
<i>b</i> (Å)	5.5263(12)	8.2971(8)	5.9441(4)	8.0493(7)	7.3147(12)	14.9687(11)	24.6214(4)
<i>c</i> (Å)	8.5110(15)	16.8366(16)	31.3477(19)	29.633(3)	29.941(4)	22.9618(16)	10.51280(10)
α (°)	90	90	90	90	90	90	90
β (°)	91.386(15)	90	95.190(3)	90	90	90	95.4650(10)
γ (°)	90	90	90	90	90	90	90
Volume (Å ³)	747.9(3)	780.29(13)	1523.73(17)	1528.2(2)	1513.8(4)	1935.5(2)	1339.54(4)

ρ_{calc} (g cm ⁻³)	1.342	1.287	1.318	1.318	1.331	1.309	1.320
Radiation type	Cu K α						
μ (mm ⁻¹)	0.806	0.772	0.791	0.823	0.830	0.822	0.819
Reflns measured	4243	4919	18234	9838	12366	11409	17685
Reflns independent	1231	1319	5155	2677	2589	3325	4582
R_{int}	0.054	0.030	0.029	0.028	0.048	0.030	0.023
Significant [$I > 2\sigma(I)$]	899	1312	4982	2662	2367	2861	4502
Parameters refined	101	101	423	202	202	255	358
Restraints	0	0	4	6	6	4	15
$\Delta\rho_{max}, \Delta\rho_{min}$ (e Å ⁻³)	0.371, -0.201	0.138, -0.174	0.102, -0.127	0.344, -0.410	0.323, -0.174	0.353, -0.176	0.249, -0.189
$F(000)$	320	320	640	640	640	816	568
R_I [$I > 2\sigma(I)$]	0.0718	0.0342	0.0277	0.0379	0.0375	0.0383	0.0314
wR_2 (all data)	0.2077	0.0906	0.0727	0.1071	0.0986	0.1113	0.0855
<i>Flack</i>	-	0.08(5)	0.05(5)	0.03(5)	0.08(10)	0.11(8)	0.10(4)
<i>CCDC</i>	2269509	2269510	2269507	2269512	2269508	2269506	2269511

6.4 Results and Discussion

Based on the molecular structures of mandelamide and both coformers, it was anticipated that the well-known amide-amide homosynths and amide-acid heterosynths would be observed in their crystal structures (Figure 6.3). A search of the CSD was undertaken to identify common supramolecular synthons for compounds containing a hydroxyl group in the alpha position to a primary or secondary amide functional group (shown in red in Figure 6.3). The $R_2^2(8)$ homosynthon between two amides is commonly observed in 82 structures, 58 of which are single component crystals. Only one structure containing the amide-acid $R_2^2(8)$ heterosynthon has been reported (Refcode NUGFAX³³).

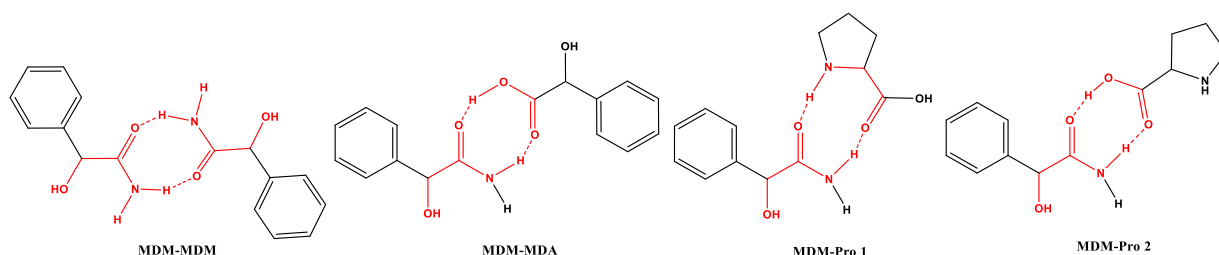


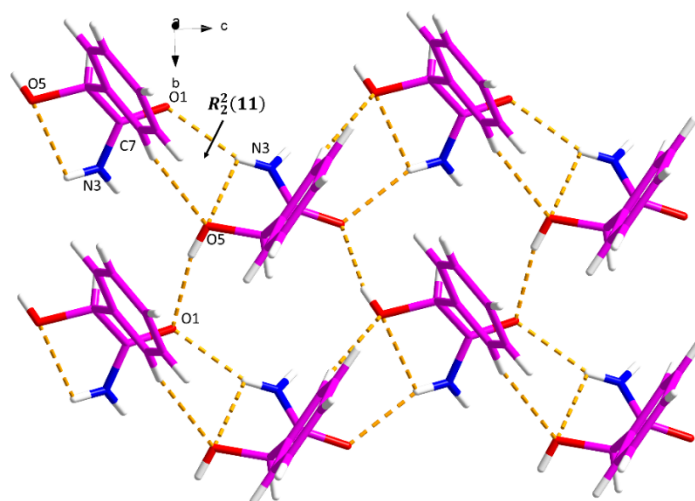
Figure 6.3. Expected hydrogen bond motifs in the MDM cocrystals.

6.4.1 Structures of Racemic MDM and *S*-MDM

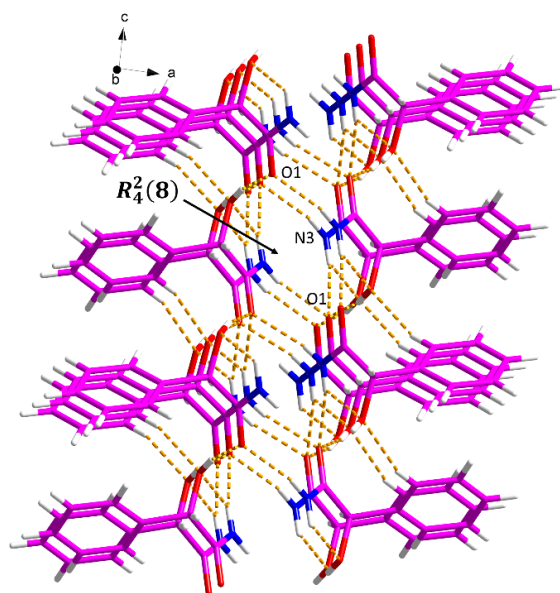
Single crystals of racemic MDM and enantiopure *S*-MDM were grown from THF and MeOH, respectively, and the structures determined as shown in Figures 6.4 and 6.5, respectively. The ellipsoid plots are shown in Figure S6.8. Hydrogen bonds geometries are displayed in Tables S6.1 and S6.2, separately.

(±)-MDM crystallizes in the monoclinic $P2_1/c$ space group with $Z' = 1$. As shown in Figure 6.4a, two (±)-MDM molecules formed an $R_2^2(11)$ motif through the N–

H \cdots O and C–H \cdots O hydrogen bonding. The hydrogen bonded network is further extended by O–H \cdots O hydrogen bonds between two (\pm)-MDM molecules. Along the b axis, an $R_4^2(8)$ motif is created among four (\pm)-MDM molecules via N–H \cdots O hydrogen bonding (Figure 4b).



(a)



(b)

Figure 6.4. Hydrogen bonding in (\pm)-MDM: (a) along the a axis, and (b) along the b axis.

S-MDM crystallizes in the $P2_12_12_1$ space group with $Z' = 1$. As shown in Figure 6.5, every two *S*-MDM molecules formed an $R_2^2(9)$ dimer between hydroxyl group and the amide group in a tail-to-tail manner through the N–H···O hydrogen bonding. The 3D hydrogen bonded network is further stabilized by O–H···O hydrogen bonds between two *S*-MDM molecules.

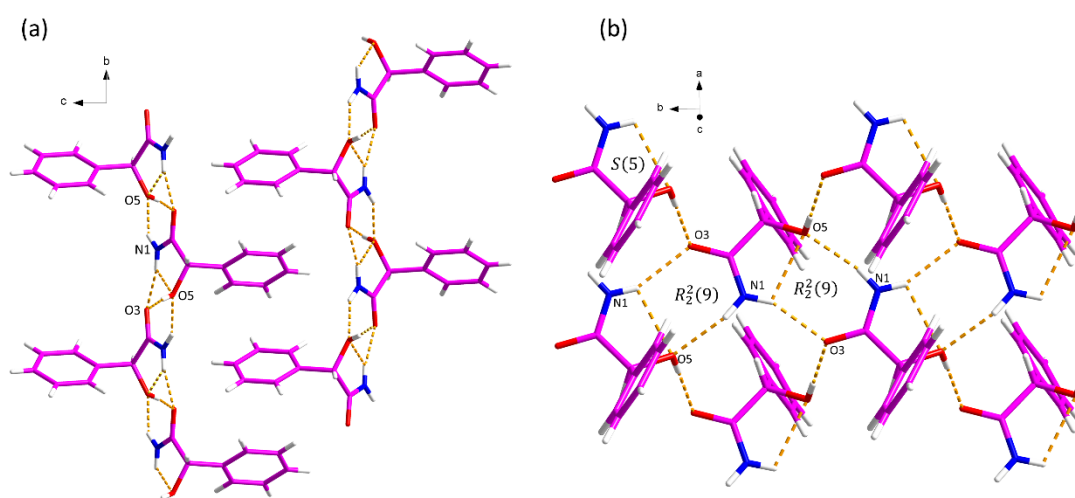
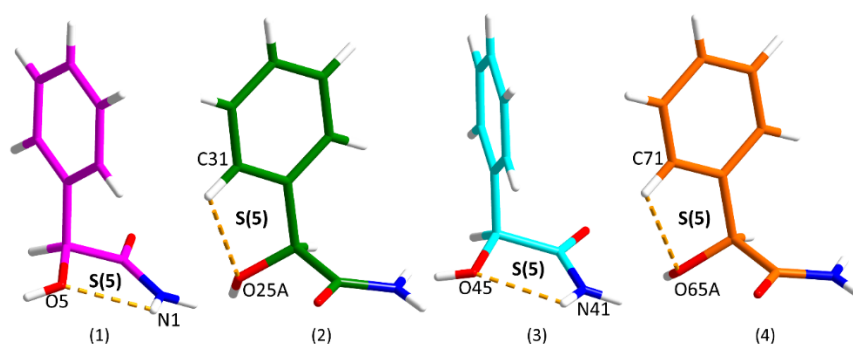


Figure 6.5. Hydrogen bonding in *S*-MDM.

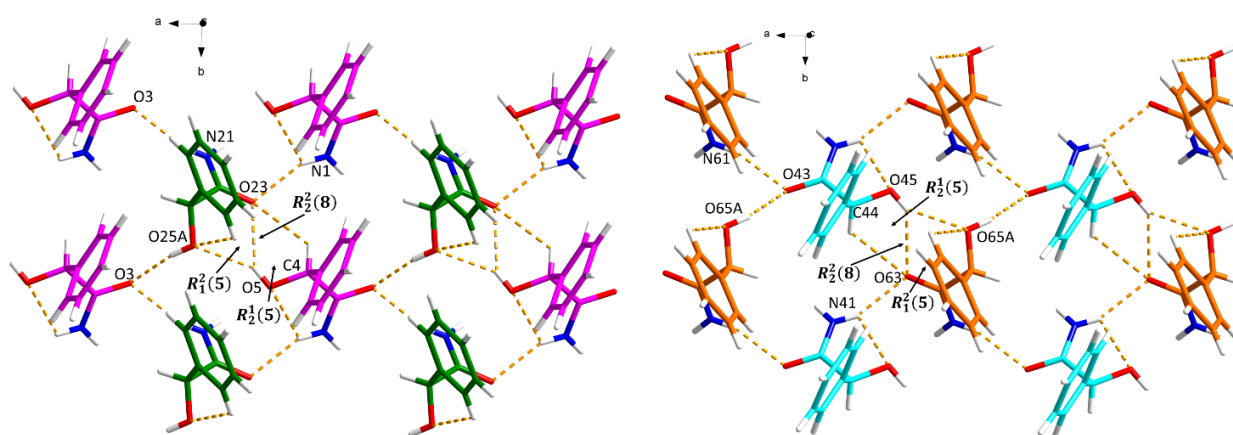
Interestingly during this study, a third crystalline form of MDM was isolated from the solvent mixture of THF and toluene. Analysis of the SCXRD showed that this contained enantio-enriched MDM (94 *S*:6 *R*) which results in a very different structure relative to either the enantiopure or racemic forms. The chiral HPLC results on another crystal from the same batch are consistent with the structural analysis. (Figure S6.11c).

MDM (94 *S*:6 *R*) crystallizes in the $P2_1$ space group with $Z' = 4$. As mentioned earlier, disorder models were created in the hydroxyl group of two MDM molecules (2 and 4). The diagrams of hydrogen bonding of the major part (88%) are presented in Figure 6.6, and Figure 6.7 illustrates the hydrogen bonded network

of the minor part (12%). In the major part, all four molecules are *S*-MDM. In addition, S(5) ring was created via N–H···O intramolecular hydrogen bond in *S*-MDM molecules 1 and 3, while for *S*-MDM molecules 2 and 4, S(5) rings were generated through C–H···O intramolecular hydrogen bond (Figure 6.6a). As shown in Figure 6.6b, two *S*-MDM molecules (1 and 2 or 3 and 4) are linked through O–H···O and C–H···O hydrogen bonds along the *c* axis, forming $R_1^2(5)$, $R_2^1(5)$ and $R_2^2(8)$ motifs. Along the *b* axis, four *S*-MDM molecules (1 and 2 or 3 and 4) are connected in a tail-to-tail fashion through N–H···O hydrogen bonds, creating an $R_4^2(8)$ motif, which further facilitates the construction of 3D structure (Figure 6.6c).



(a)



(b)

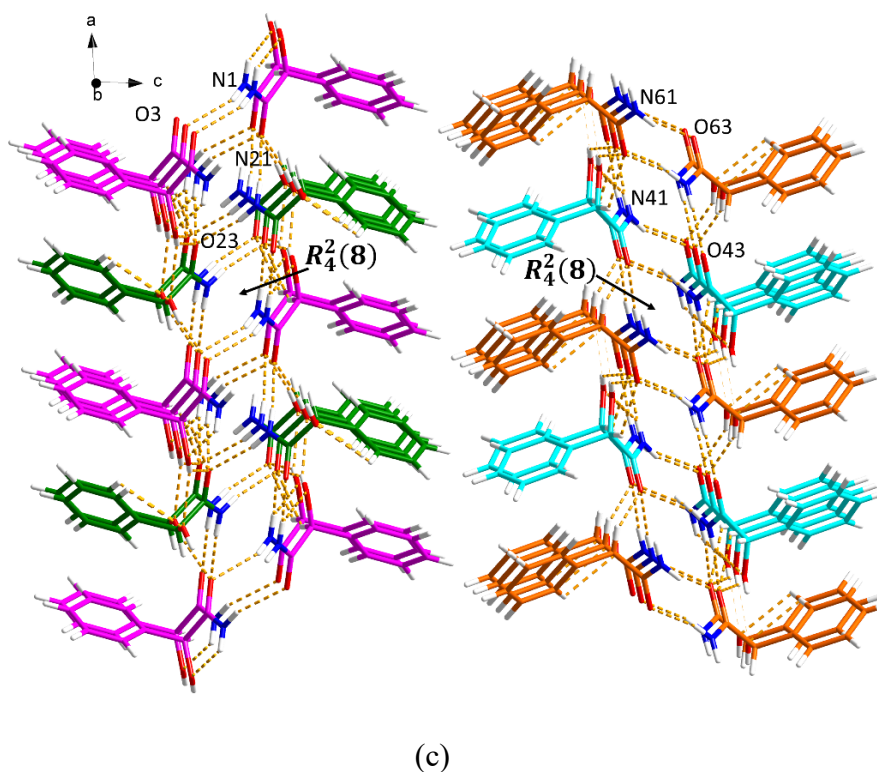
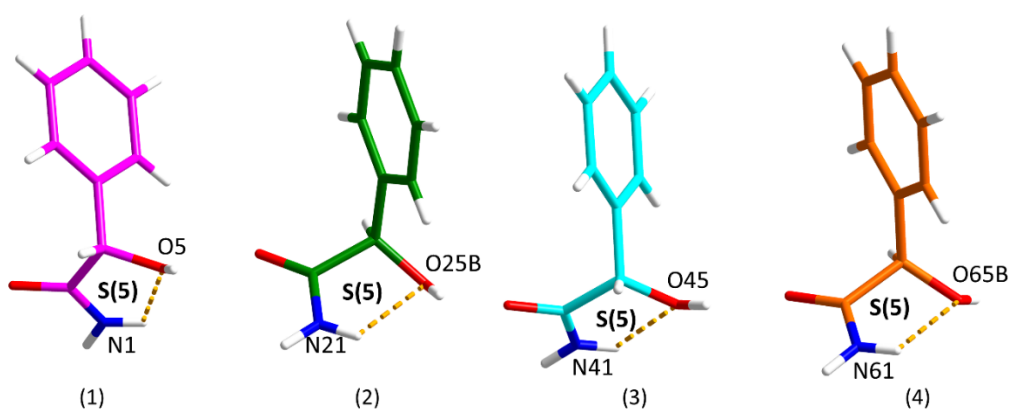


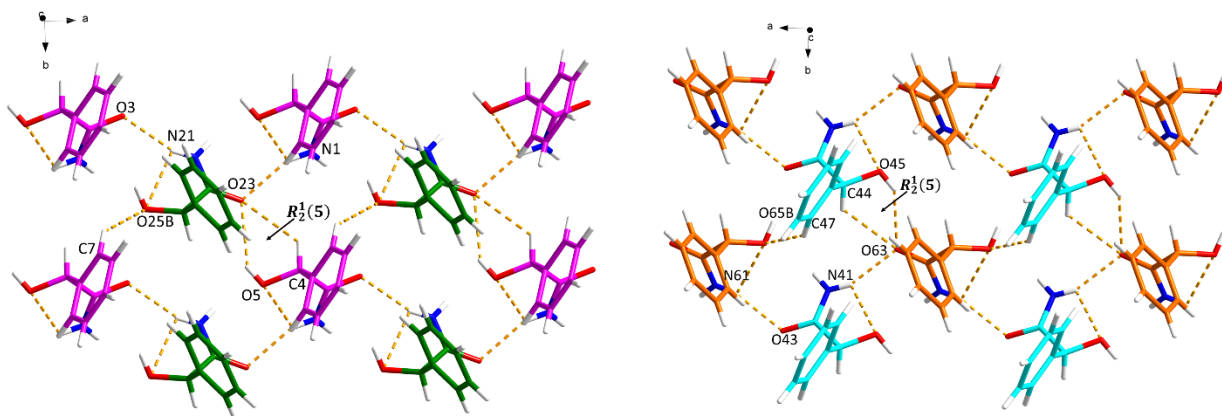
Figure 6.6. Hydrogen bonding in MDM (94 *S*:6 *R*) (major component of the disordered structure): (a) intramolecular interactions in four MDM molecules, (b) 2D hydrogen-bonding network along the *c* axis, and (c) 3D hydrogen-bonding network along the *b* axis.

In the minor part, two molecules (1 and 3) are *S*-MDM, while the other two molecules (2 and 4) are *R*-MDM. Similar S(5) ring via N–H···O intramolecular hydrogen bond was observed in all four molecules (Figure 6.7a). Along the *c* axis, $R_2^1(5)$ motifs were present between two MDM molecules (1 and 2 or 3 and 4) via O–H···O and C–H···O hydrogen bonds (Figure 6.7b). Similar to the major part, the 3D structure was further stabilized by N–H···O hydrogen bonds along the *b* axis between four MDM molecules (1 and 2 or 3 and 4) in a tail-to-tail fashion, forming an $R_4^2(8)$ motif (Figure 6.7c). The hydrogen bonding between the two MDM molecules of (\pm)-MDM is different to that in the minor component of MDM

(94 *S*:6 *R*), with the former forming an $R_2^2(11)$ motif while latter forms an $R_2^1(5)$ motif. Surprisingly, the crystal arrangement along the *b* axis in both the major and minor components of MDM (94 *S*:6 *R*) exhibits similarity to the crystal packing observed in (\pm)-MDM, rather than the expected resemblance to *S*-MDM, despite the fact that *S*-MDM constitutes 94% of MDM (94 *S*:6 *R*).



(a)



(b)

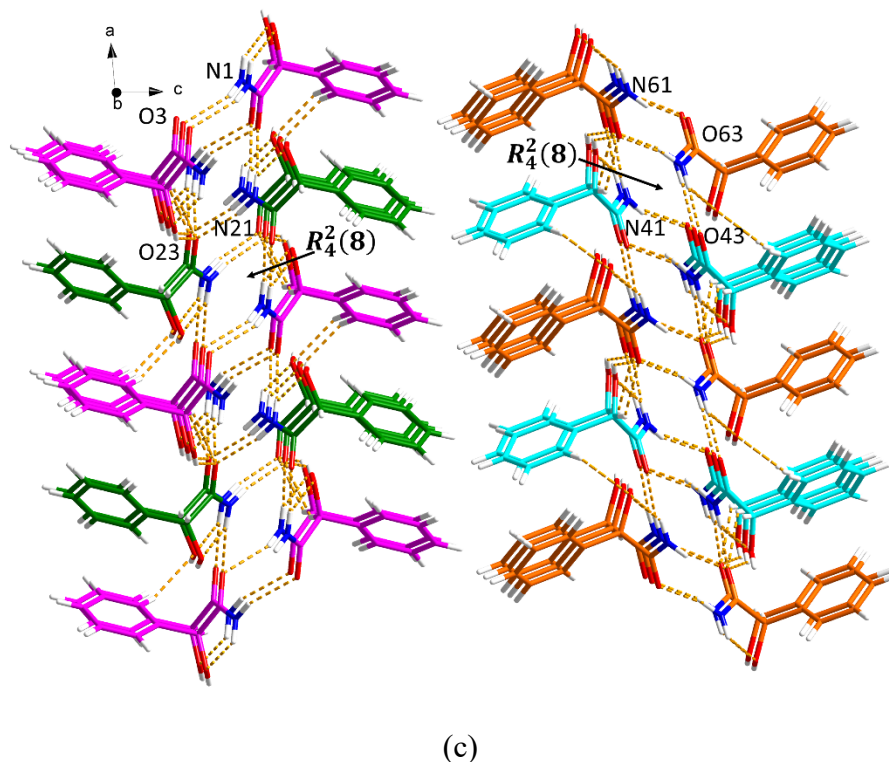


Figure 6.7. Hydrogen bonding in MDM (94 *S*:6 *R*) (minor component of the disordered structure): (a) intramolecular interactions in four MDM molecules, (b) 2D hydrogen-bonding network along the *c* axis, and (c) 3D hydrogen-bonding network along the *b* axis.

The single crystals of *S*-MDM were obtained from the synthesized *S*-MDM which contains 100% of *S*-MDM, while the formation of the MDM (94 *S*:6 *R*) could be attributed to the commercial starting material being <100% *S*. According to the chiral HPLC analysis, the commercial *S*-MDM contained 96% *S*-MDM and 4% of *R*-MDM (Figure S6.11a). The small amount *R*-MDM may fit into the crystal lattice of *S*-MDM and form “mixed crystals”. PXRD analysis of the bulk material for (±)-MDM, *S*-MDM and MDM (94 *S*:6 *R*) match the theoretical PXRD based on the single crystal analysis, Figure S6.9.

The structural analysis results revealed that the expected $R_2^2(8)$ motif between two MDM molecules is not present in any of crystal structures of MDM. Instead, motifs 1-4 (Figure 6.8) are present in these three crystal structures. Motif 1 and 3 are not found in reported structures, while motif 2 was observed in four reported structures (Refcodes: VAFVIL,³⁴ DEZKUR,³⁵ NOLCOG,³⁶ YENDEC³⁷) based on the CSD search. In addition, motif 4, consisting of four MDM molecules in (\pm)-MDM and MDM (94 *S*:6 *R*), can also be found in two reported structures (Refcodes: DEZLEC³⁵ and YENDEC³⁷).

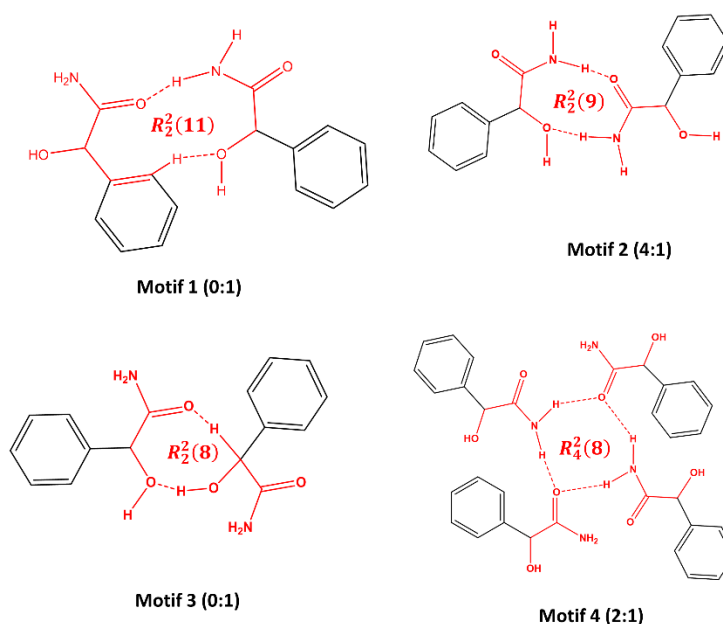


Figure 6.8. The types of motifs of MDM identified in this work. Numbers indicate occurrences in the CSD (left) and in this work (right).

The two main hydrogen bonding functional groups in MDM are the amide and hydroxyl groups. As shown in Table 6.2 and Figure S6.3, the characteristic IR bands of the N-H and O-H stretches in (\pm)-MDM and MDM (94 *S*:6 *R*) are both

increased compared with those in *S*-MDM. In contrast, the stretching vibrations of C=O in these two solids display a decrease compared to *S*-MDM.

Table 6.2. Distinctive bands (cm⁻¹) in the FTIR Spectra of MDM and cocrystals.

solid form	ν_{NH_2}	ν_{OH}	$\nu_{\text{C=O}}$
(±)-MDM	3379	3243	1633
<i>S</i> -MDM	3345	3182	1681
MDM (94 <i>S</i> :6 <i>R</i>)	3378	3197	1644
<i>S</i> -MDM- <i>S</i> -MDA	3419	3337	1719
<i>S</i> -MDM- <i>R</i> -MDA	3504	3401	1709
<i>S</i> -MDM- <i>L</i> -Pro	3431	3141	1664
<i>S</i> -MDM- <i>D</i> -Pro	3361	3150	1655

As shown in Figure 6.9, the melting point of (±)-MDM is 133-135 °C, which is in line with the reported data.³⁸ DSC analysis of the MDM (94 *S*:6 *R*) reveals its melting point is slightly lower than that of *S*-MDM. In the book "Introduction to Stereochemistry", Mislow examined the most common diastereomeric phase relationships that occur between two stereoisomers of similar substances.³⁹ One out of the four scenarios could explain the thermal behaviour of MDM (94 *S*:6 *R*). In this case, introducing a small amount of impurity (i.e., *R*-MDM) can result in a decreased melting point compared to the pure component (*S*-MDM).

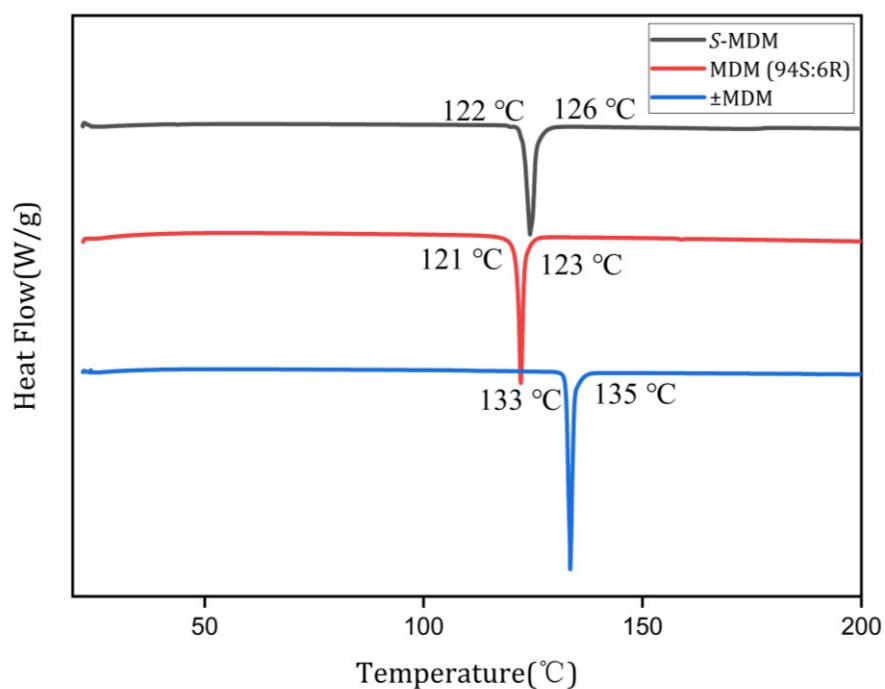


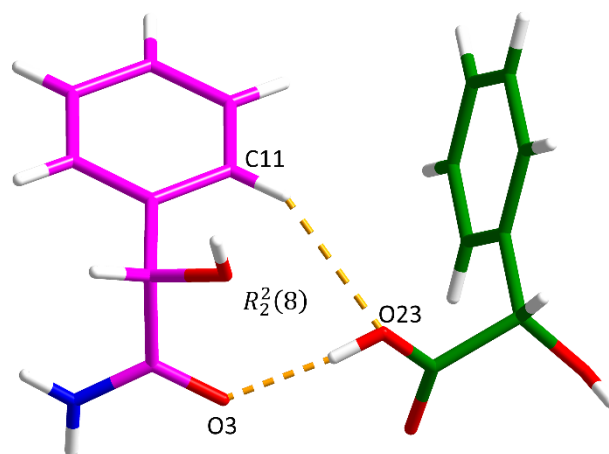
Figure 6.9. DSC curves of (\pm)-MDM, *S*-MDM and MDM (94 *S*:6 *R*).

6.4.2 The Diastereomeric Cocrystal Pair of *S*-MDM and *S* / *R*-MDA

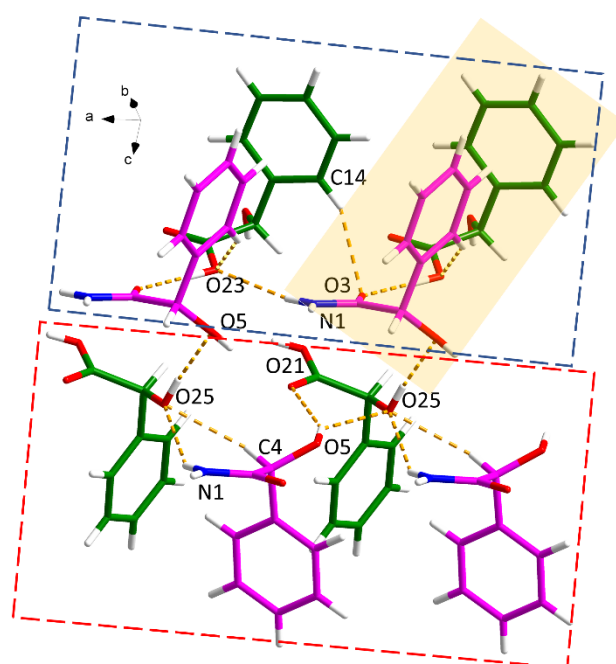
S-MDM-*S*-MDA and *S*-MDM-*R*-MDA cocrystals crystallized in the same space group ($P2_12_12_1$) of the orthorhombic system and have similar unit cell parameters (Table 6.1). Hydrogen bonds geometries are displayed in Tables S6.4 and S6.5, separately.

S-MDM-*S*-MDA crystallizes with one *S*-MDM molecule and one *S*-MDA molecule in the asymmetric unit, Figure 6.10a. These two molecules are connected via C11–H11 \cdots O23 and O23–H23 \cdots O3 discrete hydrogen bonds, forming an $R_2^2(8)$ motif. Two asymmetric unit links through N1–H1A \cdots O23 and C31–H31 \cdots O3 discrete hydrogen bonds, generating a four-molecule motif (top of Figure 6.10b). In the other four-molecule motif (bottom of Figure 6.10b), one *S*-MDM molecule and one *S*-MDA molecule interact through N1–H1B \cdots O25 and C4–H4

⋯O25 discrete hydrogen bonds, forming a similar four-molecule motif via O5–H5⋯O25 and O5–H5⋯O21 discrete hydrogen bonds. These two motifs are further assembled by an O25–H25⋯O5 hydrogen bond.



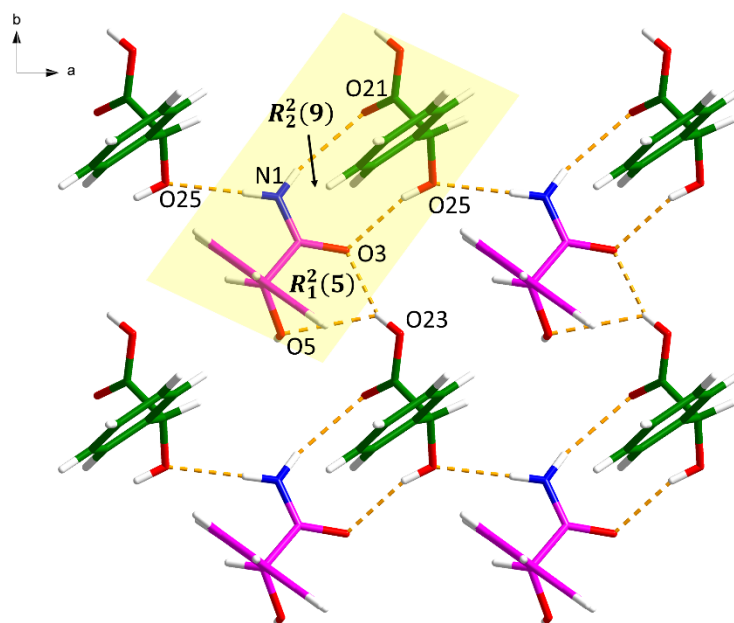
(a)



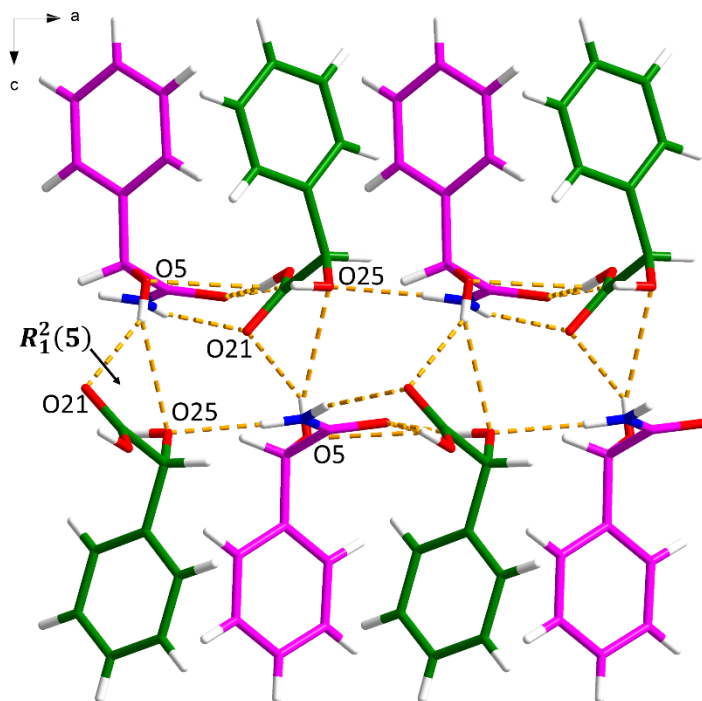
(b)

Figure 6.10. Hydrogen bonding in the *S*-MDM-*S*-MDA cocrystal: (a) asymmetric unit (pink is *S*-MDM and green is *S*-MDA) and (b) 3D hydrogen-bonded network.

The asymmetric unit of *S*-MDM-*R*-MDA contains one *S*-MDM molecule and one *R*-MDA molecule, which are connected via N1–H1A···O21 and O25–H25···O3 discrete hydrogen bonds, forming an $R_2^2(9)$ motif. Along the *c* axis, the asymmetric unit links two adjacent units to extend the 3D structure of the cocrystal through O–H···O hydrogen bonds [forming an $R_1^2(5)$ motif], and N–H···O hydrogen bond, respectively (Figure 6.11a). Additional hydrogen bonding between *S*-MDM and *R*-MDA molecules is observed in a tail-to-tail manner along the *b* axis, where an $R_1^2(5)$ motif is created via O–H···O hydrogen bonds (Figure 6.11b).



(a)



(b)

Figure 6.11. Hydrogen bonding in the *S*-MDM-*R*-MDA cocrystal (pink is *S*-MDM and green is *R*-MDA): (a) along the *a* axis, and (b) along the *b* axis.

The DSC data for the *S*-MDM-*S*-MDA and *S*-MDM-*R*-MDA cocrystals show single endothermic peaks at 85 and 81 °C, respectively, with the melting point of the cocrystals lying lower than those of the corresponding starting materials (Figure 6.12a and b). As shown in Table 6.2 and Figures S6.4 and S6.5, the -NH_2 , -OH , and C=O bands of *S*-MDM exhibit shifts in both cocrystals. All the observed differences indicated that those three moieties are involved in the formation of hydrogen bonds in the different cocrystals, which is consistent with the crystal structural analysis. As shown in Figure 6.12c and d the PXRD patterns for both *S*-MDM-*S*-MDA and *S*-MDM-*R*-MDA cocrystals match with the simulated patterns extracted from the SCXRD analysis, indicating these cocrystals can be reproduced

in bulk quantities by the LAG method. The products were the same irrespective of the source of *S*-MDM (synthesized or commercial) used in the experiments.

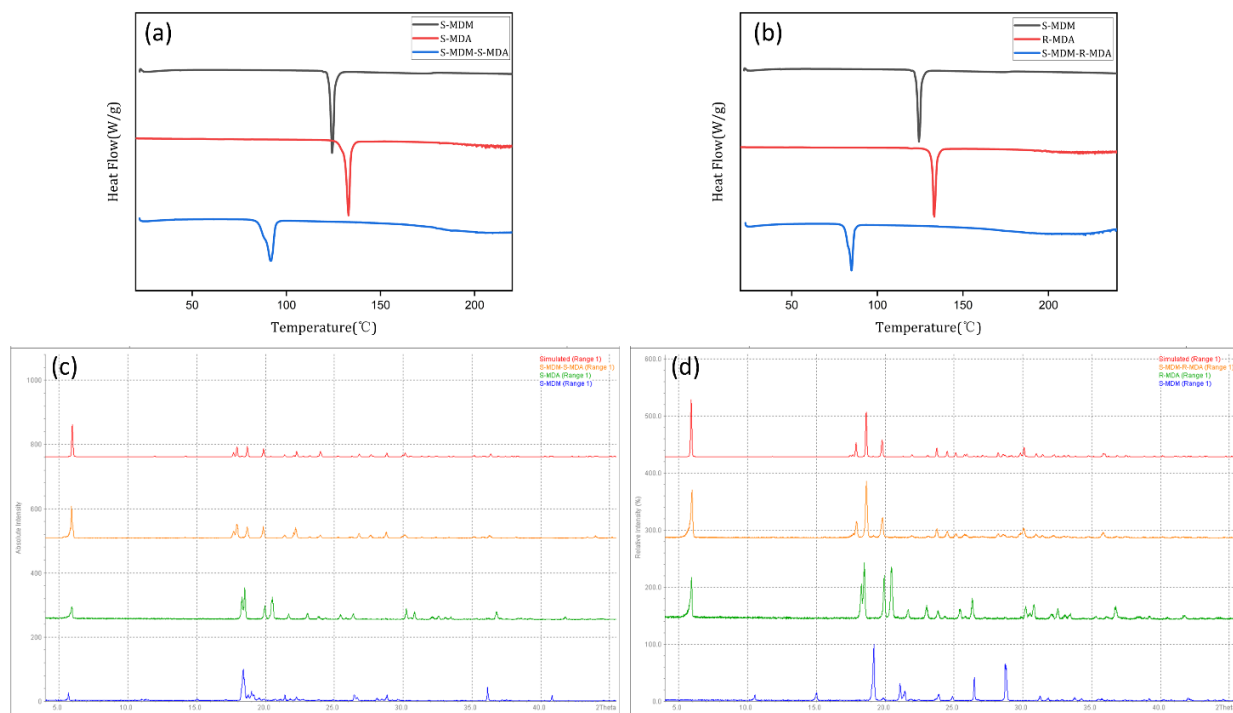


Figure 6.12. DSC plots and PXRD pattern of *S*-MDM-*R* / *S*-MDA cocrystal pair.

6.4.3 The Diastereomeric Cocrystal Pair of *S*-MDM and *L* / *D*-Pro

A stoichiometrically diverse diastereomeric cocrystal system between *S*-MDM and *L* / *D*-Pro was obtained. Hydrogen bonds geometries are displayed in Tables S6.6 and S6.7, respectively. *S*-MDM-*L*-Pro cocrystallized in the orthorhombic $P2_12_12_1$ space group with one *S*-MDM and two *L*-Pro molecules in the asymmetric unit. As shown in Figure 6.13a, *S*-MDM links *L*-Pro 1 through $O5-H5\cdots O27$ hydrogen bond and connects *L*-Pro 2 via $N-H\cdots O$ and $C-H\cdots O$ hydrogen bonds, forming an $R_2^2(8)$ motif. $R_1^2(4)$, $R_2^1(5)$ and $R_3^3(8)$ motifs between *L*-Pro

molecules interlink the chain (Figure 6.13b), stabilizing the 3D hydrogen bonded network of *S*-MDM-L-Pro cocrystal along the *a* axis (Figure 6.13c).

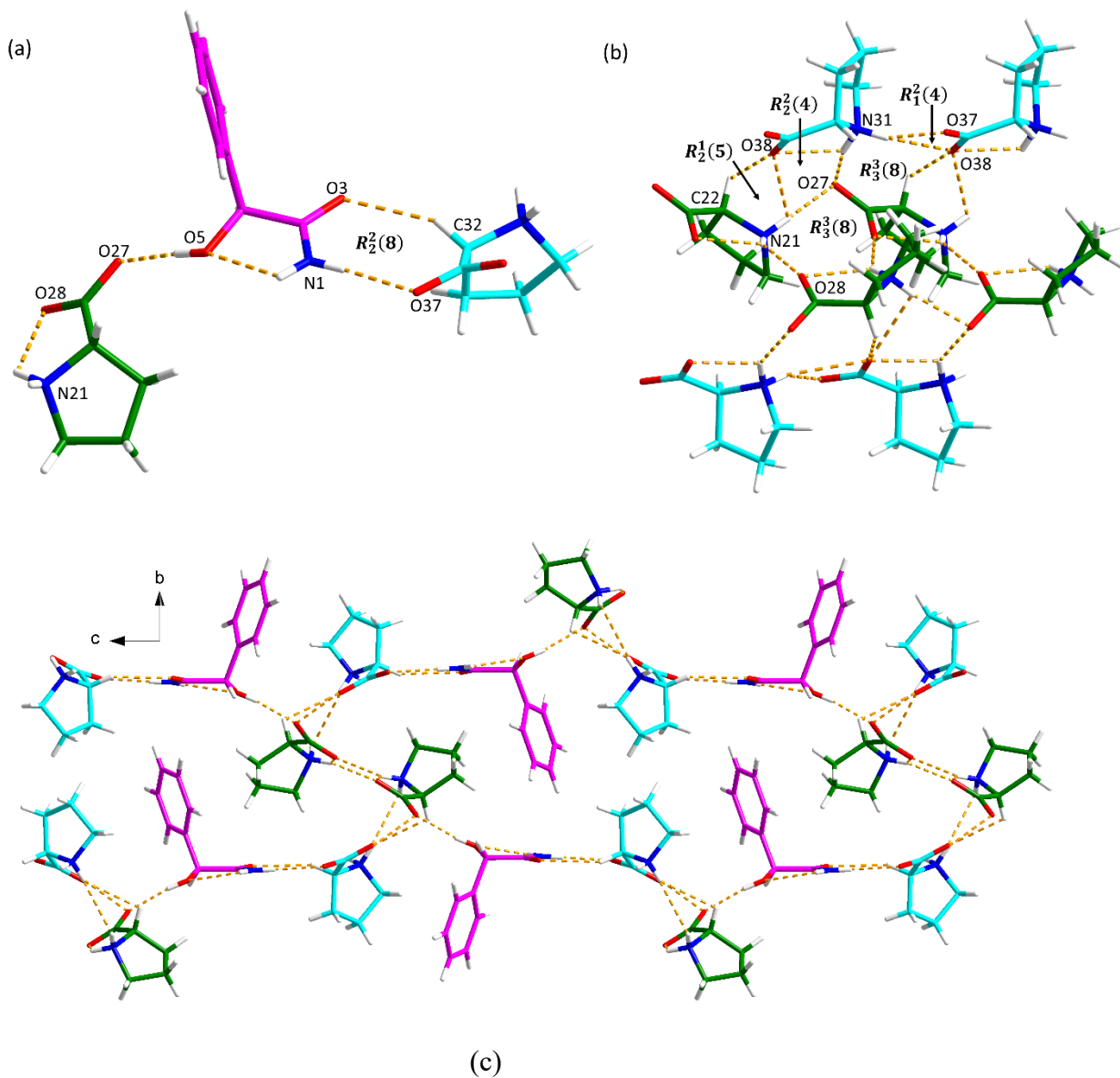
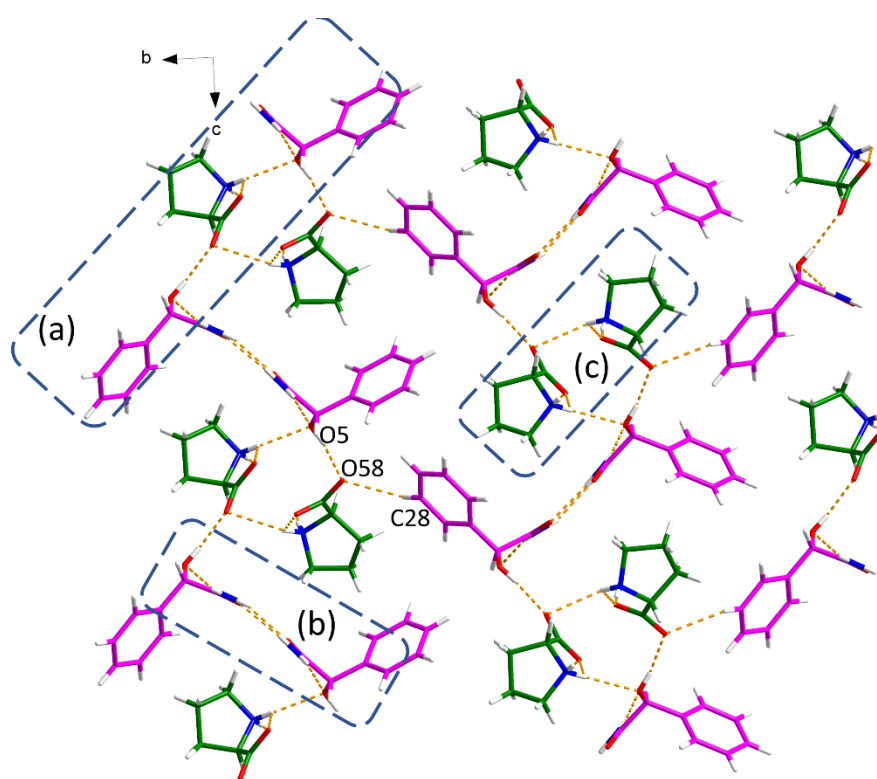


Figure 6.13. Hydrogen bonding in the *S*-MDM-L-Pro cocrystal (pink is *S*-MDM, green is L-Pro 1, and blue is L-Pro 2): (a) hydrogen bonding between *S*-MDM and two L-Pro molecules, (b) hydrogen bonding between L-Pro molecules, and (c) 3D hydrogen-bonded network along the *a* axis. One of the disordered carbon atom conformations of L-Pro 2 has been omitted for clarity.

The *S*-MDM-D-Pro cocrystal crystallizes in the monoclinic space group $P2_1$ and the asymmetric unit consists of two *S*-MDA molecules and two D-Pro molecules ($Z' = 2$). As shown in Figure 6.14, two *S*-MDA molecules and two D-Pro molecules can be regarded as the crystal packing building block, where $R_4^4(16)$ motif and $R_4^3(11)$ motif are created among four *S*-MDA molecules and two D-Pro molecules via N–H \cdots O and O–H \cdots O hydrogen bonds. An $R_4^4(13)$ motif between four D-Pro molecules is also observed in this building block through N–H \cdots O hydrogen bonding. The 3D hydrogen bonded network is extended by connecting different building block through O5–H5 \cdots O58 and C28–H28 \cdots O58 hydrogen bonds. Meanwhile, N–H \cdots O hydrogen bonds between four *S*-MDA molecules also contribute to the stabilization of the crystal structure, forming two $R_3^3(11)$ motifs.



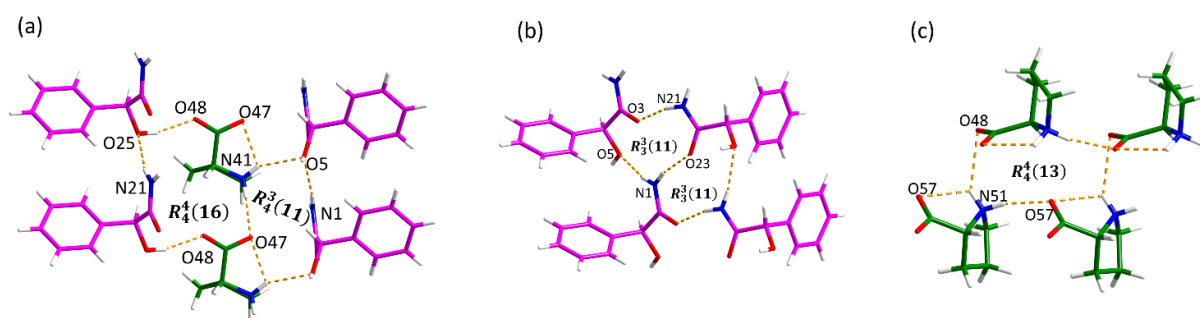


Figure 6.14. Hydrogen bonding in the *S*-MDM-D-Pro cocrystal. The minor disordered component of D-Pro has been omitted for clarity.

A significant difference of melting point between the *S*-MDM-L-Pro and *S*-MDM-D-Pro cocrystals can be observed from the DSC plots (Figure 6.15a and b). The *S*-MDM-L-Pro cocrystal shows a single endothermic peak at 116 °C, which is lower than those of its two constituents. The melting point of *S*-MDM-D-Pro cocrystal is 166 °C, which is in between that of the individual components. The IR data show differences in the $\nu_{\text{N-H}}$, $\nu_{\text{O-H}}$ and $\nu_{\text{C=O}}$, indicating re-construction of hydrogen bond networks in those solids and the formation of new crystalline solids. The experimental PXRD patterns of *S*-MDM-L-Pro and *S*-MDM-D-Pro cocrystals were found to compare well with the simulated PXRD patterns obtained from the SCXRD data (Figure 6.15 c and d). The different sources of *S*-MDM used in the cocrystallization experiments did not influence the products obtained.

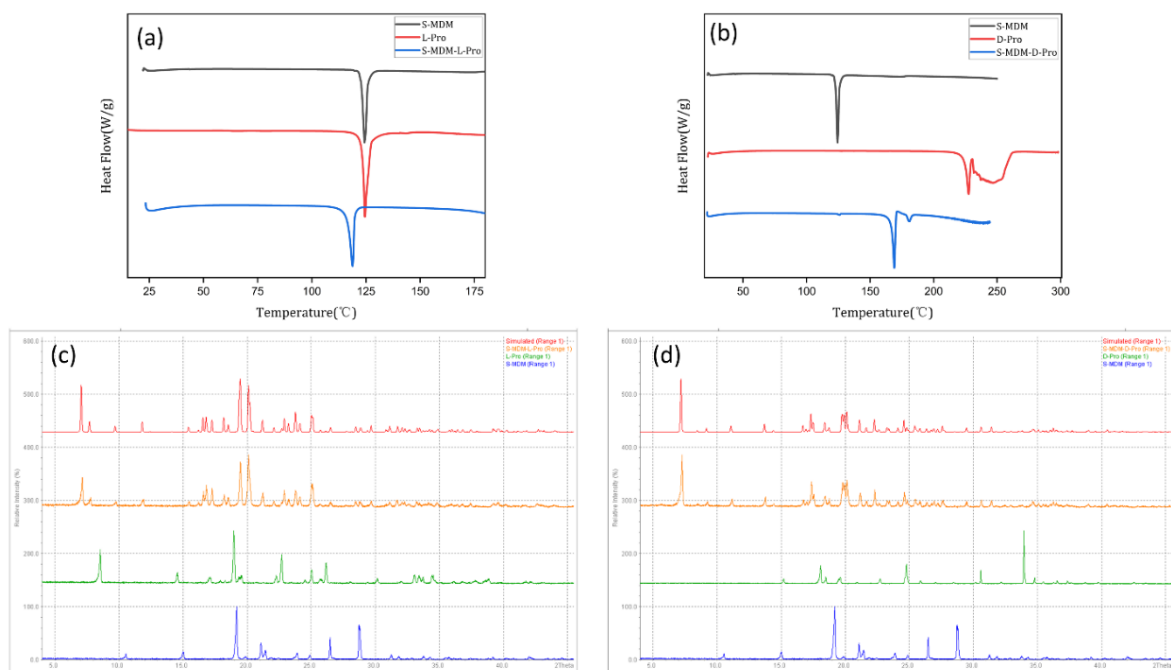


Figure 6.15. DSC plots and PXRD pattern of *S*-MDM-L / D-Pro cocrystal pair.

6.4.4 Analysis of Diastereomeric Cocrystal Pairs of *S*-MDM

When considering chiral resolution using multi-component forms, the use of salts to form a diastereomeric pair is generally observed since the ΔpK_a value is the main influence, whereas whether an enantiospecific cocrystal or a diastereomeric cocrystal pair is formed is not easy to predict due to many different factors affecting the formation of a cocrystal.⁴⁰ In previous work, Springuel *et al.* conducted a CSD search of the existing enantiospecific and diastereomeric cocrystals and found that among 44 multicomponent structures containing two optically active compounds, 38 (86%) systems behave enantiospecifically.⁴¹ This is because the stabilization free energy of cocrystal formation is usually small ($\leq 10 \text{ kJ mol}^{-1}$) as the lattice energy of a cocrystal is generally similar to that of the sum of each component.⁴¹ Strong hydrogen bonds are generally considered as the

primary drivers of cocrystal formation.^{42, 43} Factors such as secondary interactions (π - π stacking interactions, electrostatic potential of molecules), van der Waals interactions and steric hindrance, etc., also play a non-negligible role in the formation of cocrystals as the sum of these energies is similar to the total cocrystal stabilization energy (on the order of kJ mol^{-1}).^{41, 42, 44, 45} As a consequence, even a small change in the structure of the cocrystallizing component, such as a change in absolute and / or relative stereochemistry, can lead to changes in secondary interactions and steric effects, ultimately changing the outcome of cocrystal formation. Flood *et al.* demonstrated that the resolution of *S*-etiracetam (*S*-ETI) from *rac*-etiracetam can be achieved by the formation of enantiospecific cocrystallization of *S*-ETI with *S*-2-chloromandelic acid (*S*-2CLMA).⁴⁶ The reasons why the diastereomeric cocrystal pair did not form were investigated by employing crystal structure prediction and molecular simulations. Even though the predicted hypothetical crystal structure and hydrogen-bonding geometries of *R*-ETI-*S*-2CLMA are extremely similar to those of *S*-ETI-*S*-2CLMA, the differences in aromatic interactions and lattice energy were sufficient for the formation of *S*-ETI-*S*-2CLMA cocrystal to be more energetically favoured.

For the formation of a diastereomeric cocrystal pair, more changes in the hydrogen bonding network and molecular arrangement are required in order to reduce the influence of the secondary interactions and steric effects to the total cocrystal stabilization energy.⁴¹ As mentioned earlier, diastereomeric cocrystals of *S*-MDM with *S* / *R*-MDA have similar unit cell parameters, and the stoichiometric ratio between *S*-MDM and the coformers are the same. However, the hydrogen-bonding between the two components in these cocrystals differ significantly.

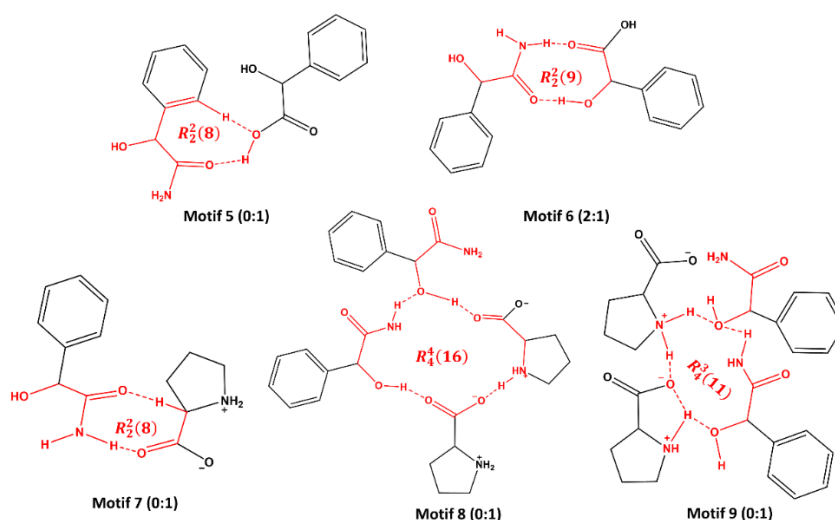


Figure 6.16. The types of motifs of *S*-MDM with coformers identified in this work. Numbers indicate occurrences in the CSD (left) and in this work (right).

As shown in Figure 6.16 binary level hydrogen bonding motifs are present in *S*-MDM-*S*-MDA (motif 5) and *S*-MDM-*R*-MDA cocrystals (motif 6), respectively. For the *S*-MDM-*S*-MDA cocrystal, only the hydroxyl group from carboxyl group of *S*-MDA, serving as both hydrogen-bonding donor and acceptor, is engaged in the hydrogen bond formation, while both the oxygen atom of the carbonyl group and a hydrogen atom (H11) from the benzene ring of *S*-MDM are involved in the hydrogen bond construction. In contrast, for the *S*-MDM-*R*-MDA cocrystal, hydrogen bonding occurs between the carbonyl oxygen atom and the hydroxyl group of *R*-MDA and the amide group of *S*-MDM. Motif 5 is not found in any structures through the CSD search, whereas motif 6 was presented in two reports (Refcodes: VASWOC⁴⁷ and ZZZRJG01⁴⁸). These orientationally restrictive interaction motifs determine the formation of diastereomeric cocrystal pairs between *S*-MDM and *S* / *R*-MDA.⁴⁹ Moreover, the different contacts in these two cocrystals can be visualized by their 2D fingerprint plots (Figure S6.10a and Table S6.8). Hydrogen-bonding in *S*-MDM-*S*-MDA cocrystal constitute a bigger

proportion compared with those in *S*-MDM-*R*-MDA cocrystal, while in contrast, van der Waals interactions account for a larger percentage in the *S*-MDM-*R*-MDA cocrystal. These significant differences lead to the remarkable changes in the crystal packing for this diastereomeric pair.

Compared to the *S*-MDM-*S* / *R*-MDA diastereomeric cocrystal pair, the differences between the *S*-MDM-*L*-Pro and *S*-MDM-*D*-Pro cocrystals are more significant. Apart from the dissimilar motifs (motif 7 from *S*-MDM-*L*-Pro, motifs 8 and 9 from *S*-MDM-*D*-Pro) resulting from different functional groups in two cocrystals and their distinct 2D fingerprint plots and corresponding contact contributions (Figure S6.10b and Table S6.8), the primary factor that overcame the obstacle of stabilization free energy for cocrystal formation is the varying stoichiometric ratios of *S*-MDM and *L* / *D*-Pro. This is similar to the recent report by Leyssens and co-workers for *L*-Pro with mandelic acid.²⁰

6.5 Conclusions

In summary, the crystal structures of racemic MDM, *S*-MDM and MDM (94 *S*:6 *R*) were identified and fully characterized in this work. The formation of MDM (94 *S*:6 *R*) can be rationalized either on the basis of solvent effects, since it was observed by crystallization from a THF / toluene mixture, or fast crystallization using the rotatory evaporator, which is a method that can produce new crystalline forms.²⁴ Additionally, this study reports the synthesis and characterization of two novel diastereomeric cocrystal pairs of *S*-MDM with both enantiomers of mandelic acid (*S*-MDM-*S*-MDA and *S*-MDM-*R*-MDA) and proline (*S*-MDM-*L*-Pro and *S*-MDM-*D*-Pro). The *S*-MDM-*S*-MDA and *S*-MDM-*R*-MDA cocrystals have similar unit cell parameters and the same stoichiometric ratio (1:1), yet significantly

different hydrogen-bonding between the two conformers plays a critical structure determining role. The formation of *S*-MDM-L-Pro and *S*-MDM-D-Pro diastereomeric cocrystals proceeds with different stoichiometries, similar to a recent report of proline with mandelic acid,²⁰ although the structure determining features are very different.

REFERENCES

- (1) Inaki, M.; Liu, J.; Matsuno, K., Cell chirality: its origin and roles in left–right asymmetric development. *Philos. Trans. R. Soc. Lond. B Biol. Sci.* **2016**, 371, (1710), 20150403.
- (2) Liu, Y.; Xiao, J.; Koo, J.; Yan, B., Chirality-driven topological electronic structure of DNA-like materials. *Nat. Mater.* **2021**, 20 638–644.
- (3) Brandt, J. R.; Salerno, F.; Fuchter, M. J., The added value of small-molecule chirality in technological applications. *Nat. Rev. Chem.* **2017**, 1, 0045.
- (4) Zhou, Y.; Wu, S.; Zhou, H.; Huang, H.; Zhao, J.; Deng, Y.; Wang, H.; Yang, Y.; Yang, J.; Luo, L., Chiral pharmaceuticals: Environment sources, potential human health impacts, remediation technologies and future perspective. *Environ. Int.* 121, 523–537.
- (5) McConathy, J.; Owens, M. J., Stereochemistry in Drug Action. *Prim. Care Companion J. Clin. Psychiatry.* **2003**, 5, (2), 70–73.
- (6) Blessington, B.; Beiraghi, A., Study of the stereochemistry of ethambutol using chiral liquid chromatography and synthesis. *J. Chromatogr. A* **1990**, 522, 195–203.
- (7) Brooks, W. H.; Guida, W. C.; Daniel, K. G., The Significance of Chirality in Drug Design and Development. *Curr. Top. Med. Chem.* **2011**, 11, (7), 760–

770.

- (8) Ault, A., The Nobel Prize in Chemistry for 2001. *J. Chem. Educ.* **2002**, *79*, (5).
- (9) Nguyen, L. A.; He, H.; Pham-Huy, C., Chiral Drugs: An Overview. *Int. J. Biol. Sci.* **2006**, *2*, (2), 85–100.
- (10) Lee, H. L.; Hung, Y. L.; Amin, A.; Pratama, D. E.; Lee, T., Green and Strategic Approach for Chiral Resolution by Diastereomeric Salt Formation: The Study of Racemic Ibuprofen. *Ind. Eng. Chem. Res.* **2023**, *62*, (4), 1946–1957.
- (11) Yang, L.-C.; Deng, H.; Renata, H., Recent Progress and Developments in Chemoenzymatic and Biocatalytic Dynamic Kinetic Resolution. *Org. Process Res. Dev.* **2022**, *26*, (7), 1925–1943.
- (12) Pinto, M. M. M.; Fernandes, C.; Tiritan, M. E., Chiral Separations in Preparative Scale: A Medicinal Chemistry Point of View. *Molecules.* **2020**, *25*, (8), 1931.
- (13) Pawar, N.; Saha, A.; Nandan, N.; Parambil, J. V., Solution Cocrystallization: A Scalable Approach for Cocrystal Production. *Crystals.* **2021**, *11*, (3), 303.
- (14) Springuel, G.; Leyssens, T., Innovative Chiral Resolution Using Enantiospecific Co-Crystallization in Solution. *Cryst. Growth Des.* **2012**, *12*, 3374–3378.
- (15) Buol, X.; Garrido, C. C.; Robeyns, K.; Tumanov, N.; Collard, L.; Wouters, J.; Leyssens, a. T., Chiral Resolution of Mandelic Acid through Preferential Cocrystallization with Nefiracetam. *Cryst. Growth Des.* **2020**, *20*, 7979–7988.
- (16) Shemchuk, O.; Song, L.; Tumanov, N.; Wouters, J.; Braga, D.; Grepioni, F.; Leyssens, a. T., Chiral Resolution of *RS*-Oxiracetam upon Cocrystallization

- with Pharmaceutically Acceptable Inorganic Salts. *Cryst. Growth Des.* **2020**, 20, (4), 2602–2607.
- (17) Harmsen, B.; Leysens, T., Dual-Drug Chiral Resolution: Enantiospecific Cocrystallization of (*S*)-Ibuprofen Using Levetiracetam. *Cryst. Growth Des.* **2017**, 18, (1), 441–448.
- (18) Shemchuk, O.; Grepioni, F.; Leysens, T.; Braga, D., Chiral Resolution via Cocrystallization with Inorganic Salts. *Isr. J. Chem.* **2021**, 61, 563–572.
- (19) Sánchez-Guadarrama, O.; Mendoza-Navarro, F.; Cedillo-Cruz, A.; Jung-Cook, H.; Arenas-García, J. I.; Delgado-Díaz, A.; Herrera-Ruiz, D.; Morales-Rojas, H.; Höpfl, H., Chiral Resolution of *RS*-Praziquantel via Diastereomeric Co-Crystal Pair Formation with L-Malic Acid. *Cryst. Growth Des.* **2015**, 16, (1), 307–314.
- (20) Zhou, F.; Collard, L.; Robeyns, K.; Leysens, T.; Shemchuk, O., L-Proline, a resolution agent able to target both enantiomers of mandelic acid: an exciting case of stoichiometry controlled chiral resolution. *Chem. Commun.* **2022**, 58, 8560–8563.
- (21) Groom, C. R.; Bruno, I. J.; Lightfoot, M. P.; Ward, S. C., The Cambridge Structural Database. *Acta Cryst.* **2016**, B72, 171–179.
- (22) Stokes, M. E.; Surman, M. D.; Calvo, V.; Surguladze, D.; Li, A.-H.; Gasparek, J.; Betzenhauser, M.; Zhu, G.; Du, H.; Rigby, A. C.; Mulvihill, M. J., Optimization of a Novel Mandelamide-Derived Pyrrolopyrimidine Series of PERK Inhibitors. *Pharmaceutics.* **2022**, 14, (10), 2233.
- (23) Lloyd-Jones, G. C.; Wall, P. D.; Slaughter, J. L.; Parker, A. J.; Laffan, D. P., Enantioselective homoallyl-cyclopropanation of dibenzylideneacetone by modified allylindium halide reagents—rapid access to enantioenriched 1-

- styryl-norcarene. *Tetrahedron*. **2006**, 62, (49), 11402–11412.
- (24) Bag, P. P.; Reddy, C. M., Screening and Selective Preparation of Polymorphs by Fast Evaporation Method: A Case Study of Aspirin, Anthranilic Acid, and Niflumic Acid. *Cryst. Growth Des.* **2012**, 12, (6), 2740–2743.
- (25) Sinha, A. S.; Rao Khandavilli, U. B.; O'Connor, E. L.; Deadman, B. J.; Maguire, A. R.; Lawrence, S. E., Novel co-crystals of the nutraceutical sinapic acid. *CrystEngComm*. **2015**, 17, (26), 4832–4841.
- (26) Sheldrick, G. M., Crystal structure refinement with SHELXL. *Acta Cryst.* **2015**, C71, 3-8.
- (27) APEX2 v2009.3-0. *Bruker AXS* **2009**.
- (28) Xu, J.; Huang, Y.; Ruan, S.; Chi, Z.; Qin, K.; Cai, B.; Cai, T., Cocrystals of isoliquiritigenin with enhanced pharmacokinetic performance. *CrystEngComm*. **2016**, 18, (45), 8776–8786.
- (29) Spek, A. L., Structure validation in chemical crystallography. *Acta Cryst.* **2009**, D65, 148-155.
- (30) Huang, S.; Xu, J.; Peng, Y.; Guo, M.; Cai, T., Facile Tuning of the Photoluminescence and Dissolution Properties of Phloretin through Cocrystallization. *Cryst. Growth Des.* **2019**, 19, (12), 6837–6844.
- (31) Spackman, P. R.; Turner, M. J.; McKinnon, J. J.; Wolff, S. K.; Grimwood, D. J.; Jayatilaka, D.; Spackman, M. A., CrystalExplorer: a program for Hirshfeld surface analysis, visualization and quantitative analysis of molecular crystals. *J. Appl. Cryst.* **2021**, 54, 1006–1011.
- (32) Bruno, I. J.; Cole, J. C.; Edgington, P. R.; Kessler, M.; Macrae, C. F.; McCabe, P.; Pearson, J.; Taylor, R., New software for searching the Cambridge Structural Database and visualizing crystal structures. *Acta Cryst.*

- 2002**, B58, 389–397.
- (33) Almog, J.; Rozin, R.; Klein, A.; Shamuilov-Levinton, G.; Cohen, S., The reaction between phloroglucinol and vic polycarbonyl compounds: extension and mechanistic elucidation of Kim's synthesis for bipolarofacial bowl-shaped compounds. *Tetrahedron*. **2009**, 65, (38), 7954–7962.
- (34) Smit, J. P., CCDC 2109758. *Experimental Crystal Structure Determination*. **2021**, DOI: 10.5517/ccdc.csd.cc28tcq6.
- (35) Pinter, E. N.; Cantrell, L. S.; Day, G. M.; Wheeler, K. A., Pasteur's tartaramide/malamide quasiracemates: new entries and departures from near inversion symmetry. *CrystEngComm*. **2018**, 20, 4213–4220.
- (36) Gawroński, J.; Gawrońska, K.; Skowronek, P.; Rychlewska, U.; Warzajtis, B.; Rychlewski, J.; Hoffmann, M.; Szarecka, A., Factors Affecting Conformation of (R,R)-Tartaric Acid Ester, Amide and Nitrile Derivatives. X-Ray Diffraction, Circular Dichroism, Nuclear Magnetic Resonance and Ab Initio Studies. *Tetrahedron*. **1997**, 53, (17), 6113–6144.
- (37) Janiak, A.; Rychlewska, U.; Marcin Kwit, U. S.; Gawrońska, K.; Gawroński, J., From Single Molecule to Crystal: Mapping Out the Conformations of Tartaric Acids and Their Derivatives. *ChemPhysChem*. **2012**, 13, 1500–1506.
- (38) Kanda, T.; Naraoka, A.; Naka, H., Catalytic Transfer Hydration of Cyanohydrins to α -Hydroxyamides. *J. Am. Chem. Soc.* **2019**, 141, (2), 825–830.
- (39) Mislow, K., Introduction to Stereochemistry. ed.; W. A. Benjamin, Inc: New York, Amsterdam, **1966**.
- (40) George, F.; Tumanov, N.; Norberg, B.; Robeyns, K.; Filinchuk, Y.; Wouters, J.; Leyssens, T., Does Chirality Influence the Tendency toward Cocrystal

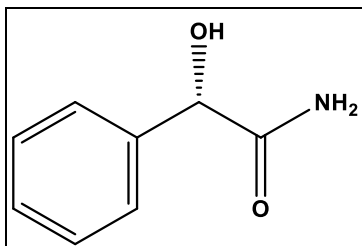
- Formation? *Cryst. Growth Des.* **2014**, *14*, 2880–2892.
- (41) Springuel, G.; Robeyns, K.; Norberg, B.; Wouters, J.; Leysens, T., Cocrystal Formation between Chiral Compounds: How Cocrystals Differ from Salts. *Cryst. Growth Des.* **2014**, *14*, (8), 3996–4004.
- (42) Taylor, C. R.; Day, G. M., Evaluating the Energetic Driving Force for Cocrystal Formation. *Cryst. Growth Des.* **2018**, *18*, 892–904.
- (43) Huang, S.; Cheemarla, V. K. R.; Tiana, D.; Lawrence, S. E., Experimental and Theoretical Investigation of Hydrogen-Bonding Interactions in Cocrystals of Sulfaguanidine. *Cryst. Growth Des.* **2023**, *23*, (4), 2306–2320.
- (44) Arunan, E.; Desiraju, G. R.; Klein, R. A.; Sadlej, J.; Scheiner, S.; Alkorta, I.; Clary, D. C.; Crabtree, R. H.; Dannenberg, J. J.; Hobza, P.; Kjaergaard, H. G.; Legon, A. C.; Mennucci, B.; Nesbitt, a. D. J., Definition of the hydrogen bond (IUPAC Recommendations 2011). *Pure Appl. Chem.* **2011**, *83*, (8), 1637–1641.
- (45) Shahi, A.; Arunan, E., Why are Hydrogen Bonds Directional? *Chem. Sci. J.* **2016**, *128*, 1571–1577.
- (46) Nulek, T.; Klaysri, R.; Cedeno, R.; Nalaoh, P.; Bureekaew, S.; Promarak, V.; Flood, A. E., Separation of Etiracetam Enantiomers Using Enantiospecific Cocrystallization with 2-Chloromandelic Acid. *ACS Omega.* **2022**, *7*, 19465–19473.
- (47) Mičová, J.; Steiner, B.; Koóš, M.; Langer, V.; Gyepesová, D., Characterisation and X-ray crystallography of products from the Bucherer–Bergs reaction of methyl 2,3-O-isopropylidene- α -D-lyxo-pentodialdo-1,4-furanoside. *Carbohydr. Res.* **2003**, *338*, (19), 1917–1924.
- (48) Rychlewska, U.; Warzajtis, B., Packing modes of (*R,R*)-tartaric acid esters

and amides. *Acta Cryst.* **2000**, B56, 833–848.

- (49) Habgood, M., Analysis of Enantiospecific and Diastereomeric Cocrystal Systems by Crystal Structure Prediction. *Cryst. Growth Des.* **2013**, 13, (10), 4549–4558.

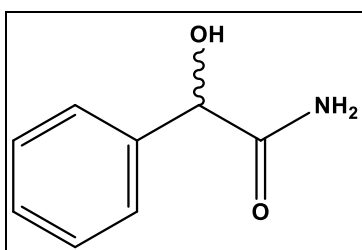
Supporting Information

(*S*)-2-Hydroxy-2-phenylacetamide¹



This was synthesized following a literature procedure.¹ (*S*)-2-Hydroxy-2-phenylacetic acid (6.00 g, 39 mmol) was dissolved in MeOH (60 mL) and cooled to 0°C. Acetyl chloride (3.38 mL, 47 mmol) was added dropwise to the solution. The reaction mixture was allowed to warm to room temperature and stirred for 24 h. The resulting solution was concentrated under reduced pressure to give a colourless liquid, which was dissolved in MeOH (25 mL). Aqueous NH₃ (85 mL, 35% w/v) was added, and the solution was stored at below 5°C for a further 24 h. The solution was then concentrated under reduced pressure to give a white solid *S*-MDM I, which was recrystallised from hot ethanol to yield white plates (2.45 g, 41%). mp 117-120°C, (lit.² 118–120 °C); [α]²⁵_D = +51.5 (c 1.05 in EtOH) [Lit.³, [α]²⁵_D = +57 (c 1.05 in EtOH)]; $\nu_{\max}/\text{cm}^{-1}$ (ATR): 3346, 3182, 1680, 1655, 1586, 1452, 1292, 1098, 1055. ¹H NMR (400 MHz, CD₃OD): 4.99 (1H, s, *CHOH*), 7.22-7.37 (3H, m, aromatic *H*), 7.46 (2H, d, *J* = 9.5 Hz, aromatic *H*); ¹³C NMR (100.6 MHz, CD₃OD): 75.4 (*CHOH*), 128.0 (aromatic CH), 129.2 (aromatic CH), 129.4 (aromatic CH), 141.7 (aromatic C_q), 178.6 (C=O).

(±)-2-Hydroxy-2-phenylacetamide¹



This was synthesized following a literature procedure.¹ (±)-Hydroxy-2-phenylacetic acid (8.09 g, 53 mmol) was dissolved in MeOH (70 mL) and cooled to 0°C. Acetyl chloride (9.95 mL, 139 mmol) was

added dropwise to the solution. The reaction mixture was allowed to warm to room temperature and stirred for 24 h. The resulting solution was concentrated under reduced pressure to give a colourless liquid, which was dissolved in MeOH (35 mL). Aqueous NH₃ (100 mL, 35% w/v) was added, and the solution was stored at below 5°C for a further 24 h. The solution was then concentrated under reduced pressure to give a white solid (±)-MDM I, which was recrystallised from hot ethanol to yield white plates (6.92 g, 86%). mp by DSC 133-135° C (lit.⁴ 132-135 °C); $\nu_{\max}/\text{cm}^{-1}$ (ATR): 3380, 3251, 1650, 1635, 1597, 1444, 1056; ¹H NMR (400 MHz, CD₃OD): 4.99 (1H, s, CHOH), 7.19-7.37 (3H, m, aromatic H), 7.45 (2H, d, $J = 8.5$ Hz, aromatic H); ¹³C NMR (100.6 MHz, CD₃OD): 75.4 (CHOH), 128.0 (aromatic CH), 129.1 (aromatic CH), 129.4 (aromatic CH), 141.7 (aromatic C_q), 178.6 (C=O).

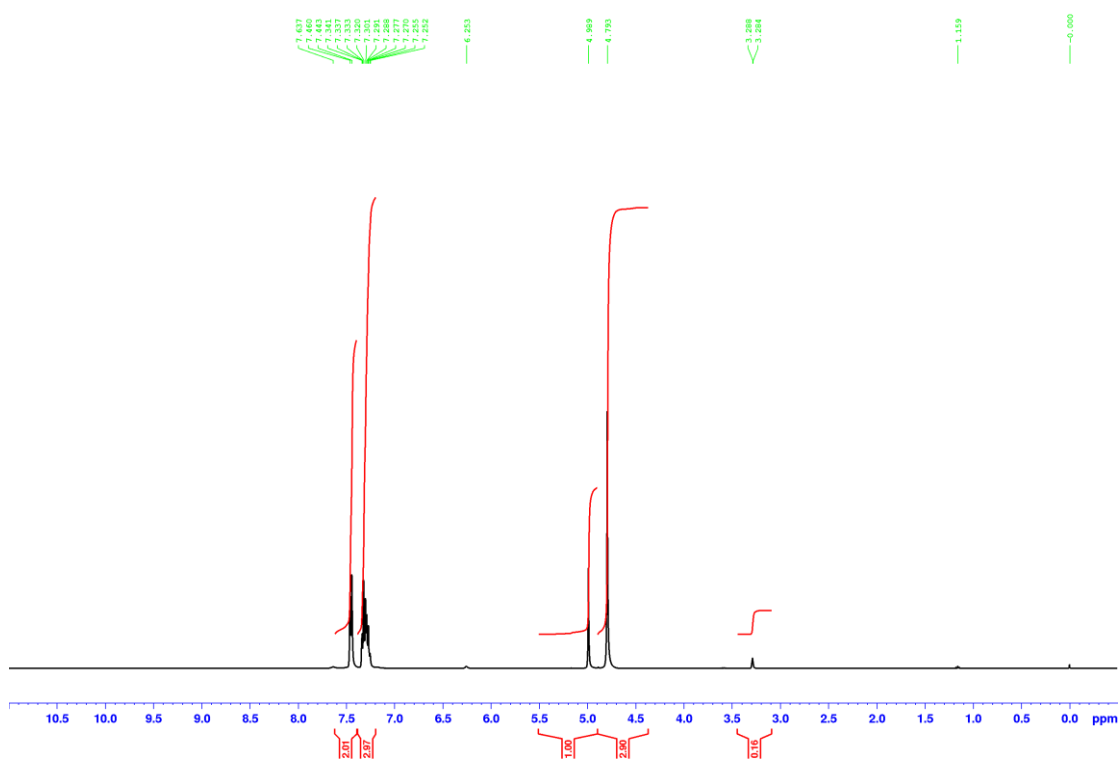


Figure S6.1. ¹H NMR spectrum of *S*-MDM (CD₃OD, 400 MHz). Peaks at 3.29 and 4.79 due to MeOH and total exchangeable hydrogens.

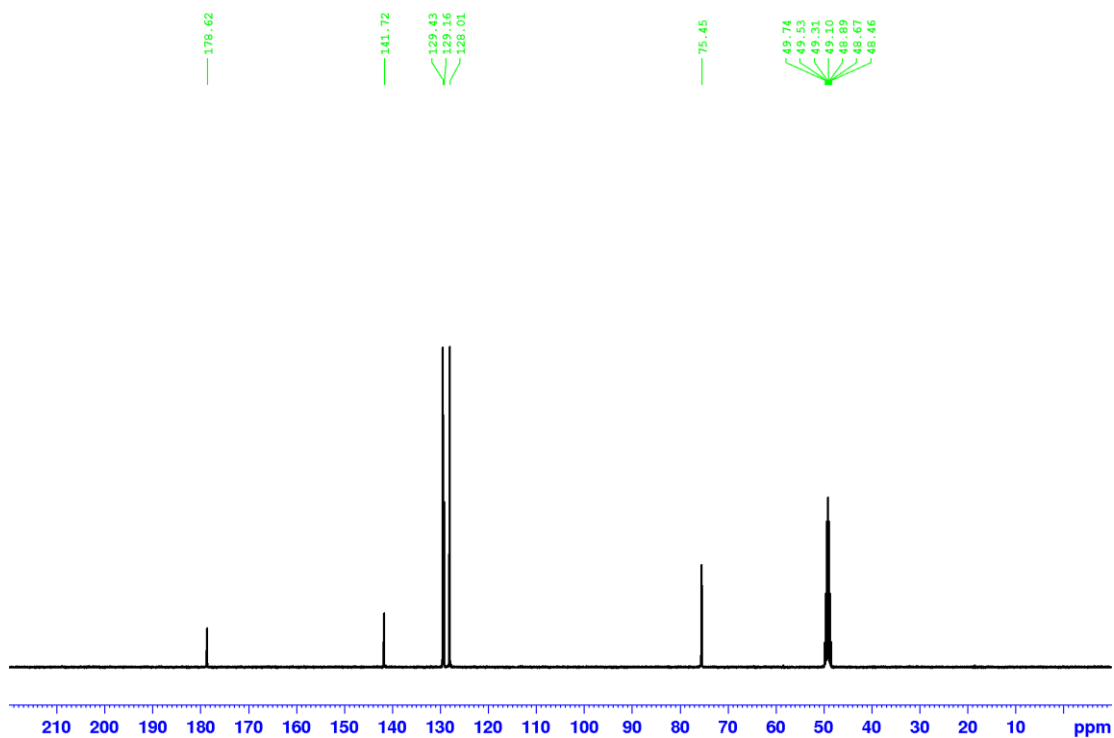


Figure S6.2. ^{13}C NMR spectrum of *S*-MDM (CD_3OD , 400 MHz). Peaks at 48.4-49.7 due to CD_3OD

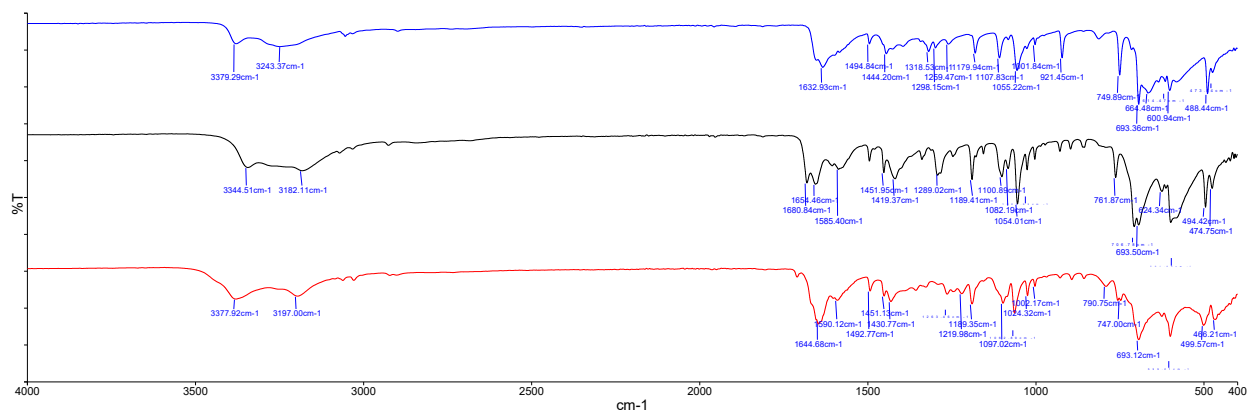


Figure S6.3. IR spectra of (\pm)-MDM (blue), *S*-MDM (black) and MDM (94 *S*:6 *R*) (red).

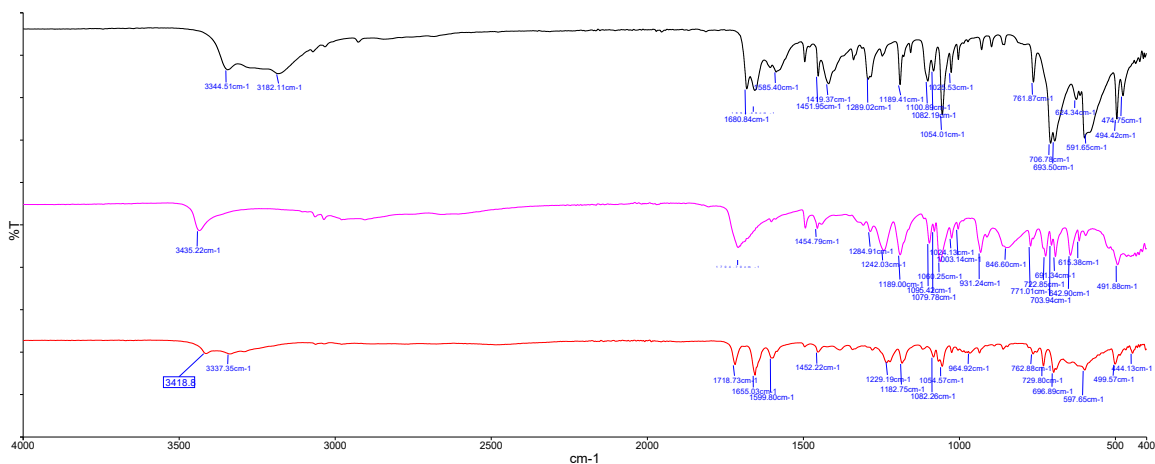


Figure S6.4. IR spectra of *S*-MDM (black), *S*-MDA (pink) and *S*-MDM-*S*-MDA cocrystal (red).

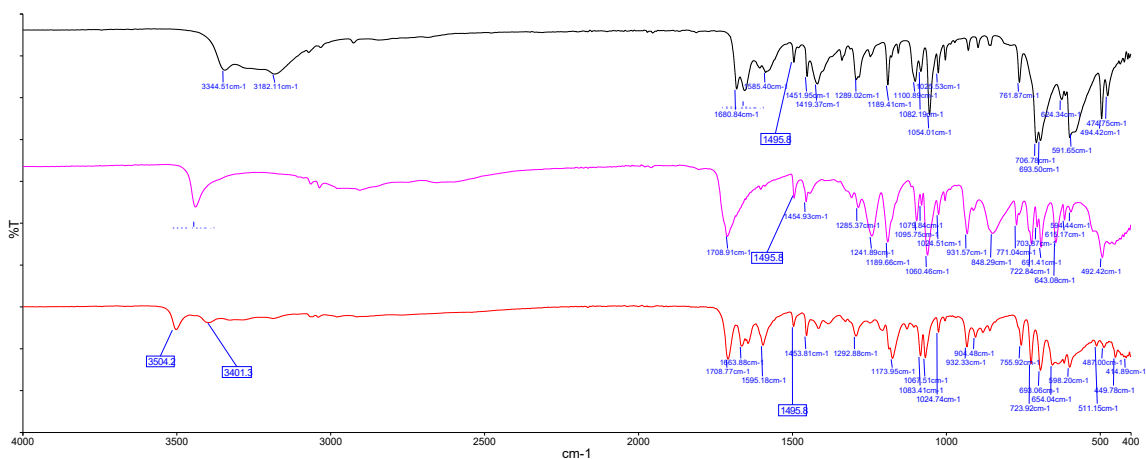


Figure S6.5. IR spectra of *S*-MDM (black), *R*-MDA (pink) and *S*-MDM-*R*-MDA cocrystal (red).

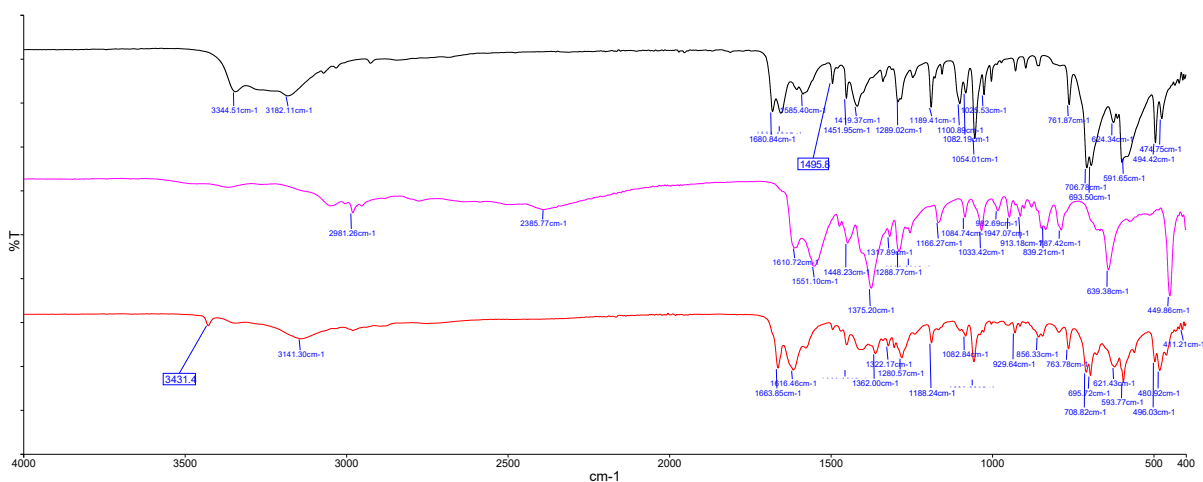


Figure S6.6. IR spectra of *S*-MDM (black), L-Pro (pink) and *S*-MDM-L-Pro cocrystal (red).

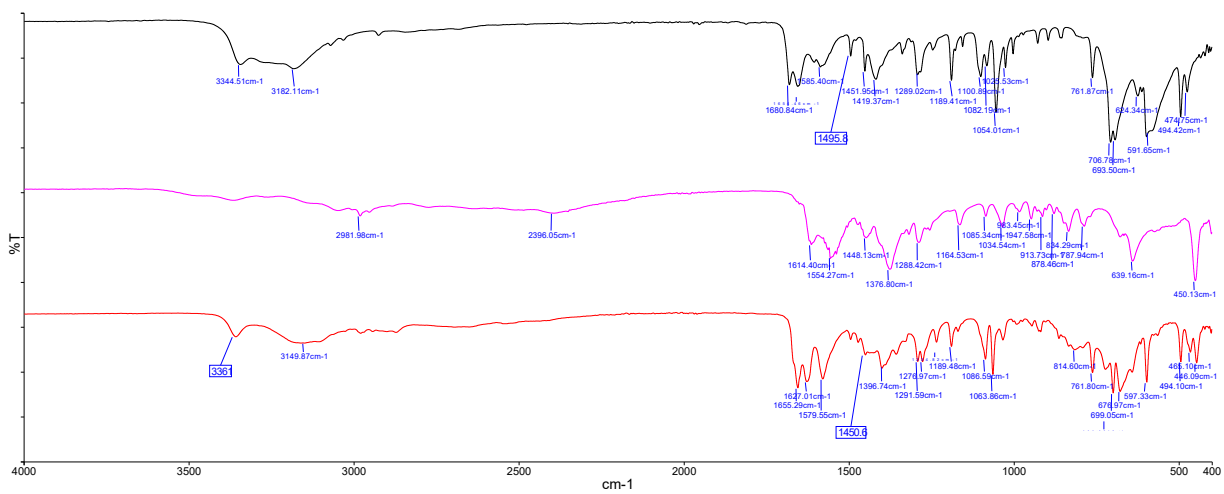
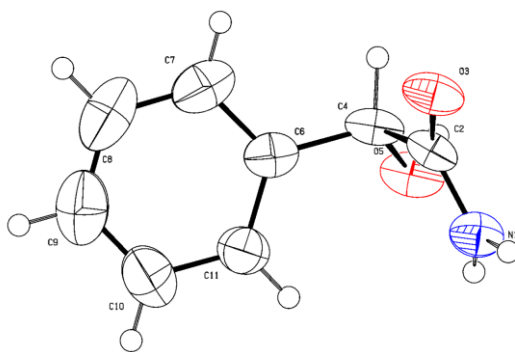
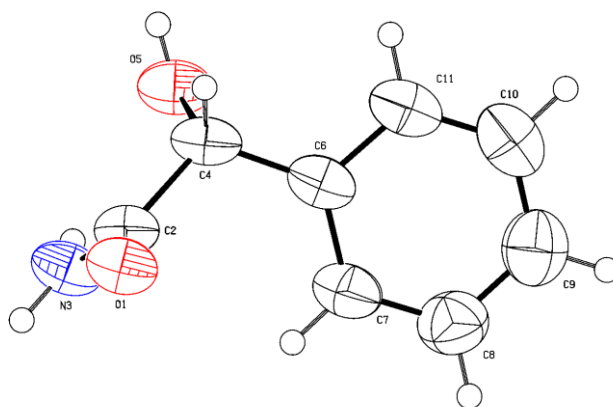
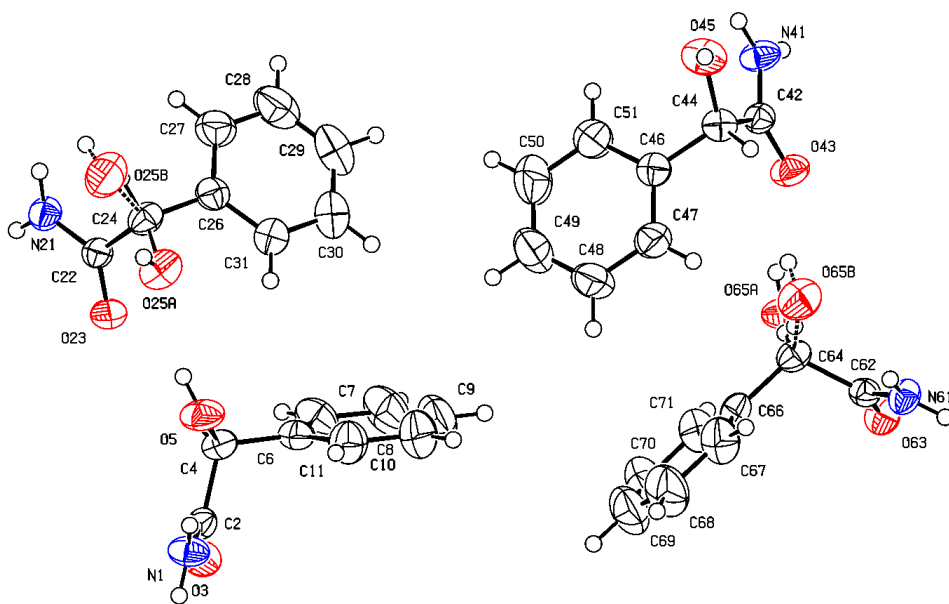
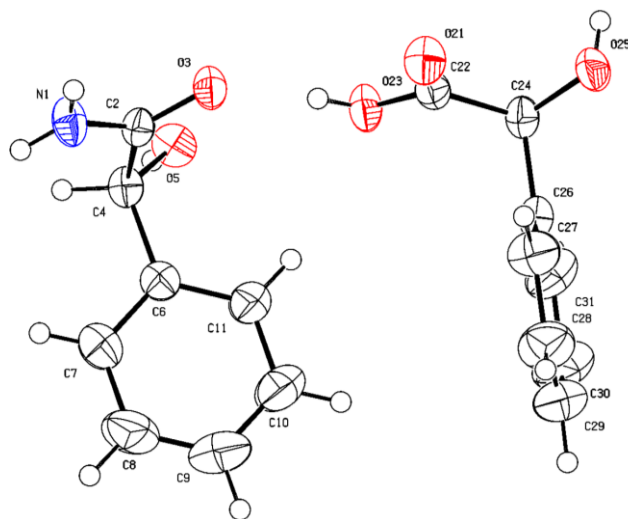


Figure S6.7. IR spectra of *S*-MDM (black), *D*-Pro (pink) and *S*-MDM-*D*-Pro cocrystal (red).

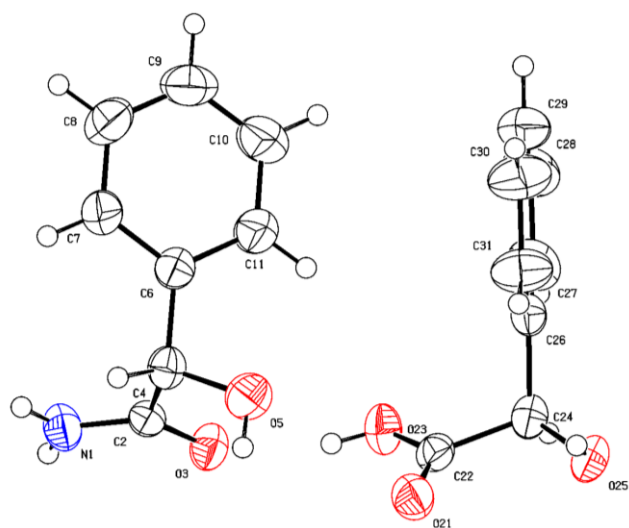




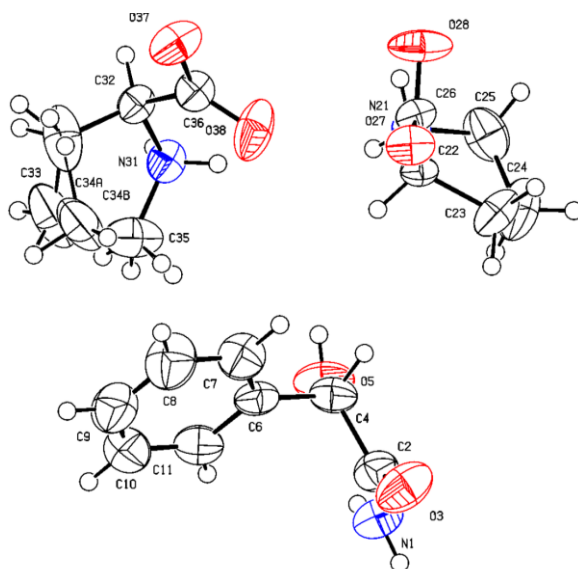
(c)



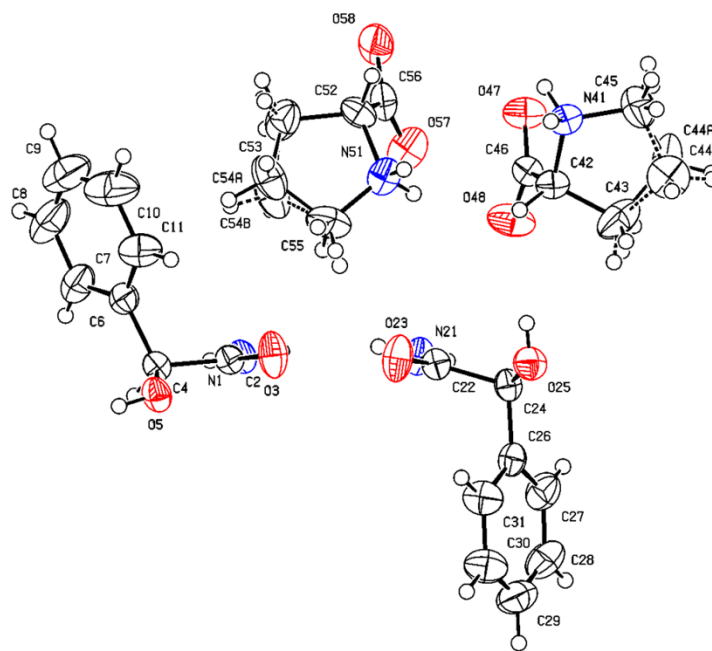
(d)



(e)

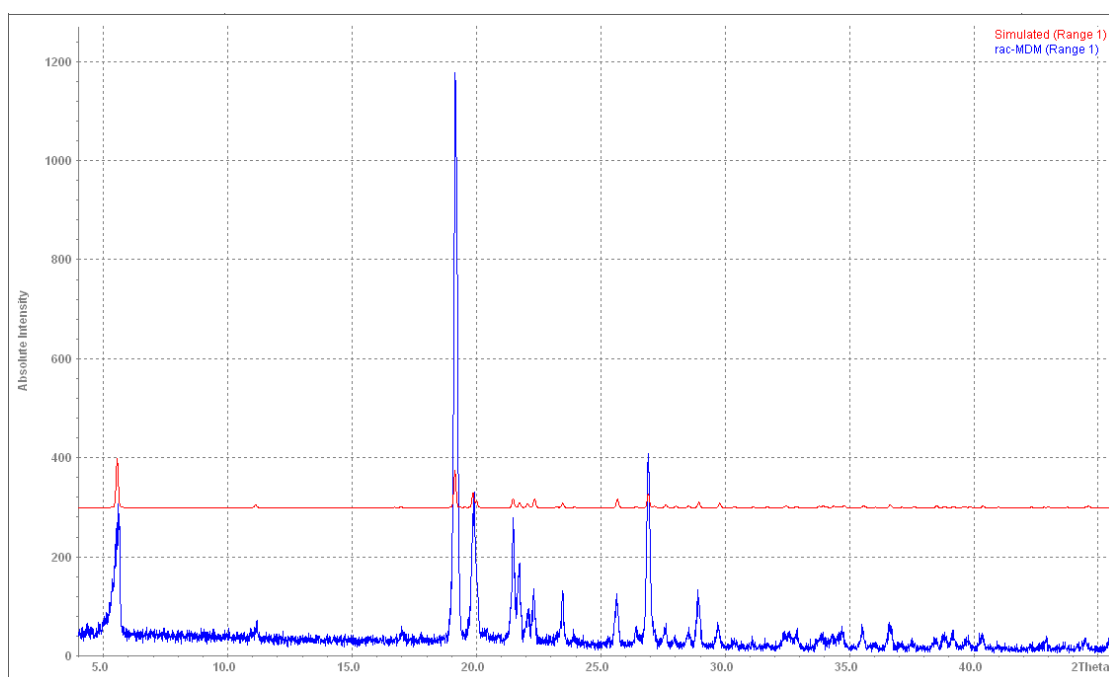


(f)



(g)

Figure S6.8. Ellipsoid plot of (a) (\pm)-MDM, (b) *S*-MDM, (c) MDM (94 *S*:6 *R*), (d) *S*-MDM-*S*-MDA, (e) *S*-MDM-*R*-MDA, (f) *S*-MDM-*L*-Pro and (g) *S*-MDM-*D*-Pro.



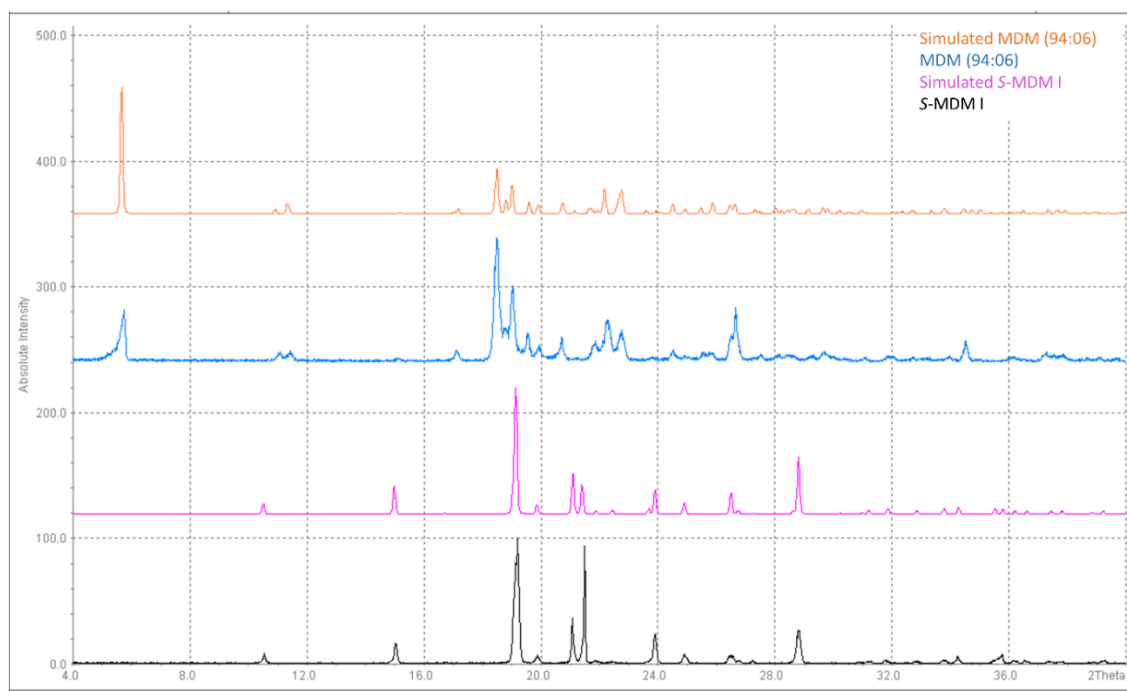
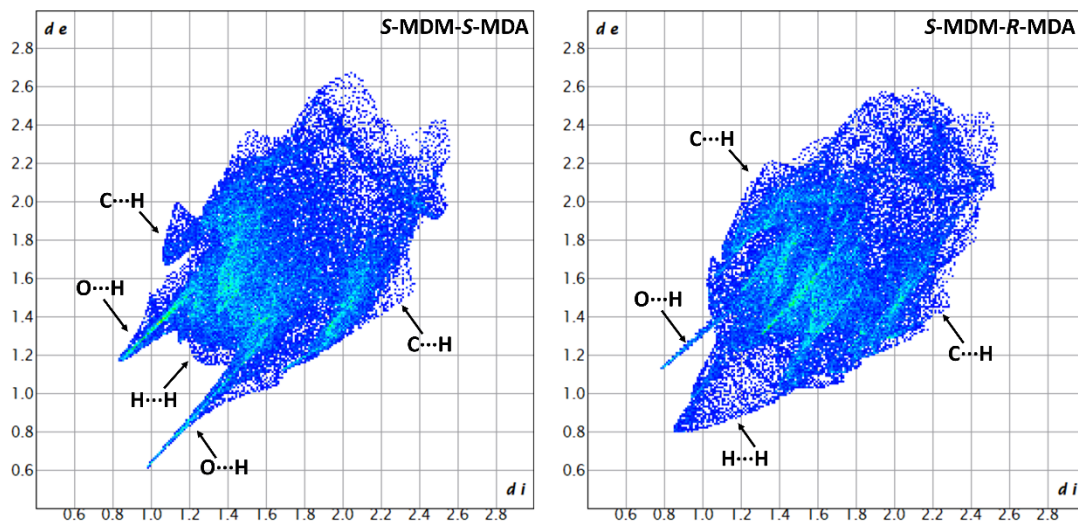
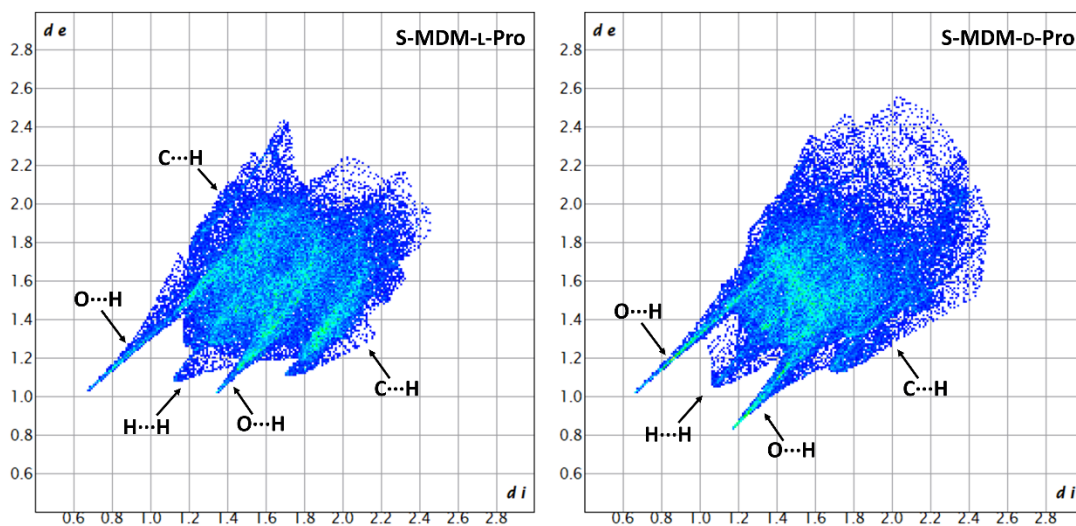


Figure S6.9. Experimental and theoretical PXRD patterns of (\pm)-MDM (top) and S-MDM and MDM (94 S:6 R) (bottom).

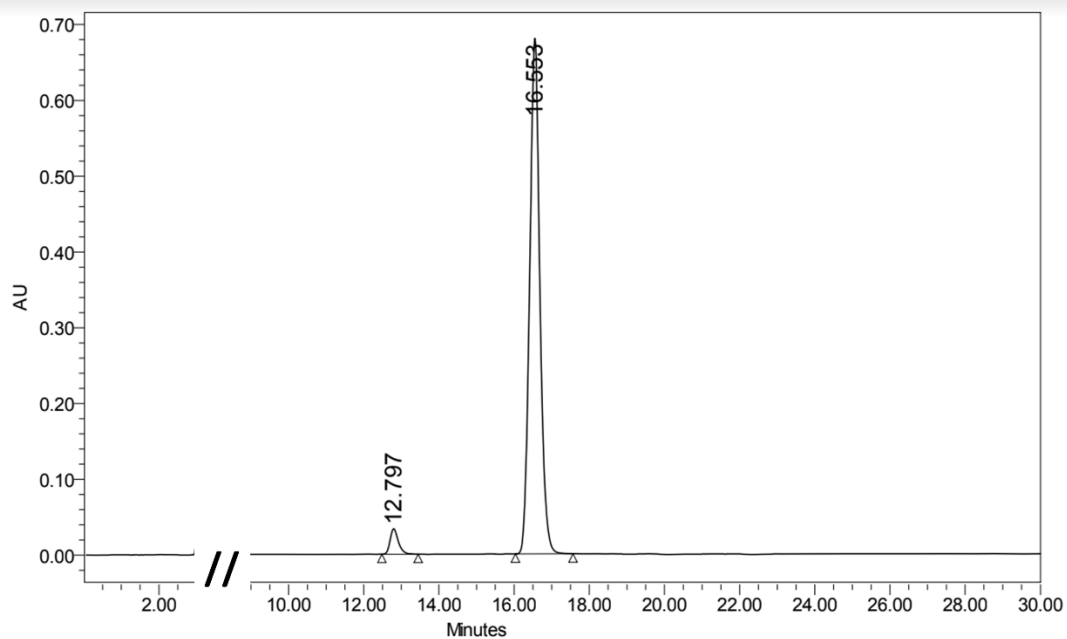


(a)



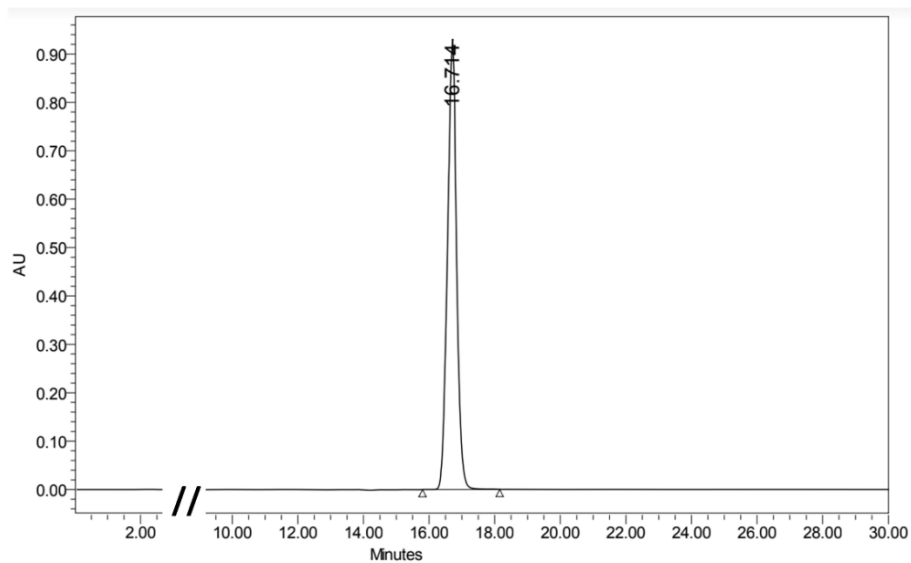
(b)

Figure S6.10. 2D fingerprint plots of *S*-MDM in (a) *S*-MDM-*S/R*-MDA cocrystal pair and (b) *S*-MDM-*L/D*-Pro cocrystal pair.



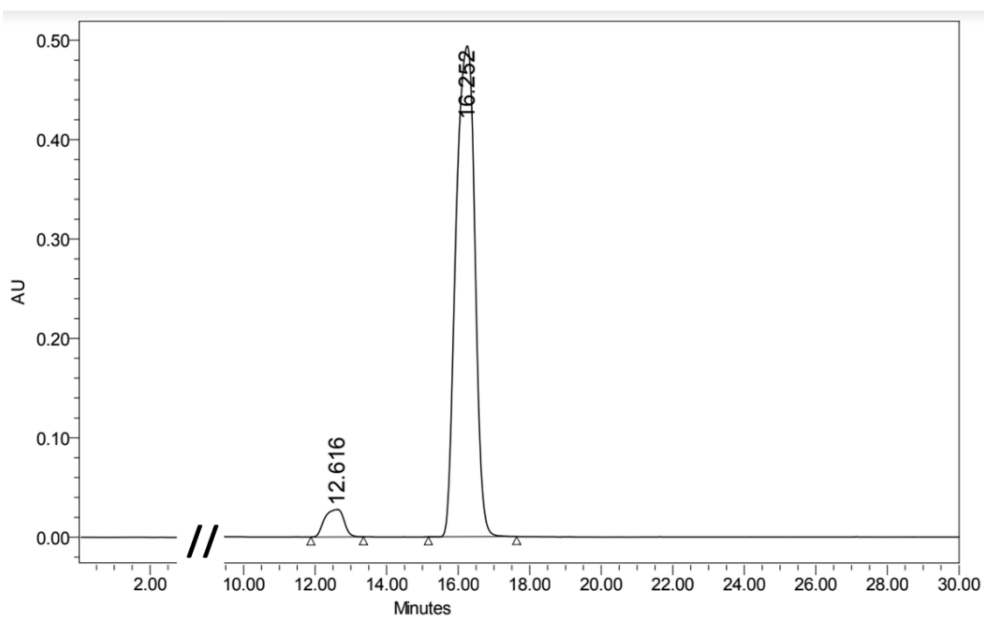
	RT	Area	% Area	Height
1	12.797	505860	3.80	33408
2	16.553	12793348	96.20	680250

(a)



	RT	Area	% Area	Height
1	16.714	17904751	100.00	929904

(b)



	RT	Area	% Area	Height
1	12.616	1033483	5.40	27552
2	16.252	18117931	94.60	493644

(c)

Figure S6.11. Chiral HPLC data of (a) commercial *S*-MDM from Sigma Aldrich, (b) synthesized *S*-MDM and (c) single crystal of MDM (94 *S*:6 *R*).

Table S6.1. Hydrogen bonds (Å, °) in (±)-MDM^a

		D-H···A	D-H	H···A	D···A	D-H···A	ARU (J)
1		N3-H3A···O1	0.86	2.15	2.984(3)	164	[2646.01]
2	Intra	N3-H3B···O5	0.86	2.29	2.658(3)	106	
3		N3-H3B···O1	0.86	2.21	3.013(3)	156	[4554.01]
4		O5-H5···O1	0.82	1.97	2.772(3)	166	[4564.01]
5		C7-H7···O5	0.93	2.52	3.433(4)	166	[4555.01]

^a Symmetry codes: [4555.] = [4_566] = x, 1/2-y, 1/2+z; [4564.] = [4_575] = x, 3/2-y, -1/2+z; [4554.] = [4_565] = x, 1/2-y, -1/2+z; [2646.] = [2_646] = 1-x, -1/2+y, 3/2-z.

Table S6.2. Hydrogen bonds (Å, °) in *S*-MDM^a

		D-H···A	D-H	H···A	D···A	D-H···A	ARU (J)
1		N1-H1A···O5	0.86	2.09	2.894(2)	155	[4656.01]
2	Intra	N1-H1B···O5	0.86	2.36	2.709(2)	105	
3		N1-H1B···O3	0.86	2.12	2.920(2)	155	[4646.01]
4		O5-H5···O3	0.82	1.89	2.7052(17)	171	[4746.01]

^a Symmetry codes: [4656.] = [3_656] = 1-x, 1/2+y, 3/2-z; [4746.] = [3_746] = 2-x, -1/2+y, 3/2-z; [4646.] = [3_646] = 1-x, -1/2+y, 3/2-z.

Table S6.3. Hydrogen bonds (Å, °) in MDM (94 *S*:6 *R*)^a

		D-H···A	D-H	H···A	D···A	D-H···A	ARU (J)
1		N1-H1A···O3	0.86	2.22	3.039(2)	159	[2556.03]
2	Intra	N1-H1B···O5	0.86	2.2	2.592(2)	107	
3		N1-H1B···O23	0.86	2.16	2.969(2)	156	[1565.01]
4		O5-H5···O23	0.82	2.41	3.098(3)	142	[1555.01]
5		O5-H5···O25A	0.82	2.23	2.950(2)	146	[1555.01]
6		N21-H21A···O23	0.86	2.1	2.944(3)	169	[2646.01]
7		N21-H21B···O3	0.86	2.18	3.007(2)	162	[1645.03]
8	Intra	N21-H21B···O25B	0.86	2.41	2.717(18)	102	
9		O25-H25A···O3	0.82	1.95	2.762(2)	169	[1655.03]
10		N41-H41A···O43	0.86	2.24	3.049(2)	157	[2647.04]
11	Intra	N41-H41B···O45	0.86	2.2	2.585(2)	107	
12		N41-H41B···O63	0.86	2.14	2.950(2)	156	[1645.02]
13		O45-H45···O63	0.82	2.42	3.063(3)	136	[1655.02]
14		O45-H45···O65A	0.82	2.19	2.923(2)	149	[1655.02]
15		N61-H61A···O63	0.86	2.13	2.970(3)	167	[2557.02]
16		N61-H61B···O43	0.86	2.16	2.995(2)	162	[1565.04]
17	Intra	N61-H61B···O65B	0.86	2.39	2.700(14)	102	
18		O65A-H65A···O43	0.82	2	2.743(2)	151	[1555.04]
19		C4-H4···O23	0.98	2.58	3.271(3)	128	[1555.01]
20		C7-H7···O25B	0.93	2.28	3.021(18)	136	[1455.01]
21	Intra	C31-H31···O25A	0.93	2.43	2.753(3)	100	
22		C44-H44···O63	0.98	2.55	3.237(3)	127	[1655.02]
23		C47-H47···O65B	0.93	2.28	3.035(14)	138	[1555.02]
24	Intra	C71-H71···O65A	0.93	2.43	2.752(3)	100	

^a Symmetry codes: [1655.] = [1_655] = 1+x, y, z; [1645.] = [1_645] = 1+x, -1+y, z; [2646.] = [2_646] = 1-x, -1/2+y, 1-z; [1565.] = [1_565] = x, 1+y, z; [2556.] = [2_556] = -x, 1/2+y, 1-z; [2647.] = [2_647] = 1-x, -1/2+y, 2-z; [2557.] = [2_557] = -x, 1/2+y, 2-z; [1455.] = [1_455] = -1+x, y, z.

Table S6.4. Hydrogen bonds (Å, °) in the *S*-MDM-*S*-MDA cocrystal ^a

	D-H...A	D-H	H...A	D...A	D-H...A	ARU (J)
1	N1-H1A...O23	0.86	2.24	3.077(2)	164	[1655.02]
2	N1-H1B...O25	0.86	2.16	2.859(2)	139	[1645.02]
3	O5-H1...O21	0.82	2.17	2.897(2)	148	[1545.02]
4	O5-H1...O25	0.82	2.44	3.109(2)	139	[1545.02]
5	O23-H23...O3	0.82	1.78	2.5946(19)	174	[1555.01]
6	O25-H25...O5	0.82	2.08	2.873(2)	164	[3466.01]
7	C4-H4...O25	0.98	2.56	3.387(3)	142	[1645.02]
8	C11-H11...O23	0.93	2.54	3.370(3)	149	[1555.02]
9	C31-H31...O3	0.93	2.52	3.389(3)	156	[1455.01]

^a Symmetry codes: [1545.] = [1_545] = x, -1+y, z; [1455.] = [1_455] = -1+x, y, z; [1655.] = [1_655] = 1+x, y, z; [1645.] = [1_645] = 1+x, -1+y, z; [3466.] = [4_466] = -1/2+x, 3/2-y, 1-z.

Table S6.5. Hydrogen bonds (Å, °) in the *S*-MDM-*R*-MDA cocrystal ^a

	D-H...A	D-H	H...A	D...A	D-H...A	ARU (J)
1	N1-H1A...O21	0.86	2.37	3.206(3)	165	[1545.02]
2	N1-H1B...O25	0.86	2.08	2.938(3)	177	[1645.02]
3	O5-H5...O21	0.82	2.26	2.947(3)	142	[3566.02]
4	O5-H5...O25	0.82	2.59	3.323(3)	151	[3566.02]
5	O23-H23...O3	0.82	1.88	2.626(2)	150	[1555.01]
6	O23-H23...O5	0.82	2.55	3.078(3)	124	[1555.01]
7	O25-H25...O3	0.82	2.06	2.846(2)	162	[1565.01]

^a Symmetry codes: [1565.] = [1_565] = x, 1+y, z; [3566.] = [4_566] = 1/2+x, 3/2-y, 1-z; [1545.] = [1_545] = x, -1+y, z; [1645.] = [1_645] = 1+x, -1+y, z.

Table S6.6. Hydrogen bonds (Å, °) in the *S*-MDM-*L*-Pro cocrystal ^a

	D-H...A	D-H	H...A	D...A	D-H...A	ARU (J)
1	N1-H1A...O37	0.86	2.05	2.909(3)	174	[2564.02]
2	Intra N1-H1B...O5	0.86	2.21	2.604(4)	107	
3	O5-H5...O27	0.82	1.87	2.688(3)	172	[1455.03]
4	N21-H21A...O27	0.89	1.98	2.823(3)	157	[1455.03]
5	N21-H21A...O38	0.89	2.58	2.905(4)	103	[1555.02]
6	Intra N21-H21B...O28	0.89	2.18	2.654(3)	113	
7	N21-H21B...O28	0.89	2.07	2.807(3)	140	[3466.03]
8	N31-H31A...O37	0.89	1.87	2.715(3)	157	[1455.02]
9	N31-H31A...O38	0.89	2.58	3.263(3)	134	[1455.02]
10	N31-H31B...O27	0.89	2.2	2.981(3)	146	[1455.03]
11	Intra N31-H31B...O38	0.89	2.21	2.637(3)	109	
12	C22-H22...O38	0.98	2.57	2.962(4)	104	[1555.02]
13	C32-H32...O3	0.98	2.46	3.360(4)	152	[2565.01]

^a Symmetry codes: [1455.] = [1_455] = -1+x, y, z; [2564.] = [2_564] = 1/2-x, 1-y, -1/2+z; [3466.] = [4_466] = -1/2+x, 3/2-y, 1-z; [2565.] = [2_565] = 1/2-x, 1-y, 1/2+z.

Table S6.7. Hydrogen bonds (Å, °) in the *S*-MDM-D-Pro cocrystal ^a

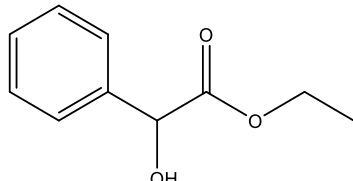
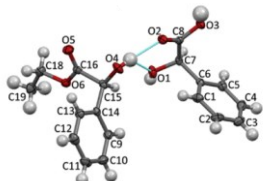
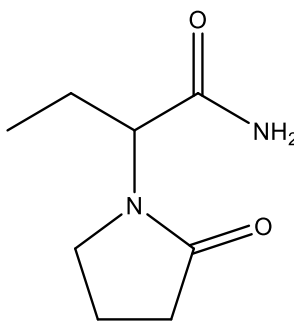
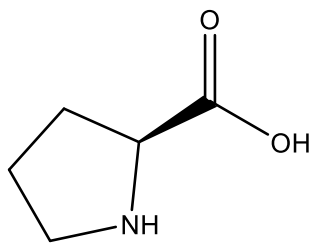
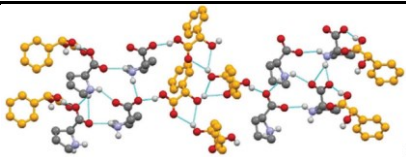
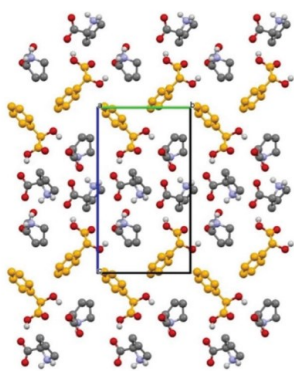
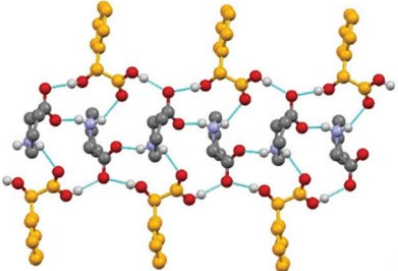
	D-H...A	D-H	H...A	D...A	D-H...A	ARU (J)
1	N1-H1A...O23	0.86	2.07	2.914(3)	166	[1455.02]
2	N1-H1B...O5	0.86	2.16	3.011(3)	169	[1455.01]
3	O5-H5...O58	0.82	1.83	2.630(3)	164	[1554.04]
4	N21-H21A...O3	0.86	2.14	2.963(3)	160	[1555.01]
5	N21-H21B...O25	0.86	2.25	3.099(3)	168	[1455.02]
6	O25-H25...O48	0.82	1.87	2.670(3)	164	[1655.03]
7	N41-H41A...O5	0.89	2.23	3.048(3)	153	[1556.01]
8	Intra N41-H41A...O47	0.89	2.16	2.622(3)	111	
9	N41-H41B...O47	0.89	1.88	2.760(3)	168	[1655.03]
10	N51-H51A...O48	0.89	2.39	3.115(3)	139	[1655.03]
11	Intra N51-H51A...O57	0.89	2.19	2.650(3)	112	
12	N51-H51B...O57	0.89	1.89	2.759(3)	164	[1655.04]
13	C28-H28...O58	0.93	2.53	3.220(4)	132	[2656.04]

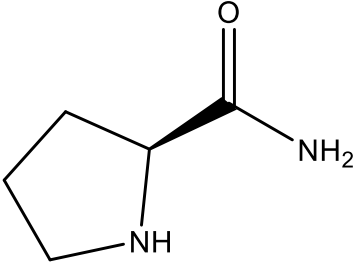
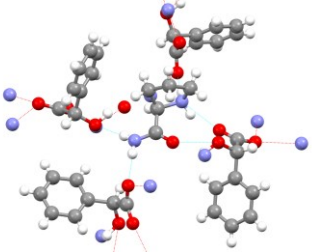
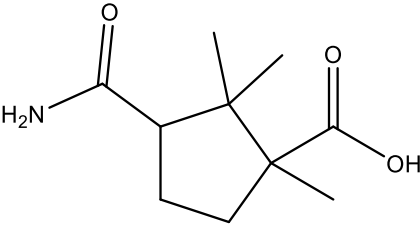
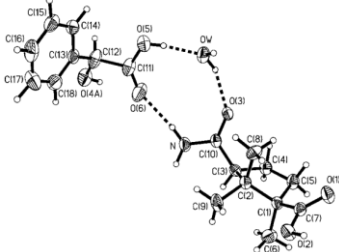
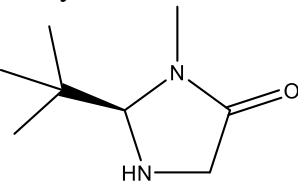
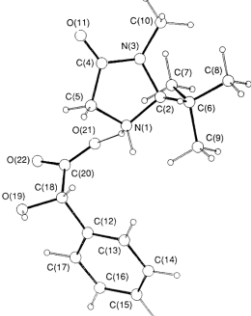
^a Symmetry codes: [1554.] = [1_554] = x, y, -1+z; [1455.] = [1_455] = -1+x, y, z; [1655.] = [1_655] = 1+x, y, z; [2656.] = [2_656] = 1-x, 1/2+y, 1-z; [1556.] = [1_556] = x, y, 1+z.

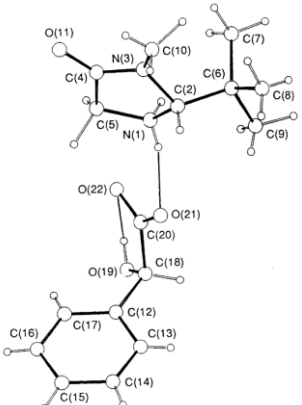
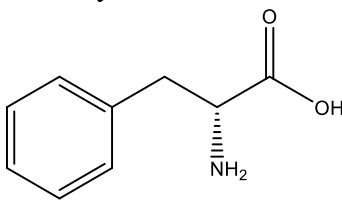
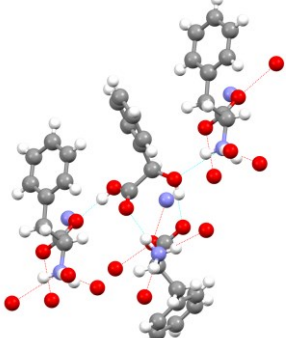
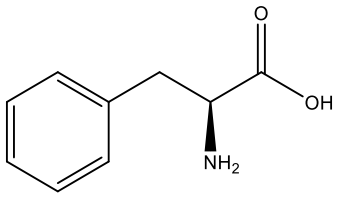
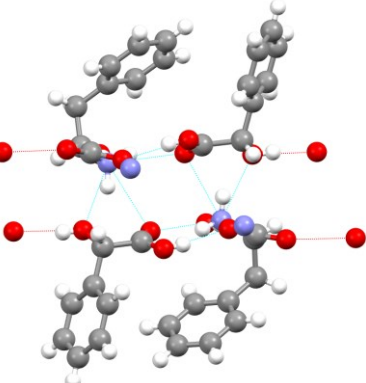
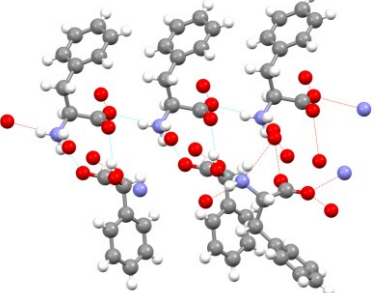
Table S6.8. Summary of the various contact contributions in *S*-MDM cocrystals.

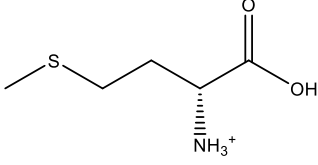
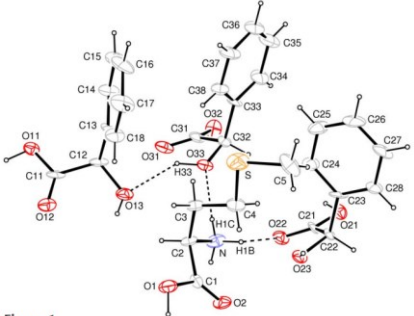
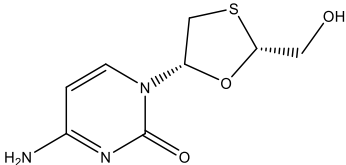
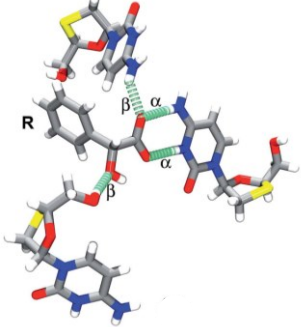
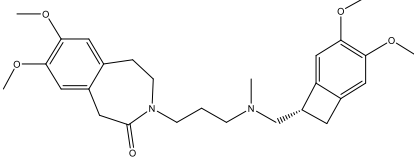
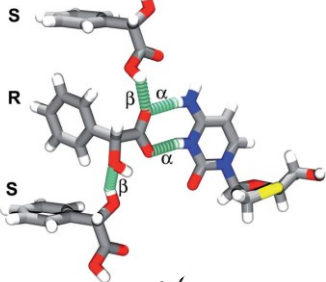
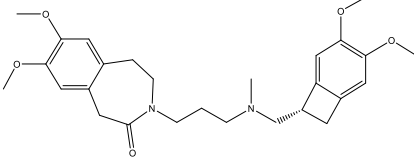
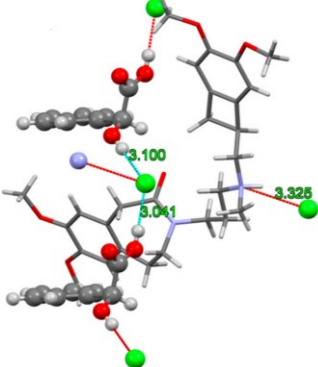
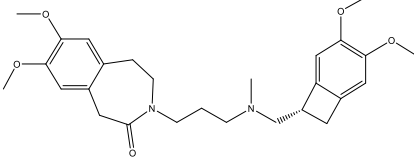
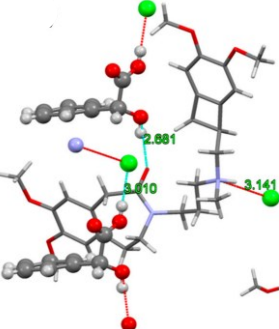
	H-H	O-H	C-H	C-O	N-H	N-O	O-O
<i>S</i>-MDM-<i>S</i>-MDA	44.3%	27.3%	24.6%	1.2%	1.9%	0.2%	0.5%
<i>S</i>-MDM-<i>R</i>-MDA	45.0%	22.0%	26.2%	0.3%	1.5%	0.3%	4.6%
<i>S</i>-MDM-<i>L</i>-Pro	56.6%	25.7%	15.6%	0	2.1%	0	0
<i>S</i>-MDM-<i>D</i>-Pro	53.4%	27.1%	17.0%	0.7%	1.6%	0.2%	0

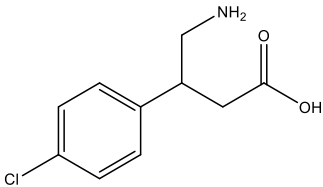
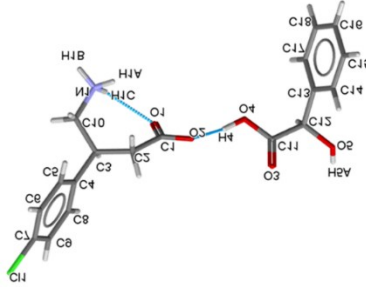
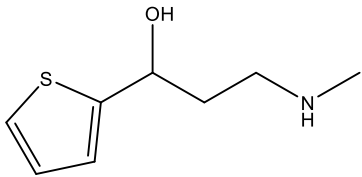
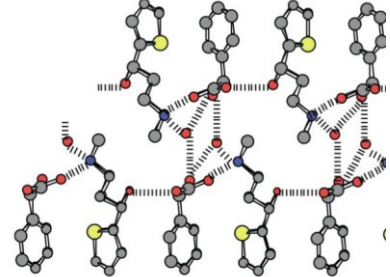
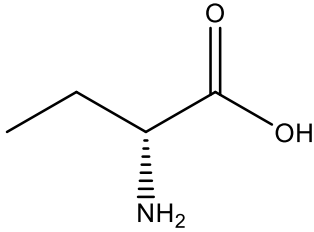
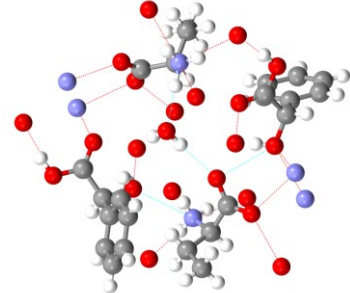
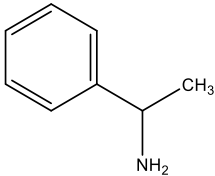
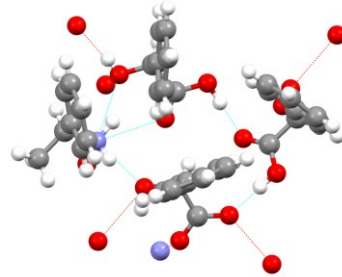
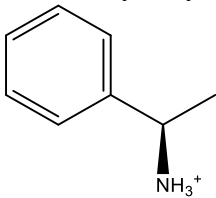
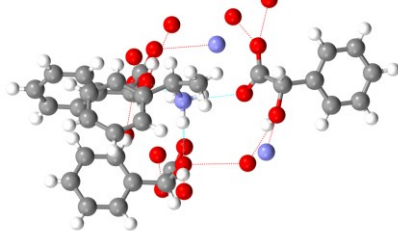
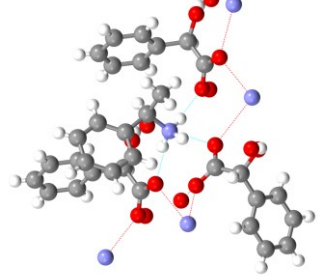
Table S6.9. Summary of reported cocrystals of mandelic acid and chiral cofomers.

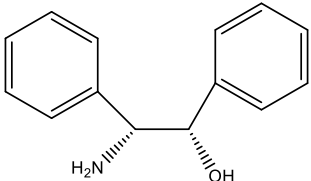
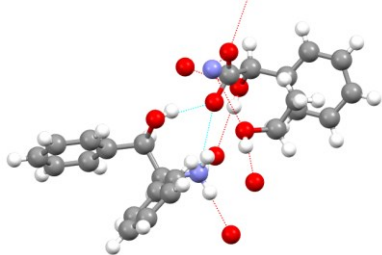
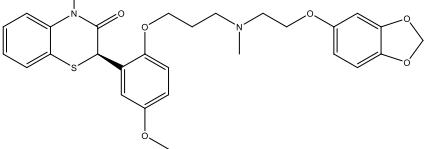
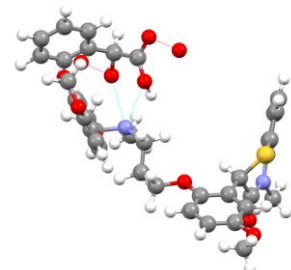
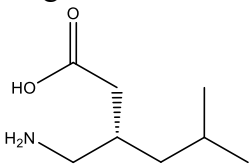
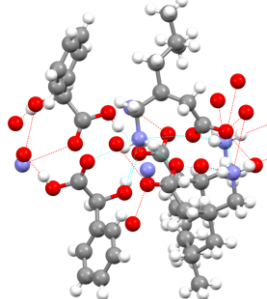
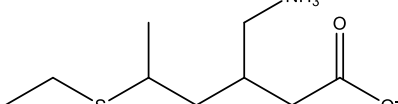
API	CCF	Crystal structures
Et-DL-mandelate ⁵ 	DL-Mandelic acid	
<i>S</i> -Etiracetam 	<i>S</i> -2-Chloromandelic acid ⁶	No crystal structure
	<i>S</i> -Mandelic acid ⁷	
	<i>Rac</i> -4-Bromomandelic acid ⁸	
	<i>Rac</i> -2-/3-/4-Chloromandelic acid ⁸	
	<i>Rac</i> -4-Fluoromandelic acid ⁸	
<i>L</i> -Proline ⁹ 	<i>S</i> -Mandelic acid (1:1)	
	<i>S</i> -Mandelic acid (2:1)	
	<i>R</i> -Mandelic acid (1:1)	

<p><i>R</i>-Proline amide¹⁰</p> 	<p><i>S</i>-Mandelic acid</p>	
<p>(1<i>R</i>,3<i>S</i>)-camphoramic acid¹¹</p> 	<p><i>R</i>-Mandelic acid</p>	
<p>(<i>R</i>)-2-<i>tert</i>-butyl-3-methylimidazolidin-4-one¹²</p> 	<p><i>S</i>-Mandelic acid</p>	

	<p><i>R</i>-Mandelic acid</p>	
<p>D-Phenylalanine</p> 	<p><i>R</i>-Mandelic acid¹³</p>	
	<p><i>S</i>-Mandelic acid¹⁴</p>	
<p>L-Phenylalanine¹⁴</p>	<p><i>S</i>-Mandelic acid</p>	

<p><i>R</i>-Methioninium¹⁹</p>  <p>Chemical structure of <i>R</i>-Methioninium, showing a methyl group attached to a sulfur atom, which is part of a propyl chain. The terminal carbon of the propyl chain is bonded to an amino group (NH₃⁺) and a carboxylic acid group (COOH).</p>	<p><i>R</i>-Mandelic acid</p>	 <p>ORTEP diagram of <i>R</i>-Mandelic acid showing the molecular structure with atom labels (C1-C18, O1-O3, N1, N2, H1A, H1B, H3A, H3B) and thermal ellipsoids at the 50% probability level. The caption below the diagram reads "Figure 1".</p>
<p>Lamivudine²⁰</p>  <p>Chemical structure of Lamivudine, featuring a pyrimidine ring with an amino group (H₂N) and a carbonyl group (C=O). The ring is substituted with a thiazolidine ring, which has a hydroxymethyl group (-CH₂OH) attached to it.</p>	<p><i>R</i>-Mandelic Acid</p>	 <p>3D ball-and-stick model of <i>R</i>-Mandelic acid, showing the spatial arrangement of atoms. The chiral center is labeled with α and β positions, and the molecule is labeled with <i>R</i>.</p>
<p>Lvabradine Hydrochloride²¹</p>  <p>Chemical structure of Lvabradine Hydrochloride, a complex molecule consisting of a piperazine ring system linked to a benzimidazole ring system, with various substituents including methoxy groups and a hydroxyl group.</p>	<p><i>S</i>-<i>R</i>-<i>S</i>-Mandelic Acid</p>	 <p>3D ball-and-stick model of <i>S</i>-<i>R</i>-<i>S</i>-Mandelic acid, showing the spatial arrangement of atoms. The chiral centers are labeled with α and β positions, and the molecule is labeled with <i>S</i>, <i>R</i>, and <i>S</i>.</p>
<p>Lvabradine Hydrochloride²¹</p>  <p>Chemical structure of Lvabradine Hydrochloride, a complex molecule consisting of a piperazine ring system linked to a benzimidazole ring system, with various substituents including methoxy groups and a hydroxyl group.</p>	<p><i>S</i>-Mandelic Acid</p>	 <p>3D ball-and-stick model of <i>S</i>-Mandelic acid, showing the spatial arrangement of atoms. The chiral center is labeled with α and β positions. Bond lengths are indicated: 3.100 Å, 3.041 Å, and 3.325 Å.</p>
<p>Lvabradine Hydrochloride²¹</p>  <p>Chemical structure of Lvabradine Hydrochloride, a complex molecule consisting of a piperazine ring system linked to a benzimidazole ring system, with various substituents including methoxy groups and a hydroxyl group.</p>	<p><i>R</i>-Mandelic Acid</p>	 <p>3D ball-and-stick model of <i>R</i>-Mandelic acid, showing the spatial arrangement of atoms. The chiral center is labeled with α and β positions. Bond lengths are indicated: 2.881 Å, 3.010 Å, and 3.141 Å.</p>

<p>Baclofen²²</p> 	<p><i>S</i>-Mandelic acid</p>	
<p>3-(methylamino)-1-(2-thienyl)propan-1-ol²³</p> 	<p><i>S</i>-Mandelic acid</p>	
<p><i>R</i>-2-aminobutanoic acid²⁴</p> 	<p><i>S</i>-Mandelic acid</p>	
<p><i>S</i>-1-Phenylethylammonium²⁵</p> 	<p><i>S</i>-Mandelic acid</p>	
<p><i>R</i>-1-Phenylethylammonium²⁶</p> 	<p><i>S</i>-Mandelic acid</p>	
	<p><i>R</i>-Mandelic acid²⁷</p>	

<p>Erythro-2-amino-1,2-diphenylethanol²⁸</p>  <p>The structure shows two phenyl rings attached to a central ethane chain. The amino group (H₂N) is on a wedge and the hydroxyl group (OH) is on a dash at the 2-position.</p>	<p>S-Mandelic acid</p>	 <p>A 3D ball-and-stick model of S-Mandelic acid, showing the spatial arrangement of atoms with red dashed lines indicating hydrogen bonds.</p>
<p>Semotiadil²⁹</p>  <p>A complex chemical structure featuring a benzothiazine ring system, a benzene ring with a methoxy group, and a piperazine ring connected via ether linkages.</p>	<p>S-Mandelic acid</p>	 <p>A 3D ball-and-stick model of S-Mandelic acid, showing the spatial arrangement of atoms with red dashed lines indicating hydrogen bonds.</p>
<p>Pregabalin³⁰</p>  <p>The structure shows a central carbon atom bonded to a carboxylic acid group (HO-C=O), an isopropyl group, and a 2-aminoethyl group (H₂N-CH₂-CH₂-).</p>	<p>S-Mandelic acid</p>	 <p>A 3D ball-and-stick model of S-Mandelic acid, showing the spatial arrangement of atoms with red dashed lines indicating hydrogen bonds.</p>
<p>3-(azaniumylmethyl)-5-(ethylsulfanyl)hexanoate³¹</p>  <p>The structure shows a hexanoate chain with a methyl group at C-3, an ethylsulfanyl group (-S-CH₂-CH₃) at C-5, and an azaniumyl group (-CH₂-NH₃⁺) at C-3.</p>	<p>S-Mandelic acid</p>	<p>No crystal structure</p>

REFERENCES

- (1) Lloyd-Jones G.C.; Wall P. D.; Slaughter J.L.; Parker A.J.; Laffan D.P., Enantioselective homoallyl-cyclopropanation of dibenzylideneacetone by modified allylindium halide reagents—rapid access to enantioenriched 1-styryl-norcarene, *Tetrahedron*, **2006**, 62, 11402–11412.
- (2) Ebbers E.J.; Ariaans G.J.; Bruggink A.; Zwanenburg B., Controlled racemization and asymmetric transformation of α -substituted carboxylic

- acids in the melt, *Tetrahedron: Asymmetry*, **1999**, 10, 3701–3718.
- (3) Bai J.; Zambron K.; Vogel P., Amides in one pot from carboxylic acids and amines via sulfinylamides, *Organic Letters*, **2014**, 16, 604–607.
- (4) Mandelamide|C₈H₉NO₂|Chemspider.
<https://www.chemspider.com/Chemical-Structure.66240.html> (accessed 2023-06-09).
- (5) Tumanova, N.; Payen, R.; Springuel, G.; Norberg, B.; Robeyns, K.; Duff, C. L.; Wouters, J.; Leyssens, T., Cocrystallization out of the blue: DL-mandelic acid/ethyl-DL-mandelate cocrystal. *J. Mol. Struct.* **2017**, 1127, 397-402.
- (6) Nulek, T.; Klaysri, R.; Cedeno, R.; Nalaoh, P.; Bureekaew, S.; Promarak, V.; Flood, A. E., Separation of Etiracetam Enantiomers Using Enantiospecific Cocrystallization with 2-Chloromandelic Acid. *ACS Omega* **2022**, 7, (23), 19465–19473.
- (7) Springuel, G.; Leyssens, T., Innovative Chiral Resolution Using Enantiospecific Co-Crystallization in Solution. *Cryst. Growth Des.* **2012**, 12, (7), 3374–3378.
- (8) Wang, J.; Peng, Y., Resolution of Halogenated Mandelic Acids through Enantiospecific Co-Crystallization with Levetiracetam. *Molecules* **2021**, 26, (18), 5536.
- (9) Zhou, F.; Collard, L.; Robeyns, K.; Leyssens, T.; Shemchuk, O., L-Proline, a resolution agent able to target both enantiomers of mandelic acid: an exciting case of stoichiometry controlled chiral resolution. *Chem. Commun.* **2022**, 58, 8560-8563.
- (10) Bock, D. A.; Lehmann, C. W., Chirality determination from X-ray powder

data—diastereomeric co-crystals of mandelic acid and proline amide. *CrystEngComm* **2012**, 14, 1534-1537.

- (11) Hu, Z.-Q.; Nie, J.-J.; Xu, D.-J.; Xu, Y.-Z.; Chen, C.-L., The crystal structure of the molecular complex of camphoramic acid with mandelic acid: A partial separation of a racemic mixture of mandelic acid by (1R,3S)-camphoramic acid. *J. Chem. Crystallogr.* **2001**, 31, 109–113
- (12) Acs, M.; Novotny-Bregger, E.; Simon, K.; Argay, G., Structural aspects of optical resolutions. Optical resolution of (R,S)-mandelic acid. DSC and X-ray studies of the diastereoisomeric salts. *J. Chem. Soc., Perkin Trans. 2* **1992**, 2011-2017.
- (13) Hu, Z.-Q.; Xu, D.-J.; Xu, Y.-Z.; Wu, J.-Y.; M.Y.Chiang, *Chin. J. Struct. Chem.*, **2004**, 23, 38.
- (14) Okamura, K. A.; Hiramatsu, H.; Nishimura, N.; Sato, T.; Hashimoto, K., Crystal Structures of Diastereomeric 1:1 Complexes of (R)-and (S)-Phenylalanine (S)-Mandelic Acid. *Anal. Sci.* **1997**, 13, 315.
- (15) Fujii, I.; Baba, H.; Takahashi, Y., Crystal Structures of L-(R)-Cysteine-Mandelic Acid Diastereomers. *Anal. Sci.: X-Ray Struct. Anal. Online* **2005**, 21, x175-x176.
- (16) Hu, Z.-Q.; Xu, D.-J.; Xu, Y.-Z., (S)-Alanine–(S)-mandelic acid (1/1). *Acta Crystallogr., Sect. E: Struct. Rep. Online* **2004**, 60, o269-o271.
- (17) Hu, Z.-Q.; Xu, D.-J.; Xu, Y.-Z.; Wu, J.-Y.; Chiang, M. Y., (R)-Mandelic acid (S)-alanine hemihydrate. *Acta Crystallogr. C Struct. Chem.* **2002**, 58, o612-o614.
- (18) Fujii, I., Crystal Structure of L-(S)-Tryptophane D-(R)-mandelate 1.5H₂O. *Anal. Sci.: X-Ray Struct. Anal. Online* **2009**, 25, 35-36.

- (19) Su, J.-R.; Xu, D.-J., (R)-Methioninium–(R)-mandelate–(R)-mandelic acid (1/1/2). *Acta Crystallogr. E: Crystallogr. Commun.* **2005**, 61, o1933-o1935.
- (20) Silva, C. C.; Martins, F. T., The enantiopreference in the solid state probed in lamivudine crystal forms with mandelic acid. *RSC Adv.* **2015**, 5, 20486-20490.
- (21) Sládková, V.; Dammer, O.; Sedmak, G.; Skořepová, E.; Kratochvíl, B., Ivabradine Hydrochloride (S)-Mandelic Acid Co-Crystal: In Situ Preparation during Formulation. *Crystals* **2017**, 7, (1), 13.
- (22) Songsermsawad, S.; Nalaoh, P.; Promarak, V.; Flood, A. E., Chiral Resolution of RS-Baclofen via a Novel Chiral Cocrystal of R-Baclofen and L-Mandelic Acid. *Cryst. Growth Des.* **2022**, 22, (4), 2441–2451.
- (23) Sakai, K.; Sakurai, R.; Yuzawa, A.; Kobayashi, Y.; Saigo, K., Resolution of 3-(methylamino)-1-(2-thienyl)propan-1-ol, a new key intermediate for duloxetine, with (S)-mandelic acid. *Tetrahedron: Asymmetry* **2003**, 14, 1631.
- (24) Teng, M.-Y.; Sun, J.; Ma, C.-A.; Song, Q.-B., (S)-2-Hydroxy-2-phenyl-acetic acid–(R)-2-amino-butanoic acid–water (1/1/0.5). *Acta Crystallogr., Sect. E: Struct. Rep. Online* **2006**, 62, o2454.
- (25) Diego, H. L., (S)-1-Phenylethylammonium (S)-Mandelate–Mandelic Acid (1/2), $C_8H_{12}N^+.C_8H_7O_3^-.2C_8H_8O_3$. *Acta Crystallogr., Sect. C: Cryst. Struct. Commun.* **1995**, 51, 253-256.
- (26) Larsen, S.; Diego, H. L., Isolation of different enantiomers caused by variation in the stoichiometric ratio of racemate and resolving agent. The crystal structure of (R)-1-phenylethylammonium (S)-mandelate·dimandelic acid. *J. Chem. Soc., Perkin Trans. 2*, **1993**, 469-473.

- (27) Karamertzanis, P. G.; Anandamanoharan, P. R.; Fernandes, P.; Cains, P. W.; Vickers, M.; Tocher, D. A.; Florence, A. J.; Price, S. L., Toward the Computational Design of Diastereomeric Resolving Agents: An Experimental and Computational Study of 1-Phenylethylammonium-2-phenylacetate Derivatives. *J. Phys. Chem. B* **2007**, 111, (19), 5326–5336.
- (28) Shitara, H.; Shintani, T.; Kodama, K.; Hirose, T., Solvent-Induced Reversed Stereoselectivity in Reciprocal Resolutions of Mandelic Acid and erythro-2-amino-1,2-diphenylethanol. *J. Org. Chem.* **2013**, 78, (18), 9309–9316.
- (29) Ota, A.; Kawashima, Y.; Ohishi, H.; Ishida, T., Conformational Studies of Semotiadil (SD-3211), a Novel Ca²⁺ Antagonist. *Chem. Pharm. Bull.* **1993**, 41, 1681-1685.
- (30) Samas, B.; Wang, W.; Godrej, D. B., 1:1 Cocrystal of (S)-3-(ammonio-meth-yl)-5-methyl-hexa-noate and (S)-mandelic acid. *Acta Crystallogr. E: Crystallogr. Commun.* **2007**, 63, o3938.
- (31) Shimada, K.; Ohata, Y.; Kobayashi, J.; Onishi, Y.; Kawamura, A.; Domon, Y.; Arakawa, N.; Inoue, T.; Kitano, Y.; Matsuda, F.; Abe, Y.; Deguchi, T., Alkylsulfanyl analogs as potent $\alpha_2\delta$ ligands. *Bioorg. Med. Chem. Lett.* **2018**, 28, 2000-2002.



Chapter 7 Conclusions and Future Work



Cocrystallization involves the formation of a multi-component crystalline material (such as salts, hydrates / solvates, and cocrystals) consisting of two or more different molecules held together by non-covalent interactions, such as hydrogen bonding, π - π stacking, or van der Waals forces. Cocrystals and salts are the common solid-state forms employed. The differences between pharmaceutical cocrystals and salts have consistently remained a compelling subject of interest for researchers and crystallographers. Chapter 2 placed emphasis on the differences between pharmaceutical cocrystals and salts of sulfasalazine. Fully structural analysis and computational studies (Hirshfeld surface and HOMO-LUMO analyses) of three sulfasalazine cocrystals and three sulfasalazine salts were conducted, suggesting that sulfasalazine cocrystals are chemically more stable than sulfasalazine salts. Non-covalent interactions, especially hydrogen-bonding interactions play an important role in multi-component crystalline materials. In Chapter 3, to gain an in-depth insight into the hydrogen-bonding interactions, detailed crystal structural analyses of eight sulfaguanidine cocrystals (five were synthesized in this work and three already reported) together with the computational calculations including Hirshfeld surface, MEPS, and QTAIM analyses have been performed, which indicates that the formation of those SGD cocrystals is both experimentally and computationally favourable. Over the past decades, cocrystallization has gained increasing attention as a compelling technique for modifying the physicochemical properties of APIs. In Chapter 4, the focus was on the solubility and luminescent properties of six novel pharmaceutical salts of piroxicam and meloxicam, incorporating three distinct organic counterions. The results demonstrated notable improvements in apparent solubility and dissolution rates compared to the parent APIs. Additionally, the three piroxicam

salts exhibited distinct luminescent properties in contrast to pure piroxicam. This phenomenon could be elucidated by the mechanism of proton-transfer-induced enhanced luminescence, which resulted in a significant longer emission wavelengths, i.e. red shift.¹ The analysis of HOMO-LUMO further supported these findings.

Cocrystal formation has also been employed as an alternative to achieve chiral separation in recent years. Chapter 5 included a comprehensive cocrystal screening of 19 L-amino acids with both enantiomers of tartaric acid, mandelic acid, malic acid and 3-phenyllactic acid. Twenty-two new phases were obtained, consisting of seven diastereomeric cocrystal pairs and eight enantiospecific cocrystals. Based on the analysis of graph-set motifs, the presence of hydrogen bonding in enantiospecific cocrystals may contribute to the formation of energetically favorable systems, while more changes in hydrogen bonding network and / or stoichiometric ratio of diastereomeric cocrystal pairs were observed. Chapter 6 continued to explore the study of cocrystal formation involving two chiral compounds. Notably, *S*-mandelamide demonstrated its potential as a resolution agent for chiral separation by forming diastereomeric cocrystal pairs with both enantiomers of mandelic acid and proline. Moreover, the structures of racemic and enantiopure *S*-mandelamide, as well as a mixed crystal mandelamide (94 *S*:6 *R*), were determined, providing the foundation for future investigations into the potential of *S*-mandelamide as a resolution agent.

Future work could continue to focus on chiral resolution by cocrystallization, aiming to advance the understanding and application of cocrystallization in chiral resolution, opening up new possibilities for the efficient separation of enantiomers. Diastereomeric cocrystal pairs with large differences in melting points, such as the

S-MDM-Pro and the L-Met-MDA systems, would be suitable for generating separation protocols based on cooling crystallization. Furthermore, phase diagrams play a crucial role in designing robust and reliable crystallization processes of complex multicomponent systems, especially for the separation of racemic compounds by cocrystal formation.² Separation strategies can be developed by generating ternary phase diagrams for the systems of *S*-MDM with racemic MDA and Pro, respectively. The future exploration of chiral resolution through cocrystal formation can be broadened by developing more chiral resolution agents, optimizing cocrystallization conditions and exploring different techniques such as the addition of chiral coupling agents,^{3,4} dynamic kinetic resolution,^{5,6} and dynamic preferential crystallization,⁷ etc.

REFERENCES

- (1) Wang, Y.; Liu, T.; Bu, L.; Li, J.; Yang, C.; Li, X.; Tao, Y.; Yang, W., Aqueous Nanoaggregation-Enhanced One- and Two-Photon Fluorescence, Crystalline J-Aggregation-Induced Red Shift, and Amplified Spontaneous Emission of 9,10-Bis(*p*-dimethylaminostyryl)anthracene. *J. Phys. Chem. C* **2012**, 116, (29), 15576–15583.
- (2) Charpentier, M. D.; Venkatramanan, R.; Rougeot, C.; Leysens, T.; Johnston, K.; Horst, J. H. t., Multicomponent Chiral Quantification with Ultraviolet Circular Dichroism Spectroscopy: Ternary and Quaternary Phase Diagrams of Levetiracetam. *Mol. Pharmaceutics* **2023**, 20, (1), 616–629.
- (3) Kolesinska, B.; Kaminski, Z. J., Design, Synthesis, and Application of Enantioselective Coupling Reagent with a Traceless Chiral Auxiliary. *Org. Lett.* **2009**, 11, (3), 765–768.

- (4) Xiouras, C.; Horst, J. H. T.; Gerven, T. V.; Stefanidis, G. D., Coupling Viedma Ripening with Racemic Crystal Transformations: Mechanism of Deracemization. *Cryst. Growth Des.* **2017**, 17, (9), 4965–4976.
- (5) Würges, K.; Petruševska-Seebach, K.; Elsner, M. P.; Lütz, S., Enzyme-assisted physicochemical enantioseparation processes—Part III: Overcoming yield limitations by dynamic kinetic resolution of asparagine via preferential crystallization and enzymatic racemization. *Biotechnol. Bioeng.* **2009**, 104, (6), 1047–1244.
- (6) Benren, L., Crystallization-Induced Dynamic Kinetic Resolution of Phenylglycine Amide. *Chinese J. Org. Chem.* **2011**, 31 (9), 1495–1498.
- (7) Rougeot, C.; Hein, J. E., Application of Continuous Preferential Crystallization to Efficiently Access Enantiopure Chemicals. *Org. Process Res. Dev.* **2015**, 19, (12), 1809–1819.